The role of solubility in the toxicity of metal oxide nanoparticles

By

Andrey Boyadzhiev

Thesis submitted to the University of Ottawa in partial fulfillment of the requirements for the degree of

Doctor of Philosophy In Biology (*With a specialization in* Chemical and Environmental Toxicology)
Department of Biology
Faculty of Science
University of Ottawa

Abstract

Metal oxide nanoparticles (MONPs) represent one of the largest classes of engineered nanomaterials (ENM) in the world. As with ENM in general, MONPs present a challenge for regulatory risk assessment due to the numerous physicochemical properties impacting their toxicity. One of the most critical properties of MONPs is their solubility in biological microenvironments, affected by factors such as their surface area, surface reactivity, and chemical composition. The relative contribution of the particulate and dissolved fractions to toxicity induced by MONPs remains poorly understood. In this context, the underlying question this thesis sought to address was: what is the relative contribution of particulate and dissolved fractions to MONP induced toxicity?

To address the question, this thesis employed 21st century toxicological tools in an *in vitro* lung epithelial model system (FE1) examining MONPs with varying solubility (including ZnO, CuO, NiO, Al_2O_3, TiO_2). In the first approach, FE1 cells were exposed to MONPs, their microparticle analogues, and dissolved metal salts for 2 – 48 h for transcriptomic characterization. In the second approach, the genotoxic potential of the same MONPs and equivalents was assessed using two high-throughput screening assays (CometChip® and Microflow®). Finally, fluorescence darkfield hyperspectral imaging was used to determine the co-localization of a set of MONPs with lysosomes, while the impact of lysosomal dissolution / interaction on MONP toxicity was assessed by measuring changes in viability with and without co-exposure to a lysosomal acidification inhibitor.

The results of the transcriptomic characterization and genotoxicity screening indicated compound-specific effects of solubility and the particulate and dissolved species on MONP toxicity; with the 'HIF1α Signaling' pathway being identified as a putative biomarker of response to acutely toxic MONPs. Based on microscopy analysis, all MONPs localized to lysosomes, with TiO_2 MONPs showing the greatest co-localization. Out of the MONPs tested, lysosomal dissolution only contributed to the toxicity of CuO MONPs.

In conclusion, adverse effects of MONPs are not captured solely by their solubility properties, raising concern that existing hazard groupings are based on oversimplified

generalizations. While solubility is a key influence, mechanistic results from 21st century toxicity approaches should be considered at the outset of regulatory priority-setting.

Acknowledgments

Numerous people have been instrumental in the completion of this thesis, and deserve sincere acknowledgement.

I would first like to extend my deepest gratitude to my thesis supervisors Sabina Halappanavar and Pat Rasmussen. To Sabina, there is so much to say and I don't have the words to fully express my appreciation. Over the past 8 years and you have shaped me into the scientist I am today. I remember when I first started in your lab, I was a wide-eyed undergrad with only the faintest understanding of toxicology and the world of nanomaterials. Over the years, you nurtured my curiosity and enthusiasm and provided me with endless opportunities to challenge myself and grow as a researcher. You have been patient, understanding, and above all an amazing mentor. Your willingness to discuss and dissect problems when I felt lost was crucial. It was the highlight of my graduate studies to attend NanOEH with you in the UK and to meet your many influential collaborators who up until that point I only knew by name. It has truly been a privilege to be your PhD student, and this thesis would not have been possible without your invaluable support and tutelage.

To Pat, your infectious tenacity and cheer have been a buoy over the course of my research track, inspiring me to persevere when the going got tough. The in-depth and thoughtful comments you provided on each document I sent your way demonstrated your genuine care about my work and really made me think about the context of my experiments and the questions I sought to answer. I wish you a joyful and well-deserved retirement!

Being part of Sabina's Nanotoxicology laboratory for the past eight years has been an honor and I am deeply grateful for the incredible colleagues and friends I've made along the way. To Luna Rahman, Dongmei Wu, and Silvia Aidee Solorio Rodriguez, I offer my heartfelt thanks for your unwavering support and camaraderie. Luna, thank you for your kindness over the years and for earnestly seeking my input which helped me develop confidence as a scientist. To Mei, you were an absolute fount of knowledge, and you were always so willing to take the time and impart a bit of it onto me. I will never forget when you trained me as a fresh-faced COOP student and how impressed you were that I had asked

so many questions. That memory will stay with me always, and it makes me proud to think of. To Silvia, it has been so great to work alongside such a meticulous and careful researcher. I've often remarked on what an exceptional colleague you are, and I sincerely hope our professional paths will cross again in the future. Although not part of our lab, I would like to extend my gratitude to Andrew Williams for his statistical assistance, without which this thesis would not have been possible.

I would also like to thank my thesis advisory committee members, Laurie Chan, Cory Harris, and Amy Rand for their insightful feedback and comments throughout my research journey.

A special thanks also goes out to my grade 12 biology teacher, Dr. Andrea Davidson. You were the absolute best biology teacher anyone could have asked for, and kindled my life-long passion for biology and the wonders of the biomolecular world.

To my mom and dad. I made it! I know this path wasn't the one you envisioned for me but you supported me every step of the way. All you cared about, was whether I was happy and doing something that I was interested in. You supported me when I needed it, and never asked for anything in return. To dad, I am saddened that you are not here to see how far I've come, but I like to think you'd be proud of me if you were. To mom, you're the best mother anyone could ask for and I'm so happy to have gotten so close over the years. Your baby boy is finally out of school!

Finally I would like to thank my amazing, beautiful wife Courtney. Even when I doubted myself, your faith in me never wavered. You were my emotional and psychological anchor over the course of my research, the foundation at my core. When times were good, you reveled with me. When the going got tough, you picked me back up. You have been my rock throughout this whole process, and are the main reason I have this degree. You are my best friend, the light in my days, and the primary reason I persevered. Words cannot express how much you mean to me, and this achievement is as much yours as it is mine. Time to start the next chapter of our lives!

Thank you everyone, from the bottom of my heart!

Table of Contents

List of Abbreviations

AIC	Akaike Information Criterion
ALF	Artificial lysosomal fluid
ANOVA	Analysis of variance
AO	Adverse outcome
AOP	Adverse outcome pathway
APTES	3-Aminopropyl triethoxysilane
BafA1	Bafilomycin A1
BALF	Bronchoalveolar lavage fluid
BET	Brunauer–Emmett–Teller
BMC	Benchmark concentration
BMCL	Lower 95th BMC percentile
BMCU	Upper 95th BMC percentile
BMR	Benchmark response
BSA	Bovine serum albumin
CAS-RN	Chemical Abstract Services Registry Numbers
CNT	Carbon nanotube
DEG	Differentially expressed gene
Dh	Hydrodynamic diameter
DLS	Dynamic light scattering
dPBS	Dulbecco's phosphate buffered saline
DSL	Domestic substances list
EBC	Exhaled breath condensate
ECHA	European CHemical Agency
ECM	Extracellular matrix
EDF-HSI	Enhanced darkfield hyperspectral imaging
EGF	Epidermal growth factor
ELS	Electrophoretic light scattering
EMA	Ethidium monoazide
ENM	Engineered nanomaterial
EPA	Environmental Protection Agency
FBS	Fetal bovine serum
FDA	Federal Drug Administration
FDR	False discovery rate
GO	Gene ontology
h	Hour
HC	High-content
HSP	Heat shock protein

HTS	High-throughput screening
HUVEC	Human umbilical vein endothelial cell
IARC	International agency for research on cancer
IATA	Integrated approach to toxicity assessment
ICP-OES	Inductively coupled plasma optical emission spectroscopy
iMONP	Incidental metal oxide nanoparticle
IPA	Ingenuity pathway analysis
ISO	International Organization for Standardization
KE	Key event
KER	Key event relationship
LC_{50}	Lethal concentration 50%
LDH	Lactate dehydrogenase
LOEL	Lowest observed effect level
LOWESS	Locally weighted scatterplot smoothing
MAANOVA	Microarray analysis of variance
MIE	Molecular initiating event
MMS	Methyl methanesulfonate
MN	Micronucleus
MO	Metal oxide
MOMP	Metal oxide microparticle
MONM	Metal oxide nanomaterials
MONP	Metal oxide nanoparticle
MP	Microparticle
MT	Metallothionein
MWCNT	Multiwalled carbon nanotube
NAM	New Approach Methodologies
NM	Nanomaterial
NNM	Natural nanomaterial
NOEL	No observed effect level
NP	Nanoparticle
NW	Nanowire
OECD	Organization for Economic Cooperation and Development
PBS	Phosphate buffered saline
PBST	0.1% Tween-PBS
PC	Principle component
PCA	Principle component analysis
PCLS	Precision cut lung slices
PDI	Poly dispersity index
POD	Point of departure
PPS	Primary particle size

PSF	Point spread function
PVP	Polyvinylpyrrolidone
REACH	Registration, Evaluation, Authorization and Restriction of Chemicals
ROS	Reactive oxygen species
RS	Relative survival
SEM	Scanning electron microscope
SSA	Specific surface area
TEM	Tunneling electron microscope
tPOD	Transcriptional point of departure
TSCA	Toxic Substances Control Act
UFP	Ultrafine particulate matter
ZP	Zeta potential

List of Tables

List of Figures

List of Appendices

List of Supplementary Material

Preface

This thesis is written as a series of articles, in accordance with the University of Ottawa Academic Regulation C-7.3. Referencing in this document is formatted in the style of APA 7th edition.

The thesis begins with a general introduction (Chapter 1) which provides the purpose and scope of the thesis with a review and summary of the relevant literature needed to contextualize the research question.

Chapters 2 to 7 are a series of manuscripts: Chapters 2, 3, 4 and 5 are published, Chapter 6 is currently in peer review, while Chapter 7 has been prepared for publication and will be submitted following Health Canada review. I am the first author on the manuscripts for Chapters 2, 3, 4, 6 and 7 and a co-author on Chapter 5. Details regarding the individual contributions from each author are provided as a title page for Chapters 2 to 7.

Chapter 8 provides a summary, conclusions and recommendations.

1 Chapter 1: General Introduction

1.1 Purpose and Scope

The purpose of this thesis is to answer the question of **"What is the relative contribution of particulate and dissolved fractions to metal oxide nanoparticle (MONP) induced toxicity?"**. To address this question, this thesis utilizes 21st century toxicological tools (high content transcriptomic and high throughput genotoxicity screening assays) in an *in vitro* approach with FE1 lung epithelial cells commonly exposed to 5 metal oxide nanoparticles (MONPs), and their dissolved and microparticle analogues.

The MONPs chosen for investigation throughout this thesis were commercially procured and are widely utilized in consumer and commercial products (ZnO, CuO, Al_2O_3, and TiO_2), or utilized in niche consumer applications but for which carcinogenic hazard is known for larger size fractions (NiO NPs) (**Table *1-1***) (Hansen et al., 2021; IARC, 1990). Furthermore, three subgroups of these MONPs are considered prioritized substances for risk assessment in Canada, those being ZnO, NiO, and TiO_2 MONPs (**Proposed Plan of Priorities: substances prioritized for assessment under CEPA - Canada.ca**). For all MONPs, commercially sourced microparticle analogues > 1µm based on manufacturer reported primary particle size were included for comparative analysis due to differences in solubility between bulk and nanoscale metal oxides. Similarly, for all MONPs except TiO_2, a water soluble metal chloride equivalent was included in order to determine the contribution of the dissolved species on toxicity. At least one concentration of each dissolved equivalent used for mechanistic characterization and high-throughput screening was based on solubility determined in cell culture medium using the same MONPs investigated herein (Avramescu et al., 2020, 2022).

Table 1-1. Select MONPs used in commercial and consumer applications. *: MONPs which are the main subject of this thesis.

Element	Oxide	Application as a nanomaterial
Zinc	ZnO*	- Sensors (Yoon et al., 2021) - Cosmetic additive (Fytianos et al., 2020)
Copper	CuO*	- Sensors (Yoon et al., 2021) - Insecticide (Rahman et al., 2022) - Supercapacitance (Ameri et al., 2016) - Cement additive (Ślosarczyk et al., 2023)
Manganese	MnO_2	- Supercapacitance (Mothkuri et al., 2019)
Nickel	NiO*	- Sensors (Maduraiveeran et al., 2019) - Photocatalysis (Mohamed et al., 2022)
Aluminum	Al_2O_3*	- Paints and coatings (Janković & Plata, 2019) - Sensors (Chavali & Nikolova, 2019) - Catalysis (Chavali & Nikolova, 2019)
Cerium	CeO_2	- Biomedicine (Dhall & Self, 2018) - Waste water treatment (Chaudhary et al., 2017)
Iron	Fe_2O_3 / Fe_3O_4	- Waste water treatment (Xu et al., 2012)
Titanium	TiO_2*	- Solar energy generation (Maduraiveeran et al., 2019) - Photocatalysis (Maduraiveeran et al., 2019) - Sensors (Maduraiveeran et al., 2019) - Waste water treatment (Liu, X. et al., 2021) - Cosmetic additive (Boyadzhiev et al., 2020; Fytianos et al., 2020) - Cement additive (Ślosarczyk et al., 2023)

In addition, for a subset of MONPs (CuO, NiO, Al_2O_3, and TiO_2), nanoscale microscopy in conjunction with inhibition experiments using a specific inhibitor of v-type ATPase activity was used to assess the relationship between subcellular lysosome localization and toxicity in terms of MONP solubility.

The scope of this thesis is primarily experimental, but does include an *in vitro* grouping and prioritization component (Chapter 7) which extends the use of this data to risk assessment activities.

Included in this Introduction (Chapter 1) is a literature review to provide context for the above overarching question, followed by a statement of the four main hypotheses, an overview of the regulatory data gaps being addressed, and a short guide to the structure of the thesis and the specific objectives of each chapter.

1.2 Background

1.2.1 A Brief History of Nanomaterials

Nanomaterials (NMs) have always existed naturally; in the form of dust particles and pathogens. They can also be produced secondary to anthropogenic activities, such as welding, grinding, brazing, or combustion and as by-products from natural processes, such as volcanic eruptions and weathering (Oberdörster et al., 2005). Utilization of NMs in human life dates back to the BCE with early human ancestors inadvertently depositing layers of nanocomposites in their cave drawings, some of which date back to 40 – 34 000 BCE (Barhoum et al., 2022; Yetisen et al., 2016). Ancient cultures including the Romans, Chinese and Islamic cultures incorporated metallic nanocrystals in pottery and glass to confer brilliant colours in their finished crafts (Barhoum et al., 2022). These pieces contained well defined stratified layers of nanoparticulate copper (Cu) and silver (Ag) within the glass / ceramic matrix that induce optical plasmonic effects and produce iridescent color phenomena (Barhoum et al., 2022). While these brief examples serve to illustrate humanity's long history of NM utilization, a real appreciation for the unique effects exhibited by NM did not become apparent until modern times when our ability to manufacture increasingly smaller materials improved.

In the present age, the ability to purposefully and precisely manipulate matter at the atomic or molecular level has given rise to the field known as nanotechnology, and through it, engineered nanomaterials (ENMs). In 1959, leading physicist Richard Feynman gave a seminal lecture at the American Physical Society titled 'There's plenty of room at the bottom' which proposed how different our world would be if we can precisely manipulate matter at the atomic scale (Feynman, 1992). More importantly, he enthused that this is physically possible and all that is stopping scientists from doing it, is that 'we hadn't gotten

around to it'. In the next few decades he was shown to be correct, with the development of ENMs beginning in earnest in the 1980s, with the discovery of C_{60} fullerenes in 1985 (Kroto et al., 1985) and the elucidation of the structure of carbon nanotubes (CNTs) in 1991 (Iijima, 1991). The intense interest in nanoscale carbon chemistry lead to an explosion in research and development of many different kinds of ENM over the next decades. While the first consumer products to contain ENM by design were released in the 1990s and consisted of tennis rackets, baseball bats, and golf clubs reinforced with carbon nanotubes, by the 2010s more than 1000 ENM-containing consumer products were available in markets globally (Hansen et al., 2021; Kessler, 2011; Vance et al., 2015), and this number continues to increase yearly. With increasing production comes increased propensity for human exposure and environmental release, which can pose risks that require regulatory management.

1.2.2 Nanomaterial Definitions, Sources, and Identities

The International Organization for Standardization (ISO) defines an NM as a material with any external dimension or structure between 1 and 100 nm (ISO, 2023). The US Federal Drug Administration does not have its own NM definition and follows the ISO definition (U.S. Department of Health and Human Services et al., 2014; US Department of Health and Human Services et al., 2022). The US Environmental Protection Agency (EPA) and Health Canada both have their own working NM definitions, which closely mirror the ISO definition (ECCC & HC, 2022; EPA, 2017). According to the definition by the European Union, a material is considered to be "nanoform" if 50% or more of the material in the number size distribution in one or more external dimensions is in the size range 1 nm - 100 nm (ECHA, 2019). Additional definitions are available in the World Health Organization document "Principles and methods to assess the risk of immunotoxicity associated with exposure to nanomaterials" (World Health Organization & International Programme on Chemical Safety, 2019). For the purposes of this thesis, the ISO NM definition will be used. Similarly, the term 'bulk' in this thesis refers to materials with all dimensions and structures larger than 100 nm in size.

In the context of regulation, NMs cannot be organized like traditional chemicals because unlike traditional chemicals, NMs do not have an unambiguous identity. NMs tend to be defined by distributions of values (like primary particle size, aspect ratio, and aggregate size in suspension) whereas traditional chemicals tend to be defined by singular values (like Log_{KoW}, and vapor pressure) (Miernicki et al., 2019). Broadly, NMs can be classified based on their origin (Barhoum et al., 2022) and chemical composition. Incidental or naturally occurring NM created inadvertently through human actions or through naturally occurring processes have distributions which are broad and encapsulate many different populations. ENMs on the other hand have tightly controlled physicochemical properties to leverage specific effects at the nanoscale. They can be categorized into a few main categories based on their chemical composition, such as metals and metalloid oxides or organic ENM (ECCC & HC, 2022). ENMs can be further divided into subtypes based on their morphology, such as rods, tubes, wires, flakes, or particles (ISO, 2023). These highly diverse materials are part of a larger class of compounds known as 'Advanced Materials' which are defined by the Organization for Economic Cooperation and Development (OECD) as having been rationally designed with new or enhanced properties and/or targeted or enhanced structural features (OECD, 2022b). These enhanced properties are what have allowed ENM to inundate global markets, and are the reason for the ever expanding methods available to synthesize ENM and the diversity of these materials.

1.2.3 Synthesis, Applications, and Properties of ENM

The range of ENM produced worldwide is quite broad and heterogeneous. Many different approaches exist for ENM synthesis and many rely upon simple chemical reactions which have been known for many years, such as chemical vapour deposition. In fact, with advances in microscopy techniques numerous existing protocols have been shown to result in the accidental synthesis of NM, such as ball milling. Over the last 2 decades more complex and varied approaches have been explored however all still involve either 'top-down' or 'bottom-up' synthesis, or a combination of the two (Barhoum et al., 2022). In 'top-down' synthesis, bulk materials are progressively broken down into smaller and smaller forms until they reach the nanoscale through processes involving impaction,

or ablation. Conversely, ‘bottom-up’ approaches build an ENM atom-by-atom through deposition based methods. Hybrid approaches on the other hand combines both ‘top-down’ and ‘bottom-up’ synthesis together in an alternating fashion. The production of computer chip dyes is a hybrid ENM synthesis approach which uses nanoscale lithography to both deposit materials onto and etch a silicon substrate. Etching being the top-down component while ion growth is the bottom-up component. With the myriad of ways to produce ENM, many varieties are available for purchase on global markets but they can be divided into a few main groups.

Broadly speaking, the two major classes of ENM which make up the bulk of worldwide production and use are carbonaceous ENM which include CNTs and inorganic carbon, and metal / metal oxide ENM which includes metals, metals salts, metalloids, and metal oxides and metalloid oxides (Vance et al., 2015).

Carbonaceous ENM exist in many types and varieties; however, the main commercially available types are CNTs, carbon black nanoparticles, C_{60} fullerenes, and graphene. CNTs present attractive mechanical properties which has led to their active incorporation as strengthening agents in consumer and commercial products (e.g. tennis rackets and aerospace materials), as well as potential applications in fields such as water treatment due to their high propensity for metal ion adsorption (Santhosh et al., 2016; Vance et al., 2015). Carbon black nanoparticles are nanoscale particles of carbon, produced in an aggregated state for use as reinforcing materials in rubber tire production, as well as everyday paints, printing inks and coatings (Long et al., 2013). The C_{60} fullerene, which is a one atom thick sphere of carbon, has unique redox chemistry and photodynamic properties with many applications in fields such as photovoltaics, catalysis, and biomedicine (Bakry et al., 2007; Collavini & Delgado, 2018). More recently, the industrial production of graphene (a flat sheet of carbon with atomic thickness) and related derivatives has been achieved (Zhu, Yanwu et al., 2017). This material presents unique electrical, thermal, and physical properties, which make it attractive for the production of high-strength poly-nanocomposite materials, stimuli-responsive materials, electronics,

and next generation energy storage media (Smith et al., 2019). Despite its relative novelty, graphene is already being integrated into modern smartphones for cooling purposes.

Other than carbonaceous ENM, metal and metal oxide ENM are the most ubiquitously produced and utilized worldwide (Vance et al., 2015). Metal nanoparticles, such as silver (Ag) and gold (Au), have seen extensive utilization by the cosmetics and personal care industry due to their antimicrobial and optical properties (Fytianos et al., 2020; Niska et al., 2017). Silica (SiO_2) nanoparticles (NPs) are used extensively to strengthen concrete due to their ability to fill spaces between the particles of calcium-silicate-hydrates, and reactions with contained calcium hydroxide that results in higher densification of the concrete matrix (Aggarwal et al., 2015). Furthermore, mesoporous SiO_2 NPs have shown promise as carriers for intracellular delivery of bioactive molecules due to relatively high levels of biocompatibility, tuneable pore and particle sizes, and high loading capacity (Hoang Thi et al., 2019). Various nano-fluids containing suspensions of metal oxide nanoparticles (MONPs) have been investigated for their application in enhanced oil recovery operations due to their ability to modify oil-water interfacial tension (Cheraghian & Hendraningrat, 2015). In addition, other MONPs such as zinc oxide (ZnO) and titanium dioxide (TiO_2) NPs, have found use as invisible UV blocking ingredients in various personal products, such as sunscreens (Vance et al., 2015). The full range of applications for MONPs is much more diverse, including utilization in sensing, diagnostics, biomedicine, catalysis, electronics, and coatings & pigments (Chavali & Nikolova, 2019; Janković & Plata, 2019; Ślosarczyk et al., 2023). These applications are driven by their unique physicochemical properties.

1.2.4 Metal Oxide Nanoparticles: Properties and Applications

The applications of MONPs across sectors is extensive, of which a brief overview of major compounds is presented in **Table *1-1***. Owing to the wide assortment of applications they are used for, MONPs are present in industrial, commercial, and consumer products sold globally. As compared to their bulk counterparts, MONPs present unique electrical, optical, and reactive properties.

As compared to their bulk counterparts (metal oxide microparticles; MOMPs), MONPs possess very few edges and corners on their surface, which modifies their electronic and magnetic configurations (Chavali & Nikolova, 2019). This can dramatically increase their reactivity, such as their catalytic potential and conductive / insulative properties. For this reason, certain species of copper oxide (CuO), TiO_2, and aluminum-(II)-oxide (Al_2O_3) NPs are applied in the field of catalysis, photocatalysis, and next generation electronics (Chavali & Nikolova, 2019).

A nanoscale size form can also confer unique optical properties to metal oxide particles. As bulk substances, ZnO and TiO_2 particles have an excellent ability to filter UV-A and UV-B light, making them attractive for use in sunscreens (Newman et al., 2009). However, bulk forms leave unsightly white residue over the surface of the skin upon application, which is undesirable. By bringing ZnO and TiO_2 particles to the nanoscale, the formulation becomes transparent upon application but retain the ability to filter out UV light (Newman et al., 2009). This has resulted in widespread utilization of ZnO and TiO_2 in personal care products and sunscreens; with 85% and 72% of globally produced ZnO & TiO_2 nanoparticles (NPs) being used for this application in 2014 (Janković & Plata, 2019).

In addition to purposeful inclusion of MONPs in many products, MONPs can also comprise parts of existing formulations which were not specifically intended to be nanoparticulate. An example of this is the metal oxide microparticulate food grade pigment E171 (comprised of TiO_2) which contains a 36% particle fraction that is nanoparticulate (Weir et al., 2012; Yang & Westerhoff, 2014). These nanoparticles can be readily extracted from edible items, such as chewing gum, and highlight the potential for unintentional consumer exposure to MONPs (Chen, X. et al., 2012). This TiO_2 NP containing pigment was banned for use in foods in the EU in 2021 due to concerns regarding the toxicity of the nanoscale component when ingested (Younes et al., 2021).

Finally, nanoscale miniaturization dramatically alters the environmental stability of MONPs. By increasing the available surface area for interaction, the solubility of MONP in various biological media can markedly increase as compared to MOMPs (Avramescu et al.,

2020, 2022; Semisch et al., 2014). Leaching of metal ions into the surrounding environment is toxic to many microorganisms and has also made certain MONPs an attractive antimicrobial additive to consumer products (Abo-zeid & Williams, 2019; Vance et al., 2015). Many of these properties which make ENM and MONPs attractive to material scientists and engineers can also drive adverse effects in living organisms.

1.2.5 Nanotoxicology: The Toxicity of The Very Small

The understanding that NMs can present additional toxicological considerations as compared to bulk materials has lead to the inception of the subdiscipline of nanotoxicology (Donaldson et al., 2004; Oberdörster et al., 2005). The term was coined in the early 2000s to describe the study of the adverse effects of nanodevices and nanostructures on living organisms, however its roots can be traced back to the study of virology and metal fume inhalation in the early 20th century (Oberdörster et al., 2007). Viruses were not known to be nanoscale until the advent of the electron microscope in the 1930s, while metal fumes were not understood at the time to be composed of particles containing NM. Research in the 1970s and 80s did show that NM can translocate across barriers, and gain systemic access as well as access to the brain, however there was not much concern for their toxicological effects.

In the 1980s and 1990s, pioneering work on particle deposition in the human lung noted an enhanced propensity for deposition of ultrafine particles (UFPs, particulate matter defined as particles <100nm in size) in the deep periphery of the lung where clearance mechanisms are weaker and persistence is increased (Oberdörster et al., 2007). In the 1990s, the first comparisons between bulk substances and ENMs were made, which showed enhanced inflammation and translocation of TiO_2 and Al_2O_3 NPs, and noted that responses correlated with the surface area of the particles (Ferin et al., 1990; Oberd et al., 1990). This was the first time that the conclusion was made that NMs induce enhanced toxicity due to their larger surface area and potential for translocation as compared to bulk compounds. These studies led to the proposal of the ‘ultrafine particle hypothesis’ which states that UFPs present in the ambient air play a role in causing lung injury in sensitive populations, by inducing pulmonary inflammation and the release of mediators that affect

cardiovascular health (Oberdörster et al., 1995; Seaton, 1995). During this time, an understanding was developed that toxicity induced by UFPs, and NMs in general, can be mediated through oxidative stress and their potential to induce the formation of reactive species through surface interactions. Thus, by the end of the 90s, there was already an understanding that surface area, surface reactivity, and size potentiate toxicity induced by NM.

From 2000 – 2010 nanotoxicology was first coined as a term, and there was a recognition of the impact of biomolecule adsorption onto the surface of ENM, forming a 'corona' which mediates interactions (Lynch et al., 2007). CNTs were observed to induce similar effects to asbestos when introduced into the lungs, and there was an increased understanding of the specific hazards posed by high-aspect-ratio nanomaterials (Poland et al., 2008; Schinwald et al., 2012). IARC also classified TiO_2 as a group 2b carcinogen, using a number of studies assessing inhalation or instillation of ultrafine (nanoscale) TiO_2 (IARC, 2010). In the 2010s, the first recommended exposure limits for ENM inhalation were released by the National Institute for Occupational Safety and Health (NIOSH) for TiO_2 NPs and CNTs (NIOSH, 2011, 2013). One class of CNTs was also classified as a group 2b carcinogen by IARC during this time (IARC, 2017). These regulatory steps serve to highlight the growing understanding of the unique size associated toxicological considerations of ENM, and the inability to directly predict the toxicity of an NM from its bulk counterpart.

1.2.5.1 Human Health Risks of MONPs

From available information it can be seen that MONP production and application is increasing globally, and like ENM in general, they possess the potential to induce additional toxicity as compared to their bulk analogues. Some of the earliest evidence available regarding human health effects related to MONP exposure can be extrapolated from data available on metal fume inhalation – of which incidentally produced MONPs present a sizeable fraction (Berlinger et al., 2011; Tossavainen, 1976).

Incidentally produced MONPs (iMONPs) are generated as by-products of industrial processes involving evaporation of metals, such as welding and casting and thus have

varied composition and heterogenous physicochemical properties (Berlinger et al., 2011; Chavali & Nikolova, 2019; Tossavainen, 1976). The main route of iMONP exposure in humans is primarily inhalation in industrial environments. Welding of metals causes evaporation of the filler material and base metal. These vapours condense and react with the atmosphere, producing a heterogeneous particle mixture which contains a sizeable fraction of diverse iMONPs (Berlinger et al., 2011). Because of their small aerodynamic diameter, iMONPs have an increased propensity for alveolar deposition and pulmonary retention. Clinical reports of metal-fume induced pulmonary toxicity are numerous (Andujar et al., 2014; Antonini et al., 2002; Balkissoon, 2006; Hull & Abraham, 2002; Rohrs, 1957). The two main effects commonly noted in literature are 'metal fume fever' which presents as acute pulmonary inflammation with flu-like symptoms, and pneumoconiosis which is a progressive, fibrotic disease characterized by the persistent presence of metal oxide particles in the lungs (Antonini et al., 2002). Welding fumes were classified as a group 2b carcinogen in 1989, with a reassessment in 2017 relabeling welding fumes as a group 1 carcinogen (Guha et al., 2017). A review of nearly 30 occupational or population cohort studies in this reassessment found an increased risk of lung cancer in welders and other workers exposed to metal fumes (Guha et al., 2017). While the composition of metal fumes is heterogenous, research has shown that iMONPs are present inside fibrotic foci in welders and are at least partially responsible for the observed pathologies (Andujar et al., 2014). Due to mixture effects and the heterogenous nature of the produced particles, the toxicity of metal fumes and iMONP inhalation in humans cannot be directly extrapolated to MONPs which are engineered with tightly controlled physicochemical properties. However, they do provide preliminary evidence of potential hazards they can pose to workers if inhaled, especially during manufacture and manipulation of dry MONPs in chronic exposure conditions. In recent years, occupational biomonitoring and epidemiological studies have been carried out which provide more accurate indications as to the human health effects posed by exposure to MONPs.

Studies in workers exposed to ENM occupationally, including MONPs, have found evidence of adverse pulmonary effects (Bellisario et al., 2024; Bergamaschi et al., 2022; Bocca

et al., 2023a; Bonetta et al., 2023; Chen et al., 2021; Hemmendinger et al., 2023; Panizzolo et al., 2024; Pelclova et al., 2016). In one of the first biomonitoring studies carried out, researchers found significant associations between occupational exposure to TiO_2 NPs and 5 markers of oxidative stress in the exhaled breath condensate (EBC) of workers (Pelclova et al., 2016). Similar effects were seen in Chinese workers exposed to TiO_2 NPs in a nanomaterial production facility, with significant changes to the serum metabolite profile in exposed workers related to lipid peroxidation, also pointing towards the induction of oxidative stress (Chen et al., 2021). The EU-led NanoExplore project examined a larger international cohort of workers exposed occupationally to mixtures of ENM, including MONPs such as TiO_2, ZnO, Al_2O_3, and FeO, and did not observe indications of oxidative stress in EBC samples, but did observe significant associations between particle number and deposited lung surface area and the levels of inflammatory mediators including IL-1β and TNF-α (Hemmendinger et al., 2023; Panizzolo et al., 2024). In the same cohort, increased levels of titanium and silica in the urine in exposed workers was associated with ENM exposure, indicating absorption and systemic distribution of the inhaled material (Bellisario et al., 2024). Absorption of indium oxide NPs was similarly observed in Italian workers exposed occupationally to MONPs, with detectable 38 nm particles in the blood (Bocca et al., 2023a). Another cohort study examining the EBC of workers exposed to pigment grade TiO_2 which contains a nanoscale component, also found significantly increased levels of IL-10 and IL-1β inflammatory mediators (Bergamaschi et al., 2022). Increased levels of DNA damage was found in these workers which was associated with oxidative stress and inflammation (Bonetta et al., 2023). Importantly, these effects were noted at lower particle concentrations than TiO_2 NP exposure limits recommended by the National Institute for Occupational Safety and Health (NIOSH) (0.3 mg/m^3), indicating even more conservative limits may be needed to protect workers from hazards posed by MONPs. Overall, the current epidemiological data available on occupational exposure to MONPs indicates a pulmonary hazard, marked by inflammation and oxidative stress. Pulmonary inflammation is a central event in the development of a number of adverse outcomes relevant to ENM exposure (Halappanavar et al., 2020). The potential risk MONPs present to human health is only expected to increase

over time as their application across sectors increases and the potential for exposure grows. In order to inform safer-by-design MONP production and regulatory decision making related to potential risk, toxicological research is ongoing on a wide assortment of MONPs.

1.2.5.2 In Vivo Effects of MONPs Following Pulmonary Exposure

There has been a large amount of research conducted on pulmonary toxicity associated with MONP exposure in rodents (some noteworthy reviews discussing the subject are: (Karlsson et al., 2022; Liu et al., 2016; Murugadoss et al., 2017; Sengul & Asmatulu, 2020; Shakeel et al., 2015; Sharifi et al., 2011)). The main adverse effects commonly noted *in vivo* are 1) inflammation, 2) fibrosis and fibrosis-like pathologies, 3) and in a minority of cases emphysema and emphysema-like pathologies.

Both inhalation (nose only and full body) and intratracheal instillation of MONPs has been shown to result in pronounced lung inflammation (Gosens et al., 2016; Larsen et al., 2016; Rahman, L. et al., 2017b; Xia et al., 2011). The characteristics and severity of the inflammation, as well as its tendency to resolve is dependent on the physicochemical properties of the MONP, exposure dose and the model test system used. Acute pulmonary inflammation related to MONP exposure in rodents is characterised by pronounced infiltration of immune cells within the alveolar space and thickening of alveolar / bronchiolar walls. Increases in acute phase cytokine levels and total protein in the bronchoalveolar lavage fluid (BALF) are commonly noted, as are decreased levels of reduced glutathione indicative of oxidative stress. The potency and mode-of-action related to acute pulmonary inflammation induced by MONP exposure is related to their tendency to dissolve in biological fluids, and their surface properties (ex. Surface charge) (Cho, W. et al., 2012; Zhang et al., 2012).

If the inflammatory response to MONP exposure is sustained, a progression to fibrotic pathologies is possible. Pulmonary fibrosis is defined as a chronic lung disease characterized by excessive deposition of extracellular matrix (ECM) and remodelling of the lung architecture ((Todd et al., 2012), **https://aopwiki.org/aops/173**). This results in progressive decreases in lung function & capacity which culminates in mortality. This

condition has been shown to develop after pulmonary exposure to CuO, nickel-(II)-oxide (NiO), TiO_2, ZnO, cerium-(II)-oxide (CeO_2), and crystalline SiO_2 nanoparticles in rodent model systems (Chang, X. H. et al., 2016; Jacobsen et al., 2015; Lai et al., 2018; Ma et al., 2019; Rahman, L. et al., 2017b; Zhao, X. et al., 2019). Histopathological evidence for collagen accumulation and increased production of TGF-β and PDGF in the lung proceeds sustained inflammatory responses (Byrne & Baugh, 2008; Rockey et al., 2015). Like other ENM, MONPs have high specific surface areas and typically present enhanced surface reactivity (increasing the propensity to produce reactive species) as compared to bulk particles, which has been implicated in an increased potential to induce lung injury (Horie & Fujita, 2011). Recent research with SiO_2 nanoparticles *in vivo* and CuO nanoparticles *in vitro* indicates that vesicular localization and impairment may play a large role in potentiating downstream pulmonary toxicity / fibrosis in response to MONP exposure (Strauch et al., 2020; Wang, M. et al., 2020). Further research is needed to elucidate the exact mechanistic underpinnings of pulmonary fibrosis induced by MONPs.

In addition to fibrosis, there are sparse reports of MONP pulmonary exposure also inducing emphysema-like changes. This adverse outcome results in the destruction of alveolar walls and widening of alveolar spaces, which reduces the surface area for gas exchange. This has been noted in a single paper where authors exposed ICR mice to 100 and 500 μg of TiO_2 NPs via intra-tracheal instillation and noted airway destruction characteristic of emphysema 1 week post-exposure (Chen, H. et al., 2006).

The above highlighted adverse effects indicate a wide range of MONPs are capable of inducing local adverse outcomes in rodent lungs following pulmonary exposure, which are relevant to effects seen in humans after exposure to iMONP-containing metal fumes, and MONPs in an occupational setting. While the exact mechanistic underpinnings behind the development of these pathologies are not fully defined, there has been extensive mechanistic research conducted in lung cell line models which highlights key areas for further research.

1.2.5.3 Effects of MONPs on Lung Cells: Mechanisms of Toxicity

Cytotoxicity and genotoxicity are two important adverse effects observed and reported in the lung and lung cell lines following *in vitro* and *in vivo* exposure to MONPs. A number of physicochemical properties may influence these responses. Two of these properties which have shown a pronounced impact on toxicity are the solubility of the MONPs in various biological media, and their surface reactivity.

Solubility is defined as the maximum amount of a substance (known as the *solute*) that can dissolve in a specific solvent at a specified temperature and pressure. Factors such as the pH of the solvent and the presence of common ions in solution can affect solubility. Dissolution on the other hand is the *act* of a solute dissolving into a solvent and is defined in terms or rate. One is a point value while the other is a dynamic process, and both are inexorably linked. The solubility of MONPs can be described according to criteria proposed in (OECD, 2015), using the maximal dissolution as the solubility (**Table *1-2***).

Table 1-2. MONP solubility defined by maximal dissolution based on criteria in *(OECD, 2015)*.

Solubility Grouping	Maximal Dissolution
Highly soluble	> 70%
Soluble	10 – 70%
Poorly soluble	1 – 10%
Negligibly soluble	< 1%

For some poorly soluble and negligibly soluble MONPs, such as cobalt oxide (CoO) and chromium-(III)-oxide (Cr_2O_3), the band gap structure of the particle has been shown to strongly correlate with biological reactivity and toxic potential (Zhang et al., 2012). Specifically, particles that have conductance band gaps in the range of the cellular redox potential have the ability to disrupt redox couples and lead to reactive oxygen species (ROS) imbalances within the cell (Zhang et al., 2012). Accumulation of ROS, and direct particle interaction can lead to cytotoxicity, genotoxicity and mutagenesis. This is however, not enough to fully explain the toxicity of poorly soluble and negligibly soluble MONPs since particles like TiO_2 NPs do not have this electrical configuration, but still possess the

ability to induce pulmonary inflammation and fibrosis-like changes in lung tissue *in vivo* (Rahman, L. et al., 2017b).

For MONPs of varying solubility, subcellular localization to lysosomes and endosomes / phagosomes has been shown to strongly potentiate toxicity (Zhang et al., 2012). With respect to negligibly soluble MONPs, localization to the lysosome can induce formation of ROS due to interactions with the particle surface (Asati et al., 2010) and vesicular destabilization due to particle overload (Decan et al., 2015; Wang, M. et al., 2020). MONPs trafficked to such compartments can exhibit enhanced solubility as a consequence of the acidic conditions (Koltermann-Jülly et al., 2018; Semisch et al., 2014). The rapid liberation of metal ions can cause damage to the vesicular membrane, resulting in permeabilization, cytoplasmic leakage and toxicity. By either inhibiting endocytosis (and thereby lysosomal particle localization) or lysosomal acidification, the toxicity of some MONPs can be greatly reduced (Strauch et al., 2020; Zhang, Jun et al., 2018). Recently, a new target for MONPs has been identified in the pulmonary epithelium *in vivo* and *in vitro* (Kokot et al., 2020). In this mechanism, ENM can be endocytosed by lung epithelial cells and interact with cellular lipids and actin fibers to create what are known as 'cauliflowers' that are exocytosed and decorate the outside of the cell. These exocytotic aggregates can then be internalized by macrophages and the organic components degraded, exposing them to the ENM stressor. These macrophages can then die and release the ENM back into the extracellular space, allowing for reuptake by epithelial cells and for the cycle to begin again. This effect was shown with TiO_2 and ZnO NPs, however it is not known whether this effect is seen more consistently with MONPs of intermediate solubility.

The toxicity of MONPs depends on the degree to which they dissolve in various biological fluids, which is dependent on their size and chemical composition (Avramescu et al., 2020; Semisch et al., 2014). The ability for the exposed cells / tissue to handle imbalances in the liberated metal ion affects toxic potential. Furthermore, the intrinsic reactivity of the metal ion and its localization (extracellular vs intracellular) can strongly affect adverse outcomes (Horie & Fujita, 2011; Wongrakpanich et al., 2016). Changing the rate of dissolution of the MONPs by either coating or doping has been shown to dramatically reduce the *in*

vitro and *in vivo* toxicity of NPs such as CuO, CoO, and ZnO, showing that their dissolution is important to their toxic potential (Cai et al., 2017; Naatz et al., 2016; Xia et al., 2011). For many soluble MONPs, the toxicity mode-of-action *in vitro* is related to the kinetics of dissolution, with both the particle and dissolved species impacting the dynamics of cellular response over time. The contribution of these two species to toxicity has of yet, not been extensively explored in the context of MONPs and presents an avenue of great promise for toxicological exploration.

Aside from these important properties, additional physicochemical descriptors such as crystal phase, dustiness, specific surface area, primary particle size, and morphology all play a role in the toxic potential of MONPs. Many of these are applicable to other ENM classes, and this wide breadth of relevant properties create a challenge in the world of regulatory risk assessment.

1.2.6 Regulatory Human Health Risk Assessment and the Challenge of ENM

Risk in the context of regulation can be defined as the product of hazard and exposure, where both the potential to induce adverse effects and relevant exposure to the hazardous agent are necessary to have risk. Chemical human health risk assessment is similarly defined as the process of characterizing and quantifying potential negative effects resulting from exposure to chemical agents (Mcclellan, 1999). A chemical human health risk assessment comprises 4 main parts, those being: 1) exposure assessment, 2) hazard identification, 3) hazard characterization, and 4) risk characterization (World Health Organization, 2021). Globally, different risk assessment agencies and pieces of legislation are responsible for this task but all follow the same format.

In Canada, the Canadian Environmental Protection Act (CEPA) governs the regulation of chemicals on the Canadian market. All chemical compounds for sale in Canada introduced after 1986 must first undergo a human and environmental health risk assessment, after which point they are added to the domestic substances list (DSL) with any relevant restrictions to their use (ECCC, 2022; Health Canada, 2017). In the US, the Environmental Protection Agency is responsible for controlling substances in commerce,

originally through the Toxic Substances Control Act (TSCA) which has been amended in 2016 with the Lautenberg Chemical Safety Act. Analogous to Canada's DSL is the US TSCA Inventory which lists all non-exempt chemicals for sale on the US marketplace after they have undergone risk evaluation. In the European Union, the European CHemical Agency (ECHA) is the governing body responsible for the regulation of chemicals through Registration, Evaluation, Authorization and Restriction of Chemicals (REACH) regulations (European Parliament, 2006). Unlike Canada's DSL and the US' TSCA Inventory, the EU has 3 separate lists, 2 of which comprise past substances (EINECS: European INventory of Existing Commercial chemical Substances. NLP: No-Longer Polymers) and 1 which contains substances introduced to market post-1981 (ELINCS: European LIst of Notified Chemical Substances). For all mentioned inventories in each of these major regulatory agencies, substances are identified based on Chemical Abstract Services Registry Numbers (CAS-RNs). CAS-RN entries do not specify the size fraction of the chemical compound, which was problematic with the emergence of ENM.

Due to the inundation of ENM in global markets and the use of CAS-RNs to define substance identity, there are many MONPs for sale on global and Canadian markets which lack relevant regulatory risk assessments. Furthermore, risk assessment frameworks used in chemical toxicology required adaptation for use with ENM, taking into account the increased diversity of physicochemical properties impacting ENM toxicity. Additionally, due to the breadth of ENM in production, and the continued creation of new and complex multi-component ENM, traditional testing strategies routed in *in vivo* animal experimentation and high-dose phenotypic endpoints are unable to keep pace. The changing paradigm of toxicology in the 21st century proposes new *in vitro* based alternative approaches that are highly suited to ENM, and seek to overcome many of the economic, ethical, and practical limitations associated with traditional regulatory toxicity testing strategies.

1.2.6.1 21st Century Toxicology and ENM-Specific Risk Assessment Frameworks

Toxicological testing in the 21st century has been guided by a landmark report titled *Toxicity Testing in the 21st Century: A Vision and a Strategy,* which places a greater emphasis on the three fundamental principles of reduction, refinement, and replacement of *in vivo*

animal experiments (Gibb, 2007). Due to economic, ethical, and practical shortcomings, the report outlines a shift from *in vivo* experimentation to *in vitro* and *in silico* testing focused on high throughput / content systems biology & omics methods. This approach places greater emphasis on mechanisms underlying toxicity and uses pathway-based knowledge to glean biological meaning (Gibb, 2007). These principles are being integrated into regulatory risk assessment frameworks, which is will expedite risk assessment of ENM.

With the ever increasing use of ENM worldwide, and the ever increasing complexity in the types of ENM produced, there was a growing need for ENM-relevant risk assessment frameworks and grouping strategies which allow for rapid screening, prioritization, and evaluation of ENM toxicity. These frameworks were also necessary for manufacturers to know what kind of characterization data to include in new ENM submissions. Work on assessing and adapting current risk assessment frameworks and testing guidelines for ENM has been conducted by the OECD (OECD, 2009, 2019, 2022a), and both Canada and the EU have produced specific frameworks or guidance for regulatory risk assessment and reporting (ECCC & HC, 2022; More et al., 2021; Nielsen et al., 2021).

A common theme in both the EU and Canada ENM regulation is the requirement of rigorous physicochemical characterization which include primary particle size, shape, composition, surface area, surface charge, surface reactivity, and solubility (ECCC & HC, 2022; ECHA, 2022). These are considered the minimum characteristics required to establish the identity of an ENM in the context of regulatory risk assessment, and is a common requirement under REACH and CEPA regulations. In all frameworks, it is acknowledged that the vast variety of ENM available for a single CAS-RN makes case-by-case assessment impractical, and all call for the utilization of tiered-testing strategies centered around grouping and read across.

Grouping as defined by the OECD in the context of regulatory risk assessment is simply considering more than one chemical at a time, while read-across is defined as a technique where information from one chemical is used to predict the same information for a chemical which lacks data (OECD, 2014a). Grouping typically precedes read-across,

and there is well defined guidance for chemicals. With respect to ENM, a number of different grouping frameworks have been proposed with varying sets of physicochemical descriptors that are used to define the identity of ENM (Arts et al., 2015; ECHA, 2016b; Hund-Rinke et al., 2017; Kuempel et al., 2015; Oomen et al., 2015; Stone et al., 2020). In Canada, a combination of approaches are used for grouping, however read-across is not yet widely used for ENM and is evaluated on a case-by-case basis (ECCC & HC, 2022). Grouping and read-across are both considered alternative approaches in regulatory toxicology and can be used to fill data-gaps for regulatory assessment without the use of additional testing. For data-poor ENM which are unsuitable for read-across, New Approach Methodologies (NAMs) can be used to derive endpoint-specific data *in vitro* for hazard identification, and mechanistic characterization purposes without making use of animals.

1.2.6.2 New Approach Methodologies and Toxicity Testing of MONPs

NAMs represent a type of alternative method that can be broadly defined as technologies, methods, and approaches that provide meaningful information useful for risk assessment activities while avoiding, or reducing, the use of animals (ECHA, 2023; EPA, 2018). These approaches encompass chemical-based assays, targeted endpoint-specific *in vitro* assays, computational modelling approaches, and molecular bioassays which includes omics technologies. NAMs are particularly well suited to the challenges facing human and environmental risk assessment of MONPs, especially as the first or second levels in tiered-testing frameworks for hazard identification and prioritization (Doak et al., 2022; Hristozov et al., 2024). There are numerous NAMs which have found regulatory acceptance in chemical hazard characterization, such as defined approaches for skin sensitization and eye damage and irritation (OECD, 2023a, 2024), and assays for *in vitro* genotoxicity (OECD, 2023c), *in vitro* immunotoxicity (OECD, 2023b), and *in vitro* mutagenicity (OECD, 2016). For ENM however, it is recognized NAM-based test guidelines will require modification, as is the case for the *in vitro* micronucleus assay (TG 487) (OECD, 2022c), or in some cases are not relevant at all such as for the Ames test (TG 471) (Rasmussen et al., 2015). A recent review of ENM-specific NAMs identified 8 which have regulatory acceptance in the EU, with another 120 under development (Jagiello et al., 2022). No ENM-

specific *in vitro* tests have accompanying OECD test guidelines, but some have published ISO standards (ISO, 2016, 2021). The publishing of an associated OECD guideline is important for the regulatory uptake of a NAM, however the current NAM validation procedures outlined in OECD GD 34 are too onerous to properly keep pace with the rapid development of NAMs in the 21st century. For example, the local lymph node assay provided as an example in the aforementioned guideline had almost 10 years worth of validation studies before a formal test guideline was published in 2002 (OECD TG 429). The current OECD GD 34 is undergoing review, to consider the recent NAM framework from van der Zalm (Van Der Zalm et al., 2022), which could also result in faster validation and acceptance of ENM-specific NAMs. Numerous other challenges still require attention for regulatory uptake of NAMs which were outlined in a recent ECHA workshop on NAMs in regulation (ECHA, 2023). Even in the absence of regulatory uptake or extensive validation, NAMs can provide crucial mechanistic information that can form part of the weight-of-evidence used in screening and prioritization activities. In the context of regulatory decision making, a weight-of-evidence approach considers a variety of information sources and lines of evidence to arrive at a conclusion (Bao et al., 2018). In this way, targeted endpoint-specific NAM data can be used to supplement limited information available from more heavily validated approaches and methods. Furthermore, this sort of data is integral to the gradual uptake and acceptance of a NAM in a regulatory setting.

One of the largest bottlenecks when it comes to nanotoxicology is the throughput of existing assays (how many samples can be tested at the same time). Due to the wide breadth of existing ENM (including MONPs), and the large changes in biological response that can occur after slight alteration of particle-specific physicochemical properties, there is a need for NAM-based high-throughput screening (HTS) assays that can assess many conditions in one experiment (Collins et al., 2016; Halappanavar, S. et al., 2017). As compared to conventional assays, they are typically both time and cost-efficient, and in-line with the vision for toxicology in the 21st century (Collins et al., 2016). There has already been successful application of HTS and multiplexed platforms for the evaluation of MONP induced toxicity *in vitro*. For example, researchers have successfully applied the

ToxTracker® transgenic reporter-based assay system to mechanistically characterize the cytotoxic and genotoxic response of 6 different MONPs, and reported that DNA damage appears to be caused by oxidative stress rather than direct DNA binding (Karlsson, H. L. et al., 2014). In another example, researchers from the lab of Andre Nel developed a multi-parameter HTS assay for detection of changes in ROS levels, intracellular calcium flux, mitochondrial membrane potential, and surface membrane potential simultaneously. This tool was successfully used to conduct potency ranking of metal nanoparticles and MONPs using an *in vivo* zebrafish embryo model (George et al., 2011) and also in the elucidation of the band-gap effect related to the toxicity of insoluble and poorly soluble MONP *in vitro* (Zhang et al., 2012). Continued application of new NAM-based HTS assays to the study of MONP induced toxicity can aid in the elucidation of shared and distinct mechanisms of action useful in the context of regulatory assessment.

In addition to the development of HTS assays, the adoption of high-content 'omics' approaches to nanotoxicology has helped develop a holistic understanding of organismal response. The term 'ome' is a suffix which is used to denote objects or parts of a specific nature. For example, the genome is the entirety of the genetic landscape, and the transcriptome is the entirety of the transcriptional landscape. Therefore, omics can broadly be considered as the study of biological landscapes. The application of transcriptomics to toxicology began in the late 1990s and a new field termed 'toxicogenomics' was created (Nuwaysir et al., 1999). This field presents an attractive, cost-effective method to probe the molecular mechanisms underlying organismal response to substances in a holistic manner, with higher sensitivity than traditional toxicity endpoints (Chen, M. et al., 2012; Fröhlich, 2017). Furthermore, it presents the opportunity for the production of biomarker panels which are indicative of specific adverse responses and can be used to predict the toxicity of novel substances rapidly, while minimizing animals used. For example, a pro-fibrotic biomarker panel consisting of 17 genes (PFS17) has been developed using *in vivo* transcriptomic data sets of mice exposed to fibrotic substances (ex. Bleomycin and carbon nanotubes), and has been put forth as part of a robust method to assess the fibrotic potential of ENMs (Rahman, L. et al., 2020). Another biomarker panel, the TGx-DDI gene

panel, has been developed (using transcriptomic approaches) for the detection of DNA damage arising from chemical exposure in human cells (Li, H. et al., 2019). The latter biomarker panel is currently under review by the US FDA for use as a preclinical biomarker of DNA damage in novel drug discovery as well as chemical risk assessment (Li, H. et al., 2019). Indeed, *in vitro* transcriptomics has a high degree of application as a NAM in hazard characterization and risk assessment in general (Beal & Everett, 2023). The use of transcriptomics, therefore, lends itself well to the mechanistic study of MONP induced toxicity, and should be able to delineate how responses are modified over time with respect to particles which show different dissolution profiles.

1.2.6.2.1 Adverse Outcome Pathways and Concentration Modelling in the Context of MONPs

The mechanisms-of-action associated with MONPs, as they pertain to adverse outcomes, can be organized through what is known as the adverse outcome pathway (AOP) framework. This systematic process uses the available mechanistic information concerning an adverse response to define a linear, causal pathway describing its genesis and development (Ankley et al., 2009; Halappanavar et al., 2020; Villeneuve et al., 2014). These pathways originate at molecular initiating events (MIEs), progress through a series of key events (KEs) connected by causal key event relationships (KERs), and terminate at specific adverse outcomes (AOs). These AOPs can inform the development of novel NAMs such as *in vitro* biomarkers of response and predictive computational models that can be used as first-pass screening tools. For instance, AOP 173 describing the development of pulmonary fibrosis was used as the basis for an *in vitro* - *in vivo* extrapolation approach that identified IL-6 and IL-1β secretion in simple *in vitro* models as screening markers for *in vivo* pulmonary inflammation predictive of fibrosis development in response to ENM (Mclean et al., 2023). This AOP was also used as the basis for a quantitative structure activity (QSAR) model for multi-walled carbon nanotubes (MWCNTs) which predicts their potential to induce transcriptional pathways related to early KEs in the development of fibrosis based on their aspect ratio (Jagiello et al., 2021). This was later used to build a web-based application that can be used to predict gene expression changes in the lungs of mice based on the aspect ratio of the MWCNT ((Gromelski et al., 2022), available through **https://sea-**

lion-app-sn3wq.ondigitalocean.app/apps/aop_app). However, just as AOPs can inform the development of novel NAMs, existing NAM data from toxicogenomic and HTS assays can be used to fill gaps present in existing AOPs as well as assist in the development of novel AOPs (Halappanavar et al., 2020; Nikota et al., 2017). This is especially relevant with respect to MONP induced toxicity, and the impact of dissolution (or lack thereof) on downstream cellular responses. Integral to the development and refinement of AOPs is the production of empirical data to support key event relationships and the chronology of the pathway. This can be accomplished using the concept of benchmark concentration (BMC) modelling for point-of-departure (POD) derivation.

Targeted endpoint assays can be used to provide empirical support for AOPs, or help understand underlying mechanisms of toxicity through the use of BMC modelling. The BMC approach was introduced in the 1980s as an improvement over point-based PODs such as no observed effect levels (NOELs) or lowest observed effect levels (LOELS) (Haber et al., 2018). NOELs and LOELs are determined based on the doses used for exposure and represent the highest dose at which no effect is seen, and the first dose where a significant (typically statistically significant) effect is seen respectively. These PODs are sensitive to the precision in the dataset, and can require a large number of animals in order to achieve satisfactory sensitivity. Furthermore, differences in the effect size in different studies can make it difficult to directly compare NOELs and LOELs. The BMC approach is an alternative method that fits a series of curves to dose-responsive endpoint data and determines the dose at which a predefined response known as the benchmark response (BMR) occurs. Unlike traditional POD methods, BMC modelling utilizes the entire dose-response range, provides a measure of uncertainty around the BMC which reflects the precision of the study, and does not require the POD to be part of the dose range used for exposure. BMC modelling is regularly used in risk assessment and is the preferred method of defining health-based risk values, with guidance for regulators produced by the EU and US (EPA, 2012; More et al., 2022). There are multiple ways of defining a BMR in a regulatory setting, and it is not always a trivial task. For quantal data, extra risk is the metric most commonly employed which normalizes all responses to the zero dose control, and determines the

dose at which a response a number of percentage points over the control is achieved. Most commonly 1, 5, and 10% extra risk are used. For continuous data, more expert knowledge is required and the BMR should be selected based on what is considered an adverse response through that endpoint. In addition to use in risk assessment applications, BMC modelling is a useful tool for *in vitro* toxicity testing and potency grouping. In these applications, more leeway is available in the choice of BMR. For example, BMRs of 50 or 200% extra risk (equating to a 1.5 or 3-fold increase in response over control) have been used for BMC modelling of *in vitro* micronucleus data (Wills et al., 2015). When applied to *in vitro* endpoint screening, BMC modelling can be used to generate mechanistic hypotheses based on obtained substance or endpoint rankings, or for determining associations between physicochemical properties and endpoint response. Both of these applications are particularly relevant to ENM and MONPs, where many diverse physicochemical properties can act to influence toxicity and where many variants of similar compounds are commercially available. For example, BMC modelling was used to define cell-line dependent differences in the mechanisms underlying CuO NP mediated toxicity in A549 and BEAS-2B cells based on differences in enzyme activity and ranking of endpoint BMCs (Pink et al., 2020). In another example, BMC modelling identified ZnO NPs functionalized with triethoxycaprylylsilane as more potent than non-functionalized ZnO NPs at inducing toxicity in mice following pulmonary exposure based on hazard identification and ranking of 10 endpoints (Gosens et al., 2015). The application of BMC modelling to *in vitro* and *in vivo* endpoint data is particularly useful in the context of omics datasets, where the large scale and breadth of data can support mechanistic characterization and AOP development.

Change in gene expression is regarded as one of the most sensitive endpoints that precedes induction of apical effects. When BMC modelling is applied to transcriptomic data, transcriptional points of departure (tPODs) can be derived either at a pathway or gene level. These tPODs define the dose below which significant changes in gene expression are not expected to occur, and as such, the likelihood of experiencing downstream adverse effects is minimal (O'Brien et al., 2024). The use of tPODs in regulatory toxicology is also gaining acceptance, with the US EPA producing tools and guidance for the use of tPODs

derived from short-term *in vivo* exposures for defining chronic reference values for daily human consumption (EPA, 2023). With respect to ENM toxicity testing, BMC-derived tPODs can provide empirical data to support existing AOPs. For example, tPODs were used in a case study approach with MWCNTs and AOP 173 for pulmonary fibrosis (Labib et al., 2015). In this approach, *in vivo* pathway level tPODs anchored to the upstream key event of 'Th2 Signaling Activation' were shown to present similar BMCs to those determined for the apical induction of fibrosis. Furthermore, similar pathway responses and BMCs were noted for the different varieties of MWCNTs tested, implying a similar response to this stressor type. A later study compiled over 20 different *in vivo* ENM-exposed transcriptomic datasets and again noted similar potency response to most MWCNTs, however particularly potent tPODs were observed for long and stiff nanotubes (Halappanavar et al., 2019). This is not only relevant to *in vivo* exposures though. In a recent non-ENM multi-omics BMC approach, both tPODs and proteomic PODs were derived for pathways anchored to the KEs of AOP 432 for the development of myeloid leukemia (Q. Vuong et al., 2025). In addition to providing preliminary empirical data to support the chronology of events in the AOP, additional co-modulatory events related to cell cycle regulation, cell death, and cytoskeletal changes were identified. This study conducted *in vitro* exposures to radiation in white blood cells isolated from healthy human volunteers, and so was animal free. Overall these attempts show how existing AOPs can inform mechanistic characterization, and how tPODs and omics-derived PODs can in turn provide crucial empirical information to support key event relationships for chemicals as well as ENM. In the context of MONP toxicity, transcriptomics data represents an invaluable resource which can be used in conjunction or alone for BMC-informed mechanistic analysis to tease apart the influence of the dissolved and particulate species on response.

1.3 Hypotheses

This thesis addresses four main hypotheses presented below:

First Hypothesis (Chapters 2 and 3): Global transcriptional changes can be used to characterize mechanistic differences in response to MONPs, which can be plausibly linked back to their physicochemical properties.

Second Hypothesis (Chapters 4 and 5): The ability of MONPs to induce genotoxicity is positively associated with their solubility in the extracellular space, i.e, the more soluble an MONP is, the more genotoxic it will be in the short term. MONPs of poor or negligible solubility are hypothesized to be weak inducers of micronuclei.

Third Hypothesis (Chapter 6): Lysosomal acidification is hypothesized to drive the toxicity of MONPs soluble and poorly soluble in cell culture medium. MONPs are hypothesized to show high degrees of co-localization with lysosomes.

Fourth Hypothesis (Chapter 7): Induction of *in vitro* endpoint response can be used to group MONPs based on hazard potential, which can be used to prioritize high toxicity materials for further testing.

1.4 Regulatory Gaps Addressed In This Thesis

MONPs can present additional hazards with respect to humans and the environment as compared to their bulk analogues. While toxicological research has been conducted *in vivo* and *in vitro* with the purpose of elucidating mechanisms underlying adverse outcomes, the relative contribution of particle and dissolved species to the resulting toxicity of MONPs is still poorly understood. Considering that solubility and dissolution are characteristics that are used to define ENM in the context of regulation, and that solubility is used as a tier-0 grouping criterion in multiple ENM frameworks, this represents an important knowledge gap which can be used to refine existing grouping hypotheses or inform the development of novel grouping hypotheses. In addition, while there has been evidence to support lysosomal localization and destabilization arising from MONP exposure as integral to downstream adverse effects, this has not been examined in detail with respect to a diverse collection of MONPs and recent evidence points to other potential cellular targets. 21st century toxicological tools (transcriptomics methodologies and HTS assays) are uniquely suited to defining the impact of dissolution on MONP toxicity.

Furthermore, through the use of nanoscale microscopy in conjunction with inhibition of vesicular acidification, the impact of lysosomal localization (or lack thereof) on MONP toxicity can be explored. Addressing these knowledge gaps will advance the regulation of ENM on a global level by determining if there are specific limitations on the use of solubility as a grouping criterion for regulatory assessment of MONPs.

1.5 Thesis Organization

This thesis sought to address the above knowledge gaps through a comparative approach.

In Chapters 2 and 3, high-content transcriptomic analysis is used as a tool to mechanistically characterize *in vitro* response to 5 MONPs with varying solubility in cell culture media as well as their MOMP and dissolved equivalents (**Table 3-1**) over time. The specific objectives of these chapters were to 1) define shared and distinct response mechanisms across MONPs; and 2) to determine the impact of the dissolved and particulate fractions on MONP induced toxicity and the impact of nanoscale and bulk particle size on MONP toxicity.

In Chapters 4 and 5, HTS assays were used to probe the *in vitro* genotoxic potential of a panel of MONPs, as well as their dissolved and MOMP analogues. These included the 5 MONPs, MOMPs, and dissolved equivalents investigated in Chapters 2 and 3 in addition to 21 additional MONPs, MOMPs, and dissolved equivalents (full material overview available in **5.3.1**). The main objectives of these chapters were to 1) utilize the high-throughput CometChip® and MicroFlow® assays to determine DNA strand break and micronucleus formation after exposure to MONPs; and 2) to assess the contribution of the dissolved and particulate species to genotoxicity induced by MONPs which vary in their solubility potential.

In Chapter 6, the relevance of lysosomal localization and dissolution on MONP toxicity was assessed. FE1 cells were co-exposed with 4 MONPs and the v-type ATPase inhibitor Bafilomycin A1 to determine the relevance of lysosomal localization on toxicity by inhibiting acidification of these compartments during exposure. Nanoscale microscopy

methods were used to probe co-localization potential with lysosomes, and potential association with actin structures. The main objectives of this chapter were to 1) determine the relevance of lysosomal dissolution on MONP induced toxicity; and 2) assess the potential of MONPs of varying solubility to localize to lysosomes; with a secondary objective 3) to identify other putative compartments MONPs may traffic to following acute exposure.

Finally in Chapter 7, the genotoxicity, viability, and transcriptomic endpoint data generated in Chapters 2-5 was combined and used to explore its relevance to regulatory risk assessment. Additional viability and transcriptomic data were included from a recent thesis (Christ, 2024), which examined the impact of solubility on MONP toxicity using MnO_2 and Fe_2O_3 particles with the same level of characterization as materials used in Chapters 2-5 (**Table 7-1**).

A critical evaluation of the guiding hypotheses, a summary of the major scientific significance of each chapter, and the recommendations arising from this thesis are provided in Chapter 8.

2 Chapter 2: Impact of Copper Oxide Particle Dissolution on Lung Epithelial Cell Toxicity: Response Characterization Using Global Transcriptional Analysis

Modified from: Boyadzhiev, A., Avramescu, M. L., Wu, D., Williams, A., Rasmussen, P., & Halappanavar, S. (2021). Impact of copper oxide particle dissolution on lung epithelial cell toxicity: response characterization using global transcriptional analysis. *Nanotoxicology*, *15*(3), 380–399. **https://doi.org/10.1080/17435390.2021.1872114**

Authorship: Andrey Boyadzhiev[1,2], Mary-Luyza Avramescu[1], Dongmei Wu[1], Andrew Williams[1], Pat Rasmussen[1,3], Sabina Halappanavar[1,2]

Affiliation:
1: Environmental Health Science and Research Bureau, Health Canada, Ottawa, Canada
2: Department of Biology, University of Ottawa, Ottawa, Canada
3: Earth and Environmental Sciences Department, University of Ottawa, Ottawa, Canada

Contributions:

Experimental Design	**Andrey Boyadzhiev** Andrew Williams (Microarray random design) Sabina Halappanavar (Toxicology experiments) Pat Rasmussen (Dissolution experiments)
Particle Suspension and Characterization	Mary-Luyza Avramescu
Electron Microscopy Imaging	University of Ottawa Material Characterization Core
Dissolution Testing	Mary-Luyza Avramescu
Exposure	**Andrey Boyadzhiev** Dongmei Wu
Trypan Blue Analysis	**Andrey Boyadzhiev**
RNA Extraction and Quantification	**Andrey Boyadzhiev**
Microarray Experiments	**Andrey Boyadzhiev**
Microarray Bioinformatics	Andrew Williams
Other Statistical Analysis	**Andrey Boyadzhiev**
Pathway and GO Analysis	**Andrey Boyadzhiev**
Data Interpretation	**Andrey Boyadzhiev** Sabina Halappanavar
Manuscript Writing and Revisions	**Andrey Boyadzhiev** Sabina Halappanavar
Internal Review	Luna Rahman Silvia Solorio Rodriguez

2.1 Abstract

The *in vitro* and *in vivo* toxicity of copper oxide nanoparticles (CuO NPs) is attributed to both particlulate and dissolved copper species. However, a clear understanding of (1) the specific cellular responses that are modulated by the two species and (2) the changes in toxicity, as the proportional amount of particulate and ionic forms alter over time, is lacking. In the current study, *in vitro* responses to microparticulate CuO (CuO MPs), CuO NPs, and dissolved Cu^{2+} were characterized in order to elucidate particle and ion-induced effects over time. Particle dissolution experiments were carried out in a relevant cell culture medium, using CuO NPs and MPs. Mouse lung epithelial cells were exposed for 2–48 h with 1–25 µg/mL CuO MPs, CuO NPs, or 7 and 54 µg/mL $CuCl_2$. Cellular viability and genome-wide transcriptional responses were assessed. Concentration and time-dependent cytotoxicity were observed in CuO NP exposed cells, which was delayed and subtle in $CuCl_2$ and not observed in CuO MP treated cells. Analyses of differentially expressed genes and associated pathway perturbations showed that dissolved ions released by CuO NPs in the extracellular medium are insufficient to account for the observed potency and cytotoxicity. Further organization of gene expression results in an Adverse Outcome Pathway (AOP) framework revealed a series of key events potentially involved in CuO NP toxicity. The AOP is applicable to toxicity induced by metal oxide nanoparticles of varying solubility, and thus, can facilitate the development of *in vitro* alternative strategies to screen their toxicity.

2.2 Introduction

Metal and metal oxide nanomaterials (NM/NMs) are one of the largest classes of NMs listed in the Nanomaterial Consumer Products Inventory, making up 37% of listed entries in 2014 (Vance et al., 2015). Copper oxide (CuO) nanoparticles (NPs) are soluble metal oxide nanoparticles (MONPs) that have been utilized in many industries globally for their unique electrical and biocidal properties (Gawande et al., 2016; Grigore et al., 2016).

Owing to its large production rates and widespread utilization, the potential for accidental exposure through inhalation in an occupational setting during its manipulation

and handling is high (Hristozov, D. et al., 2018). Human exposure to CuO NPs can also occur through industrial processes that involve the evaporation of metals (Tossavainen, 1976). A wealth of toxicological information exists, which shows that CuO NPs are a particularly potent type of MONP that cause pulmonary toxicity in both *in vitro* (Akhtar et al., 2016; Semisch et al., 2014; Strauch et al., 2017; Titma et al., 2016) and *in vivo* experimental models (Cho, W. et al., 2012; Costa et al., 2018; Gosens et al., 2016; Lai et al., 2018).

Pronounced cytotoxicity, genotoxicity, and oxidative stress due to reactive oxygen species (ROS) formation (Akhtar et al., 2016; Semisch et al., 2014; Strauch et al., 2017; Titma et al., 2016) are commonly observed toxic effects *in vitro*. *In vivo,* pulmonary toxicity in rats, following nose-only inhalation exposure to CuO NPs is observed and is characterized by transient alveolitis, bronchiolitis, epithelial vacuolization (Gosens et al., 2016), as well as upregulation of cell survival and proliferation and inflammation pathways (Costa et al., 2018). However, *in vivo*, changes associated with oxidative stress pathways are not always observed (Costa et al., 2018). In another study, intranasal instillation of CuO NPs in C57BL/6 mice was shown to induce pronounced pulmonary inflammation and oxidative stress, which progressed to fibrosis 28 days post-exposure (Lai et al., 2018). A study by Cho et al. compared the pulmonary inflammogenic potential of 15 MONPs types in rats exposed via intratracheal instillations and showed that CuO NPs were among the most potent recruiters of granulocytes to the bronchoalveolar lavage fluid, inciting an acute inflammatory response 24 h post-exposure (Cho, W. et al., 2012). Thus, as compared to other MONPs, CuO NPs are particularly potent.

In vitro mechanistic research has shown that CuO NPs exert their effects through a 'Trojan Horse' mechanism, whereby particles are internalized by cells and trafficked to lysosomes for degradation (Moschini et al., 2013; Strauch et al., 2020; Wongrakpanich et al., 2016). The acidic microenvironment of lysosomes, where CuO NPs get sequestered, is conducive to rapid particle dissolution (Cho, W. et al., 2012; Semisch et al., 2014), resulting in dramatic increases in intracellular copper ion levels. These copper ions can produce ROS through interaction with bio-molecules, while CuO NPs can produce ROS via particle surface interactions (Angelé-Martínez et al., 2017). The particle overload and/or the oxidative

stress damages the lysosomal membrane, leading to permeabilization and leakage of contents into the cytoplasm (Zhang, Jun et al., 2018). The increase in oxidative stress overwhelms the antioxidant defenses of the cell and causes lipid, protein, and nucleic acid damage. Although the toxicity mechanisms of CuO NPs are fairly well understood, a clear knowledge of the proportional contribution of nanoparticulate and ionic forms to the observed toxicity remains a subject for debate (Jeong, J. et al., 2018; Strauch et al., 2017). CuO NP dissolution experiments in cell culture media have shown that CuO NPs dissolve at a much faster rate than an equal-mass concentration of copper oxide microparticles (CuO MP), due to their increased surface area, which allows for enhanced interaction with the surrounding aqueous microenvironment (Midander et al., 2009; Semisch et al., 2014). A holistic understanding of how dissolution affects the toxic responses of soluble metal oxide particles over time will inform the current mechanistic understanding of MONP induced toxicity and provide experimental evidence to support read-across approaches associated with regulatory decision making.

Transcriptomic changes have been shown to be sensitive indicators of response, which can help delineate differences in underlying property-specific toxicity mechanisms and exposure conditions (Decan et al., 2015; Halappanavar, S. et al., 2015, 2019; Labib, S. et al., 2016; Søs Poulsen et al., 2013). **Therefore, the primary objective of the present study was to apply global transcriptomic analysis to determine the impact of the dissolved and particulate fractions on toxicity induced by CuO NPs.** Specifically, the transcriptional responses, over time, of immortalized mouse lung epithelial cells (FE1) exposed to CuO NPs, CuO MPs, as well as dissolved Cu^{2+} in the form of $CuCl_2$ for 2–48 h were characterized. Genome-wide transcriptional profiles were generated and were compared between the various exposure conditions and timepoints to specifically delineate the effects of a nanoparticle size on toxicity and particle vs ion mediated effects. The results were used to establish a putative adverse outcome pathway (AOP) for *in vitro* cytotoxicity, which is applicable to a diverse group of MONPs.

2.3 Methods

2.3.1 Materials

CuO NPs with a manufacturer reported an average primary particle size of 28 nm (Lot number: MKAA0633), cell culture pure copper-(II)-dihydrate ($CuCl_2 \cdot 2H_2O$ referred to as '$CuCl_2$' in this paper), and cell culture pure sodium chloride (NaCl) were procured from Sigma-Aldrich Inc. (Darmstadt, Germany). CuO MPs with a manufacturer reported average primary particle size of 5 µm were obtained from US Research Nanomaterials Inc. (Houston, TX, USA).

2.3.2 Cell culture

Immortalized FE1 cells derived from the Muta™Mouse transgenic rodent model were used for particle and ion exposures. This cell line, which shares characteristics of type I and II alveolar epithelial cells, has been extensively used for mechanistic genotoxicity and toxicogenomic response analysis of a variety of NMs including carbon black, carbon nanotubes, and others (Decan et al., 2015; Jacobsen et al., 2011; Søs Poulsen et al., 2013; White et al., 2003). In addition, since metal oxides are known to induce oxidative stress and DNA damage if deemed necessary, FE1 cells will allow a detailed analysis of the mutagenic potential of CuO NPs, and thus, were chosen in the study.

Cells were cultured as described in (Decan et al., 2015), in Dulbecco's Modified Eagle's Medium Nutrient Mixture F-12HAM (DMEM F12HAM) supplemented with 2% fetal bovine serum (FBS), 1 ng/mL epidermal growth factor (EGF), 100 U/mL penicillin G, and 100 µg/mL streptomycin and maintained at 37 °C, with 5% CO_2

2.3.3 Preparation of particle suspensions

Both CuO NPs and CuO MPs were prepared at stock concentrations of 5 mg/mL in ultrapure, cell culture grade H_2O. The suspensions were sonicated using protocols optimized in (Avramescu et al., 2019). For sonication procedures, a Branson Ultrasonics Sonifier™ SFX550 and a ½ in horn probe with extension and the removable flat tip was used, with delivered sonication energy of 24 J/mL. The stocks were further diluted in cell culture

media with the serum to 1 mg/mL and, subsequently, to 1, 5, 10, 25, 50, and 100 µg/mL exposure dilutions.

2.3.4 Particle characterization

A JEM-2100F Field Emission transmission electron microscope (TEM) (JEOL, USA) was used to capture 7 non-overlapping transmission electron micrographs of dry CuO NPs and a JSM-7500F Field Emission scanning electron microscope (SEM) (JEOL, USA) was used to capture 5 non-overlapping scanning electron micrographs of dry CuO MPs used in this study, for primary particle size measurement. All electron microscopy images were imported into ImageJ for particle size analysis. From the TEM images of the CuO NPs, the length and width of 9–20 individual particles per image were analyzed for a total of 105 particles. From the SEM images of the CuO MPs, the length and width of 10 well-isolated particles were analyzed per image for a total of 50 particles. The size distributions were plotted in histogram format using SigmaPlot12 (Systak Software Inc., UK), and the mean length and width were reported with standard deviation.

Characterization for CuO NP suspensions was carried out using dynamic light scattering (DLS). The stocks of CuO NPs suspended in ultrapure H_2O (5 mg/mL) and in cell culture media (1 mg/mL) were diluted to 50 µg/mL in the corresponding medium, and aliquots were analyzed by DLS using a Zetasizer Nano ZSP (Malvern Panalytical, Westborough, MA, USA). For each analysis, the mean hydrodynamic diameter (aggregate size in nm), and the zeta potential (a measure of the surface charge of the particles) were determined. Each measurement was conducted in triplicate for the calculation of mean and standard deviation.

2.3.5 Dose finding study

A dose-range finding study was carried out to determine the right exposure concentrations for gene expression analysis. Lactate dehydrogenase (LDH) assay was used to assess cytotoxicity.

FE1 cells were exposed for 2, 24 and 48 h to 1, 5, 10, 25, 50, and 100 µg/mL CuO NPs. Only CuO NPs were used for dose-range finding. Cells treated with 10% lysis buffer

were used as an assay control for cytotoxicity and media-only treated cells served as negative controls. A fresh passage of FE1 cells was plated at a density of 30 000 cells/well in 96-well plates and allowed to acclimatize overnight. Subsequently, media was swapped for exposure media containing CuO NPs, 10% lysis buffer, or blank cell culture media. Cytotoxicity was assessed using the LDH Assay Kit (ab65393) from Abcam Inc. (Toronto, Canada) according to the manufacturer's instructions. All results were expressed as a percent of response observed in the vehicle only treated cells.

It was observed that copper ions interfere with LDH reagents and thus, the rest of the cytotoxicity experiments were conducted using Trypan Blue dye exclusion staining. This method of measuring cell viability is reliable with respect to CuO NPs exposure (Karlsson, H. L. et al., 2008).

2.3.6 Particle dissolution experiments

Dissolution experiments using CuO NPs and CuO MPs were conducted using a protocol adapted from (OECD, 1995) as described by (Avramescu et al., 2020). CuO NPs were suspended in ultrapure water, sonicated as previously described, and diluted to 10 or 100 µg/mL in culture media. The high concentration of 100 µg/mL conforms to the Organization for Economic Co-operation and Development guideline for water solubility experiments, which recommends the inclusion of 100 mg/L (100 µg/mL) concentration or higher for solubility testing (OECD, 1995). The 10 µg/mL concentration was selected based on the results of the dose-range finding experiments for the toxicity testing, at which an appreciable level of viability loss is observed. Nanoparticle suspensions were incubated in 50 mL polypropylene conical tubes at 37 °C for 0, 2, 24, and 48 h on an orbital shaker (MaxQ4000, Thermo Scientific, Canada) with 1 h shaking per day at 100 rpm (OECD, 1995; Semisch et al., 2014). At the designated time intervals, samples were withdrawn and used to measure the dissolved metal fraction after particle separation using centrifugation. Before separation, aliquots were sampled at each time interval, for particle characterization using DLS. The centrifugal separation was conducted sequentially, at 20 000 *g* (2 × 30 min) using an Allegra 64 R centrifuge (Beckman Coulter, Canada) using optimized protocols from (Avramescu et al., 2019). In between centrifugations, the top part of the supernatant was

carefully transferred into a new tube by pipette to avoid particle re-suspension. The absence of particles from the supernatant was confirmed via DLS. At each time point, particle size measurements of the blank medium that had been centrifuged showed a hydrodynamic diameter (Dh) of 12.1–12.4 nm, which was similar to those of the centrifugation filtrate containing dissolved Cu (Dh = 12.4–15.8 nm), as reported previously (Avramescu et al., 2020). This confirmed lack of particles in the filtrate of dissolved Cu. The final extracts were acidified to a concentration of 2.5% HNO_3 and the dissolved metal concentration was measured using inductively coupled plasma optical emission spectroscopy (ICP-OES). Blanks and spiked matrix blanks (containing 0.5 ppb to 1 ppm Cu) were incubated alongside the CuO NP and CuO MP derived samples. Dissolution was calculated as the percent of metal dissolved.

Spectroscopic measurements were conducted using a 5100 Synchronous Vertical Dual View (SVDV) ICP-OES (Agilent Technologies, Canada) at a wavelength of 327.395 nm as recommended by the manufacturer. The machine was operated at 1.2 kW power, 12 L/min plasma, 1 L/min auxiliary, 0.7 L/min nebulizer flow rates in SVDV mode. Three replicate readings were taken for the monitored wavelength for all samples.

2.3.7 Preparation of copper chloride solutions

To mimic a Cu^{2+} ion only exposure, $CuCl_2$ solution was prepared from cell culture grade copper-(II)-chloride dihydrate. $CuCl_2$ solution was prepared in FE1 cell culture media with 2% serum at two different concentrations. The high concentration of $CuCl_2$ (54 µg/mL, 570 nmol Cu) is equivalent to the total copper content contained in 25 µg/mL CuO NPs (566 nmol Cu). The 7 µg/mL concentration of $CuCl_2$, which is more relevant, represents 2.64 times the predicted extracellular Cu expected to be released from 10 µg/mL CuO NPs based on 48 h particle dissolution experiments. The 54 µg/mL concentration of $CuCl_2$ reflecting a 100% particle dissolution scenario was included in the viability experiments to assess the degree of cytotoxicity induced by exposure to an equimolar concentration of dissolved Cu compared to CuO NPs. However, this concentration was not included in the toxicogenomics experiments since it does not represent a realistic exposure scenario with relation to the extracellular dissolution of CuO NPs. In order to

account for the influence of chloride (Cl) ions on transcriptional responses, NaCl was prepared in FE1 cell culture medium at a concentration that contains an equimolar amount of Cl ions as 7 µg/mL $CuCl_2$.

2.3.8 Concentration metrics

The particle and metal salt concentrations used in this study are expressed in terms of mass-concentration. For comparative purposes, the particle and salt concentrations expressed in terms of copper molar concentration, mass-surface area concentration, and particle specific surface area are provided in **Table 2-1**.

Table 2-1. Copper oxide particle concentrations and copper chloride salt concentrations expressed in terms of copper molarity, surface area of exposure, and particle specific surface area.

Exposure	Mass concentration (µg/mL)	Copper (µM)	Well-surface area (µg/cm^2)	Specific surface area (CuO NPs) (cm^2)[a]	Specific surface area (CuO MPs) (cm^2)[b]
CuO	1	13	0.188	0.594	0.072-0.108
	5	63	0.938	2.97	0.36-0.54
	10	126	1.88	5.94	0.72-1.08
	25	314	4.49	14.85	1.80-2.70
$CuCl_2$	7	41			

[a] Values calculated based on a manufacturer provided specific surface area of 33 m^2/g. [b] Values calculated based on a manufacturer provided specific surface area of 4–6 m^2/g.

2.3.9 Cell exposure, imaging, and sample collection for cell viability and transcriptomic analyses

For the CuO NPs, CuO MPs and $CuCl_2$ experiments, cells from four individual passages were used (four biological replicates) in four separate experiments. Cells were plated at a cell density of 130 000 cells/well in 6-well plates. Following overnight incubation, cells were exposed to 1.8 mL of 1, 5, 10, and 25 µg/mL CuO NPs, CuO MPs or 7 and 54 µg/mL $CuCl_2$. For all exposures, blank media exposed cells served as negative controls. For $CuCl_2$ experiments, cells treated with 5 µg/mL NaCl were also used as an additional control to rule out the possible contribution of Cl ions to the observed cellular toxicity in $CuCl_2$ exposures. Following 2, 24, and 48 h of exposure, cell supernatant was

harvested, cells were washed with PBS. Phase-contrast images were acquired for all exposed samples at 4x, 10x, or 20x. Following imaging, cells were trypsinized and suspended in fresh cell culture media. An aliquot of cell suspension was used for Trypan Blue dye exclusion staining and the rest of the cells were pelleted by centrifugation (8000 rpm, 10 min, 4 °C) and frozen at −80 °C for subsequent analysis.

2.3.10 Trypan Blue dye exclusion staining

Trypan Blue dye exclusion staining was conducted as per (Decan et al., 2015). Briefly, 10 µL of cell suspension was combined with 10 µL Trypan Blue dye and incubated for 5–7 min at room temperature before cell counting in a hemocytometer. The number of white and blue cells were counted in four quadrants. The ratio between white and total cells was used to calculate percent cell viability for each exposure condition and timepoint. Each measurement was conducted in triplicate or quadruplicate (n = 3, 4).

2.3.11 RNA extraction, quantification, and integrity analysis

RNA extraction, quantification, and integrity analysis were conducted as in (Decan et al., 2015). Following exposure and collection of cell pellets, TRIzol reagent was used to isolate RNA in conjunction with Direct-zol RNA Miniprep Kit (Zymo Research Corp, Irvine, USA) according to manufacturer's protocol (with a 2 min incubation in water prior to elution). Total RNA concentration and purity were determined using a NanoDrop 2000 spectrophotometer (Thermo Fisher Scientific Inc., Waltham, USA). RNA integrity and quality analysis were conducted using an Agilent 2100 Bioanalyzer system (Agilent Technologies, Inc., Santa Clara, USA). RNA samples with an RNA Integrity Number (RIN) of ≥5 were used for subsequent microarray experiments.

2.3.12 Microarray hybridization

RNA microarray hybridization and scanning were performed as outlined in (Decan et al., 2015). Briefly, 200 ng of purified RNA from each exposure group (CuO NP, CuO MP, $CuCl_2$ (7 µg/mL), or vehicle control exposed; n = 3 for each) and universal reference RNA were reverse transcribed into double-stranded cDNA which were then transcribed into cyanine 5-CTP (sample) and cyanine 3-CTP (reference) labeled cRNA. Each experimental

cRNA sample was mixed with an equimolar amount of reference cRNA and hybridized to 8x60K Agilent SurePrint G3 Mouse Gene Expression v2 Microarray (Agilent Technologies, Inc., Santa Clara, USA) slides in a hybridization chamber for 17 h at 65 °C rotating at 10 rpm. Microarray slides were washed according to the manufacturer's protocol and scanned on an Agilent G2505B scanner. Data from the resulting images was extracted using Agilent Feature Extraction software version 11.01.1.

2.3.13 Statistical analysis of microarray data

Statistical analysis of microarray data sets was conducted as outlined in (Poulsen et al., 2015). In brief, a randomized reference design using reference and sample cRNA was used (Kerr & Churchill, 2001). The commonly used LOWESS method was employed to normalize the data sets and statistically significant differences between differentially expressed genes were determined using microarray analysis of variance (MAANOVA) test in the 'R' statistical software (Wu et al., 2003). The Fs statistic was used to test for treatment effects. The permutation method was used to estimate p-values for each statistical comparison, with adjustment for multiple comparisons using the false discovery rate multiple testing correction (Benjamini & Hochberg, 1995). Fold-changes of differentially expressed genes (DEGs) were based on least-square means (Searle et al., 1980). Genes showing at least 1.5-fold expression changes in either direction and corrected p-values ≤ 0.05 were considered as significantly differentially expressed. All microarray datasets used in this study have been deposited in the NCBI gene expression omnibus database and can be accessed via the accession number GSE161017.

2.3.14 Pathway analysis of microarray data

Canonical pathway analysis was conducted on statistically significant DEGs (FDR p ≤0.05, fold-change ≥1.5) using Ingenuity Pathway Analysis (IPA) software (content version 48207413, license from Ingenuity Systems, Redwood City, CA, USA). Only samples with ≥ 40 DEGs were used for IPA analysis. Pathways were considered significantly perturbed if –log(p-value) was ≥1.3. Pathways were considered significantly activated if the –log(p-value) was ≥1.3, with a Z-score ≥2. Similarly, pathways were considered significantly inactivated if the –log(p-value) was ≥1.3, with a Z-score ≤2.

In addition, targeted analysis of genes associated with processes such as oxidative stress, DNA damage, cellular stress, and cell cycle was conducted. For this, the 84-gene lists extracted from the mouse Qiagen RT^2 Profiler qPCR arrays available for Autophagy, Apoptosis, Necrosis, Cell Cycle, DNA Damage Signaling Pathway, Cellular Stress Responses, Oxidative Stress, and Antioxidant Defenses were used and the specific differences between NPs and ion mediated responses in these key processes were determined.

2.3.15 Cytoscape ClueGO annotation of low responding samples

For samples with <40 DEGs, ClueGO enrichment analysis was conducted in Cytoscape 3.7 for gene ontology (GO) biological process, cellular component, and molecular function simultaneously. Significantly up and down-regulated genes were placed in two clusters (labeled red or blue, respectively). A right-sided hypergeometric enrichment test was conducted for both sample cluster sets, with a Benjamini–Hochberg corrected p-value cutoff of ≤0.05. Enriched GO terms are displayed according to cluster specificity. If >60% of mapped genes correspond to one gene cluster, the cluster was labeled as specific to the gene list (red or blue), otherwise, the GO term was colored gray and was labeled as nonspecific to any gene cluster.

2.4 Results

2.4.1 Particle characterization and dissolution in culture media

The CuO NPs used in this study had a manufacturer-reported primary particle size of 28 nm and a specific surface area of 33 m^2/g. Supplementary TEM imaging shows that the CuO NPs have an oblong shape with an average length of 45.9 (±28.0) nm and an average width of 64.8 (±47.0) nm (**Supplementary Figure 2-1**). Detailed characterization of the primary CuO NPs can be found in (Bushell et al., 2020), which shows that the crystallite size is 49.0 (±28.1) nm. Dynamic light scattering analysis of suspended CuO NPs is summarized in **Table 2-2**, and shows a high degree of suspension stability over time, with a PDI of <0.3 for all time points tested. Multi-modal distribution analysis of DLS results shows that at 0, 2, and 24 h the particle distribution is unimodal, and at 48 h a small

secondary peak appears (1.2%) which represents 5 µm aggregates (**Supplementary Table 2-1**). Particle dissolution experiments show that the dissolution of CuO NPs increases with increasing concentration, reaching 12.6 and 51.5% dissolved particle mass after 48 h at concentrations of 10 and 100 µg/mL, respectively (**Figure 2-1**). In contrast, CuO MPs exhibited negligible dissolution across the experimental timeframe, with only 1.5% of the initial particle mass dissolving by 48 h at a concentration of 100 µg/mL. Additional information concerning the dissolution of CuO NPs and MPs in water and cell culture media can be found in (Avramescu et al., 2020).

Table 2-2. Characterization of CuO NPs used for *in vitro* FE1 exposures. PPS: primary particle size. SSA: specific surface area. PDI: poly-dispersity index. Note: Values in parentheses indicate standard deviation.

Particle	PPS[a] (nm)	SSA[a] (m^2/g)	Timepoint (h)	PDI[b]	Hydrodynamic Diameter[b] (nm)	Zeta potential[b] (mV)
CuO NPs	28	33	0	0.174 (0.009)	182 (1.4)	-10.8 (0.5)
			2	0.165 (0.002)	183 (0.5)	-12.0 (0.2)
			24	0.172 (0.008)	183 (1.0)	-12.9 (0.9)
			48	0.227 (0.007)	199 (5.2)	-9.3 (1.5)

[a] Values obtained from manufacturers. [b] Values obtained from dynamic light scattering (DLS) analysis at a particle concentration of 10 µg/mL in cell-free culture media + (2% serum).

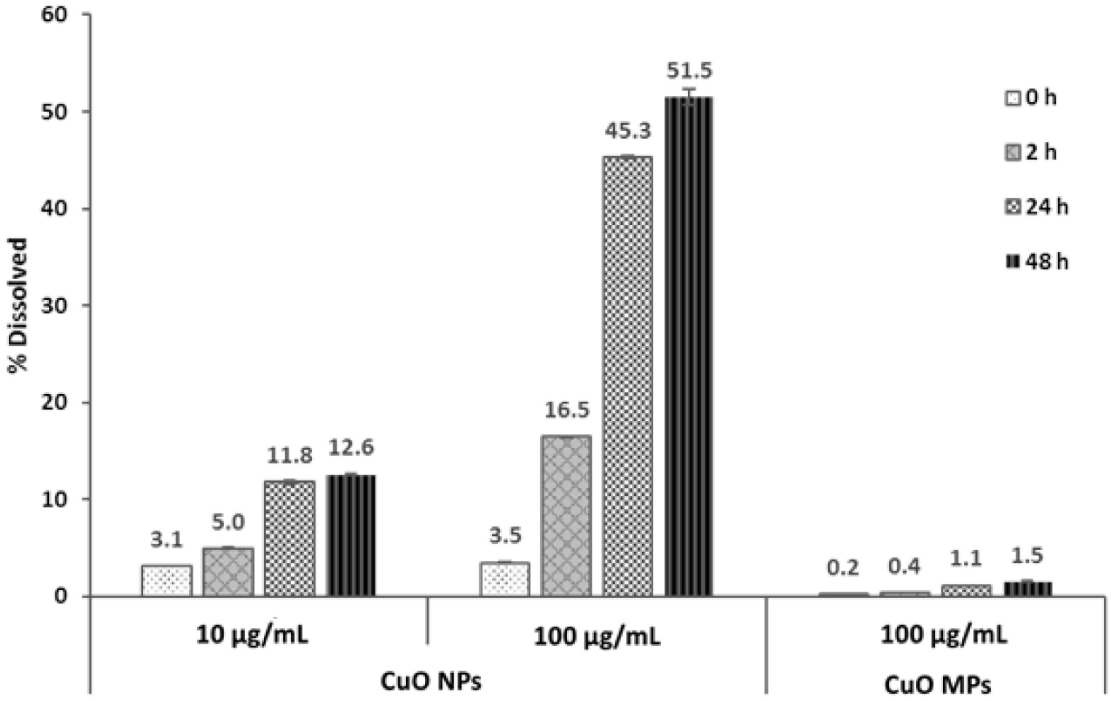

Figure 2-1. Dissolution of CuO NPs and MPs in DMEM culture medium with 2% FBS for 0–48 h. Error bars indicate one standard deviation about the mean.

The CuO MPs examined in this study had an average primary particle size of 5 µm, with a specific surface area of 4–6 m^2/g as reported by the manufacturer. Additional SEM imaging confirms the primary size reported by the manufacturer and shows that the particles have a slightly oblong shape with an average length of 4.4 (±2.9) µm and an average width of 6.3 (±3.5) µm (**Supplementary Figure 2-2**). Due to rapid sedimentation in suspension, DLS analysis could not be completed.

2.4.2 Selection of concentrations

The LDH enzymatic method of cytotoxicity assessment resulted in pronounced interference with CuO NPs (**Supplementary Figure 2-3**) at higher concentrations. Cytotoxicity was not observed for any concentrations at 2–24 h post-exposure; however, a concentration-dependent quenching of absorbance associated with the two highest concentrations (50 and 100 µg/mL) was observed at all time points. At 48 h, subtle concentration-dependent cytotoxicity was observed at the lower concentrations of 5–10 µg/mL CuO NPs. The two highest concentrations (50 and 100 µg/mL CuO NPs) showed complete quenching of absorbance at 48 h. Phase-contrast imaging showed no adherent

cells at the two highest concentrations of 50 and 100 µg/mL at 48 h (data not shown). Thus, for the purposes of subsequent experiments, 1–25 µg/mL concentrations of CuO NPs were used and the cytotoxicity assessment method was changed to cell viability assessment by Trypan Blue dye exclusion staining.

2.4.3 Viability assessment

Exposing FE1 cells to 1–25 µg/mL CuO MPs did not result in a significant decrease in viability as compared to time-matched media controls at any time point tested (**Figure 2-2**). No viability loss was observed following 2 h of exposure to any concentration of CuO NPs, at 24 h following low concentration exposure (1 and 5 µg/mL), or at 48 h after exposure to 1 µg/mL. Treatment with 10 or 25 µg/mL CuO NPs resulted in a statistically significant decrease in cell viability to 89.7% (±3.4%, $p < 0.01$) and 64.6% (±12.2%, $p < 0.01$), respectively at 24 h. At 48 h, viability was decreased to 91.6, 71.4, 13.1% (±2.9, 2.5, 10.0%, $p < 0.05$, 0.01, 0.001) after exposure to 5, 10, and 25 µg/mL CuO NPs, respectively.

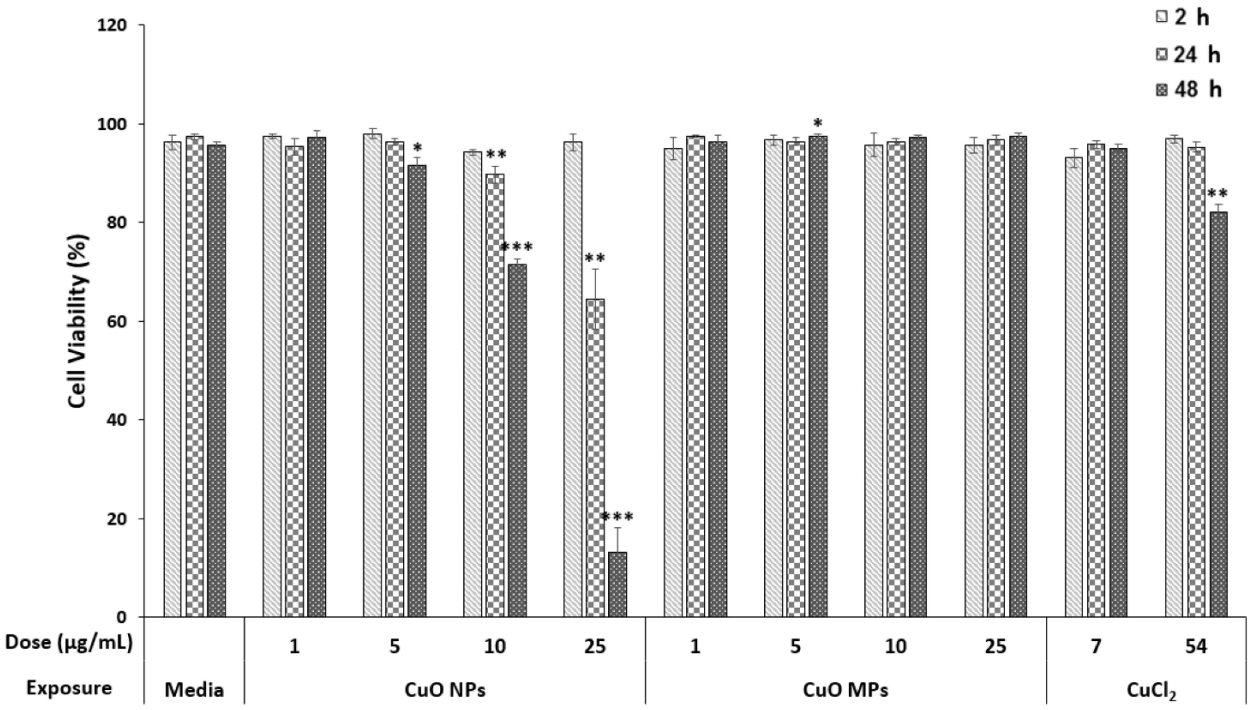

Figure 2-2. Trypan Blue exclusion assay results. FE1 cell viability following 2–48 h exposure to media control, CuO NPs, CuO MPs, or $CuCl_2$. Error bars represent standard error. Significant differences between each treatment group and media control at respective timepoints were determined using a Students' t-test (n = 4). *p <0.05; **p <0.01; ***p <0.001.

2.4.4 DEG analysis of CuO NPs and CuO MPs exposed FE1 cells

Gene expression analysis was conducted on all CuO NPs exposed sample groups (with the exception of the 25 µg/mL concentration group at the 48 h timepoint due to overt cytotoxicity and an insufficient amount of material for RNA extraction), CuO MPs, and 7 µg/mL $CuCl_2$ exposed groups (**Figure 2-3**).

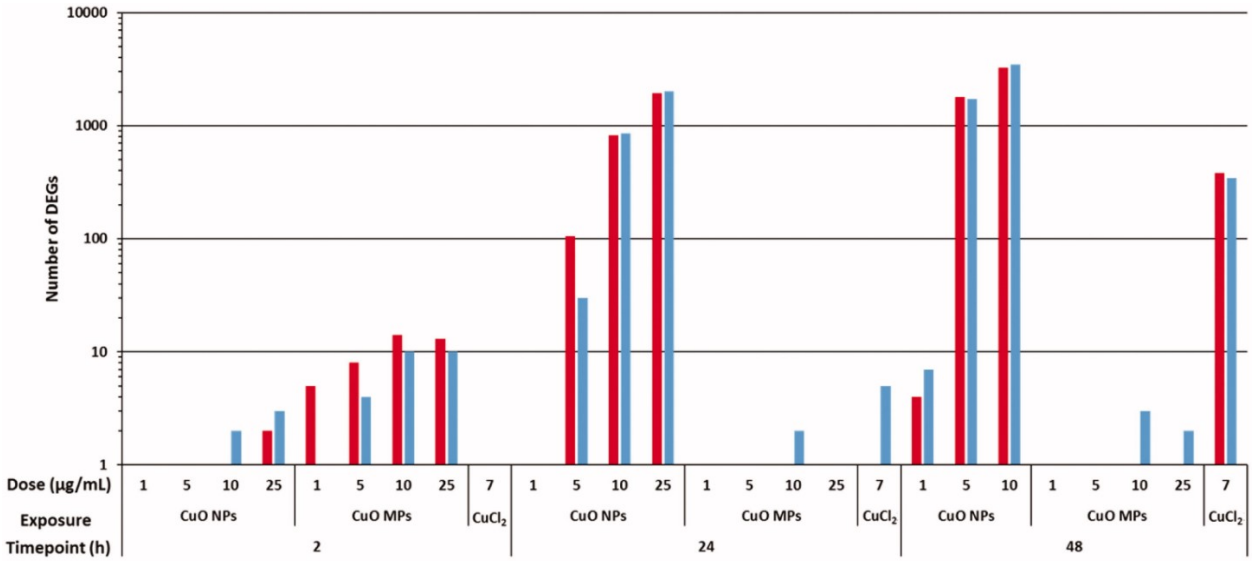

Figure 2-3. Number of DEGs (as compared to media controls) in FE1 cells exposed to CuO NPs, CuO MPs, and 7 µg/mL $CuCl_2$ for 2 h, 24 h, and 48 h. A DEG is defined as having at least 1.5-fold expression change in either direction from time matched media control with a FDR p-value ≤0.05. Red (Left bar): Upregulated; Blue (Right bar): Downregulated.

In general, the transcriptional response to CuO MPs was subtle with a maximum of 30 DEGs at any time point of assessment. The most pronounced response was observed at the 2 h timepoint, where a concentration-dependent increase in DEGs was observed (24 total DEGs at the highest concentration; 13 up-regulated, and 11 down-regulated). At 24 and 48 h, the response was reversed, with less than 5 DEGs at any concentration.

Exposure to CuO NPs resulted in pronounced gene expression changes in a concentration and time-dependent manner. The response to CuO NPs was subtle at the 2 h timepoint with less than 10 DEGs at any concentration. At 24 h, 1 (downregulated), 135 (105 upregulated, 30 downregulated), 1677 (819 upregulated, 858 downregulated), and 3934 (1924 upregulated, 2010 downregulated) DEGs were observed, for cells treated with 1, 5, 10, and 25 µg/mL CuO NPs, respectively. The response at 48 h for 5 and 10 µg/mL

treated cells was greater than at 24 h, with 3493 DEGs (1781 up, 1712 down) and 6730 DEGs (3272 up, 3458 down) respectively, however, the response was minimal for cells treated with 1 µg/mL CuO NPs (11 DEGs, 4 upregulated and 7 downregulated).

In contrast, there were only 2 and 6 DEGs in cells treated with 7 µg/mL $CuCl_2$ at 2 h and 24 h, respectively. At 48 h, $CuCl_2$ induced 725 DEGs (379 upregulated, 346 downregulated).

2.4.5 Cytoscape – ClueGO gene set enrichment of low responding experimental groups

All samples which showed a cumulative DEG count <40 were used for GO gene set enrichment analysis (molecular function, biological process, and cellular compartment) using ClueGO. From all samples analyzed, only FE1 cells exposed to 25 µg/mL CuO MPs at the 2 h timepoint had significantly enriched GO terms (**Supplementary Figure 2-4**). The enriched categories were represented by the downregulated DEGs implicated in the biological processes 'regulation of meiotic cell cycle' [GO:0051445] and 'anaphase-promoting complex-dependent catabolic process' [GO:0031145], as well as the cellular components 'nuclear ubiquitin ligase complex' [GO:0000152] and 'anaphase-promoting complex' [GO:0005680].

2.4.6 Ingenuity pathway analysis of transcriptomic response in FE1 cells treated with CuO NPs or $CuCl_2$ for 24 and 48 h

The complete list of significantly perturbed canonical pathways for all relevant samples can be found in the supplement information (**Supplementary Table 2-1**, **2-2**, **2-3**, **2-4**, **2-5**, **2-6**, **2-7**). In brief, treatment with 5, 10, or 25 µg/mL CuO NPs for 24 and 48 h resulted in a concentration and time-dependent increase in the number of perturbed pathways. At 24 h, 11, 47, and 90 canonical pathways were perturbed after treatment with 5, 10, and 25 µg/mL, respectively. At 48 h, 25 µg/mL CuO NP exposure was overtly cytotoxic and could not be assessed for transcriptional response. In cells exposed to 5 and 10 µg/mL CuO NPs for 48 h, 80 and 123 pathways were perturbed, respectively. In response to 48 h treatment with 7 µg/mL $CuCl_2$, 37 canonical pathways were perturbed.

The 10 most significantly perturbed IPA canonical pathways for all CuO NPs samples are shown in **Figure 2-4**. ‘Phagosome maturation’ and ‘Iron homeostasis’ are the most affected canonical pathways in the 5 µg/mL concentration group at 24 h (−log(p-value) >5 in both cases), with other pathways mostly related to biosynthesis and cellular metabolism. In addition, ‘Bag2 signaling pathway,’ and ‘Autophagy’ related to an unfolded protein response were also perturbed. At 10 µg/mL, pathways involved in cellular injury and stress, such as oxidative stress (‘Nrf2-mediated oxidative stress’), protein turnover (‘Protein ubiquitination pathway’), and detoxification (‘Glutathione redox reactions I,’ ‘Glutathione mediated detoxification’) were among the most significantly altered. At the highest concentration of 25 µg/mL CuO NPs at 24 h, DNA damage and repair pathways (‘Mismatch repair in eukaryotes,’ ‘Role of BRCA1 in DNA damage response’) and protein damage pathways (‘Unfolded protein response’) were among the most significantly affected. Furthermore, pathways implicated in cell death were also altered at this concentration, at 24 h (**Supplementary Table 2-4**).

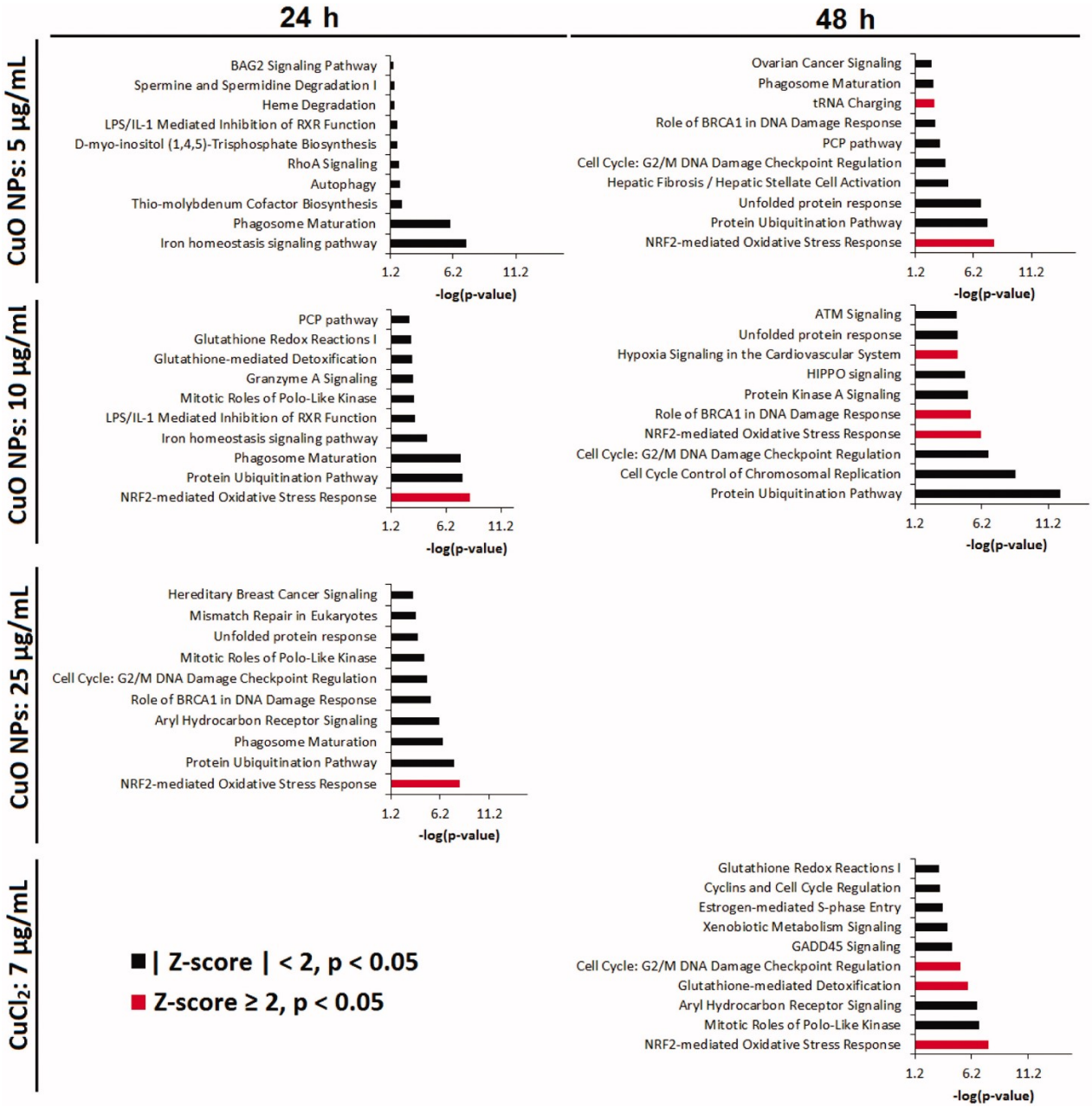

Figure 2-4. Top 10 most significantly perturbed IPA canonical pathways in relevant CuO NPs and $CuCl_2$ exposed samples. If z-score ≥ 2, the pathway is unambiguously activated.

At 48 h, cells treated with 5 and 10 µg/mL CuO NPs both exhibited substantial disturbances in cellular stress ('NRF2-mediated oxidative stress response,' 'Protein ubiquitination pathway,' 'Unfolded protein response'), and DNA damage response ('Cell cycle: G2/M DNA damage checkpoint regulation,' 'Role of BRCA1 in DNA damage response') pathways (**Figure 2-4**). Cell death pathways ('Death receptor signaling,' 'p53

signaling') were also disturbed in both concentration groups of CuO NPs at this timepoint, albeit with lower significance (**Supplementary Table 2-5**, **2-6**).

The transcriptional response to 7 µg/mL $CuCl_2$ was pronounced only at 48 h (**Figure 2-4**). Oxidative stress ('NRF2-mediated oxidative stress response'), DNA damage responses ('GADD45 signaling,' 'Cell cycle: G2/M DNA damage checkpoint regulation'), cell cycle processes ('Estrogen-mediated S-phase entry,' 'Cyclins and cell cycle regulation,' 'Mitotic roles of polo-like kinase') and detoxification responses ('Aryl hydrocarbon receptor signaling,' 'Glutathione-mediated detoxification,' 'Xenobiotic metabolism signaling,' 'Glutathione redox reactions I') were the most affected. The 'Bag2 signaling pathway' was also affected, albeit less significantly (−log(p-value) = 1.3, Z-score = 2, **Supplementary Table 2-7**).

2.4.7 Analysis of relevant cellular stress responses

From the heat maps shown (**Figure 2-5**), it can be seen that CuO NPs begin to induce differential expression of genes related to oxidative stress and cellular stress at 24 h after exposure to 5 µg/mL concentration. *Hspa1a (*25.4-fold)*, Hmox1* (6.3-fold), *Hspb1 (*2.0-fold) and *Sqstm1* (2.8-fold) were the most upregulated genes. At 10 µg/mL, the response observed at the 5 µg/mL concentration was amplified both in the number of DEGs and the magnitude of the expression fold-change. Eighteen DEGs related to oxidative stress and antioxidant defenses, and cellular stress responses, 7 DEGs associated with DNA damage signaling, and 8 cell cycle process related DEGs were observed at this concentration and timepoint. At 48 h, cells exposed to CuO NPs exhibited severe cellular stress with altered expression of genes related to all cell stress-related processes assessed. Specifically, for 5 and 10 µg/mL CuO NPs exposed cells respectively; 32 and 42 DEGs related to oxidative stress and antioxidant defenses, 39 and 22 DEGs related to cellular stress, 38 and 24 DEGs related to DNA damage signaling, and 47 and 28 DEGs related to cell cycle processes were observed.

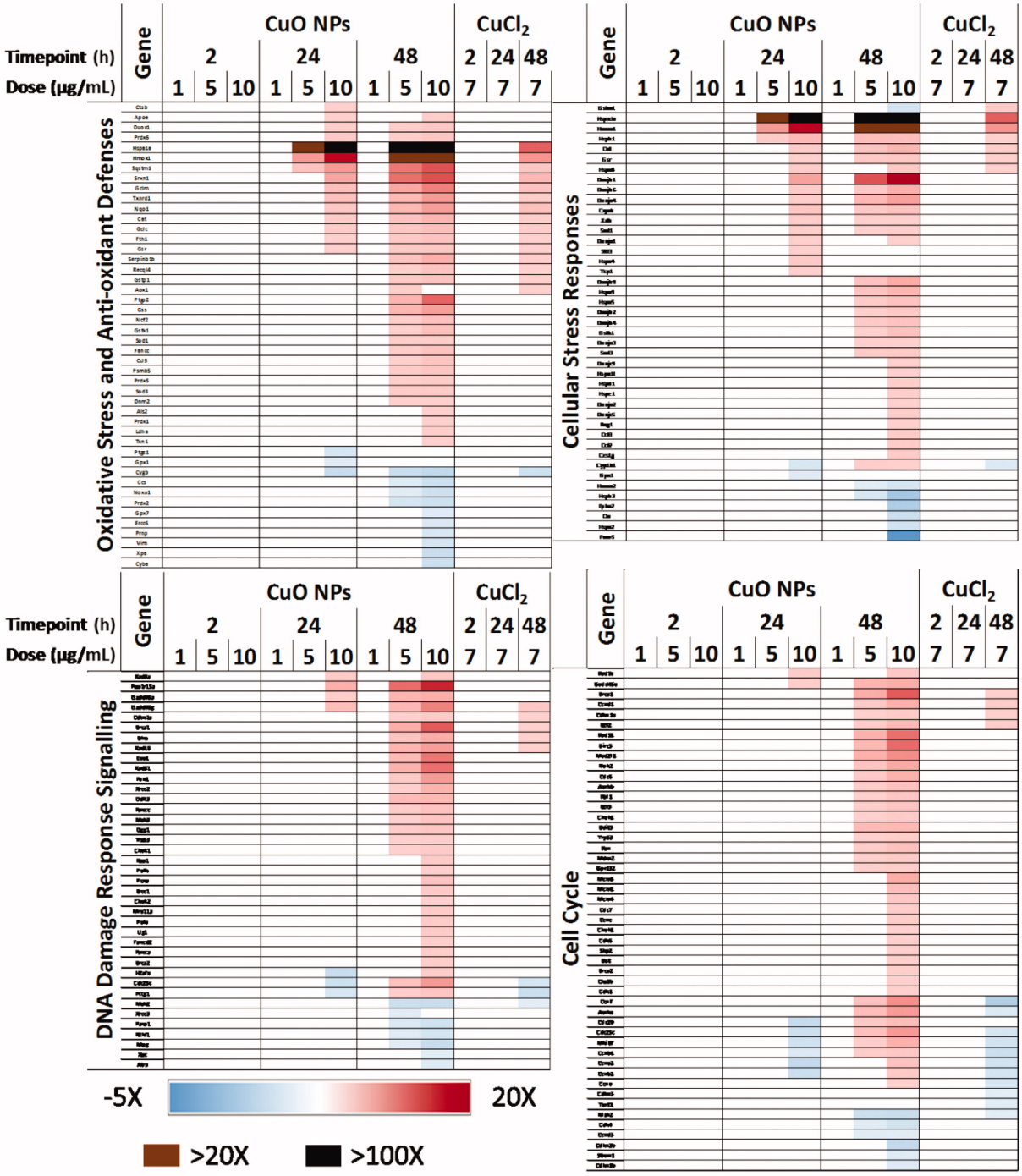

Figure 2-5. Heatmap of key differentially expressed genes related to 4 relevant cellular stress response pathways after exposure to 1–10 µg/mL CuO NPs or 7 µg/mL $CuCl_2$ for 2–48 h.

In comparison, cells exposed to 7 µg/mL $CuCl_2$ (**Figure 2-5**) show differential expression of genes related to all assessed processes, but only at 48 h and with lower severity. At this late time point, cell cycle processes, oxidative stress, and antioxidant

defenses were the most affected with 15 and 16 DEGs respectively and 8 DEGs were associated with cellular stress and DNA damage signaling.

The process of cytotoxicity was also assessed separately. A heatmap representation of key DEGs related to the cell death processes of apoptosis, autophagy, and necrosis is presented in **Figure 2-6**. A total of 6 DEGs were common to two pathways: *Dapk1, Bnip3, Trp53, Bad,* and *Bak1* are involved in apoptosis and autophagy, while *Traf2* is involved in apoptosis and necrosis. At 24 h, there was a concentration-dependent increase in DEGs related to autophagy (2 DEGs at 5 µg/mL, 8 DEGs at 10 µg/mL). Subtle changes in a few genes related to necrosis and apoptosis was also seen at 10 µg/mL (4 DEGs for both), and to a lesser extent in 5 µg/mL CuO NP treated cells (upregulation of *Pvr* is noted). After 48 h of exposure to CuO NPs, all three cell death pathways showed similar numbers of DEGs, with a concentration-dependent increase from 5 to 10 µg/mL CuO NPs (16 and 29 DEGs related to autophagy, 17 and 29 DEGs related to apoptosis, 11 and 28 DEGs related to necrosis, respectively). While all three cell death pathways have similar numbers of DEGs at 48 h after exposure to 10 µg/mL CuO NPs; autophagy and necrosis related transcripts had a larger range in differential expression as compared to apoptosis (−5 to 11.5-fold, −6.7 to 8.6-fold, −3.4 to 9.7-fold for autophagy, necrosis, and apoptosis-related transcripts respectively). In comparison, $CuCl_2$ exposed cells at 48 h displayed mild differential expression of 10 cell death-related transcripts; 2 related to apoptosis (*Bnip3*, 2.3-fold; *Bag3*, 1.6-fold), 5 related to autophagy (*Atg9b*, 3.2-fold; *Bnip3*, 2.3-fold; *Sqstm1*, 2.5-fold; *Hspa8*, 1.5-fold; *Igf1*, −1.6-fold), and 3 related to necrosis (*Ikbkg*, 2.2-fold; *S100a7a*, 1.7-fold; *Ngf*, 1.6-fold), with no differential expression noted at earlier timepoints. Phase-contrast images from the 48 h timepoint highlight extensive cytoplasmic vacuolation seen for cells exposed to 5 and 10 µg/mL CuO NPs as compared to time-matched media control and 7 µg/mL $CuCl_2$ exposed cells (**Figure 2-6**).

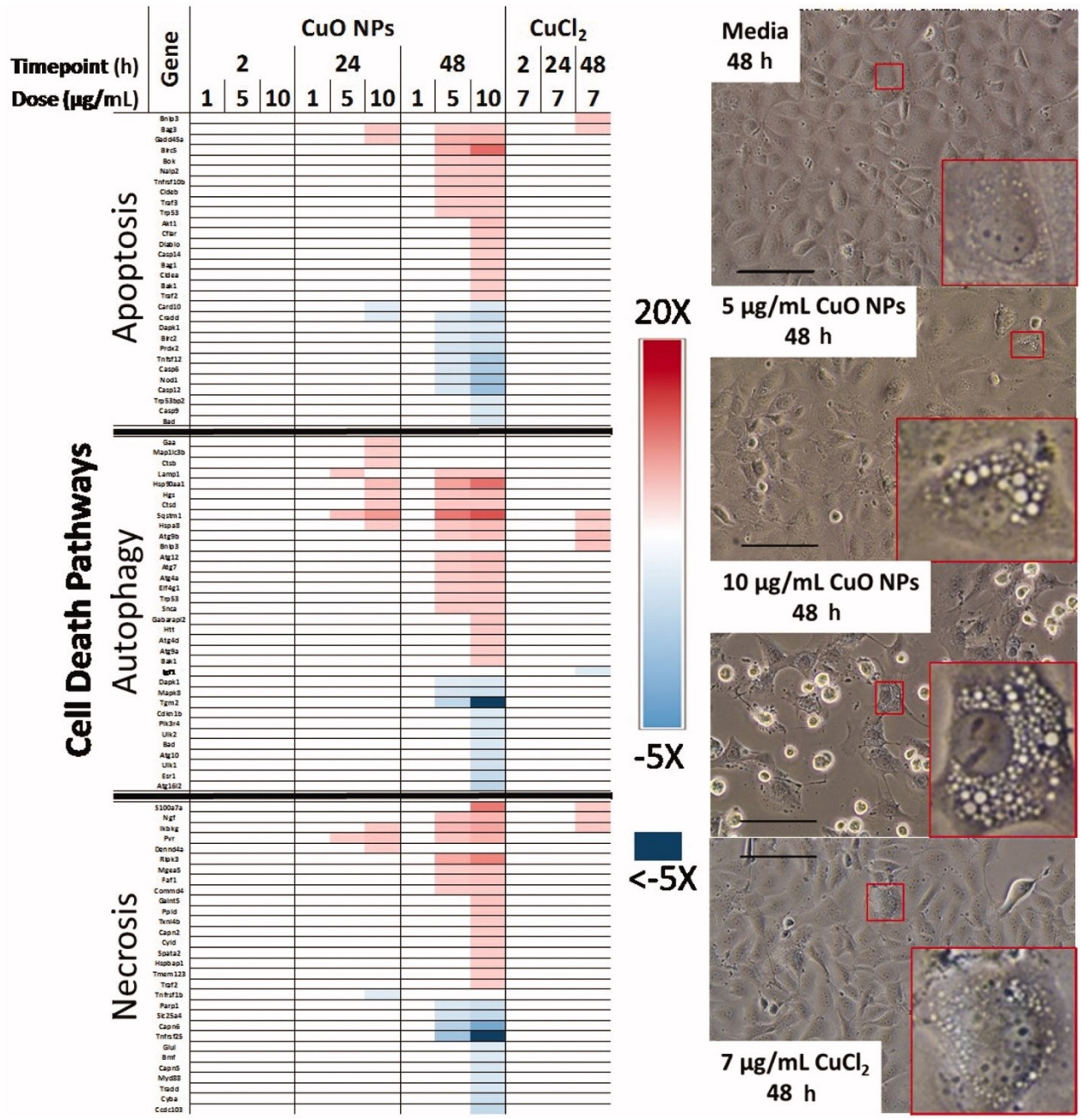

Figure 2-6. Heatmap of key DEGs related to the cell death pathways of apoptosis, autophagy, and necrosis. Phase contrast micrographs highlight cytoplasmic morphology after exposure to CuO NPs, $CuCl_2$, and media control for 48 h, scale bar = 125 µm, red insets highlight representative cells.

2.5 Discussion

The toxicity of CuO MPs and CuO NPs is well established and is mostly attributed to 1) the particles' ability to interact with cellular membranes or intracellular components and 2) their ability to dissolve in physiological environments, both of which are additionally influenced by their specific physicochemical properties such as size and concentration of particles in suspension (**Figure 2-1**; (Semisch et al., 2014)). While the toxicity mechanisms of CuO NPs have been well studied, the proportional contribution of ions and particles to toxicity has not been assessed systematically. In this study, genome-wide transcriptional profiling was carried out to elucidate the temporal transition of toxicity and the relative influence of particle size and form on cellular toxicity. A mode-of-action pathway was constructed to summarize these key differences (**Figure 2-7**).

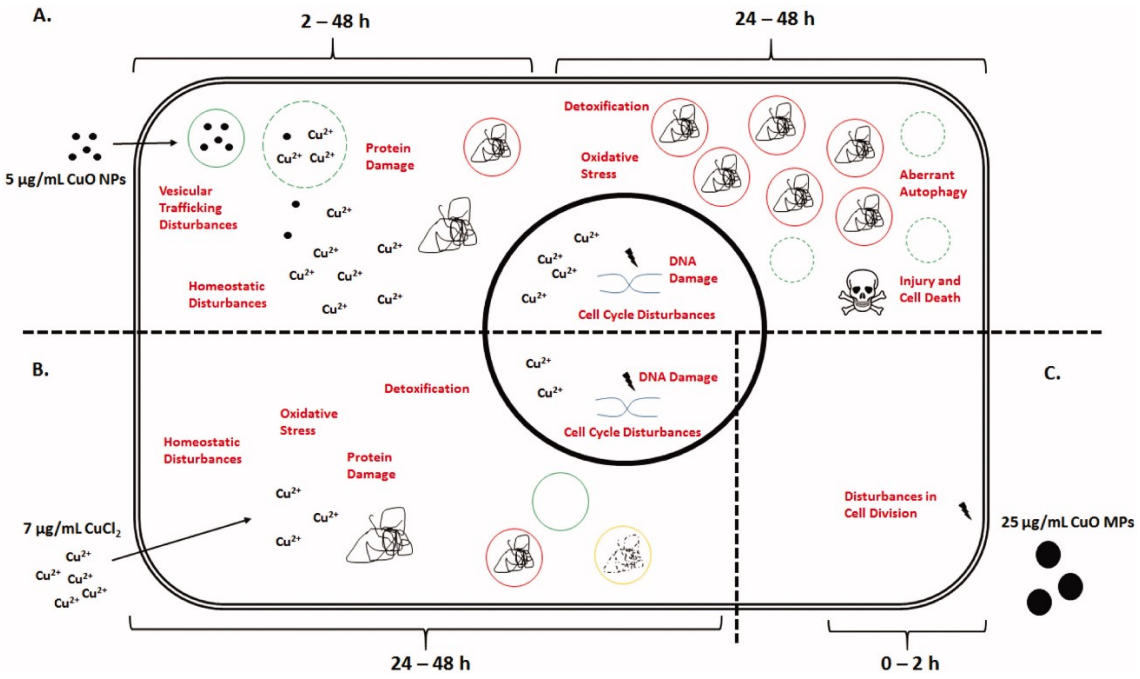

Figure 2-7. Proposed mode-of-action pathway built from transcriptional analysis for a minimally-cytotoxic concentration of CuO NPs (5 µg/mL) (A) as compared to a relevant concentration of $CuCl_2$ (7 µg/mL) (B), and the highest concentration of CuO MPs tested (25 µg/mL) (C). Labels in red within the cell indicate induced responses, for which there is pathway and gene level evidence. Squiggle represents protein aggregates. Red circles with a solid squiggle represent autophagosomes. Green solid circles represent stable lysosomes. Green dashed circles represent permeabilized lysosomes. Yellow solid circle with a dashed squiggle represents autophagolysosomes. In this model, kinetic differences in transcriptional responses are suggested to result from the CuO particle size and species-specific cellular interactions. At the time of exposure, CuO MPs have negligible or no Cu^{2+} species and CuO NPs exposure stock consist of ~3%

ions, whereas $CuCl_2$ suspension is predominantly made up of Cu^{2+} ions. The mild and acute transcriptional responses to the highest concentration of CuO MPs are transitory in nature, and are only observed sub-acutely after exposure, which is thought to be related to nonspecific interaction of large particles with the cell membrane. Lack of change in response with longer exposure duration suggests that CuO MPs are stable extracellularly and most likely will require prolonged exposure to be able to induce toxicity in whole animals or humans. In contrast, CuO NPs are rapidly internalized through nanoparticle-mediated bulk-transport mechanisms between 2 and 24 h after exposure, quickly overwhelming cellular defense mechanisms and leading to cellular injury with transcriptional disturbances in oxidative and cellular stress functions at 24–48 h. With increasing ionic concentration and overwhelmed autophagy response, leaky lysosomes can trigger cell death leading to loss of cell viability. Only a part of this response is observed in cells exposed to $CuCl_2$ and only at 48 h of exposure.

In alignment with the results of previously published studies, CuO NPs exhibited higher levels of cytotoxicity in comparison to the same mass concentrations of CuO MPs and an equimolar concentration of Cu ions (Strauch et al., 2017; Wongrakpanich et al., 2016). Cellular response to CuO MPs was negligible and only observed at the transcriptional level, with altered expression of a few genes associated with cell cycle functions (**Supplementary Figure 2-3**). The altered transcriptional response was evident early, within 2 h of exposure at the highest concentration tested, but was not observed after 24 h or 48 h of exposure. CuO MPs are slow to dissolve in culture medium (**Figure 2-1**) and the large average primary particle size of the CuO MPs (5 µm) in the present study is not conducive to uptake by lung epithelial cells, which have been shown to efficiently internalize particles up to 3 µm in size (Foster et al., 2001). It is posited that the acute transcriptional responses observed at 2 h following CuO MPs exposure are due to extracellular particle – membrane interactions. However, low levels of particle dissolution and inefficient cellular uptake of CuO MPs explain the dampened response at later post-exposure time points and cellular adaptation.

Exposure to both CuO NPs and dissolved copper ions has been shown to induce similar downstream cellular responses, such as cell cycle arrest, oxidative stress, DNA damage signaling, and apoptosis (Strauch et al., 2017). From time-dependent gene expression analysis conducted in the present study, CuO NPs mediated cellular stress responses are induced at a low concentration of 5 µg/mL at 24 h and involve a heat shock response, disturbances in metabolic pathways, and vesicular trafficking ('Autophagy,'

'Phagosome maturation') (**Figure 2-4**; **Supplementary Table 2-2**). However, there was no concomitant pathway induction of an oxidative stress response noted at this time point and concentration. Analysis of the 'Bag2 signaling pathway' mediated heat shock response shows the disturbance is caused by upregulation of heat shock protein (HSP) transcripts *Hspa1a* (25-fold), and *Hspa1b* (11-fold) (**Supplementary Figure 2-8**), responsible for proper protein folding and maintenance and whose expression is increased due to cellular stress (Daugaard et al., 2007). Furthermore, at 24 h, metallothionein (MT) transcripts *Mt1* and *Mt2* were both upregulated after exposure to 5–25 µg/mL CuO NPs (*Mt1*: 6.2, 7.4, 5.3-fold respectively; *Mt2*: 7.0, 7.8, 4.8-fold respectively; **Supplementary Figure 2-7**), which are indicative of marked intracellular Cu accumulation (Strauch et al., 2017). Similar transcriptional responses have been reported in more advanced cell culture model systems, such as 3D cultures and air–liquid interface (ALI) exposure systems. Increases in the expression of *MT1X*, *MT2A*, and *HSPA1A* have been reported in A549 cells exposed for 24 h to CuO NPs in an ALI system (Hufnagel et al., 2020). Increased expression of HSP and MT transcripts has also been seen in 3D human bronchial epithelial cell cultures exposed to CuO NPs for 25 h in ALI (*HSP90AA1, MT1M, MT2F*) and in mouse lung tissue from 24 h *in vivo* oropharyngeal CuO NP exposures (*Hsp90aa1, Mt1, Mt2*) (Ndika et al., 2020). These results suggest that the gene expression changes observed in the present study under the submerged exposure conditions are also observed in other cell types exposed under more complex exposure conditions as well as *in vivo*.

At 48 h after exposure to 5 and 10 µg/mL CuO NPs, the initial stress response is complemented by concentration-dependent induction of oxidative stress, DNA damage, cell cycle disturbances and cell death pathway signaling (**Figure 2-4**, **Figure 2-5**, **Figure 2-6**; **Supplementary Table 2-1**, **2-2**, **2-4**, **2-5**). With respect to oxidative stress-related transcripts, pronounced upregulation of *Hmox1* (32, 33-fold), *Sqstm1* (8.7, 11-fold), and *Srxn1* (9.4, 11-fold) were noted for both tested concentrations, as well as concentration-dependent downregulation of 4 transcripts including *Cygb* (−2.2, −2.4-fold) and *Ccs* (−1.6, −2.1-fold) (**Figure 2-5**). Upregulation of MT transcript expression is still evident, but to a lesser magnitude for both concentrations (*Mt1*: 2.8, 3.5-fold

respectively; *Mt2*: 2.1-fold for 5 µg/mL; **Supplementary Figure 2-7**). Treatment with 7 µg/mL $CuCl_2$ resulted in a meaningful transcriptional response only at 48 h**.** At this timepoint, *Mt1* and *Mt2* are both upregulated (5.7, 7.9-fold respectively), and similar pathways to CuO NP exposed cells are affected, including the 'Bag2 signaling pathway' with upregulated expression of *Hspa1a* (10.5-fold), *Hspa1b* (5.2-fold), *Cdkn1a* (2.6-fold), and *Hspa8a* (1.5-fold) (**Supplementary Figure 2-8**), and oxidative stress signaling with upregulation of *Hmox1* (6.7-fold), *Sqstm1* (2.5-fold) and *Srxn1* (3.6-fold) as well as downregulation of *Cygb* (−2.0-fold) (**Figure 2-5**). While the extracellular dissolution of CuO NPs in cell culture media is low at the 10 µg/mL concentration (12.6% at 48 h**, Figure 2-1**), particle dissolution is suggested to increase markedly in acidic conditions, such as those found within lysosomal and endosomal vesicles (Moschini et al., 2013; Strauch et al., 2020), resulting in marked increases in intracellular copper levels (Moschini et al., 2013; Strauch et al., 2020). In addition, while CuO NPs can be efficiently internalized through endocytosis (Strauch et al., 2020), dissolved copper ions are transported into the cell using solute carrier family transport proteins such as the high-affinity copper uptake protein 1 (Ctr1, encoded by *Slc31a1*) (Joseph R Prohaska, 2008). Finally, it is known that transcriptional regulation of heavy metal response in mice is accomplished through increased metal regulatory transcription factor 1 (*Mtf1*) expression levels (Balamurugan & Schaffner, 2006), which is seen after exposure to 5 µg/mL CuO NPs at 48 h (1.6-fold, data not shown), but not after exposure to $CuCl_2$. These results indicate, first, that similar pathways are induced at the transcriptional level after treatment with CuO NPs and dissolved $CuCl_2$ and second, that the temporal aspects of response are potentiated by the presence of elevated intracellular Cu ion levels, which is more pronounced after NP exposure due to the known 'Trojan-Horse' mechanism of toxicity as described in (Moschini et al., 2013) and (Strauch et al., 2020). Damage to intracellular organelles and biomolecules can induce the process of autophagy, which recycles deformed or malfunctioning cellular components into reagents necessary for cell growth and homeostasis. At 24 h**,** CuO NPs induce significant disturbances in the canonical pathway of 'Autophagy' (**Supplementary Table 2-2**, **2-3**, **2-4**). At 48 h post-exposure, key transcripts related to autophagy are disturbed after treatment with 5 and

10 µg/mL CuO NPs – but no longer in a way as to induce pathway disturbance (**Figure 2-5**; **Supplementary Table 2-5**, **2-6**). Concomitantly, key transcripts related to apoptosis and necrosis are recruited and there is a significant disturbance of cell death pathways (**Figure 2-6**; **Supplementary Table 2-5**, **2-6**). Phase-contrast images at 48 h post-exposure show extensive cytoplasmic vacuolization for cells treated with CuO NPs, but not for cells treated with 7 µg/mL $CuCl_2$. Despite the fact that the high concentration of $CuCl_2$ was not assessed transcriptionally, phase-contrast images of FE1 cells following 48 h exposure to 54 µg/mL show qualitatively similar vacuolization as seen in CuO NPs exposed cells (**Supplementary Figure 2-5**). The lysosomal sequestration of CuO NPs leads to lysosomal depletion through vesicular instability, resulting in a cytoplasmic overload of non-degraded autophagosomes, downstream blockage of autophagy, and cell death (Laha et al., 2014; Sun et al., 2012; Zhang, Jun et al., 2018). Our results show that cellular exposure to a high level of dissolved copper ions may induce similar disturbances in autophagy but at a slower pace compared to cells exposed to CuO NPs.

Considering that differences in transcriptional pathway induction became apparent only after a longer exposure duration (48 h), future transcriptomic studies should design experiments involving lower concentrations and longer exposure timespans.

2.5.1 An AOP for *in vitro* cytotoxicity with relevance to MONPs

Based upon the systematic analysis of the transcriptomic responses after *in vitro* exposure to different forms of CuO, and analysis of the existing literature, a putative AOP with relevance to MONPs of diverse properties is proposed for cytotoxicity, a commonly assessed and reported adverse outcome *in vitro* for NMs (**Figure 2-8**).

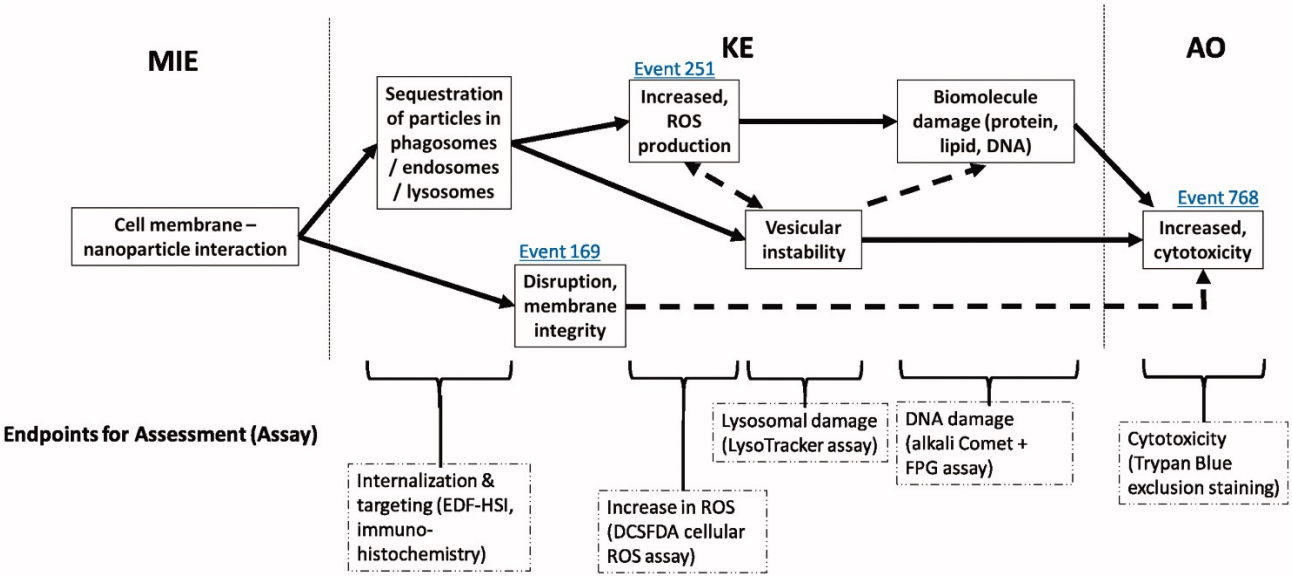

Figure 2-8. A proposed adverse outcome pathway for *in vitro* cytotoxicity relevant to MONPs. MIE: molecular initiating event; KE: key event; AO: adverse outcome. Solid arrows: adjacent key event relationship; dashed arrows: non-adjacent key event relationship. Event IDs in blue indicate a connection to a KE present in the AOPwiki. Relevant endpoints for assessment are listed, with a suggested assay for rapid screening in parentheses.

The molecular initiating event (MIE) in this putative AOP is the nano-bio interaction (not assessed in the present study). The lack of significant response after exposure to CuO MPs in this study highlights the importance of primary particle size in the induction of downstream events leading to cell death. Similar size dependence on toxic response has been shown in FE1 cells *in vitro* after exposure to silica nanoparticles (Decan et al., 2015).

From the research conducted so far, vesicular localization of MONPs seems to be a hallmark event of MONPs-induced cytotoxicity *in vitro* or *in vivo*. Endocytic or lysosomal sequestration is attributed to cytotoxicity induced by several MONPs including CuO, zinc oxide (ZnO), titanium dioxide (TiO_2), silica (SiO_2), and cerium-(IV)-oxide (CeO_2) (Asati et al., 2010; Decan et al., 2015; Lai et al., 2015; SINGH, Seema et al., 2007; Strauch et al., 2020; Zhu, Yanglong et al., 2012), which is highly influenced by the degree of solubility and particle-surface properties. Soluble MONPs, such as ZnO, CuO, and rare earth oxides are rapidly dissolved in the endosomal/lysosomal microenvironment, releasing large amounts of reactive ions (Ivask et al., 2017; Mirshafiee et al., 2018; Semisch et al., 2014; Strauch et al., 2020). While the dissolution of soluble MONPs within the vesicles causes increased vesicular

instability and ROS generation, eventually leading to cell death; insoluble or poorly soluble MONPs, such as SiO_2 and TiO_2, cause vesicular destabilization due to particle overload and inhibition of exocytosis (Decan et al., 2015; Zhu, Yanglong et al., 2012). The intrinsic reactivity of poorly soluble MONPs has a strong impact on the level of toxicity observed. For example, a strong correlation in toxicity for poorly soluble MONPs which have conductance band gaps in the range of the cellular redox potential (−4.12 to −4.84 eV) (Zhang, Haiyuan et al., 2012) was shown in a study using 24 different MONPs. Particles with band gaps in the range are liable to strongly interfere with cellular redox couples (Zhang, Haiyuan et al., 2012), which contributes to enhanced vesicular instability. The toxification of the cytoplasm (through acidification, metal ion overload, and ROS generation) leads to biomolecule damage, which culminates in cytotoxicity if left unchecked (Boya & Kroemer, 2008). Inhibition of endocytosis or endosomal/lysosomal vesicle acidification is shown to drastically reduce or inhibit MONP induced cytotoxicity (Asati et al., 2010; Strauch et al., 2020; Zhang, Jun et al., 2018).

In addition to increased cytotoxicity arising from particle internalization and vesicular localization, research has shown that direct ENM (including MONP) interaction with the cell membrane can induce membrane damage, which can also lead to cytotoxicity. SiO_2 NPs have been shown to disrupt model lipid bilayers in cell-free conditions through direct association (de Planque et al., 2011; Leroueil et al., 2008). Membrane disruption and increased permeability have also been reported in lipid bilayers exposed to cationic quantum dots, iron oxide NPs, Au NPs, and complex layered iron oxide SiO_2 NPs (Schulz et al., 2012). The specific effect on the lipid bilayer depends on physicochemical properties such as surface charge and hydrophilicity/phobicity (Schulz et al., 2012). This extracellular membrane-NP interaction leading to membrane disruption can explain residual cytotoxicity seen in cells after exposure to MONPs in the presence of endocytosis inhibitors, such as in (Asati et al., 2010). It is granted that the KEs identified in the putative AOP are influenced by the physicochemical properties of the MONP being investigated (ex. chemical composition and degree of particle solubility). The putative AOP is relevant to adverse outcomes observed *in vivo* following lung exposure to a range of

MONPs. For example, cellular uptake, vesicular instability, and cytoplasmic vacuolization, and increased cytotoxicity are all observed *in vivo* after exposure to ZnO, cobalt oxide (CoO), lanthanum oxide (La_2O_3), CuO, and TiO_2 (Cho, W. et al., 2011; Gosens et al., 2016; Rahman, L. et al., 2017b; Sisler et al., 2016). Thus, although in its preliminary roadmap version, the AOP highlights common KEs that can be targeted for measurement *in vitro* by specific endpoints and assays, and enable the development of tier-1 testing or screening strategies to prioritize MONPs for further testing by more advanced models involving animals. Moreover, specific genes highlighted in this study that showed concentration-response and relevance to one or more of KEs (ex. *Hspa1a, Hspa1b*) can aid in the design of biomarker gene panels for measuring single or multiple KEs. However, more work is warranted before a quantitative AOP is built and specific biomarkers are validated. The putative AOP presented here specifically addresses the cytotoxicity mechanism induced by MONPs of varying solubility, where particle interaction with the cellular membrane and consequent cellular uptake plays an important role. It does not, however, include the specific interaction of released ions with the surrounding biomolecules, which may also be one of the MIEs triggering toxicity.

2.6 Conclusion

In conclusion, transcriptomic analysis of lung epithelial cells treated with CuO MPs, CuO NPs, and $CuCl_2$ indicates temporal differences in response between the three exposure types plausibly related to the dynamics of cell-stressor interaction. Particle dissolution experiments in relevant culture media show differences based on particle size as well as concentration.

Mode-of-action analysis using transcriptional response as a basis highlights NP-specific effects related to vesicular internalization of NPs as integral to downstream toxicity. It is shown that there is a concentration-dependent temporal stratification of injury type response after CuO NPs exposure, indicating that homeostatic disturbances and heat shock precede significant disturbances in oxidative stress, DNA damage, cell cycle, and cell death-related processes.

Using the mechanistic knowledge gathered from the transcriptomic response analyses and the existing literature on metal oxide-induced toxicity, a putative AOP for *in vitro* cytotoxicity induced by MONPs was proposed. The AOP describes the most essential KEs implicated in MONP induced toxicity *in vitro* and provides easily assessable endpoints with suggested rapid screening assays that can facilitate high-throughput tier-1 screening of MONPs toxicity in support of regulatory decision making.

3 Chapter 3: Toxicity of Metal Oxide Nanoparticles: Looking Through the Lens of Toxicogenomics

Modified from: Boyadzhiev, A., Wu, D., Avramescu, M. L., Williams, A., Rasmussen, P., & Halappanavar, S. (2023). Toxicity of Metal Oxide Nanoparticles: Looking through the Lens of Toxicogenomics. *International journal of molecular sciences*, *25*(1), 529. **https://doi.org/10.3390/ijms25010529**.

Authorship: Andrey Boyadzhiev[1,2], Dongmei Wu[1], Mary-Luyza Avramescu[1], Andrew Williams[1], Pat Rasmussen[1,3], Sabina Halappanavar[1,2]

Affiliation:
1: Environmental Health Science and Research Bureau, Health Canada, Ottawa, Canada
2: Department of Biology, University of Ottawa, Ottawa, Canada
3: Earth and Environmental Sciences Department, University of Ottawa, Ottawa, Canada

Contributions:

Experimental Design	**Andrey Boyadzhiev** Andrew Williams (Microarray random design) Sabina Halappanavar (Toxicology experiments) Pat Rasmussen (Dissolution testing)
Particle Suspension and Characterization	Mary-Luyza Avramescu
Electron Microscopy Imaging	University of Ottawa Material Characterization Core
Dissolution Testing	Mary-Luyza Avramescu
Exposure	**Andrey Boyadzhiev** Dongmei Wu
Trypan Blue Analysis	**Andrey Boyadzhiev** Dongmei Wu
RNA Extraction and Quantification	Dongmei Wu
Microarray Experiments	**Andrey Boyadzhiev**
Microarray Bioinformatics	Andrew Williams
Other Statistical Analysis	**Andrey Boyadzhiev**
Pathway Analysis	**Andrey Boyadzhiev**
Benchmark Concentration Modelling	**Andrey Boyadzhiev**
Data Interpretation	**Andrey Boyadzhiev** Sabina Halappanavar
Manuscript Writing and Revisions	**Andrey Boyadzhiev** Sabina Halappanavar
Internal Review	Luna Rahman Silvia Solorio Rodriguez

3.1 Abstract

The impact of solubility on the toxicity of metal oxide nanoparticles (MONPs) requires further exploration to ascertain the impact of the dissolved and particulate species on response. In this study, FE1 mouse lung epithelial cells were exposed for 2–48 h to 4 MONPs of varying solubility: zinc oxide, nickel oxide, aluminum oxide, and titanium dioxide, in addition to microparticle analogues and metal chloride equivalents. Previously published data from FE1 cells exposed for 2–48 h to copper oxide and copper chloride were examined in the context of exposures in the present study. Viability was assessed using Trypan Blue staining and transcriptomic responses via microarray analysis. Results indicate material solubility is not the sole property governing MONP toxicity. Transcriptional signaling through the 'HIF1α Signaling' pathway describes the response to hypoxia, which also includes genes associated with processes such as oxidative stress and unfolded protein responses and represents a conserved response across all MONPs tested. The number of differentially expressed genes (DEGs) in this pathway correlated with apical toxicity, and a panel of the top ten ranked DEGs was constructed (*Hmox1, Hspa1a, Hspa1b, Mmp10, Adm, Serpine1, Slc2a1, Egln1, Rasd1, Hk2*), highlighting mechanistic differences among tested MONPs. The HIF1α pathway is proposed as a biomarker of MONP exposure and toxicity that can help prioritize MONPs for further evaluation and guide specific testing strategies.

3.2 Introduction

Engineered metal oxide nanoparticles (MONPs) are increasingly investigated for their applications in engineering and biomedical fields due to their attractive physicochemical properties. MONPs have been used in the production of electronics, energy generation and catalysis, biomedicine, and have even seen incorporation into personal care products and foods (Bischoff et al., 2020; Hassanpour et al., 2018; Solano et al., 2021). Market research indicated that the global MONP market was valued at 0.9 billion USD in 2021 and is expected to double in value by 2030 (A.M Research). This has resulted in an increased risk of human exposure to these materials in occupational settings, including through the pulmonary system when handling the dry material or via the processing of

MONP-containing products (A.M Research; Basinas et al., 2018; Schulte et al., 2019a). However, the human health impacts of exposure to these materials are not entirely understood.

Epidemiological or cohort studies focusing on human pulmonary exposure to engineered MONPs to date are few, but a handful of studies have shown that workers involved in the manufacturing of titanium dioxide (TiO_2) and human volunteers exposed to engineered zinc oxide (ZnO) nanoparticles (NPs) present elevated levels of markers of cardiopulmonary and systemic toxicity, respectively (Schulte et al., 2019a). For workers employed in TiO_2 NP manufacturing facilities, elevated levels of leukotrienes (markers of inflammation) in exhaled breath condensate were shown to be positively associated with exposure to TiO_2 NPs (Pelclova et al., 2016; Pelclova, D. et al., 2015). In another study, in a Chinese TiO_2 manufacturing plant, where 39% of the airborne particle fraction was nanoscale, increased levels of surfactant protein D (SP-D, a marker of inflammation), superoxide dismutase and malondialdehyde (indicative of oxidative stress), and pro-inflammatory markers interleukin-6 and interleukin-1β were observed in the serum of exposed workers (Zhao, L. et al., 2018). With respect to ZnO exposure, human volunteers exposed to 0.5–2 mg/m^3 ZnO NPs (primary particle size of 10 nm) via inhalation resulted in symptoms of systemic toxicity known as metal fume fever, including elevated body temperature and elevated levels of acute phase proteins and neutrophils in the serum (Monsé et al., 2018). Systemic symptoms of toxicity became clear at and above 1 mg/m^3 ZnO NPs, which is below international workplace exposure limits for respirable ZnO dust (available through the GESTIS—Substance Database, **https://limitvalue.ifa.dguv.de/**, accessed on 1 October 2023).

Activities such as welding can lead to the generation of incidental MONPs. Welding fumes have been classified as Group 1 carcinogens by the International Agency for Research on Cancer, based on evidence presented in over 30 occupational and population cohort studies showing an increased risk of lung cancer in welders and workers exposed to welding fumes (Guha et al., 2017). The composition of welding fumes is heterogeneous, but research has shown that MONPs are present within lesions found in the lungs of welders

and are at least partially responsible for the lung pathologies reported in these individuals (Andujar et al., 2014). While limited in scope, the above studies show that there is a human health risk associated with pulmonary exposure to MONPs and that the potential toxicity is not the same across MONP types.

In both animal and cell model systems, exposure to MONPs is shown to result in varying degrees of toxicity (recently reviewed in (Bi et al., 2023; Chang, H. et al., 2022; Czyżowska & Barbasz, 2022; Naz et al., 2020; Sengul & Asmatulu, 2020; Solano et al., 2021; Vassal et al., 2021; Wang, Z. & Tang, 2021)). For example, C57BL/6 mice exposed to low and moderate doses of insoluble TiO_2 NPs via single intratracheal instillation developed an acute inflammatory response 24 h post-exposure, which was resolved by the 28 day post-exposure timepoint (Halappanavar, S. et al., 2015), whereas single intratracheal instillation of high doses of TiO_2 NPs in C57BL/6 mice resulted in a subtle fibrotic response 90 days post-exposure (Rahman, L. et al., 2017b). Acute inflammation is also a hallmark of pulmonary exposure to soluble MONPs such as ZnO and copper oxide (CuO), which have been shown to proceed to fibrotic or emphysemic outcomes depending on the model organism, method of exposure employed, and duration of exposure. In rats exposed via nose-only inhalation to CuO NPs, acute lung inflammation, emphysema, and gene expression changes related to inflammation were noted one day post-exposure, which mostly resolved after a 22 day recovery period (Costa et al., 2018; Gosens et al., 2016). On the contrary, intranasal administration of CuO NPs in C57BL/6 mice resulted in a fibrotic outcome 21 days post-exposure (Lai et al., 2018), which was also observed following intratracheal instillation of ZnO NPs in C57BL/6 mice 2 months post-exposure (Jacobsen et al., 2015).

In cell model systems, cytotoxicity and oxidative stress have been commonly reported after exposure to MONPs, with soluble MONPs generally presenting stronger responses compared to insoluble or poorly soluble MONPs (Ivask et al., 2015; Titma et al., 2016; Zhang, Haiyuan et al., 2012). *In vitro* mechanistic research has shown that MONPs exert their toxicity through (1) the production of reactive oxygen species (ROS), (2) particle dissolution and subsequent metal ion toxicity, and (3) direct interaction between the MONP and cellular components such as membranes or organelles (Bi et al., 2023; Hou et al., 2019;

Martin & Sarkar, 2017; Wang, Z. & Tang, 2021). These mechanisms can then lead to DNA damage, homeostasis disruption, organelle damage, pro-inflammatory signaling, and calcium signaling alterations. The specific mechanisms and severity of adverse outcomes are influenced by the physicochemical properties of the MONPs, one of the most important of which is particle solubility in biological environments.

Previous research has shown that MONP dissolution is a function of time, particle concentration, particle size, chemical composition, and the solvent medium (Avramescu et al., 2020, 2022). Due to the time-dependent nature of dissolution, the toxicity of soluble MONPs is a function of both the particulate and dissolved species, whereas MONPs with negligible solubility induce toxicity through interactions with the particle surface. A knowledge gap exists, however, concerning the contribution of the dissolved and particulate species to response over timepoints relevant to MONP dissolution. It is also not completely understood if soluble, poorly soluble, and insoluble MONPs act via similar toxicity mechanisms. Toxicogenomics (the application of genomics technologies to study adverse effects of exposure to substances) tools are particularly well suited for filling this data gap, as they provide mechanistic toxicity information through the analysis of the proteome, genome, or transcriptome of a model system. Recently, using *in vitro* global transcriptional analysis and cytotoxicity monitoring, Boyadzhiev et al., 2021 demonstrated that, for CuO NPs showing moderate solubility in cell culture medium, the toxicity is potentiated by the particle size, even though apical and molecular responses may be qualitatively similar between NP and dissolved Cu exposures (Boyadzhiev et al., 2021). Furthermore, the same authors recently examined the DNA damage potential of ZnO, CuO, and TiO_2 NPs, associated microparticles (MPs), and metal chloride salts and showed that ZnO NPs and MPs behaved similarly to dissolved Zn with respect to DNA damage induction, whereas significant differences were observed between CuO forms, with only NPs inducing DNA damage compared to MPs or dissolved Cu (Boyadzhiev et al., 2022). For the TiO_2 NPs of negligible solubility tested, silica and silica-alumina coatings and a rutile crystal structure potentiated a muted DNA damage response. These studies showed that (1) soluble MONPs can induce pronounced cytotoxic, transcriptional, and genotoxic

responses, but the relative influence of the dissolved and particulate species is chemical compound dependent, and (2) the surface chemistry of MONPs exhibiting negligible solubility is important to their response. Additional research is necessary to ascertain whether these observations hold true for MONPs in a broader sense, in which case prioritization and grouping strategies for nanomaterial risk assessment may be expedited.

The first objective of the present study was to characterize and compare mechanisms of toxicity induced by MONPs of varying solubility in lung epithelial cells, with the goal of defining shared and distinct response mechanisms. The second objective of this study was to determine the impact of the dissolved and particle fractions on MONP induced toxicity, and the impact of nanoscale size on response. To accomplish these objectives, mouse lung epithelial cells (FE1) were exposed to ZnO, nickel oxide (NiO), aluminum oxide (Al_2O_3), and TiO_2 MONPs with varying solubility in cell culture medium, as well as metal chloride and bulk (metal oxide microparticle; MOMP) analogues for 2–48 h. Cytotoxicity and global transcriptional changes were assessed via Trypan Blue staining and microarray analysis, respectively. Benchmark concentration (BMC) modeling was used to delineate differences in potency between the MONPs and their different forms. Previously published viability and transcriptomic responses of CuO NPs, MPs, and $CuCl_2$ from (Boyadzhiev et al., 2021), were used for comparison with the results of the present study.

3.3 Methods

3.3.1 Nanoparticles, microparticles, and metal chlorides

A total of 4 MONPs, 4 MOMPs, and 3 metal chloride salts were used to probe the impact of solubility over time on the toxicity of MONPs, with the Cu materials assessed in (Boyadzhiev et al., 2021) used for comparison (**Table 3-1**). All nanoparticles were purchased commercially and selected to have a pristine surface without coatings or functionalizations and similar manufacturer-reported primary particle sizes (<50 nm). The microparticles were also commercially procured and selected to have a reported mean primary particle

size range of around 1 µm. In certain cases where particles of approximately 1 µm were not available, larger particles with a reported size of 5 µm were purchased.

Table 3-1. Nanoparticles, microparticles, and metal chlorides used for toxicity investigation in this study. NP: nanoparticle. MP: microparticle. PPS: primary particle size. SSA: specific surface area. N/A: not available.

Metal	Material	Catalogue Number (Manufacturer)	PPS [a] [nm]	SSA (Average) [m^2/g]
Zn	ZnO NP	US3580 (US Research Nanomaterials Inc., Houston, TX, USA)	35–45	35 [b]
	ZnO MP	US1003M (US Research Nanomaterials Inc., Houston, TX, USA)	1000	2–15.8 (8.9) [a]
	$ZnCl_2$	Z0152-100G (Sigma Aldrich, Oakville, ON, Canada)		
Ni	NiO NP	US3355 (US Research Nanomaterials Inc., Houston, TX, USA)	15–35	38.7 [c]
	NiO MP	US1014M (US Research Nanomaterials Inc., Houston, TX, USA)	5000	5–20 (12.5) [a]
	$NiCl_2 \bullet 6H_2O$	N6136-100G (Sigma Aldrich, Oakville, ON, Canada)	$NiCl_2 \bullet 6H_2O$	N6136-100G (Sigma Aldrich, Oakville, ON, Canada)
Al	Al_2O_3 NP	544833 (Sigma Aldrich, Oakville, ON, Canada)	<50	129 [b]
	Al_2O_3 MP	1331DL (Sky Spring Nanomaterials Inc., Houston, TX, USA)	400–1500	110

	$AlCl_3 \bullet 6H_2O$	A0718-500G (Sigma Aldrich, Oakville, ON, Canada)		
Ti	TiO_2 NP	NIST 1898 (National Institute of Standards and Technology, Gaithersburg, MD, USA)	19 nm (Anatase) 37 nm (Rutile)	55.5 [a]
	TiO_2 MP	US1017M (US Research Nanomaterials Inc., Houston, TX, USA)	1500	5–8 (6.5) [a]
Cu [d]	CuO NP	544868 (Sigma Aldrich, Oakville, ON, Canada)	<50	4.6 [b]
	CuO MP	US1140M (US Research Nanomaterials Inc., Houston, TX, USA)	5000	4–6 (5) [a]
	$CuCl_2 \bullet 2H_2O$	C3279-100G (Sigma Aldrich, Oakville, ON, Canada)		

[a] Manufacturer provided. [b] Data from (Bushell et al., 2020). [c] Data from (Kunc et al., 2022). [d] Material evaluated in (Boyadzhiev et al., 2021)

3.3.2 Cell culture

The immortalized mouse alveolar epithelial cell line, FE1, was utilized for toxicity testing in this study. These cells retain characteristics of both type I and type II alveolar epithelial cells with a doubling time of 18.7 ± 2 h (Berndt-Weis et al., 2009; White et al., 2003) and used for genotoxicity testing and global response characterization of both nanomaterials and chemicals (Boyadzhiev et al., 2022; Maertens et al., 2017; OECD, 2015).

FE1 cells were maintained in phenol-red-containing DMEM/F12 medium (DMEM/F12 (1:1); Cat#: 11320-033, Life Technologies, Burlington, ON, Canada), with 2% fetal bovine serum (FBS; Cat#: 12483-020, Life Technologies, Burlington, ON, Canada), 1 ng/mL of human epidermal growth factor (Cat#: PHG0311, Life Technologies, Burlington, ON, Canada), 100 U/mL of penicillin G, and 100 µg/mL of streptomycin (Cat#: 15140-122, Life Technologies, Burlington, ON, Canada), in a climatized incubator (37 °C, 5% CO_2). For exposures, phenol-red-free medium was used (Cat#: 21041-025, Life Technologies, Burlington, ON, Canada).

3.3.3 Particle characterization

To assess the particle size of the Al_2O_3 and NiO NPs and the morphology of the Al_2O_3 and NiO MPs, transmission electron microscopy (TEM) and scanning electron microscopy (SEM) imaging were respectively employed. For Al_2O_3 and NiO NPs, a JEM-2100F Field Emission TEM (JEOL Ltd., Peabody, MA, USA) was used to collect 10 non-overlapping micrographs of the dry particles. From each image, the length and width of 9–20 well-defined particles were measured for a total of 100–200 particles per MONP. The size distributions of each of the particles were plotted as histograms in SigmaPlot 12.5 (Systat Software Inc., San Jose, CA, USA), and the mean length and width were reported with a standard deviation, along with the aspect ratio. With respect to Al_2O_3 and NiO MPs, a JSM-7500F Field Emission SEM (JEOL Ltd., Peabody, MA, USA) was used to collect 10 non-overlapping micrographs of the dry particles. For ZnO and TiO_2 materials investigated here, TEM and SEM analyses were conducted and described in (Boyadzhiev et al., 2022).

Particle size and zeta potential of each MONP suspension were carried out using dynamic light scattering (DLS) and electrophoretic light scattering (ELS) as described in (Boyadzhiev et al., 2021). MONP stock suspensions in UltraPureTM DNase/RNase-Free distilled water (dH_2O) (Cat#: 10977015, Life Technologies, Burlington, ON, Canada; 5 mg/mL, details in section 3.3.4) were diluted to 50 µg/mL in phenol red-free DMEM/F12 (1:1) medium + 2% FBS (described in 3.3.2), and aliquots were analyzed by DLS/ELS using a Zetasizer Nano ZSP (Malvern Panalytical, Westborough, MA, USA). Mean hydrodynamic diameter (Dh, nm; as a measure of aggregate size) and PDI, as well as zeta potential (ZP, mV: a measure of the surface charge of the particles), were determined for each aliquot. Each measurement was conducted in triplicate for the calculation of the mean and standard deviation.

3.3.4 Preparation of stock particle suspensions and metal chloride solutions

Stock dispersions of MONPs and MOMPs were prepared at 5 mg/mL in dH_2O. The suspensions were sonicated using a Branson Digital Ultrasonics Sonifier™ SFX550 (Branson Ultrasonics, Brookfield, CT, USA) equipped with a half inch disruptor horn probe with an extension and removable flat tip according to procedures described in (Avramescu et al., 2019, 2022). The sonicated particle stock dispersions in water were diluted in phenol-red-free cell culture medium to 0.5–100 µg/mL concentrations and subsequently used for exposures. For the metal chloride exposure series, all compounds were first dissolved in dH_2O at stock concentrations of 1–5 mg/mL and subsequently diluted in phenol-red-free cell culture medium for cell exposures.

3.3.5 Concentration selection

The exposure concentrations of MONPs, MOMPs, and metal chlorides used in this study are provided in **Table 3-2**. Multiple metrics are included to allow for intercomparison between the materials. The average specific surface area (SSA) from the range provided by the manufacturer was used to calculate the SSA-based concentration of MOMPs. With respect to ZnO NPs, concentrations in the 0–25 µg/mL range were initially selected based on 48 h toxicity reported in other lung epithelial cell lines such as A549 and BEAS-2B, which show high levels of cytotoxicity above this range (Lai et al., 2015; Tolliver et al., 2020). The NiO

and Al_2O_3 NP exposure concentrations ranged from 0–50 µg/mL, while for TiO_2 NPs, concentrations in the 0–100 µg/mL range were selected due to the lower cytotoxicity generally reported using this material. For each metal oxide, equivalent concentrations of MOMPs were used.

With respect to concentrations used for each of the metal chloride exposures, selection was based on the 48 h dissolution of the MONP in acellular conditions within cell culture medium (Avramescu et al., 2020, 2022), with the aim of recapitulating the level of dissolved metal ions as an estimate of extracellular particle dissolution. In the context of ZnO NPs, particles display 95% dissolution at 10 µg/mL, and the concentrations of $ZnCl_2$ used correspond to 100% particle dissolution. With respect to both NiO and Al_2O_3 NPs, 48 h dissolution was ~1% in cell culture medium, and the lowest concentrations used for $NiCl_2$ (1.6 µg/mL) and $AlCl_3$ (2.37 µg/mL) correspond to a 1% dissolution of 50 µg/mL of NPs. With respect to Al_2O_3 NPs, it is worth noting that analyte loss was reported in $AlCl_3$ control experiments, and so the 1% solubility represents 'apparent solubility' based on the fraction of Al that is not matrix bound (Avramescu et al., 2022). The upper concentrations of 40 and 80 µg/mL for $NiCl_2$ and 47 and 118 µg/mL for $AlCl_3$ represent higher levels of solubility with equivalency to particle concentrations (**Table 3-2**). Due to the insoluble nature of TiO_2 NPs, no dissolved metal equivalent was used for this particle type.

Table 3-2. Summary of FE1 exposure concentrations for each of the 4 different types of metal oxides and 3 metal chlorides assessed, in addition to Cu materials previously examined. MO: metal oxide. MONP: metal oxide nanoparticle. MOMP: metal oxide microparticle. MeCl: metal chloride. Me: Metal. (-): particle of metal chloride concentration not assessed. N/A: not applicable/available.

Metal	Concentration [µg/mL MO]	Concentration [cm^2/mL MONP]	Concentration [cm^2/mL MOMP]	Concentration [µg/mL MeCl]	Concentration [µg/mL Me]	Concentration [µM Me]
Zn	5.00	1.75	0.45	8.50	4.00	61.44
	(-)	(-)	(-)	5.10	2.45	37.42
	1.00	0.35	0.09	1.70	0.80	12.29
	0.50	0.18	0.04	(-)	0.40	6.14
Ni	50.00	19.35	6.25	(-)	40.00	669.41
	25.00	9.68	3.13	80.00	20.00	334.70
	(-)	(-)	(-)	40.00	10.00	167.40
	10.00	3.87	1.25	(-)	8.00	133.88
	5.00	1.94	0.63	(-)	4.00	66.94
	(-)	(-)	(-)	1.60 [a]	0.40	6.69
Al	50.00	64.50	N/A	(-)	26.50	980.78
	25.00	32.25	N/A	118.00	13.25	490.39
	10.00	12.90	N/A	47.00	5.30	196.16
	5.00	6.45	N/A	(-)	2.65	98.08
	(-)	(-)	(-)	2.37 [b]	0.27	9.81
Ti	100.00	55.50	6.50	N/A	60.00	1252.10
	50.00	27.75	3.25	N/A	30.00	626.05
	25.00	13.88	1.63	N/A	15.00	313.02
	10.00	5.55	0.65	N/A	6.00	125.20
Cu	25.00	1.15	1.25	54.00	20.00	314.29
	10.00	0.46	0.50	(-)	8.00	125.72
	5.00	0.23	0.25	(-)	4.00	62.86
	(-)	(-)	(-)	7.00 [c]	2.60	41.06
	1.00	0.05	0.05	(-)	0.80	12.57

[a] Represents the expected amount of dissolved Ni based on the 1% dissolution of 50 µg/mL NiO NPs at 48 h (Avramescu et al., 2020). [b] Represents the expected amount of dissolved Al based on the 1% dissolution of 50 µg/mL Al_2O_3 NPs at 48 h (Avramescu et al., 2022). [c] Represents 2.64 times the expected amount of dissolved Cu from 10 µg/mL CuO NPs at 48 h (Boyadzhiev et al., 2021)

3.3.6 Cell exposures, phase contrast imaging, and sample collection

Cellular exposures to MONP, MOMP, and metal chlorides were conducted in 3–4 biological replicates under submerged culture conditions. The day preceding exposures, cells were seeded at a density of 130,000 cells / well in 6-well plates and incubated overnight (37 °C, 5% CO_2). The next day, cells of ~20% confluence were exposed to 3–4 concentrations of ZnO, NiO, Al_2O_3, and TiO_2 MONPs, MOMPs, and metal chlorides in cell culture medium (**Table 3-2**). For all experiments, an unexposed blank medium served as a negative control. After 2, 24, and 48 h of exposure, the medium from each sample was removed, cells were washed with 0.5 mL of PBS, and phase contrast images were acquired using an EVOS XL microscope (Thermofisher Scientific, Waltham, MA, USA). The cells were then dissociated with 0.25% trypsin-EDTA (Cat#: 25200-056, Life Technologies, Burlington, ON, Canada) and resuspended in fresh phenol-red-free cell culture medium. An aliquot from each suspension was used for Trypan Blue exclusion staining. The remaining suspensions were pelleted (8000 rpm, 10 min, 4 °C), resuspended in 0.5 mL PBS, pelleted again (8000 rpm, 10 min, 4 °C), and then frozen at −80 °C for downstream analysis.

3.3.7 Trypan Blue exclusion staining

Trypan Blue exclusion staining was performed as described in (Boyadzhiev et al., 2021), and (Boyadzhiev et al., 2022), with some modifications. In brief, for each sample, 10 µL of cell suspension was combined with 10 µL of trypan blue dye (Cat#: 15250-061, Life Technologies, Burlington, ON, Canada) and incubated at room temperature for 5–10 min. The mixtures were then loaded onto a hemocytometer for manual white (viable) and blue (non-viable) cell counting. The percent viability was calculated as the ratio of white and blue cells in a sample. All data were arcsine normalized via the equation arcsine (%viability/100). Statistically significant differences compared to time-matched medium controls were determined through a two-way ANOVA with a Dunnett's post-hoc in SigmaPlot 12.5 (Systat Software Inc., San Jose, CA, USA).

A second metric was calculated based on the density of viable cells for MONP, MOMP, and metal chloride-exposed samples compared against the density of viable cells for time-matched medium controls:

percent viable cell density =
density_of_viable_cells_SAMPLE/density_of_viable_cells_MEDIUM)*100.

This metric takes into account differences in cell density at harvest between exposed and control cells. For this calculation, the viability data from (Boyadzhiev et al., 2021) were included for comparison with the other examined metal oxides. The square root normalized densities of viable cells for MONP, MOMP, and metal chloride-exposed samples were compared in SigmaPlot 12.5 (Systat Software Inc., San Jose, CA, USA) against the square root normalized density of viable cells for time-matched medium controls using a two-way ANOVA with a Dunnett's post-hoc in the case of a significant difference.

3.3.8 RNA extraction, purification, and integrity analysis

Frozen FE1 cell pellets harvested from 2–48 h MONP, MOMP, and metal chloride exposures to 2–48 h were lysed using TRIzol (Cat#: 15596026, Invitrogen, Burlington, ON, Canada), and then RNA was extracted and purified using the Direct-zol RNA miniprep kits (Cat#: R2052, Zymo Research, Irvine, CA, USA) according to the manufacturer's protocol. The RNA concentration was measured using a NanoDrop One spectrophotometer (Thermofisher Scientific, Waltham, MA, USA), while RNA integrity was assessed using both an Agilent 2100 BioAnalyzer (Agilent Technologies, Inc., Santa Clara, CA, USA) and an Agilent 4200 Tapestation System (Agilent Technologies, Inc., Santa Clara, CA, USA) according to the manufacturer's instructions. All extracted samples that showed RNA integrity numbers >6.5 were used for gene expression analysis.

3.3.9 Microarray hybridization

Microarray hybridization was conducted as described in (Boyadzhiev et al., 2021). A randomized block design was used for each sample group (Kerr & Churchill, 2001). For each sample, 200 ng of purified RNA as well as 200 ng of universal mouse reference RNA were reverse transcribed into cDNA, which was subsequently transcribed into cyanine 5-CTP-labeled (sample) and cyanine 3-CTP-labeled (reference) cRNA. Next, 300 ng of cyanine 5-CTP-labeled sample RNA and 300 ng of cyanine 3-CTP-labeled reference were mixed and hybridized onto 8 × 60K Agilent SurePrint G3 Mouse Gene Expression v2 Microarray slides

(Agilent Technologies, Inc., Santa Clara, CA, USA) in a hybridization oven for 17 h (65 °C, 10 rpm). The next day, slides were washed according to the manufacturer's instructions and scanned on an Agilent G4900DA Microarray Scanner and an Agilent G2505B Microarray Scanner (Agilent Technologies, Inc., Santa Clara, CA, USA). Data from the resulting images were extracted using the Agilent Feature Extraction 11.01.1 software (Agilent Technologies, Inc., Santa Clara, CA, USA).

3.3.10 Statistical analysis of microarray data

Normalization and statistical analysis of microarray data were conducted as in (Boyadzhiev et al., 2021). First, the data were normalized using the LOWESS method (locally weighted scatterplot smoothing), after which statistically significant differential gene expression was determined using a microarray analysis of variance (MAANOVA) in 'R' (Wu et al., 2003). To test for treatment effects, the Fs statistic was used, while p-values were estimated using the permutation method with adjustments made for multiple comparisons using the false discovery rate multiple testing correction (Benjamini & Hochberg, 1995). For differentially expressed genes (DEGs), the fold-change was based on the least-square means (Searle et al., 1980). Genes were considered differentially expressed if they exhibited adjusted p-values <0.05 and |fold-change| ≥1.5 (n = 2–4). The microarray datasets used in this manuscript can be found in the NCBI gene expression omnibus, under the accession number GSE246159.

3.3.11 Ingenuity Pathway Analysis

For all samples, canonical pathway analysis was conducted on the probe list (Differential expression cut-offs: p ≤0.05, |fold-change| ≥1.5) using Ingenuity Pathway Analysis (IPA) (content version 81348237, license from Qiagen). While Cu samples were analyzed using IPA in (Boyadzhiev et al., 2021) (microarray dataset available from the NCBI GEO database under accession number GSE161017), the samples were reanalyzed due to content differences between the subsequent IPA database updates in order to allow for comparative hierarchical clustering with the four metal oxides examined in this study. In addition, with respect to the ZnO MP samples, there were too many significant molecules (>8000) to conduct an enrichment using the standard cut-offs. Thus, the ZnO MP probe

lists were subdivided into 2 sets: the low fold-change set and the high fold-change set. The low list contained transcripts with fold-changes between 1.5 and 2-fold in either direction, while the high list contained all transcripts with a fold-change greater than or equal to 2 in either direction. The IPA enrichment was conducted on both lists separately. Pathways were considered to be significantly enriched if the −log(p-value) >1.3 and the total amount of DEGs was ≥3. Similarly, enriched pathways were considered to be activated if the Z-score ≥2, and inactivated if the Z-score ≤−2.

In order to identify clusters of exposure groups with similar transcriptional responses, hierarchical clustering was conducted using the z-score of significantly enriched IPA canonical pathways as the clustering metric. The z-score is a statistical measure used to define how closely the expression of DEGs in a pathway corresponds to the literature-derived gene expression patterns indicative of pathway (in)activation (Krämer et al., 2014). A value ≥2 indicated strong concordance with expected expression patterns for activation of the pathway, while values ≤−2 indicated strong negative concordance or inactivation of the pathway. Values between −2 and 2 indicated mixed signaling or no readily apparent state of activation or inactivation. For all samples where a pathway was non-significant, the z-score was adjusted to 0. This was to ensure a complete data matrix for clustering. Average linkage clustering was conducted using Cluster 3.0 (de Hoon et al., 2004), using uncentered Pearson's correlation as the similarity measure. The resulting heatmap was visualized using Treeview 1.2.0 (SALDANHA, 2004).

3.3.12 Benchmark concentration modeling

BMC modeling was conducted using both viability and microarray data. Viable cell densities (cells/cm^2) were utilized for BMC modeling of viability data using BMDS Online2 (EPA). The benchmark response factor used was hybrid extra risk, at a benchmark response of 0.5 (50% increase over control), using normal and nonconstant variance settings. In each case, the 'Viable–Recommended' model was used (EPA, 2022), unless unavailable, in which case the 'Questionable' model with the lowest AIC without model saturation and a definite BMC interval was used. BMCs were reported alongside the lower 95th percentile BMCL and the upper 95th percentile BMCU values.

Log_2 normalized fluorescence ratios from microarray experiments were input into BMDExpress2 for benchmark concentration modeling. Similar cutoffs were used as in (Rowan-Carroll et al., 2021), including pre-filtering with the Williams' Trend test with 100 permutations, a 1.5-fold-change cutoff, and an unadjusted p-value <0.05. Probes that passed this initial filter were modeled using the linear, hill, power, polynomial (2°, 3°), and exponential (2^{nd}, 3^{rd}, 4^{th}, 5^{th}) functions to determine their BMCs (benchmark response = 1 standard deviation relative to controls, confidence level = 0.95, power function restricted to ≥1, max 250 iterations, 300 s max model compute time). The resulting BMC data and probe information were exported from BMDExpress2 and further filtered in Excel. First, all probes with a best-fit p-value <0.1 and/or BMCU/BMCL ≥40 were removed. Next, probes were removed if the best BMC > the highest tested concentration. Finally, all probes without a matching entrez ID and gene symbol were removed. The final probe list was collapsed down to gene symbol level, and the best BMC, BMCL, and BMCU values were summarized by their median for genes with multiple matching probes. For the purposes of relative potency ranking, the 25^{th}-ranked gene was used as the transcriptional point of departure (tPOD).

3.4 Results

3.4.1 Exposure characterization

For CuO, ZnO, and TiO_2 NPs, TEM imaging was previously conducted (Boyadzhiev et al., 2021, 2022), and the results showed their measured particle sizes to be <50 nm. The TEM sizing of both NiO and Al_2O_3 NPs also showed mean measured particle sizes <50 nm (**Table 3-3**, **Supplementary Figure 3-1**).

Table 3-3. MONP characterization in DMEM + 2% FBS. All particles were suspended at 50 µg/mL for DLS and ELS characterization. Values in parentheses indicate ± standard deviation (n = 3–4). PPS: primary particle size [length × width]. PDI: polydispersity index.

MONP	PPS Measured (nm)	Aspect Ratio	PDI	Aggregate Size (Dh, nm)	Zeta Potential (mV)
ZnO	23.9 × 19.4 (7.2 × 5.5) [a]	1.23 (0.17) [a]	0.52 (0.05)	346 (46)	−9.5 (0.1)
NiO	27.3 × 21.9 (10.3 × 7.91)	1.25 (0.20)	0.33 (0.01)	178 (7)	−12.3 (0.6)
Al_2O_3	23.9 × 10.7 (11.8 × 6.86)	2.63 (1.40)	0.44 (0.01)	276 (16)	−12.2 (0.2)
TiO_2	26.8 × 20.8 (8.9 × 6.8) [a]	1.30 (0.26) [a]	0.23 (0.06)	421 (31)	−11.5 (0.2)
CuO	64.8 × 45.9 (47 × 28) [b]	1.39 (0.39) [a]	0.174 (0.009) [b]	182 (1.4) [b]	−10.8 (0.5) [b]

[a] Data from (Boyadzhiev et al., 2022). [b] Data from (Boyadzhiev et al., 2021).

The aspect ratio of the measured particles showed that four out of five MONPs had a spherical morphology, while Al_2O_3 NPs exhibited a rod-like morphology (**Table 3-3**). DLS and ELS analyses showed that mean aggregate sizes did not exceed 450 nm, and all particle suspensions presented a negative surface charge in cell culture medium based on zeta potential (**Table 3-3**). With respect to the distribution of aggregate sizes, the polydispersity index (PDI) ranged from 0.23 (TiO_2 NPs) to 0.52 (ZnO NPs), with the CuO NPs previously examined producing the most monodisperse suspension with a PDI of 0.174 (**Table 3-3**).

With respect to MOMPs, SEM images showed a roughly spherical morphology for NiO and Al_2O_3 MPs (**Supplementary Figure 3-2**), which was also reported for CuO and TiO_2 MPs, while ZnO MPs had a fraction of rod-shaped particles present (Boyadzhiev et al., 2021, 2022). Particles under 100 nm in size could be seen within aggregates of NiO MPs (**Supplementary Figure 3-2**), as well as for ZnO and TiO_2 MPs (Boyadzhiev et al., 2022).

For the metal chloride solutions, both $ZnCl_2$ and $NiCl_2$ were soluble in cell culture medium, but not $AlCl_3$, which was soluble in water but immediately formed a precipitate in cell culture medium (**Supplementary Figure 3-3**).

Dissolution testing for all relevant MONPs and MOMPs was carried out by (Avramescu et al., 2020) and (Avramescu et al., 2022), the results of which were used to inform the toxicity testing conducted in the present study (**Supplementary Table 3-1**). MONPs were grouped as negligible (<1% dissolved), low (1–10% dissolved), moderate (10–70% dissolved), or highly soluble (>70% dissolved) according to (Avramescu et al., 2022), which was based on criteria reported in ENV/JM/MONO (2015) (OECD, 2015). In cell culture medium, at a low initial concentration of 10 µg/mL, % dissolution varied in the following order: ZnO NPs (94.5%, high), CuO NPs (12.6%, moderate), Al_2O_3 NPs (1.11%, low), and negligible for NiO NPs and TiO_2 NPs (0.94% and 0.17%, respectively). At a high initial concentration of 100 µg/mL, % dissolution was moderate for ZnO NPs (19.3%) and CuO NPs (51.6%), low for NiO NPs (1.81%), and negligible for Al_2O_3 NPs and TiO_2 NPs (0.73% and 0.045%, respectively). For bulk MOMP analogues at 100 µg/mL, dissolution varied from moderate for ZnO MPs (11.8%), to low for CuO MPs (1.51%), and negligible for NiO, Al_2O_3, and TiO_2 NPs (<0.07%).

3.4.2 Trypan Blue viability analysis

Cytotoxicity following exposure to the four MONPs, MOMPs, and three metal chlorides was assessed using the Trypan Blue exclusion method (**Supplementary Figure 3-4**). In general, the observed response was concentration-dependent for all compounds that induced a reduction in cell viability.

At the 2 h post-exposure timepoint, NiO NPs significantly reduced percent viability down to 74, 74, and 70% at 10, 25, and 50 µg/mL concentrations. A small but significant reduction in viability, down to 90 and 85% at 25 and 50 µg/mL, respectively, was seen in cells exposed to Al_2O_3 NPs. Similarly, for TiO_2 NPs, a significant reduction in viability down to 88% was observed after exposure to 100 µg/mL. No other exposures at the 2 h timepoint resulted in a significant percent viability reduction.

At the 24 h timepoint, 5 µg/mL of ZnO NPs, MPs, and 8.5 µg/mL $ZnCl_2$ resulted in a significant reduction in percent viability down to 77, 72, and 90%, respectively. A significant reduction in percent viability (74%) was observed in cells exposed to 80 µg/mL $NiCl_2$. NiO

NPs presented a non-significant decrease in viability, from 78–74% after exposure to 5–50 µg/mL concentrations, compared to matched controls, which also showed cytotoxicity (85% viability). With respect to Al materials, 25 and 50 µg/mL Al_2O_3 NPs significantly reduced viability down to 87 and 82%, respectively, while Al_2O_3 MPs and $AlCl_3$ did not affect cell viability. Lastly, for TiO_2 NPs, small but significant reductions in percent viability were seen after exposure to 25 and 100 µg/mL (89%, 85%) but not after exposure to 50 µg/mL (91%). Cells exposed to TiO_2 MPs did not show any change in viability at this timepoint.

At 48 h post-exposure, 5 µg/mL of ZnO NPs, MPs, and 8.5 µg/mL $ZnCl_2$ significantly reduced viability down to 71%, 52%, and 82%, respectively. Both $NiCl_2$ and NiO NPs induced significant reductions in percent viability down to 67 and 45% after exposure to 40 and 80 µg/mL $NiCl_2$, and 74 and 52% after exposure to 25 and 50 µg/mL NiO NPs, with no response for NiO MP-exposed cells. Response to Al forms was the same as the 24 h timepoint, with 25–50 µg/mL NPs resulting in a significant reduction in percent viability down to 88–86%, and with no response seen with respect to Al_2O_3 MPs and $AlCl_3$. Finally, exposure to 50–100 µg/mL TiO_2 NPs resulted in a significant reduction in viability to 85–83%, with no response seen for TiO_2 MPs.

In addition to percent viability, the differences in the density of viable cells for exposed and time-matched medium controls were computed (**Figure 3-1**). For comparative purposes, the viability data pertaining to FE1 cells exposed for 2–48 h to CuO NPs, MPs, and $CuCl_2$ reported in (Boyadzhiev et al., 2021) was analyzed alongside the four metal oxides investigated in this study.

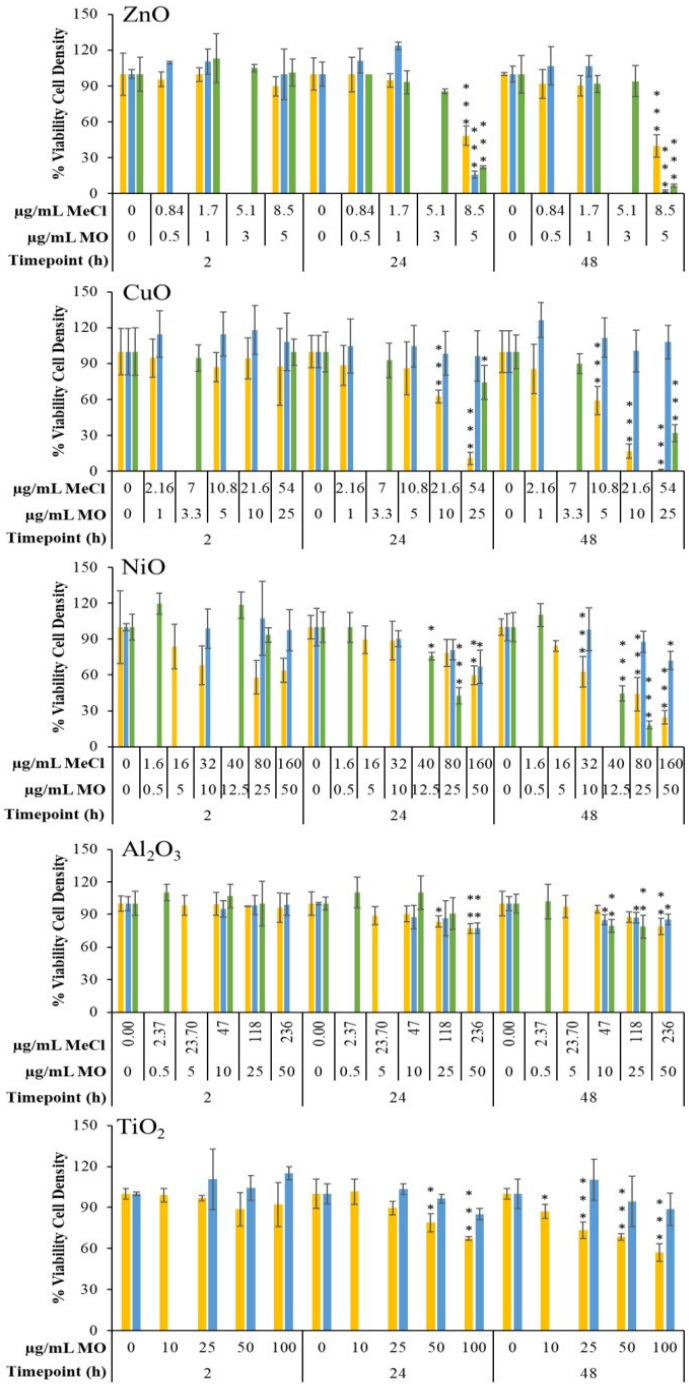

Figure 3-1. Percent viable cell density of FE1 cells following 2, 24, and 48 h of exposure to MONPs, MOMPs, and metal chlorides compared to time-matched medium controls. Error bars indicate the standard deviation (n = 3–4). Graphs were labeled based on the type of metal oxide. Yellow: MONPs. Blue: MOMPs. Green: metal chloride salts. MO: metal oxide. MeCl: metal chloride. Statistical significance against time-matched medium controls was determined through a 2-way ANOVA with a Dunnett's post-hoc. *: $p < 0.05$. **; $p < 0.01$. ***; $p < 0.001$.

At the 2 h timepoint, no significant differences in the density of viable cells were seen, although NiO NP-exposed cells showed decreases in percent viable cell density vs. medium control with 84, 68, 57, and 64% at 5–50 µg/mL concentrations.

At the 24 h timepoint, 5 µg/mL of ZnO NPs, MPs, and 8.5 µg/mL of $ZnCl_2$ resulted in significant reductions in viable cell density down to 48%, 16%, and 22% of the time-matched medium control, respectively. For Cu materials previously investigated, cells exposed to 10 and 25 µg/mL NPs showed a significant reduction in the density of viable cells down to 62% and 10% of the medium control, respectively, whereas cells exposed to 54 µg/mL $CuCl_2$ significantly reduced viable cell density to 74%, with no response seen for CuO MPs. For cells exposed to Ni materials, a 50 µg/mL concentration of NiO NPs and MPs resulted in significant reductions in viable cell density (60% and 67% of medium control for NPs and MPs, respectively), while 40 and 80 µg/mL $NiCl_2$ resulted in significant reductions down to 76% and 42%, respectively. Exposure to Al materials at the 24 h timepoint resulted in reductions in viable cell density down to 83 and 77% of time-matched medium control for 25 and 50 µg/mL NPs and 77% for 50 µg/mL MPs, with no difference seen with respect to $AlCl_3$. Finally, for TiO_2 particles, exposure to 50 and 100 µg/mL of NPs significantly reduced the viable cell density down to 79% and 67% of the medium control in a concentration-dependent manner, while MPs did not have an impact.

At the 48 h timepoint, 5 µg/mL ZnO NPs, MPs, and 8.5 µg/mL $ZnCl_2$ resulted in significant reductions in the density of viable cells (40%, 2%, and 6% of time-matched medium controls, respectively). For Cu materials previously investigated, significant reductions in viable cell density were noted down to 59, 7, and 1% of the medium control for 5–25 µg/mL concentrations, while the 54 µg/mL concentration of $CuCl_2$ significantly reduced viable cell density to 31% of the medium control, with CuO MPs not affecting response at any tested concentration. For cells exposed to Ni materials, 10–50 µg/mL of NiO NPs significantly reduced the viable cell density to 63, 44, and 24% of the medium control, as did 50 µg/mL of NiO MPs (72%), while $NiCl_2$ significantly reduced the viable cell density to 45 and 18% of the medium control at 40–80 µg/mL. With respect to Al materials, 50 µg/mL of Al_2O_3 NPs resulted in a significant reduction in viable cell density down to 79%

of the medium control, while 10, 25, and 50 µg/mL of Al_2O_3 MPs significantly reduced the viable cell density to 85, 87, and 86% of the medium control, which was not concentration-dependent, and 47–118 µg/mL of $AlCl_3$ featured a mild but significant reduction in viable cell density down to 79% for both concentrations. Lastly, for cells exposed to 10–100 µg/mL TiO_2 NPs (but not MPs), significant and concentration-dependent reductions in viable cell density to 87, 73, 69, and 57% of the time-matched medium control were noted.

3.4.3 Differentially expressed genes

All tested metal oxide and metal chloride samples presented concentration and time-dependent transcriptional responses, as assessed by the number of DEGs at each timepoint (**Figure 3-2**).

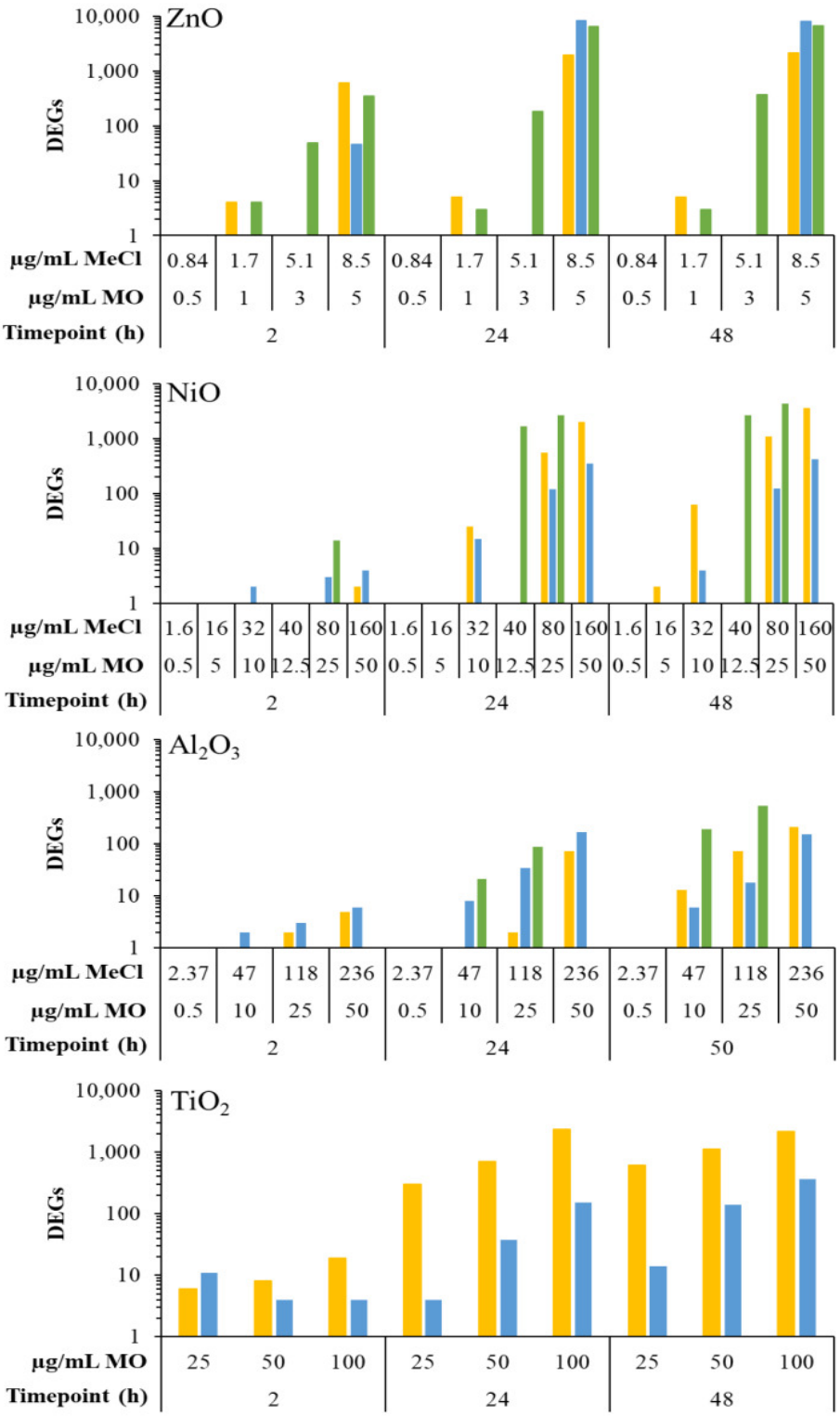

Figure 3-2. Total number of differentially expressed genes following 2–48 h exposure to MONPs, MOMPs, and metal chloride salts. Graphs were labeled based on the type of metal oxide. Yellow: MONPs. Blue: MOMPs. Green: metal chloride salts. MO: metal oxide. MeCl: metal chloride.

With respect to Zn compounds, response to all three forms began at the earliest timepoint of 2 h. There were 1, 4, and 608 DEGs at 0.5, 1, and 5 µg/mL of ZnO NPs, 46 DEGs at 5 µg/mL of ZnO MPs, and 4, 49, and 346 DEGs at 1.7, 5.1, and 8.5 µg/mL of $ZnCl_2$. At 24 h, the response increased for all three Zn forms with 1, 5, and 1942 DEGs, 0, 1, and 8367 DEGs, and 3, 184, and 6562 DEGs for ZnO NPs, MPs, and $ZnCl_2$, respectively. At 48 h post-exposure, the 0.5 and 1 µg/mL concentrations of ZnO NPs and MPs showed negligible responses, with less than 10 DEGs in each group, while the high concentration of 5 µg/mL induced 2130 and 7907 DEGs for NPs and MPs, respectively. With respect to $ZnCl_2$ at the 48 h timepoint, a concentration-dependent response was seen with 3, 371, and 6634 DEGs at 1.7, 5.1, and 8.5 µg/mL concentrations.

A strong transcriptional response was observed for Ni compounds starting at 24 h, with $NiCl_2$ inducing more DEGs than NPs or MPs. At the early timepoint of 2 h, both NiO NPs and MPs induced less than 10 DEGs, while the 80 µg/mL concentration of $NiCl_2$ induced 14 DEGs. At 24 h, a concentration-dependent response was observed for NPs, MPs, and $NiCl_2$, with 0, 25, 554, and 2048 DEGs noted for 5–50 µg/mL NPs, 15, 119, and 335 DEGs observed for 10–50 µg/mL MPs, and 0, 1699, and 2640 DEGs noted for 1.6–80 µg/mL $NiCl_2$. Similarly, an increase in DEGs was observed for NPs, MPs, and $NiCl_2$ at 48 h, with 2, 63, 1084, and 3668 DEGs for 5–50 µg/mL NPs, 4, 122, and 422 DEGs for 10–50 µg/mL MPs, and 0, 2640, and 4448 DEGs for 1.6–80 µg/mL $NiCl_2$.

The Al compounds tested induced the lowest transcriptomic responses out of the four metal oxide materials investigated in this study. At 2 h, all forms and concentrations of Al induced a negligible transcriptional response with less than 10 DEGs. At 24 h, a concentration-dependent response was seen for all three Al compounds, with 0, 2, and 72 DEGs at 10–50 µg/mL NPs, 8, 34, 169 DEGs at 10–50 µg/mL MPs, and 1, 21, 87 DEGs for 2.37–118 µg/mL $AlCl_3$ exposed cells. At 48 h there was an increase in response, with 13, 72, 211 DEGs seen for 10–50 µg/mL NPs, 6, 18, 154 DEGs noted for 10–50 µg/mL MPs and 0, 189, 537 DEGs noted for 2.37–118 µg/mL $AlCl_3$.

Finally, with respect to TiO_2 particles, NPs induced a more pronounced DEG response than MPs at all timepoints assessed. At 2 h, a subtle concentration-dependent response with 6, 8, and 19 DEGs was observed for 25, 50, and 100 µg/mL TiO_2 NPs, but not after exposure to TiO_2 MPs, which induced 11, 4, and 4 DEGs. At 24 h, the response to both NPs and MPs increased, with 298, 702, and 2299 DEGs for NPs and 4, 37, and 153 DEGs for MPs at 25, 50, and 100 µg/mL concentrations. At 48 h, the response continued to increase, with 606, 1125, and 2127 DEGs and 14, 129, and 358 DEGs noted for 25–100 µg/mL concentrations of NPs and MPs, respectively.

3.4.4 Enriched canonical pathways

The total number of enriched pathways closely followed the trends observed for DEG responses across exposure groups (**Figure 3-3**). An in-depth overview of specific enriched pathways per exposure group is provided in **Appendix II Chapter 3 Supplementary Document 1**, with a list of all significantly enriched canonical pathways available in **Supplementary File 3-1**, **3-2**, **3-3**, **3-4**, **3-5**.

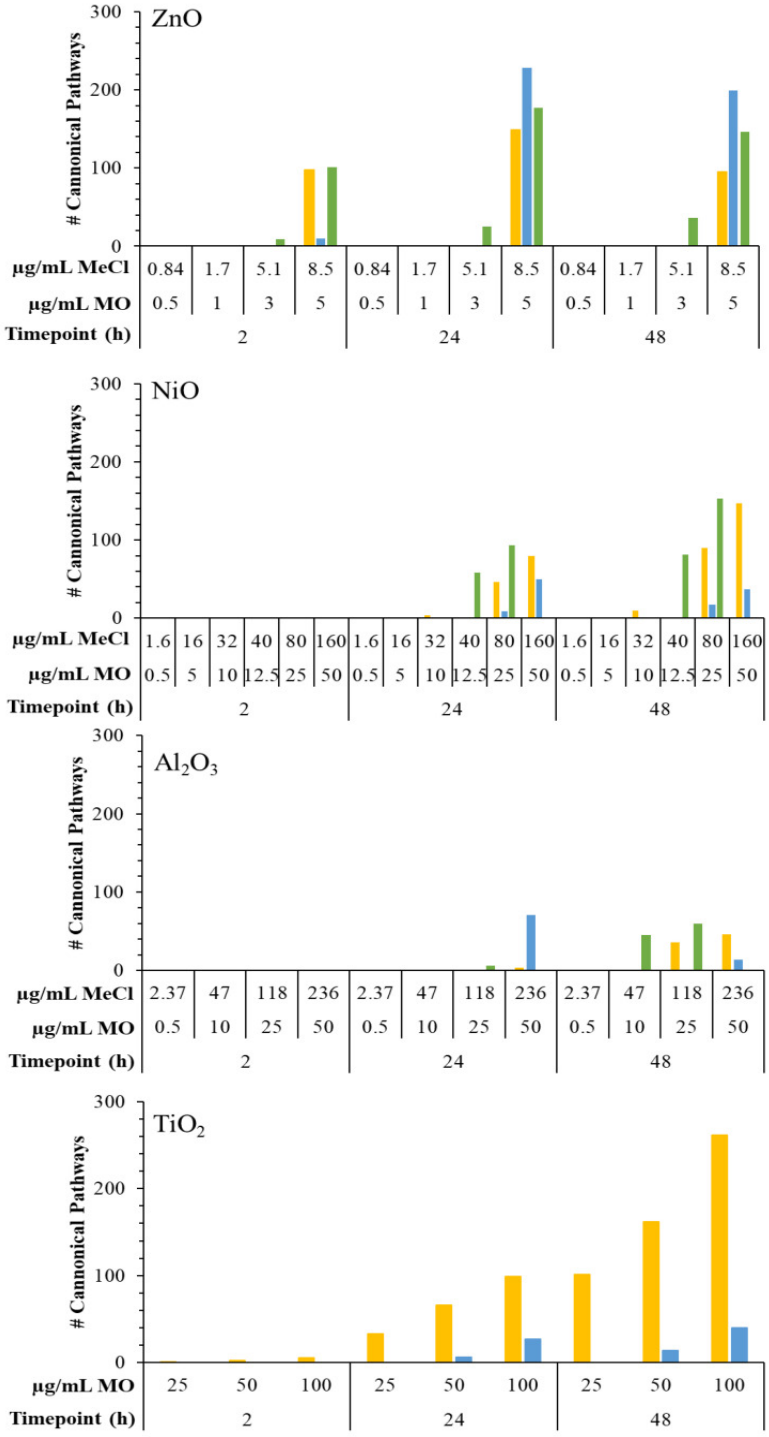

Figure 3-3. Total number of perturbed IPA canonical pathways following 2–48 h exposure to MONPs, MOMPs, and metal chloride salts. Graphs were labeled based on the type of metal oxide. Yellow: MONPs. Blue: MOMPs. Green: metal chloride salts. MO: metal oxide. MeCl: metal chloride. Significantly enriched pathways were combined in the case of ZnO MPs from enrichment of both the low fold-change and high fold-change datasets.

With respect to ZnO, dissolved $ZnCl_2$ enriched the most pathways at 2 h, while ZnO MPs showed the strongest pathway response at 24 and 48 h. At 2 h, $ZnCl_2$ presented the largest number of enriched pathways, with 9 and 101 pathways at 5.1 and 8.5 µg/mL, while ZnO NPs and MPs presented 98 and 10 significantly enriched pathways at 5 µg/mL, respectively. At 24 h, ZnO MPs had the greatest number of enriched pathways (228 unique perturbed pathways at 5 µg/mL across low and high-fold-change exposure groups), with $ZnCl_2$ presenting 25 and 177 enriched pathways at 5.1 and 8.5 µg/mL, respectively, and ZnO NPs enriching 149 pathways at 5 µg/mL. At 48 h, the number of enriched pathways was reduced compared to 24 h for all forms of Zn (**Figure 3-3**). Specifically, ZnO MPs exposure resulted in 199 total unique pathways at 5 µg/mL, which includes low and high-fold-change DEG groups; $ZnCl_2$ exposed samples presented 36 and 146 enriched pathways at 5.1 and 8.5 µg/mL; and ZnO NPs presented the lowest number of enriched pathways with 95 pathways at 5 µg/mL.

With respect to NiO, dissolved Ni in the form of $NiCl_2$ showed the most pronounced response at the pathway level compared to NiO NPs and MPs (**Figure 3-3**). At 2 h, no pathway enrichment was seen for any Ni compound. At 24 h, all Ni forms had concentration-dependent increases in enriched pathways, with $NiCl_2$ presenting the largest number (58 and 93 pathways at 40 and 80 µg/mL, respectively), followed by NiO NPs (4, 46, and 80 significant pathways at 10, 25, and 50 µg/mL), and MPs (9 and 50 enriched pathways at 25 and 50 µg/mL). At 48 h, $NiCl_2$ exhibited the most enriched pathways with 81 and 153 at 40 and 80 µg/mL, respectively, followed by NiO NPs with 10, 90, and 147 pathways for 10, 25, and 50 µg/mL, and NiO MPs with 17 and 37 pathways at 25 and 50 µg/mL concentrations. It is important to note that 1.6 µg/mL $NiCl_2$, which corresponded to the extracellular dissolution of 50 µg/mL NiO NPs in DMEM at 48 h, showed no response at any timepoint tested.

For Al_2O_3, the largest number of enriched pathways was seen for $AlCl_3$ when the concentration was expressed in terms of µg/mL Al (**Figure 3-3**). At 2 h, no significantly enriched pathways were seen for any Al form. At 24 h, both the Al_2O_3 NPs and MPs perturbed pathways at the highest concentration of 50 µg/mL, with 3 and 71 enriched

pathways, respectively, for NPs and MPs, while $AlCl_3$ enriched 1 and 6 pathways at 47 and 118 µg/mL. At 48 h, $AlCl_3$ enriched 45 and 60 pathways at 47 and 118 µg/mL, followed by Al_2O_3 NPs with 36 and 46 enriched pathways at 25 and 50 µg/mL, and Al_2O_3 MPs showing the lowest response with 14 enriched pathways at 50 µg/mL.

Finally, for TiO_2 particles, NPs presented a greater number of enriched pathways at each timepoint compared to MPs (**Figure 3-3**). At the earliest timepoint of 2 h, TiO_2 NPs enriched 1, 2, and 5 pathways, and at 24 h, 33, 66, and 99 enriched pathways were seen for NPs at 25, 50, and 100 µg/mL concentrations, respectively. There were 6 and 27 enriched pathways seen for 50 and 100 µg/mL MP concentrations. At 48 h, a greater response was noted for the NPs, with 101, 162, and 262 significantly enriched pathways at 25, 50, and 100 µg/mL compared to 14 and 40 pathways for 50 and 100 µg/mL MPs.

3.4.5 Hierarchical clustering of pathway responses

Hierarchical clustering was applied across all exposure groups and significantly enriched IPA canonical pathways in order to infer similarities and differences in response across the compounds tested (**Supplementary Figure 3-5**). For this purpose, significantly enriched pathways were clustered based on their z-score, which is a metric used to denote directionality in pathway response. The previously published gene expression data from cells exposed to Cu forms (Boyadzhiev et al., 2021) were included in this analysis. Samples that cluster close together are expected to enrich similar pathways with expression of DEGs showing similar directionality (upregulation or downregulation).

From the dendrogram in **Figure 3-4**, four main clusters are apparent and are separated mainly by the type of metal. Overall, the pathway responses seen across exposure conditions were largely MO form-specific, with metal salts and NPs inducing qualitatively similar responses, albeit with differences in timing and magnitude of response. With respect to ZnO materials, hierarchical clustering showed that ZnO NPs and $ZnCl_2$ had similar transcriptional responses at 2 h (appear on the same node in cluster 3), while ZnO MPs were dissimilar. By 24 and 48 h, all Zn materials (ZnO NPs, MPs, and $ZnCl_2$) enriched similar pathways with the same directionality and appeared in cluster 4. For CuO

materials, clustering showed that CuO NPs had different pathway responses at 24 h and 48 h (present in cluster 1 (24 h) and cluster 4 (48 h)). Response to 7 µg/mL $CuCl_2$ at 48 h was more akin to CuO NPs at 24 h than NPs at 48 h (**Figure 3-4**). Exposure to CuO MPs did not yield any enriched pathways with z-scores at any timepoint or concentration. Furthermore, there were no enriched pathways for CuO NPs or $CuCl_2$ at 2 h. All Ni materials (NiO NPs, MPs, and $NiCl_2$) showed similar pathway responses across time, with all exposure groups appearing within cluster 2 and no pathway enrichment seen at 2 h (**Figure 3-4**). With respect to Al materials, no pathway response was seen at 2 h for any compound, while at 24 h, only $AlCl_3$ and Al_2O_3 MPs presented pathways with z-score directionality. At 24 h, the response was varied, with 118 µg/mL $AlCl_3$ appearing in cluster 2 alongside NiO MP samples, whereas 50 µg/mL Al_2O_3 MPs appeared in cluster 3 alongside ZnO NP and $ZnCl_2$ at 2 h. No pathways were enriched for Al_2O_3 NPs at 24 h. By 48 h, significantly enriched pathways and their directionality were similar between Al_2O_3 NPs and $AlCl_3$ (all appeared in cluster 3), whereas 50 µg/mL Al_2O_3 MPs appeared outside of identified clusters. Finally, for TiO_2 NPs and MPs, hierarchical clustering indicated that pathway responses between NPs and MPs were dissimilar. At 2 h, only 100 µg/mL TiO_2 NPs samples presented enriched pathways and were grouped away from identified clusters. At 24 h, 25–100 µg/mL of TiO_2 NPs appeared in cluster 2, whereas at 48 h, both 25 and 50 µg/mL of TiO_2 NPs appeared in cluster 3, with 100 µg/mL of TiO_2 NPs still present in cluster 2 on the same node as 24 h TiO_2 NP samples. On the other hand, 100 µg/mL of TiO_2 MPs at 24 h appeared in cluster 1, while at 48 h 50 µg/mL of TiO_2 MPs appeared outside of identified clusters, and 100 µg/mL of MPs appeared in cluster 3.

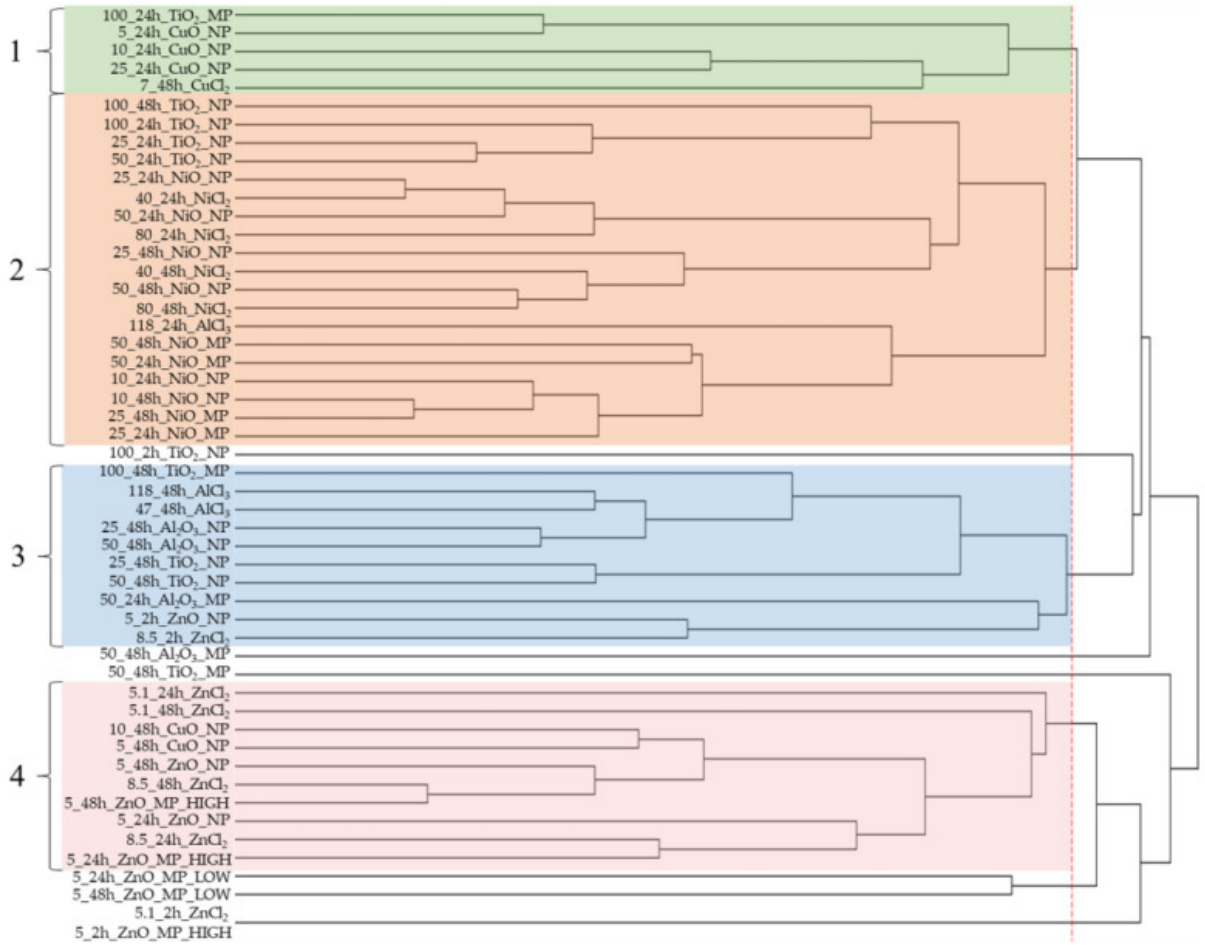

Figure 3-4. Hierarchical clustering of metal oxide and metal chloride-induced canonical pathway perturbation. The clustering was conducted on the z-scores of significantly enriched pathways. The red dashed line indicates where the dendrogram was cut to produce groupings. Each grouping was numbered and highlighted with a colored box.

3.4.6 'HIF1α Signaling' as a commonly enriched pathway across metal groups

All significantly enriched IPA canonical pathways were ranked by the number of samples showing enrichment to identify pathways commonly enriched across the exposure groups. Rank ordering of the top 10 most commonly enriched pathways (**Table 3-4**) showed the 'HIF1α Signaling' canonical pathway as the most ubiquitously enriched across all exposures, with 35/58 samples showing pathway enrichment (a list of all samples showing enrichment of this pathway is found in **Figure 3-5A**, with a high resolution heat map available in **Supplementary Figure 3-6**, and a pathway diagram found in **Appendix III 'HIF1α Signaling' IPA Canonical Pathway**).

Table 3-4. The top ten most commonly enriched IPA canonical pathways following 2–48 h of exposure to MONPs, MOMPs, and metal chlorides.

Pathway	Total Number of Samples Where Pathway Is Enriched
HIF1α Signaling	35/58
Pulmonary Fibrosis Idiopathic Signaling Pathway	31/58
Role of Macrophages, Fibroblasts and Endothelial Cells in Rheumatoid Arthritis	31/58
ID1 Signaling Pathway	30/58
Aryl Hydrocarbon Receptor Signaling	29/58
Hepatic Fibrosis / Hepatic Stellate Cell Activation	29/58
IL-10 Signaling	28/58
Hepatic Fibrosis Signaling Pathway	28/58
LPS/IL-1 Mediated Inhibition of RXR Function	28/58
Osteoarthritis Pathway	27/58
Tumor Microenvironment Pathway	27/58

The ‘HIF1α Signaling’ IPA pathway was the most commonly enriched across all MONPs (17/26 samples showing enrichment, **Supplementary Table 3-2**), while for MOMPs and metal chlorides it was the 2nd most commonly enriched pathway (8/17 and 10/15 samples showing enrichment, **Supplementary Table 3-2**). Clustering of DEGs associated with the ‘HIF1α Signaling’ pathway showed treatment groups cluster mainly based on parent metal (**Figure 3-5**). Spearman’s correlation analysis showed that pathway coverage (number of DEGs / total genes in the pathway) of the ‘HIF1α Signaling’ pathway was significantly negatively correlated with the percent viable cell density (p <0.001; Spearman’s correlation coefficient = −0.905).

A.

HIF1α Signalling

Compound	Sample (concentration_ timepoint_compound)	−log(*p*-value)	Pathway Coverage Ratio	z-score	# DEGs
Ti & Al	50_48h_Al_2O_3_NP	2.22	0.0354	0.378	7
	25_48h_Al_2O_3_NP	2.22	0.0202	1	4
	50_48h_TiO_2_NP	4.22	0.131	0.784	26
	25_48h_TiO_2_NP	3.27	0.0808	0.5	16
	100_48h_TiO_2_NP	5.04	0.212	1.234	42
	100_24h_TiO_2_NP	2.27	0.0303	1.633	6
	118_24h_$AlCl_3$	2.01	0.0202	1	4
Ni	50_24h_NiO_NP	1.34	0.141	2.502	28
	40_24h_$NiCl_2$	3.53	0.157	3.286	31
	80_24h_$NiCl_2$	2.83	0.237	1.18	47
	25_24h_NiO_NP	2.95	0.0707	2.673	14
	50_24h_NiO_MP	5.65	0.0707	3.207	14
	25_24h_NiO_MP	4.27	0.0354	1.89	7
	50_48h_NiO_NP	4.16	0.293	−0.788	58
	80_48h_$NiCl_2$	3.87	0.323	−0.25	64
	25_48h_NiO_NP	5.13	0.136	1.347	27
	40_48h_$NiCl_2$	2.54	0.197	2.082	39
	50_48h_NiO_MP	4.89	0.0758	2.84	15
	25_48h_NiO_MP	2.2	0.0253	1.342	5
	10_48h_NiO_NP	4.47	0.0303	0.816	6
Zn & Cu	10_24h_CuO_NP	2.58	0.146	0.186	29
	10_48h_CuO_NP	2.53	0.444	−1.294	88
	5_48h_CuO_NP	2.2	0.253	−1	50
	25_24h_CuO_NP	1.63	0.253	0.849	50
	8.5_24h_$ZnCl_2$	3.44	0.419	−1.207	83
	5_24h_ZnO_MP_HIGH	5.66	0.328	0.124	65
	7_48h_$CuCl_2$	2.86	0.0808	0	16
	8.5_2h_$ZnCl_2$	3.38	0.0556	0.302	11
	5_2h_ZnO_MP_HIGH	4.25	0.0202	−1	4
	5_2h_ZnO_NP	2.83	0.0707	0	14
	5.1_2h_$ZnCl_2$	3.01	0.0202	−1	4
	5_48h_ZnO_NP	2.97	0.182	0.169	36
	8.5_48h_$ZnCl_2$	4.37	0.455	−1.706	90
	5_48h_ZnO_MP_HIGH	4.76	0.323	−1.638	64
	5_24h_ZnO_NP	2.71	0.162	0	32

B.

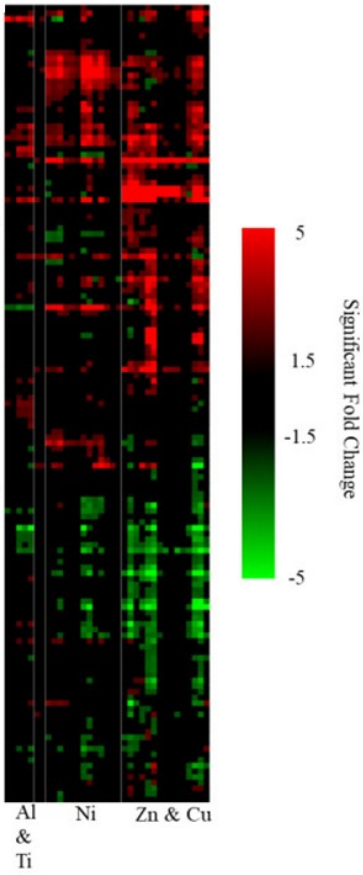

C.

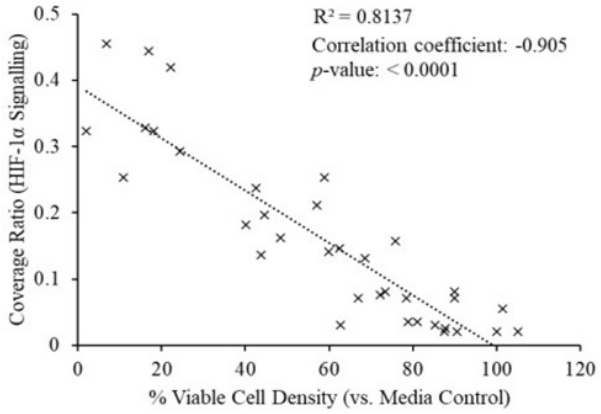

Figure 3-5. Perturbation of the 'HIF1α Signaling' pathway by MONPs, MOMPs, and metal chloride samples from 2–48 h. (A) Number of DEGs, pathway coverage ratio (# DEGs/total genes in the pathway), p-value, and z-score for all samples for which this pathway was enriched. (B) Heatmap showing clustering of samples and DEGs associated with the pathway. Lines indicate groups formed from the sample dendrogram. (C) Percent viable cell density plotted against the coverage ratio of the 'HIF1α Signaling' pathway for samples where the pathway was significantly enriched. A Spearman's correlation was conducted, with the resulting correlation coefficient and p-value displayed and a trendline fit to the graph.

To identify DEGs from the 'HIF1α Signaling' pathway that may be indicative of MONP toxicity, a weighted rank-ordering of all DEGs was conducted using scores calculated as follows: score = (average significant fold-change across samples) + (number of samples where the DEG fold-change >5)*100. This weighting puts emphasis on DEGs which show a high fold-change in many samples as opposed to a very high fold-change in a few samples.

The top ten ranked DEGs using the approach are listed in **Figure 3-6**. All Cu and Zn samples strongly upregulated the expression of heat shock protein A member 1A (*Hspa1a*), heat shock protein A member 1B (*Hspa1b*), and heme oxygenase 1 (*Hmox1*) (1.6 to 337-fold, −1.6 to 151-fold, and 4.3 to 48-fold, respectively).
Conversely, *Hspa1a* and *Hspa1b* were not differentially expressed in Ni samples (with three minor exceptions), whereas solute family carrier member 1 (*Slc2a1*) and egl-9 family hypoxia-inducible factor 1 (*Egln1*) were both ubiquitously expressed with high fold-change (1.7 to 16-fold, 1.9 to 8.4-fold). For Al and Ti samples, all of the top 10 ranked DEGs showed fold-changes <5 fold in either direction. It should be noted that while Zn, Cu, and Ni materials upregulate the expression of adrenomedullin (*Adm*), both Al and Ti materials lead to downregulation of this gene. For matrix metallopeptidase 10 (*Mmp10*) and serpin family E member 1 (*Serpine1*), upregulation was seen for Zn, Cu, Ni, Al, and Ti materials, with the highest fold-changes noted in CuO NP-exposed samples (9.9 to 69-fold and 3.2 to 12-fold, respectively). The last gene was ras related dexamethasone induced 1 (*Rasd1*), which showed high fold-change expression in ZnO MP and $ZnCl_2$-exposed samples at 24 and 48 h exclusively (7.6 to 49-fold).

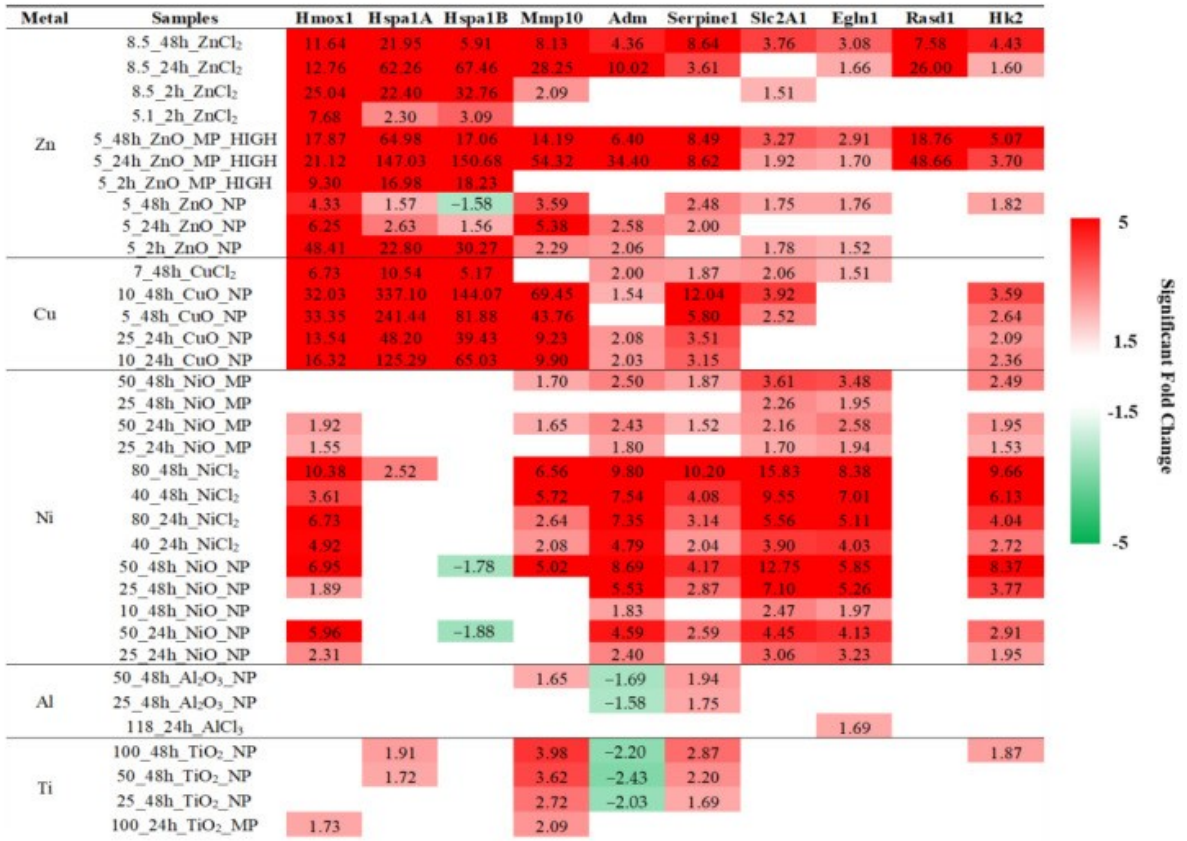

Metal	Samples	Hmox1	Hspa1A	Hspa1B	Mmp10	Adm	Serpine1	Slc2A1	Egln1	Rasd1	Hk2
Zn	8.5_48h_$ZnCl_2$	11.64	21.95	5.91	8.13	4.36	8.64	3.76	3.08	7.58	4.43
	8.5_24h_$ZnCl_2$	12.76	62.26	67.46	28.25	10.02	3.61		1.66	26.00	1.60
	8.5_2h_$ZnCl_2$	25.04	22.40	32.76	2.09			1.51			
	5.1_2h_$ZnCl_2$	7.68	2.30	3.09							
	5_48h_ZnO_MP_HIGH	17.87	64.98	17.06	14.19	6.40	8.49	3.27	2.91	18.76	5.07
	5_24h_ZnO_MP_HIGH	21.12	147.03	150.68	54.32	34.40	8.62	1.92	1.70	48.66	3.70
	5_2h_ZnO_MP_HIGH	9.30	16.98	18.23							
	5_48h_ZnO_NP	4.33	1.57	−1.58	3.59		2.48	1.75	1.76		1.82
	5_24h_ZnO_NP	6.25	2.63	1.56	5.38	2.58	2.00				
	5_2h_ZnO_NP	48.41	22.80	30.27	2.29	2.06		1.78	1.52		
Cu	7_48h_$CuCl_2$	6.73	10.54	5.17		2.00	1.87	2.06	1.51		
	10_48h_CuO_NP	32.03	337.10	144.07	69.45	1.54	12.04	3.92			3.59
	5_48h_CuO_NP	33.35	241.44	81.88	43.76		5.80	2.52			2.64
	25_24h_CuO_NP	13.54	48.20	39.43	9.23	2.08	3.51				2.09
	10_24h_CuO_NP	16.32	125.29	65.03	9.90	2.03	3.15				2.36
Ni	50_48h_NiO_MP				1.70	2.50	1.87	3.61	3.48		2.49
	25_48h_NiO_MP							2.26	1.95		
	50_24h_NiO_MP	1.92			1.65	2.43	1.52	2.16	2.58		1.95
	25_24h_NiO_MP	1.55				1.80		1.70	1.94		1.53
	80_48h_$NiCl_2$	10.38	2.52		6.56	9.80	10.20	15.83	8.38		9.66
	40_48h_$NiCl_2$	3.61			5.72	7.54	4.08	9.55	7.01		6.13
	80_24h_$NiCl_2$	6.73			2.64	7.35	3.14	5.56	5.11		4.04
	40_24h_$NiCl_2$	4.92			2.08	4.79	2.04	3.90	4.03		2.72
	50_48h_NiO_NP	6.95		−1.78	5.02	8.69	4.17	12.75	5.85		8.37
	25_48h_NiO_NP	1.89				5.53	2.87	7.10	5.26		3.77
	10_48h_NiO_NP					1.83		2.47	1.97		
	50_24h_NiO_NP	5.96		−1.88		4.59	2.59	4.45	4.13		2.91
	25_24h_NiO_NP	2.31				2.40		3.06	3.23		1.95
Al	50_48h_Al_2O_3_NP				1.65	−1.69	1.94				
	25_48h_Al_2O_3_NP					−1.58	1.75				
	118_24h_$AlCl_3$								1.69		
Ti	100_48h_TiO_2_NP		1.91		3.98	−2.20	2.87				1.87
	50_48h_TiO_2_NP		1.72		3.62	−2.43	2.20				
	25_48h_TiO_2_NP				2.72	−2.03	1.69				
	100_24h_TiO_2_MP	1.73			2.09						

Figure 3-6. Heatmap showing the differential expression of the top-10-ranked DEGs from the 'HIF1α Signaling' pathway across all samples for which this pathway is significantly enriched. The values in each cell indicate the fold-change over the control. The left-most DEG is the top-ranked, whereas the right-most DEG is the bottom-ranked. Blank cells indicate no significant differential expression. Red: increased fold-change. Green: decreased fold-change.

3.4.7 Benchmark concentration modeling

Benchmark concentration modeling of viable cell density responses (**Figure 3-7**) and transcriptomic responses (**Figure 3-8**) was employed for comparative potency ranking of the MONPs, MOMPs, and metal chlorides used in this study, with the concentrations normalized to the amount of constituent metal in the exposure medium. Viable cell density was used instead of percent viability, as it more accurately captured the toxicity induced by Zn compounds compared to white and blue cell ratios in this study. Transcriptomic and cell density data from Cu exposures in (Boyadzhiev et al., 2021) were included in the analysis.

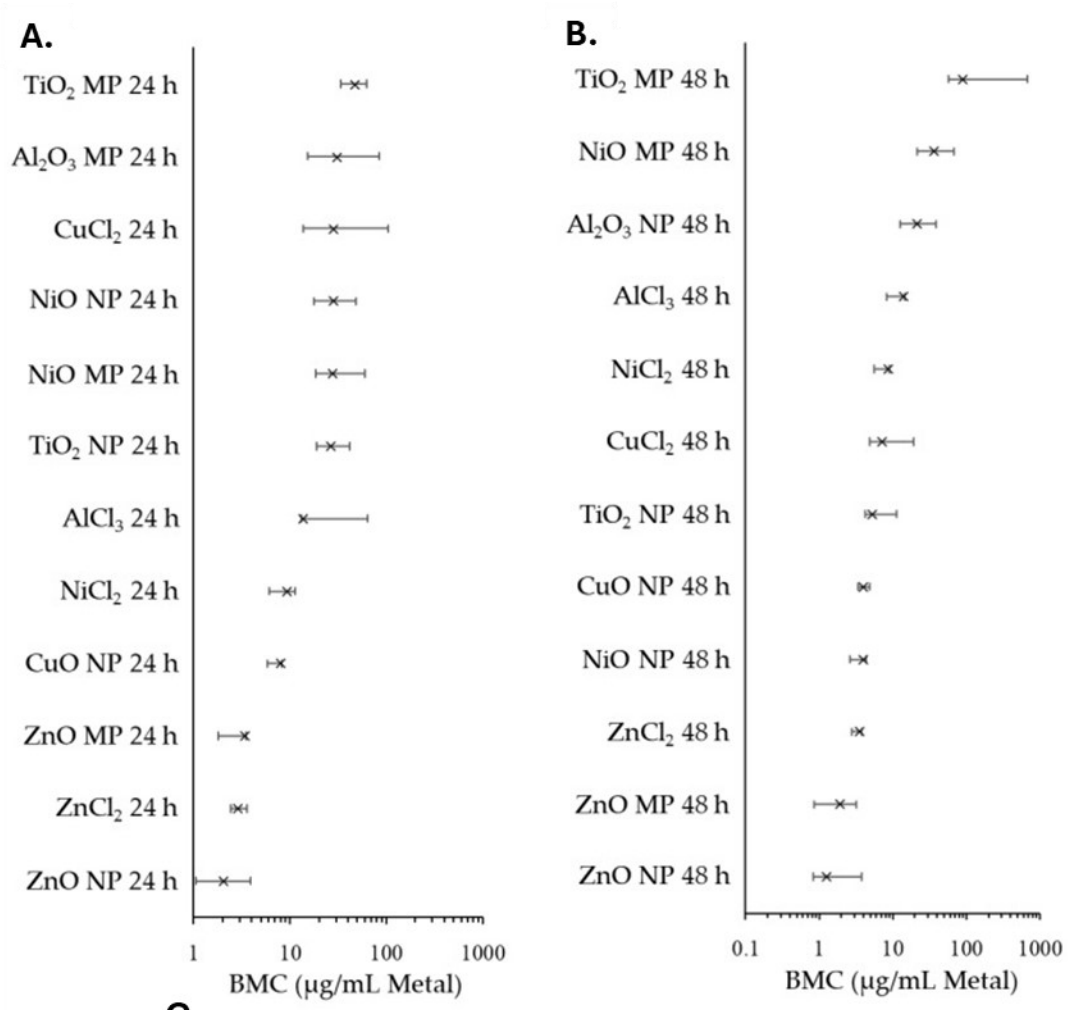

C.

Metal	24 h Potency Ranking	48 h Potency Ranking
Zn	$ZnO\ NP \sim ZnO\ MP \sim ZnCl_2$	$ZnO\ NP \sim ZnO\ MP \sim ZnCl_2$
Ni	$NiCl_2 > NiO\ NP \sim NiO\ MP$	$NiO\ NP > NiCl_2 > NiO\ MP$
Al	$Al_2O_3\ MP \sim AlCl_3$	$Al_2O_3\ NP \sim AlCl_3$
Ti	$TiO_2\ NP \sim TiO_2\ MP$	$TiO_2\ NP > TiO_2\ MP$
Cu	$CuO\ NP > CuCl_2$	$CuO\ NP \sim CuCl_2$

Figure 3-7. BMDS-based BMC modeling of viable cell density reduction following (A) 24 h and (B) 48 h exposure to metal oxides and metal chlorides, with (C) differences in potency for each metal variety. Benchmark response: 0.5 (hybrid risk). The 'x' indicates the BMC. Left and right bars indicate lower and upper 95% confidence intervals around the BMC, respectively. Potencies for different compounds are considered equivalent if the confidence intervals overlap.

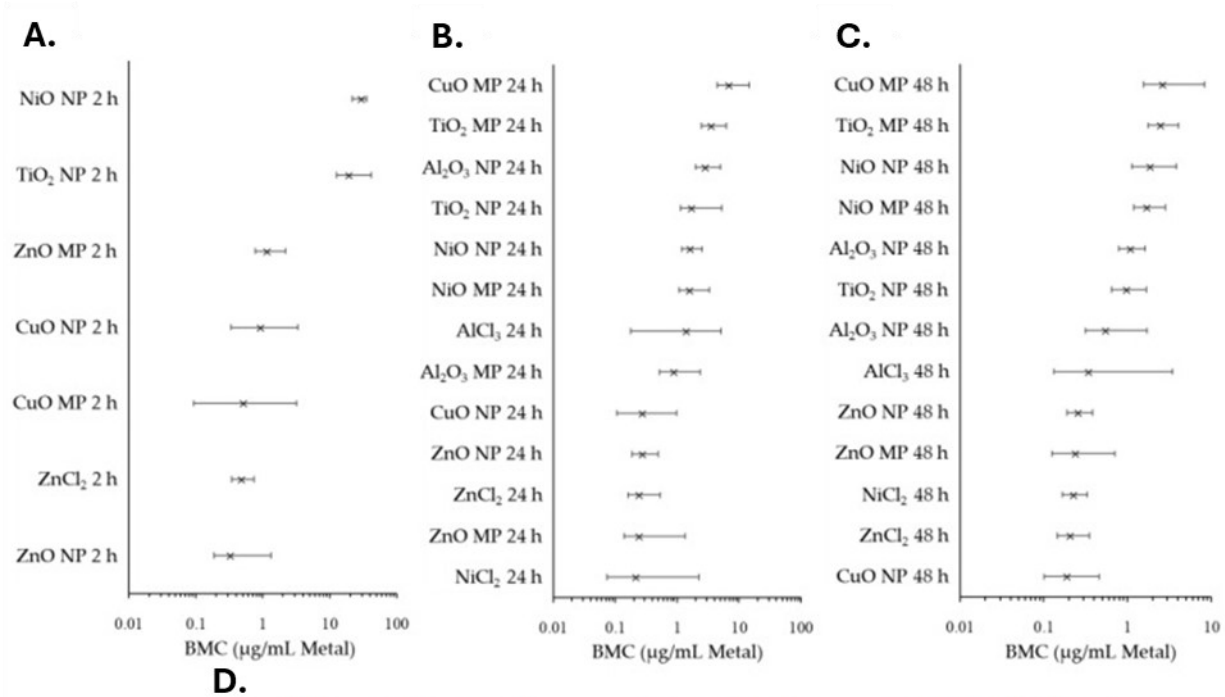

D.

Metal	2 h Potency Ranking	24 h Potency Ranking	48 h Potency Ranking
Zn	($ZnCl_2$ > ZnO MP) ~ ZnO NP	ZnO NP ~ ZnO MP ~ $ZnCl_2$	ZnO NP ~ ZnO MP ~ $ZnCl_2$
Ni	(-)	$NiCl_2$ ~ NiO NP ~ NiO MP	$NiCl_2$ > NiO NP ~ NiO MP
Al	(-)	Al_2O_3 NP ~ $AlCl_3$ ~ Al_2O_3 MP	Al_2O_3 NP ~ $AlCl_3$ ~ Al_2O_3 NP
Ti	(-)	TiO_2 NP ~ TiO_2 MP	TiO_2 NP > TiO_2 MP
Cu	CuO NP ~ CuO MP	CuO NP > CuO MP	CuO NP > CuO MP

Figure 3-8. The transcriptomic-based BMC determined through BMDExpress2 BMC modeling for (A) 2 h, (B) 24 h, and (C) 48 h metal oxide and metal chloride exposures, with (D) differences in potency for each metal variety. Benchmark response: 1 (standard deviation). The 'x' indicates the BMC. Left and right bars indicate lower and upper 95% confidence intervals around the BMC, respectively. Potencies for different compounds are considered equivalent if the confidence intervals overlap.

BMC modeling of viable cell densities was only attempted for 24 and 48 h timepoints due to the minimal response at the 2 h timepoint for all compounds. At 24 h, the materials were ranked as follows: ZnO NP ~ ZnO MP ~ $ZnCl_2$ > CuO NP ~ $NiCl_2$ > TiO_2 NP ~ NiO MP ~ NiO NP ~ $CuCl_2$ ~ Al_2O_3 MP ~ $AlCl_3$ ~ TiO_2 MP. At 48 h, a similar trend was observed, although the BMC ranges largely overlapped (**Figure 3-7B**). There were differences noted within the three forms of each metal compound at 48 h (**Figure 3-7C**). For Zn compounds, all three forms presented the same potency at 48 h, which was also seen for Al_2O_3 NPs and $AlCl_3$, as well as for CuO NPs and $CuCl_2$. In contrast, NiO NPs were more potent compared to $NiCl_2$, while TiO_2 NPs and NiO NPs were more potent than MP analogues.

With respect to the transcriptomic data, the tPOD chosen was the 25th ranked gene for 2, 24, and 48 h timepoints (**Figure 3-8**). At 2 h, TiO_2 NPs and NiO NPs were less potent than ZnO NPs, ZnO MPs, $ZnCl_2$, CuO NPs, and CuO MPs at inducing transcriptional signaling. At 24 h, Zn compounds presented equivalent potency between the NP, MP, and $ZnCl_2$ forms, an equivalency that was also displayed by the three forms of Ni and Al and the two forms of TiO_2 (**Figure 3-8D**). In contrast, CuO NPs were more potent than MPs at inducing transcriptional signaling. By 48 h, Zn, Al, and Cu compounds presented the same potency trends as the 24 h timepoint, while $NiCl_2$ was more potent than NiO NPs and NiO MPs at inducing transcriptional signaling, and TiO_2 NPs presented greater potency than TiO_2 MPs.

For both viable cell density and transcriptomic BMC modeling, the concentrations were also expressed in terms of SSA (cm^2/mL), using experimentally measured SSA values for NPs and manufacturer-provided SSA values for MPs (**Supplementary Figure 3-7**, **3-8**). The SSA-based BMC ranges at 24 h indicated MPs present equal or greater potency than NPs for reduction of viable cell density (ZnO MP > ZnO NP; NiO NP ~ NiO MP; TiO_2 MP > TiO_2 NP), with a similar trend for the induction of transcriptional response (ZnO NP ~ ZnO MP; CuO NP > CuO MP; NiO MP > NiO NP; Al_2O_3 MP ~ Al_2O_3 NP; TiO_2 MP > TiO_2 NP). By 48 h of exposure, substances showed compound-specific potency differences for reduction of viable cell density (ZnO MP > ZnO NP; NiO NP > NiO MP; TiO_2 NP ~ TiO_2 MP), while MPs generally presented a greater potency than NPs to induce transcriptional response (ZnO MP > ZnO NP; CuO NP > CuO MP; NiO MP > NiO NP; Al_2O_3 MP ~ Al_2O_3 NP; TiO_2 MP > TiO_2 NP).

3.5 Discussion

The solubility of MONPs in biological environments can have an impact on their potential to induce toxicity. Recent research has shown that size and concentration both affect the dissolution of MONPs, with MOMPs dissolving to a lesser extent (Avramescu et al., 2020, 2022). In the present study, *in vitro* global transcriptomic analysis was applied to characterize the impact of solubility on cellular toxicity induced by MONPs over short

exposure durations, using MOMPs and metal chloride salts as bulk and dissolved metal analogues. Overall, the results show that (1) extracellular dissolution was an important contributor to the toxicity of ZnO and CuO MONPs with high–moderate solubility in cell culture medium, while extracellular dissolution did not contribute to toxicity induced by NiO and Al_2O_3 MONPs with low–negligible solubility; (2) responses were generally specific to the parent metal (Zn, Cu, Ni), with MONPs and metal salts inducing similar transcriptional responses albeit with differences in magnitude and timing, while MOMPs showed less consistency; (3) signaling through the 'HIF1α Signaling' pathway was a common response underlying the toxicity of MONPs, as well as their bulk and dissolved metal analogues; however, the DEGs within the pathway for each metal differed, implying differences in underlying mechanisms and the eventual toxicity; and (4) BMC-derived relative potency ranking of apical and transcriptomic endpoints indicated similar toxicity for ZnO NPs, MPs, and Zn ions, whereas differences were observed in the case of MONPs that have lower solubility in biological media.

3.5.1 The impact of solubility on the toxicity of MONPs

The contribution of extracellular dissolution to the response induced by MONPs depended on the solubility of the material. For ZnO NPs, which display high solubility and instantaneous dissolution in cell culture medium at low concentrations (**Supplementary Table 3-1**), an equivalent concentration of $ZnCl_2$ induced a similar cytotoxic and transcriptomic response as early as 2 h post-exposure, which markedly increased for $ZnCl_2$ at 24 and 48 h post-exposure (**Figure 3-1**, **Figure 3-2**, and **Figure 3-3**). Other *in vitro* studies in the past have reported similar levels of acute cytotoxicity for dissolved Zn and ZnO NPs when the concentration was normalized to the constituent metal (Kononenko et al., 2017) or markedly higher toxicity in response to dissolved Zn exposure (Jeong, J. et al., 2018). For the moderately soluble CuO NPs (**Supplementary Table 3-1**), extracellular dissolution contributed to cellular toxicity, as 7 µg/mL $CuCl_2$ induced transcriptional signaling at 48 h, which clustered alongside 24 h CuO NP samples (**Appendix II Chapter 3 Supplementary Document 1**, **Figure 3-4**, (Boyadzhiev et al., 2021)). However, the results showed a lag in time at which the cytotoxicity or significant transcriptional perturbance became apparent post-

exposure to $CuCl_2$. Also, extracellular dissolution alone was insufficient to account for the magnitude of the responses seen for NPs at 24 and 48 h (described in detail in (Boyadzhiev et al., 2021)), implying a role for the particulate form of CuO NPs in the observed toxicity. In the case of NiO and Al_2O_3, NPs that showed low-negligible solubility in cell culture medium, concentrations of metal chlorides representing possible extracellular dissolution of NPs (1.6 and 2.4 µg/mL, respectively) did not result in loss of viability or induce transcriptional response at any timepoint assessed (**Figure 3-1**, **Figure 3-2**, and **Figure 3-3**). For NiO NPs, this indicates that toxicity is induced either through cell-material interactions or through particle internalization and intracellular dissolution, rather than from exposure to ions via extracellular dissolution. For Al_2O_3 NPs, however, the result is less straightforward. Upon addition of dissolved $AlCl_3$ to FE1 cell culture medium, an insoluble precipitate was quickly formed at a concentration of 1 mg/mL (**Supplementary Figure 3-3**). Similar analyte loss during control experiments was reported by (Avramescu et al., 2022) at a lower $AlCl_3$ concentration of 1 mg/L. Considering the observed analyte loss, the authors suggested that the solubility reported may be considered an 'apparent solubility', which represents the portion of released Al that is not matrix bound (Avramescu et al., 2022). Furthermore, particle formation has been noted by others when conducting *in vitro* exposures using $AlCl_3$ as well as within simulated intestinal fluid (Sieg et al., 2017, 2018). The formation of aluminum phosphate and calcium phosphate precipitate has been reported when $AlCl_3$ was introduced into A549 cell culture medium (Helmig et al., 2018). The results of these studies, as well as the results reported here, imply that loss of dissolved Al within neutral or slightly basic biological environments is an anticipated behavior and may be caused by precipitation, surface adsorption, and/or interactions with proteins. Moreover, the present study indicates that extracellular dissolution based on 'apparent solubility' does not contribute to responses induced by Al_2O_3 NPs. In summary, while extracellular dissolution was a factor contributing to the observed toxicity of certain MONPs with high-moderate solubility, it was not a significant factor impacting the toxicity of MONPs with low-negligible solubility.

Based on transcriptional profiling, MONPs and dissolved salts of the same parent metal (e.g., Ni) perturbed similar pathways at the same timepoints of the assessment when equivalent metal concentrations, or concentrations equivalent to high levels of NP dissolution (≥50%) were used (**Figure 3-4** and **Supplementary Figure 3-5**). With respect to bulk MP analogues, responses were less consistent, with ZnO and NiO MPs clustering alongside their NP and dissolved analogues, but with Al_2O_3 and TiO_2 MPs showing less consistency. Detailed analysis of significantly enriched pathways (**Appendix II Chapter 3 Supplementary Document 1**) indicated a conserved stress and cell death response for ZnO NPs, MPs, and dissolved Zn beginning at the earliest post-exposure timepoint of 2 h and increasing in severity up to 48 h at equivalent Zn concentrations (4 µg/mL Zn). However, it is important to note that the number of enriched pathways at the highest concentration decreased for all forms of Zn from 24 to 48 h. For NiO NPs, MPs, and dissolved Ni, pathways implicated in hypoxia signaling beginning at 24 h were seen, with concentration- and time-dependent increases in pathways involved in cell stress, death, and immune response (**Appendix II Chapter 3 Supplementary Document 1**). It was commonly seen that 50 µg/mL NPs (40 µg/mL Ni) clustered close to 80 µg/mL $NiCl_2$ (20 µg/mL Ni) at the same timepoints (**Figure 3-4**), implying a similar pathway response between the two forms but with an increased magnitude and breadth of transcriptional induction for dissolved Ni. For Al_2O_3 NPs, the pathway response was negligible for all concentrations of NPs and $AlCl_3$ at 24 h (<10 significant pathways), with 48 h responses for both materials featuring mainly aberrant wound healing responses, immune signaling, and disease pathways noted at the highest exposure concentrations of 50 µg/mL of NPs (26.5 µg/mL Al) and 118 µg/mL of $AlCl_3$ (13.25 µg/mL Al). Recent reports examining MONPs alongside dissolved metal equivalents in human cell lines support this view, with ZnO NPs and $ZnCl_2$ showing a transcriptionally similar response in A549 cells after 24 h of exposure (Dekkers et al., 2018); and NiO NPs and $NiCl_2$ exposures both showing cytotoxicity and genotoxicity in BEAS-2B cells following chronic (6-week) and acute (24 h) *in vitro* exposures, with $NiCl_2$ inducing the most DEGs after 6 weeks of exposure compared to NiO NPs at the same concentration of Ni (Di Bucchianico et al., 2018; Gliga et al., 2020). While some

commonalities were observed, for example, enrichment of 'HIF1α Signaling' across all samples, the results showed that mechanistically, each metal type differs from the other, and thus, eventual toxicity may also be different.

3.5.2 'HIF1α Signaling' as a common underlying response to MONP toxicity

Based on shared enriched canonical pathways, it could be seen that 'HIF1α Signaling' was the most commonly enriched pathway across all exposures except for Al_2O_3 MPs (**Table 3-4**), with DEG responses clustering based on parent metal (**Figure 3-5B**). Higher coverage in this pathway (more DEGs) was strongly associated with decreases in the density of viable cells in this study (**Figure 3-5C**). Signaling through the 'HIF1α Signaling' pathway showed MONPs with low-negligible solubility in cell culture medium of low acute toxicity (Al_2O_3, TiO_2) altered the expression of lower numbers of DEGs in general, with lower fold-change differences in comparison to toxic MONPs with higher solubility (ZnO, CuO) (**Supplementary Figure 3-6**).

The 'HIF1α Signaling' pathway is a stress-induced signaling pathway that controls the expression of over 100 downstream genes (Masoud & Li, 2015). Cellular processes directly controlled by HIF1α include angiogenesis, metabolism, iron transport and cycling, extracellular matrix remodeling, and cell survival and differentiation (Ke & Costa, 2006; Masoud & Li, 2015). Cellular response to hypoxia is controlled by both oxygen and iron availability, and dysregulation in iron homeostasis is known to induce a hypoxic response in a similar manner to low oxygen (Hirota, 2019). Responses associated with hypoxia include a shift in energy generation away from oxygen-intensive pathways (e.g., mitochondrial cellular respiration) and towards anoxic processes (e.g., glycolysis), as well as the induction of stress responses such as autophagy, endoplasmic reticulum stress, oxidative stress, and unfolded protein responses (Galanis et al., 2009; Luo et al., 2022; McGarry et al., 2018; Wouters & Koritzinsky, 2008). High levels of oxidative stress can lead to oxidative damage of biomolecules such as lipids, proteins, and nucleic acids, which, in turn, leads to DNA damage and unfolded protein response induction, which are two main mechanisms of MONP toxicity (Sengul & Asmatulu, 2020). Furthermore, the accumulation of unfolded proteins in cells can result in endoplasmic reticulum stress, while disturbances in

the endo-lysosomal network can cause autophagic stress, both of which have been associated with the toxicity of MONPs such as ZnO, CuO, and iron oxide nanoparticles (Bi et al., 2023). The ability to monitor these important stress pathways, along with HIF1α's direct association with cellular homeostasis and specifically metal homeostasis, makes this pathway an attractive candidate as an *in vitro* biomarker of MONP toxicity. While all MONPs responded by inducing 'HIF1α Signaling', the specific DEGs and consequently, associated processes varied. Oxidative stress and unfolded protein responses were commonly seen in Zn, Cu, and Ni-exposed cells and, to a lesser extent, in TiO_2 NP exposed cells; however, important pathways implicated in glycolysis were for the most part not enriched (**Appendix II Chapter 3 Supplementary Document 1**). NiO NPs exhibit low-negligible solubility in cell culture medium (Avramescu et al., 2022) and moderate-low solubility in acidic environments (Shinohara et al., 2017), with dissolved Ni shown to induce a state of cellular hypoxia akin to the hypoxia-mimetic compound cobalt chloride (Davidson et al., 2006; Jorge Muñoz-Sánchez & María E. Chánez-Cárdenas, 2019). Transcriptional induction of hypoxia was seen for NiO NPs, MPs, and $NiCl_2$, which all enriched and activated 'HIF1α Signaling', in addition to activation of glycolysis for all Ni compounds and inactivation of oxidative phosphorylation for NiO NPs and $NiCl_2$ (**Appendix II Chapter 3 Supplementary Document 1**, **Supplementary File 3-3**). It should be noted that while all metal compounds lead to the enrichment of 'HIF1α Signaling', only NiO NPs, MPs, and $NiCl_2$ lead to activation of this pathway based on z-score directionality (**Figure 3-5A**).

The 'HIF1α Signaling' IPA canonical pathway consists of 198 genes, based on IPA content version 81348237. Using weighted rank-ordered genes from samples where the 'HIF1α Signaling' pathway was enriched, the top 10 DEGs were selected with high fold-change induction across the sample set (**Figure 3-6**). These genes consist of *Hmox1*, *Hspa1a*, *Hspa1b*, *Mmp10*, *Adm*, *Serpine1*, *Slc2a1*, *Egln1*, *Rasd1*, and *Hk2*. The genes *Hmox1, Hspa1a,* and *Hspa1b* are implicated in iron recycling, response to oxidative stress, iron homeostasis, and protein folding and are transcriptionally responsive to reactive oxygen species, heavy metal exposure, as well as homeostatic disruption (Daugaard et al., 2007; Moreno-Navarrete et al., 2017; Ryter, 2022). Both HSP genes were highly

expressed in response to Zn and Cu exposures, but not Ni, Al, or Ti, whereas *Hmox1* was highly expressed in Zn, Cu, and Ni samples. Two genes implicated in glucose uptake and metabolism, *Slc2a1* and *Hk2*, showed the highest fold-change in 25 and 50 µg/mL at 48 h of NiO NPs and 40 and 80 µg/mL at 24 and 48 h of $NiCl_2$ exposed groups. Next was *Egln1*, which showed high fold-change induction in Ni-exposed samples. This gene encodes a prolyl hydroxylase domain-containing protein used to post-translationally control the stability of HIF1A (Ke & Costa, 2006). The gene *Adm* encodes the multi-functional peptide adrenomedullin, which has recently been shown to have increased expression in the mouse lung epithelium in hypoxic conditions (Han, Jihye et al., 2022). This gene was upregulated in Zn, Ni, and Cu-exposed samples and downregulated in Al and Ti-exposed samples. The next two genes, *Mmp10* and *Serpine1,* encode a matrix metalloprotease and a serine protease inhibitor, respectively, and show upregulation in response to Zn, Cu, Ni, Al, and Ti exposures. Differential expression of *Serpine1* has been associated with pulmonary disease (Ghosh & Vaughan, 2012; Morrow & Mutch, 2023), and increased expression has been noted in the lungs of mice exposed to carbon nanotubes and TiO_2 (Rahman, L. et al., 2017b; Søs Poulsen et al., 2013). Similarly, *Mmp10* has been implicated in pulmonary inflammation and the development of pathologies such as emphysema and chronic obstructive pulmonary disease (Wight et al., 2017), with high levels of MMP10 expression noted in the lungs of rats under hypoxic stress (Chi et al., 2022). The final DEG in the list was *Rasd1*, which only showed expression in ZnO MP and $ZnCl_2$-exposed samples at 24 and 48 h, but with a high fold-change. The gene *Rasd1* encodes a RAS small GTPase protein involved in many mammalian signaling cascades, including iron cycling and calcium signaling (Bouchard-Cannon & Cheng, 2018). These 10 genes involved in HIF1α signaling showed strong induction in response to highly toxic MONPs, such as ZnO, CuO, and NiO NPs, but minimal perturbation in low-responding Al_2O_3 and TiO_2 NPs. Therefore, it is posited that their expression levels may serve as putative *in vitro* markers of exposure to toxic MONPs.

3.5.3 Relative potency ranking of apical and transcriptomic points of departure

In order to delineate differences in potency amongst MONPs, MOMPs, and metal chlorides with respect to their ability to induce cytotoxicity and transcriptomic signaling, BMC modeling was employed (**Figure 3-7**, **Figure 3-8**, **Supplementary Figure 3-7**, **3-8**). Compound-specific differences in potency were observed. When concentrations were expressed in terms of the mass volume of the constituent metal, there were no observable differences in potency amongst the three Zn compounds at 24 or 48 h with respect to transcriptomic response and cytotoxicity. CuO NPs with moderate solubility showed a greater ability to induce cytotoxicity than dissolved Cu (as $CuCl_2$) at 24 h, but this difference in potency disappeared at 48 h. Transcriptionally, NPs were more potent than MPs at both 24 and 48 h, with no similar comparison possible for $CuCl_2$ due to the paucity of concentrations used. NiO NPs with low-negligible solubility presented mixed potency compared to MPs and dissolved Ni, with $NiCl_2$ presenting greater potency than NPs and MPs at inducing cytotoxicity at 24 h, and equivalent potency to induce transcriptional response. However, by 48 h, NiO NPs presented greater potency to induce cytotoxicity compared to both $NiCl_2$ and NiO MPs, whereas $NiCl_2$ was more potent at inducing transcriptional responses at this timepoint. For Al_2O_3 NPs with low-negligible solubility, no difference in potency was seen for cytotoxicity at 48 h between NPs and $AlCl_3$, a trend similarly seen for NPs, MPs, and $AlCl_3$ transcriptomic exposures at 24 and 48 h. It must be reiterated, however, that dissolved Al precipitated in cell culture medium (**Supplementary Figure 3-3**) and therefore does not represent Al fully in solution. Overall, MOMPs tended to present equivalent or lower cytotoxic and transcriptional potencies in comparison to both MONPs and dissolved metals. Together, the results of this BMC modeling provide support for the notion that cellular toxicity resulting from exposure to ZnO NPs with high-moderate solubility in cell culture medium is comparable to exposure to fully dissolved ions. However, MONPs of lower solubility show compound-specific trends in potency between nano, bulk, and dissolved forms.

The BMC concentration was also expressed in terms of the SSA of each particle, which takes into account the available surface atoms for interaction, and which is proposed as a more appropriate dose metric for MONPs with negligible solubility compared to mass dose (Schmid & Stoeger, 2016). For the NPs used in this study, experimentally derived SSA values were available from recent publications (Bushell et al., 2020; Kunc et al., 2022). However, for MPs, only the manufacturer-provided ranges were available. Using the mean SSA estimates for MPs, it was observed that MOMPs were either more potent or showed equivalent potency to MONPs for both endpoints, with the exception of CuO NPs, which were more potent than CuO MPs at inducing transcriptional signaling at 24 and 48 h, and NiO NPs, which were more potent than MPs at inducing reductions in viable cells at 48 h (**Supplementary Figure 3-7**, **3-8**). The use of manufacturer-provided SSA values for MOMPs precluded a more precise potency comparison between NPs and MPs, but the current results concur with reports indicating that differences in potency between NPs and MPs can at least partially be explained by the larger SSA of NPs (Waters et al., 2009).

3.6 Conclusion

There is a pressing need to derive consistent information concerning the impacts of physicochemical properties on the toxicity mechanisms of nanomaterials, such as MONPs, in order to allow for a timely and accurate assessment of the risks these materials pose to both human and environmental health. Solubility has been used as a case-study method for binning materials for environmental risk assessment by determining which species (particulate, dissolved, or both) should be the focus of the risk assessment (OECD, 2015). Furthermore, solubility has been proposed as an aspect of a tiered testing approach to the human health risk assessment of nanomaterials in Canada (ECCC & HC, 2022). The present study provides evidence of compound-specific effects of solubility on MONP toxicity, with a key conclusion that there are limits on the applicability of solubility in read-across and grouping strategies for the purposes of risk assessment. That is, solubility cannot be considered a sole determinant of the toxicity of MONPs, with further systematic

studies required to identify other properties that act in parallel or in conjunction to influence toxicity.

Through transcriptomic analysis, this study identified signaling through the 'HIF1α Signaling pathway' as a conserved response across not only MONPs, but also metal chlorides and most MOMPs, with the number of differentially expressed genes in this pathway closely tied to cytotoxicity. Due to the association of HIF1α signaling with cell death, cellular homeostasis, as well as with key stress processes such as oxidative stress, protein damage, and material turnover (autophagy), key genes in this pathway can be explored for use as prognostic *in vitro* biomarkers for acutely toxic MONPs in a tiered testing approach. Fold-change induction in these reporters can prioritize MONPs for toxicity testing using more advanced *in vitro* techniques or toxicity verification by animal testing methods.

4 Chapter 4: The High-Throughput *In Vitro* CometChip® Assay for the Analysis of Metal Oxide Nanomaterial Induced DNA Damage

Modified from: Boyadzhiev, A., Solorio-Rodriguez, S. A., Wu, D., Avramescu, M. L., Rasmussen, P., & Halappanavar, S. (2022). The High-Throughput In Vitro CometChip Assay for the Analysis of Metal Oxide Nanomaterial Induced DNA Damage. Nanomaterials (Basel, Switzerland), 12(11), 1844. **https://doi.org/10.3390/nano12111844**.

Authorship: Andrey Boyadzhiev[1], Silvia Aidee Solorio-Rodriguez[1], Dongmei Wu[1], Mary-Luyza Avramescu[1], Andrew Williams[1], Pat Rasmussen[1], Sabina Halappanavar[1]

Affiliation:
1: Environmental Health Science and Research Bureau, Health Canada, Ottawa, Canada

Contributions:

Experimental Design	**Andrey Boyadzhiev (Toxicological experiments)** Sabina Halappanavar (Toxicology experiments) Pat Rasmussen (Dissolution testing)
Particle Suspension	**Andrey Boyadzhiev (ZnO US3580, CuO 544868, TiO_2 NIST1898)** Silvia Solorio Redriguez (coated TiO_2)
Dynamic Light Scattering Analysis	Dongmei Wu
Dissolution Testing	Mary-Luyza Avramescu
Electron Microscopy Imaging	University of Ottawa Material Characterization Core
Exposure	**Andrey Boyadzhiev** Silvia Solorio Rodriguez
Trypan Blue Analysis	**Andrey Boyadzhiev** Silvia Solorio Rodriguez
CometChip Imaging and Analysis	**Andrey Boyadzhiev** Silvia Solorio Rodriguez
Statistics	**Andrey Boyadzhiev**
Benchmark Concentration Modelling	**Andrey Boyadzhiev**
Data Interpretation	**Andrey Boyadzhiev**
Manuscript Writing and Revisions	**Andrey Boyadzhiev** Silvia Solorio Rodriguez Sabina Halappanavar
Internal Review	Paul White Julie Cox

4.1 Abstract

Metal oxide nanomaterials (MONMs) are among the most highly utilized classes of nanomaterials worldwide, though their potential to induce DNA damage in living organisms is known. High-throughput *in vitro* assays have the potential to greatly expedite analysis and understanding of MONM induced toxicity while minimizing the overall use of animals. In this study, the high-throughput CometChip® assay was used to assess the *in vitro* genotoxic potential of pristine copper oxide (CuO), zinc oxide (ZnO), and titanium dioxide (TiO_2) MONMs and microparticles (MPs), as well as five coated/surface-modified TiO_2 NPs and zinc-(II)-chloride ($ZnCl_2$) and copper-(II)-chloride ($CuCl_2$) after 2–4 h of exposure. The CuO NPs, ZnO NPs and MPs, and $ZnCl_2$ exposures induced concentration- and time-dependent increases in DNA damage at both timepoints. TiO_2 NPs surface coated with silica or silica–alumina and one pristine TiO_2 NP of rutile crystal structure also induced subtle concentration-dependent DNA damage. Concentration modelling at both post-exposure timepoints highlighted the contribution of the dissolved species to the response of ZnO, and the role of the nanoparticle fraction for CuO mediated genotoxicity, showing the differential impact that particle and dissolved fractions can have on genotoxicity induced by MONMs. The results imply that solubility alone may be insufficient to explain the biological behavior of MONMs.

4.2 Introduction

Metal oxide (MO) nanomaterials (NMs) are among some of the most highly utilized engineered NMs worldwide, with an estimated global market share of USD 5.55 billion in 2019 and an anticipated 9.3% growth by 2027 (Marketysers Global Consulting LLP). MONMs have many varied applications such as food and cosmetic-grade pigments and additives, catalytic reagents, and as advanced electronics and complex materials fabrication components (Chavali & Nikolova, 2019; Huang, Y. et al., 2017). With increased utilization, manufacturing, and manipulation of MONMs, there are increased concerns for risks associated with exposure to these materials.

MONMs are known to induce a wide variety of effects in laboratory experimental models. Evidence for health impacts in humans comes from occupational studies involving mining activities, welding fumes and diesel exhaust (ANTONINI, J. M. et al., 2013; Ghio et al., 2012; Graczyk et al., 2016; Martell & Guidotti, 2022; Oliver et al., 2022; Verma, 2013). Studies conducted in mammalian *in vitro* and *in vivo* model systems have shown pulmonary toxicity and DNA damage resulting from exposure to different kinds of MONMs (Sengul & Asmatulu, 2020), the exact nature and magnitude of which are suggested to be dependent upon their physicochemical properties such as particle size, solubility and particle surface (Huang, Y. et al., 2017). Recent research has shown that, in human volunteers, inhalation of zinc oxide (ZnO) nanoparticles (NPs) at concentrations under the US-recommended exposure limit for zinc fumes significantly increases markers of lung and systemic inflammation (Monsé et al., 2018). With respect to genotoxicity, NMs (including MONMs) have the potential to induce DNA damage through both primary and secondary mechanisms, which involve the direct interaction of NMs with DNA, the production of reactive intermediates such as reactive oxygen species (ROS) that can cause DNA damage, or through reactive molecules produced during an inflammatory response (Kohl et al., 2020). Moreover, some MONMs (e.g., titanium dioxide (TiO_2) NPs) exhibit photoactivation. TiO_2 NPs induce oxidative DNA damage in acellular conditions upon visible or UV irradiation (Petersen et al., 2014). Although early ROS production may be protective in nature, improperly repaired DNA damage arising from ROS can lead to mutagenic and carcinogenic effects. Three widely utilized and commercially available MONMs—ZnO, copper oxide (CuO) and TiO_2—have been examined for their genotoxic potential using mammalian *in vitro* and *in vivo* model systems (MAGAYE et al., 2012; Singh, Sanjiv, 2019; Wani & Shadab, 2020). Both ZnO and CuO NPs are soluble in a biological medium (Boyadzhiev et al., 2021; Reed et al., 2012) and their toxicity is thought to be a combination of both particulate and dissolved metal species. The microparticle (MPs) counterparts of CuO and ZnO NP types are shown to be less soluble (Boyadzhiev et al., 2021; Tada-Oikawa et al., 2015) and differ in their toxicity potential compared to their nano forms. While both ZnO and CuO NPs have been consistently shown to induce DNA damage both *in vitro* and *in vivo*, there

are conflicting reports with respect to TiO_2 NPs (Wani & Shadab, 2020). With respect to TiO_2 NPs, their insoluble nature precludes the impact of an ionic or dissolved fraction on response and any resulting genotoxicity is suggested to be the result of particle–cell interactions, or through the production of reactive intermediates; both of which are impacted by the material's physicochemical properties (Carriere et al., 2020; Wani & Shadab, 2020). With respect to crystal phase and surface coating, most studies have evaluated the anatase form of TiO_2 NPs and mixtures of anatase/rutile, while few studies have assessed the genotoxicity of coated TiO_2 NPs (Charles et al., 2018). Thus, a clear understanding of how size, solubility and other material properties affect the genotoxic potential of MONMs is still needed.

There are numerous tests available for measuring the genotoxicity of NMs *in vitro*, with varying levels of throughput and applicability. The most commonly used assays include the comet assay, the micronucleus assay, the chromosomal aberration test, and the hypoxanthine phosphoribosyl transferase forward mutation assay (OECD, 2018). Of these, the comet assay has been the most widely utilized test for measuring DNA damage in eukaryotic cells (Elespuru et al., 2018; Langie et al., 2015; OECD, 2018). This assay has been used to investigate the DNA damaging properties of NMs (Magdolenova et al., 2012). However, the traditional comet assay is low throughput, which makes it challenging for the purposes of screening a large number of NMs in a time- and resource-effective manner. Recent developments of this assay have yielded a commercially available high-throughput version, the CometChip® assay (Sykora et al., 2018b), which holds great potential for routine screening of DNA damage induced by NMs.

The high-throughput alkaline CometChip® assay relies on the same principles as the standard alkaline comet, however, it increases the throughput ~200-fold by utilizing a micro-patterned agarose chip in a 96-well format instead of glass slides (Sykora et al., 2018b). Each of the 96 wells in the chip contains ~500 micropores, fitting one cell per pore, which allows for 96 different exposures simultaneously on one gel. This system has been used to successfully measure chemical-induced DNA damage in suspension and adherent mammalian cell cultures as well as in peripheral blood monocytes (Sykora et al., 2018a,

2018b). Similar in-house made micro-patterned agarose-gel comet chip systems have been used to assess the *in vitro* genotoxicity of ZnO, cerium dioxide (CeO_2), iron oxide (Fe_2O_3), silica (SiO_2), and silver (Ag) NPs as well as ZnO nanorods (Sotiriou et al., 2014; Watson et al., 2014). The high-throughput assay enables side-by-side comparison of all three species of metal oxides (NP, MP, and dissolved metal salt) for their DNA damaging potential and allows a systematic understanding of the contribution of different properties of MONMs to genotoxicity. This type of data is a prerequisite to applying approaches such as read-across in human health risk assessment of nanomaterials.

Thus, the overarching goal of the present study was to apply the high-throughput CometChip® assay to investigate the role of size, solubility and surface coatings on NM-induced genotoxicity. Specifically, the study investigated DNA damaging effects in adherent murine lung epithelial (FE1) cells exposed for 2–4 h to different concentrations of ZnO, CuO, and TiO_2 NPs, MPs as well as zinc and copper chloride salts. No-observed-effect-concentration (NOEC) and the lowest-observed-effect-concentration (LOEC) were used alongside benchmark concentration (BMC) modelling to determine points of departure (PODs) to delineate the differences in relative potency between the various exposures.

4.3 Methods

4.3.1 Metal oxide nanomaterials and metal chloride salts

A total of 10 NPs with primary particle sizes of ≤ 50 nm, and one metal oxide nanowire (NW) were procured from five different manufacturers (**Table 4-1**). In addition, three pristine bulk analogues of TiO_2, ZnO, and CuO (**Table 4-1**), copper-(II)-dihydrate (referred to as $CuCl_2$; Sigma Aldrich, Catalogue #: C3279-100G), and zinc-(II)-chloride ($ZnCl_2$; Sigma Aldrich, Catalogue #: Z0152-100G) were procured to assess the effects of particle size fraction and particle solubility on genotoxic response. A 30% hydrogen peroxide (H_2O_2) solution in dH_2O (Sigma Aldrich, Catalogue #:216763) was used as a positive assay control for DNA damage.

Table 4-1. Particle characterization of the CuO, ZnO, and TiO_2 NMs used for genotoxicity screening. Measured primary NP sizes are presented in terms of width and length, with standard deviation in parentheses for each respective measurement (n = 100–200). For TiO_2 NW (774510) only the width was directly measured due to the tangled nature of the fibres. PPS: primary particle size. SSA: specific surface area.

Metal Oxide	Manufacturer (Catalogue Number)	Coating	PPS Reported [a]	PPS Measured (Standard Deviation)	Aspect ratio (Standard Deviation)	SSA (m^2/g) [a]
ZnO	US Research Nanomaterials Inc. (US3580)	Pristine	35-45 nm	23.9 × 19.4 nm (7.2 × 5.5 nm)	1.23 (0.17)	65
CuO	Sigma Aldrich (544868)	Pristine	28 nm	64.8 × 45.9 nm [b] (28.0 × 47.0 nm)	1.39 (0.39)	33
TiO_2	National Institute of Standards and Technology (1898)	Pristine	19 nm Anatase (76%) 37 nm Rutile (24%)	26.8 × 20.8 nm (8.9 × 6.8 nm)	1.30 (0.26)	55.55
TiO_2	Nanostructured & Amorphous Materials, f. (5422HT)	Silica	20 nm (80–90% Anatase; 10–20% Rutile)	52.6 × 32.7 nm (25.3 × 12.4 nm)	1.63 (0.51)	≥40
TiO_2	Nanostructured & Amorphous Materials, Inc. (5423HT)	Silica & Alumina	20 nm (80–90% Anatase; 10–20% Rutile)	37.6 × 30.1 nm (23.1 × 18.3 nm)	1.32 (0.71)	≥40
TiO_2	Nanostructured & Amorphous Materials, Inc. (5424HT)	Silica & Stearic Acid	20 nm (80–90% Anatase; 10–20% Rutile)	49.5 × 32.9 nm (20.4 × 12.4 nm)	1.54 (0.42)	≥10
TiO_2	Nanostructured & Amorphous Materials, Inc. (5425HT)	Silica & Silicone Oil	20 nm (80–90% Anatase; 10–20% Rutile)	50.3 × 32.5 nm (42.8 × 13.3 nm)	1.53 (0.75)	≥10
TiO_2	MKNano (MK-TiO_2-A050)	Hydrophilic	50 nm (Anatase)	30.7 × 26.3 nm	1.17 (0.15)	N/A

				(8.57 × 7.01 nm)		
TiO_2	MKNano (MKN-TiO_2-R050P)	Pristine	50 nm (Rutile)	82.4 × 52.9 nm (34.6 × 14.6 nm)	1.56 (0.51)	N/A
TiO_2	MKNano (MKN-TiO_2-A005)	Pristine	<5 nm (Anatase)	7.6 × 5.4 nm (2.1 × 1.6 nm)	1.42 (0.30)	356
TiO_2	Sigma Aldrich (774510)	Pristine	100 nm × 10 000 nm	106.5 nm (147.5 nm)	----	N/A

[a] Information obtained from manufacturer. [b] Information obtained from (Boyadzhiev et al., 2021).

4.3.2 Cell culture

Immortalized FE1 cells derived from the Muta™ Mouse transgenic rodent model were utilized for particle and metal chloride exposures. These cells retain the characteristics of type I and type II pulmonary alveolar epithelial cells, and have been used in the past to assess the genotoxicity and mutagenicity of both chemicals and NPs (Arlt et al., 2008; Bengtson et al., 2016; Decan et al., 2015; Jacobsen et al., 2008b; Maertens et al., 2017; White et al., 2003).

Cells were maintained in phenol-red-containing Dulbecco's Modified Eagle's Medium Nutrient Mixture: F12 HAM (1:1) culture media (DMEM/F12 (1:1) (1X), Life Technologies, Burlington, ON, Canada) supplemented with 2% fetal bovine serum (FBS, Life Technologies, Burlington, ON, Canada), 1 ng/mL human epidermal growth factor (EGF, Life Technologies, Burlington, ON, Canada), 100 U/mL penicillin G, and 100 µg/mL streptomycin (Life Technologies, Burlington, ON, Canada) in an incubator at 37 °C, with 5% CO_2. For CometChip® exposures, the same conditions were used, except for the absence of phenol-red in the exposure media.

4.3.3 Primary particle size determination

A JEM-2100F Field Emission transmission electron microscope (TEM) (JEOL, Peabody, MA, USA) was used to capture 9–10 non-overlapping transmission electron micrographs of dry ZnO and TiO_2 MONMs used in this study for primary particle size analysis, as described in (Boyadzhiev et al., 2021). All electron microscopy images were

imported into ImageJ for particle size measurement. From the TEM images of the MONMs, the length and width of 9–18 individual particles per image were analyzed for a total of at least 100 particles per NM. For the TiO_2 NW, only the width was measured due to the tangled nature of the material in the micrographs. The size distributions were plotted in histogram format (GraphPad Prism 9.2.0, GraphPad Software, San Diego, CA, USA), and the mean length and width were reported with standard deviation.

With respect to the metal oxide MPs, a JSM-7500F Field Emission scanning electron microscope (SEM) (JEOL, Peabody, St. Louis, MO, USA) was used to capture 10 non-overlapping scanning electron micrographs of the ZnO and TiO_2 MPs used in this study. Due to the aggregated nature of the particles, it was not possible to conduct size analysis from the resulting micrographs. The CuO NPs and MPs have been similarly analysed for their primary particle size and results have been published (Boyadzhiev et al., 2021).

4.3.4 Particle dissolution experiments

The release of Zn from the ZnO NPs and MPs was assessed as outlined in (Avramescu et al., 2020; Boyadzhiev et al., 2021). The ZnO NPs were suspended at a concentration of 1 mg/mL in ultrapure dH_2O as described in (Avramescu et al., 2019). The NP stock dispersions were sonicated at a delivered sonication energy of 265 J/mL. From this stock, serial dilutions in cell culture media +2% fetal bovine serum were made to final concentrations of 10 and 100 µg/mL. With respect to the ZnO MPs, the particles were directly suspended in cell culture media +2% fetal bovine serum at a concentration of 100 µg/mL and mixed by vortexing. ZnO particle suspensions were incubated on an orbital shaker (1 h shaking per day at 100 rotations per minute shaking rate) within polypropylene 50 mL conical tubes at 37 °C for 0, 24, and 48 h. At the designated times, samples were withdrawn and the dissolved metal fraction was measured following sequential centrifugation (20,000× g, 3 × 30 min; Alegra 64R centrifuge, Beckman Coulter, Mississauga, ON, Canada). The final extracts were acidified to a concentration of 2.5% HNO_3 (SCP Science, Graham Baie D'Urfé, QC, Canada) and the Zn fraction was measured using an Inductively Coupled Plasma Optical Emission Spectrophotometer (ICP-OES, Agilent Technologies, Santa Clara, CA, USA). Blank samples as well as spiked matrix blanks were incubated alongside the ZnO

NP and MP suspensions. Analysis of the dissolved fraction was conducted using a 5100 Synchronous Vertical Dual View ICP-OES at a wavelength of 213.857 nm as recommended by the manufacturer. The instrument was operated at 1.2 kW power, 12 L/min plasma, 1 L/min auxiliary, 0.7 L/min nebulizer flow rate in SVDV mode, with 3 replicates per sample. The CuO NPs and MPs have been similarly assessed for their solubility and results have been published (Boyadzhiev et al., 2021).

4.3.5 Preparation of exposure suspension

MONM and MP stock suspensions were prepared in ultrapure dH_2O, based upon delivered sonication energies determined to produce a stable suspension for the NP in question. Sonication conditions for each particle can be found in **Supplementary Table 4-1**. For all sonication procedures, a Branson Ultrasonics Sonifier™ 450 (Branson Ultrasonics Markham, ON, Canada) with a ½ inch disruptor horn and a removable flat tip was used. The tip was immersed into the suspension, 1–1.5 inches from the surface of the air–liquid interface. Rapid sedimentation of the TiO_2 NPs, MK-TiO_2-A050 (**Table 4-1**), was observed to occur in water. In order to improve the dispersion, bovine serum albumin (BSA; Sigma Aldrich, Oakville, ON, Canada) was used as a stabilizing agent (**Supplementary Figure 4-1**). NPs were suspended in ultrapure dH_2O at 5 mg/mL. This suspension was sonicated as described above, immediately following which BSA was added to a final concentration of 2 mg/mL. The suspension was then vortexed and incubated for 10 min. Sonicated stock suspensions were used to produce desired serial dilutions in a cell culture medium. Each exposure dilution was inverted 20 times to mix and the dilutions were used within 15 min of preparation. Three to five concentrations of MONMs, MPs, $CuCl_2$, and $ZnCl_2$ were chosen for exposure. Concentration interconversions for each are available in **Supplementary Table 4-2**.

4.3.6 Dynamic light scattering analysis of NP suspensions

Particle characterization in the relevant medium was conducted using dynamic light scattering (DLS), as described in (Boyadzhiev et al., 2021). Sonicated and suspended NP stocks in ultrapure dH_2O were diluted in cell culture medium (+2% fetal bovine serum) to a final concentration of 50 µg/mL, and aliquots were used for DLS analysis in a Zetasizer

Nano ZSP (Malvern Panalytical, Westborough, MA, USA). The hydrodynamic diameter (aggregate size measured in nm) and the poly-dispersity-index (PDI; a measure of the broadness of size distribution) were calculated. For each particle sample, 2–3 independent runs were conducted, with 5 measurements conducted per run for a total of 10–15 measurements per particle. For MK-TiO_2-A050 TiO_2 NPs, DLS characterization was conducted in DMEM (+ 2% fetal bovine serum) and 0.02 mg/mL BSA.

4.3.7 Trypan Blue exclusion assay

In order to determine that the concentrations chosen for genotoxicity analysis do not induce overt cytotoxicity, the Trypan Blue exclusion method for cell viability assessment was utilized. FE1 cells were plated in 6-well plates at a density of ~130,000 cells/well. Following overnight incubation, the cells were exposed to 1.8 mL of 3–5 concentrations (0–108 µg/mL) of MONMs, MPs, and $ZnCl_2$ or $CuCl_2$ as outlined in **Supplementary Table 4-2**. In all cases, blank media exposed cells served as negative controls. For MK-TiO_2-A050 TiO_2 NPs, negative controls were exposed to medium containing 0.04 mg/mL BSA (the amount of BSA that was present in the medium at 100 µg/mL NP concentration). Following 2 and 4 h of exposure, cell supernatant was removed and cells were washed once with 0.5 mL of PBS. Phase-contrast images of each condition were acquired at 4x and 20x in order to assess morphology. Cells were detached from the surface with 0.15 mL of 0.25% Trypsin-EDTA (1x) (Thermofisher Scientific, Whitby, ON, Canada), and resuspended in 0.5 mL of fresh culture medium. Trypan Blue staining was conducted as described in (Boyadzhiev et al., 2021; Decan et al., 2015). In brief, 10 µL of cell suspension was combined with 10 µL of Trypan Blue dye (Thermofisher Scientific, Whitby, ON, Canada) and incubated at room temperature for 5–10 min before counting in a hemocytometer. The number of blue and white cells was counted, and the ratio between the number of white cells and the total number of cells were used as a measure of cell viability. Each sample was assessed in triplicate (n = 3), and the statistical difference between the negative control (time-matched blank media samples) was determined through a one-way ANOVA with a Dunnett's post hoc in the case of significant results in SigmaPlot 12.5 (Systat Software Inc., San Jose, CA, USA).

4.3.8 CometChip® assay

The protocol utilized for the CometChip® experiments was a slight modification of the manufacturer protocol. On the day of exposure, FE1 cells were trypsinized and suspended at a density of ~150,000 cells/mL in fresh phenol red free growth medium. The suspension was passed through a 70 µm cell strainer (Fisher Scientific, Whitby, ON, Canada) in order to ensure that the suspension was single-celled. After 30 min of equilibration in 100 mL PBS (room temperature; Thermofisher Scientific, Whitby, ON, Canada), the micro-patterned agarose CometChip® (Cedarlane Laboratories, Burlington, ON, Canada) was loaded into the macrowell former system, and the residual PBS was aspirated using a VacuSafe system (Integra LifeSciences, Toronto, ON, Canada). Next, 100 µL of the single-cell suspension was loaded into each well of the chip. The system was incubated at 37 °C for 15 min, after which the system was rocked east–west and north–south 4 times each in order to aid cell loading into the micropores and placed in the incubator for 5 additional minutes. Following loading, the cell-containing loading medium was aspirated from each well using a VacuSafe system and 50 µL of fresh phenol red free cell culture medium was loaded into each well. The system was placed back into the incubator until the exposure. For each experiment, a 4 h blank medium negative control was used and cells treated with 100 µM H_2O_2 in cell culture media for 1 h were used as positive assay controls. For MK-TiO_2-A050, negative controls were exposed to medium containing 0.04 mg/mL BSA. Following exposure, the chip was washed with PBS and a low melting agarose (Cedarlane Laboratories, Burlington, ON, Canada) overlay was deposited onto the chip to fix the cells in place. The agarose was allowed to harden at room temperature before being transferred to a 4 °C cold room to fully polymerise under light occlusion. The chip was then lysed for an hour in the dark using 100 mL of the lysis buffer solution (Cedarlane Laboratories, Burlington, ON, Canada) and acclimatized in alkaline solution (pH ≥13, 200 mM NaOH (Sigma Aldrich, Oakville, ON, Canada) + 1 mM EDTA (Thermofisher Scientific, Whitby, ON, Canada) + 0.1% Triton-X (Fisher Scientific, Whitby, ON, Canada)) for 40 min. Electrophoresis was carried out in the dark in alkaline conditions (pH ≥13, 200 mM NaOH + 1 mM EDTA + 0.1% Triton-X), under constant voltage (20 V, 1

V/cm) and variable current (280 mA) for 50 min. The chip was neutralized in 400 mM and 20 mM Tris-HCl buffer (1M pH 7.4 Tris-HCl procured from Sigma Aldrich, Oakville, ON, Canada), followed by 14 h of overnight staining in dark in a solution of 0.2x SYBR GOLD stain (10,000× SYBR GOLD in DMSO procured from Life Technologies Corporation, Burlington, ON, Canada) in 20 mM Tris-HCl.

The following day, the chip was de-stained for one hour in 100 mL of room temperature 20 mM Tris-HCl and imaged using a Leica DMi8 automated confocal fluorescence microscope (Leica Microsystems, Wetzlar, Germany) at 5x magnification, and the resulting TIFF images were uploaded into the proprietary Trevigen Comet Software (Bio-Techne, Devens, MA, USA) for analysis. Quality control was conducted on the comets, in order to remove misidentified artefacts as well as to adjust improperly labelled comet tails and heads. Individual wells with less than 50 valid comets after quality control were not included in the final analysis. For all controls and experimental conditions, each biological replicate contained between 2–8 technical replicates. The mean percentage DNA in the tail was used as the metric for DNA damage. The final data, containing 3–4 biological replicates per condition were normalized via a log transformation and the resulting transformed data sets were statistically analyzed using a one-way analysis of variance (ANOVA) with a Dunnett's multiple comparison post hoc against the respective media control in SigmaPlot 12.5 (Systat Software Inc., San Jose, CA, USA).

4.3.9 Benchmark concentration modelling

PROAST version 67.0 (**https://www.rivm.nl/en/proast**; accessed on 1 June 2020) was used to conduct concentration-response modelling of percentage DNA in the tail from FE1 cells exposed for 2–4 h. The benchmark response (BMR) was set to 1.0 (100% increase over baseline) according to the structure of the data and the magnitude of responses seen. BMC modelling was carried out (1) without using covariate analysis, and (2) by setting the exposure compounds as a covariate in PROAST, then carrying out modelling for the 2 and 4 h timepoints. All resulting models were assessed for goodness of fit, normality (through quantile-quantile plots), and homogeneity of variance (through residual plots). Outlier samples (samples with standardized residuals >3) were removed for BMC modelling. Two

concentration metrics were used for BMC computation, µg/mL of the compound, and µg/mL of the constituent metal. All PROAST markdowns and model fitting graphs, quantile–quantile plots, and residuals plots can be found in the **Supplementary File 4-1**, **4-2**.

4.4 Results

4.4.1 Primary particle and particle suspension characterization

All MONMs used in this study had a manufacturer reported primary particle size < 50 nm and specific surface areas between 33–65 m^2/g. Regarding TiO_2 NPs, the primary particle size was 20–50 nm for all except MKN-TiO_2-A005, which was 8 nm in size with a surface area of 356 m^2/g (**Table 4-1**). The MPs examined in this study had primary particle sizes ranging from 1000–5000 nm with specific surface areas between 2–8 m^2/g (**Table 4-2**). SEM images were acquired for the ZnO and TiO_2 MPs used in this study, however, the materials were too aggregated to conduct an accurate particle size analysis (**Supplementary Figure 4-2**, **4-3**). What can be seen from the representative micrographs is that the ZnO MPs have an irregular particle shape, with many rod-like crystallites present. The TiO_2 MPs are largely spherical in appearance. Additional TEM imaging and primary particle size analysis of the NPs used in this study show that almost all NPs used in this study are roughly spherical, with measured sizes in the range of the manufacturer reported values (**Table 4-1**) (**Supplementary Figure 4-4**; CuO NP data previously published in (Boyadzhiev et al., 2021)). TiO_2 NWs were extremely long (greater than 10 µm), and the length could not be reliably measured.

Table 4-2. Particle characterization information of the ZnO, CuO, and TiO_2 MPs used for genotoxicity screening. PPS: primary particle size. SSA: specific surface area.

Metal Oxide	Manufacturer (Catalogue Number)	Coating	PPS Reported (nm) [a]	SSA (m^2/g) [a]
ZnO	US Research Nanomaterials Inc. (US1003M)	Pristine	1000	2–5.8
CuO	US Research Nanomaterials Inc. (US1140M)	Pristine	5000	4–6
TiO_2	US Research Nanomaterials Inc. (US1017M)	Pristine	1500 nm Anatase 1500 nm Rutile	5–8

[a] Information obtained from manufacturer.

Dynamic light scattering analysis conducted on 50 µg/mL NP suspensions in cell culture medium containing serum shows that ZnO and CuO NPs have similar aggregate sizes of 323 and 337 nm, respectively. All TiO_2 NPs showed values from 400–730 nm, except the TiO_2 NIST 1898 NPs which aggregated to a larger extent with an average size of ~1250 nm. All suspensions were heterodisperse in the cell culture medium, with PDI values ranging from 0.39 for TiO_2 NPs to 0.56 for ZnO NPs (**Table 4-3**).

Table 4-3. Dynamic light scattering analysis of MONPs within DMEM cell culture media +2% fetal bovine serum.

Metal Oxide	Manufacturer (Catalogue Number)	Hydrodynamic Diameter (50 µg/mL DMEM)	Polydispersity Index (50 µg/mL DMEM)
ZnO	US Research Nanomaterials Inc. (US3580)	323 ± 125 nm	0.56 ± 0.12
CuO	Sigma Aldrich (544,868)	337 ± 17.4 nm	0.40 ± 0.04
TiO_2	National Institute of Standards and Technology (1898)	1251 ± 83.1 nm	0.39 ± 0.25
TiO_2	Nanostructured & Amorphous Materials, Inc. (5422HT)	663 ± 49.7 nm	0.35 ± 0.05
TiO_2	Nanostructured & Amorphous Materials, Inc. (5423HT)	726 ± 85.3 nm	0.31 ± 0.06
TiO_2	Nanostructured & Amorphous Materials, Inc. (5424HT)	563 ± 23.6 nm	0.41 ± 0.05
TiO_2	Nanostructured & Amorphous Materials, Inc. (5425HT)	553 ± 27.2 nm	0.33 ± 0.04
TiO_2	MKNano (MK-TiO_2-A050)	460 ± 66.6 nm [a]	0.37 ± 0.07 [a]
TiO_2	MKNano (MKN-TiO_2-R050P)	373 ± 11.3 nm	0.27 ± 0.02
TiO_2	MKNano (MKN-TiO_2-A005)	407 ± 17.6 nm	0.23 ± 0.02

[a] DMEM + 0.02 mg/mL BSA.

4.4.2 Dissolution of ZnO and CuO particles

With respect to ZnO and CuO particles, both are known to be soluble in biological environments. The dissolution of ZnO NPs and MPs was measured in FE1 cell culture medium over 0–48 h (**Figure 4-1**). From the data presented, it can be seen that at a concentration of 100 µg/mL, both the ZnO NPs and MPs undergo immediate dissolution to a similar level. Concentration-dependent dissolution is seen with respect to the ZnO NPs,

with the lower concentration showing a higher propensity to dissolve over the experimental time span (94.5% vs. 19.3% dissolved at 48 h for 10 and 100 µg/mL). The amount of dissolved material stays relatively consistent from 0–48 h for all Zn materials, albeit a slight increase over time can be seen for the 100 µg/mL concentration of ZnO NPs (14.6–19.3% dissolved from 0–48 h).

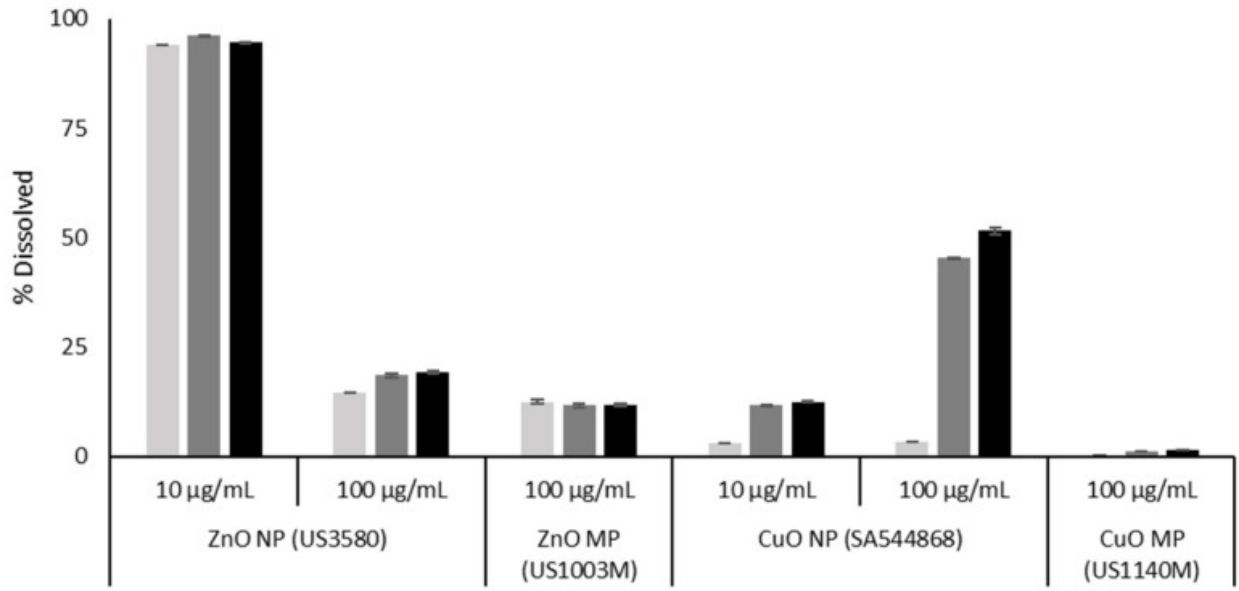

Figure 4-1. Percentage dissolution of CuO and ZnO NPs (US3580; SA544868) and MPs (US1003M; US1140M) in DMEM F12 cell culture media, with 2% serum, after 0–48 h of incubation at 37 °C. Error bars represent ± standard deviation (n = 3). Light grey: 0 h. Dark grey: 24 h. Black: 48 h. CuO data were reproduced from *(Boyadzhiev et al., 2021)*.

The CuO dissolution data were reproduced from (Boyadzhiev et al., 2021) (**Figure 4-1**). From the data presented, it can be seen that the CuO particles exhibit concentration, time, and size dependent dissolution from 0–48 h and dissolve to a greater extent than the same concentration of MPs (51.5% vs. 1.51% for NPs and MPs, respectively at 48 h). However, unlike ZnO, CuO NPs exhibit a higher degree of dissolution at higher concentrations (12.6% vs. 51.5% dissolved at 48 h for 10 and 100 µg/mL, respectively).

4.4.3 Viability analysis of cells treated with NPs, MPs, and metal chlorides

Trypan Blue exclusion assay was conducted to assess viability after 2–4 h MONM exposure. Phase-contrast images and percentage of cell viability results are shown in **Figure 4-2**, and **Supplementary Figure 4-5**, **4-6**. With respect to the ZnO and CuO, only the

highest concentration of ZnO NPs resulted in a statistically significant decrease in percentage viability as compared to control, down to 88% at 40 µg/mL ($p < 0.05$) after 4 h of exposure (**Figure 4-2**). From all the TiO_2 forms assessed, only TiO_2 5424HT exposure resulted in a statistically significant loss of cell viability at 100 µg/mL at 2 h (89%, $p < 0.05$). Although at other concentrations of ZnO, there was no decrease in cell viability, phase-contrast images of ZnO NP, ZnO MP, and $ZnCl_2$ showed significant cell rounding (**Supplementary Figure 4-5**, **4-6**) at both time points. Exposure to 100 µM H_2O_2 for 4 h did not result in a reduction of viability as compared to time-matched media controls (data not shown). Exposure to particle concentrations over 100 µg/mL resulted in significant particle overload for TiO_2 NPs, which impaired accurate cell counting (data not shown). As such, concentrations over 100 µg/mL were not used for subsequent experiments.

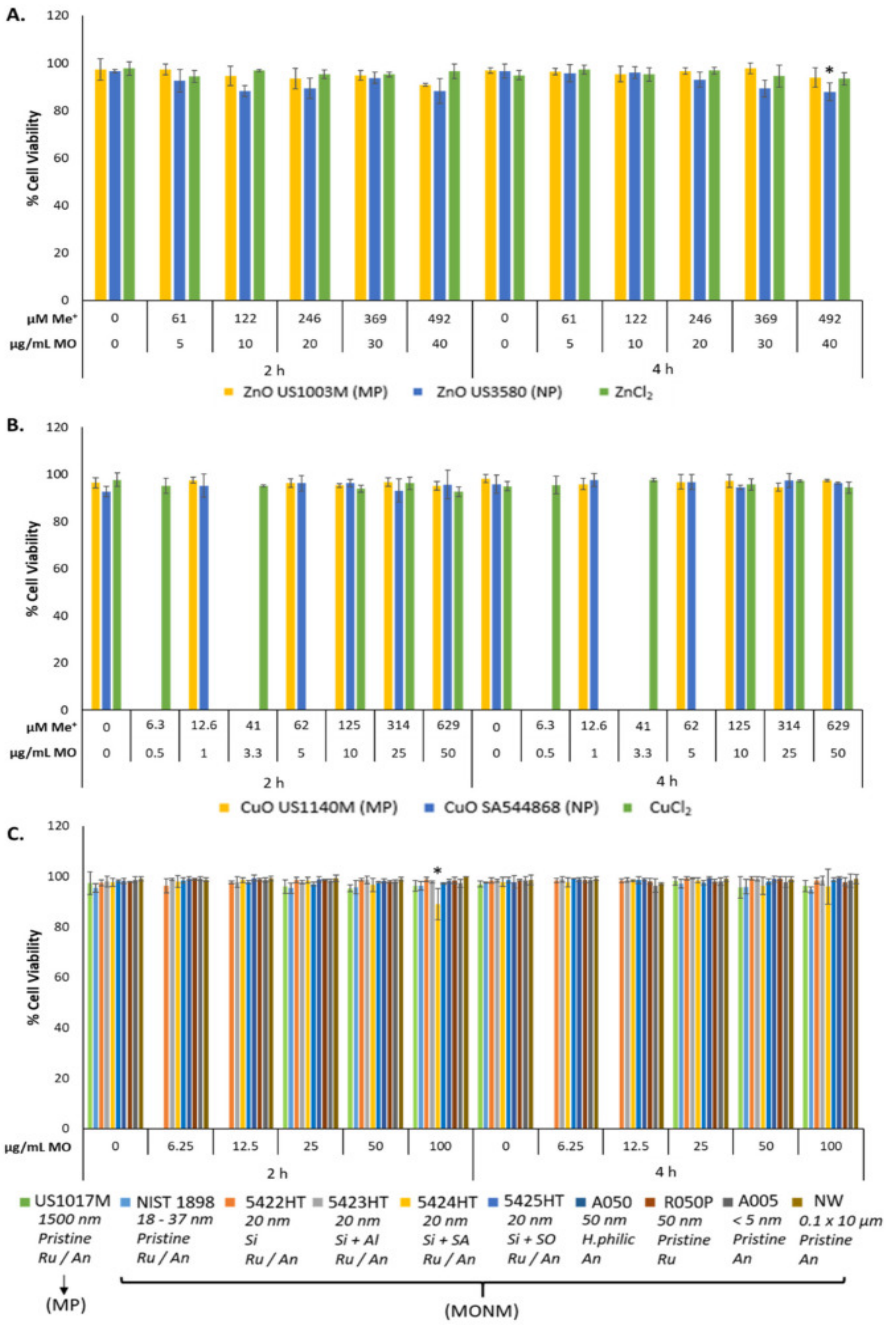

Figure 4-2. FE1 percentage cell viability analysis following 2–4 h exposure to (A) Zn forms, (B) Cu forms, and (C) TiO_2 NPs and MPs. Statistically significant differences between the exposed samples and the media control were determined through a one-way ANOVA with a Dunnett's post hoc in the case of significant results. * p <0.05. Error bars are +/−SD (n = 3–4). µM Me+: concentration expressed in terms of µM of the constituent metal. µg/mL MO: concentration expressed as mass concentration of metal oxide. NW: nanowire, Ru/An: anatase + rutile mix, An: anatase, Ru: rutile, Si: silica coated, Si + Al: silica and alumina coated, Si + SA: silica and stearic acid coated, Si + SO; silica + silicone oil, H.philic: hydrophilic coating.

4.4.4 Metal oxide and metal chloride induced DNA damage

DNA damage, as assessed by the CometChip® assay via percentage DNA in the tail, is most prominently seen with respect to soluble MONM exposures (**Figure 4-3**). Treatment with ZnO NPs induced concentration- and time-dependent DNA damage, with 18 and 57% DNA in the tail at 2 and 4 h of exposure at 40 µg/mL (**Figure 4-3A**). The ZnO MPs induced significant DNA damage at all concentrations tested at both time points, with 12 and 52% DNA in the tail at 2 and 4 h at a concentration of 40 µg/mL (**Figure 4-3A**). With respect to $ZnCl_2$, concentration- and time-dependent increases in DNA damage were seen but with a lower magnitude than that seen for ZnO NPs and ZnO MPs with equimolar amounts of metal. A maximal response of 7 and 27% DNA in the tail was observed in the 67 µg/mL $ZnCl_2$ concentration group at 2 and 4 h, respectively (**Figure 4-3A**). Similarly, at both post-exposure timepoints, CuO NPs induced concentration- and time-dependent DNA strand breaks, with 24 and 58% DNA in the tail at 2 and 4 h, respectively, at 50 µg/mL. CuO MPs did not induce DNA damage at any concentration or timepoint tested (**Figure 4-3B**). Treatment with $CuCl_2$ did not induce any DNA damage (**Figure 4-3B**).

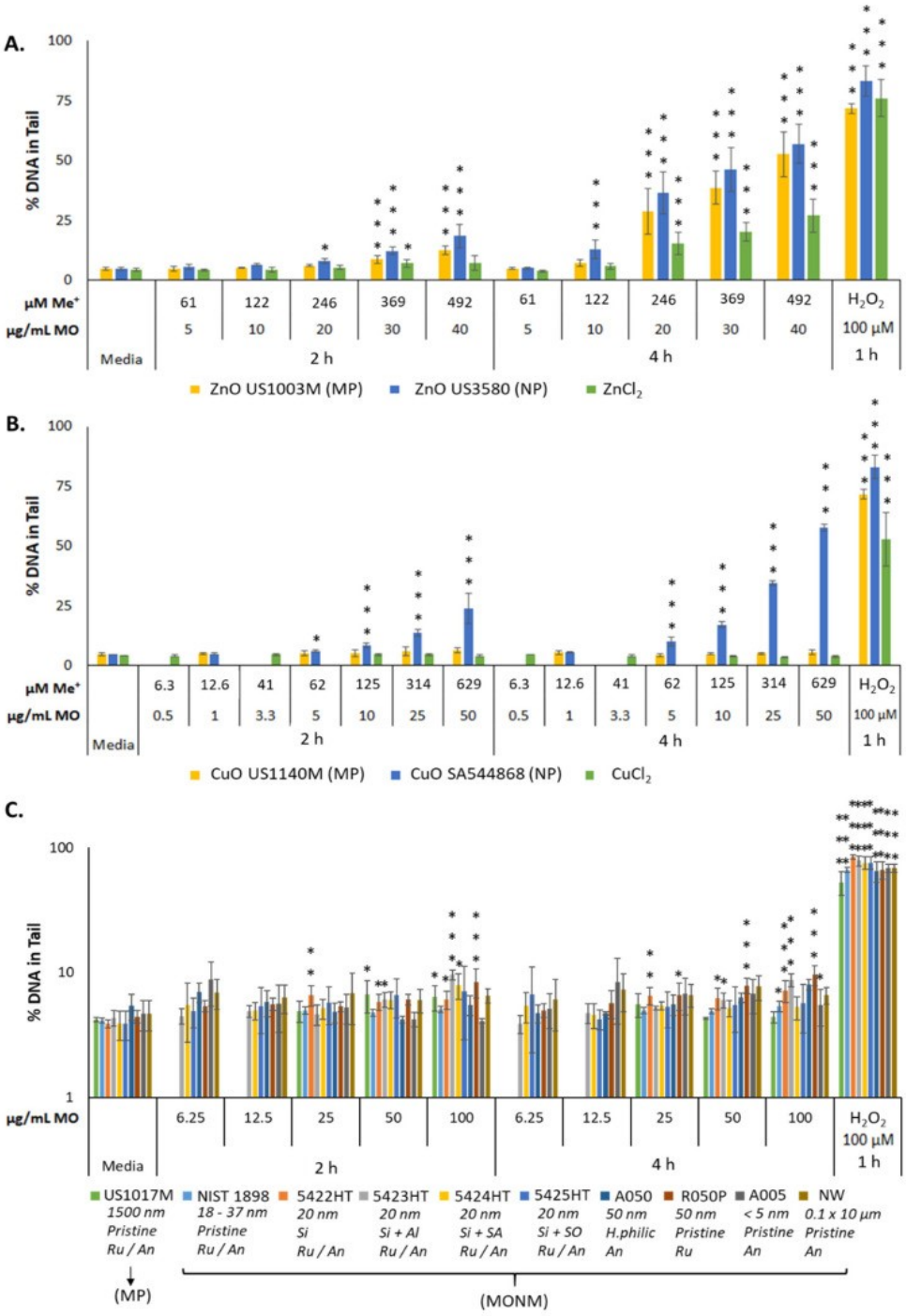

Figure 4-3. DNA damage, as measured by percentage DNA in tail, in FE1 cells after 2–4 h exposure to (A) Zn forms, (B) Cu forms, and (C) TiO_2 materials. Statistically significant differences between the exposed samples and the media control were determined through a one-way ANOVA with a Dunnett's post hoc in the case of significant results. * p <0.05. ** p <0.01. *** p <0.001. Error bars are ±SD (n = 3–4). NW: nanowire, Ru/An: anatase + rutile mix, An: anatase, Ru: rutile, Si: silica coated, Si + Al: silica and alumina coated, Si + SA: silica and stearic acid coated, Si + SO; silica + silicone oil, H.philic: hydrophilic coating.

With respect to the insoluble TiO_2 MONMs and MPs, the overall response was subtle compared to the responses observed in cells treated with ZnO and CuO NPs (**Figure 4-3**). TiO_2 5422 HT, 5423 HT, and R050P NPs exhibited a statistically significant increase in DNA damage at 50 and 100 µg/mL after 2 and 4 h of exposure (~10% DNA in tail). TiO_2 5422 HT induced a small but statistically significant response starting from 25 µg/mL at 2 h. The NIST TiO_2 NPs were the least responsive, with ~5% DNA in the tail at 4 h, at concentrations of 50 and 100 µg/mL.

Media-only exposed negative controls consistently exhibited ~4.5% DNA in the tail and cells treated for 1 h with 100 µM H_2O_2 exhibited variation, with between 53–83% DNA in the tail.

4.4.5 DNA damage points of departure for metal oxide and metal chloride treated cells

For the purposes of BMC modelling of comet data, the concentration was expressed as either µg/mL of the material used (**Figure 4-4**) or as µg/mL of the constituent metal (**Figure 4-5**). The PODs (µg/mL material) determined through both BMC modelling with a BMR of 1.0 (100% increase in response over baseline), and classical methods are summarised in **Table 4-4**. Using univariate BMC modelling, it can be seen that there is distinct separation in potency at 2 h between CuO NPs, ZnO NPs, ZnO MPs, and $ZnCl_2$, TiO_2 5423HT, TiO_2 R050P with the following order of potency: CuO NP > ZnO NP > ZnO MP > $ZnCl_2$, TiO_2 5423HT, TiO_2 R050P (**Figure 4-4**). Covariate analysis at 2 h post-exposure, using the exposure compound as the covariate, increased confidence intervals for 2 samples and differences in BMC ranges became less distinguishable, although CuO NPs, ZnO NPs, and ZnO MPs consistently appeared more potent than $ZnCl_2$ and the TiO_2 NPs that showed concentration–response. At 4 h, the trend in potency was largely the same as what was observed at the 2 h time point with respect to univariate modelling, albeit $ZnCl_2$ appears distinctly more potent than the TiO_2 NPs showing concentration–response, exhibiting the following potency ranking: CuO NPs > ZnO NPs > ZnO MPs > $ZnCl_2$ > TiO_2 R050P, TiO_2 5423HT, TiO_2 5422HT. For the covariate analysis at the 4 h time point, Zn forms and Ti forms were treated as covariates. From the covariate analysis, there was no difference in

potency between the three TiO_2 NPs showing concentration–response, while the ZnO NPs and MPs appeared more potent than $ZnCl_2$ (**Figure 4-4**) In all BMC modelling instances, the NOEC/LOEC values were within the range of the lower and upper 95th percentile of the benchmark concentration (BMCL/BMCU) (**Figure 4-4**).

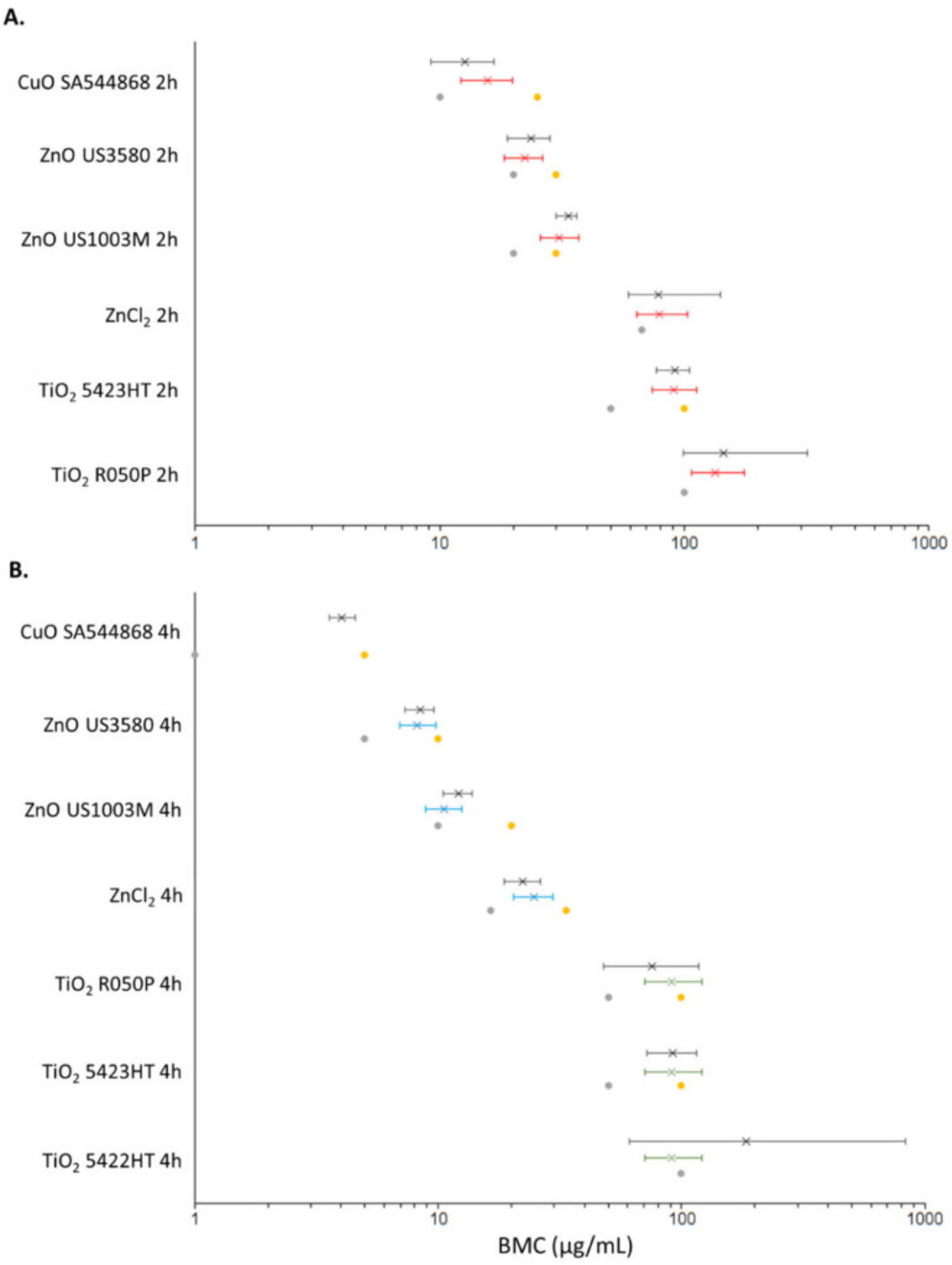

Figure 4-4. BMC plots showing the results of PROAST BMC modelling (BMR = 1.0, 100% increase over baseline) at 2 h (A) and 4 h (B) for metal oxides and metal chlorides which exhibit a concentration–response. Left error bars: BMCL. Right error bars: BMCU. X: BMC. Grey dot: NOEC. Yellow dot: LOEC. Red: BMC modelling with exposure type (NP, MP, metal chloride) as covariate. Black: BMC modelling with no covariate. Blue: BMC modelling with Zn type as covariate. Green: BMC modelling with TiO_2 type as covariate.

Table 4-4. Classical and benchmark concentration modelling to derive points of departure (µg/mL) based upon percentage DNA in tail measurements after 2–4 h exposure to NPs, MPs, and metal chlorides. For all BMC modelling, the benchmark response was set to 1.0 (100% extra risk). NOEC: no-observed-effect-concentration. LOEC: lowest-observed-effect-concentration. BMC: benchmark concentration. BMCL: the lower 95% confidence interval of the BMC. BMCU: the upper 95% confidence interval of the BMC. No Covariate: All BMC analyses were computed for each individual particle and timepoint. Covariate: BMC modelling conducted using covariate approach.

Timepoint	Metal Oxide	Particle Type	Classical		BMC Modelling (No Covariate)			BMC Modelling (Covariate)		
			NOEC [a]	LOEC [b]	BMCL	BMC	BMCU	BMCL	BMC	BMCU
2 h	ZnO	US3580	20	30	18.9	23.7	28.2	18.4 [c]	22.3 [c]	26.3 [c]
		US1003M	20	30	29.9	33.5	36.5	25.9 [c]	30.9 [c]	37 [c]
		$ZnCl_2$	67	>67	59.2	78.7	141	64.2 [c]	79.1 [c]	103 [c]
	CuO	SA544868	10	25	9.16	12.7	16.7	12.2 [c]	15.7 [c]	19.8 [c]
		US1140M	50	>50	-	-	-	-	-	-
		$CuCl_2$	108	>108	-	-	-	-	-	-
	TiO_2	NIST1898	100	>100	-	-	-	-	-	-
		5422HT	100	>100	-	-	-	-	-	-
		5423HT	50	100	77.1	91.4	105	73.9 [c]	90.4 [c]	112 [c]
		5424HT	100	>100	-	-	-	-	-	-
		5425HT	100	>100	-	-	-	-	-	-
		A050	100	>100	-	-	-	-	-	-
		R050P	100	>100	99	145	318	107 [c]	134 [c]	176 [c]
		A005	100	>100	-	-	-	-	-	-
		Nano Wires	100	>100	-	-	-	-	-	-
		US1017M	100	>100	-	-	-	-	-	-
4 h	ZnO	US3580	5	10	7.32	8.48	9.6	6.94 [d]	8.24 [d]	9.77 [d]
		US1140M	10	20	10.5	12.1	13.8	8.87 [d]	10.6 [d]	12.5 [d]
		$ZnCl_2$	16.5	33.5	18.7	22.3	26.2	20.5 [d]	24.9 [d]	29.6 [d]
	CuO	A544868	1	5	3.56	4.04	4.55	-	-	-
		US1003M	50	>50	-	-	-	-	-	-
		$CuCl_2$	108	>108	-	-	-	-	-	-
	TiO_2	NIST1898	100	>100	-	-	-	-	-	-

		5422HT	100	>100	61.1	184	832	70.4 [e]	91.5 [e]	121 [e]
		5423HT	50	100	72.3	91.8	115	70.4 [e]	91.5 [e]	121 [e]
		5424HT	100	>100	-	-	-	-	-	-
		5425HT	100	>100	-	-	-	-	-	-
		A050	100	>100	-	-	-	-	-	-
		R050P	50	100	47.7	75.4	118	70.4 [e]	91.5 [e]	121 [e]
		A005	100	>100	-	-	-	-	-	-

[a] NOEC is defined as the first concentration preceding the LOEC. [b] LOEC is defined as the first concentration where there is a statistically significant ($p < 0.05$) increase in percentage DNA in the tail of at least 2-fold as compared to the media control. [c] Exposure type set as covariate. [d] Zn exposure type set as covariate. [e] TiO_2 particle type set as covariate.

An additional concentration metric was employed for BMC modelling, µg/mL of constituent metal, in order to determine whether the potency differences between the materials hold true when normalized to metal content (**Figure 4-5**). From the BMC modelling shown, it can be seen that the potency rankings largely remain the same, albeit a smaller separation in BMC ranges between the materials. At the 2 h timepoint, using univariate modelling the following potency ranking is obtained: CuO NP > ZnO NPs > ZnO MPs > TiO_2 5423HT, TiO_2 R050P. The BMC interval for $ZnCl_2$ overlapped with ZnO MPs, TiO_2 5423HT, and TiO_2 R050P. Using covariate modelling, with all exposures as covariate, the separation in BMC intervals was lesser, with potency ranking showing CuO NPs, ZnO NPs, ZnO MPs > $ZnCl_2$, TiO_2 5423HT, and TiO_2 R050P. $ZnCl_2$ also appeared more potent than TiO_2 R050P. At the 4 h time point, the potency rankings for the univariate analysis are almost identical to results shown in **Figure 4-4**, with CuO NPs > ZnO NPs > ZnO MPs ~ $ZnCl_2$ > TiO_2 R050P, TiO_2 5423HT, TiO_2 5422HT, while covariate BMC modelling indicates ZnO NPs, ZnO MPs > $ZnCl_2$ > TiO_2 R050P, TiO_2 5423HT, TiO_2 5422HT. In all BMC modelling cases, the NOEC/LOEC values were within the BMCL/BMCU range (**Figure 4-5**).

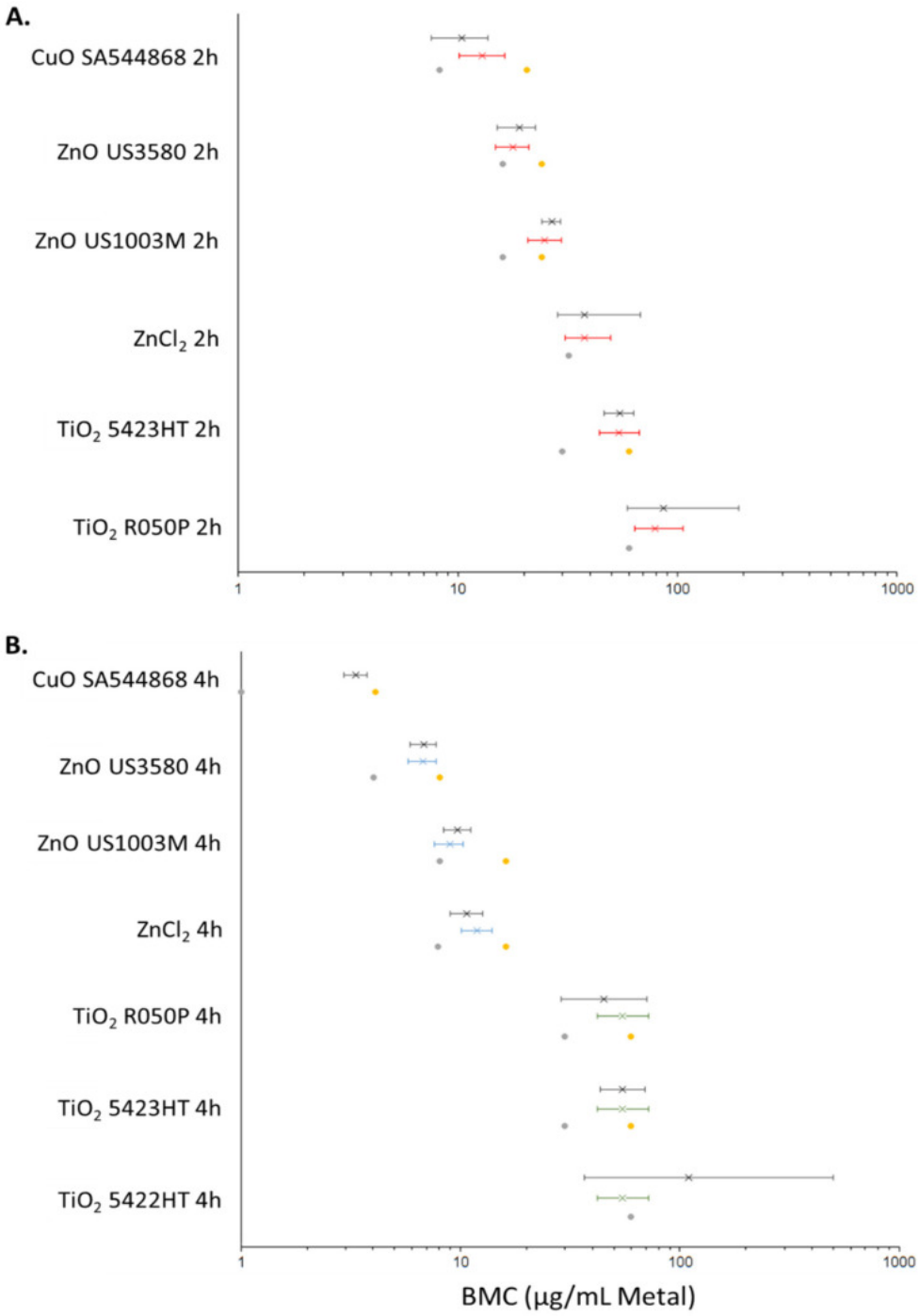

Figure 4-5. BMC plots showing the results of PROAST BMC modelling (BMR = 1.0, 100% increase over baseline) at 2 (A) and 4 (B) h for metal oxides and metal chlorides which exhibit a concentration–response. The concentration is represented in terms of µg/mL of the constituent metal. Left error bars: BMCL, lower 95 percentile or BMC. Right error bars: BMCU, upper 95 percentile of BMC. X: BMC. Grey dot: NOEC. Yellow dot: LOEC. Red: BMC modelling with exposure type (NP, MP, metal chloride) as covariate. Black: BMC modelling with no covariate. Blue: BMC modelling with Zn type as covariate. Green: BMC modelling with TiO_2 type as covariate.

4.5 Discussion

The genotoxic potential of the MONMs investigated in this study has been assessed previously, both *in vitro* and *in vivo* (reviewed in (MAGAYE et al., 2012; Singh, Sanjiv, 2019; Wani & Shadab, 2020)). While material size and solubility have been suggested to significantly impact the observed genotoxicity, systematic studies investigating the relative contributions of size and solubility to the levels of DNA damage to derive genotoxicity potency have not been conducted. In this study, the high-throughput CometChip® assay was tested for its applicability for routine potency screening of NM induced genotoxicity using an *in vitro* lung cell culture model. Three MONMs were investigated including, ZnO, CuO, and TiO_2 MONMs and MPs, as well as the dissolved metal equivalents $ZnCl_2$ and $CuCl_2$.

4.5.1 Genotoxicity of ZnO, CuO, and TiO_2 MONMs

Genotoxicity resulting from ZnO, CuO, and TiO_2 particle exposure has been consistently documented in a number of *in vitro* and *in vivo* model systems (Hou et al., 2018; Kazimirova et al., 2019; MAGAYE et al., 2012; May et al., 2022; Singh, Sanjiv, 2019; Wani & Shadab, 2020). In A549 lung cells, pristine ZnO particles with a primary particle size of ~140 nm and aggregate sizes of 210 nm induced concentration-dependent increases in percentage DNA in the tail in the comet assay, with statistically significant responses from 10 µg/cm^2 after 3 h of exposure (~30 µg/mL concentration used in this study) (El Yamani et al., 2017). In the same study, the authors also examined TiO_2 NPs with an average size of ~110 nm with an aggregate size of ~220 nm in media and reported no statistically significant increase in DNA damage, although an increasing, non-significant, concentration-dependent trend was observed (May et al., 2022). More recently, the genotoxic potential of uncoated ZnO NPs (particle sizes ~ 16 nm) alongside uncoated TiO_2 NPs (particles sizes <25 nm) was investigated in human T-lymphocytes after 3–24 h exposure, and showed significant genotoxicity in the case of ZnO NPs (concentrations up to 100 µg/mL, both 3 and 24 h timepoints) but not TiO_2 NPs (Kazimirova et al., 2019). With respect to the CuO NPs, using the same CuO NP type used in the present study (SA544868), Siivola et al., (2020) showed statistically significant increases in percentage DNA damage starting at a concentration of

10 μg/cm^2 (equivalent to 32 μg/mL in this study) after 3–24 h in BEAS-2B cells using the traditional alkaline comet assay (Boyadzhiev et al., 2021; Siivola et al., 2020). The CuO MPs were shown to be genotoxic at the very high concentration of 50 μg/cm^2. With respect to TiO_2 NPs, literature is inconsistent with both negative and positive genotoxicity results reported for seemingly similar particles, although studies published between 2013–2020 note more positive responses than negative (Carriere et al., 2020; Wani & Shadab, 2020). In the present study, CuO NPs were considerably more genotoxic compared to ZnO NPs but ZnO MPs induced DNA damage and not CuO MPs (**Figure 4-3A,B**). While TiO_2 materials were largely inert, subtle but concentration-dependent increases in DNA breaks were observed for some TiO_2 NPs investigated (**Figure 4-3C**). The overall response profile of the ZnO and CuO NPs, and TiO_2 materials generated in the high-throughput CometChip® assay are in concordance with the reported literature.

For the soluble NPs—ZnO and CuO—cellular response depends upon both the dissolved and particulate fractions, which change in abundance over time. For ZnO NPs, dissolution experiments from the literature (Reed et al., 2012) as well as from this study (**Figure 4-1**) have shown that particles can undergo instantaneous dissolution in DMEM depending on the particle characteristics, with similar levels of dissolved Zn present in the suspension media at 0, 24, and 48 h post-suspension. On the other hand, CuO NPs undergo slower dissolution over time in DMEM, with ~3% dissolved at 0 h and up to 51% dissolved by 48 h post-suspension (Avramescu et al., 2020; Boyadzhiev et al., 2021). Comparatively, both CuO and ZnO MPs are shown to dissolve less in DMEM at the same post-suspension timepoints (**Figure 4-1**), which may be related to the decreased surface area for interaction as compared to their NP equivalents. The genotoxicity results in **Figure 4-4** show that both CuO and ZnO NPs induce potent time and concentration-dependent genotoxicity at 2 and 4 h, however for the MP and metal chloride exposures, only ZnO MPs and $ZnCl_2$ initiated the DNA damage, and with lower potency than their respective NP (**Table 4-4**, **Figure 4-4** and **Figure 4-5**). A study examining the genotoxicity of ZnO NPs, MPs, and $ZnCl_2$ in MDCK kidney cells following 24 h exposure using the comet assay only reported positive results with respect to the NPs (Kononenko et al., 2017). Similar responses

were seen in A549 cells exposed to ZnO NPs and $ZnCl_2$ for 24 h, where only the ZnO NPs induced significant induction of double-strand breaks (Heim et al., 2015). Both studies indicate that toxicity is induced by Zn uptake, however, the magnitude of response cannot be explained by the dissolved fraction alone. In another study examining the genotoxic potential of CuO NPs, CuO MPs, and $CuCl_2$ via alkaline DNA unwinding, only the CuO NPs were able to induce DNA damage after 24 h of incubation (Semisch et al., 2014). This was proposed to be due to high levels of Cu detected in the cell nucleus after NP exposure, as compared to MPs and $CuCl_2$. This was also observed in another study focusing on these three CuO species, with CuO NPs producing significantly higher Cu levels in the nucleus and cytoplasm than $CuCl_2$ and CuO MPs after 24 h of exposure (Strauch et al., 2017). Together, in alignment with published *in vitro* genotoxicity literature, high-throughput CometChip® assay results shown in **Figure 4-4** and **Figure 4-5** show evidence that the NP fractions are crucial to the genotoxic response in FE1 cells, but suggest that for ZnO NPs, the ionic fraction is a critical contributor to the observed DNA damage compared to dissolved Cu from CuO NP. Although not investigated in this study, the results suggest that Cu ions are slower to be internalised compared to Zn ions and may involve different membrane transport mechanisms, impacting their uptake and intracellular availability for reactions.

Unlike soluble ZnO and CuO NPs, TiO_2 MONMs are insoluble and induce genotoxicity through interactions with the particle surface and through the formation of ROS or reactive nitrogen species (Charles et al., 2018; Wani & Shadab, 2020). Cellular responses, in this case, are dependent on particle properties such as size, crystallinity, and surface coating/functionalization, although a thorough assessment of the impact of surface coating on TiO_2 genotoxicity is lacking (Charles et al., 2018). In this study, the genotoxicity of nine different TiO_2 MONMs and a TiO_2 MP were examined, five of which are surface coated and five of which are pristine (**Table 4-1** and **Table 4-2**). For the coated particles, four are coated in silica or silica in conjunction with another compound, and one is coated in a manufacturer-described 'hydrophilic' coating. With respect to particle size, of the 10 materials tested, 5 are ~50 nm in size, 2 are ~30 nm, 1 is ~5 nm, 1 is ~1500 nm, and

another is a high-aspect ratio NW. Finally, 10 TiO_2 NMs comprised of 3 different crystalline configurations—6 consisting of anatase/rutile mixture, 2 anatase, and 1 rutile only in composition (**Table 4-1** and **Table 4-2**). With respect to the CometChip® screening of the 10 different TiO_2 metal oxides, only 3 induced a concentration-dependent increase in DNA damage at either time point of assessment (**Table 4-4**). For two variants (5422HT, 5423HT), the surface was coated with silica or a silica–alumina formulation and both particle types had measured primary sizes of ~30 nm, with a predominant anatase crystal phase. The third type (R050P) that induced a concentration-dependent DNA damage response is an uncoated type, with a primary particle size of ~50 nm and a rutile crystal phase. In all three cases, the response did not exceed 10% DNA in the tail indicating a relatively subtle potential to induce DNA damage among the active TiO_2 forms assessed. Research into the toxicity of silica has shown that surface silanol groups and siloxane bridges are key mechanistic players involved in its pathogenicity, with the reactivity of these surface groups impacting endpoints such as DNA damage, and cytotoxicity through membranolysis (Pavan et al., 2019), providing a potential explanation for the activity of TiO_2 5422HT and 5423HT. With respect to crystallinity, the rutile crystal arrangement has exhibited greater toxic potential than anatase both *in vitro* and *in vivo* (Fresegna et al., 2021; Rahman, L. et al., 2017b), although contradictory results do exist (Carriere et al., 2020). Analysis of radicals generated from TiO_2 particles indicates differential reactivity based on crystal structure, with rutile being able to catalyze the formation of hydroxyl radicals under light occlusion, while anatase induces the formation of superoxide anions (Fenoglio et al., 2009). This may potentially explain the significant (but small) concentration-dependent response of TiO_2 R050P, as this particle was uncoated and entirely of rutile configuration (**Table 4-4**). Currently, there is no consensus in the literature concerning the impact of coating, particle size, or crystallinity on the genotoxicity of TiO_2 (recent positive and negative studies summarised in (Carriere et al., 2020; Charles et al., 2018; Wani & Shadab, 2020)). However, results from the high-throughput CometChip® screening indicate a rutile configuration and silica coating increase the material's DNA damage potential. While the results of the

present study reflect acute responses, long-term studies using advanced cell culture models may be required to truly evaluate the potential of 5422HT, 5423HT and R050P.

In addition to mechanistic research using *in vitro* systems, all three MONMs have been used to assess pulmonary effects *in vivo* (Cho, W. et al., 2011; Costa et al., 2018; Danielsen et al., 2020; Gosens et al., 2016; Jain et al., 2013; Rahman, L. et al., 2017b). In Wistar rats, inhalation of CuO NPs and ZnO NPs has been shown to result in an acute inflammatory response, punctuated by inflammation and damage of alveolar and bronchiolar tissue (Gosens et al., 2016; Jain et al., 2013). The effects of these are thought to be mediated by the intracellular dissolution of the particle within acidic lysosomes (Cho, W. et al., 2011; Gosens et al., 2016). With respect to ZnO exposure, a recovery period has been shown to reduce the inflammatory response, however, detectable levels of inflammatory markers are still present 15 days post-exposure (Jain et al., 2013), and 4 weeks post-exposure (Cho, W. et al., 2011) depending on the exposure conditions. Using a dose range relevant for occupational exposures, inflammation and lung damage resulting from CuO NP exposure in rats was shown to largely ameliorate by 22 days post-exposure, with the exception of the highest dose used (Gosens et al., 2016). With respect to TiO_2 NPs, intratracheal instillation in mice has been shown to result in inflammatory and fibrotic pathologies, with crystal phase, particle size, shape, surface area, and surface composition shown to be important predictors of response (Danielsen et al., 2020; Rahman, L. et al., 2017b). Of note, even though inflammation and lung damage was noted after intratracheal exposure to TiO_2 NPs, no pronounced DNA damage as assessed by comet assay was noted in BALF cells, lung cells, or liver cells after 1, 3, 28, or 90 days post-exposure (Danielsen et al., 2020). Thus, while some of these materials may be DNA damage-inducing, the long-term impact of early DNA damage remains to be assessed.

4.5.2 Mechanisms of toxicity underlying CuO, ZnO, and TiO_2 responses

With respect to CuO and ZnO, genotoxicity is thought to be induced through interactions of both the particulate and dissolved fractions through (1) the formation of ROS, (2) direct interaction with the DNA or DNA maintenance machinery by gaining access to the nuclear compartment, or (3) during mitosis where the nuclear membrane dissolves

(Magdolenova et al., 2014). For these particles, toxicity is suggested to act via the 'Trojan Horse' mechanism (Cho, W. et al., 2011; Moschini et al., 2013; Strauch et al., 2020), which involves active transport of the particulate ZnO and CuO into the cells (typically via endocytic pathways), sequestration in acidic vesicles before ending up in the lysosomes and undergoing rapid dissolution. Vesicular dissolution releases large amounts of metal ions within the lysosomal lumen, changing the pH of the microenvironment. The dissolved particles generate ROS and cause damage to the integrity of the vesicle membrane, resulting in vesicular rupture and release of the contents into the cytoplasm. Consequently, antioxidant defences are overwhelmed, resulting in damage to biomolecules (proteins, lipids, nucleic acids) either directly or through ROS imbalances. These effects culminate in genotoxicity and cytotoxicity if left unchecked. With respect to ZnO, dissolution results in **Figure 4-1** seem to indicate that the 'Trojan Horse' mechanism may have less of an influence on toxicity than previously surmised and that the dissolved fraction is the main mediator of genotoxicity (**Figure 4-3A**). It is important to note that ZnO NPs are less genotoxic but more cytotoxic compared to CuO NPs, suggesting the underlying mode of action for the two responses may be different. In one of our recent publications involving the same CuO NPs, CuO MPs, and $CuCl_2$ compound used in this study, a differential impact of size and ionic fraction on transcriptional response was shown (Boyadzhiev et al., 2021). Both CuO NPs and $CuCl_2$ were shown to induce both oxidative stress responses and DNA damage responses at the canonical pathway level, however, the $CuCl_2$ mediated response was shown to have a slower onset than the CuO NP mediated response, and induced cytotoxicity to a lesser extent. Although no genotoxicity was reported for $CuCl_2$ for up to 4 h as assessed by the CometChip® assay in the present study, the possibility that DNA damage may be seen at a longer exposure duration cannot be disregarded.

TiO_2 is insoluble and interplay between dissolved and particulate fractions is not anticipated, precluding a 'Trojan Horse' mechanism of action or metal-ion-induced toxicity. Instead, genotoxicity induced by TiO_2 can proceed through the formation of ROS from the particle surface, interaction with the DNA in the nucleus, and also through interaction with

mitosis/DNA maintenance and repair machinery (Magdolenova et al., 2014). With respect to the formation of ROS, the crystal configuration (anatase vs. rutile) dictates the reactivity of the particle, with anatase showing enhanced reactivity under UV irradiation (Sanders et al., 2012) although both crystal configurations can generate radicals even under light occlusion (Fenoglio et al., 2009). These reactive molecules can induce oxidative DNA damage in an indirect manner. In addition to ROS formation, TiO_2 NPs within the cell have been shown to interact with the mitotic spindle *in vitro*, resulting in improper chromosomal segregation and the formation of micronuclei (Huang, S. et al., 2009). It has also been proposed that TiO_2 particle loaded vesicles can impinge upon and deform the nucleus, resulting in chromosomal damage and the formation of micronuclei (Di Virgilio et al., 2010). Results from the DNA damage screening (**Figure 4-3C**) do not provide indications for any of the above mechanisms, and while TiO_2 aggregates can be seen associated with exposed FE1 cells (**Supplementary Figure 4-6**), their subcellular localization cannot be determined. Due to the particle size of the three DNA damage-inducing TiO_2 NPs (30–50 nm, **Table 4-1**), direct nuclear access is unlikely. Therefore, TiO_2 NP DNA damage noted in this study may have proceeded through ROS production, interaction with DNA during mitosis when the nuclear membrane is dissolved, or through interaction with mitosis/DNA repair and maintenance machinery. It is important to note that while responses noted are minimal, it is possible that additional DNA damage may result from longer exposure regimens.

4.5.3 Benchmark concentration modelling and relative potency ranking of MONMs

Classical methods for determining points of departure (PODs) include the lowest-observed-effect-concentration (LOEC) and the no-observed-effect-concentration (NOEC), which are based upon point estimates of endpoint response and do not rely on the whole concentration-response relationship to determine the POD. In contrast, BMC modelling makes use of the entire concentration-response relationship and determines a POD (known as the BMC) with confidence intervals related to the variation inherent in the dataset used to conduct modelling. Within PROAST, it is possible to conduct BMC modelling with or without using a covariate approach. If the underlying data structure is

adequate, covariate analysis can produce tighter BMC confidence intervals, as highlighted in (Wills et al., 2016).

Currently, the preferred method of deriving PODs is the benchmark modelling approach (Haber et al., 2018), which has recently been used to rank 28 chemicals for their potential to induce *in vitro* DNA damage in the CometChip® assay (Seo et al., 2019). A similar approach was utilized here to conduct a potency ranking of DNA damage induced by concentration-responding metal oxides and chlorides at 2 and 4 h. A BMR of 1.0, with or without covariate analysis was used, with mass-concentrations of the compound (**Figure 4-4**) or constituent metal (**Figure 4-5**) as concentration metrics. Covariate analysis has been suggested to increase the precision of BMC estimation, as long as response data at each level of the covariate can be described using models with constant shape parameters (Wills et al., 2016). A noticeable increase in precision (BMCL–BMCU range) was seen between univariate and covariate analyses with respect to concentration-responding TiO_2 at 4 h, although this effect was less pronounced, and even opposite, with respect to the Zn forms and CuO NPs at both time points (**Table 4-4**, **Figure 4-4** and **Figure 4-5**). The covariate approach was not uniformly applicable across exposures due to inherent differences in concentration–response structures, and further subdivision of exposures at the 4 h time point was necessary (**Figure 4-4** and **Figure 4-5**; TiO_2 nanoforms and Zn forms as covariates). Due to the difficulties in uniformly applying the covariate approach, potency ranking and trends seen are based on univariate modelling only.

With respect to compound-based potency ranking, a similar rank amongst the concentration-responding exposures is seen at both time points; although the differences in potency were more distinct at 4 h, with the following trend seen: CuO NPs (SA544868) > ZnO NPs (US3580) > ZnO MPs (US1003M) > $ZnCl_2$ > TiO_2 R050P, TiO_2 5423HT, TiO_2 5422HT. Expressing the concentration as a function of the constituent metal markedly decreases the difference in potency between the various compounds (**Figure 4-5**), although a similar trend is retained at the 4 h time point: CuO NPs (SA544868) > ZnO NPs (US3580) > ZnO MPs (US1003M) ~ $ZnCl_2$ > TiO_2 R050P, TiO_2 5423HT, TiO_2 5422HT. The ranking trends indicate that 1) soluble MONMs induce more pronounced DNA damage than insoluble MONMs, 2)

dissolved ions contribute substantially to the observed damage of ZnO, and 3) the DNA damage induced by TiO_2 nanoforms is subtle and is not specific to material properties. This study represents one of the first to use the CometChip® assay to show differential potency of soluble and insoluble particles to induce DNA damage. Some results are in alignment with published literature (Ivask et al., 2015; Titma et al., 2016); however, the results from this study suggest that soluble NPs differ in the toxicity mode of action and in their relative potency, implying further studies are needed before the application of read-across strategies in risk assessment of soluble MONMs.

As compared to the traditional alkaline comet assay, the CometChip® assay allows for greatly enhanced throughput with a reduced labour cost, which makes it an attractive genotoxicity test for NM. The increase in throughput allowed for 20 separate particle exposures to be conducted on a single plate, with four technical replicates per condition, which produced enough information to allow for BMC modelling and relative potency estimation. Thus, this assay can be used in tier-1 testing strategies and screening approaches to identify potentially hazardous NM. In all, this study provides support for the use of the CometChip® assay for routine *in vitro* screening of NM genotoxic potential.

4.6 Conclusion

In conclusion, this study provides evidence for the applicability of the commercially available CometChip® assay for routine screening of NM induced DNA damage. The ZnO, CuO, and select TiO_2 NPs investigated exhibited concentration- and time-dependent DNA damage, with maximal responses of 58, 57, and 10% DNA in the tail, respectively, at 4 h. The results of concentration–response modelling highlight the differential impact of the dissolved and particulate fractions on the DNA damage potential of CuO and ZnO, as well as the importance of surface coating and crystallinity on genotoxicity induced by TiO_2. With the increasing number and variety of NM and MONMs in use, traditional low-throughput genotoxicity testing methods are insufficient to meet regulatory needs for their assessment. By leveraging mechanistically based high-throughput *in vitro* screening assays, a large number of relevant endpoint-specific data can be generated which can aid

in prioritization, grouping, and read-across endeavors. The screening data generated for these 5 MONMs can serve as part of the weight-of-evidence for prioritization in a tiered toxicity testing strategy for ENM.

5 Chapter 5: A Systematic Genotoxicity Assessment of a Suite of Metal Oxide Nanoparticles Reveals Their DNA Damaging and Clastogenic Potential

Modified from: Solorio-Rodriguez, S. A., Wu, D., Boyadzhiev, A., Christ, C., Williams, A., & Halappanavar, S. (2024). A Systematic Genotoxicity Assessment of a Suite of Metal Oxide Nanoparticles Reveals Their DNA Damaging and Clastogenic Potential. *Nanomaterials (Basel, Switzerland)*, *14*(9), 743. **https://doi.org/10.3390/nano14090743**.

Authorship: Silvia Aidee Solorio-Rodriguez[1], Dongmei Wu[1], Andrey Boyadzhiev[1,2], Callum Christ[1], Andrew Williams[1], Sabina Halappanvar[1,2]

Affiliation:
1: Environmental Health Science and Research Bureau, Health Canada, Ottawa, Canada
2: Department of Biology, University of Ottawa, Ottawa, ON K1N6N5, Canada

Contributions:

Experimental Design	Silvia Aidee Solorio Rodriguez Dongmei Wu **Andrey Boyadzhiev** Sabina Halappanavar
Particle Suspension	Silvia Solorio Rodriguez Dongmei Wu **Andrey Boyadzhiev (uncoated NiO NP, MP, Al_2O_3 NP, MP; for CometChip®)**
Dynamic Light Scattering Analysis	Dongmei Wu
Electron Microscopy Imaging	University of Ottawa Material Characterization Core
Specific Surface Area Characterization	McGill University
Exposure	Silvia Solorio Rodriguez Dongmei Wu **Andrey Boyadzhiev (uncoated NiO NP, MP, $NiCl_2$, Al_2O_3 NP, MP, $AlCl_3$; CometChip®)**
Trypan Blue Analysis	Silvia Solorio Rodriguez **Andrey Boyadzhiev (uncoated NiO NP, MP, $NiCl_2$, Al_2O_3 NP, MP, $AlCl_3$; CometChip®)**
CometChip® Imaging and Analysis	Silvia Solorio Rodriguez **Andrey Boyadzhiev (uncoated NiO NP, MP $NiCl_2$, Al_2O_3 NP, MP, $AlCl_3$)**
Microflow Assay	Dongmei Wu Silvia Aidee Solorio Rodriguez
Flow Cytometry	Health Canada Scientific Services
Statistics	**Andrey Boyadzhiev**

	Silvia Solorio Rodriguez
Benchmark Concentration Modelling.....	Andrew Williams
Data Interpretation.....	Silvia Solorio Rodriguez
	Andrey Boyadzhiev
Manuscript Writing and Revisions.....	Silvia Solorio Rodriguez
	Andrey Boyadzhiev
	Sabina Halappanavar
Internal Review.....	Eunnara Cho
	Luna Rahman

5.1 Abstract

Metal oxide nanoparticles (MONPs) induce DNA damage, which is influenced by their physicochemical properties. In this study, the high-throughput CometChip® and micronucleus (MicroFlow®) assays were used to investigate DNA and chromosomal damage in mouse lung epithelial cells induced by nano and bulk sizes of zinc oxide, copper oxide, manganese oxide, nickel oxide, aluminum oxide, cerium oxide, titanium dioxide, and iron oxide. Ionic forms of MONPs were also included. The study evaluated the impact of solubility, surface coating, and particle size on response. Correlation analysis showed that solubility in the cell culture medium was positively associated with response in both assays, with the nano form showing the same or higher response than larger particles. A subtle reduction in DNA damage response was observed post-exposure to some surface-coated MONPs. The observed difference in genotoxicity highlighted the mechanistic differences in the MONP-induced response, possibly influenced by both particle stability and chemical composition. The results highlight that combinations of properties influence response to MONPs and that solubility alone, while playing an important role, is not enough to explain the observed toxicity. The results have implications on the potential application of read-across strategies in support of human health risk assessment of MONPs.

5.2 Introduction

Engineered Nanomaterials (ENMs) are materials that are manufactured at or within the nanoscale (1 to 100 nanometers inclusive) or have internal or surface structures in the nanoscale (Health Canada, a). The internal and external structures are expected to break down into component nanomaterials (Health Canada, b). Metal oxide nanoparticles (MONPs) are among the most synthesized and utilized ENMs globally, with a wide variety of applications, including in consumer products, electronics, energy, food, agriculture, and medicine sectors (Chavali & Nikolova, 2019), with an approximate worldwide production from less than 10 tons to over 10,000 tons per year (Piccinno et al., 2012). This increase in synthesis and application has led to enhanced risks of human exposure to these materials, potentially resulting in adverse health effects (Directorate-General for Environment, 2016; Naghdi et al., 2017). Inhalation is the main route of exposure to MONPs occupationally,

where workers may be exposed during material handling (weighing, embedding, cleaning, filtration, etc.), whereas consumers could be exposed via inhalation of powders and sprays containing MONPs (Bierkandt et al., 2018; Brenner et al., 2016; Kuhlbusch et al., 2011). Because of their small size, once inhaled, they can bypass the upper and lower respiratory clearance mechanisms to reach the alveolar region and potentially induce pulmonary toxicity by various mechanisms (Oberdorster et al., 2005).

Inhalation of mixtures containing incidental MONPs, such as welding fumes, has been associated with an increased risk of lung disease in humans (Li, G. et al., 2022). A recent exposure monitoring study positively identified chromium oxide and nickel oxide nanoparticles (NiO NPs) in the plasma of stainless-steel welders post-shift (Bocca et al., 2023b). Furthermore, analysis of lung samples taken from welders has shown evidence that MONPs co-localize with macrophages and fibrotic foci in lungs in diseased individuals . These data are complemented by recent studies of humans exposed occupationally or on a volunteer basis to engineered MONPs, indicating the potential risk associated with these materials (Schulte et al., 2019b).

Limited epidemiological and biomonitoring studies in recent years have raised concerns about occupational exposure to MONPs. In workers employed in titanium dioxide (TiO_2) nanoparticles (NPs) manufacturing facilities, increased levels of biomarkers associated with cardiopulmonary and systemic toxicity were found in their blood, which was correlated with workers' exposure to MONPs (Schulte et al., 2019b). Similarly, researchers involved in the production of metal-containing nanocomposite compounds have been shown to have elevated levels of nucleic acid and protein oxidation in their exhaled breath condensate in comparison with non-exposed control subjects (Pelclova, D. et al., 2018). In addition, human volunteers exposed via inhalation to zinc oxide (ZnO) NPs at 1 mg/m^3 showed signs of systemic toxicity, including increases in blood neutrophils and acute phase proteins (Monsé et al., 2018). In many countries, such as the US (U.S. Department of Labor Occupational Safety and Health Administration), occupational exposure limits to ZnO fume are set at 5 mg/m^3, which indicates that current occupational exposure limits for metal oxides (MO) may not be protective enough for the nanoforms (i.e., MONPs).

These scarce studies underscore the need to better understand the mechanisms involved in the toxicity of MONPs to better protect workers and consumers. Research using *in vivo* model systems in past years has helped better define the hazard that MONPs can pose in mammalian organisms. For example, exposure to ZnO NPs, copper oxide (CuO) NPs, NiO NPs, manganese oxide (MnO_2) NPs, aluminum oxide (Al_2O_3) NPs, cerium oxide (CeO_2) NPs, TiO_2, and iron-(III)-oxide (Fe_2O_3) NPs induce inflammation, oxidative stress, and tissue injury in different animal models (Guo et al., 2019; Hadrup et al., 2020; Jeong, M. et al., 2022; Kim et al., 2018; Kwon et al., 2022; Rahman, L. et al., 2017b; Sárközi et al., 2009; Wang, D. et al., 2017).

Besides inflammation, MONPs have been reported to induce primary and secondary genotoxicity both *in vivo* and *in vitro* (Cao et al., 2023; Hadrup et al., 2022). Primary genotoxicity is the result of direct interactions of NPs with DNA or cellular proteins involved in mitosis or via the generation of reactive oxygen species (ROS) (Magdolenova et al., 2014). Secondary genotoxicity occurs when activated phagocytes produce ROS and oxidative DNA damage during inflammation (Magdolenova et al., 2014). The comet and micronucleus (MN) assays are two of the most commonly used techniques to evaluate the genotoxic potential of compounds due to their high sensitivity to detect DNA breaks and chromosome damage, respectively (Araldi et al., 2015). The comet assay (also known as single-cell gel electrophoresis) has three different versions based on the pH of the buffers used for the electrophoresis. The alkaline version with a pH higher than 13 detects single- and double-strand breaks that result from direct interactions with DNA, alkali labile sites, or transient DNA strand breaks from DNA excision repair (Araldi et al., 2015; OECD, 2014b). The MN assay determines the frequency of MN (also known as Howell-Jolly bodies) that are formed by clastogenesis (chromosomal breaks) or aneugenesis (miss-segregation of entire chromosomes due to disruption of the mitotic apparatus) when the chromosomal fragment or chromosome that is not integrated into the nucleus of a daughter cell is enveloped by a nuclear membrane (Araldi et al., 2015; OECD, 2023c). Recent advances in technology have led to the development of commercially available high-throughput

versions of these methodologies, which are uniquely suited for the task of *in vitro* genotoxicity screening.

The genotoxicity of MONPs is influenced by their physicochemical properties, such as chemical composition, size, surface properties, agglomeration/aggregation state, and solubility (Huang, Y. et al., 2017). However, the knowledge of how MONP properties impact their toxicity is not complete. Because of the high number of ENMs with different physicochemical properties that require testing, *in vitro* high-throughput screening techniques are desired for the rapid screening of potentially hazardous ENMs (Collins, A. R. et al., 2017). In a previous study, the high-throughput CometChip® assay was used to evaluate the genotoxic potential of three types of MONPs, CuO, ZnO, and TiO_2 NPs and metal oxide microparticles (MOMPs), as well as their equivalent metal chloride salts, zinc-(II)-chloride ($ZnCl_2$) and copper-(II)-chloride ($CuCl_2$) in mouse lung epithelial cells (FE1) (Boyadzhiev et al., 2022). It was found that ZnO NPs and CuO NPs induced a concentration-dependent genotoxic response, with CuO NPs being more genotoxic than ZnO NPs. For Zn, all forms, including NPs, microparticles (MPs), and dissolved Zn, induced DNA damage, suggesting that the metal ion Zn^{2+} is the main contributor to toxicity (Boyadzhiev et al., 2022). Of the TiO_2 NP variants tested, uncoated, silica, and silica-alumina-coated TiO_2 NPs induced a concentration-dependent increase in DNA breaks, which was lower in magnitude compared to that observed after exposure to other MONPs. In another study, the genotoxicity of NPs with different chemical compositions, including silicon dioxide (SiO_2), ZnO, Fe_2O_3, silver (Ag), and CeO_2 NPs, was evaluated in human lymphoblastoid (TK6) and Chinese hamster ovary (H9T3) cell lines using a high-throughput comet assay. ZnO, Ag, and Fe_2O_3 NPs induced a concentration-dependent increase in DNA damage with different genotoxic responses between the two cell lines (Watson et al., 2014). The potential genotoxicity of Ag NPs coated with citrate or polyvinylpyrrolidone (PVP) and positively and negatively charged SiO_2 NPs were evaluated in primary human lymphocytes and B lymphocyte human cells (WIL2-NS) using a high-throughput cytokinesis-block MN assay (a version of MN assay for human lymphocytes) at different concentrations. It was observed that NPs of 10 nm size were more genotoxic than 70 nm, and citrate-coated NPs were more

genotoxic than PVP-coated NPs, whereas SiO_2 did not induce MN (Vecchio et al., 2014). In another study, HBEC3-KT cells (an hTERT-immortalized epithelial cell line) were exposed to several types of NPs (silver [Ag], gold [Au], and platinum [Pt]) of two sizes, 5 or 50 nm. Au NPs of 5 nm caused more DNA damage than Au NPs of 50 nm, whereas Pt NPs of 50 nm induced more damage than the smaller size Pt (Lebedová et al., 2018). From these studies, it can be concluded that several properties of MONPs, including chemical composition, surface coating, and size, play a significant role in this response, in addition to solubility. The use of high-throughput screening tools makes it practical to assess many concentrations and property variants simultaneously, allowing for the elucidation of links between physicochemical properties and genotoxicity.

Using such tools, the objective of the current study was to evaluate the genotoxic potential of a wide panel of MONPs with varying solubility profiles (i.e., ZnO, CuO, MnO_2, NiO, Al_2O_3, CeO_2, TiO_2, Fe_2O_3 (Avramescu et al., 2022)). Bulk and dissolved metal analogs were included in order to determine the contribution of the dissolved and particulate fractions on response, and the impact of particle size on genotoxicity. Surface coated variants were also included to determine the impact of surface functionalization on toxicity. Health Canada has identified these MONPs and their coatings (PVP, 3-Aminopropyl triethoxysilane [APTES], stearic acid, and silane) as priority nanomaterials due to their commercialization in Canada (Avramescu et al., 2019, 2022; Bushell et al., 2020).

This study examined DNA strand breaks in FE1 Muta™Mouse lung epithelial cells via the high-throughput CometChip® assay and chromosomal damage by the high-throughput MicroFlow® MN assay. The data generated in (Boyadzhiev et al., 2022) were used to compare coated and uncoated nanoparticles.

5.3 Methods

5.3.1 MONPs, MOMPs, and dissolved metal analogs

A total of 21 individual uncoated and coated ZnO, CuO, MnO_2, NiO, Al_2O_3, CeO_2, TiO_2, and Fe_2O_3 MONPs were investigated in this study. The material purity ranged from 97.8

to 99+%, and the primary particle size ranged from 10 to 60 nm. **Table 5-1** lists the catalog numbers, the vendor, and the physicochemical characteristics of MONPs as provided by the manufacturer.

Table 5-1. Characteristics of MONPs as provided by the manufacturer.

MONPs	Manufacturer	Coating	Purity (%)	Primary Size (nm)	SSA (m^2/g)
ZnO US3580	US Research Nanomaterials, Inc., Houston, TX, USA	Uncoated	99+	35–45	65
ZnO 5811HT	Nanostructured and Amorphous Materials, Inc., Katy, TX, USA	Uncoated	99+	30	>15
ZnO 5812HT	Nanostructured and Amorphous Materials, Inc., Katy, TX, USA	APTES-coated	98+	30	>8
ZnO 8412DL	SkySpring Nanomaterials, Inc., Houston, TX, USA	Stearic acid-treated	99	10–30	>60
CuO 544868	Sigma–Aldrich, Oakville, ON, Canada	Uncoated	97.8	<50	29
CuO US3070	US Research Nanomaterials, Inc., Houston, TX, USA	Uncoated	99	40	~45
CuO US3070	US Research Nanomaterials, Inc., Houston, TX, USA	PVP-coated	99	40	~45
CuO US3070	US Research Nanomaterials, Inc., Houston, TX, USA	Silane-coated	99	40	~45
MnO_2 4910DX *	SkySpring Nanomaterials, Inc., Houston, TX, USA	Uncoated	98+	40–60	~13.5
NiO US3355	US Research Nanomaterials, Inc., Houston, TX, USA	Uncoated	99.5+	15–35	50–100
NiO US3352	US Research Nanomaterials, Inc., Houston, TX, USA	Uncoated	99.98	18	50–100
NiO US3352	US Research Nanomaterials,	PVP-coated	99.98	18	50–100

	Inc., Houston, TX, USA				
NiO US3352	US Research Nanomaterials, Inc., Houston, TX, USA	Stearic acid-coated	99.98	18	50–100
NiO US3352	US Research Nanomaterials, Inc., Houston, TX, USA	Silane-coated	99.98	18	50–100
Al_2O_3 544833	Sigma–Aldrich, Oakville, ON, Canada	Uncoated	-	<50	>40
CeO_2 US3136	US Research Nanomaterials, Inc., Houston, TX, USA	Uncoated	99.97	50	30–35
CeO_2 US3036	US Research Nanomaterials, Inc., Houston, TX, USA	Uncoated	99.97	10–30	30–50
CeO_2 US3037	US Research Nanomaterials, Inc., Houston, TX, USA	PVP-coated	99.99	10	35–70
CeO_2 US3037	US Research Nanomaterials, Inc., Houston, TX, USA	Stearic acid-coated	99.99	10	35–70
TiO_2 NIST #	National Institute of Standards and Technology (NIST,1989), Gaithersburg, MD, USA	Uncoated	99.4 [a]	19-Anatase (76%) 37-Rutile (24%)	55.55
Fe_2O_3 US3160	US Research Nanomaterials, Inc., Houston, TX, USA	Uncoated	99.5+	30	20–60

SSA: Specific surface area. APTES: (3-Aminopropyl) triethoxysilane. PVP: Polyvinylpyrrolidone. * 4910DX is sold as Mn_2O_3, but it was identified as MnO_2 by X-ray diffraction in (Avramescu et al., 2019). # TiO_2 NIST NPs will be referred to as "uncoated TiO_2 NPs". - Not provided by the manufacturer. [a] (Avramescu et al., 2020).

The study also included the uncoated bulk analogs of ZnO, CuO, MnO_2, NiO, Al_2O_3, CeO_2, TiO_2, and Fe_2O_3 (**Table 5-2**) and the dissolved metal analogs to evaluate the effects of particle size and solubility on potential genotoxicity. $ZnCl_2$ (Cat#Z0152), $CuCl_2$ dihydrate ($CuCl_2{\cdot}2H_2O$, Cat#C3279), manganese-(II)-sulfate monohydrate ($MnSO_4{\cdot}H_2O$, Cat#M7899), nickel-(II)-chloride hexahydrate ($NiCl_2{\cdot}6H_2O$, Cat#N6136), aluminum-(III) -chloride hexahydrate ($AlCl_3{\cdot}6H_2O$, Cat#A0718) and cerium-(III)-chloride heptahydrate ($CeCl_3{\cdot}7H_2O$,

Cat#228931) were obtained from Sigma–Aldrich (Oakville, ON, Canada). The physicochemical characterization, the results of cell viability and DNA damage assay (as evaluated by comet assay) for ZnO NPs (Cat#US3580), CuO NPs (Cat#544868), TiO_2 NIST NPs (referred to as "uncoated TiO_2 NPs"), ZnO MPs (Cat#US1003M), CuO MPs (Cat#US1140M), TiO_2 MPs (Cat#US1017M), $ZnCl_2$ and $CuCl_2$ were previously reported (Boyadzhiev et al., 2022) and are included in this study for comparison purposes.

Table 5-2. Characteristics of MOMPs as provided by the manufacturer.

MOMPs	Manufacturer	Purity (%)	Primary Size (µm)	SSA (m^2/g)
ZnO US1003M	US Research Nanomaterials, Inc., Houston, TX, USA	99.9+	1	2–15.8
CuO US1140M	US Research Nanomaterials, Inc., Houston, TX, USA	99.5	5	4–6
MnO_2 4930DX	SkySpring Nanomaterials, Inc., Houston, TX, USA	99+	~5 (50%), <10 (90%)	-
NiO US1014M	US Research Nanomaterials, Inc., Houston, TX, USA	99+	5	5–20
Al_2O_3 1331DL	SkySpring Nanomaterials, Inc., Houston, TX, USA	99.9	0.4–1.5	~110
CeO_2 2118CG	SkySpring Nanomaterials, Inc., Houston, TX, USA	99.9	5–20	5–8
TiO_2 US1017M	US Research Nanomaterials, Inc., Houston, Tx, USA	99.9+	1.5 (Anatase) 1.5 (Rutile)	5–8
Fe_2O_3 US1139M	US Research Nanomaterials, Inc., Houston, TX, USA	99	5	-

5.3.2 Primary particle size analysis of MONPs by transmission electron microscopy (TEM)

In addition to the characterization details provided by the manufacturer, the primary particle size of MONPs was also analyzed in-house using transmission electron microscopy (TEM). In brief, dry MONPs were analyzed by a JEM-2100F Field Emission TEM (JEOL, Peabody, MA, USA). Several images of each MONP dry suspension were obtained, and at least 100 individual NPs were sized using ImageJ 1.53g to determine the length and

width of NPs. GraphPad Prism Software 9.5.0 (San Diego, CA, USA) was used to create distribution histograms. Scanning electron micrographs of the MOMPs were taken using a JSM-7500F Field Emission scanning electron microscope (SEM) (JEOL, Peabody, MA, USA). The primary size of the MOMPs was not determined due to their size and aggregate state.

5.3.3 Specific surface area measurement for MONPs and MOMPs

The specific surface area (SSA) of each MONP and MOMP was experimentally determined using the Brunauer–Emmett–Teller (BET) method with nitrogen adsorption. For this purpose, an Autosorb iQ (Anton Paar Canada Inc., Montreal, QC, Canada) instrument was used. The samples were weighed before degassing and then again after degassing. For MO without an organic coating, the samples were heated at 20 °C/min to 120 °C and held for 12 h. Organically coated MO were heated at 20 °C/min to 85 °C and held for 12 h. Samples were run through a built-in leakage detection method to ensure no moisture or organic volatiles were remaining in the sample before proceeding with surface area analysis. SSA was determined by the multipoint BET method.

5.3.4 MONPs and MOMPs exposure suspensions

MONPs and MOMPs stock suspensions were prepared according to (Boyadzhiev et al., 2022) and (Avramescu et al., 2019, 2022). In brief, materials were weighed on an analytical mass balance (XSR105 Mettler Toledo), suspended in UltraPure™ DNase/RNase-Free distilled water (dH_2O) (Cat#10977015, Life Technologies, Burlington, ON, Canada) and sonicated in an ice-water bath. All suspensions were sonicated using a Branson Ultrasonics Sonifier™ 450 (Branson Ultrasonics Markham, ON, Canada), equipped with a ½ inch disruptor horn (with extension for volumes greater than 8 mL) and a removable flat tip. The tip was immersed 1–1.5 inches into the suspension from the surface. **Supplementary Table 5-1** summarizes the sonication details and the delivered sonication energy for each material suspension in water. An aliquot of the stock suspension was used to characterize the particle suspension, as described in section **5.3.5**. Serial dilutions were prepared from the stock suspension in DMEM/F12 (Dulbecco's Modified Eagle Medium/Nutrient Mixture F-12) cell culture medium without phenol red (Cat#21041-025, Life Technologies,

Burlington, ON, Canada) to obtain different concentrations for cell exposure. Dilutions were inverted 20 times to mix and used within 15 min of preparation.

Following the exposure suspension preparation, it was observed that a fraction of stearic acid-coated CeO_2 NPs and stearic acid-coated NiO NPs remained unsuspended, floating at the top of the suspension. The well-suspended fraction was transferred to a new vial, and two aliquots from this vial were used to characterize the suspension as described in section **5.3.5** and prepare the serial dilutions in the cell culture medium; the remaining unsuspended fraction was stored at −20 °C to determine the exact concentration of the stock suspension as described in (Rahman, L. et al., 2017a), with a slight modification to the protocol.

In brief, aluminum weighing boats (43 mm, Cat#HS14521A, Sigma–Aldrich, Oakville, ON, Canada) were weighed on an analytical mass balance (XSR105 Mettler Toledo), resulting in $Weight_1$. A total of 3 mL of each suspension or 3 mL of dH_2O (the same dH_2O used to prepare the suspension) was deposited on the top of each boat. All samples were dried with aluminum boats closed in an oven at 80 °C for 8 h. Once the suspensions were dried, boats were acclimatized at room temperature overnight and weighed on the same balance, resulting in $Weight_2$. The exact concentrations were calculated by subtracting $Weight_2$ from $Weight_1$ and dividing the final mass by the sample volume (3 mL). The weight of the boats with dH_2O was the same before and after the drying process, which corroborated the purity of the dH_2O and indicated that 8 h was enough to dry NP suspensions. Two or three independent stock suspensions were dried to determine the exact concentrations. The results for the stock suspension of stearic acid-coated CeO_2 NPs and stearic acid-coated NiO NPs were 0.67 ± 0.14 mg/mL and 2.96 ± 0.43 mg/mL, respectively. The exact concentrations in the medium of those two NPs are presented in parenthesis in the respective figures.

5.3.5 MONPs characterization by dynamic light scattering and electrophoretic light scattering

The hydrodynamic size (Dh) and polydispersity index (PDI) were determined by dynamic light scattering (DLS), whereas the surface charge (zeta potential; ZP) was characterized by electrophoretic light scattering (Jiang et al., 2009). MONPs stock suspensions were diluted to 50 µg/mL in dH_2O or DMEM/F12 without phenol red with 2% fetal bovine serum (FBS) (Cat#12483-020, Life Technologies, Burlington, ON, Canada), 100 U/mL penicillin G and 100 µg/mL streptomycin (Cat#15140-122, Life Technologies, Burlington, ON, Canada), and 1 ng/mL human epidermal growth factor (EGF) (Cat#PHG0311, Life Technologies, Burlington, ON, Canada). From each dilution, 7–10 individual measurements were conducted on a Zetasizer Nano ZSP (Malvern Panalytical, Westborough, MA, USA).

5.3.6 Cell culture

Immortalized FE1 cells derived from the transgenic Muta™Mouse model were used in this study. FE1 cells have the characteristics of type I and II pulmonary alveolar cells and have been used previously to evaluate the genotoxicity and mutagenicity of different chemicals and nanomaterials (Bengtson et al., 2016; Boyadzhiev et al., 2021; Decan et al., 2015; Jacobsen et al., 2008b; Maertens et al., 2017; White et al., 2003) and are under validation to be used in a standard *in vitro* mammalian mutagenicity test (Hölzl-Armstrong et al., 2020; Maertens et al., 2017; White et al., 2019). Cells were maintained in Dulbecco's Modified Eagle's Medium Nutrient Mixture: F12 HAM (1:1) cell culture medium (DMEM/F12) (Cat#11320-033, Life Technologies, Burlington, ON, Canada) with 2% FBS, 100 U/mL penicillin G and 100 µg/mL streptomycin, 1 ng/mL EGF at 37 °C in an incubator at 95% humidity and 5% CO_2. DMEM/F12 without phenol red cell culture medium was used for all exposures under the previously described conditions (section **5.3.4**).

5.3.7 Cell viability assay to determine the experimental conditions for the CometChip® assay

Trypan Blue exclusion analysis was used to determine the viability following MO or dissolved metal exposure. Cells were plated at 130,000 cells/well in a 6-well plate using

DMEM/F12 without phenol red and were incubated for 24 h. The following day, cells were exposed to different particle concentrations for 2 and 4 h at 37 °C with 95% humidity and 5% CO_2. Each well was washed with 0.5 mL Dulbecco's phosphate-buffered saline (dPBS; (Cat#14190-144, Life Technologies, Burlington, ON, Canada) three times and trypsinized for 3 min with 150 µL of trypsin-EDTA (disodium ethylenediaminetetraacetic acid) 0.25% (Cat#25200-056, Life Technologies, Burlington, ON, Canada). A total of 500 µL of DMEM/F12 without phenol red was added to harvest cells. From each sample, 10 µL of cell suspension was mixed with 10 µL of 0.4% Trypan Blue dye (Cat#15250061, Life Technologies, Burlington, ON, Canada), incubated for 5 min, and then counted on a hemocytometer. At least three independent experiments were conducted with two technical replicates per condition. The results are represented as the % cell viability ([Live cells/Total cell count] × 100) and the percentage of relative survival (% relative survival = [Number of live cells/cm^2 of samples]/[number of live cells/cm^2 of the control] × 100). Data were analyzed using a Kruskal–Wallis test with a Dunnett's post hoc to compare each exposure vs. the matched negative control in SigmaPlot 14.5 (Systat Software Inc., San Jose, CA, USA).

5.3.8 CometChip® assay

The Trevigen's 96-well CometChip® system (Cedarlane Laboratories, Burlington, ON, Canada) was used as a high-throughput platform to expose cells, electrophorese, and fluorescently measure DNA damage. The comet assay was performed according to a previous study (Boyadzhiev et al., 2022).

In brief, the CometChip® (Cat#4260-096-01, Cedarlane Laboratories, Burlington, ON, Canada) was equilibrated in 100 mL dPBS at room temperature for 30 min, following which 100 µL of single-cell suspension (150,000 cells/mL in DMEM/F12 without phenol red) was loaded into each well of the 96-well plate and the CometChip® was incubated for 20 min. Post-incubation, media was removed, and 50 µL of DMEM/F12 without phenol red was added to each well. MONPs suspensions, MOMPs suspensions, and dissolved metal analog solutions in the cell culture medium were prepared at 2x concentrations, and 50 µL of suspension was added to individual wells to obtain a final concentration of 1x in a final

volume of 100 µL. For the negative control, cells were incubated in the cell culture medium for 4 h, and for the positive control, cells were exposed for 1 h to 100 µM H_2O_2 (Cat#216763, Sigma–Aldrich, Oakville, ON, Canada). After 2 and 4 h of exposure, the medium was removed from wells, the CometChip® was washed with dPBS and overlaid with 5 mL of LMAgarose (Cat#4250-500-02, Cedarlane Laboratories, Burlington, ON, Canada), which solidified after 3 min at room temperature and 12 min at 4 °C. The CometChip® with embedded cells was incubated in 100 mL of lysis solution (Cat#4250-050-01, Cedarlane Laboratories, Burlington, ON, Canada) for 1 h at 4 °C and equilibrated for 20 min two times in 250 mL of alkaline solution (pH > 13, 200 mM sodium hydroxide [NaOH] [Cat#S8045-500, Sigma–Aldrich, Oakville, ON, Canada], 1 mM EDTA [Cat#15575-020, Life Technologies, Burlington, ON, Canada], and 0.1% Triton-X [Cat#BP-151-500, Fisher Scientific, Whitby, ON, Canada]). The electrophoresis was performed at 4 °C for 50 min at a constant 21 V (variable current 280 mA) using 700 mL of alkaline solution. The CometChip® was neutralized 2 times for 15 min in 100 mL of 400 mM Tris-HCl buffer (prepared from 1 M pH 7.4 Tris-HCl [Cat#T2194-1L, Sigma–Aldrich, Oakville, ON, Canada]), and then in 100 mL of 20 mM Tris-HCl for 30 min (prepared from 1 M pH 7.4 Tris-HCl). The neutralized chip was stained for 14 h in 100 mL 0.2X SYBR® Gold (Cat#S11494, Life Technologies, Burlington, ON, Canada) in 20 mM Tris-HCl. After that, the CometChip® was destained for 1 h at room temperature in 100 mL 20 mM Tris pH 7.4 and kept in 100 mL of dPBS. TIFF Images were generated using a Leica DMI8 automated confocal fluorescence microscope (Leica Microsystems, Wetzlar, Germany) at 5x magnification and were analyzed using the Trevigen Comet Software 1.3d (Bio-Techne, Devens, MA, USA). Artifacts were excluded from each well (double comet, debris, etc.).

Wells with more than 50 comets were included in the final analysis, except for cells treated with high concentrations (50 µg/mL or 100 µg/mL) of CuO NPs, MnO_2 NPs, NiO NPs, Fe_2O_3 NPs, MnO_2 MPs, and Fe_2O_3 MPs, which resulted in non-uniform or incomplete staining of comet heads (**Supplementary Figure 5-1**). This resulted in less than 50 comets/well. Thus, for high-concentration exposures, a decision was made to count the wells with less than 50 comets. Each experiment considered a minimum of 2 and a

maximum of 8 technical replicates, with at least three independent experiments performed. The mean percentage of DNA in the tail was used as the metric for DNA damage. Data were normalized via a $\log_{10}$ transformation and passed the normality test (Shapiro–Wilk). The transformed datasets were analyzed using a one-way analysis of variance (ANOVA) with a Dunnett's post hoc to compare each exposure to the respective negative control in SigmaPlot 14.5.

5.3.9 *In vitro* MicroFlow® assay

A total of 5000 FE1 cells were seeded in each well of a 96-well plate using DMEM/F12 cell culture medium without phenol red and were incubated at 37 °C in a humidified atmosphere of 5% CO_2. Following 24 h incubation, cells were exposed to varying concentrations of MONPs, MOMPs, or dissolved metal analogs for 40 h. According to the MicroFlow® MN assay, cells should be exposed for a duration that approximates 1.5 to 2 normal cell cycles to evaluate the MN induction. The doubling time of FE1 cells is 17 h; therefore, 40 h of exposures reflected cell division over 2 normal cell cycles. For the negative control, cells were incubated for 40 h in the cell culture medium, whereas for the positive control, cells were exposed to 500 µM of methyl methanesulfonate (MMS) (Cat# 129925, Sigma–Aldrich, Oakville, ON, Canada) for 40 h. The MicroFlow® kit (In Vitro MicroFlow® kit, 1000/200, 96 well; Litron Laboratories, Rochester, NY, USA) was used to measure cytotoxicity, fold-increase of apoptotic/necrotic cells, and MN frequency using flow cytometry. Sample preparation, staining, and flow cytometry analysis were performed according to the manufacturer's instructions. In brief, following the 40 h exposure, cells were washed with DMEM/F12 cell culture medium without phenol red and placed on ice for 20 min. The supernatant was removed, and 50 µL of freshly prepared Complete Nucleic Acid Dye A was added to each well. The plate was placed under a visible light source on ice for 30 min, and 150 µL of cold 1X Buffer Solution was added to each well. The supernatant was carefully removed. Cells were lysed, stained with 100 µL of Complete Lysis Solution 1, incubated at 37 °C for 1 h, and then in 100 µL of freshly prepared Completed Lysis Solution 2 at room temperature for 30 min. A Becton–Dickinson LSRFortessa™ 5 laser analyzer (Becton–Dickinson, San Jose, CA, USA) was used to collect data. An analysis stop gate of

5000 ethidium monoazide (EMA)-negative nuclei was applied. The % relative survival, the increase of apoptotic/necrotic cells (EMA-fold increase), and the MN frequency (%MN) were determined (Fortin et al., 2023).

In brief, % relative survival was determined using intact viable nuclei-to-bead ratios in exposed cells versus the negative control by spiking the cell suspensions with 6-micron fluorescent microspheres (Cat#C-16508, Life Technologies, Burlington, ON, Canada), which function as the internal standards. Apoptotic/necrotic cells were stained using EMA dye (contained in the kit), which crosses the outer membrane of necrotic and apoptotic cells. EMA-fold increase was determined using % Parent apoptotic/necrotic in exposed cells versus the average of %Parent apoptotic/necrotic in the negative control. % MN was scored in exposed cells and negative control using the double staining procedure outlined in the instruction manual. % MN was calculated as % MN = (MN Events/Nucleated Events) × 100. Then, % MN was converted to MN-fold increase values relative to negative controls (Avlasevich et al., 2021). The final data represents 3–4 biological replicates per condition. Statistical significance was determined using the Student's *t*-test, which was used when both groups passed the normality test (Shapiro–Wilk) and equal variance test (Brown-Forsythe). For groups that were normally distributed (Shapiro–Wilk) but did not pass the equal variance, a Welch's *t*-test was conducted. Mann–Whitney Rank Sum Test was conducted for some groups that did not pass the normality and equal variance tests. The statistical analysis was performed in SigmaPlot 14.5.

5.3.10 Correlation analysis

To evaluate whether significant monotonic relationships were present between the two genotoxicity endpoints (% DNA in the tail, MN-fold increase) and the physicochemical properties of the MO tested, a Spearman's rank-order correlation analysis was conducted. For this purpose, the response at the highest concentration at the latest timepoint for each MO form was used for % DNA in the tail, whereas the response at the highest concentration for each MO form where % relative survival was 40% or higher was used for MN-fold increase. The data from both genotoxicity endpoints were normalized to the concentration of MO expressed in terms of µM of constituent metal. The responses were correlated with

nine physicochemical properties: % solubility at 10 µg/mL, % solubility at 100 µg/mL, valence state of the constituent metal, atomic mass of the metal constituent (g/mol), primary particle size (nm), SSA (m^2/g) experimentally determined by BET, and Dh (nm), PDI, and ZP (mV) in cell culture medium. A correlation was considered significant if $p < 0.05$.

5.3.11 Benchmark concentration modeling

BMC modeling of the % DNA in the tail and % MN responses was conducted using PROAST (RIVM National Institute for Public Health and the Environment). The Benchmark response (BMR), which is a predetermined change in response as compared to negative control, was set to the commonly used value of 10% relative risk. Data with BMC/lower 95% confidence interval of the BMC (BMCL) >20, BMC with values higher than the highest concentration, and samples with a non-significant trend according to the Akaike information criterion were removed.

All materials previously evaluated and reported in (Boyadzhiev et al., 2022), uncoated ZnO NPs (US3580), uncoated CuO NPs (544868), uncoated TiO_2 NPs, silica-coated TiO_2 NPs (5422HT), silica and alumina-coated TiO_2 NPs (5423HT), silica and stearic acid-coated TiO_2 NPs (5424HT), silica and silicone oil coated TiO_2 NPs (5425HT), uncoated TiO_2 NPs (MKA050), uncoated rutile TiO_2 NPs (MKNR050P), uncoated TiO_2 NPs (MKNA005), TiO_2 nanowires (774510), ZnO MPs, CuO MPs, TiO_2 MPs, $ZnCl_2$ and $CuCl_2$ were included in the analysis.

5.4 Results

5.4.1 MONPs characterization

The primary size determined by TEM, the Dh, PDI, and ZP in the cell culture medium are summarized in **Table 5-3**. Part of the characterization of uncoated ZnO NPs (US3580), uncoated CuO NPs (544868), uncoated NiO NPs (US3355), uncoated Al_2O_3 NPs (544833), uncoated TiO_2 NPs, ZnO MPs, CuO MPs, NiO MPs, Al_2O_3 MPs, and TiO_2 MPs were previously reported and are indicated with letters “a”, “b”, and “c” in **Table 5-3**. The characterization of Dh, PDI, and ZP in dH_2O is found in **Supplementary Table 5-2**, and the BET SSA characterization is found in **Supplementary Table 5-3**. The frequency distribution of the

MONPs can be found in **Supplementary Figure 5-2**, **5-3**, **5-4**, **5-5**, **5-6**, **5-7**.

The **Supplementary Figure 5-8** shows representative SEM images of MnO_2 MOMPs, CeO_2 MOMPs, and Fe_2O_3 MPs. The images of the previously reported MONPs and MOMPs can be found in (Boyadzhiev et al., 2022, 2023).

Table 5-3. Characterization of MONPs as determined by TEM, DLS, and ELS.

MONPs	Primary Size [d] (nm) Length Width	Aspect Ratio [e]	Cell Culture Medium [f]		
			Dh (nm)	PDI	ZP (mv)
Uncoated ZnO (US3580)	(23.9 ± 7.2) [a] (19.4 ± 5.5) [a]	1.23 ± 0.17 [a]	323 ± 125 [a]	0.56 ± 0.12 [a]	−9.21 ± 1.15
Uncoated ZnO (5811HT)	(44.06 ± 19.4) (33.88 ± 13.2)	1.31 ± 0.32	290 ± 13.5	0.27 ± 0.05	−9.05 ± 0.65
APTES-coated ZnO (5812HT)	(53.51 ± 38.5) (40.4 ± 25.6)	1.31 ± 0.30	322 ± 24.8	0.29 ± 0.05	−10.8 ± 0.60
Stearic acid-treated ZnO (8412DL)	(33.69 ± 16.57) (25.06 ± 9.56)	1.35 ± 0.36	361 ± 65.9	0.42 ± 0.04	−9.00 ± 0.96
Uncoated CuO (544868)	(64.8 ± 47.0) [b,c] (45.9 ± 28.0) [b,c]	1.39 ± 0.39 [b,c]	396 ± 34.9	0.35 ± 0.05	−11.7 ± 0.73
Uncoated CuO (US3070)	(75.97 ± 42.87) (58.06 ± 34.36)	1.35 ± 0.32	265 ± 8.79	0.26 ± 0.03	−11.7 ± 0.73
PVP-coated CuO (US3070)	(63.07 ± 34.05) (48.07 ± 24.7)	1.32 ± 0.28	272 ± 12.6	0.29 ± 0.04	−11.3 ± 0.57
Silane-coated CuO (US3070)	(84.21 ± 55.46) (62.35 ± 36.28)	1.35 ± 0.41	494 ± 49.1	0.34 ± 0.11	−14.9 ± 0.75
Uncoated MnO_2 (4910DX)	(36.06 ± 34.88) (13.12 ± 6.33)	2.80 ± 1.97	151 ± 2.42	0.19 ± 0.03	−12.3 ± 0.87
Uncoated NiO (US3355)	(27.29 ± 10.26) [c] (21.84 ± 7.90) [c]	1.25 ± 0.20 [c]	229 ± 18.5	0.30 ± 0.05	−12.9 ± 1.03
Uncoated NiO (US3352)	(25.56 ± 13.16) (20.71 ± 10.08)	1.23 ± 0.24	231 ± 4.11	0.21 ± 0.02	−14.4 ± 1.06
PVP-coated NiO (US3352)	(31.99 ± 14.7) (24.66 ± 11.28)	1.31 ± 0.29	213 ± 4.37	0.20 ± 0.02	−13.6 ± 0.52
Stearic acid-coated NiO (US3352)	(29.59 ± 14.42) (22.81 ± 10.38)	1.30 ± 0.25	285 ± 9.62	0.28 ± 0.05	−16.7 ± 0.82
Silane-coated NiO (US3352)	(29.51 ± 12.46) (23.90 ± 9.98)	1.24 ± 0.19	222 ± 8.49	0.29 ± 0.04	−13.6 ± 0.83
Uncoated Al_2O_3 (544833)	(23.92 ± 11.84) [c] (10.68 ± 6.85) [c]	2.63 ± 1.40 [c]	385 ± 48.6	0.37 ± 0.05	−12.4 ± 0.81
Uncoated CeO_2 (US3136)	(39.78 ± 14.55) (31.25 ± 9.66)	1.27 ± 0.22	345 ± 6.72	0.27 ± 0.03	−14.0 ± 1.12
Uncoated CeO_2 (US3036)	(12.05 ± 3.42) (9.90 ± 2.73)	1.22 ± 0.20	357 ± 15.2	0.32 ± 0.05	−13.9 ± 1.91
PVP-coated CeO_2 (US3037)	(14.12 ± 4.54) (10.92 ± 3.42)	1.29 ± 0.22	383 ± 20.4	0.32 ± 0.05	−11.9 ±0.99
Stearic acid-coated CeO_2 (US3037)	(10.61 ± 2.71) (8.23 ± 2.05)	1.30 ± 0.20	405 ± 23.4	0.40 ± 0.05	−12.2 ± 0.68
Uncoated TiO_2 NPs	(26.8 ± 8.9) [a,c] (20.8 ± 6.8) [a,c]	1.30 ± 0.26 [c]	421 ± 31 [c]	0.23 ± 0.06 [c]	−11.5 ± 0.2 [c]
Uncoated Fe_2O_3 (US3160)	(30.95 ± 13.12) (24.99 ± 11.24)	1.26 ± 0.24	193 ± 12.9	0.28 ± 0.03	−11.4 ± 0.86

[a] Characterization described by (Boyadzhiev et al., 2022). [b] Characterization described by (Boyadzhiev et al., 2021). [c] Previously reported in (Boyadzhiev et al., 2023). [d] Primary size

determined by TEM. [e] Aspect ratio: Length/Width. [f] DMEM/F12 cell culture medium without phenol red + 2% FBS + 1 ng/mL EGF. Dh, PDI, and ZP were determined by DLS and ELS.

The lengths of all ZnO NPs ranged from 23.9 ± 7.2 to 53.51 ± 38.5 nm, whereas the lengths of CuO NPs ranged from 63.07 ± 34.05 to 84.21 ± 55.46 nm. The size of uncoated MnO_2 NPs (4910DX) was from 36.06 ± 34.88 nm. All NiO NPs exhibited similar lengths from 25.56 ± 13.16 nm to 31.99 ± 14.7 nm. Uncoated Al_2O_3 NPs (544833) exhibited 23.92 nm ± 11.84 nm size (reported in (Boyadzhiev et al., 2023)). Uncoated CeO_2 NPs (US3136) showed 39.78 ± 14.55 nm, and the rest of the CeO_2 NPs (Uncoated-US3036, PVP-coated and stearic acid-coated [US3037]) exhibited smaller lengths, ranging from 10.61 ± 2.71 to 14.12 ± 4.54 nm. The uncoated TiO_2 NPs were 26.8 ± 8.9 nm in length (reported previously in (Boyadzhiev et al., 2022, 2023)). Uncoated Fe_2O_3 NPs (US3160) were 30.95 ± 13.12 nm (**Table 5-3**). Almost all MONPs had an aspect ratio spanning from 1.22 ± 0.20 to 1.39 ± 0.39 and showed a spherical morphology, except uncoated MnO_2 NPs (4910DX) and uncoated Al_2O_3 NPs (544833), which exhibited an aspect ratio of ~2.7 with a rod-like shape (reported previously in (Boyadzhiev et al., 2023) and **Supplementary Figure 5-4**).

The characterization of MONPs in dH_2O showed Dh and PDI values ranging from ~134 to 647 nm and from ~0.14 to 0.5, respectively, suggesting that all of them were polydisperse suspensions (**Supplementary Table 5-2**). The Dh and PDI in the cell culture medium were closer to the values observed in water, which ranged from ~151 to 494 nm and ~0.19 to 0.56, respectively (**Table 5-3**). The decrease in ZP values to ~−12 mV and their polydispersity state in the cell culture medium is expected due to the cell culture medium components and its high osmolarity (**Table 5-3**) (Jiang et al., 2009).

The SSA as determined by BET was from 16.52 to 28.28 m^2/g for ZnO NPs, 6.11–10.34 m^2/g for CuO NPs (showed the lowest SSA), 42.16 m^2/g for uncoated MnO_2 NPs (4910DX), 14.63 to 36.68 m^2/g for NiO NPs, 145.3 m^2/g for uncoated Al_2O_3 NPs (544833), which was the highest of all the MONPs, 14.06 to 67.11 m^2/g for CeO_2 NPs, and 52.73 and 44.88 m^2/g for uncoated TiO_2 NPs and uncoated Fe_2O_3 NPs (US3160), respectively (**Supplementary Table 5-3**). From SSA analysis of the MOMPs, CuO MPs showed the lowest value of SSA with 0.797 m^2/g, whereas Al_2O_3 MPs showed the highest value with

22.32 m^2/mg. The rest of the MOMPs exhibited SSA values ranging from 2.52 to 10.8 m^2/g (**Supplementary Table 5-3**). The SSA experimentally determined by BET for all TiO_2 variants included in the BMC analysis is found in **Supplementary Table 5-3**.

5.4.2 Cell viability and relative survival

Cell viability and relative survival were evaluated by the Trypan Blue exclusion method as indicators of cytotoxicity following exposure to different concentrations of MONPs, MOMPs, and dissolved metal analogs for 2 and 4 h. Uncoated MnO_2 NPs (4910DX), MnO_2 MPs, $MnSO_4$, uncoated Fe_2O_3 NPs (US3160) and Fe_2O_3 MPs were evaluated after 24 h of exposure because their NP and MP forms did not induce a decrease in cell viability, no cytotoxicity evaluation was conducted at 2 and 4 h. The % cell viability results of uncoated ZnO NPs (US3580), ZnO MPs, $ZnCl_2$, uncoated CuO NPs (544868), CuO MPs, $CuCl_2$, uncoated TiO_2 NPs, and TiO_2 MPs were reported previously in (Boyadzhiev et al., 2022) and are included here for comparison purposes. The term "variants" refers to uncoated or coated MONPs and MOMPs.

The highest concentration evaluated for ZnO variants in this study was set to 20 µg/mL, as higher concentrations than this induced cell rounding and significant loss in viability at 4 h post-exposure in a previous study (Boyadzhiev et al., 2022). Similar cytotoxicity was not observed after exposure to other materials tested in the current study. Percent cell viability did not alter after exposure to MO variants and dissolved metal analogs at any concentrations or post-exposure time points (**Supplementary Figure 5-9**, **5-10**, **5-11**, **5-12**), except for uncoated Fe_2O_3 NPs (US3160), which showed 93% and 89% viability at 50 and 100 µg/mL after 24 h compared to their matched negative control (**Supplementary Figure 5-12B**).

With regards to % relative survival, although a decreasing trend was observed at the highest concentration of 20 µg/mL of the uncoated or coated ZnO NPs or 33 µg/mL of $ZnCl_2$, none of them induced a statistically significant decrease compared to the matched negative control at 2 or 4 h (**Supplementary Figure 5-13A**), the exposure durations used for the comet assay. With respect to Cu, Mn, and Ni, a majority of variants and dissolved metal

analogs tested did not induce a decrease in % relative survival at any of the timepoints except for $MnSO_4$, which induced reduction in the relative survival to 60% after 24 h of exposure (**Supplementary Figure 5-13B**, **5-14**) and stearic acid-coated NiO NPs (US3352), NiO MPs and $NiCl_2$ which exhibited a tendency to affect the % relative survival only at 4 h (**Supplementary Figure 5-15A**). Uncoated Al_2O_3 NPs (544833), Al_2O_3 MPs, and $AlCl_3$ exposure did not impact the % relative survival after 4 h; therefore, no cytotoxicity evaluation was conducted at 2 h of exposure (**Supplementary Figure 5-15B**). However, exposure to stearic acid-coated CeO_2 NPs (US3037) resulted in a significant decrease in % relative survival (71%) at 134 µg/mL after 4 h post-exposure (**Supplementary Figure 5-16A**). Since uncoated CeO_2 NPs (US3036) did not decrease % relative survival after 24 h of exposure, this NP was not evaluated at an earlier post-exposure time point. $CeCl_3$ did not change the % relative survival with respect to the matched negative control (**Supplementary Figure 5-16A**).

After 2 and 4 h of exposure to uncoated TiO_2 NPs, the % relative survival did not decrease at any concentration (**Supplementary Figure 5-16B**). The exposure for 24 h to Fe_2O_3 variants did not induce any statistically significant decrease at any concentration after 24 h of exposure; thus, no evaluation was conducted at 2 or 4 h (**Supplementary Figure 5-17**).

5.4.3 DNA strand break induction

Only the statistically significant results are described based on differences between the exposed samples and the matched negative controls.

Only stearic acid-treated ZnO NPs (8412DL) induced an increase in % DNA in the tail (6.7%) at 10 µg/mL at 2 h. All other ZnO NP variants, except the ZnO MPs, induced ~8–15% DNA in the tail compared to the matched negative controls (~4–5%) at the higher concentration of 20 µg/mL. At 4 h, uncoated ZnO NPs (US3580), uncoated ZnO NPs (5811HT), APTES-coated ZnO NPs (5812HT), and stearic acid-treated ZnO NPs (8412 DL) showed 13, 11, 12 and 24% DNA in the tail, respectively, at 10 µg/mL, and, at 20 µg/mL, the % DNA in the tail increased to 36, 33, 46 and 33%, respectively (**Figure 5-1**). ZnO MPs and

$ZnCl_2$ exposure induced DNA strand breaks after 4 h of exposure only at 20 µg/mL and 33 µg/mL with 29 and 15% DNA in the tail, respectively (**Figure 5-1**).

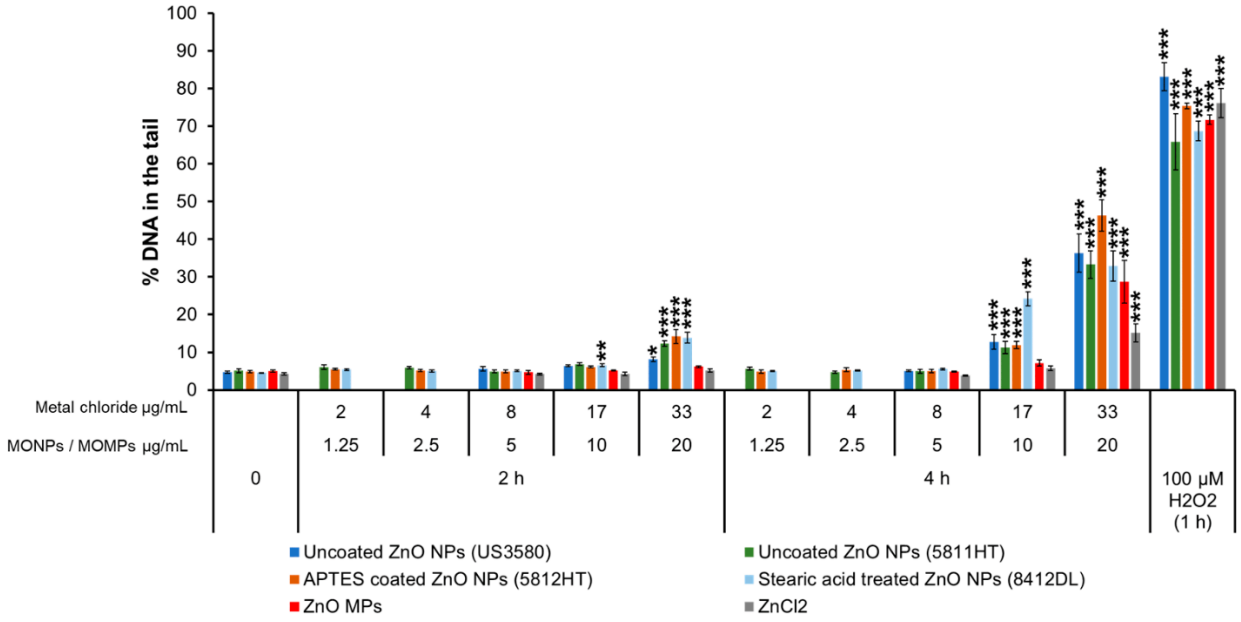

Figure 5-1. Percentage of DNA in the tail in FE1 cells after exposure to ZnO variants and $ZnCl_2$ at 2 and 4 h. Data are presented as mean and standard error (n = 3–4). Statistically significant differences between the exposed samples and the matched negative control (4 h) were determined through one-way ANOVA with a Dunnett's post hoc. * $p < 0.05$, ** $p < 0.01$, *** $p < 0.001$. Uncoated ZnO (US3580), ZnO MPs, and $ZnCl_2$ data were previously reported *(Boyadzhiev et al., 2022)*.

Among all CuO NPs, uncoated CuO NPs (544868, US3070) exhibited significant DNA damage at the lowest concentration of 5 µg/mL with ~6–6.8% and ~10–12% DNA in the tail at 2 and 4 h, respectively, compared to matched negative controls (~4.6%). Uncoated CuO NPs (544868) caused 6, 8, 14, and 24% DNA in the tail at 2 h and 10, 17, 34, and 58% DNA in the tail at 4 h at the concentrations of 5, 10, 25, and 50 µg/mL, respectively. A similar response was observed for uncoated CuO NPs (US3070) with 7, 10, 22, and 28% DNA in the tail at 2 h and 12, 25, 42, and 51% at 4 h after exposure to 5, 10, 25 and 50 µg/mL, respectively. PVP-coated CuO NPs (US3070) and silane-coated CuO NPs (US3070) showed 7, 14, and 19–24% at 2 h after exposure to 10, 25 and 50 µg/mL. At 4 h, both PVP and silane-coated CuO NPs induced 9, 15, ~ 30, and 38% DNA in the tail at 5, 10, 25, and 50 µg/mL concentrations, respectively (**Figure 5-2**). CuO MPs and $CuCl_2$ did not induce DNA damage (**Figure 5-2**).

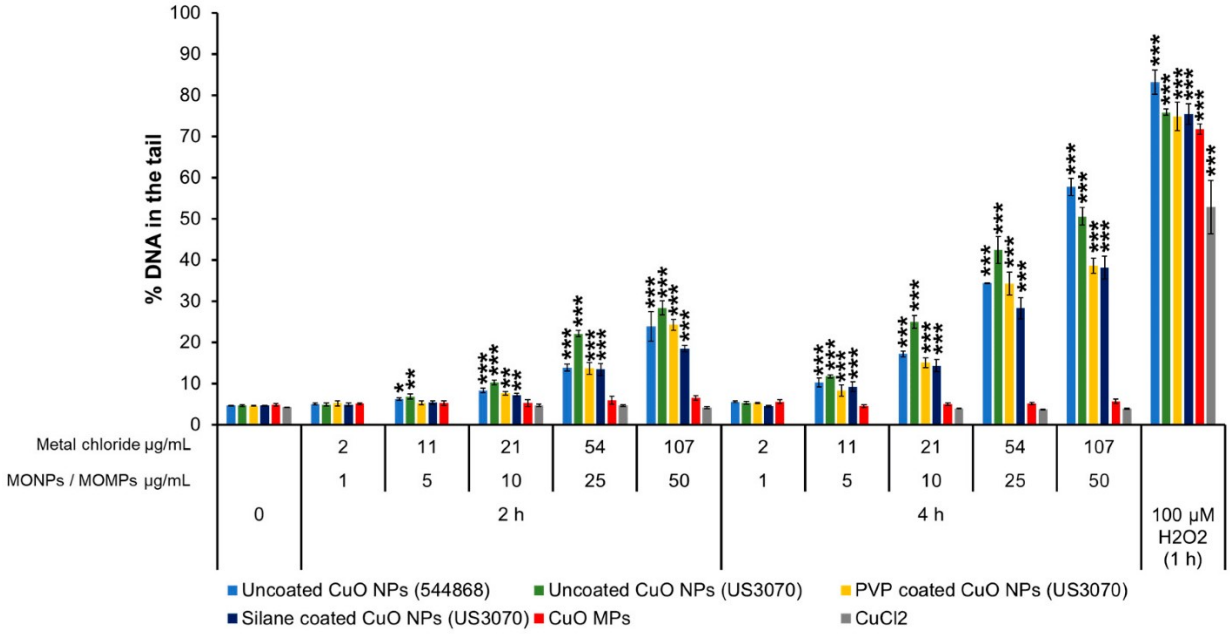

Figure 5-2. Percentage of DNA in the tail in FE1 cells after exposure to CuO variants and $CuCl_2$ at 2 and 4 h. Data are presented as mean and standard error (n = 3–4). Statistically significant differences between the exposed samples and the matched negative control (4 h) were determined through one-way ANOVA with a Dunnett's post hoc. * $p < 0.05$, ** $p < 0.01$, *** $p < 0.001$. Uncoated CuO NPs (544868), CuO MPs, and $CuCl_2$ data were previously reported *(Boyadzhiev et al., 2022)*.

Uncoated MnO_2 NPs (4910DX) induced 14 and 22% DNA in the tail after 2 h of exposure and 22 and 34% after 4 h of exposure to 50 and 100 µg/mL. MnO_2 MPs also induced DNA breaks with up to 13% DNA in the tail at 100 µg/mL at 4 h, compared to the matched negative controls (~4.58%) (**Figure 5-3**). $MnSO_4$ did not increase the % DNA in the tail at any concentrations tested (**Supplementary Figure 5-18**). Concentrations higher than 15 µg/mL of $MnSO_4$ were not evaluated at 4 h because 15 µg/mL showed high cytotoxicity at 24 h (60% relative survival, **Supplementary Figure 5-14B**).

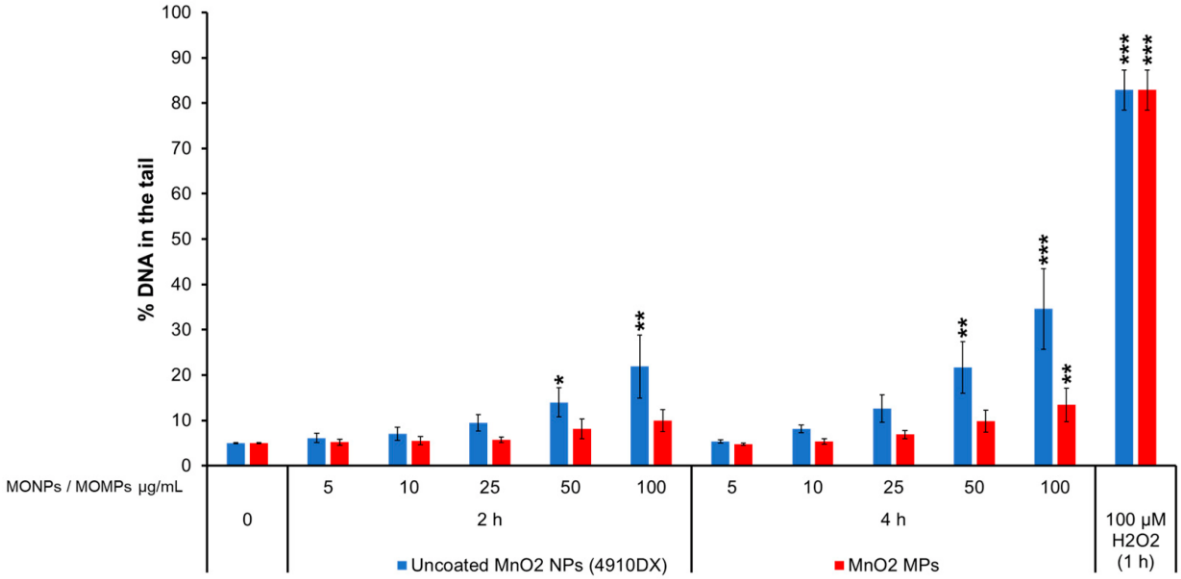

Figure 5-3. Percentage of DNA in the tail in FE1 cells after exposure to MnO_2 variants at 2 and 4 h. Data are presented as mean and standard error (n = 3–4). Statistically significant differences between the exposed samples and the matched negative control (4 h) were determined through one-way ANOVA with a Dunnett's post hoc. * $p < 0.05$, ** $p < 0.01$, *** $p < 0.001$.

At 2 h post-exposure, DNA damage was evident in cells treated with uncoated/coated NiO NPs and after treatment with NiO MPs, showing 7–9% of DNA in the tail at 5 and 10 µg/mL and 16–27% at 25, 50 and 100 µg/mL. At 4 h post-exposure, these particles showed 9–17% of DNA in the tail at 5 and 10 µg/mL and 15–26% at 25, 50 and 100 µg/mL concentrations. The exception was PVP-coated NiO NPs (US3352), which did not induce significant DNA strand breaks at 5 or 10 µg/mL at both the time points tested. Similarly, $NiCl_2$ did not induce a response compared to the matched negative controls at 2 or 4 h (~5%) (**Figure 5-4**).

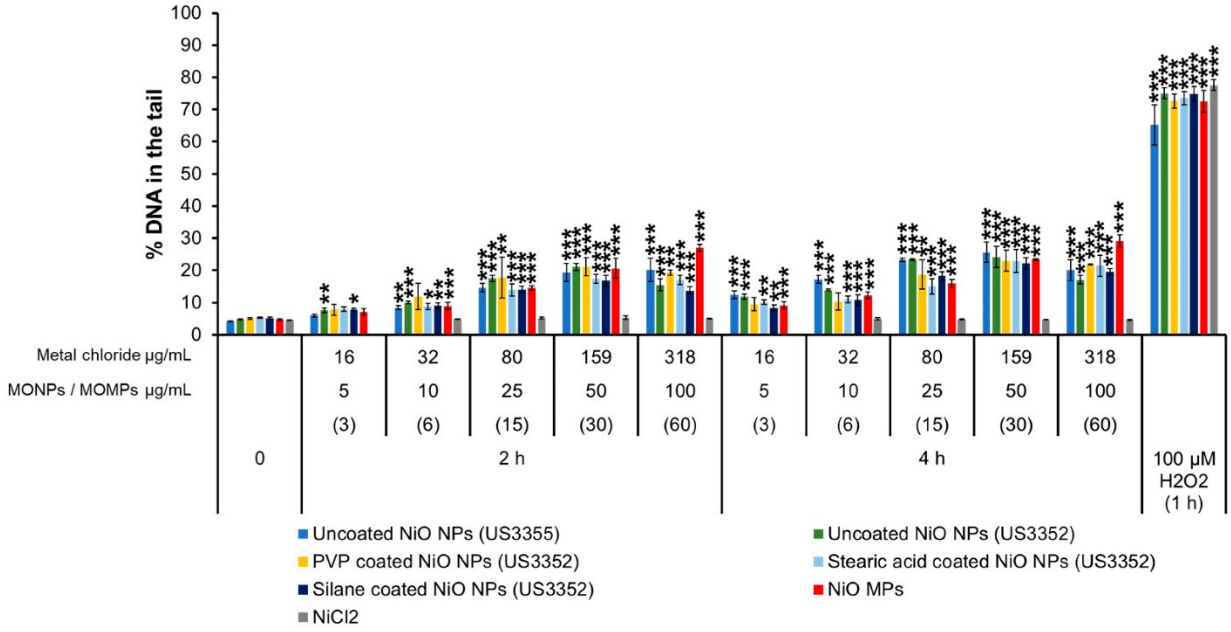

Figure 5-4. Percentage of DNA in the tail in FE1 cells after exposure to NiO variants and $NiCl_2$ at 2 and 4 h. Data are presented as mean and standard error (n = 3–4). Statistically significant differences between the exposed samples and the matched negative control (4 h) were determined through one-way ANOVA with a Dunnett's post hoc. * $p < 0.05$, ** $p < 0.01$, *** $p < 0.001$. Data in parenthesis indicates the concentration of stearic acid-coated NiO NPs.

Regarding Al_2O_3 variants (uncoated Al_2O_3 NPs [544833], Al_2O_3 MPs) and $AlCl_3$, all of them showed values from 4 to 7% of DNA in the tail, but there was no statistically significant difference versus the negative controls (~5% DNA in the tail) (**Figure 5-5**).

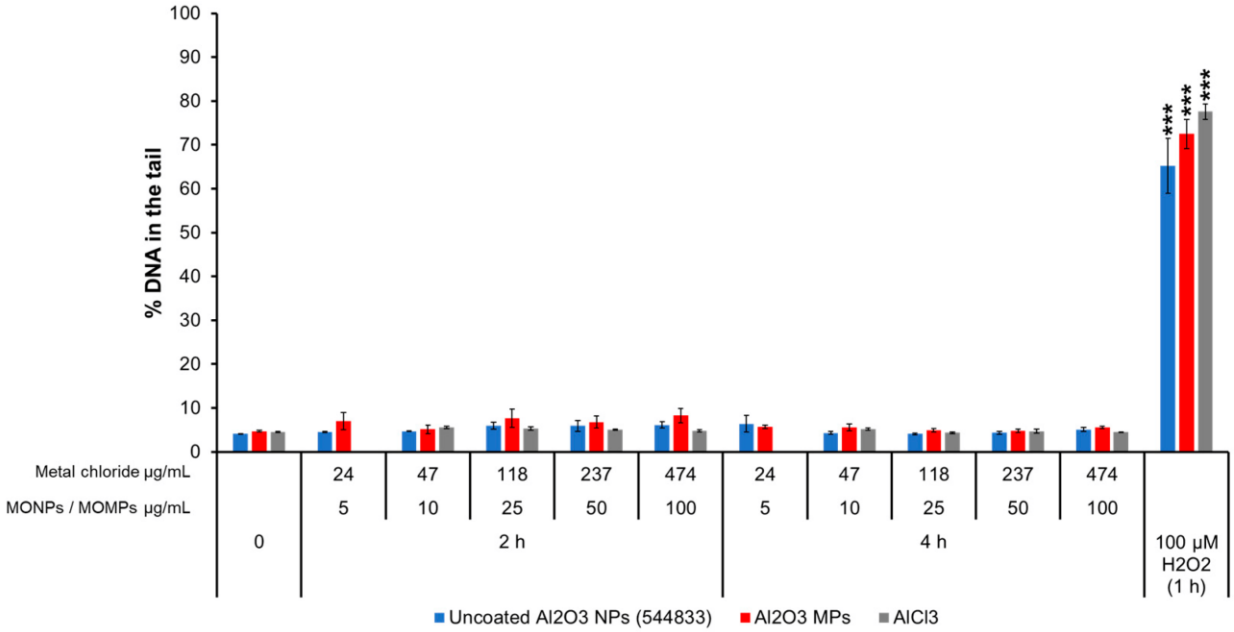

Figure 5-5. Percentage of DNA in the tail in FE1 cells after exposure to Al_2O_3 variants and $AlCl_3$ at 2 and 4 h. Data are presented as mean and standard error (n = 3–4). Statistically significant differences between the exposed samples and the matched negative control (4 h) were determined through one-way ANOVA with a Dunnett's post hoc. *** $p < 0.001$.

For CeO_2 variants and $CeCl_3$, the negative controls showed ~5% of DNA in the tail. A subtle but significant increase in % DNA in the tail was observed after exposure to uncoated CeO_2 NPs (US3136) at 100 µg/mL after 2 h and 4 h (~6.7%) and CeO_2 NPs (US3036) at the same concentration at 2 h (6.6%). The PVP-coated CeO_2 NPs (US3037) increased % DNA in the tail to 6.8–9.5% at 50 and 100 µg/mL at 2 h and to 6–7.14% at 10, 25, 50, and 100 ug/mL at 4 h of exposure. Stearic acid-coated CeO_2 NPs (US3037) showed ~5–5.7% DNA in the tail at 3, 7, 17, and 134 µg/mL at 2 h and 5–5.8% at 4 h following exposure to 34, 67, and 134 µg/mL concentrations. However, a concentration or time response for all uncoated and coated CeO_2 NPs was not observed. CeO_2 MPs and $CeCl_3$ did not induce DNA breaks (**Figure 5-6**).

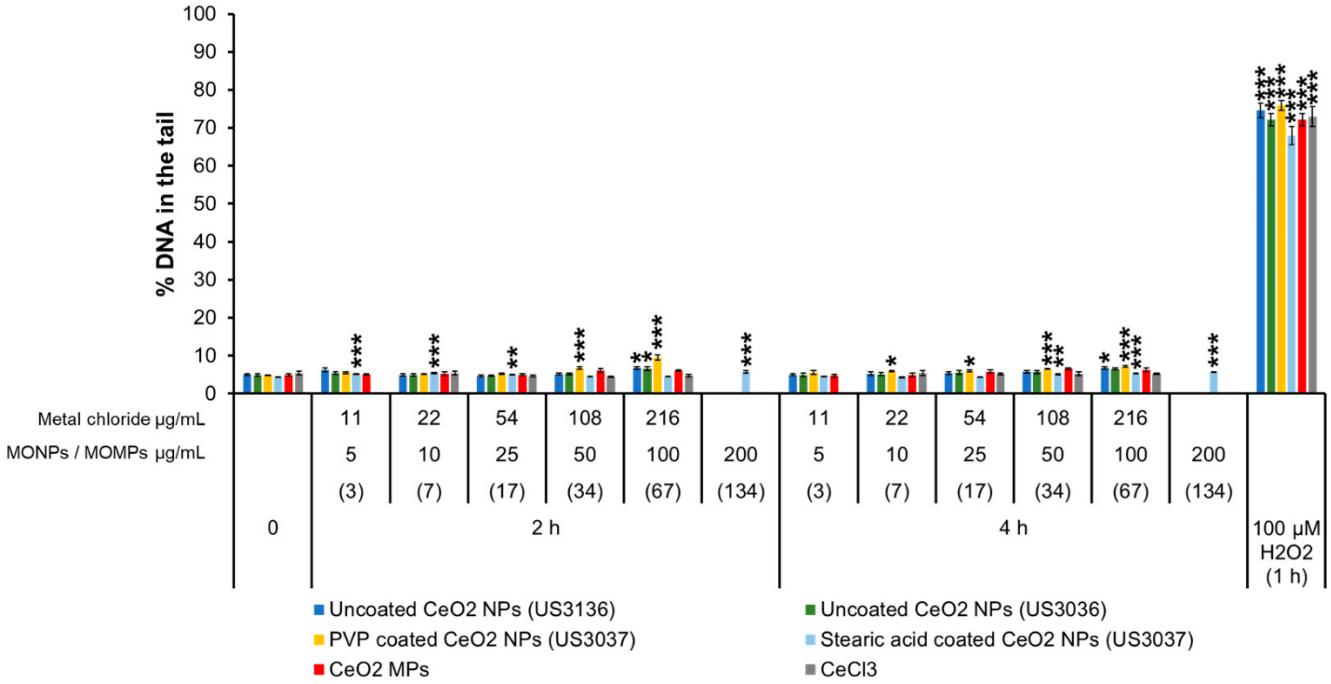

Figure 5-6. Percentage of DNA in the tail in FE1 cells after exposure to CeO_2 variants and $CeCl_3$ at 2 and 4 h. Data are presented as mean and standard error (n = 3–4). Statistically significant differences between the exposure and the matched negative control (4 h) were determined through one-way ANOVA with Dunnett's post hoc. * $p < 0.05$, ** $p < 0.01$, *** $p < 0.001$. Data in parenthesis indicates the concentration of stearic acid-coated CeO_2 NPs.

Uncoated Fe_2O_3 NPs (US3160) induced a slight significant increase after 2 and 4 h of exposure at 100 µg/mL of 5.9% DNA in the tail. Fe_2O_3 MPs did not increase the % DNA in the tail compared to the matched negative controls (4.4%) (**Figure 5-7**).

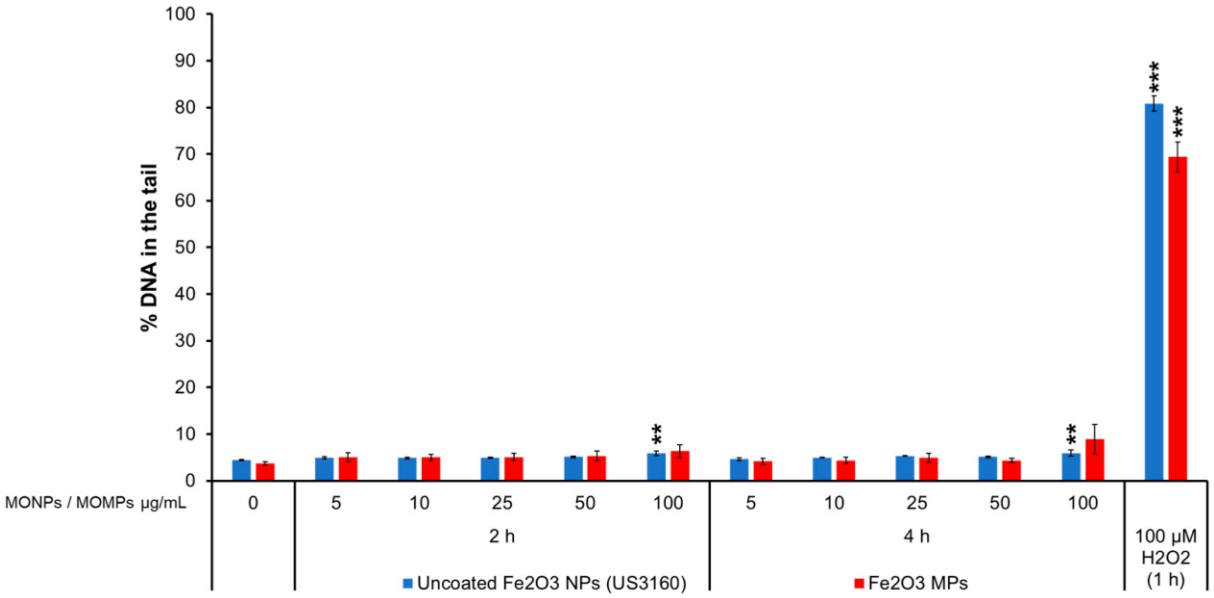

Figure 5-7. Percentage of DNA in the tail in FE1 cells after exposure to Fe_2O_3 variants at 2 and 4 h. Data are presented as mean and standard error (n = 3–4). Statistically significant differences between the exposed samples and the matched negative control (4 h) were determined through one-way ANOVA with a Dunnett's post hoc. ** $p < 0.01$, *** $p < 0.001$.

Supplementary Figure 5-19, **5-20**, **5-21**, **5-22** show representative comet images from MO variants that induced higher levels of % DNA in the tail (ZnO, CuO, MnO_2, and NiO). The images from the previously published data can be found in (Boyadzhiev et al., 2022). The results for all TiO_2 variants were previously published in (Boyadzhiev et al., 2022). In brief, a minimal response of ~10% DNA in the tail was observed after exposure to silica-coated TiO_2 NPs (5422HT), silica and alumina-coated TiO_2 NPs (5423HT), and uncoated rutile TiO_2 (MKNR050P) NPs.

5.4.4 MN induction

Cells were exposed to different concentrations of MO variants for 40 h, and % relative survival and MN-fold increase relative to the unexposed controls were determined (**Figure 5-8**). Some exposures induced high toxicity, reducing the relative survival to less than 40%, which could contribute to false positive results. These results are denoted by the letter "a" in the bar graphs.

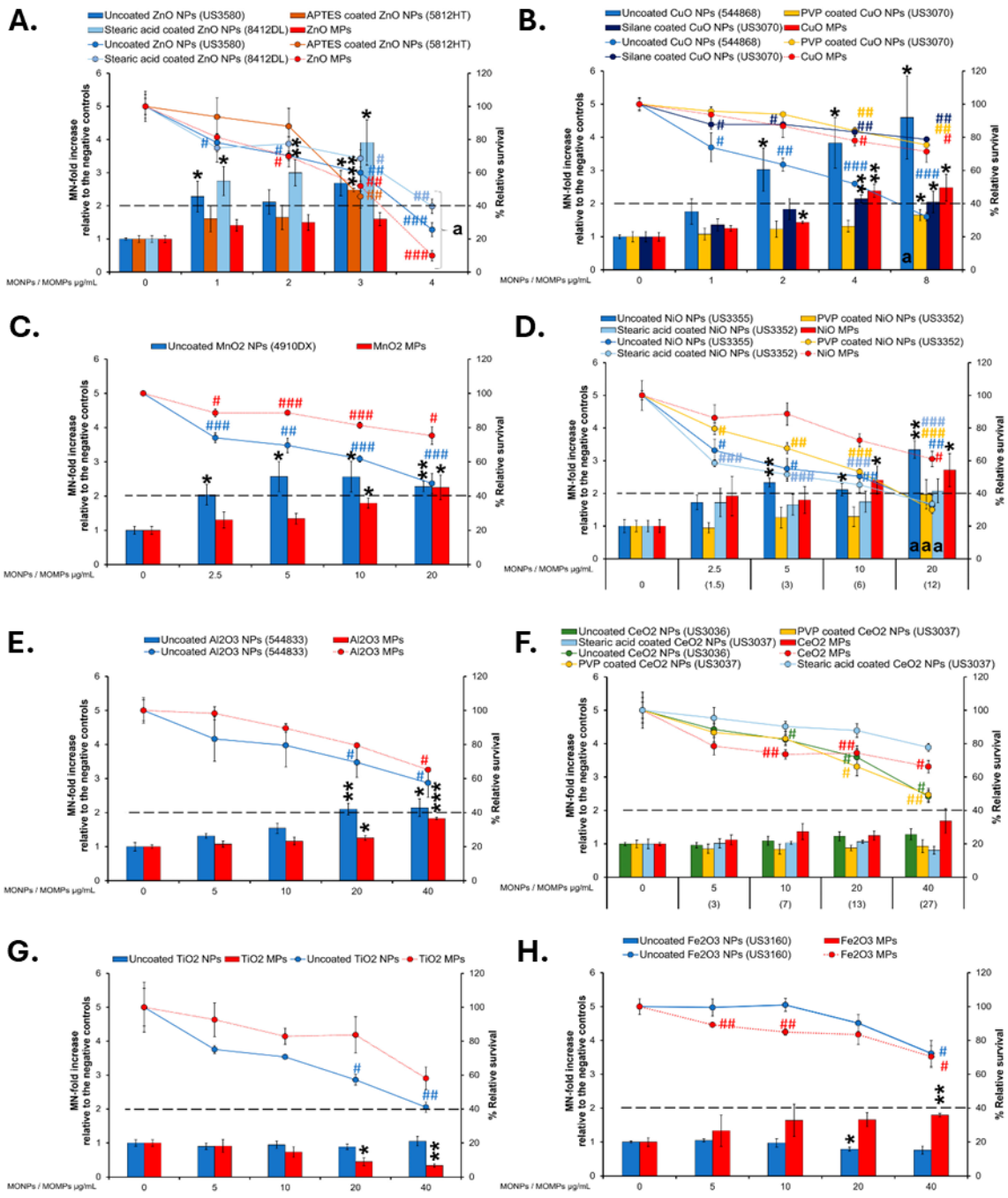

Figure 5-8. Cytotoxicity assessment (% relative survival) and MN-fold increase in FE1 cells after 40 h of exposure to MO variants. (A) ZnO variants, (B) CuO variants, (C) MnO_2 variants, (D) NiO variants, (E) Al_2O_3 variants, (F) CeO_2 variants, (G) TiO_2 variants, (H) Fe_2O_3 variants. Data are presented as mean and standard error (n = 3–4). Data in parenthesis indicates the concentration of stearic acid-coated NiO NPs or stearic acid-coated CeO_2 NPs. Statistically significant differences between the exposed samples and the matched negative controls were determined. % relative survival: $^{\#}$ p <0.05, $^{\#\#}$ p <0.01, $^{\#\#\#}$ p <0.001. MN-fold increase: * p <0.05, ** p <0.01, *** p <0.001. The letter "a" indicates that the exposure was overtly cytotoxic, with relative survival dipping below 40%. The dashed line represents 40% of the relative survival threshold.

Uncoated ZnO NPs (US3580) induced 2.3- and 2.7-MN-fold increases at 1 and 3 µg/mL, whereas APTES-coated ZnO NPs (5812HT) induced a 2.5-MN-fold increase only at 3 µg/mL and stearic acid-coated ZnO NPs (8412DL) induced 2.7-, 3-, and 3.9-MN-fold increases at 1, 2 and 3 µg/mL (**Figure 5-8A**). ZnO MPs did not induce MN formation (**Figure 5-8A**), whereas $ZnCl_2$ induced a significant increase of 1.8-MN-fold increase only at 1.6 µg/mL (**Figure 5-9A**). The highest concentration of all ZnO variants and $ZnCl_2$ showed the highest level of cytotoxicity with less than 40% relative survival, and thus, the MN induction results are not reported for this concentration (**Figure 5-8A** and **Figure 5-9A**).

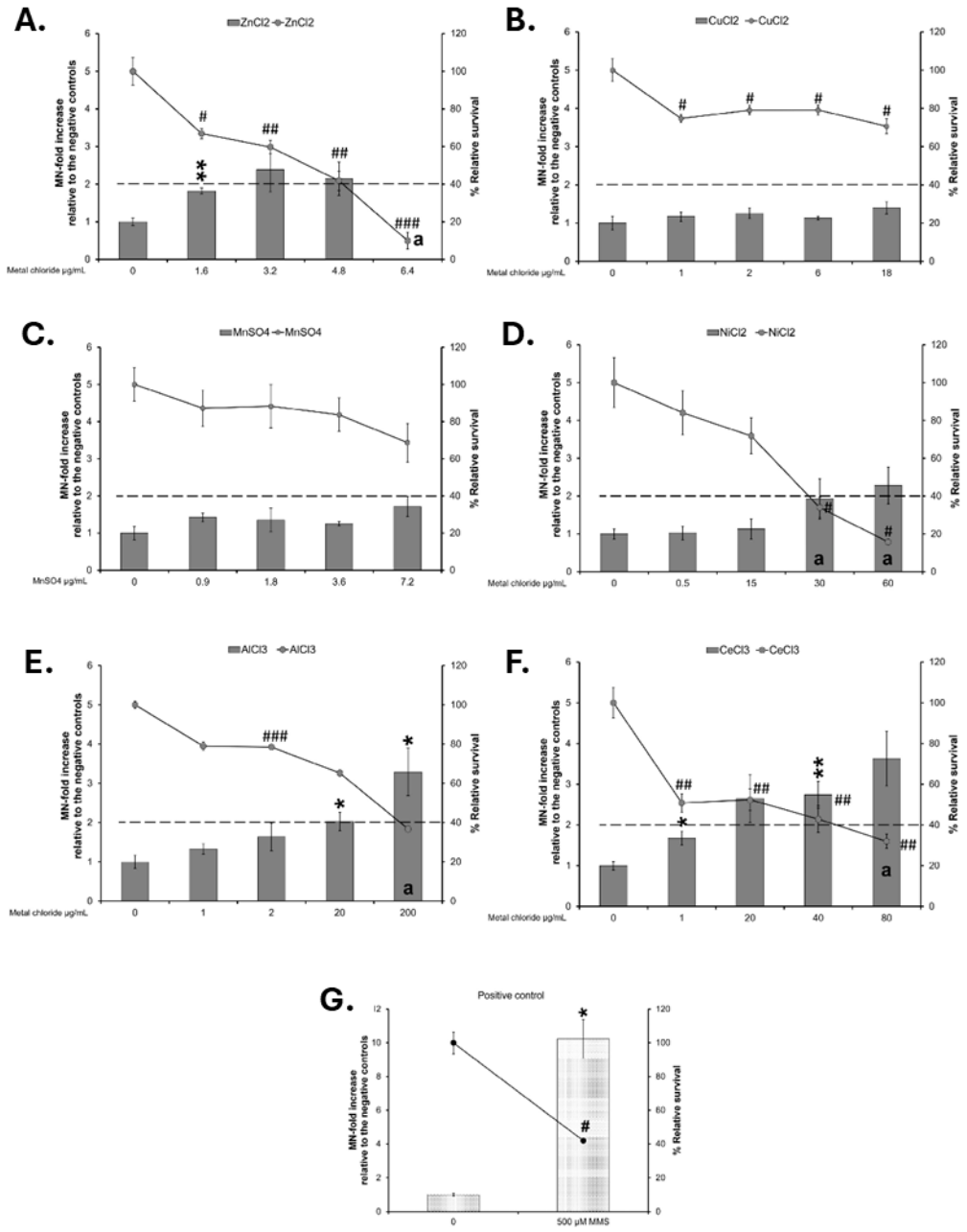

Figure 5-9. Cytotoxicity assessment (% relative survival) and MN-fold increase in FE1 cells after 40 h of exposure to dissolved metal analogs. (A) $ZnCl_2$, (B) $CuCl_2$, (C) $MnSO_4$, (D) $NiCl_2$, (E) $AlCl_3$, (F) $CeCl_3$, (G) Positive control: 500 µM MMS for 40 h. Data are presented as mean and standard error (n = 3–4). Statistically significant differences between the exposed samples and the matched negative controls were determined. % relative survival: $^{\#}$ $p < 0.05$, $^{\#\#}$ $p < 0.01$, $^{\#\#\#}$ $p < 0.001$. MN-fold increase: * $p < 0.05$, ** $p < 0.01$. The letter "a" indicates that the exposure was overtly cytotoxic, with less than 40% relative survival. The dashed line represents 40% of the relative survival threshold.

With respect to CuO variants, uncoated CuO NPs (544868) induced the highest response at the lower concentrations of 2 and 4 µg/mL with 3- and 3.8-MN-fold increase, and at 8 µg/mL, a 4.6-MN-fold increase was observed. However, the 8 µg/mL concentration also induced high cytotoxicity (32% relative survival). PVP-coated CuO NPs (US3070) induced a response only at the 8 µg/mL (1.6-MN-fold increase) concentration. Silane-coated CuO NPs (US3070) showed 2.1- and 2-MN-fold increases at 4 and 8 µg/mL, whereas CuO MPs caused 1.4, 2.4, and 2.5-MN-fold increases at 2, 4, and 8 µg/mL, respectively (**Figure 5-8B**). $CuCl_2$ did not induce MN or cytotoxicity at any concentration (**Figure 5-9B**).

Uncoated MnO_2 NPs (4910DX) showed 2, 2.6, 2.6 and 2.3-MN-fold increases at 2.5, 5, 10 and 20 µg/mL. MnO_2 MPs induced MN only at the highest concentrations of 10 and 20 µg/mL with 1.8 and 2.3-MN-fold increases (**Figure 5-8C**). $MnSO_4$ did not induce MN or cytotoxicity (**Figure 5-9C**).

Uncoated NiO NPs (US3355) showed 2.3- and 2.11-MN-fold increases at 5 and 10 µg/mL, while at 20 µg/mL, the induction of MN could not be reliably determined due to high cytotoxicity (32% relative survival). PVP-coated NiO NPs (US3352) and stearic acid-coated NiO NPs (US3352) did not induce MN but decreased the % relative cell survival to ~30% at the highest concentrations of 20 µg/mL and 12 µg/mL, respectively (**Figure 5-8D**). NiO MPs induced 2.4- and 2.7-MN-fold increases at 10 and 20 µg/mL (**Figure 5-8D**). $NiCl_2$ did not induce a response but showed high cytotoxicity at 30 and 60 µg/mL (34 and 16% relative survival, respectively) (**Figure 5-9D**).

Uncoated Al_2O_3 NPs (544833) induced a 2.1-MN-fold increase at 20 and 40 µg/mL. Al_2O_3 MPs induced a 1.2 and 1.8-MN-fold increases at 20 and 40 µg/mL (**Figure 5-8E**), whereas $AlCl_3$ caused a 2-MN-fold increase at 20 µg/mL (**Figure 5-9E**). A 3.2-MN-fold increase was observed after exposure to 200 µg/mL of $AlCl_3$, but the cytotoxicity was greater than 60% (**Figure 5-9E**).

Uncoated CeO_2 NPs (US3036), PVP-coated CeO_2 NPs (US3037), stearic acid-coated CeO_2 NPs (US3037), and CeO_2 MPs did not induce MN formation (**Figure 5-8F**). A

concentration-dependent increase (1.6- and 2.7-MN-fold increase) was observed after exposure to 1 and 40 µg/mL of $CeCl_3$, respectively (**Figure 5-9F**). $CeCl_3$ at 80 µg/mL induced a non statistically significant increase (3.6-MN-fold increase) but with high cytotoxicity (32% relative survival) (**Figure 5-9F**).

Uncoated TiO_2 NPs and TiO_2 MPs did not cause MN formation at any concentrations tested, but the response decreased after exposure to TiO_2 MPs in a concentration-dependent manner, indicating potential interference (**Figure 5-8G**). Although both TiO_2 variants showed a decreasing trend in % relative survival, the cytotoxicity was not above 60% (**Figure 5-8G**).

Uncoated Fe_2O_3 NPs (US3160) showed a trend to decrease MN induction at all concentrations tested (potential interference) and induced a significant decrease relative to negative control only at 20 µg/mL, whereas Fe_2O_3 MPs induced a 1.8-MN-fold increase at the highest concentration of 40 µg/mL (**Figure 5-8H**).

The % relative survival (42) and the MN-fold increase (10.2) after exposure to 500 µM MMS (positive control) are shown in **Figure 5-9G**.

5.4.5 Spearman's correlation of genotoxicity with physicochemical properties of MO

To assess whether monotonic relationships are present between the physicochemical properties of the MO assessed and genotoxicity, a Spearman correlation was conducted (**Figure 5-10**, **Supplementary File 5-1**).

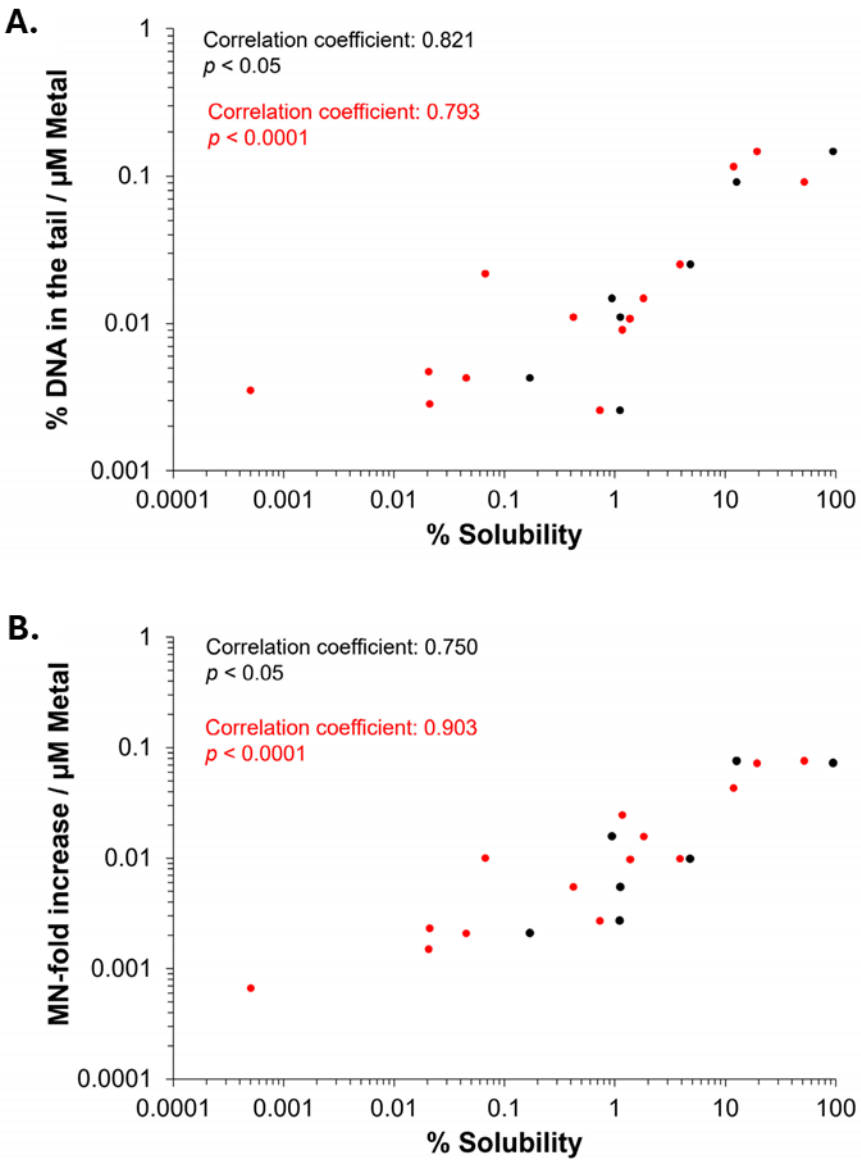

Figure 5-10. The relationship between solubility at 10 and 100 µg/mL, and (A) % DNA in the tail at 4 h and (B) MN-fold increase at 40 h when concentration is normalized to µM of constituent metal. The highest admissible concentration for each endpoint was used. Black circles: Solubility at 10 µg/mL (n = 7). Red circles: Solubility at 100 µg/mL (n = 14).

With respect to correlations between physicochemical properties, solubility in DMEM cell culture medium at 10 and 100 µg/mL was significantly positively correlated, as were the atomic mass of the constituent metal and HD and PDI in cell culture medium. Conversely, primary particle size was significantly negatively correlated with particle SSA (**Supplementary File 5-1**).

When % DNA in the tail was expressed in terms of μM of constituent metal, it can be seen that response at the highest tested concentration at 4 h is significantly positively correlated with % solubility at 10 and 100 μg/mL (**Figure 5-10**), as well as ZP, and negatively correlated with the valence state of the constituent metal. Similarly, MN-fold increase at 40 h normalized to μM of constituent metal at the highest admissible concentration was significantly correlated with solubility at 10 and 100 μg/mL (but not ZP) and significantly negatively correlated with the valence state of the constituent metal. Neither genotoxicity endpoint correlated with particle size or SSA for the MO assessed; however, responses for both endpoints were strongly positively correlated with each other (**Supplementary File 5-1**).

5.4.6 BMC analysis and potency ranking of metal oxide materials

BMC modeling was employed to determine differences in potency for samples showing a concentration-dependent response in both 4 h comet and 40 h MN endpoints. The responses were compared with concentration normalized to constituent metal (μg metal/mL, **Figure 5-11**) and SSA (cm^2 particles/cm^2 well plate, **Figure 5-12**).

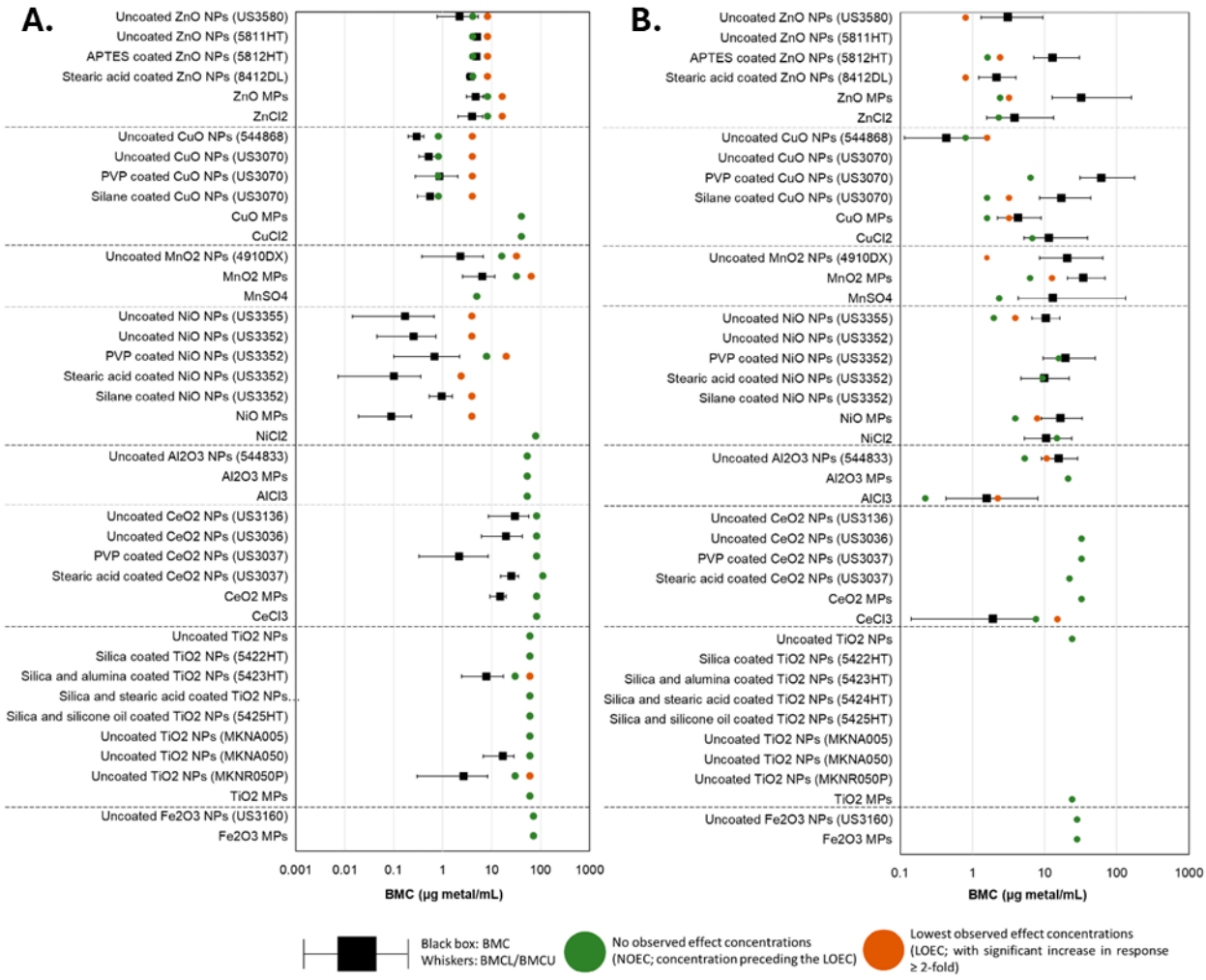

Figure 5-11. BMC analysis of (A) 4 h % DNA in tail, and (B) 40 h % MN induction endpoints for MONPs, MOMPs, and dissolved metal exposures. Concentration is expressed in terms of the mass volume of constituent metal. Black dashed lines denote the separation between MO types. BMCL: Lower 95% confidence interval of the BMC. BMCU: Upper 95% confidence interval of the BMC.

When the response was normalized to the amount of constituent metal in the exposure medium, differences were seen between % DNA in the tail (**Figure 5-11A**) and % MN induction (**Figure 5-11B**). For both endpoints, there were no apparent trends related to specific surface coatings, and there was widespread overlap of BMC confidence intervals between different forms (NP, MP, ionic) as well as between different constituent metals (Zn, Cu, Ni, etc.). A trend was apparent for % DNA in the tail at 4 h, with compounds with the same constituent metal showing similar BMCs. Zn materials had BMCs in the range of 2.2–5.1 µg metal /mL; for Cu materials, the BMCs were in the range of 0.3–0.9 µg metal /mL; for

Mn materials, the range was 2.3–6.4 µg metal /mL; for Ni materials, the range was 0.09–0.96 µg metal /mL; Al materials presented no concentration response; Ce materials presented a BMC range of 2.2–29.6 µg metal /mL and Ti particles had BMCs in the range of 2.7–17.1 µg metal /mL.

With respect to % MN induction, no trends were observed. Uncoated CuO NPs (544868) showed the lowest BMC of all tested materials (0.43 µg metal /mL), but its confidence intervals overlapped with numerous other samples. All CeO_2, TiO_2, and Fe_2O_3 particles tested did not induce a concentration-dependent response.

When concentration is expressed in terms of the surface area of the particles to the surface area of the cell culture well in which the exposure was conducted (**Figure 5-12**), confidence intervals largely overlapped between samples for both endpoints. With respect to % DNA in the tail at 4 h, a trend was apparent in the BMCs between NPs and MPs analogs. For ZnO, MnO_2, NiO, and CeO_2, uncoated MPs present lower BMCs (but with overlapping confidence intervals) than all respective NP variants when the response was expressed in terms of particle surface area (cm^2 particles/cm^2 well plate). For CuO, Al_2O_3, and TiO_2 MPs, a concentration response was not present, and therefore, they were not included in the analysis.

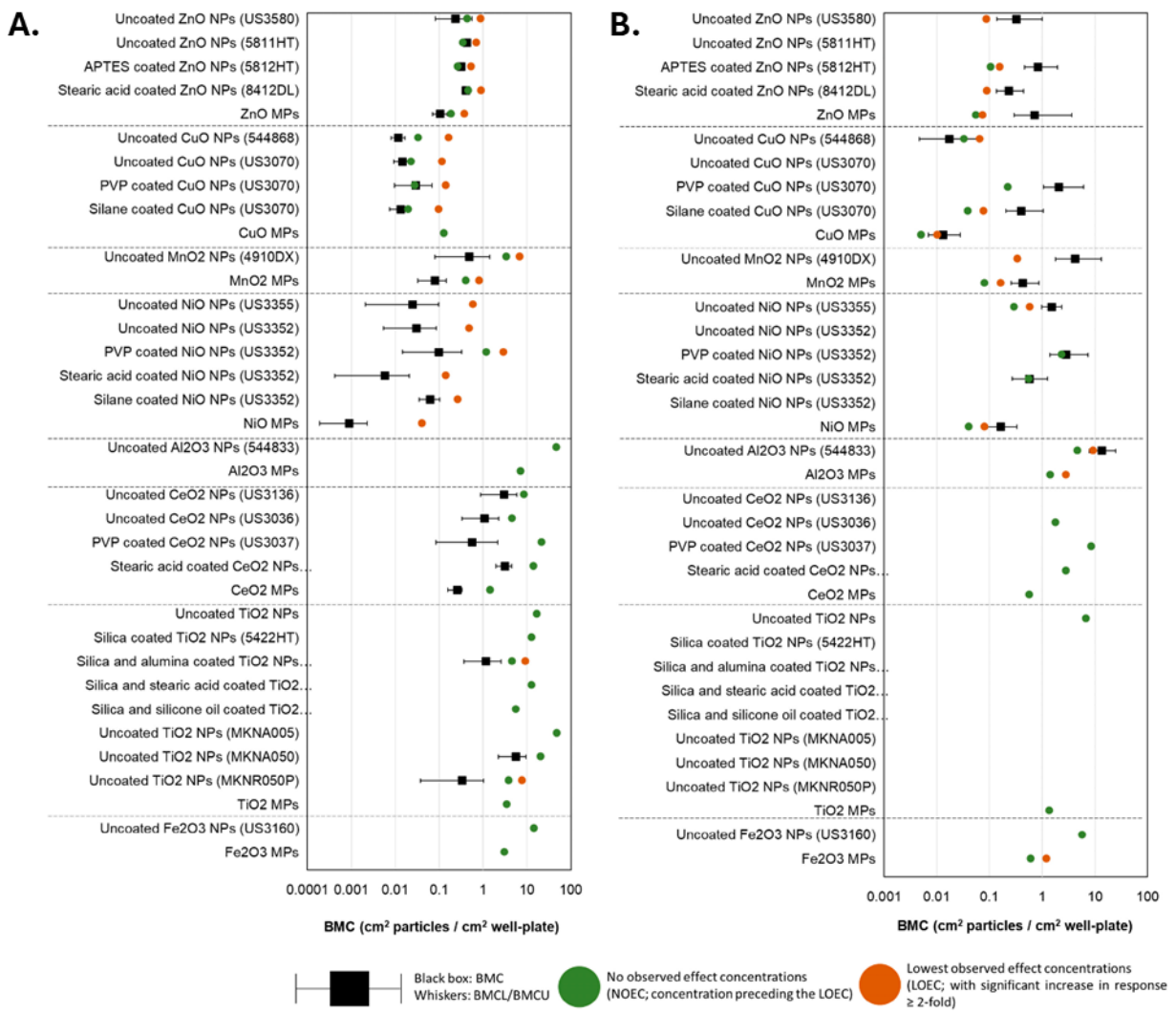

Figure 5-12. BMC analysis of (A) 4 h % DNA in tail, and (B) 40 h % MN induction endpoints for MONPs and MOMPs exposures. Concentration is expressed in terms of the SSA of the particles per surface area of the well plate. Black dashed lines denote the separation between MO types. BMCL: Lower 95% confidence interval of the BMC. BMCU: Upper 95% confidence interval of the BMC.

With respect to % MN induction, CuO, MnO_2, and NiO MPs showed lower BMCs than NPs, with some overlap present between confidence intervals. For ZnO, MPs were in the range of NPs tested, and for Al_2O_3, CeO_2, TiO_2, and Fe_2O_3, this comparison was not possible as MPs did not present calculable BMCs.

Due to the fact that multiple sample types did not feature a prominent concentration response, which precluded the calculation of an accurate BMC, potency ranking based on the no observed effect concentration (NOEC) values was conducted for

both endpoints, using the exposure concentration normalized to μg metal/mL medium (**Supplementary Table 5-4**) and cm^2 particles/cm^2 well plate (**Supplementary Table 5-5**).

When the concentration was normalized to the amount of constituent metal in the exposure medium, it was seen that for comet and MN endpoints, uncoated MONPs were as potent or more potent than uncoated MOMPs (**Figure 5-11**, **Supplementary Table 5-4**). It should be kept in mind, however, that both TiO_2 and Fe_2O_3 particles showed interference with respect to MN scoring, as reductions in the response were observed with respect to exposed samples as compared to negative controls. It can also be observed that dissolved metal equivalents are among the least potent forms of the MO assessed with respect to DNA damage.

However, for MN formation, divalent dissolved metals ($ZnCl_2$, $CuCl_2$, $NiCl_2$, but not $MnSO_4$) were among the least potent forms assessed, whereas the trivalent dissolved metals ($AlCl_3$, $CeCl_3$) were the most potent forms assessed of the respective MO. Surface-coated NP variants typically presented reduced or equal potency compared to uncoated MONPs. Two notable exceptions include the stearic acid-coated NiO NPs (US3352) and stearic acid-coated CeO_2 NPs (US3037), which showed higher potency to induce DNA and chromosomal damage compared to uncoated NPs, respectively. This difference was due to difficulties in suspending stearic acid-coated particles, reducing the expected exposure concentration delivered to cells and offsetting the NOEC relative to other variants. No other trends were apparent.

When the concentration was normalized to the SSA of the particles and surface area of the cell culture well, the trends for both endpoints changed (**Figure 5-12**, **Supplementary Table 5-5**). MOMPs presented equal or greater potency than uncoated MONPs at inducing DNA or chromosomal damage (except for CuO MPs for the 4 h comet endpoint). For coated MONP variants, potency was reduced compared to uncoated MONPs for both endpoints, except in the case of Zn materials. For ZnO NPs, APTES-coated ZnO NPs (5812HT) were more potent than uncoated ZnO NPs at inducing comet response (NOEC: 0.26 vs. 0.34 and 0.43 cm^2 particles/cm^2 well plate). As well, for TiO_2 materials

previously assessed, all coated varieties showed less potency than uncoated rutile TiO_2 NPs (MKNR050P) but more potent than the three other uncoated varieties tested (uncoated TiO_2 NPs, MKNA050, MKNA005).

5.5 Discussion

In the present study, the genotoxic potential of MONPs of different sizes, solubility, and surface coatings was evaluated in FE1 lung epithelial cells at different post-exposure time points and concentrations using the high-throughput CometChip® and MicroFlow® MN assays. Eight types of commercially acquired MONPs of varying solubility were included in the study—ZnO, CuO, MnO_2, NiO, Al_2O_3, CeO_2, TiO_2, and Fe_2O_3. For each MONP type, respective bulk particles, surface coated variants, and soluble forms were included, where possible. The many varied forms of each metal oxide assessed allowed for the analysis of relationships between size, coating, solubility, and genotoxic potential.

5.5.1 Impact of particle size, solubility, and surface coating on MONP genotoxicity

The results of material dissolution testing conducted for the 8 MONPs used in this study in both water and DMEM cell culture medium have been previously published (**Supplementary Table 5-3**, (Avramescu et al., 2020, 2022)). Based on their dissolution in DMEM at 100 µg/mL, the materials were binned as highly soluble (>70% dissolution), moderately soluble (10–70% dissolution; CuO, ZnO NPs), low solubility (1–10% dissolution; NiO, MnO_2), and negligibly soluble (<1% dissolution; CeO_2, Al_2O_3, TiO_2, Fe_2O_3). For some materials, dissolution in DMEM changed at a lower concentration of 10 µg/mL, which showed that ZnO is highly soluble (94.5% dissolved), CuO is moderately soluble (12.6% dissolved), MnO_2, Al_2O_3, and CeO_2 are low soluble (4.79%, 1.11%, 1.12% dissolved, respectively), and NiO and TiO_2 to be negligibly soluble particles (0.94%, 0.17%). A lower concentration was not assessed for Fe_2O_3 NPs (**Supplementary Table 5-3**).

Correlation analyses of 9 individual physicochemical properties with the 2 genotoxicity endpoints showed both endpoint responses are positively correlated with solubility in the cell culture medium at 10 and 100 µg/mL, indicating solubility is an

important property for MO-induced genotoxicity (**Figure 5-10**). In addition to extracellular solubility, material solubility in acidic environments, such as in lysosomes, is also of key importance for MONPs due to their potential to localize to such compartments. Dissolution testing in (Avramescu et al., 2022) examined the solubility of ZnO, CeO_2, and MnO_2 NPs (also used in the present study) in artificial lysosomal fluid and noted that these materials exhibit high solubility, negligible solubility, and low solubility, respectively. For the other 5 MONPs examined, previous research using similar materials has indicated that CuO NPs are highly soluble (Chakraborty & Misra, 2019), NiO NPs are moderate to highly soluble depending on the specific ENM characteristics (Shinohara et al., 2017), Al_2O_3 NPs are moderately soluble (Holmfred et al., 2022), and both TiO_2 and Fe_2O_3 NPs are negligibly soluble in lysosomes (Zhong et al., 2017). All these studies indicate that the solubility pattern of the MONPs tested in this study is the same in cell culture medium and artificial lysosome fluid. While the solubility of specific MONP variants can change based on physicochemical properties, the results of the genotoxicity testing carried out in this study indicate that, in general, MONPs of negligible solubility in DMEM do not induce DNA strand breaks in the short term (**Figure 5-1**, **Figure 5-2**, **Figure 5-3**, **Figure 5-4**, **Figure 5-5**, **Figure 5-6**, **Figure 5-7**), whereas MONPs of negligible solubility in lysosomal fluid do not lead to increases in MN induction (**Figure 5-8**). There was also a difference in the behavior of dissolved trivalent metals (Ce, Al) as compared to divalent metals (Zn, Cu, Ni) with respect to MN induction, where dissolved trivalent metals were more potent than NPs and MPs at inducing response, the dissolved divalent metals were less potent or showed similar potency to NP and MP analogs (**Supplementary Table 5-4**). Dissolution studies of Al_2O_3 and $AlCl_3$ have shown that dissolved Al has the propensity to precipitate in neutral biological environments (Avramescu et al., 2022; Helmig et al., 2018). Similarly, while CeO_2 is insoluble in lysosomes, dissolved cerium in the form of $CeCl_3$ has been shown to localize to lysosomes where it forms an insoluble precipitate containing phosphorus (Berry et al., 1989). It is possible that depletion of media resources due to precipitation of the dissolved fractions may explain MN induction in response to Al_2O_3 NPs, $AlCl_3$, and $CeCl_3$ and not by bivalent types. Together, these findings imply that in addition to MONP solubility, the stability of the dissolved form is

another defining property governing their genotoxic potential, with instability in neutral and acidic environments leading to increases in DNA damage.

In addition to the impacts of solubility on MONP genotoxicity, this study also evaluated the impacts of particle surface coating on response. The particle surface mediates the first interaction between particles and cells or the biological milieu, defining the mode of internalization, the extent of distribution, accumulation, and eventual fate of NPs (Schubert & Chanana, 2018). The surface of MONPs can be modified to protect the particles, decrease their state of agglomeration, increase particle stability, improve wettability, and increase their bioavailability (Schubert & Chanana, 2018). Two coated variants of ZnO NPs (APTES, stearic acid-coated), two coated variants of CuO NPs (PVP, silane-coated), two coated variants of CeO_2 NPs (PVP, stearic acid-coated), and three coated variants of NiO NPs (PVP, stearic acid, silane-coated) were examined for their potential to induce genotoxicity in lung epithelial cells. No separate solubility experiments were conducted for coated MONP variants. Based on both DNA strand break and MN induction, no pattern was observed with respect to the influence of specific surface coatings on toxicity (**Figure 5-11** and **Figure 5-12**). Both PVP and silane surface coatings were shown to reduce DNA strand breaks and MN induced by exposure to uncoated CuO NPs (**Figure 5-2** and **Figure 5-8**). A similar but more subtle response was observed with respect to NiO NPs, where stearic acid and PVP coatings reduced MN induction (**Figure 5-8**). In an *in vivo* study examining the pulmonary toxicity of paint-embedded TiO_2 NPs, hyperspectral imaging showed they remain embedded in the paint matrix up to 28 days post-exposure, which was suggested as the reason for a decrease in their ability to alter gene expression and associated biological pathways as compared to non-embedded particles (Halappanavar, S. et al., 2015). Surface coating of MONPs can protect their cores from dissolution, reducing ion leaching and toxicity (Cai et al., 2017; García-Torra et al., 2021). This depends on the stability of the coating and the solubility of the MONPs in different microenvironments. Since no solubility testing was conducted with coated variants, it is possible that the observed reduction in genotoxicity after exposure to coated CuO and NiO

NPs as compared to uncoated NPs could also be attributed to changes to particle surface-cell interaction and their solubility.

The study also examined the differences in genotoxic potential of MONPs and MOMPs. In general, NPs either induce the same or higher levels of both DNA strand break and MN induction as compared to matched MPs equivalents, with no significant correlation between primary particle size and genotoxicity noted (**Supplementary File 5-1**). The only exception to this trend was with respect to NiO MPs, which showed a heightened DNA strand break response at 2 and 4 h as compared to NPs at a concentration of 100 µg/mL (**Figure 5-4**). However, this result was not observed at the lower concentrations. The observations from this study are in alignment with our previously published results (Boyadzhiev et al., 2022) that showed DNA damage induced by ZnO, CuO, and TiO_2 NPs with similar primary particle sizes was either higher or equal to their MPs analogs. Higher levels of genotoxicity with NPs compared to MPs are most commonly thought to result from their small volume and large SSA that increases the surface molecules available for interaction and, as a result, increases their surface reactivity, allowing for enhanced interaction of NPs with the biological medium, cellular membranes, and subcellular structures (Oberdorster et al., 2005). For materials such as CuO, particle size greatly influences the potential to induce DNA strand breaks, with MPs showing no response in the CometChip® assay while both CuO NPs (544868 and US3070) induced pronounced concentration and time-dependent genotoxicity (**Figure 5-2**). A similar trend is seen with MnO_2, with NPs leading to DNA strand break and MN induction at lower concentrations than what was observed for MPs. In addition, Al_2O_3 NPs showed significant MN induction at a concentration of 20 µg/mL, a response that was only observed at 20 and 40 µg/mL MPs concentration (**Figure 5-8**). For ZnO, CeO_2, NiO, and TiO_2, DNA strand break and MN induction were similar between MPs and NPs, with response mainly related to the specific metal in question (ex. Ce vs. Ni). These results suggested that while some MPs were not genotoxic, others showed delayed responses that also differed in magnitude. In recent years, some studies have shown that, in general, smaller NPs are more genotoxic than larger NPs or MPs (Boyadzhiev et al., 2022; Shi et al., 2022; Zhou et al., 2019). For instance, in human umbilical vein endothelial cells

exposed to 1, 5, and 25 µg/mL SiO_2 NPs of different sizes (10, 25, 50, and 100 nm) for 4 and 24 h, the observed DNA strand breaks at 4 h and MN induction at 24 h showed an inverse relationship with size, with higher responses recorded for smaller sized NPs (Zhou et al., 2019). In another study, polystyrene NPs induced more MN than polystyrene MPs at 50 and 100 µg/mL following 24 h exposure in A549 cells (Shi et al., 2022). The results of the present study agree with the above observations, showing that the smaller primary particle size of MONPs vs. MOMPs contributes to an increased potential for DNA damage; however, chemical composition is also a critical property affecting genotoxicity.

5.5.2 Relative potency ranking of MONP genotoxic potential

As compared to classical points of departure (PODs), such as the lowest observed effect concentration (LOEC), NOEC, or lethal concentration 50 (LC_{50}), BMC modeling can utilize the whole concentration-response curve to estimate potency. This can make it more accurate than classical PODs, but it requires a complete concentration response in order to have a precise estimation of the BMC and resulting confidence intervals. This means that for materials that do not show concentration-dependent responses, it is not possible to compute a BMC. In this study, BMC modeling was attempted in an effort to rank all compounds based on their genotoxic potency for both endpoints. Due to the large degree of overlap in BMC confidence intervals and the absence of calculable BMCs for numerous compounds, the ranking was also conducted using the NOEC (**Supplementary Table 5-4**, **5-5**).

When concentration was normalized to the amount of constituent metal in the exposure medium, MOMPs were less potent or as potent as MONPs at inducing DNA strand breaks and MN formation; however, this trend flipped when concentration was normalized to the SSA of the particles (**Figure 5-11**, **Supplementary Table 5-4**). The same trend was reported in a recent transcriptomic study examining 5 of the same uncoated MONPs (ZnO, CuO, NiO, Al_2O_3, TiO_2), with potency trends based on SSA-normalized concentrations showing that MPs are either as potent or more potent than corresponding MONPs. In general, SSA is inversely proportional to particle size, with smaller particles showing larger surface areas. In this study, the primary particle size of NPs and MPs is significantly

negatively correlated with SSA; however, both genotoxicity endpoints did not show a correlation with size or SSA (**Supplementary File 5-1**), suggesting these properties may not be the defining ones for the toxicity response. A retrospective analysis of 9 individual *in vivo* studies involving rats and mice exposed to different types of NPs (polystyrene, TiO_2, carbonaceous materials, Co_3O_4, Ni, ZnO, and nanoquartz) reported very strong correlations between the SSA dose and acute pulmonary toxicity (Schmid & Stoeger, 2016). However, a more recent analysis examining 88 individual *in vivo* studies including 13 different ENMs (NMs of Ag, carbon, Ce, cobalt, Cu, Fe, Ni, silicium, TiO_2, and Zn) did not find such strong associations between SSA-dose and resulting toxicity (Hadrup et al., 2023). The results of the current study and the recent large-scale transcriptomic analysis, in addition to available *in vivo* data, imply that higher SSA may be associated with increased toxicity; however, MONP stability and other physicochemical properties discussed above can override this response.

5.5.3 Mechanisms affecting genotoxic potential of MONPs

Based on the activity for each of the two genotoxicity endpoints (**Figure 5-13**), inferences can be derived regarding the type of DNA damage seen and potential mechanisms at play across the MONPs tested.

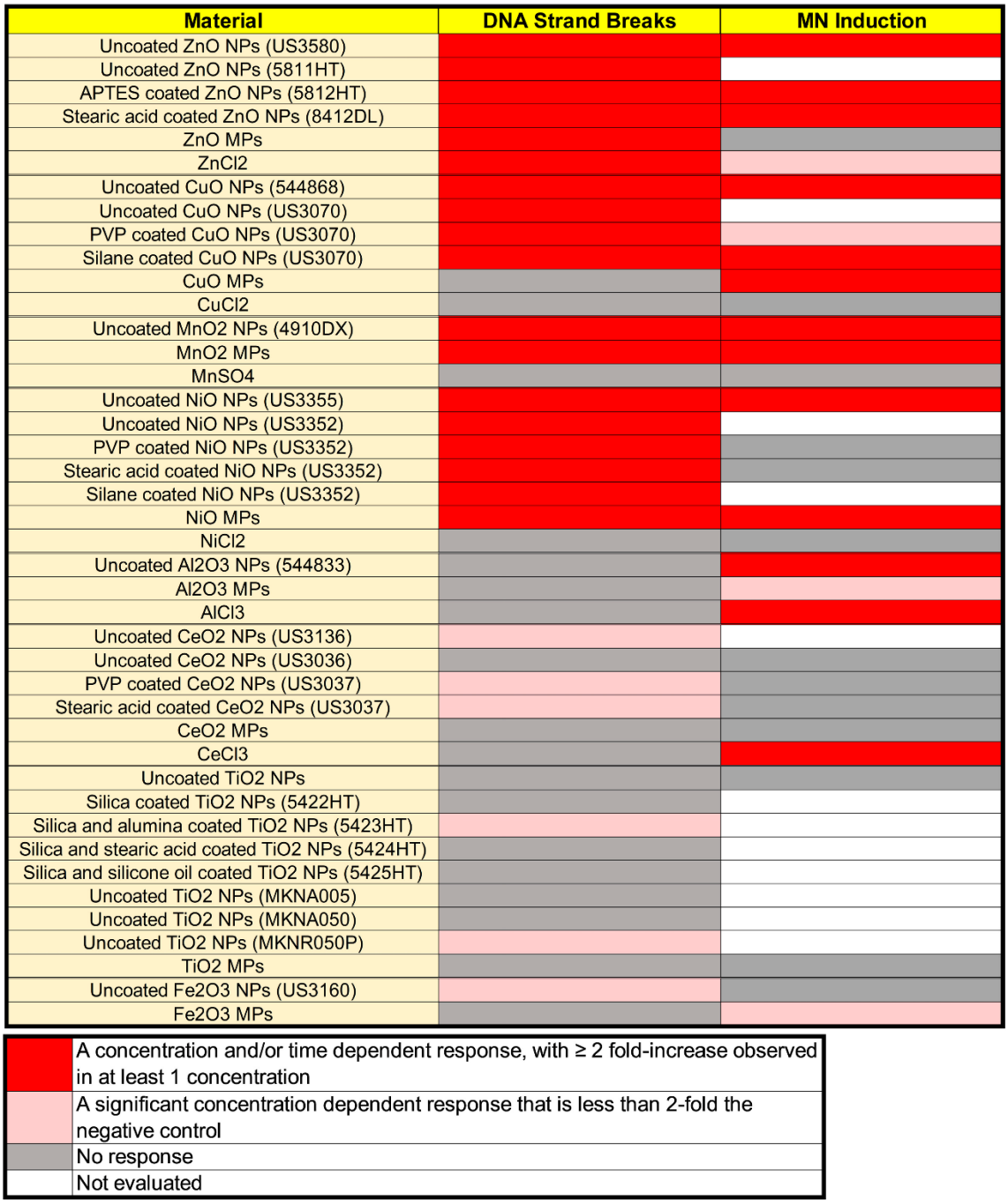

Figure 5-13. Summary of the results of 4 h comet and 40 h MN assays for all MO and dissolved metal analogs.

Based on the results of previously evaluated DNA damage responses of FE1 cells exposed to ZnO, CuO and TiO_2 NPs, the dissolved component was determined to be the main mediator of DNA damage for ZnO NPs, whereas for CuO NPs, a “Trojan Horse” mechanism was considered more likely, and for TiO_2 NPs surface interactions and

subsequent ROS generation was suggested as a putative underlying mechanism (Boyadzhiev et al., 2022). The summary in **Figure 5-13** shows that for Zn and Cu forms, their clastogenic/aneugenic activity is much the same across all sizes, coatings, and forms, except for ZnO MPs and $CuCl_2$. In the case of ZnO MPs, a non-significant concentration-dependent increase was seen (**Figure 5-8**). Conversely, uncoated TiO_2 NPs and MPs did not induce increases in MN induction, although interference of the assay was seen for TiO_2 MPs and Fe_2O_3 NPs (**Figure 5-8**). For both CuO and ZnO NPs, genotoxicity is surmised to be due to ion homeostatic disturbances, with the dissolved fraction being the main mediator of ZnO NP response, whereas the nanoparticulate nature of CuO NPs is critical for its response. The positive MN call and negative comet call for CuO MPs indicate that larger-sized CuO particles require longer interaction times to induce DNA damage, potentially related to reduced uptake or reduced intracellular dissolution. For dissolved Cu, reduced uptake of the ionic form as compared to NPs and MPs is a possible explanation for its lack of response. Dissolved Cu is taken up via metal transporters, mainly through the high-affinity copper transporter known as hCTR1 in humans or Ctr1 in mice (Kaplan & Maryon, 2016). While not much is known about copper flux through murine Ctr1, hCTR1 is considered a relatively slow transporter with the ability to transport 5–10 Cu ions per second (Kaplan & Maryon, 2016; Maryon et al., 2013), compared to typical transporters which have transport rates of 100–10,000 molecules per second (Nies, 2008). The slower rate of uptake of dissolved Cu as compared to CuO NPs could allow cells the time to respond to the stressor, reducing downstream toxicity resulting in a negative genotoxicity call (as described in (Boyadzhiev et al., 2022)).

For NiO, Al_2O_3, MnO_2, CeO_2, and Fe_2O_3 NPs not previously assessed, NiO and MnO_2 NPs and MPs were DNA strand break and clastogen/aneugen positive, while the respective dissolved analog was negative for both. In mammalian cells, Mn functions as an essential micronutrient like Cu and Zn. In cellular model systems, elevated levels of Mn are associated with oxidative stress, mitochondrial dysfunction, and cell death (Daiana Silva Avila et al., 2013). From dissolution testing in (Avramescu et al., 2022), it can be seen that MnO_2 NPs are soluble in both the cell culture medium as well as in artificial lysosomal

fluid. It is surmised that genotoxicity resulting from MnO_2 NP exposure proceeds according to the same mechanisms as CuO NPs, through a 'Trojan Horse' mechanism whereby the particles are internalized into the acidic compartments, followed by intracellular dissolution, resulting in disturbances of Mn homeostasis, oxidative stress, and subsequent DNA damage. The lower response of the MPs as compared to NPs in both comet and MN endpoints (**Figure 5-3** and **Figure 5-8**) provides credence to this hypothesis, as MPs show lower dissolution than NPs at the same concentration in the cell culture medium (Avramescu et al., 2022). For dissolved $MnSO_4$, the concentrations were chosen to represent extracellular dissolution, and from the lack of response seen, the extracellular dissolved component does not contribute to the genotoxicity induced by MnO_2 NPs.

With respect to NiO NPs, the potential mechanisms are different. Ni is considered an essential micronutrient in certain prokaryotic organisms but not in mammals, and as such, no homeostatic system exists to specifically regulate its bioavailability. While NiO NPs are poorly to negligibly soluble in cell culture medium, they show solubility in lysosomal fluid (Shinohara et al., 2017). Research on the genotoxicity of Ni compounds has shown that they function as weak mutagens via indirect mechanisms, with Ni ions showing preferential interaction with proteins as opposed to DNA (Buxton et al., 2019). The mechanism behind this toxicity involves the generation of ROS, inhibition of DNA repair enzymes, and epigenetic alterations, with carcinogenicity dependent upon the delivery of dissolved Ni to the nucleus (Buxton et al., 2019). From the summary in **Figure 5-13**, it can be seen that all Ni compounds, except for $NiCl_2$, induce DNA strand breaks. Furthermore, both NiO NPs and MPs are positive for clastogenicity/aneugenicity, with non-significant upward trends seen for coated NPs and dissolved Ni. The lack of DNA strand break induction for $NiCl_2$ in this study may be related to insufficient exposure time to allow for cellular uptake. From the comet responses, it can be surmised that NiO NPs and MPs are rapidly internalized into the cell, wherein dissolution or particle interaction begins to occur, resulting in DNA strand breaks as early as 2 h post-exposure (**Figure 5-4**). Due to the propensity for Ni to interact with proteins as well as induce DNA strand breaks, the positive MN call for uncoated NiO NPs could be due to either clastogenicity (accumulation of

strand breaks culminating in chromosomal breakage) or aneugenicity (through interference with mitotic machinery).

In contrast, based on the negative DNA strand break and positive clastogenicity/aneugenicity calls, Al_2O_3 NPs seem to act indirectly with indications for a potential aneugenic mechanism. From the high-content transcriptomic analysis of the same Al_2O_3 NPs, MPs, and $AlCl_3$ used in this study, minimal indications of oxidative stress and no indications of DNA damage responses were seen after up to 48 h of exposure (Boyadzhiev et al., 2023). Furthermore, it can be seen that Al_2O_3 NPs show low-negligible solubility in cell culture medium but can dissolve under acidic conditions in lysosomes (Avramescu et al., 2022; Holmfred et al., 2022); however, dissolved Al is known to precipitate in the presence of biological material (Avramescu et al., 2022; Helmig et al., 2018). Evidence exists for the ability of Al to induce chromosomal aberrations in plants and to induce cross-linking of chromosomal proteins in mammals, but with little to no potential to induce DNA strand breaks, mutagenesis, or carcinogenicity (Krewski et al., 2007). Based on this information, it is proposed that the positive MN call and negative comet call for Al_2O_3 NPs are indicative of interference with mitotic machinery rather than accumulation of single- and double-stranded DNA breaks. This may be the result of the dissolved fraction, as $AlCl_3$ was able to induce the formation of MN at much lower concentrations than Al_2O_3 NPs (**Figure 5-11**) or through direct interaction of NPs with mitotic machinery.

Finally, with respect to CeO_2 NPs and Fe_2O_3 NPs, based on the results of both genotoxicity endpoints, these MONPs are considered to be non-genotoxic (**Figure 5-13**). For CeO_2 NPs, minimal comet induction (<10%) and negative responses were seen in the MN assays; however, the dissolved $CeCl_3$ was MN-positive. The lack of genotoxicity in CeO_2 NPs is ascribed to limited surface reactivity as well as negligible solubility in both cell culture medium and lysosomal fluid (Avramescu et al., 2022), while dissolved Ce^{3+} may behave similarly to Al^{3+} as both are known to form phosphate-containing complexes in cells and cell culture medium. As seen for CeO_2 NPs; TiO_2 NPs, and Fe_2O_3 NPs are negligibly soluble in the cell culture medium as well as lysosomal fluid (Avramescu et al., 2022; Zhong et al., 2017). DNA strand break induction for both NPs and MPs is minimal (**Figure 5-7**);

however, interference was seen for TiO_2 NPs and Fe_2O_3 NPs in the MN assay, with a reduction in response across the concentration range (**Figure 5-8**). Thus, it was not possible to deduce the potential mechanistic differences conclusively, but the negative comet and MN call for the NPs suggest that they have a low surface reactivity, which could mitigate downstream toxicity resulting from particle interactions. *In vivo* studies from our lab have shown that TiO_2 NPs induce inflammation in mouse lungs (Husain et al., 2013; Rahman, L. et al., 2017b). At low doses, TiO_2 NPs have been shown to perturb pathways associated with ion homeostasis, which could be due to their tissue persistence and interference with the cellular cytoskeleton functions (Husain et al., 2013).

From the available literature, both negative and positive genotoxicity responses have been seen with regard to different types of Fe_2O_3 NPs and cell lines, with DNA strand break induction and oxidative DNA damage being the main mechanisms cited (Valdiglesias et al., 2015). The Fe_2O_3 NPs assessed in this study do not appear to be reactive, based on comet results.

5.6 Conclusion

In conclusion, this study utilized the high-throughput CometChip® and MicroFlow® assays to assess the *in vitro* genotoxic potential of ZnO, CuO, MnO_2, NiO, Al_2O_3, CeO_2, TiO_2, and Fe_2O_3, NPs, MPs, and dissolved metal analogs, with the purpose of identifying the role of solubility, particle size, and surface coating on response. Based on correlation analyses between concentration normalized endpoint responses and physicochemical properties, strong positive correlations were seen between particle solubility in cell culture medium, % DNA in the tail and MN induction across all tested particles, indicating that as solubility in medium increases, the propensity to induce genotoxicity increases as well. When concentration is normalized to constituent metal, MONPs exhibited the same or greater potency than MPs to induce both DNA strand breaks and MN formation; however, this trend reversed when concentration was normalized to SSA, indicating the larger surface area of NPs may at least partially explain the difference in potency between MONPs and MOMPs. Surface coating of MONPs inconsistently affected genotoxicity, with CuO and NiO NP

coatings seen to reduce comet and MN responses. Differences in DNA strand break activity and clastogenicity/aneugenicity across the tested materials denote mechanistic differences in MONP response, which is related to both particle stability and chemical composition. The results of this study highlight that combinations of properties influence response to MONPs and that solubility alone, while playing an important role, cannot be solely accountable for the observed toxicity. This may have implications on the potential application of read-across in support of human health risk assessment of MOs in their nano form.

6 Chapter 6: Acute Toxicity of Metal Oxide Nanoparticles - Role of Intracellular Localization

In preparation: Undergoing peer review

Authorship: Andrey Boyadzhiev[1,2], Sabina Halappanvar[1,2]

Affiliation:
1: Environmental Health Science and Research Bureau, Health Canada, Ottawa, Canada
2: Department of Biology, University of Ottawa, Ottawa, ON K1N6N5, Canada

Contributions:

Experimental Design.....	**Andrey Boyadzhiev** Sabina Halappanavar
Nanomaterial Suspension.....	**Andrey Boyadzhiev**
Exposures.....	**Andrey Boyadzhiev**
Inhibition Experiments.....	**Andrey Boyadzhiev**
Immunocytochemistry.....	**Andrey Boyadzhiev**
Microscopy.....	**Andrey Boyadzhiev**
Data Interpretation.....	**Andrey Boyadzhiev**
Manuscript Writing and Revisions.....	**Andrey Boyadzhiev** Sabina Halappanavar
Internal Review.....	Silvia Solorio Rodriguez Luan Rahman

6.1 Abstract

Endocytic uptake and lysosomal localization are suggested to be the key mechanisms underlying the toxicity of metal oxide nanoparticles (MONPs), with dissolution in the acidic milieu driving response. In this study, we aimed to investigate if MONPs of varying solubility are similarly sequestered intracellularly, including in lysosomes and the role of the acidic lysosomal milieu on toxicity induced by copper oxide (CuO) nanoparticles (NPs), nickel oxide (NiO) NPs, aluminum oxide (Al_2O_3) NPs, and titanium dioxide (TiO_2) NPs of varying solubility in FE1 lung epithelial cells. Mitsui-7 multi-walled carbon nanotubes (MWCNTs) served as contrasts against particles. Enhanced darkfield hyperspectral imaging (EDF-HSI) with fluorescence microscopy was used to determine their potential association with lysosomes. The v-ATPase inhibitor Bafilomycin A1 (BafA1) was used to assess the role of lysosomal acidification on toxicity. The results showed co-localization of all MONPs with lysosomes, with insoluble TiO_2 NPs showing the greatest co-localization. However, only acute toxicity induced by soluble CuO NPs was affected by the presence of BafA1. In addition, all MONPs were found associated with large actin aggregates; however, treatment with insoluble TiO_2 NPs, but not soluble CuO NPs, impaired the organization of F-actin and α-tubulin. These results indicate that MONPs are sequestered similarly intracellularly; however, the nature or magnitude of their toxicity is not similarly impacted by it. Future studies involving a broader variety of NPs is needed to fully appreciate the role of differential sequestration of NPs on cellular toxicity.

6.2 Introduction

Engineered nanomaterials (ENMs; materials designed for a specific purpose or function exhibiting at least 1 dimension or structure in the size range of 1 – 100 nm) have become endemic in consumer markets over the last 20 years (Vance et al., 2015). Engineered metal oxide nanoparticles (MONPs) represent one of the largest classes of ENM used worldwide, which present a risk for occupational exposure through accidental inhalation when the material is manipulated in its dry, dusty state (Mccormick et al., 2023). As with all ENM, the toxicity of MONPs is influenced by particle-specific physicochemical

properties, of which solubility in biological environments is considered to be of importance.

In previous studies, we systematically investigated the role of material solubility in cellular toxicity induced by MONPs, including the toxicity of zinc oxide (ZnO), copper oxide (CuO), nickel oxide (NiO), aluminum oxide (Al_2O_3), and titanium dioxide (TiO_2) nanoparticles (NPs) that exhibited varying solubility profiles and chemical composition (Boyadzhiev et al., 2021, 2023). The results showed that particulate and dissolved forms of all MONPs induced similar transcriptional responses in lung cells exposed under submerged conditions; however, the contribution of dissolution was dependent on the solubility of the material in the culture medium (Boyadzhiev et al., 2023).

In these studies, extracellular dissolution contributed to the toxicity induced by highly soluble particles. For soluble MONPs both particle and ionic forms contributed to the toxicity, while dissolution did not play a role in toxicity of poorly soluble MONPs (Boyadzhiev et al., 2023). CuO NPs, NiO NPs, and Al_2O_3 NPs have shown higher solubility in the caustic environment of lysosomes (Chakraborty & Misra, 2019; Holmfred et al., 2022; Shinohara et al., 2017). A study involving BEAS-2B bronchial epithelial lung cells noted that inhibition of lysosomal acidification using the v-type ATPase inhibitor Bafilomycin A1 (BafA1) significantly reversed the cytotoxic response induced by CuO NPs (Strauch et al., 2020), suggesting CuO NPs are taken up by cells prior to their dissolution in lysosomes, which is responsible for the toxicity observed. Other MONPs, such as iron oxide nanoparticles and labelled cerium oxide nanoparticles, have been directly observed localizing to lysosomes and endosomes *in vitro* (Feng et al., 2018; Vassie et al., 2017). For certain MONPs such as ZnO and TiO_2 NPs, particle sequestration in actin-lipid aggregates called 'cauliflowers' has recently been shown, which act as both nanoparticle reservoirs as well as a mechanism for repeated exposure through a cycle of exocytosis and endocytosis (Kokot et al., 2020). While particle localization has been assessed independently for some MONPs in the past, it is not clear if intracellular particle localisation is driven by their solubility profiles or if all MONPs are transported and sequestered similarly in cells regardless of solubility.

Determining the subcellular location of ENM post-exposure can be a non-trivial endeavour, especially when dealing with unlabelled particles. Transmission electron microscopy (TEM) has been used because of its high sensitivity and resolution to detect particles in specific cellular compartments (Ostrowski et al., 2015). However, it is not conducive to routine analysis owing to the specialised skillset for sample processing, microscope operation, as well as the costs involved. Enhanced darkfield microscopy with hyperspectral imaging (EDF-HSI) has been applied to locate unlabelled ENM in both tissues *in vivo* (Boyadzhiev et al., 2020; Guttenberg et al., 2017; Peña et al., 2016), and cells *in vitro* (Decan et al., 2015; Vallotton et al., 2014; Zucker et al., 2020). When equipped with fluorescence capabilities, EDF-HSI enables simultaneous detection of ENM and its cellular localisation post-exposure. EDF-HSI with fluorescence has been utilized in the past to assess co-localization of silica (SiO_2) NPs with Lysosomal-Associated Membrane Protein 1 (Lamp1), a lysosomal marker, in mouse lung epithelial cells (Decan et al., 2015), and more recently to show the uptake and localization of folate conjugated SiO_2 NPs in relation to the nucleus and actin cytoskeleton (Miclea et al., 2022). Furthermore combined EDF-HSI and 3D imaging approach has been applied to show direct interaction of multi-walled carbon nanotubes (MWCNTs) with lung cells in mice following *in vivo* exposure and in precision cut lung slices after *ex vivo* exposure (Rahman, L. et al., 2017a, 2020).

Therefore, the objectives of the present study were to 1) determine if CuO, Al_2O_3, NiO, and TiO_2 MONPs that vary in their solubility are similarly sequestered in lysosomes and the relevance of vesicular acidification on their toxicity in lung cells *in vitro*, and 2) utilize EDF-HSI in conjunction with fluorescence microscopy and 3D imaging to assess the degree of co-localization of the four individual MONPs with lysosomes and potentially with actin sequestering structures. In brief, lung epithelial cells (FE1) were exposed to individual MONPs with or without the lysosomal acidification inhibitor BafA1. Using immunocytochemistry, cellular sequestration and the potential impact on cellular structures were identified. Mitsui-7 (a type of MWCNT) was used as a non-metal control, which is known to induce cytoskeletal disturbances *in vitro* (Hevia & Fanarraga, 2020; Zhang et al., 2020).

6.3 Methods

6.3.1 Materials and reagents

Four individual MONPs, CuO, NiO, Al_2O_3, and TiO_2 NPs as well as Mitsui-7 MWCNTs were included in the study and their physicochemical properties are listed in **Table 6-1**. For NiO, Al_2O_3, and TiO_2 NPs, the primary particle sizes were very similar with mean size of 23.9 – 27.3 nm, whereas CuO NPs were larger with mean size of 64.8 nm. The aspect ratios indicate that CuO, NiO, and TiO_2 NPs are roughly spherical, whereas the Al_2O_3 NPs have a rod-like morphology. Similarly, CuO, NiO, and TiO_2 NPs have specific surface areas (SSAs) in the range of 10.3 – 52.7 m^2/g whereas Al_2O_3 NPs have an SSA of 145.3 m^2/g. Based on 24 h dissolution experiments conducted in the cell culture medium used for toxicity testing at a 10 µg/mL concentration following the Organization for Economic Cooperation and Development (OECD) guidelines on dissolution testing of ENMs (OECD, 2015), CuO NPs are considered soluble (10 - 70% dissolution), Al_2O_3 NPs as poorly soluble (1 - 10% dissolution), and NiO and TiO_2 NPs as negligibly soluble (<1% dissolution). The characteristics of Mitsui-7 MWCNTs used in this study have been reported in previous publications, revealing a range of sizes (**Table 6-1**). Based on a summary provided in Rahman *et al.,* 2017, Mitsui-7 MWCNTs have tube diameters in the range of 40 - 100 nm whereas the lengths range from 3 – 9.4 µm, with the aspect ratio between 30 - 235 and surface area between 22 – 28 m^2/g. No additional characterisation work was carried out on these materials in the present manuscript.

Table 6-1. Nanomaterials used in the study. Sizes are provided in terms of length (longest dimension) and width (shortest dimension) of the particles. Numbers in parentheses represent standard deviation. SSA: Specific surface area. D: diameter. L: Length. N/A: Not available. Dissolution: data pertains to 24 h dissolution in cell culture media at 10 µg/mL from *(Avramescu et al., 2020, 2022)*.

Material	Catalogue Number	Manufacturer	Size (nm)		Aspect Ratio	SSA (m^2/g)	Dissolution (%)
CuO NPs	544868	Sigma Aldrich	64.8 x 45.9 (47 x 28)[a]		1.39 (0.39)[a]	10.3[e]	11.8
Al_2O_3 NPs	544833	Sigma Aldrich	23.9 x 10.7 (12 x 7)[b]		2.63 (1.40)[b]	145.3[e]	1.25
NiO NPs	US3355	US Research Nanomaterials Inc.	27.3 x 21.9 (10 x 8)[b]		1.25 (0.20)[b]	36.6[e]	0.81
TiO_2 NPs	NIST 1898	National Institute of Standards and Technology	26.8 x 20.9 (9 x 7)[c]		1.30 (0.26)[c]	52.7[e]	0.17
Mitsui-7	N/A	Mitsui & Co.	D: 40 - 100[d]	L: 3000 – 9400[d]	30 – 235[d]	22 – 28[d]	N/A

[a] Data from (Boyadzhiev et al., 2021). [b] Data from (Boyadzhiev et al., 2023). [c] Data from (Boyadzhiev et al., 2022). [d] Data from (Rahman, L. et al., 2017a). [e] Data from (Solorio-Rodriguez et al., 2024).

Cell culture and other reagents: Lyophilized Bafilomycin A1 (Millipore Sigma: Cat# 196000-10UG) was dissolved in 100% dimethyl sulfoxide (DMSO; Fisher Scientific: Cat # BP231-100) to a stock concentration of 32 µM. Stock vials were aliquoted and stored at -20 °C in the dark away from light. $CuCl_2$ (Millipore Sigma, ON, Canada: Cat # C3279-100G) was dissolved in DNAse/RNAse free ultra pure water (dH_2O; Life Technologies, ON, Canada: Cat # 10977015) at a 5 mg/mL stock concentration followed by sterile filtration and storage at 4 °C. For immunofluorescence experiments, 18x18-1 square glass coverslips (Fisher Scientific, Whitby, ON, Canada: Cat # 12-548A), formalin (Millipore Sigma, ON, Canada: Cat # F8775-500ML), Triton X-100 (Fisher Scientific, ON, Canada: Cat # BP151-500), bovine serum albumin (BSA; Millipore Sigma, ON, Canada: A9647-100G), Tween-20 (Millipore Sigma, ON, Canada: Cat # P9416-100ML), and ProLong™ Glass Antifade Mountant with NucBlue™ Stain were used (ThermoFisher, ON, Canada: Cat # P36983). Anti-LAMP1 antibody (Abcam, MA, USA: ab24170), Anti-alpha tubulin antibody (Rabbit monoclonal) from (Abcam, MA, USA: Cat # ab52866), Phalloidin-iFluor 594 from (Abcam, MA, USA: Cat # ab176757) were used as primary antibodies. Secondary antibodies included Goat Anti-

Rabbit IgG H&L (Alexa Fluor® 488) (Abcam, MA, USA: Cat # ab150077), and Goat Anti-Rabbit IgG H&L (Alexa Fluor 568) (Abcam, MA, USA: Cat # ab175471). Acidotrophic Lysotracker Red DND-99 stain was purchased from (Thermofisher Scientific, ON, Canada: Cat # L7529).

6.3.2 Cell culture and maintenance

Immortalized mouse lung cells (FE1), with characteristics of type I and II alveolar epithelial cells were used for exposure. FE1 cells have been utilized to conduct high content global gene expression analysis (Boyadzhiev et al., 2021, 2023), and genotoxicity screening (Boyadzhiev et al., 2022; Solorio-Rodriguez et al., 2024) of the MONPs tested in the present study, as well as in cellular uptake and localisation studies involving SiO_2 NPs (Decan et al., 2015). These cells have also been utilized by other groups to screen for genotoxicity induced by ENM *in vitro* (Bengtson et al., 2016; Jacobsen et al., 2008a, 2008c; Wils et al., 2021).

FE1 cells were maintained in Dulbecco's Modified Eagle's Medium Nutrient Mixture: F12 HAM (1:1) phenol red containing medium (DMEM/F12; Life Technologies, ON, Canada: Cat # 21041-025), supplemented with 2% fetal bovine serum (FBS; Life Technologies, ON, Canada: Cat # 12483-020), 100 U/mL penicillin G & 100 µg/mL streptomycin (Life Technologies, ON, Canada: Cat # 15140-122), and 1 ng/mL human epidermal growth factor (EGF; Life Technologies, ON, Canada: Cat # PHG0311). Cells were cultured in a 37 °C incubator with 95% humidity and 5% CO_2.

6.3.3 ENM suspension

CuO, NiO, and Al_2O_3 NPs were prepared for exposure as described in (Boyadzhiev et al., 2022), whereas TiO_2 NPs were prepared according to (Boyadzhiev et al., 2023). Methods described in (Rahman, L. et al., 2017a) were followed to prepare Mitsui-7 MWCNTs. All materials were weighed out on an XSR105 analytical mass balance (Mettler Toledo, ON, Canada), and suspended in dH_2O using a Branson Ultrasonics Sonifier™ 450 (Crystal Electronics Inc, ON, Canada), on an ice bath, according to sonication conditions listed in **Error! Reference source not found.**. For all materials, a ½ inch disruptor horn and r

emovable flat tip was used, with the tip of the probe immersed 1.5 inches deep into the solution. For TiO_2 NPs, a removable extension was used for sonication to allow the flat tip to reach the appropriate depth. For Mitsui-7 MWCNTs, the fibres were suspended in ultra pure water + 2% FBS and shaken vigorously by hand for 15 minutes to allow for fibres to enter suspension prior to initial sonication. The suspended Mitsui-7 stock was frozen at -20 °C until use. The stock was thawed just before cell exposure and mixed by gentle pipetting prior to resonication and dilution.

Table 6-2. Sonication parameters for ENM used for exposure. DSE: delivered sonication energy, DSE = (P x T)/V. P=power (W), T=time (s), V=volume (mL).

Material	Concentration (mg/mL)	Volume (mL)	DSE (J/mL)	% Amplitude	Frequency	Active Sonication Time (s)
CuO NPs	1	8	109.5	10	8 sec on / 2 sec off	144
NiO NPs	5	8	733	60	8 sec on / 2 sec off	90
Al_2O_3 NPs	5	8	1270	55	8 sec on / 2 sec off	180
TiO_2 NPs	5	50	1013	55	8 sec on / 2 sec off	900
Mitsui-7 MWCNTs	1	10.61	550[a] / 172[b]	10	Always on	960[a] / 300[b]

[a] Initial sonication of stock Mitsui-7.[b] Subsequent sonication of thawed primary stock.

6.3.4 Cell seeding and exposure to ENM

For all exposures carried out in this study, FE1 cells were seeded at a density of 125 - 130 000 cells/well in 6-well plates. For Trypan Blue exclusion analysis, cells were seeded directly onto the well plates. For microscopy analyses, cells were seeded on 18x18-1 sterile glass coverslips in each well of a 6-well plate. In each case, sonicated ENM in ultrapure water were diluted into fully supplemented DMEM/F12 without phenol red (Life Technologies, ON, Canada: Cat # 21041-025) and used for 24 h exposures. Cells were allowed to recover for 24 h after initial seeding before treatment with ENM.

6.3.5 Trypan Blue exclusion assay

Following 24 h of exposure, cells were washed once with 0.5 mL phosphate buffered saline (PBS), dissociated using 150 µL Trypsin (3 minute incubation, 37 °C, 95% humidity, 5% CO_2; Life Technologies, ON, Canada: Cat # 25200-056), and resuspended in 0.5 – 1 mL of fresh phenol-red free cell culture medium (depending on cell density as assessed via phase contrast at the time of harvest). A 10 µL aliquot of control or exposed cell suspension was combined with 10 µL of 0.4% Trypan Blue dye (Life Technologies, ON, Canada: Cat # 15250061) and incubated at room temperature for 5-10 min before manual cell counting on a hemocytometer. The relative survival was calculated using the equation below:

*Relative survival = (exposed viable cell count [white] / control viable cell count [white]) *100*

6.3.6 LysoTracker Red DND-99 staining

To assess the integrity of acidic vesicles, LysoTracker Red DND-99 staining was used. After 24 h of exposure, media was removed and FE1 cells were washed with 1 mL fresh, prewarmed phenol-red free media. Next, fresh phenol-red free media complemented with 60 nM LysoTracker Red DND-99 was added to each well and the plates were incubated under light-occlusion for 1 h. The plates were washed with 1 mL fresh media, and with 1 mL PBS. Cells were fixed with 4% formalin in PBS for 11 minutes, washed 3 times with fresh PBS, and mounted onto slides for analysis using ProLong™ Glass Antifade Mountant with NucBlue™ counterstain. Slides were allowed to cure for 24 h at room temperature in the dark, before storage in the dark at 4 °C for analysis.

6.3.7 Bafilomycin A1 dose range finding

A dose-range finding study was carried out to identify the appropriate concentration of BafA1 to achieve the desired inhibition of lysosomal acidification in FE1 cells without causing overt toxicity. Cells were seeded for Trypan Blue exclusion staining as described in section **6.3.4** and were exposed to 1.8 mL of 1 – 200 nM BafA1 in fully supplemented phenol red-free cell culture medium for 24 h. Cells exposed to medium only or medium containing 0.625% DMSO were used as negative controls. Trypan Blue analysis was carried out as described in section **6.3.5**, with one biological replicate assessed for each concentration in technical duplicates.

In parallel, cells were seeded for imaging analysis as described in section **6.3.4** and acidic vesicles were labelled as described in section **6.3.6** with LysoTracker Red following 24 h exposure to 1 – 25 nM BafA1. Cells treated with 0.02% DMSO served as a solvent control.

6.3.8 Bafilomycin A1 nanomaterial co-exposures and viability analysis

To determine the impact of inhibition of vesicular acidification on acute MONP cellular toxicity, FE1 cells were seeded for Trypan Blue Exclusion analysis as described in section **6.3.4**, and co-exposed to 25 µg/mL CuO NPs, 50 µg/mL NiO NPs, 50 µg/mL Al_2O_3 NPs, or 100 µg/mL TiO_2 NPs with or without 5 nM BafA1 for 24 h. The concentrations of

MONPs chosen for exposure have been shown to result in reductions in relative survival at 24 h in FE1 cells (Boyadzhiev et al., 2023). A concentration of 54 µg/mL $CuCl_2$ (equivalent to dissolved copper concentration from 25 µg/mL CuO NPs) was utilized to represent fully dissolved copper metal, the toxicity of which is expected to remain unaltered in the presence of BafA1. Furthermore, a concentration of 100 µg/mL Mitsui-7 MWCNTs was utilized as a non-metal oxide non-particle contrast for comparison. This concentration induced a pronounced transcriptional response in FE1cells and represents the highest concentration tested *in vitro* (Søs Poulsen et al., 2013). In each experiment, a blank media control and a DMSO solvent control were included. All particles were sonicated according to section **6.3.3** (**Error! Reference source not found.**).

Following exposure, Trypan Blue exclusion staining was conducted according to section **6.3.5**. For each condition, 2 technical and 3 biological replicates were conducted. Significant differences in relative survival (using the density of viable cells measured as cells/cm^2) were compared in R, with the 'multcomp' package, using a one-way ANOVA with a Tukey's post-hoc in the case of significant results. Normality and variance structure were confirmed for each sample set using the Shapiro-Wilks and Levene's tests respectively prior to ANOVA computation.

6.3.9 Measuring CuO NP induced vesicular instability

Particle suspension and cell exposure were conducted as described in **6.3.3** and **6.3.4**. Cells were treated for 24 h to blank media or 6, 12.5, and 25 µg/mL CuO NPs. Lysotracker Red staining was conducted according to **6.3.6**.

6.3.10 Lysosome and cytoskeleton labelling

To test for particle localisation to lysosomes and the effects of particle exposure on the cytoskeleton, FE1 cells were seeded for imaging analysis (section **6.3.4**). Following 24 h of recovery, cells were exposed to 6 or 12.5 µg/mL CuO, NiO, Al_2O_3, and TiO_2 NPs. A concentration of 12.5 µg/mL had been used in the past to conduct co-localization analysis of SiO_2 NPs with Lamp1 in FE1 cells (Decan et al., 2015), while a lower concentration of 6 µg/mL was included in the case that 12.5 µg/mL presented too many particles for analysis.

In a parallel experiment, FE1 cells were seeded for imaging analysis as in section **6.3.4**. After 24 h recovery, cells were exposed for 24 h to 100 µg/mL Mitsui-7 MWCNTs, 50 µg/mL TiO_2 NPs, or 25 µg/mL CuO NPs. Mitsui-7 MWCNTs were included as a non-MONP contrast that has been shown to induce cytoskeletal instabilities (Hevia & Fanarraga, 2020; Zhang et al., 2020). The concentrations of MONPs chosen are known to induce cytotoxicity or strong transcriptional signalling in FE1 cells, with between 10 – 77% relative survival at 24 h (Boyadzhiev et al., 2023; Søs Poulsen et al., 2013). Cells were used for Lamp1, F-actin, and α-tubulin immunofluorescent staining according to section **6.3.11**, and imaged as described in section **6.3.12**-**6.3.14**.

6.3.11 Immunofluorescent staining with Lamp1, F-actin or α-tubulin

Following 24 h FE1 cell exposure, glass coverslips were washed 2 times with fresh, warm media followed by 1 wash with PBS. Cells were fixed with 4% formalin in PBS for 11 minutes. Cells were washed 3 times with fresh PBS, then permeabilized using 1% Triton X-100 in PBS for 5 minutes before antibody staining. In all cases, fixation, permeabilization, and staining were conducted at room temperature (21 °C).

Lamp1 + α-tubulin staining: Cells were blocked with 0.1% Tween-PBS (PBST) solution containing 1% BSA for 30 minutes. Cells were then labelled with Anti-Lamp1 antibody at a 1/1000 dilution in 1% BSA + PBST solution for 1 h. Cells were washed 3 times with fresh PBS, then incubated with Goat Anti-Rabbit IgG H&L at a 1:200 dilution in PBST BSA solution for 1 h in the dark. Cells were washed 3 times with fresh PBS, transferred to a new plate, and blocking was repeated one more time for 30 minutes in PBST BSA solution. Cells were next incubated with Anti-alpha tubulin antibody (Rabbit monoclonal) at a 1:1000 dilution in PBST BSA solution for 1 h in the dark. Cells were washed 3 times with fresh PBS, then labelled with Goat Anti-Rabbit IgG H&L at a 1:200 for 1 h in the dark. Cells were washed three more time with PBS and mounted onto slides using hard curing ProLong™ Glass Antifade Mountant with NucBlue™ Stain (containing Hoechst 33342 nuclear counterstain). After 24 h of curing at room temperature in the dark, slides were placed at 4 °C until analysis.

F-actin staining: Cells were blocked using PBST BSA solution for 30 minutes, after which cells were incubated with Phalloidin-iFluor 594 Reagent at a 1:1000 dilution in PBST BSA. Incubation time was optimised and 30 minutes to 1 h was used for incubation with primary antibody coverslips were washed 3 times with fresh PBS and were mounted onto slides using ProLong™ Glass Antifade Mountant with NucBlue™ Stain (containing Hoechst 33342 nuclear counterstain). After 24 h of curing at room temperature in the dark, slides were placed at 4 °C until analysis and kept away from light.

6.3.12 Enhanced Darkfield Hyperspectral Imaging

All imaging was conducted on a Cytoviva 3D enhanced darkfield hyperspectral microscope (Cytoviva Inc., NJ, USA), with an attached dual mode fluorescence module with DAPI, FITC, and Texas Red filters installed. All darkfield and fluorescence images were captured on a monochrome QI825 camera (Teledyne Vision Solutions, MA, USA) to allow for channel merging. Fluorescence and 40X darkfield signals were captured using an Xcite Series 120Q light source (Excelitas Technologies Corp., QC, Canada). Hyperspectral images (HSI, HSIs for plural) and darkfield images at 60 and 100x were captured using a Fiber-Lite DC-950 light source (Dolan-Jenner Industries, MA, USA).

Particle spectral library preparation: To create pure particle libraries for mapping purposes, aliquots of suspended and sonicated particles were diluted in ProLong mounting medium, deposited onto glass slides and coverslipped. The slides were allowed to cure for 24 h at room temperature in the dark, after which at least 3 hyperspectral images per slide were captured using a 100x oil immersion objective. For each particle, the darkfield light source was set to 50% total illumination, the collar on the objective was reduced to its smallest diameter (NA = 0.6) and the exposure conditions were set to 0.25 sec exposure, with 501 lines per image. In order to remove non-specific spectra from the libraries, and control for artifacts, images of blank dH_2O diluted in ProLong medium were also captured with the same conditions used for particle imaging. The initial pure particle libraries created using the 'Particle Finder' algorithm were filtered at a spectral angle mapping (SAM) angle of 0.1 radians using control HSIs of dH_2O in ProLong.

Imaging sequence: The images were taken in the following sequence: First 40x images were taken using an air objective of the whole coverslip, across 9 fields of view covering the full surface of the slip. For each field of view, the fluorescence images were taken in DAPI (nuclear), FITC (Lamp1), and Texas Red (α-tubulin or F-actin) channels. Next, the filter wheel on the Dual Mode Fluorescence module of the Cytoviva was moved between filter positions bathing the sample in white light and producing darkfield illumination. Due to the scattering properties of MONPs and MWCNTs, they can be clearly seen against the dark background. A short exposure image (5 ms) was taken to serve as the darkfield channel. This was repeated for 9 separate fields of view. The darkfield condenser was adjusted at each new field of view in order to maintain maximal fluorescence and scattering intensity.

After 40x imaging, higher magnification images were captured at 60 and 100x using oil immersion objectives in which 3 fields of view per coverslip were analyzed. At each field of view, the 60x image was taken; with the fluorescence channels imaged first (collar fully open, NA = 1.25), followed by the darkfield channel imaging with the collar fully closed (NA = 0.65). Once the 60x image was collected, the 100x objective was placed and the imaging repeated as for the 60x objective, however with the NA = 1.3 for fluorescence imaging and 0.6 for darkfield imaging. The darkfield light source was set to 50% or 35% power at 60 and 100x (depending on the strength of scattering of the ENM), however for imaging control cells, the light source was always set to 50% intensity as this produces the stronger signal. At 60x, 5 ms of exposure time was used whereas at 100x, 20 ms of exposure time was used. During the 100x imaging, HSI imaging proceeded darkfield image acquisition. For HSI acquisition, the darkfield light source was set to 50% intensity in all cases, the collar was fully closed on the 100x objective (NA = 0.6), exposure time was set to 0.25 seconds and line number was set to 501. For identification purposes, HSIs from cells exposed to the material of interest were mapped using the SAM algorithm and filtered spectral libraries, using a critical angle of 0.1 (same as what was used to filter the reference libraries). The final 2D fluorescence images were created by combining the fluorescence and darkfield

channels in ImageJ 1.54f, however the HSI imaging could not be directly overlaid due to small differences in the field of view and are shown side-by-side for comparison instead.

6.3.13 2D Particle / Lamp1 colocalization

To determine in an objective manner the degree of overlap between the signals for particles and Lamp1, the 'Colocalization Threshold' plugin in Fiji was used. This plugin utilizes an objective statistical approach originally published in (Costes et al., 2004) to conduct thresholding on two separate fluorescent channels and then determine the degree of pixel overlap from both channels. Statistical significance of this overlap was not determined. For Lamp1 images, a rolling ball background subtraction was conducted (50 pixel ball width) prior to colocalization analysis. Three separate 100x fields of view were analyzed per sample. Pixels of overlap between the two channels are presented in white in the generated maps.

6.3.14 3D imaging

At each high magnification field of view, 3D image stacks of fluorescence and darkfield channels were captured using a 100x oil immersion objective, with the collar fully open for fluorescent (NA = 1.3) images and fully closed for darkfield images (NA = 0.6). Z-stack size and imaging parameters varied depending on the specific field of view imaged. For MONP localization, 'Just Locate Nanoparticles' was used which determines the location of spherical particles based on the slice showing maximal intensity for areas with scattering intensity past a certain threshold. NPs are visualized as red, 4 pixel spherical voxels in the 3D space. Fluorescence deconvolution was conducted in ImageJ using Cytoviva's 3D analysis plugins. For deconvolution, point spread functions (PSFs) were generated based on the emission wavelength of the fluorophore in question for each target (Lamp1: 520 nm; α-tubulin: 603 nm; Hoechst 33342: 454 nm; Phalloidin: 618 nm). To create the final 3D visualizations, the NP localization file, and the 3 deconvoluted fluorescence channels were opened in the '3D Viewer' plugin in ImageJ and overlayed. In the case of Mistui-7 MWCNTs, a PSF was generated based on the main peak of the lamp spectrum of the darkfield light source used for channel imaging (661 nm). This PSF was used to deconvolute the channel in the same manner as for the fluorescent channels.

6.4 Results

6.4.1 Inhibition of vesicular acidification and impacts on cell viability

Treatment of FE1 cells with 1-200 nM BafA1 for 24 h induced a concentration-dependent reduction in viable cells, beginning at the 5 nM (**Figure 6-1A**). LysoTracker Red DND-99 staining of untreated control cells showed strong, punctate, mainly perinuclear but non-uniform staining of lysosomes, the intensity of which significantly reduced in cells treated with different BafA1 concentrations, apparent at 10 and 25 nM with diffuse cytoplasmic staining starting at 5 nM (**Figure 6-1B**). Due to the high toxicity of BafA1 in FE1 cells, a concentration of 5 nM was chosen for all subsequent exposures.

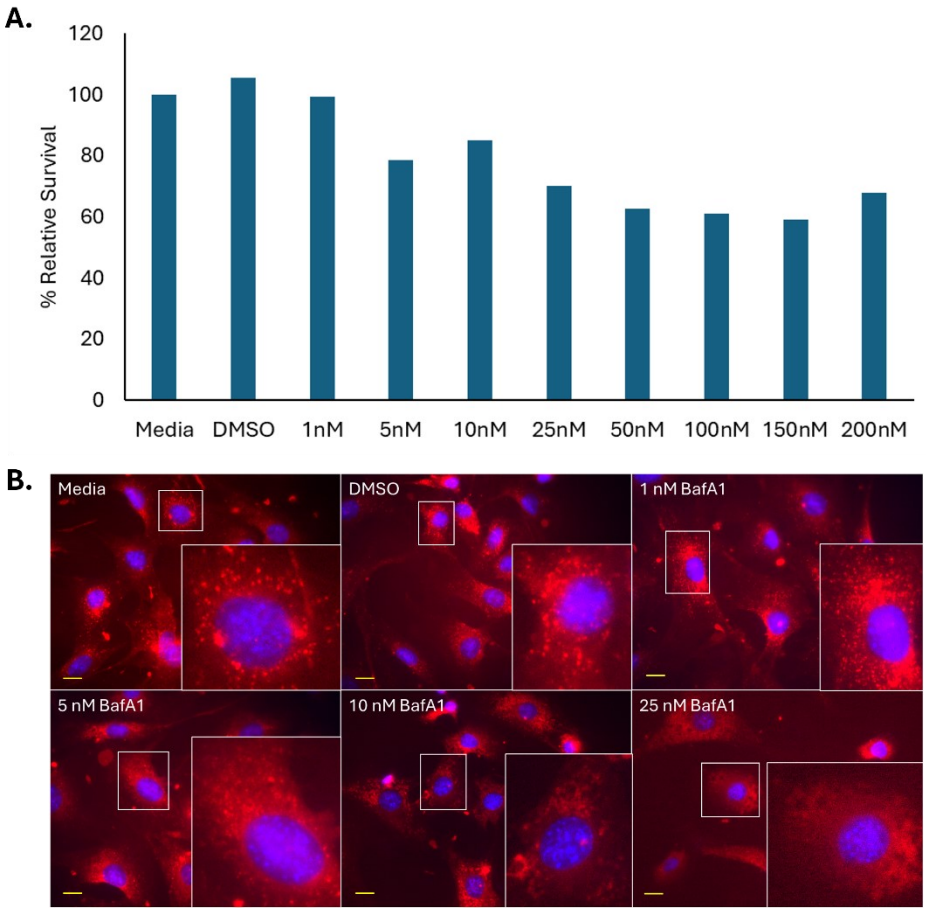

Figure 6-1. A) BafA1 dose-range finding study (n=1). B) 40X Fluorescent imaging of FE1 cells after 24 h exposure. Lysotracker DND (Red) and Hoechst 33342 (Blue). Yellow scale bars = 10 µm for each image. Insets represent enlargements of areas in white boxes.

When FE1 cells were co-exposed for 24 h with 5 nM BafA1 and CuO, NiO, Al_2O_3, TiO_2 NPs, or Mitsui-7 MWCNTs an improvement in % relative survival was only observed in cells exposed to 25 µg/mL CuO NPs (52% cell survival with 5 nM BafA1, 38% in the absence of BafA1) (**Figure 6-2**). Both conditions were statistically significantly different compared to DMSO treated cells, but were not significantly different from each other. Treatment with 54 µg/mL $CuCl_2$ did not change in the presence or absence of BafA1 (60-62% relative survival). For cells co-exposed to NiO, Al_2O_3, or TiO_2 MONPs and 5 nM BafA1, an increase in toxicity was observed in the presence of BafA1 compared to cells exposed to ENM alone. With respect to NiO NPs, this difference was statistically significant ($p < 0.01$).

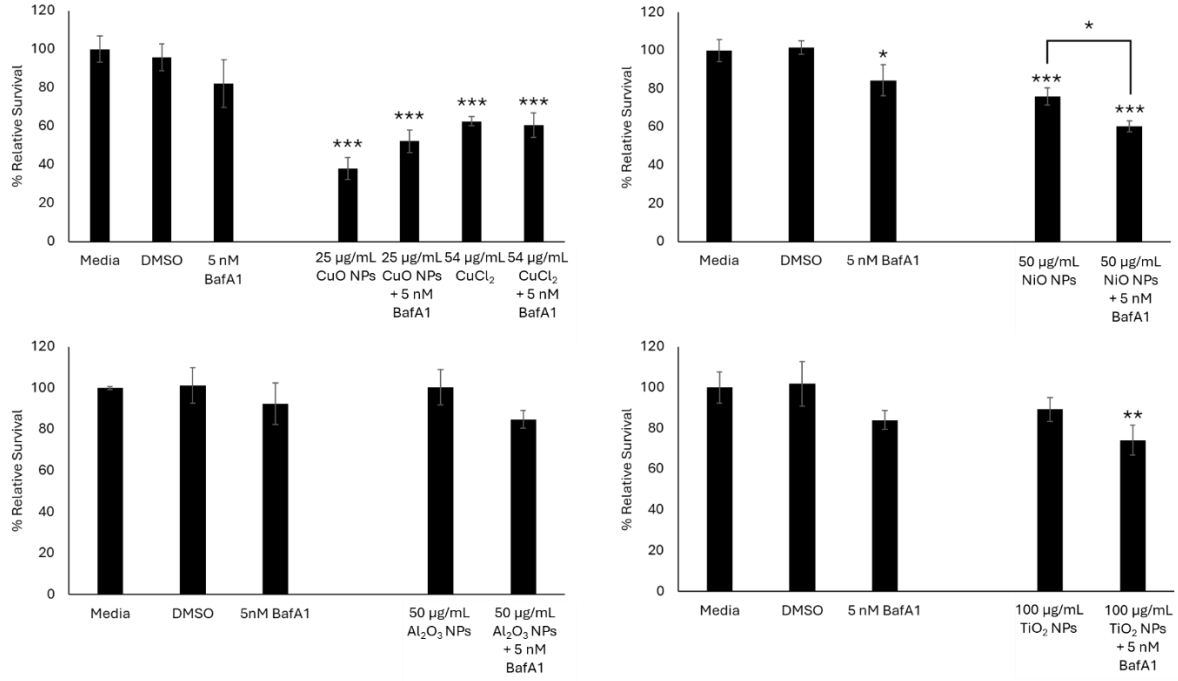

Figure 6-2. % Relative survival of FE1 cells following 24 h treatment with MONPs ± 5 nM BafA1. Error bars represent standard deviation (n = 3). Significance determined through a one-way ANOVA with a Tukey's post-hoc in the case of significant result. *: $p < 0.05$. **: $p < 0.005$. ***: $p < 0.0005$.

Since 5 nM BafA1 was able to induce a modest improvement in viability only in cells exposed to CuO NPs, the effect of CuO NPs on acidic vesicle integrity in FE1 cells was tested using LysoTracker Red DND-99 staining (**Figure 6-3**). In control untreated cells, Lysotracker staining was pronounced and appeared as bright red foci (**Figure 6-3**).

Noticeable reduction in LysoTracker Red staining was seen at 25 µg/mL CuO NPs, which co-located with the distribution of particles.

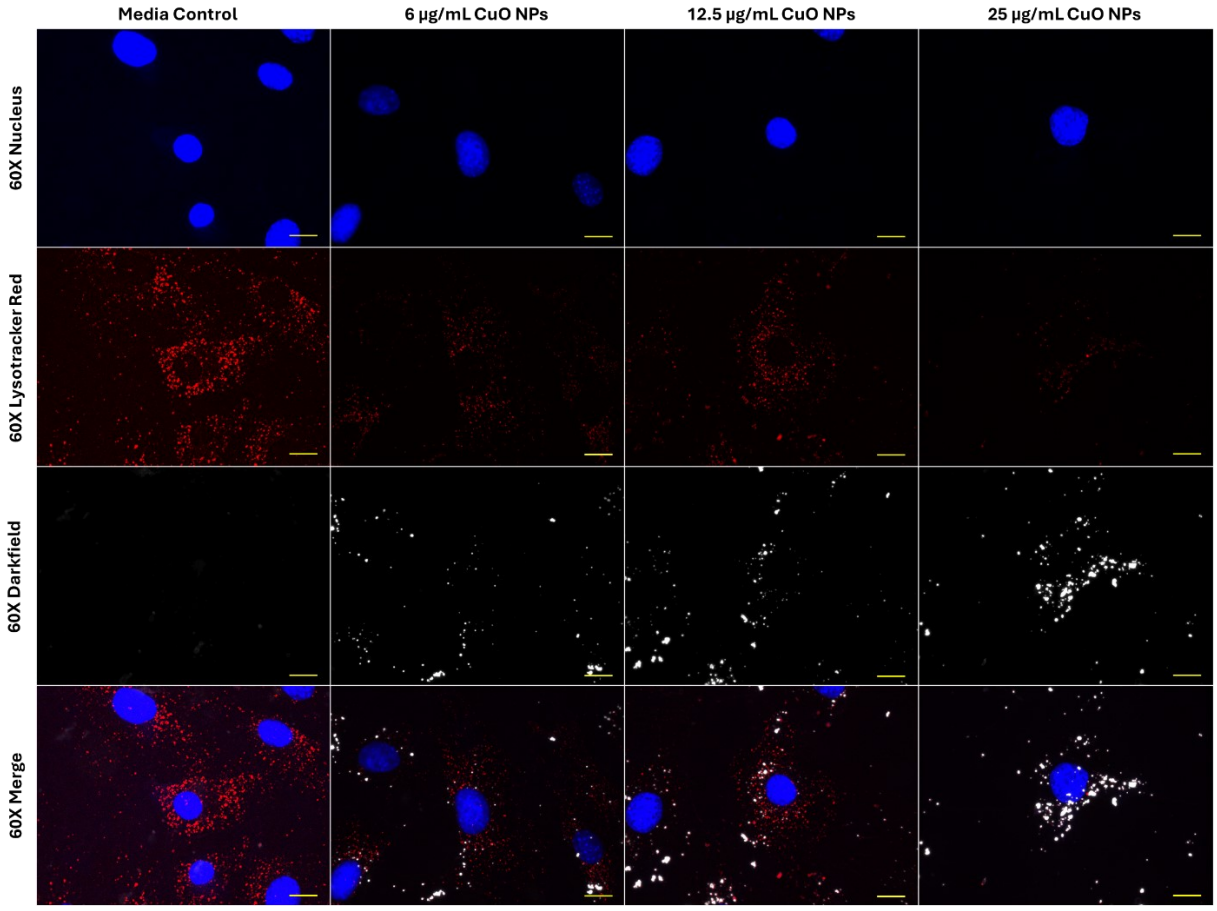

Figure 6-3. 60X enhanced darkfield fluorescent imaging of FE1 cells after 24 h of exposure to blank media or ENM. Yellow scale bars = 10 µm for each image. Blue: Nucleus (Hoechst 33342). Red: acidic vesicles (Lysotracker Red DND-99). White: particles.

6.4.2 Hyperspectral libraries for particle mapping

While nanoscale objects can be visualized to an extent using enhanced darkfield illumination, spectral matching is used to differentiate between non-specific bright objects from actual nanomaterials. Pure particle libraries for MONPs dispersed in ProLong mounting medium are shown in (**Supplementary Figure 6-1**). For CuO NPs, two separate spectral profiles were observed; one at 670 nm and the other at 720 nm. Similarly, for NiO NPs two spectral profiles were observed, at 610 nm and at 645 nm. Al_2O_3 and TiO_2 NPs were blue-shifted relative to CuO and NiO NPs, with a main broad peak at 570 nm for Al_2O_3 NPs and two spectral populations for TiO_2 NPs at 540 nm and 580 nm.

6.4.3 Co-localization of MONPs with Lamp1 and impacts on α-tubulin

Since treatment with BafA1 did not improve cytotoxicity induced by NiO, Al_2O_3, and TiO_2 NPs, their association with lysosomes was assessed and compared with CuO NPs via Lamp1 staining.

Shown in **Figure 6-4**, are representative 40x images of Lamp1 and particle distributions in FE1 cells after 24 h exposure to 6 and 12.5 µg/mL of CuO, NiO, Al_2O_3, or TiO_2 NPs. The distribution of Lamp1 in control and all exposed cells appeared perinuclear, showing no change in response to MONP treatment at either concentration. MONPs can be identified as bright white objects in the images, which are absent in unexposed cells. Aggregates of MONPs can be seen associated with cells in all instances, with no obvious pattern in their organization.

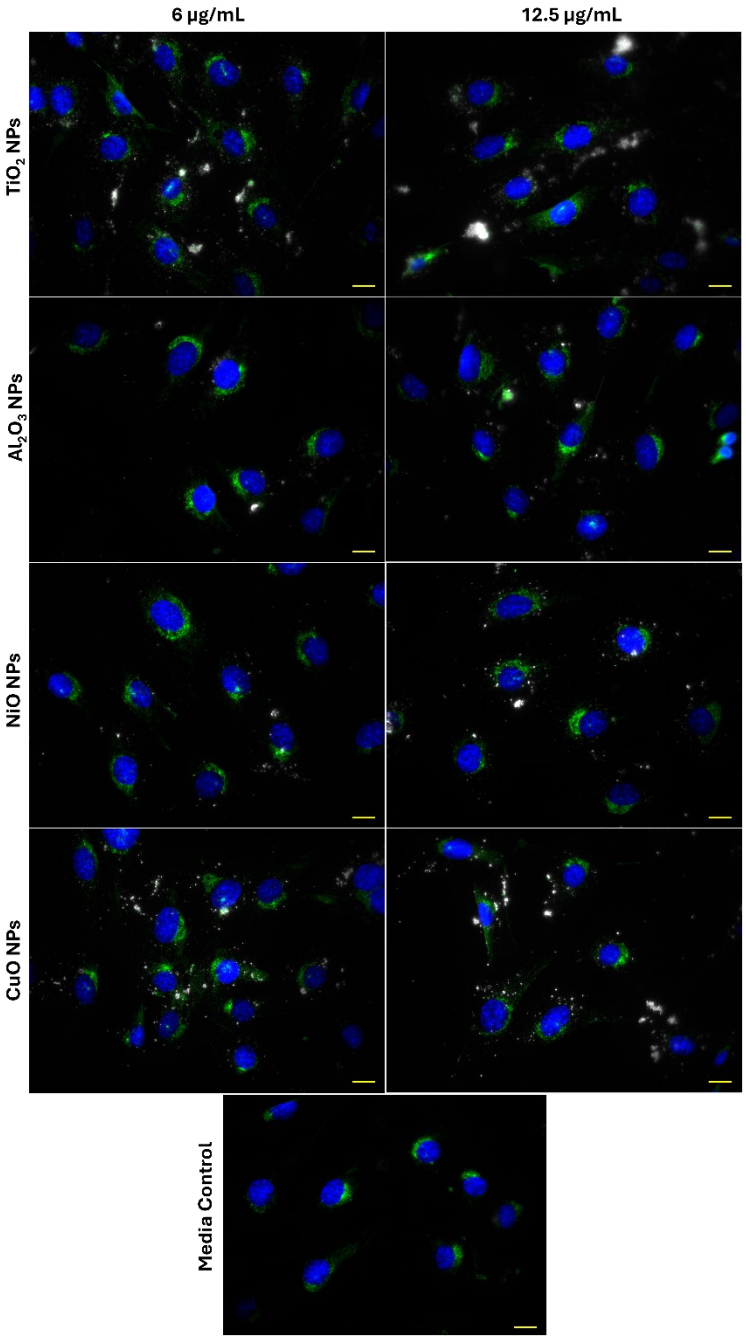

Figure 6-4. Lysosome distribution in FE1 cells following 24 h exposure to MONPs and blank media . Yellow scale bar = 10 µm in each image. Blue: Nucleus (Hoechst 33342). Green: Lysosomes (Lamp1). White: MONPs.

To determine the degree of co-localization of MONP and Lamp1 signals, the overlap between Lamp1 and darkfield channels in 100x oil immersion images was measured in ImageJ. Co-labelling with α-tubulin was used to visualize the cellular boundaries. **Figure 6-5** and **Supplementary Figure 6-2** confirm that darkfield and Lamp1 signals showed

subtle co-localization in all instances. For CuO and NiO NPs at 6 and 12.5 µg/mL and for 12.5 µg/mL Al_2O_3 NPs, only 1 image in 3 showed colocalization using this approach (**Table 6-3**). For CuO and Al_2O_3 NPs at 6 and 12.5 µg/mL and NiO NPs at 12.5 µg/mL, the maximum proportion of darkfield signal which colocalizes with Lamp1 signal is <10%. More pronounced co-localization was seen for insoluble 6 and 12.5 µg/mL TiO_2 NPs, with 5/6 images showing signal colocalization. The maximum amount of co-localizing darkfield signal was concentration-dependent, with a maximum of 26.9% of the particle signal showing colocalization at 6 µg/mL and 53.0% at 12 µg/mL. The identify of the colocalized bright objects was confirmed by hyperspectral imaging using pure particle libraries. Deconvolution of 100x 3D z-stacks captured for each image shows that the matched MONPs are in the same plane as the Lamp1 signal, and in close association (**Supplementary Figure 6-3**).

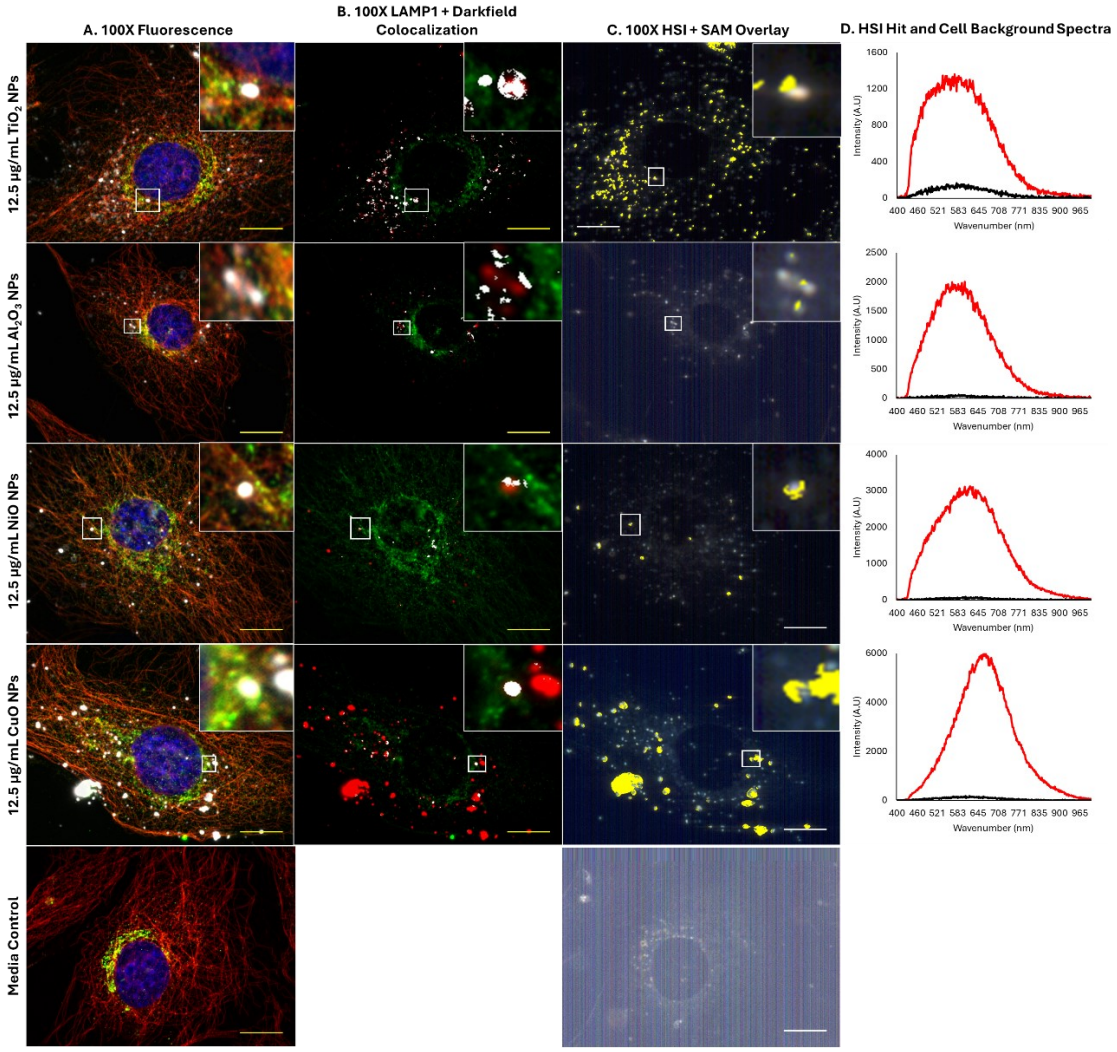

Figure 6-5. Co-localization of MONPs and lysosomes in FE1 cells following 24 h exposure. Yellow / White scale bars = 10 µm in each image. Insets represent areas highlighted by white boxes. (A) Red: α-Tubulin; Green: Lysosomes (Lamp1); Blue: Nucleus (Hoechst 33342); White: particles. (B) Red: particles; Green: Lysosomes (Lamp1); White: Areas of overlap particles and lysosomes. (C): Yellow: Areas with spectral match to the MONP of interest. (D): Red: Particle hit spectrum. Black: cell background spectrum.

Table 6-3. Maximum proportion of darkfield signal colocalizing with Lamp1 signal from three 100x fields of view. Numbers in parentheses indicate total number of images (out of 3 for each concentration) where colocalization is seen based on auto-thresholding.

MONP	6 ug/mL	12.5 ug/mL
CuO	0.0183 (1)	0.0691 (1)
NiO	0.3805 (1)	0.044 (1)
Al_2O_3	0.0625 (2)	0.0781 (1)
TiO_2	0.2693 (3)	0.5301 (2)

6.4.4 Co-localization of MONPs and F-actin aggregates

Labelling of FE1 cells with Phalloidin allowed for visualization of the F-actin cytoskeleton, which is implicated in endo / exocytosis activities and the formation of sequestering structures termed ‘cauliflowers’ in the pulmonary epithelium.

In all samples, including blank media control, rounded aggregates of F-actin were observed (**Figure 6-6**). Cytoplasmic inclusions can be seen in phase contrast images which appear at similar size and density as fluorescently labelled F-actin aggregates, with a diameter of 2-4 µm (**Supplementary Figure 6-4**). MONPs were always seen to associate with these aggregates after MONP exposure. Particles showed an increased tendency to localize to these bright staining actin aggregates compared to the colocalization observed between Lamp1 and the particles. The 3D deconvolution of the areas surrounding the aggregates in Al_2O_3 NP and NiO NP samples showed that particles appear both in-plane and above the plane of the main F-actin cytoskeleton (**Supplementary Figure 6-5**), which was also observed for CuO and TiO_2 NPs.

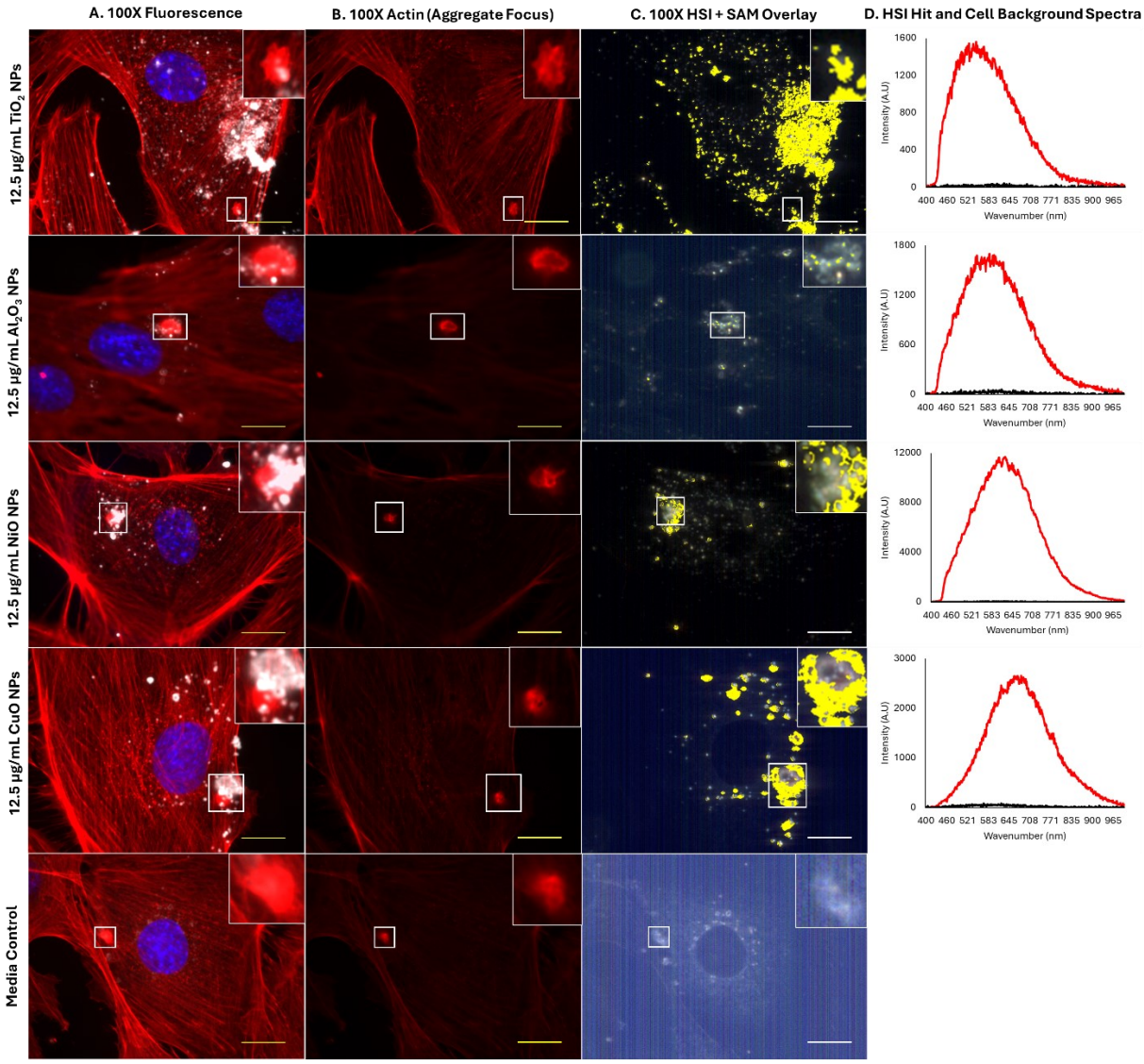

Figure 6-6. Association of MONPs and actin aggregates in FE1 cells following 24 h exposure. Yellow / White scale bars = 10 µm in each image. Insets represents enlargement of area highlighted by white squares. (A) Red: F-actin; Blue: Nucleus (Hoechst 33342); White: particles. Inset represents enlargement of area highlighted by white boxes. (B) Red: F-actin. (C): Yellow: Areas with spectral match to the MONP of interest. Inset represents enlargement of area highlighted by white arrow. (D): Red: Particle hit spectrum. Black: cell background spectrum.

6.4.5 High concentrations of MONPs and MWCNTs show differing effects on the F-actin and α-tubulin cytoskeleton, and Lamp1 signal distribution

To test for acute effects on F-actin and α-tubulin cytoskeleton structure, and on Lamp1 distribution following exposure to high concentrations of MONPs, cells were exposed to 25 µg/mL soluble CuO NPs and 50 µg/mL insoluble TiO_2 NPs, with 100 µg/mL Mitsui-7 MWCNTs serving as an insoluble non-MONP and non-particle contrast.

Based on representative 100x images in **Figure 6-7A**, cells exposed to blank media showed well defined reticular tubulin meshwork inside the cell, with the main Lamp1 signal located in the perinuclear region. No change in Lamp1 distribution was seen in response to any treatment, however differences were seen with respect to effects on the α-tubulin cytoskeleton. In response to 25 μg/mL CuO NPs, large holes were observed in the α-tubulin structure (**Figure 6-7B**). Conversely, exposure to 50 μg/mL TiO_2 NP induced fragmentation of tubulin fibres as compared to the blank media control (**Figure 6-7C**). In contrast, 100 μg/mL Mitsui-7 MWCNTs did not appear to induce differences in background tubulin structure (**Figure 6-7D**); however in cells undergoing division, association of MWCNT fibres with microtubules was observed. (**Figure 6-7E**). Deconvolution of 3D stacks of the fibre-laden dividing cell showed the presence of MWCNTs intersecting the tubulin fibres, surrounding the mitotic nuclei (**Supplementary Figure 6-6**).

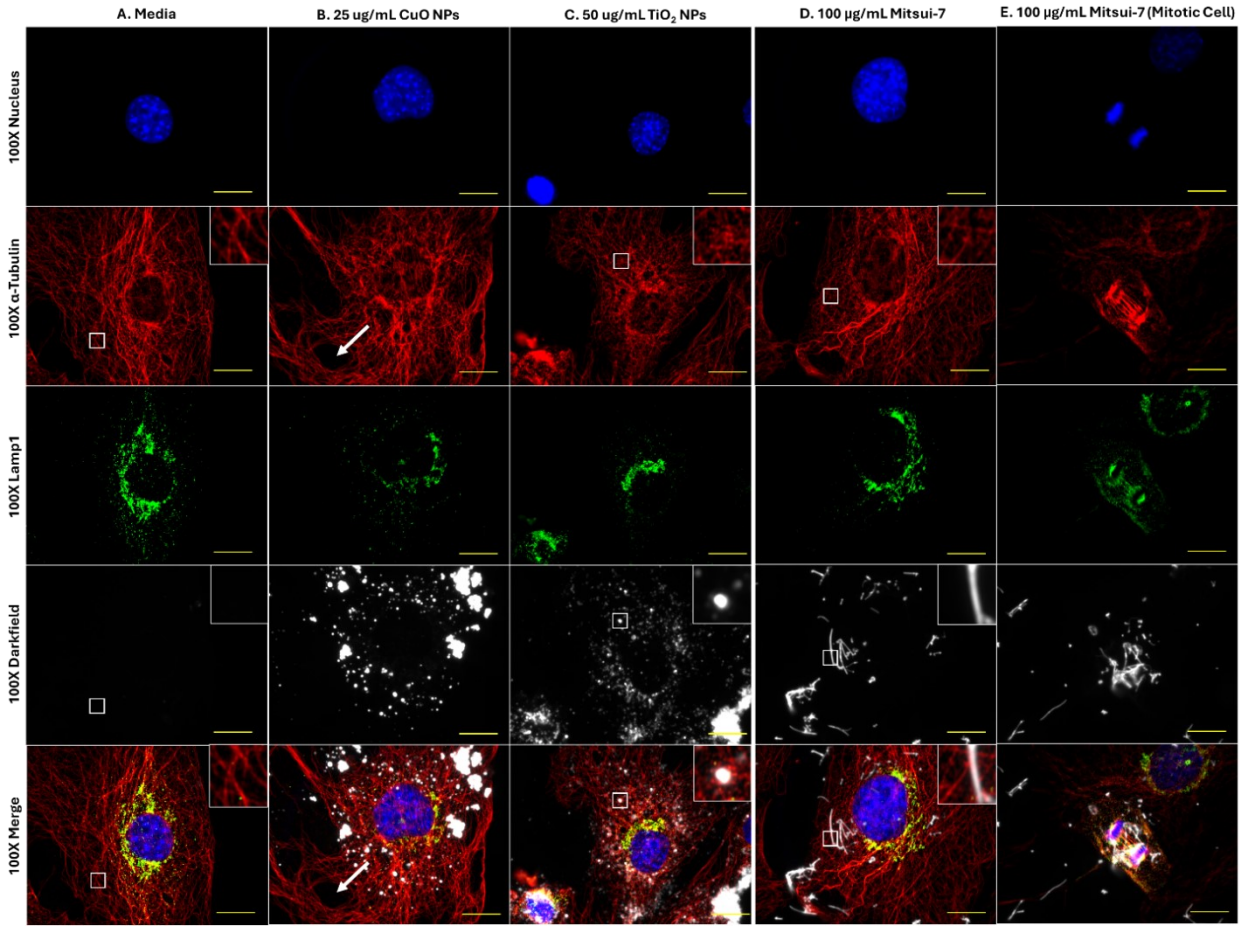

Figure 6-7. Effects of 24 h of exposure to (A) blank media, (B) 25 µg/mL CuO NPs, (C) 50 µg/mL TiO_2 NPs, or (D,E) 100 µg/mL Mitsui-7 MWCNT on lysosomes and α-tubulin structure in FE1 cells. Yellow scale bar = 10 µm in each image. Red: α-Tubulin. Green: Lysosomes (Lamp1). Blue: Nucleus (Hoechst 33342). White: particles or fibres. Insets represent enlarges areas highlighted by the white squares. White arrows highlight large hole formed in the tubulin structure of a CuO NP exposed cell.

As compared to effects on α-tubulin structure, 24 h exposure to a high concentration of CuO NPs, TiO_2 NPs, and Mitsui-7 MWCNTs, also induced changes to the F-actin cytoskeleton (**Figure 6-8**). Cells exposed to blank media showed well defined stress fibres distributed throughout the cell (**Figure 6-8A**). Treatment with 25 µg/mL CuO NPs induced the formation of holes in the actin structure, observed directly under particle aggregates (**Figure 6-8B**). Exposure to 50 µg/mL of insoluble TiO_2 NPs resulted in similar stress fibre formation as in control cells, albeit with increased incidence of areas featuring diffuse staining characteristic of unpolymerized actin (**Figure 6-8C**). Finally with respect to 100 µg/mL Mitsui-7 MWCNTs, no impact on background F-actin structure was observed

(**Figure 6-8D**); however, MWCNT-laden bi-nucleated cells lacking F-actin stress fibres were noted (**Figure 6-8E**).

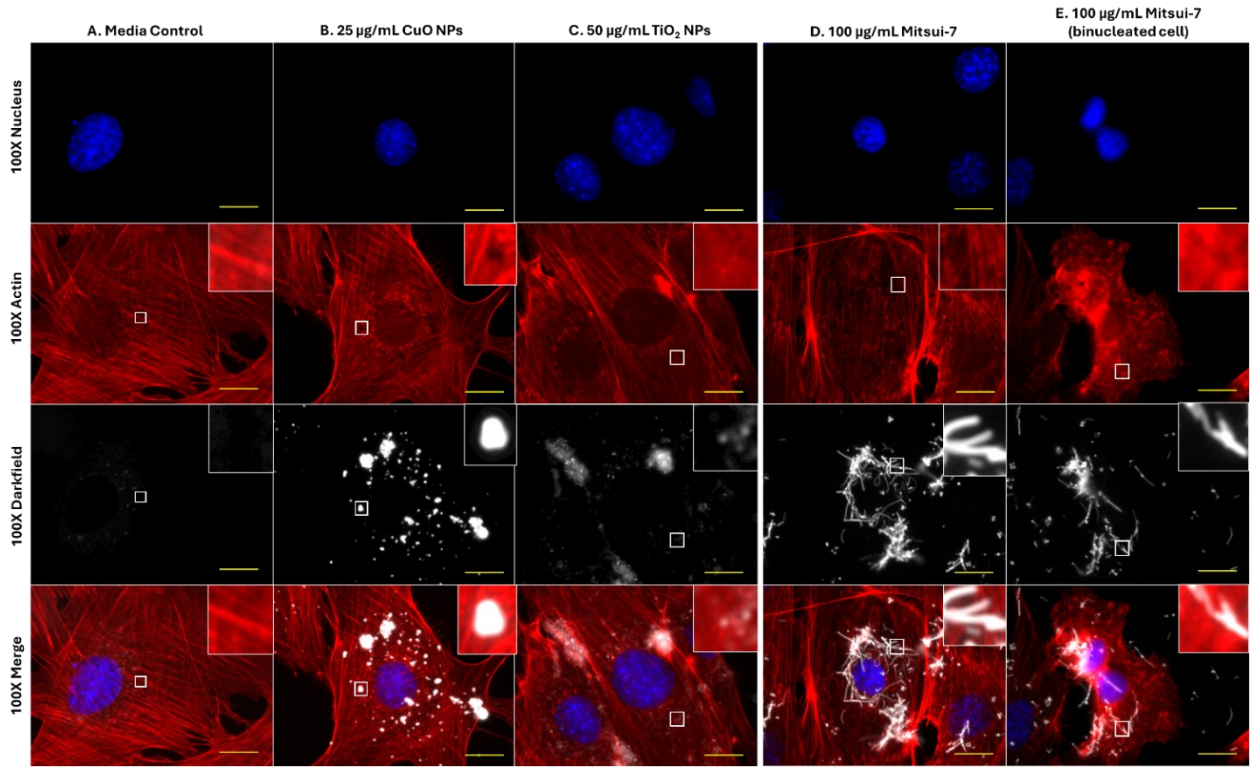

Figure 6-8. Effects of 24 h of exposure to (A) blank media, (B) 25 µg/mL CuO NPs, (C) 50 µg/mL TiO_2 NPs, or (D,E) 100 µg/mL Mitsui-7 MWCNT on the F-actin cytoskeleton in FE1 cells. Yellow scale bars = 10 µm in each image. Red: F-actin. Blue: Nucleus. White: particles or fibres. Insets represents enlargement of area highlighted by white squares.

Lastly, cells were co-exposed to 100 µg/ml Mitsui-7 MWCNTs with or without 5 nM BafA1 to determine if inhibition of lysosomal acidification influences toxicity induced by high concentrations of Mitsui-7 MWCNTs. **Figure 6-9** shows that reduction in % relative survival in cells exposed to BafA1 alone or co-exposed to BafA1 and MWCNTs, in comparison to media controls, was the same (~80%).

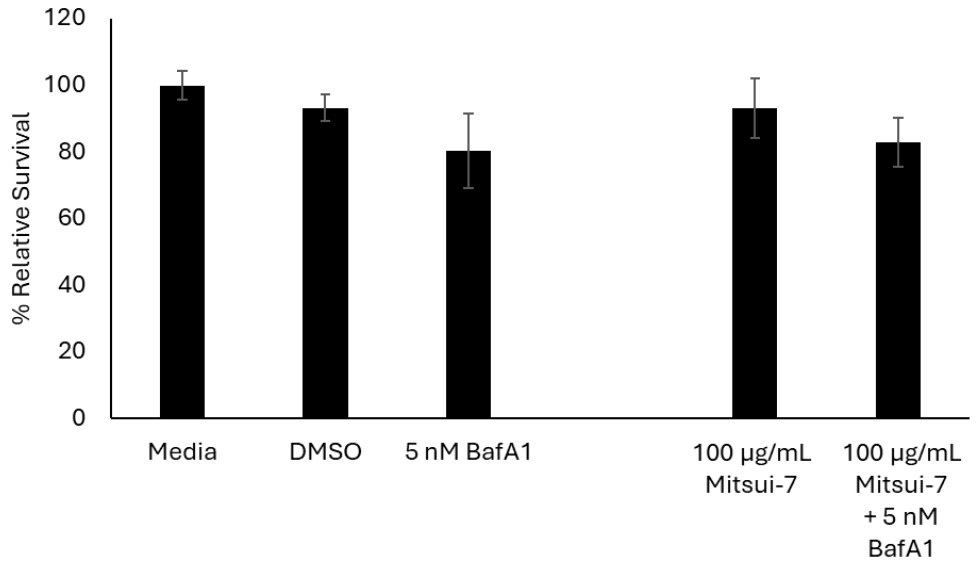

Figure 6-9. % Relative survival of FE1 cells following 24 h treatment with Mitsui-7 ± 5 nM BafA1. Error bars represent standard deviation (n = 3). Significance determined through a one-way ANOVA with a Tukey's post-hoc in the case of significant result. *: p <0.05. **: p<0.005. ***: p<0.0005.

6.5 Discussion

MONPs-induced toxicity is influenced partly by their solubility in biological environments, which in turn, is influenced by particle size, chemical composition, and pH of the biological medium. Previous studies have shown that for highly soluble ZnO, which dissolves instantaneously extracellularly, toxicity proceeds akin to a fully dissolved equivalent (Thoma et al., 2024). However, for MONPs which exhibit lower solubility, particle uptake and consequent intracellular dissolution in lysosomes is thought to play a key role in their toxic potential. Even for insoluble MONPs such as TiO_2 which are stable under acidic conditions (Zhong et al., 2017), evidence in animal models exists for lysosomal localization and subsequent instability (Zhu, Yanglong et al., 2012). In the present study, intracellular localization, including localization to lysosomes was investigated to understand if all MONPs are similarly sequestered and if cellular sequestration contributes to their toxicity.

6.5.1 Relevance of lysosomal dissolution on toxicity

Based on a BafA1 dose-range finding experiment (**Figure 6-1A**), FE1 cells were particularly sensitive to v-type ATPase inhibition, responding with decreased relative

survival noticeable from 5 nM to ~ 60% reduction in relative survival at 100 nM BafA1 as compared to the blank media treated controls. Studies using human lung epithelial cells have shown that in A549 and BEAS-2B cells, up to 24 h of exposure to concentrations as high as 100 – 200 nM BafA1 have no impact on cell viability (Miyayama & Matsuoka, 2016; Strauch et al., 2020). At the low concentration of 5 nM BafA1 in FE1 cells, destabilization of lysosomes was already noticeable (**Figure 6-1B**), suggesting that FE1 cells are particularly sensitive to inhibition of lysosomal acidification. The high sensitivity of cells to BafA1 resulted in incomplete inhibition of lysosomal acidification, which may have contributed to the subtle changes in toxicity observed following co-exposures to BafA1 and particles.

From the 4 MONPs assessed (CuO, NiO, Al_2O_3, and TiO_2) which vary in their intracellular and extracellular solubility, lysosomal dissolution over 24 h only contributed to the toxicity induced by CuO NPs (**Figure 6-2**, **Figure 6-3**). In cells co-exposed with BafA1 and CuO NPs, cytotoxicity was modestly reduced, which was not observed after $CuCl_2$-BafA1 co-exposure (**Figure 6-2**). When FE1 cells were treated with 25 µg/mL CuO NPs, lysosomal instability was noted, which was marked by decreased point focal LysoTracker Red staining (**Figure 6-3**). A similar trend in toxicity but more pronounced protection against reductions in cell number was observed following 24 h co-exposure with CuO NPs or $CuCl_2$ and 100 nM BafA1 in BEAS-2B cells (Strauch et al., 2020). In another study, a concentration-dependent reduction in LysoTracker staining was reported in A549 lung cells exposed to CuO NPs for 3 - 6 h (Moschini et al., 2013). The modest improvement in relative survival in FE1 cells co-exposed to CuO NPs and BafA1 compared to other studies using human cells is due to the higher sensitivity of FE1 cells to BafA1 treatment, which limited the use of high BafA1 concentrations that are required to completely inhibit the acidification of lysosomes. Together, these results indicate a role for lysosomal sequestration and consequent lysosomal dissolution of CuO NPs in the toxicity observed in lung cells.

Conversely, insoluble or poorly soluble TiO_2, Al_2O_3, and NiO MONPs, and Mitsui-7 MWCNTs showed an increased loss in relative survival when co-treated with BafA1, with indications of an additive response between the MONPs and the inhibitor (**Figure 6-2**). For

TiO_2 NPs, this response was expected, as they are shown to be insoluble and stable in lysosomal media (Wall et al., 2021). With respect to Al_2O_3 NPs, while increased dissolution in acidic environments compared to neutral media has been reported (Holmfred et al., 2022), dissolved Al is unstable and forms precipitates in the presence of biomolecules found in cell culture medium (Helmig et al., 2018). NiO NPs have been shown to dissolve in cell culture medium and under acidic environments (Avramescu et al., 2020; Shinohara et al., 2017), with their dissolved form stable in the presence of bioligands. However, the results showed higher cytotoxicity in cells co-exposed to NiO NPs and BafA1. In addition to inhibiting lysosomal acidification, BafA1 is also known to block autophagic flux by inhibiting the fusion of autophagosomes and lysosomes (Mauvezin et al., 2015). At present, it is not possible to inhibit lysosomal acidification without also affecting autophagy in some capacity. With respect to NiO NPs, experiments in HeLa cells identified a protective role for autophagy in NiO NP mediated cytotoxicity (Cho, Y. et al., 2020). Thus, a lack of protection against cellular toxicity in the absence of lysosomal dissolution may be due to decreased autophagic flux. Finally for Mitsui-7 MWCNTs, BafA1 co-exposure resulted in the same level of toxicity as BafA1 alone, ~80% relative survival (**Figure 6-2**). MWCNTs in general are known to be stable in acidic conditions, however they may leach metal impurities into the surrounding microenvironment (Ge et al., 2012). Together, these results indicate lysosomal dissolution over a 24 h span does not contribute to the toxicity of Al_2O_3 NPs, nor does the acidic lysosomal lumen potentiate toxicity induced by TiO_2 NPs, while a more complex interaction may be occurring with respect to poorly soluble NiO NPs.

6.5.2 Localization of MONPs to lysosomes

ENMs in general are reported to be sequestered in lysosomes. To understand if differences in levels of MONP sequestration in lysosomes was responsible for differences observed in BafA1 co-exposures, EDF-HSI fluorescence microscopy was used to determine the degree of co-localization between MONPs and Lamp1, a lysosomal marker.

All tested MONPs showed some level of co-localization with Lamp1 (**Figure 6-5B**). 2D hyperspectral imaging and spectral mapping, along with 3D darkfield-fluorescence imaging confirmed the spectral signature of MONPs colocalizing with Lamp1 signal for

each particle (**Figure 6-5C,D**, **Supplementary Figure 6-3**), with a much higher likelihood of co-localization after TiO_2 NP exposure as compared to CuO, NiO, and Al_2O_3 NPs (**Table 6-3**). As compared to the other MONPs, it is clear that TiO_2 NPs present many more small, visible aggregates with large parts of the field of view positively mapping with the spectral library for nano TiO_2 (**Figure 6-5C**, **Figure 6-6C**). There are a few possible explanations for this observation. It is possible the scattering properties and consequently, the spectral profiles of CuO NPs, NiO NPs, and Al_2O_3 NPs, which have enhanced dissolution in acidic environments and which also showed some level of dissolution in cell culture medium, are modified due to interactions in lysosomes or the cellular medium. A shift in HSI spectral profiles was reported for polymer coated gold / copper sulfide particles suspended in media at different pH levels, relative to spectra in neutral pH media (Zamora-Perez et al., 2021). Similar high levels of co-localization has been observed between poorly soluble SiO_2 NPs and lysosomes in FE1 cells. SiO_2 NPs are also known to be stable in lysosomes as is seen for TiO_2 NPs (Wall et al., 2021; Yoo et al., 2021). Another explanation is that EDF-HSI analysis is not sensitive enough to accurately detect all MONPs associated with lysosomes at the single cell level. EDF-HSI has been validated with traditional techniques, such as Raman microscopy and electron microscopy, for its ability to detect metal oxides in tissue (Peña et al., 2016), and has been used in conjunction with automated detection algorithms for highly sensitive and specific detection of nano gold in mice tissues following injection (SoRelle et al., 2016). However, at a single cell level, similar validation has not been carried out. Therefore, the co-localization seen should not be taken to represent the full breadth of association between Lamp1 and MONPs.

6.5.3 Localization of MONPs to F-actin aggregates

In order to understand if different ENM are sequestered or trafficked differently, impacting their intracellular localization and dissolution, the F-actin cytoskeleton was stained with Phalloidin post-exposure to CuO, NiO, Al_2O_3, and TiO_2 MONPs (Sousa De Almeida et al., 2021).

Based on EDF-HSI fluorescence summarized in **Figure 6-6** and 3D deconvolution of Z-stacks in **Supplementary Figure 6-5**, it can be seen that all MONPs traffic to and co-

localize with bright actin aggregates that appear both within and above the focal plane of the cells (**Figure 6-5**). These aggregates appear infrequently, with most cells featuring between 1 – 3, and with sizes in the range of what is seen for cytoplasmic inclusions visualized through phase contrast imaging (**Supplementary Figure 6-4**). A mechanism for the formation of actin-lipid cauliflowers with similar characteristics has been described both *in vivo* in mice, and *in vitro* in mouse LA-4 cells after exposure to MONPs (Kokot et al., 2020). In this mechanism, endocytosed MONPs interact with lipid molecules inside pulmonary epithelial cells to make an initial aggregate, that is then coated in actin and exocytosed out of the cell, decorating the plasma membrane in ENM-actin-lipid structures. In the present study involving FE1 cells, bright F-actin aggregates were seen in MONP treated cells as well as in cells treated with blank media (**Figure 6-6**), suggesting that these structures represent a physiological process for sequestering particles. FE1 lung epithelial cells have been described as having both type I and II alveolar epithelial characteristics, with distinct subcellular inclusions visible under phase contrast (White et al., 2003). Based on the phenotype of FE1 cells, it is possible these aggregates represent a subtype of lamellar body or secretory vesicles, which may be produced in type II alveolar epithelial cells and are responsible for surfactant secretion in the lung. They are characterized by an acidic microenvironment with large concentrations of phospholipids (Dietl & Frick, 2021). Subtypes of actin-coated lamellar bodies have been characterized in rat lung cells, however they are smaller in size and more abundant than the actin aggregates seen here (Van Weeren et al., 2004). Further work is necessary to fully characterize these structures in FE1 cells, however based on the results shown here, these inclusions naturally present in the cytoplasm may act to sequester particles upon their uptake in addition to lysosomes.

6.5.4 Differential effects of soluble CuO and negligibly soluble TiO_2 NPs on lysosomes and cytoskeleton structure

In order to understand the effects of cellular sequestration of particles on cytoskeletal structures and lysosome dynamics, FE1 cells were exposed to high concentrations of soluble CuO NPs or insoluble TiO_2 NPs shown to induce a cytotoxic

response *in vitro* (Boyadzhiev et al., 2021, 2023). Mitsui-7 MWCNTs were included as a non-MONP and non-particle contrast (**Figure 6-7**, **Figure 6-8**).

Changes in Lamp1 abundance or distribution was not seen for any ENM (**Figure 6-7**). While 20 µg/mL CuO NPs have been shown to result in increased Lamp1 staining in human endothelial cells following 24 h of exposure (Zhang, Jun et al., 2018), it is possible the response takes longer to manifest in FE1 cells. With respect to TiO_2 NPs, studies have reported an increase in lysosomal membrane permeabilization after 72 h of incubation and that long term exposure to TiO_2 NPs leads to a blockage in autophagic flux (Popp et al., 2018). While clear evidence for changes to lysosome dynamics via Lamp1 staining was not observed in the present study, transcriptional responses in FE1 cells post-exposure to CuO or TiO_2 NPs showed enrichment and activation of the 'Autophagy' and 'CLEAR Signaling Pathway' canonical pathways at 24 h, at the same concentrations tested here ((Boyadzhiev et al., 2023) **Supplementary File 3-2**, **3-5**), with CuO NPs inducing the buildup of vesicles within the cytoplasm after 48 h of exposure (Boyadzhiev et al., 2021). Together, these responses indicate that transcriptomic changes in response to MONPs are a sensitive indicator of lysosomal disturbances, which manifest prior to apical changes in Lamp1 abundance or distribution and that the post-exposure sampling time used in the study may need further optimization for capturing the manifested events. Similar associations can also be made between the differential effects seen on the cytoskeleton.

Both CuO NPs and TiO_2 NPs were also observed to induce disturbances in F-actin and α-tubulin organization at high concentrations (**Figure 6-8**). The large holes in the α-tubulin cytoskeleton in cells exposed to CuO NPs may indicate an indirect result of its toxicity, whereas the holes in the F-actin cytoskeleton could simply be due to optical occlusion from a dense particle cluster directly over top of the actin cytoskeleton, as the hole was the same size as the particle cluster. At the concentrations tested in this study, TiO_2 NPs and not CuO NPs, enriched multiple actin related pathways at 48 h ((Boyadzhiev et al., 2023), **Supplementary File 3-2**, **3-5**). These were the 'Regulation of Actin-based Motility by Rho', 'Actin Cytoskeleton Signaling', and 'Actin Nucleation by ARP-WASP Complex' canonical pathways, which were enriched at 25, 50, and 100 µg/mL with a concentration-

dependent increase in the number of differentially expressed genes in each pathway. No tubulin related pathways were available in the Ingenuity Pathway Analysis database as of 2023, precluding this specific comparison. Disorganization of actin was associated with the endocytic uptake of TiO_2 NPs in H9c2 cardiomyoblasts (Huerta-García et al., 2019). Furthermore, disorganization and disruption of both actin and tubulin networks has been seen in SaOS-2 osteoblast-like cells (Ibrahim et al., 2018), and more recently in A549 lung epithelial cells (Déciga-Alcaraz et al., 2020) exposed for 24 h to TiO_2 NPs. While the mechanism behind this interference is not fully understood, evidence suggests TiO_2 NPs can directly bind to microtubules and induce conformational changes that decrease tubulin polymerization (Gheshlaghi et al., 2008). It is possible a similar physical mechanism may be at play with respect to F-actin destabilization. Overall, the results of this study indicate insoluble TiO_2 NPs, but not soluble CuO NPs, can impair the stability or polymerization of both actin and tubulin.

In comparison to MONPs, Mitsui-7 MWCNTs did not induce noticeable changes in Lamp1 mobilization, or F-actin and α-tubulin cytoskeletal structure (**Figure 6-7D**, **Figure 6-8D**). However, Mitsui-7 fibers were observed interacting with the mitotic spindle in dividing cells, and fiber-laden bi-nucleated cells were observed lacking actin stress fibers (**Figure 6-7E, Figure 6-8E**). Transcriptional response characterization in FE1 cells exposed to 100 µg/mL Mitsui-7 MWCNTs showed that the GO biological process 'extra cellular matrix organization [GO: 30198]' and 'cell cycle arrest [GO:7050]' were uniquely enriched at this concentration, along with 'regulation of cell proliferation [GO: 42127]' (Søs Poulsen et al., 2013). Exposure to Mitsui-7 MWCNTs induced aneuploidy and cell cycle arrest in BEAS-2B lung epithelial cells, with MWCNTs surrounding and even penetrating the cell nuclei (Siegrist et al., 2019). These results indicate that cellular interaction with MONPs vs MWCNTs is different and that ENM aspect ratio and size may influence their toxicity in addition to their solubility behavior.

6.6 Conclusion

Our previous investigations have identified differential impacts of solubility on the toxicity of MONPs and shown that extracellular solubility is not sufficient to explain their toxicity potential. In this study, the relevance of lysosomal acidification and cellular localisation on acute toxicity induced by CuO, Al_2O_3, NiO, and TiO_2 NPs of varying solubility was investigated. All MONPs were found to co-localize with the Lamp1 lysosomal marker, with insoluble TiO_2 NPs which are stable in neutral and acidic environments showing the greatest co-localization potential. Furthermore, only soluble CuO NPs showed an improvement in relative survival after inhibition of lysosomal acidification, implying that for MONPs with lower solubility potential, such as NiO and Al_2O_3 NPs, intracellular dissolution does not contribute to cytotoxicity for up to 24 h of exposure. At 24 h, 50 µg/mL insoluble TiO_2 NPs impacted the stability of F-actin and α-tubulin cytoskeletons. Mitsui-7 MWCNT which were included as a non-metal oxide, non-particle ENM showed no effects on cytoskeleton structure, but were notably present inside binucleated cells and associated with the mitotic spindle in dividing cells. Thus, the results suggest that cellular localisation, uptake and intracellular dissolution impact ENM's potential to induce toxicity but to different extents and via dissimilar mechanisms.

7 Chapter 7: Applicability of *in vitro* Mouse Lung Epithelial Cell Responses for Potency Grouping and Hazard Identification of Metal Oxide Nanoparticles: Impact of Form, Size, Surface Area, and Solubility on Toxicity

In preparation: Manuscript in preparation

Authorship: Andrey Boyadzhiev[1,2], Callum Christ[1,2], Andrew Williams[1,2], Sabina Halappanvar[1,2]

Affiliation:
1: Environmental Health Science and Research Bureau, Health Canada, Ottawa, Canada
2: Department of Biology, University of Ottawa, Ottawa, ON K1N6N5, Canada

Methodology.....	**Andrey Boyadzhiev** Sabina Halappanavar
Generation of Viability and Transcriptomics Data.....	Callum Christ
Benchmark Concentration Modelling.....	**Andrey Boyadzhiev** Andrew Williams (Transcriptomics)
Other Statistics (Clustering, PCA, Correlation).....	**Andrey Boyadzhiev**
Data Interpretation.....	**Andrey Boyadzhiev** Sabina Halappanavar
Manuscript Writing and Revisions.....	**Andrey Boyadzhiev** Sabina Halappanavar

7.1 Abstract

Human health risk assessment of engineered nanomaterials (ENM; materials with any dimension or structure between 1 – 100 nm) is challenged by the large number of compounds requiring assessment and the intricate association between physicochemical properties and toxicity. Over the course of this thesis, high-content and high-throughput NAM-based *in vitro* assays were applied to investigate the impact of dissolution on the toxicity of metal oxide nanoparticles (MONPs). In this chapter, the data from viability (viable cells / cm^2), transcriptomic induction (based on response through the 'HIF1α Signaling' pathway), and genotoxicity (DNA strand break and MN induction) endpoints were combined and used to conduct a potency grouping and hazard identification exercise of 18 compounds (MONPs, their dissolved equivalents, and bulk microparticle analogues). Data from a recent thesis was combined with the data generated as part of Chapters 2-5 to better inform the impact of form, solubility, size, and surface area on toxicity. Benchmark concentration modeling was performed across a range of benchmark responses (BMRs), followed by hierarchical clustering to facilitate potency grouping and hazard identification. Correlations between endpoints used for potency grouping, and between endpoints and primary particle size, specific surface area, and solubility in cell culture medium across all BMRs were determined. Instantaneously dissolving zinc oxide (ZnO) NPs presented similar potency to dissolved zinc and ZnO MPs, while aluminum oxide, iron oxide, and titanium dioxide NPs showed low potency. Thus, these particles were considered low priority for further testing. Copper oxide, nickel oxide and manganese dioxide NPs exhibited distinct potency and hazards compared to their dissolved or MPs forms, suggesting these particles warrant further assessment. Material solubility and the specific form of MOs were associated with endpoint potency. These results demonstrate the applicability of *in vitro* NAMs-based potency screening for first-tier assessment of MONP-induced acute toxicity.

7.2 Introduction

Risk assessment of ENM (engineered nanomaterials; defined as any compound with at least 1 dimension or structure within 1 – 100 nm (ISO, 2023)) is a challenge facing regulatory agencies worldwide. Due to the intrinsic relationship between toxicity and the

physicochemical properties of ENM, risk assessment activities must currently proceed on a case-by-case basis which is impractical considering the many diverse types of ENM currently available on global markets and the rate at which new ENM are synthesized. Furthermore, traditional animal testing approaches are time and cost intensive, presenting practical problems considering the number of compounds requiring assessment.

A paradigm shift is currently underway in the global approach to chemical safety testing and risk assessment, to move away from animal based testing and towards next generation new approach methodologies (NAMs) (ECHA, 2016a; EPA, 2018). NAMs are defined as technologies, methods, and approaches that provide meaningful information useful for risk assessment activities while avoiding the use of animals (ECHA, 2016a; EPA, 2018). These approaches include chemical based assays, targeted endpoint-specific *in vitro* assays, computational modelling approaches, and molecular bioassays which include omics technologies. NAM-based techniques are particularly well suited to the challenges facing human and environmental risk assessment of ENMs, as the first or second levels in tiered testing strategy frameworks for hazard identification, and prioritization (Doak, S. H. et al., 2022; Hristozov et al., 2024). At present, NAM-based data are not regularly used in formal regulatory decision-making, as most NAMs lack regulatory validation. However, *in vitro* NAM-based data can still be effective in identifying underlying toxicity mechanisms of ENM, as a means of comparing the toxicity mechanisms of different ENM, and as a first-tier testing approach to evaluate ENM-induced hazards.

In this chapter, I have used quantitative *in vitro* data that has been generated as part of my thesis to explore its relevance to regulatory decision making. **Specifically, my objectives were to utilize the data for 1) potency grouping of MONPs and their forms, and 2) for hazard identification to prioritize MONPs that may require further testing in more complex model systems.** Data from 7 *in vitro* endpoints and 18 compounds was used for this purpose; comprising 7 MONPs, and their dissolved, and microparticle equivalents. The compounds examined were zinc oxide (ZnO), copper oxide (CuO), nickel oxide (NiO), manganese oxide (MnO_2), aluminum oxide (Al_2O_3), iron oxide (Fe_2O_3), and titanium dioxide (TiO_2) nanoparticles (NPs) and microparticles (MPs), as well as zinc

chloride ($ZnCl_2$), nickel chloride ($NiCl_2$), aluminum chloride ($AlCl_3$), and manganese(II) sulfate ($MnSO_4$) dissolved metal analogues. A list of all datasets, endpoints, studies, and associated compounds is presented in **Table 7-1**.

Table 7-1. List of studies, compounds and endpoints used for hazard grouping. NPs: nanoparticles. MPs: microparticle.

Study (Chapter)	Compound	Endpoint (metric)
(Boyadzhiev et al., 2021) (Chapter 2)	CuO NPs, MPs	24, 48 h Transcriptomics
(Boyadzhiev et al., 2023) (Chapter 3)	ZnO NPs, MPs CuO NPs & MPs NiO NPs, MPs, $NiCl_2$ Al_2O_3 NPs, MPs, $AlCl_3$ TiO_2 NPs, MPs	24, 48 h Viability (viable cells/cm^2) 24, 48 h Transcriptomics
(Boyadzhiev et al., 2022) (Chapter 4)	ZnO NPs, MPs, $ZnCl_2$ CuO NPs, MPs TiO_2 NPs, MPs	2, 4 h Comet (% DNA in Tail)
(Solorio-Rodriguez et al., 2024) (Chapter 5)	ZnO NPs, MPs, $ZnCl_2$ CuO NPs, MPs NiO NPs, MPs, $NiCl_2$ Al_2O_3 NPs, MPs, $AlCl_3$ MnO_2 NPs, MPs, $MnSO_4$ Fe_2O_3 NPs, MPs TiO_2 NPs, MPs	2, 4 h Comet (% DNA in Tail) 40 h Micronucleus (% micronuclei)
(Christ, 2024)	MnO_2 NPs, MPs, $MnSO_4$ Fe_2O_3 NPs, MPs	24, 48 h Viability (viable cells /cm^2) 24, 48 h Transcriptomics

Associations between endpoints, and between endpoints and primary particle size (PPS), specific surface area (SSA), and solubility in cell culture medium were explored. The results of this chapter highlight the current benefits and limitations of using the existing *in vitro* data for risk-assessment prioritization and provide directions for future work.

7.3 Methods

7.3.1 Included datasets

In total, cellular responses to 18 compounds from 4 recently published manuscripts and a thesis were included in the analyses (**Table 7-1**). Information pertaining to the physicochemical properties of the particles as well as supplier information can be found in **Table 7-2**. Data for $CuCl_2$ was not included in the analysis as it was only investigated at one concentration transcriptionally (Boyadzhiev et al., 2021).

Table 7-2. Physicochemical properties and supplier information for the 18 compounds used for robust potency grouping. NP: nanoparticle. MP: microparticle. PPS: primary particle size. SSA: specific surface area. LxW: length x width. N/A: not applicable or not available.

Form	Compound	Supplier (Catalogue Number)	PPS Average (LxW; nm)[a]	Solubility 100 µg/mL (%)[b]	SSA (m^2/g)[c]
Dissolved	$ZnCl_2$	Sigma Aldrich (Z0152-100G)	N/A	N/A	N/A
	$MnSO_4 \cdot H_2O$	Sigma Aldrich (M7899)	N/A	N/A	N/A
	$NiCl_2 \cdot 6H_2O$	Sigma Aldrich (N6136-100G)	N/A	N/A	N/A
	$AlCl_3 \cdot 6H_2O$	Sigma Aldrich (A0718-500G)	N/A	N/A	N/A
Nanoparticle	ZnO NP	US Research Nanomaterials Inc (US3580)	21.65	19.30	27.27
	CuO NP	Sigma Aldrich (544868)	55.35	51.60	10.34
	MnO_2 NP	Sky Spring Nanomaterials Inc (4910DX)	24.59	3.87	42.16
	NiO NP	US Research Nanomaterials Inc (US3352)	24.57	1.81	36.60
	Al_2O_3 NP	Sigma Aldrich (544833)	17.30	0.73	145.29
	Fe_2O_3 NP	US Research Nanomaterials Inc (US3160)	22.04	N/A	44.88
	TiO_2 NP	NIST (1898)	23.80	0.05	52.73
Microparticle	ZnO MP	US Research Nanomaterials Inc (US1003M)	1000.00	11.80	5.85
	CuO MP	US Research Nanomaterials Inc (US1140M)	5000.00	1.17	0.80
	MnO_2 MP	Sky Spring Nanomaterials Inc (4930DX)	5000.00	1.37	2.55
	NiO MP	US Research Nanomaterials Inc (US1014M)	5000.00	0.07	2.52
	Al_2O_3 MP	Sky Spring Nanomaterials Inc (1331DL)	950.00	0.02	22.32
	Fe_2O_3 MP	US Research Nanomaterials Inc (US1139M)	5000.00	N/A	9.52
	TiO_2 MP	US Research Nanomaterials Inc (US1017M)	1500.00	0.02	10.76

[a] Average of length and width. Data from microparticles is manufacturer reported. Data for CuO NPs is taken from (Boyadzhiev et al. 2021). Data for ZnO and TiO_2 NPs is taken from (Boyadzhiev et al. 2022). Data for NiO and Al_2O_3 NPs is taken from (Boyadzhiev et al. 2023). Data for MnO_2 and Fe_2O_3 NPs is taken from (Solorio-Rodriguez et al. 2024). [b] Data for CuO, NiO, and TiO_2 particles is taken from (Avramescu et al. 2020). Data for ZnO, MnO_2, Al_2O_3, and Fe_2O_3 particles is from (Avramescu et al. 2022). [c] Data is taken from (Solorio-Rodriguez et al. 2024).

7.3.2 BMC modelling of apical endpoint data

The 24 and 48 h viability from (Boyadzhiev et al., 2021, 2023) and (Christ, 2024), in addition to 2 and 4 h comet and 40 h MN responses reported in (Boyadzhiev et al., 2022;

Solorio-Rodriguez et al., 2024) were used for benchmark concentration (BMC) modelling across a range of benchmark responses (BMR(s)). For viability (viable cells/cm^2), comet (% DNA in Tail), and MN (% MN) data, BMC modelling was conducted in PROAST Online (version 70.1) at a BMR of 5, 10, 25, and 50% relative risk. For viability and comet data which were collected at 2 different post-exposure timepoints, the timepoint was used as a covariate for each compound tested. The best model was chosen as the one with the lowest Akaike Information Criterion (AIC). If two or more models had identical AIC values, the model with the lowest BMC was chosen. All BMC values were normalized to μM of the constituent metal to allow for proper comparison between forms.

7.3.3 BMC modelling of transcriptomic data

Published datasets corresponding to GSE161017 and GSE246159, as well as transcriptomic data from (Christ, 2024) were used for BMC analysis. The $\log_2$-normalized fluorescence ratios from each sample and biological replicate were used, the Agilent probe IDs were annotated according to Gene Symbol, and then multiple transcript variants were collapsed down to one gene, taking the median response at each concentration for genes with more than one transcript variant. The data was imported into BMDExpress3.0 and a Williams Trend test was conducted to identify genes with a significant concentration-dependent response at 24 and 48 h. All genes which passed the trend test ($p < 0.05$), and with a maximum fold-change of at least 1.5-fold in either direction were used for BMC modelling with ToxicR averaging. The BMR in BMDExpress3.0 was set to 1.021, 1.349, 1.932, and 2.601 standard deviation which is equivalent to BMR5-50% extra risk. The best BMC according to the model average was chosen for each gene.

Instead of using BMC values from the entire gene expression profile, the data was trimmed to only include BMCs from 198 genes belonging to a specific pathway called the 'HIF1α Signaling' pathway. Signaling through this pathway was specifically chosen due to 1) its consistent expression across the tested MONPs, 2) its strong correlation with cell death in the FE1 model system, and 3) due to its association with stress responses relevant to the toxicity of MONPs (see section **3.5.2** for more information). The 198 genes corresponded to

the IPA content version 101138820 (Release Date: 2023-08-24). The median BMC across all concentration-responding genes in the pathway per sample was used as the transcriptional point of departure (tPOD) for that sample. Only those samples with a minimum of 3 genes showing concentration-response from this pathway were included in the analysis.

The initial BMC matrices were filtered to remove extreme outlier values resulting from imprecise BMC estimation. At BMR5 and 10, both 24 h viability BMC and MN BMC values were removed for MnO_2 NPs (8×10^{12} – 2.7×10^{-6} µM metal). At BMR25 four values were removed; with 24 h viability BMC for Al_2O_3 MPs and MnO_2 NPs (1.4×10^{5}, 8×10^{13} µM metal respectively), as well as 48 h viability BMC for Al_2O_3 MPs (1.4×10^{5} µM metal), and MN BMC for MnO_2 NPs (3.4×10^{-5} µM metal). Finally at BMR50, three values were removed including 24 h viability BMC for MnO_2 NPs and Al_2O_3 MPs (2×10^{14}, 2.4×10^{9} µM metal respectively) and 48 h viability BMC for Al_2O_3 MPs (2.4×10^{9} µM metal). No additional filtering was performed in order to keep as many original BMC values as possible for grouping purposes. The resulting BMC matrices were Winsorized in R to the 5^{th} / 95^{th} percentile, $\log_{10}$ transformed, scaled, and used for downstream analyses.

7.3.4 Potency grouping using hierarchical clustering with multiscale bootstrap resampling

Hierarchical clustering with multiscale bootstrapping was employed to identify significant clusters for each of the four BMR matrices within resulting dendrograms. For this the 'pvclust' package in R was used, with an nboot = 1000 and iterating the relative sample size of the bootstrap replications between 0.4 and 1.4x the original dataset size (along 0.1x increments). An approximately unbiased p-value >0.95 was used to identify statistically supported clusters. In order to account for different linkage and distance combinations which accentuate different relationships in the data with their own strengths and limitations, this clustering was conducted using Euclidean, Manhattan, and Minkowski distance measures using Complete, Average, Single, and Ward.D2 linkage for a total of 12 clustering attempts per BMR. Euclidean is considered straight line distance between samples, Manhattan can only travel in parallel directions to each axis (variable) but is less

influenced by outlier values. Minkowski distance is considered a generalized form of both the Euclidean and Manhattan distances, with calculated distance falling in the middle of the two measures. With regards to linkage, Ward.D2 is a variance maximization linkage measure that tends to produce circular clusters. Complete linkage determines similarity based on maximum distance across all variables, single linkage is based on minimum distance, and average linkage is based on average distance across the variables.

The best clustering attempt for each BMR was defined as the linkage-distance combination which resulted in the largest number of statistically supported clusters (approximately unbiased p >0.95). If multiple solutions resulted in the same number of statistically supported clusters, the solution with the least number of singletons (defined as a compound outside significant clusters) was selected as the best.

The presence of compounds in potency groups were tabulated across all attempts, with compounds appearing outside identified clusters treated as their own separate groups. The resulting cluster inclusion matrix was used to run a Jaccard similarity measure, which calculated the exact similarity (%) between different compounds based on significant hierarchical clustering. The resulting similarity matrices were used to identify groupings based on which compounds associate most frequently with each other across all attempts, with a value of 1 meaning samples always appear in the same significant cluster while a value of 0 means they never appear in the same significant cluster together.

7.3.5 Principle component analysis

Each filtered, winsorized, $\log_{10}$-transformed BMC matrix was used to conduct a principle component analysis (PCA) analysis in R using the 'prcomp' function (scale = TRUE). PCA is a commonly used dimensionality reduction procedure that can be used to more easily visualize high-dimensionality data while retaining important variance structure.

Endpoints were considered to significantly load onto PCs if the |loadings| >0.4 (Stevens, 2009). PCA biplots were created using the 'factoextra' plugin and the 'fviz_pca_biplot' function. Groups of compounds were highlighted on the biplots based on the clusters identified through 12 hierarchical clustering attempts at each BMR.

7.3.6 Correlation analyses between endpoints and physicochemical properties

The relationship between each of the 7 endpoints used for potency grouping were assessed through a Spearman's correlation analysis in R. For this purpose, BMC data across all BMRs was combined into one matrix and used as the input (n = 72). A correlation was considered significant if the $p < 0.05$. An association was considered negligible if $|r| < 0.3$, weak if $0.31 < |r| < 0.5$, moderate if $0.51 < |r| < 0.7$, strong if $0.71 < |r| < 0.9$, and very strong if $|r| > 0.91$ (Mukaka, 2012).

In order to determine relationships between endpoints and key physicochemical properties, the Kendall's Tau-b was used. This correlation test is specifically suited for handling ties in the data (Kendall, 1945), which are present when all BMC data across BMRs is combined with compound-specific physicochemical properties. For this purpose, 3 separate correlations were conducted. In the first, all samples were used (n = 72) along with a property called 'form'. This property defines whether the compound was a dissolved metal (form = 1), a nanoparticle (form = 2), or a microparticle (form = 3). In the second analysis, all dissolved metals were removed and PPS and SSA were included as physicochemical properties (n = 56). In the final comparison, all dissolved metals in addition to Fe_2O_3 NPs and MPs were removed and solubility at 100 µg/mL was included as a property (n = 48). Fe_2O_3 particles were not included as there was no quantifiable dissolution measured for these compounds past the 0 h timepoint (Avramescu et al., 2022). An association was considered significant if the $p < 0.05$. For simplicity, the strength of association was judged the same as for the Spearman's coefficient.

7.4 Results

7.4.1 Description of the four BMC matrices

BMC modelling was conducted across BMR5-50% and used to create the starting matrices for downstream clustering. Each starting matrix consisted of 104 computed BMC values expressed in µM of the constituent metal. After filtering and Winsorization to account for extreme outlier values resulting from imprecise BMC calculation, 88 calculated

BMCs remained for BMR5-10, 86 calculated BMCs remained for BMR25, and 87 calculated BMCs at BMR50 (**Supplementary Tables 7-1**, **7-2**, **7-3**, **7-4**).

Across the endpoints, 48 h viability was the most robust endpoint for modelling across all BMRs, with 1 BMCs replaced with the lower 5th percentile, 2 BMCs replaced with the upper 95th percentile at BMR5-25, and 3 BMCs replaced with the upper 95th percentile at BMR50.

In contrast, the 24 h 'HIF1α Signaling' tPOD was the least robust, with 7/18 compounds not having a BMC and replaced with the upper 95th percentile and 1 BMC replaced with the lower 5th percentile across at each BMR.

All filtered, winsorized, and $\log_{10}$ transformed BMC matrices were used for potency grouping at each BMR.

7.4.2 Potency grouping at each BMR

In the context of the hierarchical clustering, and subsequent grouping, a 'cluster' is taken to mean a statistically supported cluster identified during hierarchical clustering between 2 or more compounds. A 'group' is defined as a collection of 2 or more compounds, determined based on the likelihood of co-clustering during hierarchical clustering.

When 12 clustering attempts at each BMR are summarized and compared, some stable groups become evident which consistently arise across all clustering attempts (**Figure 7-1**). Across BMR5-50, 3-4 groups are formed.

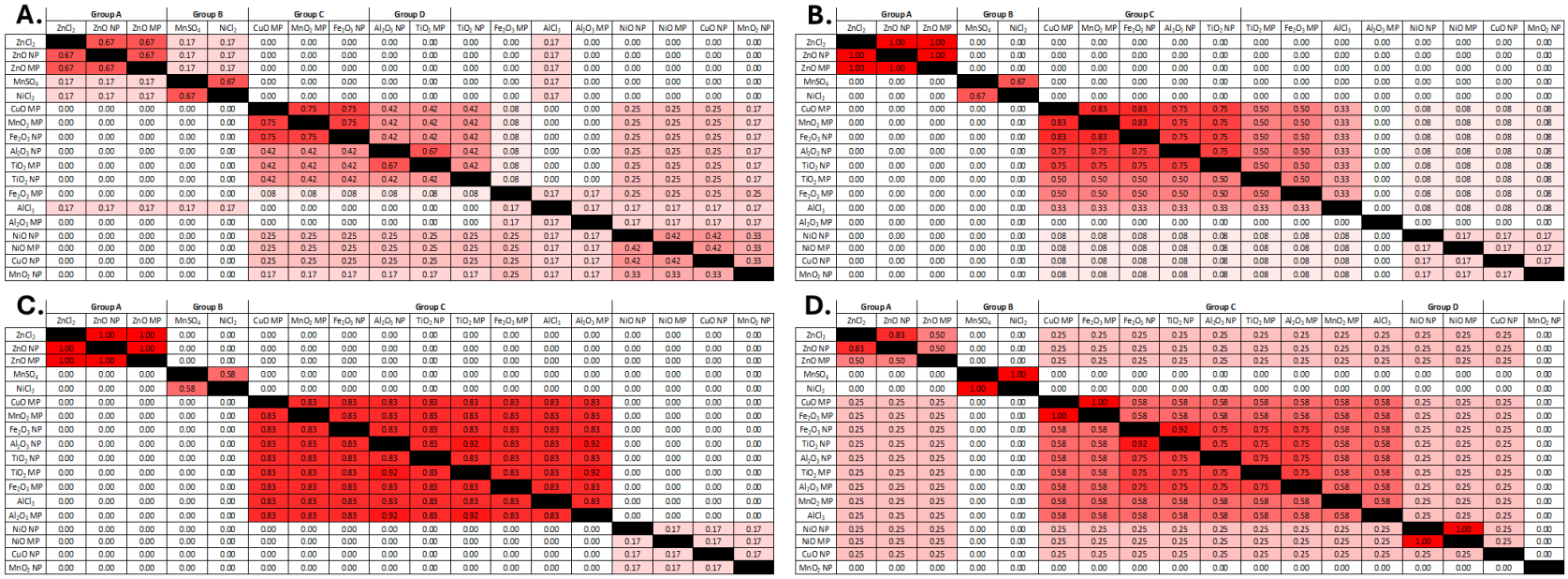

Figure 7-1. Jaccard similarity measures showing the likelihood of MONPs, MOMPs, and dissolved equivalents to cluster together based on potency across *in vitro* endpoints at a BMR of A) 5%, B) 10%, C) 25%, or D) 50%. Each matrix was constructed based on 12 hierarchical clustering attempts. Compounds were considered to group together if they appeared in the same statistically supported cluster >50% of the time. 1: substances always appear in the same statistically supported cluster. 0: substances never appear in the same statistically supported cluster. Red: higher likelihood of co-clustering. Black: non-applicable comparison. NP: nanoparticle. MP: microparticle.

Group ‘A’ was found to be relatively stable and composed of BMC responses for all Zn compounds between BMR5-25, and $ZnCl_2$ and ZnO NP at BMR50. All Zn compounds showed a 100% chance to co-cluster at BMR10-25. However at BMR50, ZnO MPs appear in the same statistically supported cluster as ZnO NPs and $ZnCl_2$ only 50% of the time.

Group ‘B’ is the most stable grouping, containing $MnSO_4$ and $NiCl_2$ with a 58 – 100% likelihood of co-clustering across all BMRs. Both dissolved equivalents show no association with any other compound, except at the lowest BMR of 5% where they co-cluster with $ZnCl_2$, ZnO NPs, ZnO MPs, and $AlCl_3$ 17% of the time.

Group ‘C’ made up of CuO MPs, MnO_2 MPs, and Fe_2O_3 NPs can be observed starting at BMR5, and continuing into BMR50, with additional compounds grouping alongside as the BMR increases. At BMR25 and 50, Al_2O_3 NPs & MPs, Fe_2O_3 NPs & MPs, TiO_2 NPs & MPs, MnO_2 MPs, and CuO MPs showed a high likelihood of appearing in the same statistically supported cluster. At BMR50, a subgrouping in Group ‘C’ is observed between TiO_2 NPs & MPs, Al_2O_3 NPs & MPs and Fe_2O_3 NPs with 75 – 92% likelihood of co-clustering. At this BMR, another subgrouping is also present which is composed of CuO MPs and Fe_2O_3 MPs which appear in the same statistically supported cluster 100% of the time.

Group ‘D’ appears only at BMR5 and BMR50. At BMR5, this group is composed of Al_2O_3 NPs and TiO_2 MPs which co-cluster 67% of the time. At BMR50, Group ‘D’ is composed of NiO NPs and MPs which co-cluster 100% of the time.

Interestingly, CuO NPs and MnO_2 NPs do not consistently or frequently co-cluster with any compound at any BMR (**Figure 7-1**). Nevertheless, if the best clustering solutions at each BMR are considered, it can be seen that CuO NPs and MnO_2 NPs frequently appear on the same branch as NiO NPs and MPs, just seldom in a significant manner (**Supplementary Figure 7-1**).

7.4.3 Visualization of groupings through PCA analysis

Based on the loading and variance analysis at each BMR (**Supplementary Table 7-5**), PC1 and PC2 explain between 70 – 91% of the variance in the system, which increases with increasing BMR. In all instances PC1 represents potency to induce decreases in viability and transcriptional signaling through the 'HIF1α Signaling' pathway at both 24 and 48 h, with these endpoints loading positively and significantly across all BMRs. Conversely, PC2 represents genotoxicity with both MN induction at 40 h and 2-4 h comet induction loading significantly and in the same direction across all BMRs, except BMR25. At BMR25, MN induction loading is still in the same direction as loadings for comet endpoints, but is under the 0.4 cutoff considered significant in this analysis (loading onto PC2 = 0.38). As the BMR increases, MN and comet endpoints load more strongly and in the same direction onto PC1 as viability and 'HIF1α Signaling' endpoints. Across BMRs, this information indicates separation along PC1 is indicative of potency to induce cell death and cell stress, and separation along PC2 is a general indicator of genotoxic potential. At higher BMRs (25-50), PC1 also starts to partially represent genotoxicity.

When the groups identified at each BMR are used to annotate the PCA biplots, it can be seen that as BMR increases, the samples become more separated and groupings identified through hierarchical clustering become more apparent, with BMR50 resulting in the greatest separation and delineation of groupings (**Figure 7-2**, **Supplementary Figure 7-2**, **7-3**, **7-4**).

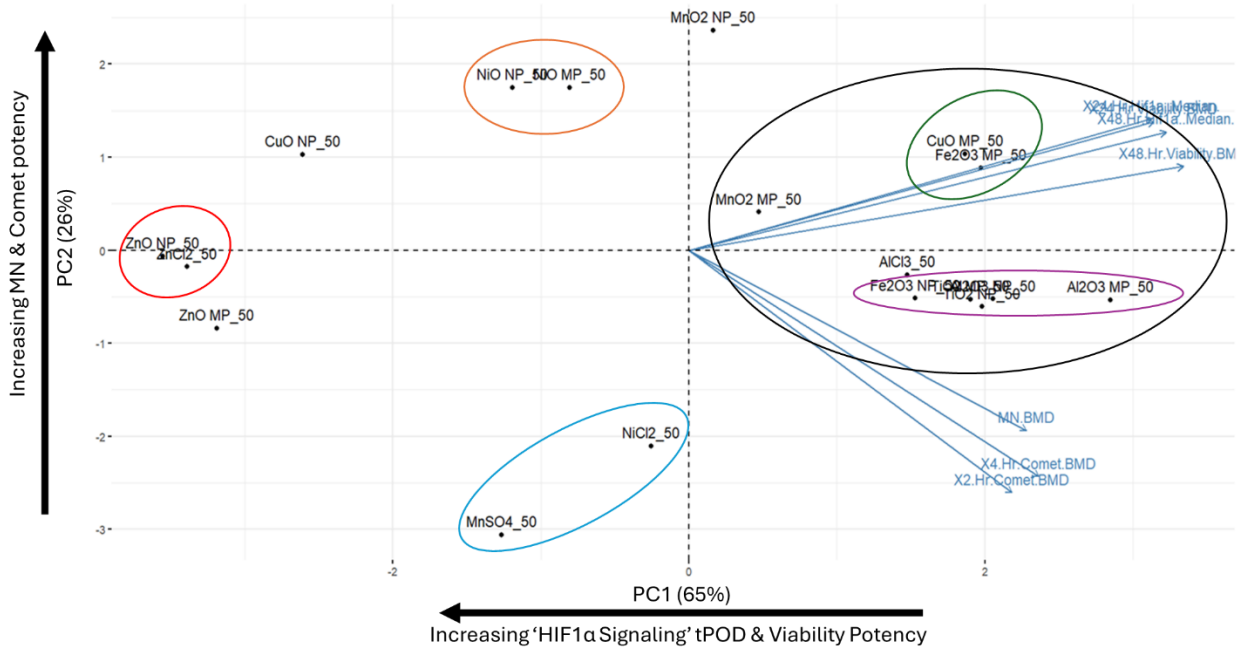

Figure 7-2. Biplot showing principle component 1 (PC1) and PC2 from principle component analysis (PCA) of the filtered, log_{10} transformed, and scaled BMR50 BMC matrix. Vectors indicate the direction of loading for each endpoint. Viability and 'Hif1α Signaling' endpoints load significantly and positively onto PC1. MN induction and comet endpoints load significantly and negatively onto PC2. Numbers in parentheses indicate the amount of variance explained by each PC. Colored circles indicate compounds likely to cluster together based on 12 hierarchical clustering attempts at BMR50.

Zn samples which appear as part of Group 'A' have highly negative values along PC1 and values around -1 to +1 along PC2 at all BMRs (**Figure 7-2**, **Supplementary Figure 7-2**, **7-3**, **7-4**). This indicates a moderate genotoxic potential, but a strong potency to induce cell death and cell stress regardless of the BMR chosen.

The consistent Group 'B' made up of $NiCl_2$ and $MnSO_4$ shows change in position on the PC1 and PC2 biplots across BMRs. At BMR5, both $NiCl_2$ and $MnSO_4$ have similar positions along the genotoxicity related PC2, while $MnSO_4$ has much more negative values along PC1 as compared to $NiCl_2$. These indicate a similar genotoxic potential, but stronger potency to induce cell death and cell stress from $MnSO_4$ as compared to $NiCl_2$. As the BMR increases, $MnSO_4$ becomes more separated along PC2 from $NiCl_2$, indicating a progressively weaker potency to induce genotoxicity as compared to $NiCl_2$. Furthermore, the relative potency to induce cell death and cell stress decreases as the BMRs increase,

with $MnSO_4$ presenting similar relative potency along PC1 as Zn samples at BMR5, whereas at BMR50 the position is similar to NiO NPs.

For the 9 compounds which make up Group 'C' at BMR25-50 (**Figure 7-1C**,**D**), they appear progressively closer together as BMR increases, with a range of negative values along PC1 and values along PC2 between +1 and -1 (**Figure 7-2**, black circle). Together this indicates a weak potential to induce cell death and cell stress, and a moderate but variable potency to induce genotoxicity.

For NiO NPs and MPs, which form Group 'D' at BMR50, it can be seen that they are in close proximity along PC1 and PC2 at all BMRs, but they get closer together as the BMR increases. Across all BMRs, NiO NPs present more negative values along PC1 than NiO MPs, indicating a relatively greater potential to induce cell stress and cell death from NPs as compared to MPs. For NiO NPs and MPs, they always present high values along PC2 indicative of strong genotoxic potency.

For MnO_2 NPs and CuO NPs which do not frequently cluster with any compound, they can both be seen in close proximity to NiO NPs and MPs at BMR5 (**Supplementary Figure 7-2**), however while MnO_2 NPs stay in relative proximity to NiO particles as BMRs increase, CuO NPs move progressively towards Zn samples presenting higher potential to induce cell death and cell stress at higher BMRs (**Supplementary Figure 7-3**, **7-4**, **Figure 7-2**). Both MnO_2 NPs and CuO NPs possess pronounced genotoxic potential based on their position along PC2, however CuO NPs have more negative values along PC1 whose magnitude increases as BMR increases. This indicates strong genotoxic potential for both CuO NPs and MnO_2 NPs, but a stronger potential to induce cell death and cell stress for CuO NPs which gets more pronounced as the BMR increases.

7.4.4 Potency grouping across BMR5-50: overall compound grouping

When statistically supported clusters across all 48 attempts from BMR5-50 are tabulated and a Jaccard similarity measure is conducted on the resulting matrix, it can be seen that overall 4 main groupings form (**Figure 7-3**). Group '1' includes all Zn substances, with ZnO NPs and $ZnCl_2$ slightly more likely to group together than with ZnO MPs. This group

appears at all BMRs. Group '2' includes dissolved $MnSO_4$ and $NiCl_2$, which also appears at all BMRs. Group '3' contains poorly soluble – insoluble Al_2O_3 NPs & MPs, TiO_2 NPs & MPs, Fe_2O_3 NPs & MPs, CuO MPs, and MnO_2 MPs. Finally, Group '4' includes NiO NPs and MPs.

	Group 1			Group 2		Group 3									Group 4			
	$ZnCl_2$	ZnO NP	ZnO MP	$MnSO_4$	$NiCl_2$	Fe_2O_3 MP	CuO MP	MnO_2 MP	Fe_2O_3 NP	Al_2O_3 NP	TiO_2 NP	TiO_2 MP	$AlCl_3$	Al_2O_3 MP	NiO NP	NiO MP	CuO NP	MnO_2 NP
$ZnCl_2$		0.88	0.79	0.04	0.04	0.06	0.06	0.06	0.06	0.06	0.06	0.06	0.10	0.06	0.06	0.06	0.06	0.00
ZnO NP	0.88		0.79	0.04	0.04	0.06	0.06	0.06	0.06	0.06	0.06	0.06	0.10	0.06	0.06	0.06	0.06	0.00
ZnO MP	0.79	0.79		0.04	0.04	0.06	0.06	0.06	0.06	0.06	0.06	0.06	0.10	0.06	0.06	0.06	0.06	0.00
$MnSO_4$	0.04	0.04	0.04		0.73	0.00	0.00	0.00	0.00	0.00	0.00	0.00	0.04	0.00	0.00	0.00	0.00	0.00
$NiCl_2$	0.04	0.04	0.04	0.73		0.00	0.00	0.00	0.00	0.00	0.00	0.00	0.04	0.00	0.00	0.00	0.00	0.00
Fe_2O_3 MP	0.06	0.06	0.06	0.00	0.00		0.60	0.50	0.50	0.50	0.50	0.50	0.48	0.40	0.15	0.15	0.15	0.08
CuO MP	0.06	0.06	0.06	0.00	0.00	0.60		0.75	0.75	0.65	0.65	0.58	0.44	0.35	0.15	0.15	0.15	0.06
MnO_2 MP	0.06	0.06	0.06	0.00	0.00	0.50	0.75		0.75	0.65	0.65	0.58	0.44	0.35	0.15	0.15	0.15	0.06
Fe_2O_3 NP	0.06	0.06	0.06	0.00	0.00	0.50	0.75	0.75		0.69	0.73	0.63	0.44	0.40	0.15	0.15	0.15	0.06
Al_2O_3 NP	0.06	0.06	0.06	0.00	0.00	0.50	0.65	0.65	0.69		0.69	0.71	0.44	0.42	0.15	0.15	0.15	0.06
TiO_2 NP	0.06	0.06	0.06	0.00	0.00	0.50	0.65	0.65	0.73	0.69		0.63	0.44	0.40	0.15	0.15	0.15	0.06
TiO_2 MP	0.06	0.06	0.06	0.00	0.00	0.50	0.58	0.58	0.63	0.71	0.63		0.44	0.42	0.15	0.15	0.15	0.06
$AlCl_3$	0.10	0.10	0.10	0.04	0.04	0.48	0.44	0.44	0.44	0.44	0.44	0.44		0.40	0.13	0.13	0.13	0.06
Al_2O_3 MP	0.06	0.06	0.06	0.00	0.00	0.40	0.35	0.35	0.40	0.42	0.40	0.42	0.40		0.10	0.10	0.10	0.04
NiO NP	0.06	0.06	0.06	0.00	0.00	0.15	0.15	0.15	0.15	0.15	0.15	0.15	0.13	0.10		0.44	0.25	0.17
NiO MP	0.06	0.06	0.06	0.00	0.00	0.15	0.15	0.15	0.15	0.15	0.15	0.15	0.13	0.10	0.44		0.25	0.17
CuO NP	0.06	0.06	0.06	0.00	0.00	0.15	0.15	0.15	0.15	0.15	0.15	0.15	0.13	0.10	0.25	0.25		0.17
MnO_2 NP	0.00	0.00	0.00	0.00	0.00	0.08	0.06	0.06	0.06	0.06	0.06	0.06	0.06	0.04	0.17	0.17	0.17	

Figure 7-3. Likelihood of MONPs, MPs, and dissolved metals to cluster together based on potency to induce 7 *in vitro* endpoints across all 48 clustering attempts from BMR5-50. 1: substances always appear in the same significant cluster. 0: substances never appear in the same significant cluster. Red: higher likelihood of appearing in the same cluster. Black: non-applicable comparison. 1-4: Potency clusters based on likelihood to appear in the same significant group across BMR5-50.

When BMCs across all BMRs are tabulated, and split-up according to the groupings formed, it can be seen that Group '1' with ZnO NPs, MPs, and $ZnCl_2$ has the most left shifted BMC distribution in terms of reduction in viable cell density and 'HIF1α Signaling' gene expression indicating it as the highest potency grouping overall with respect to these endpoints (**Figure 7-4**), but not so with respect to genotoxic potency (**Figure 7-5**). With respect to comet induction at both timepoints, Group '4' composed of NiO NPs and MPs, and also CuO NPs which appear alone, have the most left-shifted BMC distributions. With respect to MN induction, Group '1' as well as MnO_2 NPs have the most left-shifted distributions, however for both compounds the distribution is broad, indicating that potency decreases at higher BMRs. For MN induction, Group '2' has the most right-shifted distribution indicating dissolved Ni and Mn have the least potency at inducing clastogenicity / aneugenicity from the compounds tested.

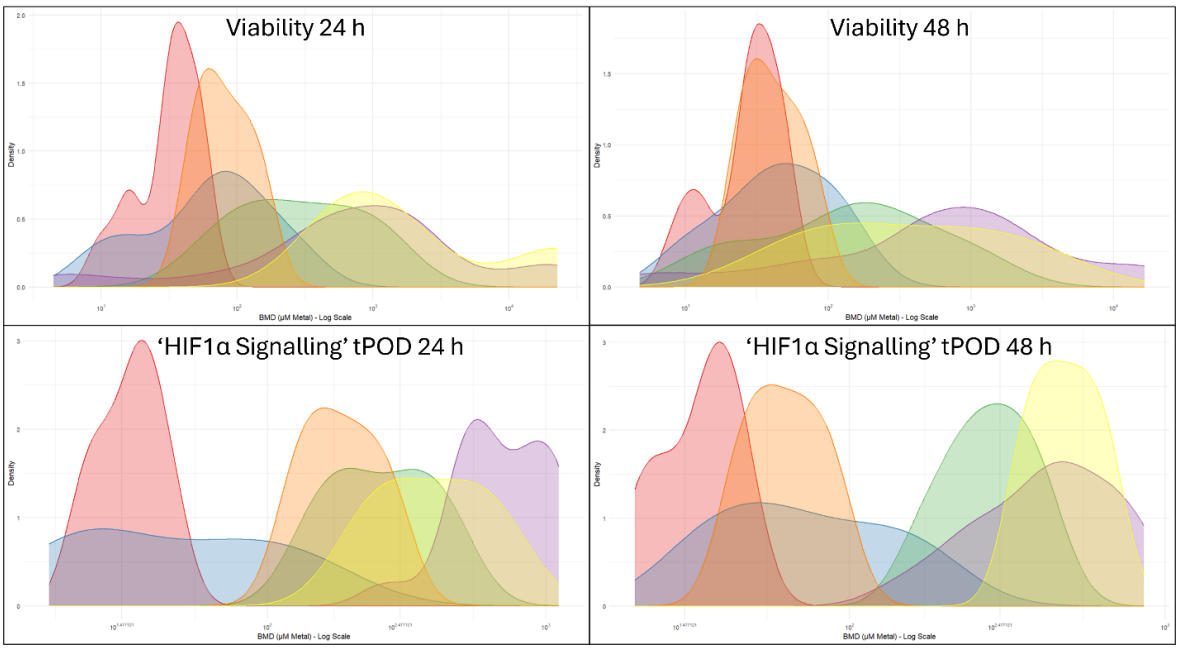

Figure 7-4. Density plots of the BMC distribution across BMR5-50 for 24 & 48 h viability reduction and 24 & 48 h transcriptomic induction for the 4 groups identified through hierarchical clustering. tPOD: transcriptomic point of departure. Red: Group '1' [$ZnCl_2$, ZnO NPs, ZnO MPs]. Blue: Group '2' [$MnSO_4$, $NiCl_2$]. Purple: Group '3' [Al_2O_3 NPs & MPs, $AlCl_3$, TiO_2 NPs & MPs, Fe_2O_3 NPs & MPs, CuO MPs, MnO_2 MPs]. Green: Group'4' [NiO NPs, NiO MPs]. Orange: CuO NPs. Yellow: MnO_2 NPs.

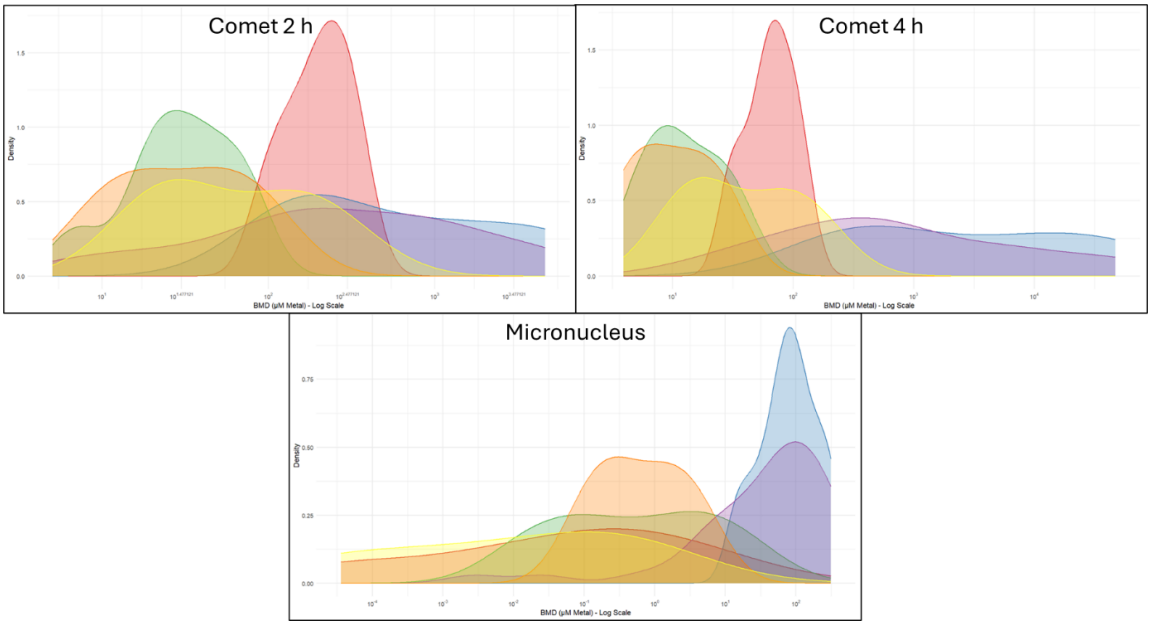

Figure 7-5. Density plots of the BMC distribution across BMR5-50 for 2 & 4 h comet and micronucleus genotoxicity endpoints for the 4 clusters identified through hierarchical clustering. Red: Cluster '1' [$ZnCl_2$, ZnO NPs, ZnO MPs]. Blue: Cluster '2' [$MnSO_4$, $NiCl_2$]. Green: Cluster '3' [NiO NPs, NiO MPs]. Purple: Cluster '4' [Al_2O_3 NPs & MPs, $AlCl_3$, TiO_2 NPs & MPs, Fe_2O_3 NPs & MPs, CuO MPs, MnO_2 MPs]. Orange: CuO NPs. Yellow: MnO_2 NPs.

7.4.5 Endpoint-endpoint and endpoint-property correlation analysis

As a final step, the Spearman's rank test and the Kendall's tau-b correlation test were utilized to assess the associations between endpoints used for potency grouping and hazard identification; and between endpoint potency and SSA, PPS, and solubility in cell culture medium respectively across all BMRs (**Figure 7-6**).

	Endpoint-Endpoint Spearmans Correlations (72)							Property-Endpoint Kendall's Tau-b Correlations			
	24 Hr Viability	48 Hr Viability	24 Hr Hif1α tPOD	48 Hr Hif1α tPOD	Micronucleus	2 Hr Comet	4 Hr Comet	Form (72)	PPS (56)	SSA (56)	Solubility (48)
24 Hr Viability		0.95	0.79	0.80	0.40	0.38	0.44	0.19			-0.30
48 Hr Viability	0.95		0.77	0.78	0.51	0.43	0.50	0.25			-0.37
24 Hr Hif1α tPOD	0.79	0.77		0.89	0.49	0.29	0.48	0.26			-0.55
48 Hr Hif1α tPOD	0.80	0.78	0.89		0.51	0.25	0.40	0.37			-0.44
Micronucleus	0.40	0.51	0.49	0.51		0.52	0.70				-0.58
2 Hr Comet	0.38	0.43	0.29	0.25	0.52		0.85				
4 Hr Comet	0.44	0.50	0.48	0.40	0.70	0.85					-0.39

Figure 7-6. Significant spearman's correlations between endpoints, and between endpoint potency and specific surface area (SSA), primary particle size (PPS), and % solubility. Blank cells designate a non-significant association. Black cells are non-applicable associations. An association was considered significant if the $p < 0.05$. Green: significant negative association. Red: Significant positive association.

All endpoints were positively correlated with each other. The genotoxicity endpoints were only weakly to moderately positively correlated with reduction in viable cell density and transcriptional 'HIF1α Signaling' induction, whereas MN induction and 4 h comet induction were more strongly associated.

With respect to physicochemical properties, PPS and SSA showed no association with respect to potency through the 7 endpoints. The property called 'form', which is an ordinal characteristic that describes whether a compound is a dissolved metal (1), an NP (2), or an MP (3), shows significant positive but negligible associations with viability reduction and 48 h 'HIF1α Signaling' potency. This association is weak with respect to 48 h 'HIF1α Signaling'. These associations indicate that reductions in viable cells and hypoxia signaling is lessened in MONPs and MOMPs as compared to fully dissolved metals when the concentration metric is normalized to the amount of constituent metal in the exposure medium.

Finally, solubility at 100 µg/mL is most strongly associated with endpoint response, showing weak to moderate significant negative associations between BMC in all endpoints

except for 2 h comet potency. This indicates that as particle solubility in the extracellular medium increases, BMC is expected to decrease and response to become more potent.

7.4.6 Hazard identification per group

Based on Spearman's correlations of endpoint-endpoint potency it was observed that potency at different timepoints for the same endpoint are strongly correlated. In order to make a positive or negative call for hazard identification, a cutoff must be made. For this purpose, the maximal response for each endpoint at the latest timepoint of assessment was used. For cell death (decreases in viable cell density), a cutoff of ≤66% viable cells remaining at the highest concentration (1.5-fold decrease in response over control) was used. For clastogenicity / aneugenicity assessed through MN induction, this was considered as a 2-fold increase at concentrations with ≥40% relative survival. For DNA strand break induction measured using the comet assay, this means >10% DNA in tail. Finally, for cell stress determined based on transcriptional response through the 'HIF1α Signaling' pathway, a positive call was made if at least 3 concentration-responsive genes were present per sample (**Table 7-3**).

Table 7-3. Hazards identified for each potency grouping determined through BMR5-50 clustering. Check mark indicates that compound is positive for that hazard category.

Group	Compound	Hazard			
		Cell Death	Cell Stress Signaling	DNA Strand Break Induction	Clastogenicity / Aneugenicity
1	$ZnCl_2$	✓	✓	✓	✓
	ZnO NP	✓	✓	✓	✓
	ZnO MP	✓	✓	✓	✓
2	$MnSO_4$	✓	✓		
	$NiCl_2$	✓	✓		
3	MnO_2 MP		✓	✓	✓
	CuO MP				✓
	Al_2O_3 NP		✓		✓
	$AlCl_3$		✓		✓
	Al_2O_3 MP				
	Fe_2O_3 NP		✓		
	Fe_2O_3 MP		✓		
	TiO_2 NP	✓	✓		
	TiO_2 MP				
4	NiO NP	✓	✓	✓	✓
	NiO MP	✓	✓	✓	✓
	CuO NP	✓	✓	✓	✓
	MnO_2 NP		✓	✓	✓

Group '1' containing Zn compounds is positive for all hazards identified, with the highest potency to induce cell death and cell stress signaling from all compounds. Group '2' containing dissolved $NiCl_2$ and $MnSO_4$ is positive for cell death and cell stress signaling hazards, but is negative for genotoxicity as measured through both endpoints. Group '4' containing NiO NPs and MPs is also positive for all hazards, with moderate potency to induce cell death and cell stress signaling, but the highest overall potency for DNA strand break induction. Group '3' containing 9 insoluble MONPs, MOMPs, and $AlCl_3$ is almost entirely negative for cell death and DNA strand break induction. However 6/9 compounds were positive for induction of cell stress signaling, although this drops to 2/9 if only the 24 h timepoint is considered (**Supplementary Table 7-4**). In Group '3', 4/9 compounds were positively identified for clastogenicity or aneugenicity based on a 2-fold increase in MN frequency without a reduction in relative survival <40% (Solorio-Rodriguez et al., 2024). Of

these samples, $AlCl_3$ presents a similar potency to CuO NPs and NiO NPs at BMR50 while the rest of the samples present moderate to low relative potency (**Supplementary Table 7-4**).

7.5 Discussion

In this chapter, the potency of MONPs and their forms to induce toxicity through quantitative endpoints in the FE1 lung epithelial cell model was used for 1) potency grouping of MONPs and their forms, and 2) for hazard identification to identify priority MONPs for additional downstream analysis in more complex model systems. Associations between endpoints, and between endpoints and physicochemical properties were explored. Through this exercise, several key observations were made regarding the impact of form (dissolved, MONP, MOMP) on toxicity, which can be used as weight-of-evidence to support grouping for risk assessment. The implications and limitations of the current data for ENM risk assessment activities, and directions for future work are discussed.

7.5.1 Endpoint potency is associated with form and MONP solubility

Primary particle size, specific surface area, and solubility are all properties considered important to the toxicity of MONPs. Based on potency across BMR5-50, only the form of the metal oxide, and solubility were significantly associated with endpoint potency (**Figure 7-6**). Form was positively correlated with reductions in viable cell density and gene expression through the 'HIF1α Signaling' pathway, but was not associated with genotoxicity endpoints. Based on this, overall dissolved equivalents were most potent in inducing cell death and cell stress signaling, followed by MONPs and then MOMPs. In addition, solubility was negatively correlated with response through all endpoints, except comet induction at 2 h, indicating that as metal oxide particle solubility in media increases, overall toxic potency increases. Since form (dissolved, MONP, MOMP) and particle solubility are associated with endpoint potency, MONPs can be prioritized for further assessment based on hazard and potency differences between the three forms assessed.

7.5.2 Potency grouping & hazard identification: MONPs with hazard akin to dissolved equivalent

Based on endpoint potency data from 18 total compounds (MONPs, MOMPs, and dissolved equivalents) there were two instances when the same *in vitro* hazard was seen for MONPs and their dissolved equivalents (**Table *7-3***). Those being highly soluble ZnO NPs, and surprisingly poorly soluble – insoluble Al_2O_3 NPs.

For highly soluble ZnO NPs which instantaneously dissolve, potency to induce all endpoints was similar to the dissolved equivalent. All three Zn compounds showed very high likelihood to group together across all BMRs. The human health risk assessment of ZnO by the EU identified the zinc cation as the determining factor for toxicity, with the caveat that the physicochemical properties of ZnO will affect toxicokinetics and bioavailability, and therefore have an impact on resulting toxicity (ECHA, 2004). In a more recent draft screening assessment by Health Canada and Environment and Climate Change Canada, ZnO was grouped alongside 75 zinc compounds for evaluation (ECCC & HC, 2019). The evaluation did not report specific hazards related to zinc inhalation other than the well characterized systemic immune response known as metal fume fever. It is important to note that this evaluation specifically did not include nano forms of Zn or ZnO. In human volunteers exposed to ZnO NPs and MPs via inhalation for 2 h, similar effects were seen between the two compounds with respect to induction of inflammatory markers in the blood, though slightly stronger effects were seen with the MPs as compared to NPs (Monsé et al., 2021). Based on the potency grouping exercise and hazard identification conducted in this chapter, the *in vitro* data generated provides support for read-across of zinc compound toxicity to that of uncoated ZnO NPs, based on both similar endpoint potency (**Figure 7-3**), ability to induce the same kinds of hazard (**Table *7-3***), and induction of similar transcriptional pathways (Boyadzhiev et al., 2023) for all three forms. While pronounced hazard was noted for ZnO NPs, the compound would not be recommended for further downstream testing due to the potential for read-across from existing zinc compounds.

On the other hand, Al_2O_3 NPs which present between 0.73 - 1.11% dissolution in cell culture media (Avramescu et al., 2022) presented similar low potency to Al_2O_3 MPs and $AlCl_3$ in FE1 cells for inducing reductions in viable cells, and comet responses at BMR50, but varied potency from BMR5-25. Since BMR50 is representative of what is considered a biologically significant *in vitro* response (1.5-fold increase), similarity in potency at this BMR was weighed more strongly than at lower BMRs. However, there was a difference with respect to the ability to induce both 'HIF1α Signaling' and MN responses across all BMRs, with $AlCl_3$ > Al_2O_3 NPs > Al_2O_3 MPs (**Supplementary Table 7-1**, **7-2**, **7-3**, **7-4**). When dissolved $AlCl_3$ is introduced into cell culture medium, insoluble precipitates are formed (Boyadzhiev et al., 2023; Helmig et al., 2018). Therefore, $AlCl_3$ behaves akin to a particle with a portion of dissolved aluminum, and not a fully dissolved equivalent in these exposures. The human health risk assessment of aluminum compounds makes note of the unstable nature of Al^{3+}, with its proclivity bind to carboxylate and phosphate groups, in addition to tyrosine residues (Krewski et al., 2007). To date, no direct comparisons between the solubility of Al_2O_3 NPs and MPs has been made in artificial lysosomal fluid (ALF), but it is known that Al_2O_3 NPs have a capacity to dissolve in ALF (Holmfred et al., 2022) and it is known that at the pH of lysosomes (4.5 – 5.0) Al^{3+} is the predominant form of dissolved Al present (Krewski et al., 2007). $AlCl_3$ was shown to have the highest potential to induce MN of the three forms (Solorio-Rodriguez et al., 2024), and $AlCl_3$ has been shown capable of binding to the phosphate groups in the DNA backbone and on the guanine site of G-C base pairs through chelation (Ahmad et al., 1996). Furthermore, $AlCl_3$ can lead to the cross-linking of chromosomes in Novikoff ascites hepatoma cells (Wedrychowski et al., 1986), and more recently has been shown to lead to chromosomal instability and clastogenicity in mammary epithelial cells (Mandriota et al., 2020). Despite these reports, aluminum compounds have not been shown to be carcinogenic in animal models (Krewski et al., 2007). I surmise that MN induction due to Al_2O_3 NPs is a result of intracellular particle dissolution releasing Al^{3+} ions which associate with the DNA in the nucleus or during mitosis, cause chromosomal cross-linking, and subsequent micronucleus formation. Increased potency for 'HIF1α Signaling' in $AlCl_3$ as compared to Al_2O_3 NPs and MPs is most likely to be due to

the presence of dissolved Al in the cell, which induced a mild concentration-dependent increase of 3-5 genes for $AlCl_3$ and Al_2O_3 NPs at 48 h, but not Al_2O_3 MPs (data not shown). Overall, based on comparisons with $AlCl_3$, and Al_2O_3 MPs and overall endpoint response, Al_2O_3 NPs are not expected to be acutely hazardous in the lung following inhalation and would not be prioritized for further testing based on the current screening results.

7.5.3 Potency grouping & hazard identification: MONPs with hazard akin to bulk forms

In total, there were 3 MONPs which showed the same *in vitro* hazard as their bulk forms (**Table *7-3***). These are poorly soluble – insoluble NiO NPs and MPs, which group together in Group '4' and are positive for all tested hazards; insoluble Fe_2O_3 NPs & MPs which group together in Group '3' and are positive only for cell stress signaling; and finally, poorly soluble MnO_2 NPs and MPs which appear in separate groupings but are positive for cell stress signaling, DNA strand break induction, and MN induction.

Both NiO NPs and MPs present a moderate potency to induce cell death and cell stress signaling through the 'HIF1α Signaling' pathway, but strong potency to induce genotoxicity through both DNA strand breaks and MN induction (**Supplementary Table 7-4**). In contrast, dissolved Ni in the form of $NiCl_2$ was more potent at inducing reductions in viable cell density and inducing cell stress signaling, but much less potent at inducing genotoxicity. A recent tier-2 human health screening assessment by the Australian government evaluated NiO and found that it merits classification as a category 1 skin sensitizer, pulmonary toxicant through repeated inhalation, and 1A carcinogen according to the GHS classification scheme (NICNAS, 2014). The carcinogenic potential of Ni compounds lies in their ability to induce epigenetic silencing and interfere with the functioning of cellular maintenance machinery, including DNA repair enzymes (Genchi et al., 2020; Hartwig et al., 2002). This is mainly believed to be the result of dissolved Ni, which is also the basis for dermal sensitization resulting from chronic skin exposure to Ni compounds. While NiO NPs exhibit poor-negligible solubility in cell culture medium (Avramescu et al., 2020), they dissolve better in artificial lysosomal media with decreased dissolution seen for larger particle sizes (Shinohara et al., 2017). The NiO MPs utilized as

analogues had a mean particle size of 5 µm as reported by the manufacturer, however scanning electron microscopy (SEM) imaging revealed the presence of a smaller size fraction of NiO which is in the nanoscale ((Boyadzhiev et al., 2023), **Supplementary Figure 3-2**). With this in mind, the similarities in NP and MP potency across the endpoints could be due to the uptake and intracellular dissolution of this nanoscale fraction. Although almost all endpoints were similarly induced by NiO NPs and MPs, NPs did present a much lower BMC for 48 h reduction in viable cell density as compared to NiO MPs at all tested BMRs (**Supplementary Table 7-1**, **7-2**, **7-3**, **7-4**). Overall, endpoint screening in the FE1 model identified positive calls for all endpoints for both the NPs and MPs, and would prioritize NiO NPs for further downstream testing. While both NiO NPs and MPs induce the same acute hazards, enhanced uptake and dissolution of the NPs could manifest in more pronounced pulmonary toxicity *in vivo*.

For Fe_2O_3 NPs and MPs which have negligible solubility in cell culture medium, a positive call was only seen for cell stress induction, and signaling was minor with 3-6 genes showing concentration dependent response at either timepoint (Data not shown). Fe_2O_3 NPs present weak cytotoxic and genotoxic potency and a weak ability to induce cell stress signaling through the 'HIF1α Signaling' pathway (**Supplementary Table 7-4**). They present similar potency as was seen for Fe_2O_3 MPs, with the greatest similarity seen at the largest BMR of 50%. Pronounced differences are only apparent once differential gene expression is examined. Exposure to Fe_2O_3 NPs results in substantially more differentially expressed genes (DEGs) and enriched pathways at the same concentration as their respective MPs (Christ, 2024). To date, no extensive human health risk assessment is available for Fe_2O_3, however research indicates a pulmonary hazard from inhalation exposure (EFSA Panel on Additives and Products or Substances used in Animal Feed (FEEDAP), 2016). Since Fe_2O_3 is a persistent particle with low solubility in both neutral and acidic pH environments, it can accumulate in the lung after inhalation. This leads to the development of an interstitial lung disease known as siderosis (Akar et al., 2018; Doğrul, 2017). With respect to Fe_2O_3 NPs, they have shown limited dissolution potential inside artificial lysosomal fluid based on work in a recent thesis (Cook, 2022), and analysis of DEGs induced by Fe_2O_3 NPs over a 48 h period

shows the induction of genes related to the transport of iron (Christ, 2024). Based on this, while Fe_2O_3 bulk particles can be considered insoluble and present a persistent particle hazard with low potential for acute pulmonary toxicity, Fe_2O_3 NPs may present an additional hazard related to dissolved iron ions in the lung due to dissolution within lysosomes. Endpoint screening in the FE1 system is insufficient to capture this effect, and both Fe_2O_3 NPs and MPs present low acute hazard across all endpoints. Based on these responses, Fe_2O_3 NPs would not be prioritized for further downstream testing.

The last MONP which presents the same hazard as their respective MPs based on *in vitro* screening is MnO_2 NPs. Both MnO_2 NPs and MPs induce cell stress signaling and genotoxicity through both endpoints with a weak ability to induce reductions in viable cell density (**Table 7-3**). At BMR50, MnO_2 NPs were more potent at inducing genotoxicity than MnO_2 MPs, while the MPs were more potent at inducing cell stress through the 'HIF1α Signaling' pathway. However, when the genes are examined MnO_2 NPs result in more concentration-responsive genes than MnO_2 MPs, even though the latter presents lower overall BMC (**Supplementary Table 7-1**, **7-2**, **7-3**, **7-4**). Manganese is an essential micronutrient, and like nickel, can result in stabilization of HIF1α (Li, Q. et al., 2006) and the induction of chemical hypoxia in exposed cells and tissues (Han, Jeongoh et al., 2009). The induction of cellular hypoxia is associated with oxidative stress, protein folding stress, and changes in metabolism from oxygen intensive processes like cellular respiration to glycolysis which results in mitochondrial dysfunction. The main target organ for Mn induced toxicity is the brain, where neurotoxicity manifests as the pathology known as manganism with similarities to Parkinson's syndrome (Racette, 2014). A human health risk assessment has been conducted for inhalation of manganese, which also included information pertaining to MnO_2 (Health Canada, 2010). Due to the target organ for toxicity being the brain, the assessment mainly focused on neurotoxic effects of manganese exposure, however mixed effects were reported for the cardiovascular system. As for the risk evaluation of zinc compounds, this evaluation did not specifically address manganese ENM or MnO_2 NPs. Exposure via inhalation to manganese compounds can result in dissolution in the lung, and systemic absorption of manganese which bypasses

homeostatic controls available when manganese is ingested. Solubility testing of MnO_2 NPs and MPs shows that both have poor solubility in cell culture medium, but that NPs present higher solubility than MPs at the same concentration (Avramescu et al., 2022). Furthermore incubation of MnO_2 NPs in ALF resulted in a 5-fold higher release of dissolved Mn as compared to cell culture medium (Avramescu et al., 2022). When this is taken in the context of endpoint potency in the FE1 model system, while the same hazards are induced by MnO_2 NPs and MPs, NPs present a greater genotoxic potency than the MPs which could be driven by intracellular MnO_2 dissolution and cellular manganese overload. Overall, *in vitro* endpoint screening identified the same hazards for both MnO_2 NPs and MPs, however MnO_2 NPs should be prioritized for further testing due to their enhanced potency (as determined based on different potency clustering for both compounds) and solubility as compared to the bulk compound, potentially allowing for more intense local effects in the lung and greater systemic absorption of dissolved manganese when inhaled.

7.5.4 Potency grouping & hazard identification: MONPs with distinct hazard

Finally, there were two MONPs which had distinct hazard calls as compared to their bulk and dissolved counterparts. First is TiO_2 NPs from Group '3', which present positive calls for cell death and cell stress signaling and whose MOMP analogue does not present any positive calls. Next is CuO NPs which cluster independently with positive calls in all hazard categories and whose MOMP analogue in Group '3' is only positive for clastogenicity / aneugenicity.

Based on hazard identification in FE1 cells, TiO_2 NPs present additional hazard compared to MPs, however both compounds appear in the same potency Group '3' (**Table 7-3**). Based on the potential to induce tumorigenesis in rats following inhalation, the International Agency for Research on Cander (IARC) classified TiO_2 as a class 2b carcinogen (IARC, 2010). More recently, the TiO_2 NP containing food-grade pigment E171 was banned from use in the EU due to concerns relating to immunotoxicity, genotoxicity, and potential neurotoxicity arising from the nano component (Younes et al., 2021). In Canada, a recent draft screening assessment of titanium compounds, which included TiO_2, concluded that there was a low risk for human and environmental harm and do not

meet the criteria for regulation, however it was stated that titanium ENM were not specifically considered (ECCC & HC, 2023). Genotoxicity screening in FE1 cells indicates no potential to induce strand breaks or micronuclei for the uncoated TiO_2 NPs tested here. At BMR50, TiO_2 NPs and MPs presented similar potency across all endpoints due to highly imprecise estimation of viability potency for TiO_2 NPs at this BMR (BMC = 66.21 – 720 µM Ti at BMR5 – 25, while BMC = 2712 – 5747 µM Ti at BMR50 for 24 and 48 h viability endpoints; **Supplementary Table 7-4**, data not shown), however from BMR5-25 TiO_2 NPs consistently presented higher potency for reductions in viable cells than TiO_2 MPs, as well as higher potency to induce cell stress signaling through the 'HIF1α Signaling' pathway (**Supplementary Table 7-1**, **7-2**, **7-3**). When transcriptomic responses are compared, TiO_2 NPs are shown to induce much more pronounced gene expression changes than MPs with respect to both DEG induction and pathway enrichment at the same concentrations ((Boyadzhiev et al., 2023), **Supplementary File 3-5**). TiO_2 MP and NPs tended to cluster separately based on canonical pathway enrichment, indicating differences in the types of pathways enriched, and their activation states ((Boyadzhiev et al., 2023), **Figure 3-4**). Based upon potency clustering and hazard identification in the FE1 model system, similar potency is seen for TiO_2 NPs and MPs in most endpoints, with no potential to induce primary genotoxicity from both compounds. However, TiO_2 NPs presented greater cytotoxicity and cell stress signaling, especially at 48 h, which could manifest in greater pro-inflammatory potential *in vivo*. Based on this, screening in the FE1 model system indicates low-level acute hazard potential in the lung, which would not prioritize it for further testing.

The final MONP with distinct *in vitro* hazard calls from its dissolved and bulk equivalents is CuO NPs. CuO NPs were positive for all hazards, and clustered by themselves away from all other compounds (**Table 7-3**), with high potency (**Figure 7-4**, **Figure 7-5**). In contrast, CuO MPs only presented a positive hazard call for clastogenicity / aneugenicity. While $CuCl_2$ was not included as part of this grouping and hazard identification exercise, it has positive cell death and negative genotoxicity calls based on maximum response through each of the endpoints (Boyadzhiev et al., 2023; Solorio-Rodriguez

et al., 2024). Solubility testing in cell culture medium showed pronounced differences between CuO NPs and MPs, with NPs being soluble while MPs are poorly soluble (Boyadzhiev et al., 2021). Testing in ALF shows that CuO NPs are highly soluble, indicating a rapid ability to dissolve when endocytosed (Chakraborty & Misra, 2019). In a 2008 human health risk assessment on copper containing substances, risk evaluators made note of the classification of copper-(I)-oxide and copper oxychloride as acutely hazardous following inhalation, however there was a specific derogation for CuO (copper-(II)-oxide) due to poor bioavailability and large particle size available at the time (ECHA, 2008). As compared to CuO MPs, it is clear that based on both potency grouping and hazard identification that CuO NPs present a distinct acute hazard from the bulk compound, with much higher solubility potential and greater bioavailability due to their small particle size. Based on acute hazard identification in the FE1 model system, greater potential for uptake and greater dissolution potential as compared to MPs, CuO NPs merit further downstream testing.

7.5.5 Limitations and future directions

Currently, *in vitro* validated NAMs with regulatory uptake that are relevant to ENM are rare, although there are many ongoing activities globally to develop and adapt regulatory testing guidelines and assays for ENM (Hristozov et al., 2024). In the absence of regulatory validation, *in vitro* endpoint data can still be used for tier-1 screening for organ-specific toxicity, as was conducted in this chapter. However, there are limitations which must be considered when using the data for this purpose.

The first limitation is that the data generated is only relevant for acute hazards induced by MONPs, and the genotoxicity screening can only detect primary (direct or indirect) genotoxicity. For persistent MONPs like TiO_2 or Fe_2O_3 NPs, chronic toxicity would be an important consideration, with the potential for secondary genotoxicity arising from chronic inflammation. To test for ENM-induced chronic effects, more complex models would be required that better capitulate the cellularity and architecture of the lung environment. One such NAM model is precision cut lung slices (PCLS), which can be cultured *ex vivo* for up to 7 days and have been used to develop a gene panel to predict the

pro-fibrotic effects of ENM (Rahman, L. et al., 2020). Although PCLS still uses animals to an extent, it represents a strong refinement over existing techniques which reduces the overall number of animals used.

Another limitation of the current data, is a lack of similar *in vivo* data on the same MONPs that can be used to assess the accuracy of the *in vitro* generated groupings and predictions. A similar paired exposure series was carried out as part of the EU led PLATOX project, where paired *in vitro* and *in vivo* exposures to graphene nanoplatelets and single layer graphene found that cytotoxicity and DNA strand break induction *in vitro* was predictive of genotoxicity and inflammation *in vivo* following 28 day inhalation, and that *in vitro* potency ranking matched what was seen *in vivo* (Creutzenberg et al., 2022). This type of paired exposure was also conducted with Mitsui-7 carbon nanotubes *in vitro* in FE1 cells and *in vivo* via intratracheal instillation in C57BL/6 mice (Søs Poulsen et al., 2013). Using transcriptomic analysis, similar pathways of inflammation and oxidative stress were found to be perturbed in both model systems, albeit with a different series of DEGs. A similar *in vitro – in vivo* paired exposure using a subset of the same MONPs, primary human lung epithelial cells, and inhalation in mice would provide valuable information concerning the accuracy of the groupings determined in the FE1 model. It would also provide empirical evidence of the association between *in vitro* endpoints and *in vivo* apical toxicity induction, and differences between signaling in mice and human cells. This would be crucial for the development of conversion factors which can be used to predict *in vivo* response for MONPs which have only been screened in the FE1 model. Furthermore, the use of signaling through the 'HIF1α Signaling' pathway as a biomarker of cell stress induced by MONPs can be further developed, identifying genes in common between *in vivo* and *in vitro* model systems that can be used as prognostic markers of toxicity.

7.6 Conclusion

In conclusion, in this chapter genotoxicity, viability, and transcriptomic endpoint data generated on 18 compounds (MONPs, MOMPs, and their dissolved equivalents) in the FE1 model system was used for a robust potency grouping and hazard identification

exercise. Solubility in cell culture medium was associated with potency in all measured endpoints, with increasing potency (decreasing BMC) seen as solubility increases. The form of the metal oxide was also associated with cell death and cell stress signaling, with dissolved metals showing higher potency overall for these endpoints, followed by NPs and MPs. In a first-tier screening approach which relied on the potency groupings and hazards identified for each of the forms tested; CuO NPs, NiO NPs, and MnO_2 NPs were prioritized for further downstream testing due to predicted acute pulmonary toxicity potential.

8 Chapter 8: Summary, Conclusions and Perspectives

The general purpose of this thesis was to systematically assess the impact of solubility on the toxicity of metal oxide nanoparticles (MONPs), using well characterized materials with similar physicochemical properties that can be used to answer the question of **"What is the relative contribution of particulate and dissolved fractions to MONP induced toxicity?"**. What follows is an empirical evaluation of the 4 guiding hypothesis of this thesis, followed by an in-depth summary of the objectives completed in Chapters 2-7 and the significant scientific contributions of each chapter; with a discourse on the perspectives the data provides to the field of nanotoxicology. This chapter finished with some conclusions and recommendations based on the main findings of this thesis.

8.1 Empirical Evaluation of Hypotheses

In this thesis, each chapter had a specific hypothesis (or hypotheses) relating to the impact of solubility on MONP toxicity, and the impact of the dissolved and particulate form on response. Not all hypotheses were supported by the generated data. What follows is a statement of each chapter hypothesis and the degree of support (or lack of support) provided by the generated data.

First Hypothesis (Chapters 2 and 3): Global transcriptional changes can be used to characterize mechanistic differences in response to MONPs, which can be plausibly linked back to their physicochemical properties.

Hypothesis Support: The results provide support for this hypothesis. In Chapter 2, detailed analysis of transcriptional pathways affected by CuO NPs, MP and copper chloride ($CuCl_2$) allowed for the construction of 3 comparative mode-of-action pathways that highlighted the differences in toxicity mechanisms between dissolved, bulk, and nano CuO. These corresponded to the known toxicity mechanisms of CuO NPs and provide support for this hypothesis. In Chapter 3, hierarchical clustering based on pathway directionality showed that MONPs and their forms create 4 main groups that represent the different response profiles seen. The composition of these groups highlights the form and time-dependent

differences in response profiles across the MONPs, while the in-depth pathway analysis (**Appendix II Chapter 3 Supplementary Document 1**) detailed the similarities and differences in enriched pathways between MONPs and between forms.

Second Hypothesis (Chapters 4 and 5): The ability of MONPs to induce genotoxicity is positively associated with their solubility in the extracellular space, i.e, the more soluble an MONP is, the more genotoxic it will be in the short term. MONPs of poor or negligible solubility are hypothesized to be weak inducers of micronuclei.

Hypothesis Support: The results provide support that acute genotoxicity increases as the solubility of the MONP increases, as solubility is correlated with both DNA strand break induction and micronucleus formation. However, the results do not support the hypothesis that poorly-negligibly soluble MONPs are weak inducers of micronuclei and instead provide evidence that the stability of the dissolved fraction is integral to chromosomal damage induced by MONPs which can dissolve in either acidic or neutral conditions.

Third Hypothesis (Chapter 6): Lysosomal acidification is hypothesized to drive the toxicity of MONPs soluble and poorly soluble in cell culture medium. MONPs are hypothesized to show high degrees of co-localization with lysosomes.

Hypothesis Support: Overall, the results of this chapter do not support the hypothesis that lysosomal dissolution drives the toxicity of both soluble and poorly soluble MONPs, at least in the short term. Only soluble CuO NPs featured recovery in the presence of an acidification inhibitor, and the recovery was not statistically significantly different from the no-inhibitor condition. While some localization to lysosomes was observed for all studied MONPs, the results also do not support the hypothesis that MONPs show high degrees of localization to lysosomes. The results do show that localization differences are seen based on MONP solubility, with insoluble MONPs showing the highest co-localization potential.

Fourth Hypothesis (Chapter 7): Induction of *in vitro* endpoint response can be used to group MONPs based on hazard potential, which can be used to prioritize high toxicity materials for further testing.

Hypothesis Support: The results from the analysis in Chapter 7 support this hypothesis. Through the use of BMC modelling and hierarchical clustering of endpoint potency, groupings were derived which relate to the mechanism of action of the materials. For example, nickel chloride ($NiCl_2$) and manganese sulfate ($MnSO_4$) tended to group together and both materials are known to induce a state of chemical hypoxia in cells. All Zn materials also grouped together, indicating an ion-mediated toxicity mechanism with high potential for acute toxicity for all forms. Finally, based on both potency and hazard differences, MONPs with unique response as compared to their bulk and dissolved counterparts were able to be identified and prioritized for downstream testing.

8.2 Scientific Significance

8.2.1 Transcriptomic Characterization (Chapters 2 and 3)

The objectives of Chapters 2 and 3 were to 1) compare and contrast transcriptomic responses and reductions in viability after exposure to MONPs of varying solubility in cell culture medium in order to define shared and distinct response mechanisms, and 2) to determine the impact of the dissolved fraction and nanoparticle size on acute toxicity induced by MONPs.

Scientific Significance: A thorough characterization of particle characteristics, as well as consistent and reproducible suspension procedures are needed in order to be able to accurately relate physicochemical properties to ENM response. The MONPs used in these two studies have been extensively characterized and have well developed sonication parameters that result in consistent suspension characteristics (Avramescu et al., 2019; Bushell et al., 2020). Furthermore, concentrations of dissolved metal equivalents were determined based on direct dissolution testing of the materials in question (NPs and MPs), in the medium used for exposure and therefore approximate the response to an extracellular dissolved proportion as accurately as possible. These studies represent one of the most thorough and systematic response characterization endeavors for MONPs to date, resulting in the production of over 5 million datapoints across the entire sample set. Furthermore, these results were used in the production of a putative (adverse outcome

pathway) for MONP induced cytotoxicity based on time-dependent changes in transcriptional response to CuO NP treatment, and also identified signaling through the 'HIF1α Signaling' pathway as a common response to all MONPs tested that can be used to distinguish acutely toxic particles. Differences in potency between fully dissolved metal equivalents and MONPs was dependent on the solubility of the MONP, however these studies show that solubility is insufficient by itself to account for differences in response between MONPs with similar solubility. In the context of regulation, signaling through the 'HIF1α Signaling' pathway represents a biomarker candidate that can be used as a rapid tier-1 screening tool to identify MONPs likely to result in acute pulmonary injury in the event of exposure, while simultaneously providing mechanistic information concerning the type of toxicity seen (oxidative stress, protein folding stress, hypoxia induction).

8.2.2 High-throughput Genotoxicity Screening (Chapters 4 and 5)

In the comparative mechanistic characterization as part of Chapter 3; ZnO, CuO, NiO, and TiO_2 NPs showed the potential to perturb DNA damage response pathways, indicating some level of genotoxic potential. In Chapters 4 and 5 the high-throughput versions of the comet assay (CometChip®), and the micronucleus assay (MicroFlow®) were applied as screening tools for the assessment of MONP induced DNA damage. The objectives in these chapters were to 1) screen the potential of MONPs with different solubilities in cellular medium to induce acute DNA strand breaks and large scale chromosomal damage, and 2) to assess the contribution of the dissolved species and particle size on MONP induced genotoxicity by using bulk analogues and dissolved metal equivalents for comparison.

Scientific Significance: Reliable HTS assays are needed to expeditiously assess ENM for both regulatory risk assessment in a tiered-testing approach, and also for mechanistic response analysis; due to the large variety of ENM needing risk assessment worldwide, as well as the intimate association between physicochemical properties and biological response, and even the interdependence between physicochemical properties. These studies represent one of the first attempts to conduct large scale high-throughput

screening of ENM induced genotoxicity and provide support for the use of the CometChip® and MicroFlow® assays for tier-1 *in vitro* testing of ENM. Furthermore, it was shown that the solubility of MONPs in neutral cellular environments is positively correlated with their ability to induce genotoxicity *in vitro* both in terms of strand breaks as measured by CometChip® and micronuclei as measured through MicroFlow®. With respect to solubility as a hazard grouping criterion in MONP risk assessment, results from these chapters further corroborate findings from Chapters 2 and 3 and indicate that solubility is insufficient to account for MONP toxicity by itself, with the stability of the dissolved form being another defining property governing their genotoxic potential.

8.2.3 Subcellular Localization and Lysosome-Mediated Toxicity (Chapter 6)

In Chapters 2 and 3, transcriptional response and cytotoxicity resulting from exposure to MONPs was related to both their solubility and their chemical composition, with the impact of the dissolved form dependent on the constituent metal. These effects were again seen with respect to their ability to induce genotoxicity in Chapters 4 and 5. For all MONPs except for ones which instantly dissolve with high solubility, trafficking to acidic lysosomes and dissolution or interaction within lysosomes is thought to mediate downstream toxicity, including genotoxicity. In Chapter 6, the objectives were to 1) assess the relevance of vesicular acidification on the toxicity of MONPs of varying solubility, 2) determine whether there are differences in lysosomal localization between MONPs based on solubility, and 3) to identify other putative compartments or structures MONPs may associate with in the FE1 cell model.

Scientific Significance: The rapid and accurate detection of ENM within tissues and exposed cells is a challenging task most commonly accomplished through laborious electron microscopy analysis. EDF-HSI has been shown to be an effective tool for rapid qualitative detection of ENM in a variety of matrices. This study utilized EDF-HSI with fluorescence microscopy to show, in three dimensions, that MONPs exhibit differing co-localization potential with lysosomes in FE1 cells depending on their solubility. Lysosomal co-localization was limited in many instances, with MONPs also localizing to bright staining actin aggregates which merits further examination. Inhibition of vesicular acidification

identified differential effects depending on the solubility of the MONP, indicating that dissolution or interaction in these acidic microenvironments is not crucial to the toxicity of all MONPs in the short term.

8.2.4 Grouping and Prioritization (Chapter 7)

In the previous chapters, the overall cellular response to MONPs and their forms was characterized (Chapters 2, 3), their ability to induce acute genotoxicity through two endpoints was screened (Chapters 4, 5), and their subcellular localization and role of endolysosomal particle dissolution was probed (Chapter 6). In Chapter 7, the concentration-response endpoint data was synthesized and used for a holistic potency grouping and prioritization exercise, combining viability and transcriptomic data from a recent thesis (Christ, 2024) to draw more informed conclusions concerning the impact of MONP solubility on cell toxicity and to explore the relevance of the data for regulatory risk assessment. Specifically, the objectives were to 1) use the generated high-content and high-throughput screening data for potency grouping of MONPs and their forms, and 2) conduct *in vitro* hazard identification and prioritization to identify MONPs for further downstream testing.

Significance: In the context of ENM regulation, the best case scenario is when read-across or grouping is possible; either between different ENM, or between ENM and their bulk or dissolved forms. When this is feasible and valid, no additional testing is required to come to a conclusion on hazard. So far, no regulatory risk assessments have been published that specifically address MONPs, although regulatory guidance and frameworks have been made available in recent years and this is expected to change in the near future. In this chapter, evidence was presented in support of read-across for instantaneously dissolving ZnO NPs with high solubility in cell culture medium based on known hazards for dissolved Zn. While this would not cover all forms of ZnO, it would be relevant for any ZnO NP which features similar solubility and dissolution rate and provides a basis to group all such Zn materials together in the context of human health hazard. In contrast, CuO, MnO_2, and NiO MONPs were identified as possessing additional hazard, or enhanced potency compared to their dissolved or MP equivalents which when taken in the context of toxicity induced by

the traditional bulk variety, would prioritize them for additional testing. The current data generated in the FE1 model system was shown to be useful for *in vitro* grouping and prioritization.

8.3 Conclusions and Perspectives

8.3.1 Use of Solubility and Dissolution for Grouping and Read-Across of MONPs

Solubility and dissolution are both properties important to the toxicity of traditional chemicals as well as ENM. Regarding MONPs, differences in toxicodynamics and kinetics have been recognized with respect to insoluble and soluble particles since the early 2000s (Oberdörster, G. et al., 2005). In 2015, the first guidance document regarding the use of dissolution data for ENM in risk assessment was published by the OECD (OECD, 2015). In this approach, 4 dissolution categories (high: >70%; moderate: 10-70%; low: 1 – 10%; and negligible <1%; **Table 1-2**) were proposed which could help regulators determine the form (dissolved or particulate) to focus their assessments. Even before this guidance was released however, grouping guidelines were being proposed using qualitative cutoffs for ENM solubility, such as in the control banding framework from 2012 which used two categories of ENM related to solubility, those being 'higher solubility' and 'poorly soluble' (Kuempel, E. D. et al., 2012). In the current chemical regulation frameworks in both the EU and Canada, requirements for registering an ENM specify the need for determination of solubility and dissolution rate in water and relevant media (ECCC, 2022; ECHA, 2022). Furthermore, in the GRACIOUS framework for grouping and read-across for ENM in the context of both regulation and safer-by-design ENM production, every one of the developed pre-defined grouping hypotheses related to inhalation, oral, or dermal exposure had a dissolution criteria as the very first component (instantaneous, quick, gradual, or very slow) (Murphy et al., 2023). These developments show that solubility and dissolution are considered critical physicochemical properties of ENM that are currently used in the context of regulation and risk assessment. While the understanding is there that solubility and dissolution in relevant media impact stability, which will impact persistence both in the body and in the environment, an in-depth understanding of the impact of the dissolved

and particulate species on resulting toxicity has been lacking. This was particularly true with respect to MONPs which can leach dissolved metal into their surroundings.

The results of this thesis improved our understanding of solubility and MONP induced toxicity. They support one colloquially held belief concerning solubility and dissolution, but find that overall effects are compound-specific. In an integrated approach to toxicity assessment (IATA) for inhalation exposure to ENM derived from the GRACIOUS framework, 4 pre-defined hypotheses for grouping and read-across were proposed based on dissolution rate in lung lining fluid and lysosomal fluid (**Table 8-1**) (Braakhuis et al., 2021). The MONP dissolution data in cell culture medium can be used as a proxy for dissolution in lung lining fluid. While dissolution rate was not determined for any of the MONPs tested, it can be seen that ZnO instantaneously dissolve with 94 – 13% dissolved by the 0 h timepoint at 10 and 100 µg/mL respectively (Avramescu et al., 2022), and would therefore fit the criteria for hypothesis 1 at low concentrations. Based on the data generated in this thesis, endpoint response is highly similar between ZnO NPs and fully dissolved Zn at each timepoint, providing empirical support for the assumptions behind hypothesis 1. For all other MONPs except ZnO, compound-specific effects were seen. For NiO NPs and Al_2O_3 NPs which feature between 0.73 – 1.81% dissolution in cell culture medium at 48 h, extracellular dissolution did not contribute to any endpoint response tested. Therefore, toxicity will either be mediated through particle-surface interactions or through intracellular dissolution via a 'Trojan-Horse'-like mechanism. This cannot be generalized to all poorly soluble MONPs however, as MnO_2 NPs which feature between 3.87 – 4.79% dissolution in cell culture medium at 48 h saw an impact of extracellular dissolution on toxicity (Christ, 2024). The same effect was observed with soluble CuO NPs as well, which have between 12.6 - 51.6% dissolution in the same medium at 10 and 100 µg/mL. Tentatively this suggests that for MONPs for which dissolution borders on negligible by 48 h, the extracellular dissolved fraction shows no contribution to toxicity, whereas the dissolved fraction contributes to response for MONPs with higher solubility even if it is still considered poor (1 – 10% dissolved).

Table 8-1. Grouping and read-across hypotheses for the inhalation exposure to ENM IATA. $T_{1/2}$: half life. LLF: lung lining fluid. ALF: artificial lysosomal fluid. Adapted from *(Braakhuis et al., 2021)*.

Hypothesis	Explanation	Criteria
1: Instantaneous dissolution	Toxicity is driven by the constituent ion.	$T_{1/2}$ <10 minutes in LLF
2: Fast dissolution	Toxicity driven by particle and ion effects. Toxicity depends on the location of ion release.	$T_{1/2}$ < 48 h in LLF / ALF
3: Slow dissolution	Toxicity driven by particle and ion effects. Toxicity depends on the location of ion release. Concern for pulmonary accumulation.	48 h < $T_{1/2}$ < 60 days in LLF / ALF
4: Very slow dissolution	Toxicity driven by particle effects. Concern for pulmonary accumulation.	$T_{1/2}$ > 60 days in ALF

8.3.2 Relevance of Lysosomal Localization & Dissolution on MONP Induced Toxicity

In addition to effects attributable to dissolved and particle species for MONPs based on their solubility, the commonly held idea that MONPs traffic primarily to endosomes and lysosomes following exposure (which mediates downstream response) was challenged for short term exposures, though additional experiments will be required to fully characterize trafficking and localization in the FE1 cell model. With respect to what 'relevant media' means for dissolution testing in the context of pulmonary exposure to ENM, this means artificial lung lining fluid and artificial phagosomal or lysosomal media. This speaks to the importance placed on vesicular localization and resulting downstream effects from ENM instability. I have found however, that while lysosomal localization is seen with respect to all tested MONPs, many particles could be found not associated with these structures. These could have potentially diffused into the cell, leaked out of endocytic vesicles, or were internalized through other mechanisms (ex. pinocytosis). The identification of large actin aggregates into which particles can traffic represents another potential reservoir for MONPs inside lung epithelial cells. These results highlight that

additional mechanisms other than lysosomal localization and dissolution should be considered with regards to toxicity induced by MONPs, and that cell-type specific localization mechanisms can be at play that drive resulting response.

8.3.3 Hypoxia Signaling as a Common Underlying Response to MONPs

Cellular response to hypoxia is mediated through the HIF1α pathway. This hypoxia pathway can also be activated in tumour cells and promotes angiogenesis and epithelial-mesenchymal transition (Zhang, Jiayi et al., 2025). This pathway is associated with many stress responses implicated in the mechanisms underlying MONP toxicity, including metal ion homeostasis, oxidative stress, protein folding, and inflammation. Hypoxia and HIF1α signaling are also implicated in pulmonary disorders and inflammation *in vivo*. The finding that the HIF1α pathway represents a conserved transcriptional response across the tested MONPs harkens back to what is known about the constituent metals. Since the early 2000s, it has been observed that heavy metals in solution can lead to the stabilization of HIF1α and downstream transcriptional activity to different extents (Aschner et al., 2023; Maxwell & Salnikow, 2004).

This thesis has shown this activity to also occur after exposure to MONPs which would be considered poorly soluble in water, but which feature enhanced dissolution in cellular environments. Using just 10 genes from this pathway, mechanistic differences in response could be determined for each MONP type investigated. Both TiO_2 and Al_2O_3 NPs presented the weakest response through this gene panel, and both materials act as materials of negligible solubility with low potential to induce cell stress. For Al_2O_3 NPs, this is due to the instability of the dissolved component. In contrast poorly soluble NiO NPs whose mechanism of action relies upon induction of cellular hypoxia, showed strong gene expression through almost all genes except for the heat shock protein folding chaperones. And finally, soluble CuO and ZnO NPs showed a varied potential to induce glycolysis related transcripts but showed strong induction of protein chaperones and the oxidative stress marker *Hmox1*. This preliminary gene panel only focused on highly upregulated genes across the investigated MONP set, and this can be expanded to include both down regulated and upregulated genes. In this way, this panel can represent an *in vitro* biomarker

for acutely toxic MONPs which can be assessed either independently through custom PCR arrays, or included as part of transcriptomic biomarker panels. Further development and validation of this panel comprises a promising future direction, where paired *in vitro* exposures in human cell lines as well as short term murine *in vivo* exposures are conducted to help define the limitations of the gene panel and its relevance to both human signalling and the *in vivo* pulmonary environment in relation to MONP exposure.

8.3.4 Use of *In Vitro* NAMs in an AOP Context for ENM Toxicity Screening

The global movement away from animal-based toxicity testing methods and towards *in vitro* and *in silico* based new approach methodologies (NAMs) is occurring at a fortuitous time with regards to ENM. Many of the challenges facing ENM risk assessment could be mitigated using targeted endpoint assays capable of evaluating many conditions simultaneously. Through the use of well characterized materials, concentration response modelling, and comparative analysis, the influence of physicochemical properties on endpoint response can be teased apart; as was done in this thesis with respect to solubility and the impact of the particulate and dissolved fractions on MONP toxicity.

In order for a NAM to see acceptance and uptake NAM by research and risk assessment communities, it is important to generate data using the approach with appropriate controls which can be compared and contrasted to results in more well characterized systems. Over the course of this thesis, 3 *in vitro* NAM testing approaches, and 1 alternative imaging approach were applied to a variety of MONPs in the context of a putative AOP for cytotoxicity. For all MONPs, the adverse outcome (AO) was also assessed, allowing for critical analysis of the relevance of key event induction on the resulting AO. Finally, the quantitative endpoint information generated through omics and HTS NAM-based assays, as well as AO induction were used in a potency grouping and prioritization exercise which highlighted the utility of the data in the context of tier-1 ENM screening. While further validation is required for regulatory application of the HTS NAMs applied in this thesis, the data generated on the diverse set of MONPs and analogues indicates the assays are readily applicable to ENM endpoint screening with caveats concerning specific ENM classes and high particle concentration ranges.

8.3.5 Unanswered Questions, Limitations, and Future Directions

The data generated as part of this thesis has improved our understanding of MONP toxicity and the influence of particle dissolution on response. It has further developed our understanding of shared and distinct mechanisms of response between different types of MONPs with varying solubility profiles and has provided support for the use of HTS assays for genotoxicity testing of ENM. However, there are still unanswered questions and experimental limitations which present additional avenues for further research.

The most challenging aspect of nanotoxicology is the many physicochemical properties which act in concert to elicit toxicity. In this thesis, 5 MONPs of varying solubility were used throughout as model compounds to assess the impacts of dissolution on cellular response. While these MONPs do indeed cover the spectrum between highly soluble and instantaneously dissolving to negligibly soluble, it only comprised 5 different constituent metals. Therefore, while the insights and conclusions drawn during this thesis were extrapolated to MONPs in general, overall more data is needed to support these conclusions from a larger repertoire of particles. For example, different redox states were not considered in this thesis, like Cu_2O or Ni_2O_3 compared to CuO or NiO. Therefore, while similar transcriptomic and genotoxic responses were seen with regards to constituent metal, it remains to be seen whether this holds across redox states for a specific MONP. This presents an avenue for further research, especially considering that at least for transition metal oxides, multiple redox states can exist as stable compounds. By applying the same transcriptomic and HTS genotoxicity testing approach used in this thesis to redox variants of the same MONPs, this understanding could be developed and used to enrich the associations described here between chemical composition, solubility, and toxicity.

Another limitation of the current study is the sole use of immortalized mouse lung epithelial cells for mechanistic characterization. While murine model systems have been extensively used for MONP toxicity testing, use of *in vitro* mouse cells for this purpose necessitates a second degree of extrapolation to the human condition (*in vitro – in vivo*, mouse – human). Therefore, a key direction for future research would be to confirm some of the main findings from this thesis in an *in vitro* human model system, as well as *in vivo*

using carefully designed mouse inhalation studies. While toxicology in the 21st century is moving away from animal testing, the ability to relate *in vitro* signaling to *in vivo* response is critical. In the world of ENM, this is best accomplished using paired exposures, using the same particles in each set of exposures and making sure that the stability of the suspension or aerosol is similar across the exposures and model systems. This represents another promising avenue for future research, and would be an important step towards the development of a response biomarker for MONPs based on hypoxia signaling.

8.4 Conclusions and Recommendations

With regards to the initially posed question of **"What is the relative contribution of particulate and dissolved fractions to MONP induced toxicity?"**, the results indicate that the nature of the constituent metal and the stability of this dissolved component are crucial parameters contributing to differences in toxicity for MONPs that share similar solubility (Chapters 3 and 5). The results of this thesis also show the complexity of the relationship between lysosomal localization and dissolution (Chapter 6), and that other relevant reservoirs exist within lung epithelial cells which merit further research. Based on the observations of compound-specific effects of the dissolved fraction on MONP toxicity (Chapter 7), caution is recommended if hazard grouping is to be attempted based solely on the solubility of the MONP. While mechanistic research is not directly applicable to human health risk assessment frameworks, the results generated herein, for these well-characterized model MONPs, can be used as part of a weight-of-evidence to support tier-1 MONP screening and prioritization.

This thesis identified a stress signaling pathway (HIF1α) which is perturbed across the tested MONPs and which can serve as a biomarker of metal oxide-induced toxicity. Since genes in this pathway are implicated in important stress responses associated with MONP exposure, a gene biomarker can be developed from this pathway to provide quick tier-1 mechanistic information in addition to identifying acutely toxic materials. Further investigation using a wider diversity of MONPs, as well as variants which have different

physicochemical properties is warranted to confirm the results obtained with the model MONPs used in this thesis, and to determine the limitations of its predictive capacity.

References

A.M Research. *Metal Oxide Nanoparticles Market by Type (Aluminium Oxide, Titanium Dioxide, Copper Oxide, Magnesium Oxide, Zinc Oxide, and Others), and End Use Industry (Optics & Electronics, Healthcare, Automotive, Construction, Ceramic & Glass, Personal Care, Paints & C)*. **https://www.alliedmarketresearch.com/metal-oxide-nanoparticles-market-A15611.** Retrieved September 14 2023, from

Abo-zeid, & Williams. (2019). *The potential anti-infective applications of metal oxide nanoparticles: A systematic review*. Wiley. 10.1002/wnan.1592

Aggarwal, P., Singh, R. P., & Aggarwal, Y. (2015). Use of nano-silica in cement based materials—A review. *Cogent Engineering, 2*(1)10.1080/23311916.2015.1078018

Ahmad, R., Naoui, M., Neault, J. F., Diamantoglou, S., & Tajmir-Riahi, H. A. (1996). An FTIR Spectroscopic Study of Calf-thymus DNA Complexation with Al(III) and Ga(III) Cations. *Journal of Biomolecular Structure & Dynamics, 13*(5), 795–802. 10.1080/07391102.1996.10508892

Akar, E., Yildiz, T., & Atahan, S. (2018). Pulmonary siderosis cases diagnosed with minimally invasive surgical technique: A retrospective analysis of 7 cases. *Annals of Thoracic Medicine, 13*(3), 163–167. 10.4103/atm.ATM_152_17

Akhtar, M. J., Kumar, S., Alhadlaq, H. A., Alrokayan, S. A., Abu-Salah, K. M., & Ahamed, M. (2016). Dose-dependent genotoxicity of copper oxide nanoparticles stimulated by reactive oxygen species in human lung epithelial cells. *Toxicology and Industrial Health, 32*(5), 809–821. 10.1177/0748233713511512

Ameri, B., Davarani, S. S. H., Roshani, R., Moazami, H. R., & Tadjarodi, A. (2016). A flexible mechanochemical route for the synthesis of copper oxide nanorods/nanoparticles/nanowires for supercapacitor applications: The effect of morphology on the charge storage ability. *Journal of Alloys and Compounds, 695*, 114. 10.1016/j.jallcom.2016.10.144

Andujar, P., Simon-Deckers, A., Galateau-Sallé, F., Fayard, B., Beaune, G., Clin, B., Billon-Galland, M., Durupthy, O., Pairon, J., Doucet, J., Boczkowski, J., & Lanone, S. (2014). Role of metal oxide nanoparticles in histopathological changes observed in the lung of welders. *Particle and Fibre Toxicology, 11*(1), 23–23. 10.1186/1743-8977-11-23

Angelé-Martínez, C., Nguyen, K. V. T., Ameer, F. S., Anker, J. N., & Brumaghim, J. L. (2017). Reactive oxygen species generation by copper(II) oxide nanoparticles determined by DNA damage assays and EPR spectroscopy. *Nanotoxicology, 11*(2), 278–288. 10.1080/17435390.2017.1293750

Ankley, Bennett, Erickson, Hoff, Hornung, Johnson, Mount, Nichols, Russom, Schmieder, Serrrano, Tietge, & Villeneuve. (2009). Adverse outcome pathways: A conceptual framework to support ecotoxicology research and risk assessment. *Environmental Toxicology and Chemistry, 29*(3), 730. 10.1002/etc.34

ANTONINI, J. M., ROBERTS, J. R., SCHWEGLER-BERRY, D., & MERCER, R. R. (2013). Comparative Microscopic Study of Human and Rat Lungs After Overexposure to Welding Fume. *The Annals of Occupational Hygiene, 57*(9), 1167–1179. 10.1093/annhyg/met032

Antonini, Lewis, Roberts, & Whaley. (2002). Pulmonary effects of welding fumes: Review of worker and experimental animal studies. *American Journal of Industrial Medicine, 43*(4), 350. 10.1002/ajim.10194

Araldi, R. P., de Melo, T. C., Mendes, T. B., de Sá Júnior, P. L., Nozima, B. H. N., Ito, E. T., de Carvalho, R. F., de Souza, E. B., & de Cassia Stocco, R. (2015). Using the comet and micronucleus assays for genotoxicity studies: A review. *Biomedicine & Pharmacotherapy, 72*, 74–82. 10.1016/j.biopha.2015.04.004

Arlt, V. M., Gingerich, J., Schmeiser, H. H., Phillips, D. H., Douglas, G. R., & White, P. A. (2008). Genotoxicity of 3-nitrobenzanthrone and 3-aminobenzanthrone in MutaMouse and lung epithelial cells derived from MutaMouse. *Mutagenesis, 23*(6), 483–490. 10.1093/mutage/gen037

Arts, Hadi, Irfan, Keene, Kreiling, Lyon, Maier, Michel, Petry, Sauer, Warheit, Wiench, Wohlleben, & Landsiedel. (2015). A decision-making framework for the grouping and testing of nanomaterials (DF4nanoGrouping). *Regulatory Toxicology and Pharmacology, 71*(2), S1. 10.1016/j.yrtph.2015.03.007

Asati, A., Santra, S., Kaittanis, C., & Perez, J. M. (2010). Surface-Charge-Dependent Cell Localization and Cytotoxicity of Cerium Oxide Nanoparticles. *ACS Nano, 4*(9), 5321–5331. 10.1021/nn100816s

Aschner, M., Skalny, A. V., Lu, R., Santamaria, A., Zhou, J., Ke, T., Karganov, M. Y., Tsatsakis, A., Golokhvast, K. S., Bowman, A. B., & Tinkov, A. A. (2023). The role of hypoxia-inducible factor 1 alpha (HIF-1α) modulation in heavy metal toxicity. *Archives of Toxicology, 97*(5), 1299–1318. 10.1007/s00204-023-03483-7

Avlasevich, S., Pellegrin, T., Godse, M., Bryce, S., Bemis, J., Bajorski, P., & Dertinger, S. (2021). Biomarkers of DNA damage response improve in vitro micronucleus assays by revealing genotoxic mode of action and reducing the occurrence of irrelevant positive results. *Mutagenesis, 36*(6), 407–418. 10.1093/mutage/geab039

Avramescu, M., Chénier, M., Beauchemin, S., & Rasmussen, P. (2022). Dissolution Behaviour of Metal-Oxide Nanomaterials in Various Biological Media. *Nanomaterials (Basel, Switzerland), 13*(1), 26. 10.3390/nano13010026

Avramescu, M., Chénier, M., Gardner, H. D., & Rasmussen, P. E. (2019). Solubility of metal oxide nanomaterials: cautionary notes on sample preparation. *Journal of Physics. Conference Series, 1323*(1), 12001. 10.1088/1742-6596/1323/1/012001

Avramescu, M., Chénier, M., Palaniyandi, S., & Rasmussen, P. E. (2020). Dissolution behavior of metal oxide nanomaterials in cell culture medium versus distilled water. *Journal of Nanoparticle Research, 22*(8)10.1007/s11051-020-04949-w

Bakry, R., Vallant, R. M., Najam-Ul-Haq, M., Rainer, M., Szabo, Z., Huck, C. W., & Bonn, G. K. (2007). Medicinal applications of fullerenes. *International Journal of Nanomedicine, 2*(4), 639–649.

Balamurugan, K., & Schaffner, W. (2006). Copper homeostasis in eukaryotes: Teetering on a tightrope. *Biochimica Et Biophysica Acta, 1763*(7), 737–746. 10.1016/j.bbamcr.2006.05.001

Balkissoon, R. (2006). A 26-Year-Old Welder with Severe Non-Reversible Obstructive Lung Disease. *COPD: Journal of Chronic Obstructive Pulmonary Disease, 3*(1), 63. 10.1080/15412550500513878

Bao, T., Bhuller, Y., Bonvalot, Y., Hill, M., Klein, A., Kozak, G., Plante, I., & Robert, N. (2018). *Weight of Evidence:*
General Principles and Current
Applications at Health Canada. Health Canada.

Barhoum, A., García-Betancourt, M. L., Jeevanandam, J., Hussien, E. A., Mekkawy, S. A., Mostafa, M., Omran, M. M., S. Abdalla, M., & Bechelany, M. (2022). *Review on Natural, Incidental, Bioinspired, and Engineered Nanomaterials: History, Definitions, Classifications, Synthesis, Properties, Market, Toxicities, Risks, and Regulations*. MDPI AG. 10.3390/nano12020177

Basinas, I., Jiménez, A. S., Galea, K. S., Tongeren, M. v., & Hurley, F. (2018). A Systematic Review of the Routes and Forms of Exposure to Engineered Nanomaterials. *Annals of Work Exposures and Health, 62*(6), 639–662. 10.1093/annweh/wxy048

Beal, M. A., & Everett, L. J. (2023). Editorial: In vitro toxicogenomics (TGx) in hazard and risk assessment. *Frontiers in Toxicology, 5*10.3389/ftox.2023.1284932

Bellisario, V., Garzaro, G., Squillacioti, G., Panizzolo, M., Ghelli, F., Mariella, G., Bono, R., Guseva Canu, I., & Bergamaschi, E. (2024). Occupational Exposure to Metal-Based Nanomaterials: A Possible Relationship between Chemical Composition and Oxidative Stress Biomarkers. *Antioxidants, 13*(6)10.3390/antiox13060676

Bengtson, S., Kling, K., Madsen, A. M., Noergaard, A. W., Jacobsen, N. R., Clausen, P. A., Alonso, B., Pesquera, A., Zurutuza, A., Ramos, R., Okuno, H., Dijon, J., Wallin, H., & Vogel, U. (2016). No cytotoxicity or genotoxicity of graphene and graphene oxide in murine lung epithelial FE1 cells in vitro. *Environmental and Molecular Mutagenesis, 57*(6), 469–482. 10.1002/em.22017

Benjamini, Y., & Hochberg, Y. (1995). Controlling the False Discovery Rate: A Practical and Powerful Approach to Multiple Testing. *Journal of the Royal Statistical Society Series B: Statistical Methodology, 57*(1), 289–300. 10.1111/j.2517-6161.1995.tb02031.x

Bergamaschi, Bellisario, Macrì, Buglisi, Garzaro, Squillacioti, Ghelli, Bono, Fenoglio, Barbero, Riganti, Marrocco, Bonetta, & Carraro. (2022). A Biomonitoring Pilot Study in Workers from a Paints Production Plant Exposed to Pigment-Grade Titanium Dioxide (TiO2). *Toxics, 10*(4)10.3390/toxics10040171

Berlinger, B., Benker, N., Weinbruch, S., L`Vov, B., Ebert, M., Koch, W., Ellingsen, D. G., & Thomassen, Y. (2011). Physicochemical characterisation of different welding aerosols. *Analytical and Bioanalytical Chemistry, 399*(5), 1773–1780. 10.1007/s00216-010-4185-7

Berndt-Weis, M. L., Kauri, L. M., Williams, A., White, P., Douglas, G., & Yauk, C. (2009). Global transcriptional characterization of a mouse pulmonary epithelial cell line for use in genetic toxicology. *Toxicology in Vitro, 23*(5), 816–833. 10.1016/j.tiv.2009.04.008

Berry, J. P., Masse, R., Escaig, F., & Galle, P. (1989). Intracellular Localization of Cerium. A Microanalytical Study using an Electron Microprobe and Ionic Microanalysis. *Human & Experimental Toxicology, 8*(6), 511–520. 10.1177/096032718900800614

Bi, J., Mo, C., Li, S., Huang, M., Lin, Y., Yuan, P., Liu, Z., Jia, B., & Xu, S. (2023). Immunotoxicity of metal and metal oxide nanoparticles: from toxic mechanisms to metabolism and outcomes. *Biomaterials Science, 11*(12), 4151–4183. 10.1039/d3bm00271c

Bierkandt, F. S., Leibrock, L., Wagener, S., Laux, P., & Luch, A. (2018). The impact of nanomaterial characteristics on inhalation toxicity. *Toxicology Research, 7*(3), 321–346. 10.1039/c7tx00242d

Bischoff, N. S., de Kok, T. M., Sijm, D. T. H. M., van Breda, S. G., Briedé, J. J., Castenmiller, J. J. M., Opperhuizen, A., Chirino, Y. I., Dirven, H., Gott, D., Houdeau, E., Oomen, A. G., Poulsen, M., Rogler, G., & van Loveren, H. (2020). Possible Adverse Effects of Food Additive E171 (Titanium Dioxide) Related to Particle Specific Human Toxicity, Including the Immune System. *International Journal of Molecular Sciences, 22*(1), 207. 10.3390/ijms22010207

Bocca, B., Battistini, B., Leso, V., Fontana, L., Caimi, S., Fedele, M., & Iavicoli, I. (2023a). Occupational Exposure to Metal Engineered Nanoparticles: A Human Biomonitoring Pilot Study Involving Italian Nanomaterial Workers. *Toxics, 11*(2)10.3390/toxics11020120

Bocca, B., Leso, V., Battistini, B., Caimi, S., Senofonte, M., Fedele, M., Cavallo, D. M., Cattaneo, A., Lovreglio, P., & Iavicoli, I. (2023b). Human biomonitoring and personal air monitoring. An integrated approach to assess exposure of stainless-steel welders to metal-oxide nanoparticles. *Environmental Research, 216*(Pt 3), 114736. 10.1016/j.envres.2022.114736

Bonetta, Macrì, Acito, Villarini, Moretti, Bonetta, Bosio, Mariella, Bellisario, Bergamaschi, & Carraro. (2023). DNA damage in workers exposed to pigment grade titanium dioxide (TiO2) and association with biomarkers of oxidative stress and inflammation. *Environmental Toxicology and Pharmacology, 105*10.1016/j.etap.2023.104328

Bouchard-Cannon, P., & Cheng, H. M. (2018). RASD1. *Encyclopedia of Signaling Molecules* (pp. 4474–4481). Springer International Publishing. 10.1007/978-3-319-67199-4_101764

Boya, P., & Kroemer, G. (2008). Lysosomal membrane permeabilization in cell death. *Oncogene, 27*(50), 6434–6451. 10.1038/onc.2008.310

Boyadzhiev, A., Avramescu, M., Wu, D., Williams, A., Rasmussen, P., & Halappanavar, S. (2021). Impact of copper oxide particle dissolution on lung epithelial cell toxicity: response characterization using global transcriptional analysis. *Nanotoxicology, 15*(3), 380–399. 10.1080/17435390.2021.1872114

Boyadzhiev, A., Solorio-Rodriguez, S. A., Wu, D., Avramescu, M., Rasmussen, P., & Halappanavar, S. (2022). The High-Throughput In Vitro CometChip Assay for the Analysis of Metal Oxide Nanomaterial Induced DNA Damage. *Nanomaterials (Basel, Switzerland), 12*(11), 1844. 10.3390/nano12111844

Boyadzhiev, A., Trevithick-Sutton, C., Wu, D., Decan, N., Bazin, M., Shah, G. M., & Halappanavar, S. (2020). Enhanced Dark-Field Hyperspectral Imaging and Spectral Angle Mapping for Nanomaterial Detection in Consumer Care Products and in Skin Following Dermal Exposure. *Chemical Research in Toxicology, 33*(5), 1266. 10.1021/acs.chemrestox.0c00090

Boyadzhiev, A., Wu, D., Avramescu, M., Williams, A., Rasmussen, P., & Halappanavar, S. (2023). Toxicity of Metal Oxide Nanoparticles: Looking through the Lens of Toxicogenomics. *International Journal of Molecular Sciences, 25*(1), 529. 10.3390/ijms25010529

Braakhuis, H. M., Murphy, F., Ma-Hock, L., Dekkers, S., Keller, J., Oomen, A. G., & Stone, V. (2021). An Integrated Approach to Testing and Assessment to Support Grouping and Read-Across of Nanomaterials After Inhalation Exposure. *Applied in Vitro Toxicology, 7*(3), 112–128. 10.1089/aivt.2021.0009

Brenner, S. A., Neu-Baker, N. M., Eastlake, A. C., Beaucham, C. C., & Geraci, C. L. (2016). NIOSH field studies team assessment: Worker exposure to aerosolized metal oxide nanoparticles in a semiconductor fabrication facility. *Journal of Occupational and Environmental Hygiene, 13*(11), 871–880. 10.1080/15459624.2016.1183015

Bushell, M., Beauchemin, S., Kunc, F., Gardner, D., Ovens, J., Toll, F., Kennedy, D., Nguyen, K., Vladisavljevic, D., Rasmussen, P. E., & Johnston, L. J. (2020). Characterization of Commercial Metal Oxide Nanomaterials: Crystalline Phase, Particle Size and Specific Surface Area. *Nanomaterials (Basel, Switzerland), 10*(9), 1812. 10.3390/nano10091812

Buxton, S., Garman, E., Heim, K. E., Lyons-Darden, T., Schlekat, C. E., Taylor, M. D., & Oller, A. R. (2019). Concise Review of Nickel Human Health Toxicology and Ecotoxicology. *Inorganics, 7*(7), 89. 10.3390/inorganics7070089

Byrne, J. D., & Baugh, J. A. (2008). The significance of nanoparticles in particle-induced pulmonary fibrosis. *McGill Journal of Medicine, 11*(1), 43–50. **https://www.ncbi.nlm.nih.gov/pubmed/18523535**

Cai, X., Lee, A., Ji, Z., Huang, C., Chang, C. H., Wang, X., Liao, Y., Xia, T., & Li, R. (2017). Reduction of pulmonary toxicity of metal oxide nanoparticles by phosphonate-based surface passivation. *Particle and Fibre Toxicology, 14*(1), 13–11. 10.1186/s12989-017-0193-5

Cao, Y., Chen, J., Bian, Q., Ning, J., Yong, L., Ou, T., Song, Y., & Wei, S. (2023). Genotoxicity Evaluation of Titanium Dioxide Nanoparticles In Vivo and In Vitro: A Meta-Analysis. *Toxics (Basel), 11*(11), 882. 10.3390/toxics11110882

Carriere, M., Arnal, M., & Douki, T. (2020). TiO2 genotoxicity: An update of the results published over the last six years. *Mutation Research. Genetic Toxicology and Environmental Mutagenesis, 854-855*, 503198. 10.1016/j.mrgentox.2020.503198

Chakraborty, S., & Misra, S. K. (2019). A comparative analysis of dialysis based separation methods for assessing copper oxide nanoparticle solubility. *Environmental Nanotechnology, Monitoring & Management, 12*, 100258. 10.1016/j.enmm.2019.100258

Chang, H., Wang, Q., Meng, X., Chen, X., Deng, Y., Li, L., Yang, Y., Song, G., & Jia, H. (2022). Effect of Titanium Dioxide Nanoparticles on Mammalian Cell Cycle In Vitro: A Systematic Review and Meta-Analysis. *Chemical Research in Toxicology, 35*(9), 1435–1456. 10.1021/acs.chemrestox.1c00402

Chang, X. H., Zhu, A., Liu, F. F., Zou, L. Y., Su, L., Liu, S. K., Zhou, H. H., Sun, Y. Y., Han, A. J., Sun, Y. F., Li, S., Li, J., & Sun, Y. B. (2016). Nickel oxide nanoparticles induced pulmonary fibrosis via TGF-β1 activation in rats. *Human &Amp; Experimental Toxicology, 36*(8), 802. 10.1177/0960327116666650

Charles, S., Jomini, S., Fessard, V., Bigorgne-Vizade, E., Rousselle, C., & Michel, C. (2018). Assessment of the in vitro genotoxicity of TiO2 nanoparticles in a regulatory context. *Nanotoxicology, 12*(4), 357–374. 10.1080/17435390.2018.1451567

Chaudhary, S., Sharma, P., Singh, D., Umar, A., & Kumar, R. (2017). Chemical and Pathogenic Cleanup of Wastewater Using Surface-Functionalized CeO2 Nanoparticles. *ACS Sustainable Chemistry & Engineering, 5*(8), 6803–6816. 10.1021/acssuschemeng.7b01041

Chavali, M. S., & Nikolova, M. P. (2019). Metal oxide nanoparticles and their applications in nanotechnology. *SN Applied Sciences, 1*(6), 607. 10.1007/s42452-019-0592-3

Chen, H., Su, S., Chien, C., Lin, W., Yu, S., Chou, C., Chen, J. J. W., Yang, P., Chen, H., Su, S., Chien, C., Lin, W., Yu, S., Chou, C., Chen, J. J. W., & Yang, P. (2006). *Titanium dioxide nanoparticles induce emphysema-like lung injury in mice*. Wiley. 10.1096/fj.06-6485fje

Chen, M., Zhang, M., Borlak, J., & Tong, W. (2012). A Decade of Toxicogenomic Research and Its Contribution to Toxicological Science. *Toxicological Sciences, 130*(2), 217. 10.1093/toxsci/kfs223

Chen, X., Cheng, B., Yang, Y., Cao, A., Liu, J. H., Du, L. Y., Liu, Y., Zhao, Y., & Wang, H. (2012). Characterization and Preliminary Toxicity Assay of Nano-Titanium Dioxide Additive in Sugar-Coated Chewing Gum. *Small, 9*(9-10), 1765. 10.1002/smll.201201506

Chen, Han, Zhang, Zheng, Liu, Zhang, & Jia. (2021). Metabolomics screening of serum biomarkers for occupational exposure of titanium dioxide nanoparticles. *Nanotoxicology, 15*(6), 832. 10.1080/17435390.2021.1921872

Cheraghian, G., & Hendraningrat, L. (2015). A review on applications of nanotechnology in the enhanced oil recovery part B: effects of nanoparticles on flooding. *International Nano Letters, 6*(1), 1. 10.1007/s40089-015-0170-7

Chi, P., Cheng, C., Hung, C., Wang, M., Liu, H., Ke, M., Shen, M., Lin, K., Kuo, S., Hsieh, P., Wann, S., & Huang, W. (2022). MMP-10 from M1 macrophages promotes pulmonary vascular remodeling and pulmonary arterial hypertension. *International Journal of Biological Sciences, 18*(1), 331–348. 10.7150/ijbs.66472

Cho, W., Duffin, R., Howie, S. E. M., Scotton, C. J., Wallace, W. A. H., Macnee, W., Bradley, M., Megson, I. L., & Donaldson, K. (2011). Progressive severe lung injury by zinc oxide nanoparticles; the role of Zn2+ dissolution inside lysosomes. *Particle and Fibre Toxicology, 8*(1), 27–27. 10.1186/1743-8977-8-27

Cho, W., Duffin, R., Thielbeer, F., Bradley, M., Megson, I. L., Macnee, W., Poland, C. A., Tran, C. L., & Donaldson, K. (2012). Zeta Potential and Solubility to Toxic Ions as Mechanisms of Lung Inflammation Caused by Metal/Metal Oxide Nanoparticles. *Toxicological Sciences, 126*(2), 469–477. 10.1093/toxsci/kfs006

Cho, Y., Tan, H. W. S., Saquib, Q., Ren, Y., Ahmad, J., Wahab, R., He, W., Bay, B., & Shen, H. (2020). Dual role of oxidative stress-JNK activation in autophagy and apoptosis induced by nickel oxide nanoparticles in human cancer cells. *Free Radical Biology and Medicine, 153*, 173. 10.1016/j.freeradbiomed.2020.03.027

Christ, C. (2024). *Establishing the impact of metal oxide nanoparticle size and solubility on lung epithelial cell toxicity*

Collavini, S., & Delgado, J. L. (2018). Fullerenes: the stars of photovoltaics. *Sustainable Energy &Amp; Fuels, 2*(11), 2480. 10.1039/c8se00254a

Collins, A. R., Annangi, B., Rubio, L., Marcos, R., Dorn, M., Merker, C., Estrela-Lopis, I., Cimpan, M. R., Ibrahim, M., Cimpan, E., Ostermann, M., Sauter, A., Yamani, N. E., Shaposhnikov, S., Chevillard, S., Paget, V., Grall, R., Delic, J., de-Cerio, F. G., . . . Dusinska, M. (2017). High throughput toxicity screening and intracellular detection of nanomaterials. *Wiley Interdisciplinary Reviews. Nanomedicine and Nanobiotechnology, 9*(1), n/a. 10.1002/wnan.1413

Collins, Annangi, Rubio, Marcos, Dorn, Merker, Estrela-lopis, Cimpan, Ibrahim, Cimpan, Ostermann, Sauter, Yamani, Shaposhnikov, Chevillard, Paget, Grall, Delic, De-cerio, . . . Dusinska. (2016). High throughput toxicity screening and intracellular detection of nanomaterials. *WIREs Nanomedicine and Nanobiotechnology, 9*(1)10.1002/wnan.1413

Cook, S. (2022). *Investigating the Impact of Metallic Nanoparticles on Biological Systems and Lysosomal Function* Available from ProQuest Dissertations & Theses: UK & Ireland: Business **https://www.proquest.com/docview/2732231341**

Costa, P. M., Gosens, I., Williams, A., Farcal, L., Pantano, D., Brown, D. M., Stone, V., Cassee, F. R., Halappanavar, S., & Fadeel, B. (2018). Transcriptional profiling reveals gene expression changes associated with inflammation and cell proliferation following short-term inhalation exposure to copper oxide nanoparticles. *Journal of Applied Toxicology, 38*(3), 385–397. 10.1002/jat.3548

Costes, S. V., Daelemans, D., Cho, E. H., Dobbin, Z., Pavlakis, G., & Lockett, S. (2004). Automatic and Quantitative Measurement of Protein-Protein Colocalization in Live Cells. *Biophysical Journal, 86*(6), 3993. 10.1529/biophysj.103.038422

Creutzenberg, O., Oliveira, H., Farcal, L., Schaudien, D., Mendes, A., Menezes, A. C., Tischler, T., Burla, S., & Ziemann, C. (2022). PLATOX: Integrated In Vitro/In Vivo Approach for Screening of Adverse Lung Effects of Graphene-Related 2D Nanomaterials. *Nanomaterials (Basel, Switzerland), 12*(8), 1254. 10.3390/nano12081254

Czyżowska, A., & Barbasz, A. (2022). A review: zinc oxide nanoparticles - friends or enemies? *International Journal of Environmental Health Research, 32*(4), 885–901. 10.1080/09603123.2020.1805415

Daiana Silva Avila, Robson Luiz Puntel, & Michael Aschner. (2013). Manganese in Health and Disease. *Metal Ions in Life Sciences, 13*, 199–227. 10.1007/978-94-007-7500-8_7

Danielsen, P. H., Knudsen, K. B., Štrancar, J., Umek, P., Koklič, T., Garvas, M., Vanhala, E., Savukoski, S., Ding, Y., Madsen, A. M., Jacobsen, N. R., Weydahl, I. K., Berthing, T., Poulsen, S. S., Schmid, O., Wolff, H., & Vogel, U. (2020). Effects of physicochemical properties of TiO2 nanomaterials for pulmonary inflammation, acute phase response and alveolar proteinosis in intratracheally exposed mice. *Toxicology and Applied Pharmacology, 386*, 114830. 10.1016/j.taap.2019.114830

Daugaard, M., Rohde, M., & Jäättelä, M. (2007). The heat shock protein 70 family: Highly homologous proteins with overlapping and distinct functions. *FEBS Letters, 581*(19), 3702–3710. 10.1016/j.febslet.2007.05.039

Davidson, T. L., Chen, H., Di Toro, D. M., D'Angelo, G., & Costa, M. (2006). Soluble nickel inhibits HIF-prolyl-hydroxylases creating persistent hypoxic signaling in A549 cells. *Molecular Carcinogenesis, 45*(7), 479–489. 10.1002/mc.20176

de Hoon, M. J. L., Imoto, S., Nolan, J., & Miyano, S. (2004). Open source clustering software. *Bioinformatics, 20*(9), 1453–1454. 10.1093/bioinformatics/bth078

de Planque, M. R. R., Aghdaei, S., Roose, T., & Morgan, H. (2011). Electrophysiological Characterization of Membrane Disruption by Nanoparticles. *ACS Nano, 5*(5), 3599–3606. 10.1021/nn103320j

Decan, Wu, Williams, Bernatchez, Johnston, Hill, & Halappanavar. (2015). Characterization of in vitro genotoxic, cytotoxic and transcriptomic responses following exposures to amorphous silica of different sizes. *Mutation Research/Genetic Toxicology and Environmental Mutagenesis, 796*, 8. 10.1016/j.mrgentox.2015.11.011

Déciga-Alcaraz, A., Delgado-Buenrostro, N. L., Ispanixtlahuatl-Meráz, O., Freyre-Fonseca, V., Flores-Flores, J. O., Ganem-Rondero, A., Vaca-Paniagua, F., Pilar Ramos-Godinez, M. D., Morales-Barcenas, R., Sánchez-Pérez, Y., García-Cuéllar, C. M., & Chirino, Y. I. (2020). Irreversible disruption of the cytoskeleton as induced by non-cytotoxic exposure to titanium dioxide nanoparticles in lung epithelial cells. *Chemico-Biological Interactions, 323*10.1016/j.cbi.2020.109063

Dekkers, S., Williams, T. D., Zhang, J., Zhou, J. (., Vandebriel, R. J., De La Fonteyne, L. J. J., Gremmer, E. R., He, S., Guggenheim, E. J., Lynch, I., Cassee, F. R., De Jong, W. H., & Viant, M. R. (2018). Multi-omics approaches confirm metal ions mediate the main toxicological pathways of metal-bearing nanoparticles in lung epithelial A549 cells. *Environmental Science. Nano, 5*(6), 1506–1517. 10.1039/C8EN00071A

Dhall, A., & Self, W. (2018). Cerium Oxide Nanoparticles: A Brief Review of Their Synthesis Methods and Biomedical Applications. *Antioxidants, 7*(8), 97. 10.3390/antiox7080097

Di Bucchianico, S., Gliga, A. R., Åkerlund, E., Skoglund, S., Wallinder, I. O., Fadeel, B., & Karlsson, H. L. (2018). Calcium-dependent cyto- and genotoxicity of nickel metal and nickel oxide nanoparticles in human lung cells. *Particle and Fibre Toxicology, 15*(1), 32–32. 10.1186/s12989-018-0268-y

Di Virgilio, A. L., Reigosa, M., Arnal, P. M., & Fernández Lorenzo de Mele, M. (2010). Comparative study of the cytotoxic and genotoxic effects of titanium oxide and aluminium oxide nanoparticles in Chinese hamster ovary (CHO-K1) cells. *Journal of Hazardous Materials, 177*(1), 711–718. 10.1016/j.jhazmat.2009.12.089

Dietl, P., & Frick, M. (2021). Channels and Transporters of the Pulmonary Lamellar Body in Health and Disease. *Cells, 11*(1)10.3390/cells11010045

DiPeso, L., Pendyala, S., Huang, H. Z., Fowler, D. M., & Hatch, E. M. (2025). Image-based identification and isolation of micronucleated cells to dissect cellular consequences. *bioRxiv,* 10.1101/2023.05.04.539483

Directorate-General for Environment. (2016). *In: Support for 3rd Regulatory Review on Nanomaterials-Environmental Legislation*. Luxembourg: **https://doi.org/10.2779/49879**

Doak, S. H., Clift, M. J. D., Costa, A., Delmaar, C., Gosens, I., Halappanavar, S., Kelly, S., Pejinenburg, W. J. G. M., Rothen-Rutishauser, B., Schins, R. P. F., Stone, V., Tran, L., Vijver, M. G., Vogel, U., Wohlleben, W., & Cassee, F. R. (2022). The Road to Achieving the European Commission's Chemicals Strategy for Nanomaterial Sustainability—A PATROLS Perspective on New Approach Methodologies. *Small (Weinheim an Der Bergstrasse, Germany), 18*(17), e2200231–n/a. 10.1002/smll.202200231

Doak, Clift, Costa, Delmaar, Gosens, Halappanavar, Kelly, Pejinenburg, Rothen-rutishauser, Schins, Stone, Tran, Vijver, Vogel, Wohlleben, & Cassee. (2022). *The Road to Achieving the European Commission's Chemicals Strategy for Nanomaterial Sustainability—A PATROLS Perspective on New Approach Methodologies*. Wiley. 10.1002/smll.202200231

Doğrul, Z. (2017). Nonfibrinogenic Pneumoconiosis, Siderosis: A Case Report. *Eurasian Journal of Medical Investigation,* 10.14744/ejmi.2017.33043

Donaldson, K., Stone, V., Tran, C. L., Kreyling, W., & Borm, P. J. A. (2004). *Nanotoxicology*. BMJ. 10.1136/oem.2004.013243

ECCC. (2022). *New Substances Notification Regulations (Chemicals and Polymers) Guidance document for the Version 1.0*. Gatineau, Quebec: Government of Canada.

ECCC & HC. (2019). Draft Screening Assessment
Zinc and Its Compounds. **https://www.canada.ca/en/environment-climate-change/services/evaluating-existing-substances/draft-screening-assessment-zinc-compounds.html**

ECCC & HC. (2022). *Environment and Climate Change Canada Helath Canada Framework for the Risk Assessment of Manufactured Nanomaterials under the Canadian Environmental Protection Act, 1999 (Draft) 2022*. Retrieved September 14 2023, from : **https://www.canada.ca/en/environment-climate-change/services/evaluating-existing-substances/framework-risk-assessment-manufactured-nanomaterials-cepa-draft.html**

ECCC & HC. (2023). *Draft assessment - Titanium-containing Substances Group.* ECCC & HC. **https://www.canada.ca/en/environment-climate-change/services/evaluating-existing-substances/draft-assessment-titanium-containing-substances-group.html**

ECHA. (2004). *European Union Risk Assessment Report: Zinc Oxide Addendum to the Part II (Human Health) – 2004.* **https://echa.europa.eu/documents/10162/cc20582a-d359-4722-8cb6-42f1736dc820**

ECHA. (2008). *Copper, Copper II sulphate pentahydrate, Copper(I)oxide, Copper(II)oxide, Dicopper chloride trihydroxide*
Human health part.
https://echa.europa.eu/documents/10162/13630/scher_opinion_hh_en.pdf/df7fee7a-fb00-490e-9641-8d5ec1004843

ECHA. (2016a). *New Approach Methodologies in Regulatory Science*
Proceedings of a scientific workshop Helsinki,
19–20 April 2016. Helsinki, Finland: European Chemicals Agency. 10.2823/543644
https://echa.europa.eu/documents/10162/21838212/scientific_ws_proceedings_en.pdf/a2087434-0407-4705-9057-95d9c2c2cc57

ECHA. (2016b). *Usage of (eco)toxicological data for bridging data gaps between and grouping of nanoforms of the same substance. Elements to consider.* 10.2823/982046 **https://echa.europa.eu/documents/10162/13630/eco_toxicological_for_bridging_grouping_nanoforms_en.pdf/245bf47d-4955-4202-b0d0-1d3c531346d4**

ECHA. (2019). *Appendix for nanoforms applicable to the Guidance on Registration and substance identification*. European Chemicals Agency.

ECHA. (2022). *Appendix R7-1 for nanomaterials applicable to Chapter R7a (Endpoint specific guidance) Version 4.0 -December 2022 1*10.2823/496606

ECHA. (2023). *Report on the European Chemicals Agency's "New Approach Methodologies Workshop: Towards an Animal Free Regulatory System for Industrial Chemicals"*10.2823/7494

EFSA Panel on Additives and Products or Substances used in Animal Feed (FEEDAP). (2016). Safety and efficacy of iron oxide black, red and yellow for all animal species. *EFSA Journal, 14*(6), e04482–n/a. 10.2903/j.efsa.2016.4482

El Yamani, N., Collins, A. R., Rundén-Pran, E., Fjellsbø, L. M., Shaposhnikov, S., Zienolddiny, S., & Dusinska, M. (2017). In vitro genotoxicity testing of four reference metal nanomaterials, titanium dioxide, zinc oxide, cerium oxide and silver: Towards reliable hazard assessment. *Mutagenesis, 32*(1), 117–126. 10.1093/mutage/gew060

Elespuru, R., Pfuhler, S., Aardema, M. J., Chen, T., Doak, S. H., Doherty, A., Farabaugh, C. S., Kenny, J., Manjanatha, M., Mahadevan, B., Moore, M. M., Ouédraogo, G., Stankowski, L. F., & Tanir, J. Y. (2018). Genotoxicity Assessment of Nanomaterials: Recommendations on Best Practices, Assays, and Methods. *Toxicological Sciences, 164*(2), 391–416. 10.1093/toxsci/kfy100

EPA. *BMDS Online (Model Library Version 2023.03.1) [Web App].* Retrieved September 14 2023, from **https://bmdsonline.epa.gov/**

EPA. (2012). Benchmark Dose Technical Guidance. **https://www.epa.gov/sites/default/files/2015-01/documents/benchmark_dose_guidance.pdf**

EPA. (2017). *Technical Fact Sheet – Nanomaterials.* **https://nepis.epa.gov/Exe/ZyPURL.cgi?Dockey=P100TLN9.TXT**

EPA. (2018). *Strategic Plan to Promote the Development and Implementation of Alternative Test Methods Within the TSCA Program*. Office of Chemical Safety and Pollution Prevention.

EPA. (2022). *U.S. EPA. BMDS Version 3.3 User Guide (Oct 2022).* Washington DC: **https://assessments.epa.gov/bmds/document/&deid=353980**

EPA. (2023). *External Review Draft: Standard Methods for Development of EPA Transcriptomic Assessment Products (ETAPs)*

REGULATION (EC) No 1907/2006 OF THE EUROPEAN PARLIAMENT AND OF THE COUNCIL of 18 December 2006 concerning the Registration, Evaluation, Authorisation and Restriction of Chemicals (REACH), establishing a European Chemicals Agency,

amending Directive 1999/45/EC and repealing Council Regulation (EEC) No 793/93 and Commission Regulation (EC) No 1488/94 as well as Council Directive 76/769/EEC and Commission Directives 91/155/EEC, 93/67/EEC, 93/105/EC and 2000/21/EC, (2006). **https://eur-lex.europa.eu/legal-content/EN/TXT/PDF/?uri=CELEX:32006R1907**

Feng, Q., Liu, Y., Huang, J., Chen, K., Huang, J., & Xiao, K. (2018). Uptake, distribution, clearance, and toxicity of iron oxide nanoparticles with different sizes and coatings. *Scientific Reports, 8*(1), 2082–13. 10.1038/s41598-018-19628-z

Fenoglio, I., Greco, G., Livraghi, S., & Fubini, B. (2009). Non-UV-Induced Radical Reactions at the Surface of TiO2 Nanoparticles That May Trigger Toxic Responses. *Chemistry : A European Journal, 15*(18), 4614–4621. 10.1002/chem.200802542

Ferin, J., Oberdorster, G., Penney, D. P., Soderholm, S. C., Gelein, R., & Piper, H. C. (1990). INCREASED PULMONARY TOXICITY OF ULTRAFINE PARTICLES? I. PARTICLE CLEARANCE, TRANSLOCATION, MORPHOLOGY.

Feynman, R. P. (1992). There's plenty of room at the bottom [data storage]. *Journal of Microelectromechanical Systems, 1*(1), 60–66. 10.1109/84.128057

Fortin, A. V., Long, A. S., Williams, A., Meier, M. J., Cox, J., Pinsonnault, C., Yauk, C. L., & White, P. A. (2023). Application of a new approach methodology (NAM)-based strategy for genotoxicity assessment of data-poor compounds. *Frontiers in Toxicology, 5*, 1098432. 10.3389/ftox.2023.1098432

Foster, K. A., Yazdanian, M., & Audus, K. L. (2001). Microparticulate uptake mechanisms of in-vitro cell culture models of the respiratory epithelium. *Journal of Pharmacy and Pharmacology, 53*(1), 57–66. 10.1211/0022357011775190

Fresegna, A. M., Ursini, C. L., Ciervo, A., Maiello, R., Casciardi, S., Iavicoli, S., & Cavallo, D. (2021). Assessment of the Influence of Crystalline Form on Cyto-Genotoxic and Inflammatory Effects Induced by TiO2 Nanoparticles on Human Bronchial and Alveolar Cells. *Nanomaterials (Basel, Switzerland), 11*(1), 253. 10.3390/nano11010253

Fröhlich, E. (2017). Role of omics techniques in the toxicity testing of nanoparticles. *Journal of Nanobiotechnology, 15*(1)10.1186/s12951-017-0320-3

Fytianos, G., Rahdar, A., & Kyzas, G. Z. (2020). *Nanomaterials in Cosmetics: Recent Updates*. MDPI AG. 10.3390/nano10050979

Galanis, A., Karapetsas, A., & Sandaltzopoulos, R. (2009). Metal-induced carcinogenesis, oxidative stress and hypoxia signalling. *Mutation Research, 674*(1), 31–35. 10.1016/j.mrgentox.2008.10.008

García-Torra, V., Cano, A., Espina, M., Ettcheto, M., Camins, A., Barroso, E., Vazquez-Carrera, M., García, M. L., Sánchez-López, E., & Souto, E. B. (2021). State of the art on toxicological mechanisms of metal and metal oxide nanoparticles and strategies to reduce toxicological risks. *Toxics (Basel), 9*(8), 195. 10.3390/toxics9080195

Gawande, M. B., Goswami, A., Felpin, F., Asefa, T., Huang, X., Silva, R., Zou, X., Zboril, R., & Varma, R. S. (2016). Cu and Cu-Based Nanoparticles: Synthesis and Applications in Catalysis. *Chemical Reviews, 116*(6), 3722–3811. 10.1021/acs.chemrev.5b00482

Ge, C., Li, Y., Yin, J., Liu, Y., Wang, L., Zhao, Y., & Chen, C. (2012). The contributions of metal impurities and tube structure to the toxicity of carbon nanotube materials. *NPG Asia Materials, 4*(12), e32. 10.1038/am.2012.60

Genchi, G., Carocci, A., Lauria, G., Sinicropi, M. S., & Catalano, A. (2020). Nickel: Human Health and Environmental Toxicology. *International Journal of Environmental Research and Public Health, 17*(3), 679. 10.3390/ijerph17030679

George, Xia, Rallo, Zhao, Ji, Lin, Wang, Zhang, France, Schoenfeld, Damoiseaux, Liu, Lin, Bradley, Cohen, & Nel. (2011). Use of a High-Throughput Screening Approach Coupled with In Vivo Zebrafish Embryo Screening To Develop Hazard Ranking for Engineered Nanomaterials. *ACS Nano, 5*(3), 1805. 10.1021/nn102734s

Gheshlaghi, Z. N., Riazi, G. H., Ahmadian, S., Ghafari, M., & Mahinpour, R. (2008). Toxicity and interaction of titanium dioxide nanoparticles with microtubule protein. *Acta Biochimica Et Biophysica Sinica, 40*(9), 777. 10.1111/j.1745-7270.2008.00458.x

Ghio, A. J., Sobus, J. R., Pleil, J. D., & Madden, M. C. (2012). Controlled human exposures to diesel exhaust. *Swiss Medical Weekly, 142*(2122), w13597. 10.4414/smw.2012.13597

Ghosh, A. K., & Vaughan, D. E. (2012). PAI-1 in tissue fibrosis. *Journal of Cellular Physiology, 227*(2), 493–507. 10.1002/jcp.22783

Gibb, S. (2007). Toxicity testing in the 21st century: A vision and a strategy. *Reproductive Toxicology, 25*(1), 136. 10.1016/j.reprotox.2007.10.013

Gliga, A. R., Di Bucchianico, S., Åkerlund, E., & Karlsson, H. L. (2020). Transcriptome Profiling and Toxicity Following Long-Term, Low Dose Exposure of Human Lung Cells to Ni and NiO Nanoparticles—Comparison with NiCl2. *Nanomaterials (Basel, Switzerland), 10*(4), 649. 10.3390/nano10040649

Gosens, I., Cassee, F. R., Zanella, M., Manodori, L., Brunelli, A., Costa, A. L., Bokkers, B. G. H., de Jong, W. H., Brown, D., Hristozov, D., & Stone, V. (2016). Organ burden and pulmonary toxicity of nano-sized copper (II) oxide particles after short-term inhalation exposure. *Nanotoxicology, 10*(8), 1084–1095. 10.3109/17435390.2016.1172678

Gosens, I., Kermanizadeh, A., Jacobsen, N. R., Lenz, A., Bokkers, B., De Jong, W. H., Krystek, P., Tran, L., Stone, V., Wallin, H., Stoeger, T., & Cassee, F. R. (2015). Comparative Hazard Identification by a Single Dose Lung Exposure of Zinc Oxide and Silver Nanomaterials in Mice. *Plos One, 10*(5)10.1371/journal.pone.0126934

Graczyk, H., Lewinski, N., Zhao, J., Concha-Lozano, N., & Riediker, M. (2016). Characterization of Tungsten Inert Gas (TIG) Welding Fume Generated by Apprentice Welders. *Annals of Occupational Hygiene, 60*(2), 205–219. 10.1093/annhyg/mev074

Grigore, M. E., Biscu, E. R., Holban, A. M., Gestal, M. C., & Grumezescu, A. M. (2016). Methods of Synthesis, Properties and Biomedical Applications of CuO Nanoparticles. *Pharmaceuticals, 9*(4), 75. 10.3390/ph9040075

Gromelski, Stoliński, Jagiello, Rybińska-Fryca, Williams, Halappanavar, Vogel, & Puzyn. (2022). *AOP173 key event associated pathway predictor – online application for the prediction of benchmark dose lower bound (BMDLs) of a transcriptomic pathway involved in MWCNTs-induced lung fibrosis*. Informa UK Limited. 10.1080/17435390.2022.2064250

Guha, N., Loomis, D., Guyton, K. Z., Grosse, Y., El Ghissassi, F., Bouvard, V., Benbrahim-Tallaa, L., Vilahur, N., Muller, K., & Straif, K. (2017). Carcinogenicity of welding, molybdenum trioxide, and indium tin oxide. *The Lancet Oncology, 18*(5), 581–582. 10.1016/S1470-2045(17)30255-3

Guo, C., Robertson, S., Weber, R. J. M., Buckley, A., Warren, J., Hodgson, A., Rappoport, J. Z., Ignatyev, K., Meldrum, K., Römer, I., Macchiarulo, S., Chipman, J. K., Marczylo, T., Leonard, M. O., Gant, T. W., Viant, M. R., & Smith, R. (2019). Pulmonary toxicity of inhaled nano-sized cerium oxide aerosols in Sprague-Dawley rats. *Nanotoxicology, 13*(6), 733–750. 10.1080/17435390.2018.1554751

Guttenberg, M., Bezerra, L., Neu-Baker, N. M., Del Pilar Sosa Idelchik, M., Elder, A., Oberdörster, G., & Brenner, S. A. (2017). Biodistribution of inhaled metal oxide nanoparticles mimicking occupational exposure: a preliminary investigation using enhanced darkfield microscopy. *Journal of Biophotonics, 9*(10), 987. 10.1002/jbio.201600125

Haber, L. T., Dourson, M. L., Allen, B. C., Hertzberg, R. C., Parker, A., Vincent, M. J., Maier, A., & Boobis, A. R. (2018). Benchmark dose (BMD) modeling: current practice, issues, and challenges. *Critical Reviews in Toxicology, 48*(5), 387–415. 10.1080/10408444.2018.1430121

Hadrup, N., Saber, A. T., Kyjovska, Z. O., Jacobsen, N. R., Vippola, M., Sarlin, E., Ding, Y., Schmid, O., Wallin, H., Jensen, K. A., & Vogel, U. (2020). Pulmonary toxicity of Fe2O3, ZnFe2O4, NiFe2O4 and NiZnFe4O8 nanomaterials: Inflammation and DNA strand breaks. *Environmental Toxicology and Pharmacology, 74*, 103303. 10.1016/j.etap.2019.103303

Hadrup, N., Sahlgren, N., Jacobsen, N. R., Saber, A. T., Hougaard, K. S., Vogel, U., & Jensen, K. A. (2023). Toxicity dose descriptors from animal inhalation studies of 13 nanomaterials and their bulk and ionic counterparts and variation with primary particle characteristics. *Nanotoxicology, 17*(4), 338–371. 10.1080/17435390.2023.2221728

Hadrup, N., Sørli, J. B., & Sharma, A. K. (2022). Pulmonary toxicity, genotoxicity, and carcinogenicity evaluation of molybdenum, lithium, and tungsten: A review. *Toxicology (Amsterdam), 467*, 153098. 10.1016/j.tox.2022.153098

Halappanavar, S., Rahman, L., Nikota, J., Poulsen, S. S., Ding, Y., Jackson, P., Wallin, H., Schmid, O., Vogel, U., & Williams, A. (2019). Ranking of nanomaterial potency to induce pathway perturbations associated with lung responses. *NanoImpact, 14*, 100158. 10.1016/j.impact.2019.100158

Halappanavar, S., Saber, A. T., Decan, N., Jensen, K. A., Wu, D., Jacobsen, N. R., Guo, C., Rogowski, J., Koponen, I. K., Levin, M., Madsen, A. M., Atluri, R., Snitka, V., Birkedal, R. K., Rickerby, D., Williams, A., Wallin, H., Yauk, C. L., & Vogel, U. (2015). Transcriptional profiling identifies physicochemical properties of nanomaterials that are determinants of the in vivo pulmonary response. *Environmental and Molecular Mutagenesis, 56*(2), 245–264. 10.1002/em.21936

Halappanavar, S., Vogel, U., Wallin, H., & Yauk, C. L. (2017). Promise and peril in nanomedicine: the challenges and needs for integrated systems biology approaches to define health risk. *WIREs Nanomedicine and Nanobiotechnology, 10*(1)10.1002/wnan.1465

Halappanavar, Rahman, Nikota, Poulsen, Ding, Jackson, Wallin, Schmid, Vogel, & Williams. (2019). Ranking of nanomaterial potency to induce pathway perturbations associated with lung responses. *NanoImpact, 14*10.1016/j.impact.2019.100158

Halappanavar, Van Den Brule, Nymark, Gaté, Seidel, Valentino, Zhernovkov, Høgh Danielsen, De Vizcaya, Wolff, Stöger, Boyadziev, Poulsen, Sørli, & Vogel. (2020). Adverse outcome pathways as a tool for the design of testing strategies to support the safety assessment of emerging advanced materials at the nanoscale. *Particle and Fibre Toxicology, 17*(1)10.1186/s12989-020-00344-4

Han, J., Lee, J., Choi, D., Lee, Y., Hong, S., Choi, J., Han, S., Ko, Y., Kim, J., Mi Kim, Y., & Jung, Y. (2009). Manganese (II) induces chemical hypoxia by inhibiting HIF-prolyl hydroxylase: Implication in manganese-induced pulmonary inflammation. *Toxicology and Applied Pharmacology, 235*(3), 261–267. 10.1016/j.taap.2009.01.003

Han, J., Wan, Q., Seo, G., Kim, K., El Baghdady, S., Lee, J. H., Kronenberg, M., & Liu, Y. (2022). Hypoxia induces adrenomedullin from lung epithelia, stimulating ILC2 inflammation and immunity. *The Journal of Experimental Medicine, 219*(6)10.1084/jem.20211985

Hansen, Mackevica, & Hull. (2021). Nano-enabled Consumer Products: Inventories, Release, and Exposures. (pp. 85). Springer International Publishing. 10.1007/978-3-030-79808-6_4

Hartwig, A., Asmuss, M., Ehleben, I., Herzer, U., Kostelac, D., Pelzer, A., Schwerdtle, T., & Bürkle, A. (2002). Interference by Toxic Metal Ions with DNA Repair Processes and Cell Cycle Control: Molecular Mechanisms. *Environmental Health Perspectives, 110*(suppl 5), 797–799. 10.1289/ehp.02110s5797

Hassanpour, P., Panahi, Y., Ebrahimi-Kalan, A., Akbarzadeh, A., Davaran, S., Nasibova, A. N., Khalilov, R., & Kavetskyy, T. (2018). Biomedical applications of aluminium oxide nanoparticles. *Micro & Nano Letters, 13*(9), 1227–1231. 10.1049/mnl.2018.5070

Health Canada. (a). *Nanomaterials*. Retrieved September 13 2023, from **https://www.canada.ca/en/health-canada/services/chemical-substances/nanomaterials.html**

Health Canada. (b). *Policy Statement on Health Canada's Working Definition for Nanomaterial*. Retrieved March 31 2024, from **https://www.canada.ca/en/health-canada/services/science-research/reports-publications/nanomaterial/policy-statement-health-canada-working-definition.html**

Health Canada. (2010). *Human Health Risk Assessment for Inhaled Manganese*. Health Canada. **https://www.canada.ca/en/health-canada/services/publications/healthy-living/human-health-risk-assessment-inhaled-manganese-document-summary.html**

Health Canada. (2017). *The Canadian Environmental Protection Act, 1999 and the Assessment of Existing Substances*. Retrieved January 5th 2025, from **https://www.canada.ca/en/environment-climate-change/services/canadian-environmental-protection-act-registry/general-information/fact-sheets/assessment-existing-substances.html**

Heim, J., Felder, E., Tahir, M. N., Kaltbeitzel, A., Heinrich, U. R., Brochhausen, C., Mailänder, V., Tremel, W., & Brieger, J. (2015). Genotoxic effects of zinc oxide nanoparticles. *Nanoscale, 7*(19), 8931–8938. 10.1039/c5nr01167a

Helmig, S., Haibel, N., & Walter, D. (2018). In vitro toxicity studies of aluminum compounds. *Journal of Thermal Analysis and Calorimetry, 134*(1), 643–651. 10.1007/s10973-018-7480-8

Hemmendinger, Squillacioti, Charreau, Garzaro, Ghelli, Bono, Sauvain, Suarez, Hopf, Wild, Progiou, Fito, Bergamaschi, & Guseva Canu. (2023). Occupational exposure to nanomaterials and biomarkers in exhaled air and urine: Insights from the NanoExplore international cohort. *Environment International, 17*910.1016/j.envint.2023.108157

Hevia, L. G., & Fanarraga, M. L. (2020). Microtubule cytoskeleton-disrupting activity of MWCNTs: applications in cancer treatment. *Journal of Nanobiotechnology, 18*(1)10.1186/s12951-020-00742-y

Hirota, K. (2019). An intimate crosstalk between iron homeostasis and oxygen metabolism regulated by the hypoxia-inducible factors (HIFs). *Free Radical Biology and Medicine, 133*, 118–129. 10.1016/j.freeradbiomed.2018.07.018

Hoang Thi, T. T., Cao, V. D., Nguyen, T. N. Q., Hoang, D. T., Ngo, V. C., & Nguyen, D. H. (2019). Functionalized mesoporous silica nanoparticles and biomedical applications. *Materials Science and Engineering: C, 99*, 631. 10.1016/j.msec.2019.01.129

Holmfred, E., Loeschner, K., Sloth, J. J., & Jensen, K. A. (2022). Validation and Demonstration of an Atmosphere-Temperature-pH-Controlled Stirred Batch Reactor System for Determination of (Nano)Material Solubility and Dissolution Kinetics in Physiological Simulant Lung Fluids. *Nanomaterials (Basel, Switzerland), 12*(3), 517. 10.3390/nano12030517

Hölzl-Armstrong, L., Nævisdal, A., Cox, J. A., Long, A. S., Chepelev, N. L., Phillips, D. H., White, P. A., & Arlt, V. M. (2020). In vitro mutagenicity of selected environmental carcinogens and their metabolites in MutaMouse FE1 lung epithelial cells. *Mutagenesis, 35*(6), 453–463. 10.1093/mutage/geaa032

Horie, M., & Fujita, K. (2011). Toxicity of Metal Oxides Nanoparticles. (pp. 145). Elsevier. 10.1016/b978-0-444-53864-2.00004-9

Hou, J., Liu, H., Wang, L., Duan, L., Li, S., & Wang, X. (2018). Molecular Toxicity of Metal Oxide Nanoparticles in Danio rerio. *Environmental Science & Technology, 52*(14), 7996–8004. 10.1021/acs.est.8b01464

Hou, J., Wang, L., Wang, C., Zhang, S., Liu, H., Li, S., & Wang, X. (2019). Toxicity and mechanisms of action of titanium dioxide nanoparticles in living organisms. *Journal of Environmental Sciences, 75*, 40–53. 10.1016/j.jes.2018.06.010

Hristozov, D., Pizzol, L., Basei, G., Zabeo, A., Mackevica, A., Hansen, S. F., Gosens, I., Cassee, F. R., de Jong, W., Koivisto, A. J., Neubauer, N., Sanchez Jimenez, A., Semenzin, E., Subramanian, V., Fransman, W., Jensen, K. A., Wohlleben, W., Stone, V., & Marcomini, A. (2018). Quantitative human health risk assessment along the lifecycle of nano-scale copper-based wood preservatives. *Nanotoxicology, 12*(7), 747–765. 10.1080/17435390.2018.1472314

Hristozov, Badetti, Bigini, Brunelli, Dekkers, Diomede, Doak, Fransman, Gajewicz-Skretna, Giubilato, Gómez-Cuadrado, Grafström, Gutleb, Halappanavar, Hischier, Hunt, Katsumiti, Kermanizadeh, Marcomini, . . . Zabeo. (2024). Next Generation Risk Assessment approaches for advanced nanomaterials: Current status and future perspectives. *NanoImpact, 35*10.1016/j.impact.2024.100523

Huang, S., Chueh, P. J., Lin, Y., Shih, T., & Chuang, S. (2009). Disturbed mitotic progression and genome segregation are involved in cell transformation mediated by nano-TiO2 long-term exposure. *Toxicology and Applied Pharmacology, 241*(2), 182–194. 10.1016/j.taap.2009.08.013

Huang, Y., Cambre, M., & Lee, H. (2017). The Toxicity of Nanoparticles Depends on Multiple Molecular and Physicochemical Mechanisms. *International Journal of Molecular Sciences, 18*(12), 2702. 10.3390/ijms18122702

Huerta-García, E., Ramos-Godinez, M. D. P., López-Saavedra, A., Alfaro-Moreno, E., Gómez-Crisóstomo, N. P., Colín-Val, Z., Sánchez-Barrera, H., & López-Marure, R. (2019). *Internalization of Titanium Dioxide Nanoparticles Is Mediated by Actin-Dependent Reorganization and Clathrin- and Dynamin-Mediated Endocytosis in H9c2 Rat Cardiomyoblasts*. American Chemical Society (ACS). 10.1021/acs.chemrestox.8b00284

Hufnagel, M., Schoch, S., Wall, J., Strauch, B. M., & Hartwig, A. (2020). Toxicity and Gene Expression Profiling of Copper- and Titanium-Based Nanoparticles Using Air–Liquid Interface Exposure. *Chemical Research in Toxicology, 33*(5), 1237–1249. 10.1021/acs.chemrestox.9b00489

Hull, M. J., & Abraham, J. L. (2002). Aluminum welding fume-induced pneumoconiosis. *Human Pathology, 33*(8), 819. 10.1053/hupa.2002.125382

Hund-Rinke, Schlich, Kühnel, Hellack, Kaminski, & Nickel. (2017). Grouping concept for metal and metal oxide nanomaterials with regard to their ecotoxicological effects on algae, daphnids and fish embryos. *NanoImpact, 9*, 52. 10.1016/j.impact.2017.10.003

Husain, M., Saber, A. T., Guo, C., Jacobsen, N. R., Jensen, K. A., Yauk, C. L., Williams, A., Vogel, U., Wallin, H., & Halappanavar, S. (2013). Pulmonary instillation of low doses of titanium dioxide nanoparticles in mice leads to particle retention and gene expression changes in the absence of inflammation. *Toxicology and Applied Pharmacology, 269*(3), 250–262. 10.1016/j.taap.2013.03.018

IARC. (1990). *IARC monographs on the evaluation of carcinogenic risks to humans. v. 49: Chromium, nickel and welding*. Lyon (France) IARC.

IARC. (2010). Carbon black, titanium dioxide, and talc. *IARC Monographs on the Evaluation of Carcinogenic Risks to Humans, 93*, 1–413. **https://www.ncbi.nlm.nih.gov/pubmed/21449489**

IARC. (2017). *SOME NANOMATERIALS AND SOME FIBRES VOLUME 111*. Lyon, France: The International Agency for Research on Cancer.

Ibrahim, M., Schoelermann, J., Mustafa, K., & Cimpan, M. R. (2018). *TiO2 nanoparticles disrupt cell adhesion and the architecture of cytoskeletal networks of human osteoblast-like cells in a size dependent manner*. Wiley. 10.1002/jbm.a.36448

Iijima, S. (1991). Helical microtubules of graphitic carbon. *Nature (London), 354*(6348), 56–58. 10.1038/354056a0

ISO. (2016). *PD ISO/TS 19006:2016: Nanotechnologies. 5-(and 6)-Chloromethyl-2',7' Dichlorodihydrofluorescein diacetate (CM-H2DCF- DA) assay for evaluating nanoparticle-induced intracellular reactive oxygen species (ROS) production in RAW 264.7 macrophage cell line*. British Standards Institute.

ISO. (2021). *PD ISO/TR 22455:2021: Nanotechnologies. High throughput screening method for nanoparticles toxicity using 3D model cells*. British Standards Institute.

ISO. (2023). *BS EN ISO 80004-1:2023: Nanotechnologies. Vocabulary*. British Standards Institute.

Ivask, A., Scheckel, K. G., Kapruwan, P., Stone, V., Yin, H., Voelcker, N. H., & Lombi, E. (2017). Complete transformation of ZnO and CuO nanoparticles in culture medium and lymphocyte cells during toxicity testing. *Nanotoxicology, 11*(2), 150–156. 10.1080/17435390.2017.1282049

Ivask, A., Titma, T., Visnapuu, M., Vija, H., Kakinen, A., Sihtmae, M., Pokhrel, S., Madler, L., Heinlaan, M., Kisand, V., Shimmo, R., & Kahru, A. (2015). Toxicity of 11 Metal Oxide Nanoparticles to Three Mammalian Cell Types In Vitro. *Current Topics in Medicinal Chemistry, 15*(18), 1914–1929. 10.2174/1568026615666150506150109

Jacobsen, N. R., Møller, P., Cohn, C. A., Loft, S., Vogel, U., & Wallin, H. (2008a). Diesel exhaust particles are mutagenic in FE1-Muta™Mouse lung epithelial cells. *Mutation Research/Fundamental and Molecular Mechanisms of Mutagenesis, 641*(1-2), 54. 10.1016/j.mrfmmm.2008.03.001

Jacobsen, N. R., Pojana, G., White, P., Møller, P., Cohn, C. A., Korsholm, K. S., Vogel, U., Marcomini, A., Loft, S., & Wallin, H. (2008b). Genotoxicity, cytotoxicity, and reactive oxygen species induced by single-walled carbon nanotubes and C(60) fullerenes in the FE1-Mutatrade markMouse lung epithelial cells. *Environmental and Molecular Mutagenesis, 49*(6), 476–487. 10.1002/em.20406

Jacobsen, N. R., Pojana, G., White, P., Møller, P., Cohn, C. A., Smith Korsholm, K., Vogel, U., Marcomini, A., Loft, S., & Wallin, H. (2008c). Genotoxicity, cytotoxicity, and reactive oxygen species induced by single-walled carbon nanotubes and C60 fullerenes in the FE1-Muta™Mouse lung epithelial cells. *Environmental and Molecular Mutagenesis, 49*(6), 476. 10.1002/em.20406

Jacobsen, N. R., Stoeger, T., van den Brule, S., Saber, A. T., Beyerle, A., Vietti, G., Mortensen, A., Szarek, J., Budtz, H. C., Kermanizadeh, A., Banerjee, A., Ercal, N., Vogel, U., Wallin, H., & Møller, P. (2015). Acute and subacute pulmonary toxicity and mortality in mice after intratracheal instillation of ZnO nanoparticles in three laboratories. *Food and Chemical Toxicology, 85*, 84–95. 10.1016/j.fct.2015.08.008

Jacobsen, N. R., White, P. A., Gingerich, J., Møller, P., Saber, A. T., Douglas, G. R., Vogel, U., & Wallin, H. (2011). Mutation spectrum in FE1-MUTATMMouse lung epithelial cells exposed to nanoparticulate carbon black. *Environmental and Molecular Mutagenesis, 52*(4), 331–337. 10.1002/em.20629

Jagiello, K., Halappanavar, S., Rybińska-Fryca, A., Willliams, A., Vogel, U., & Puzyn, T. (2021). Transcriptomics-Based and AOP-Informed Structure–Activity Relationships to Predict Pulmonary Pathology Induced by Multiwalled Carbon Nanotubes. *Small (Weinheim an Der Bergstrasse, Germany), 17*(15), e2003465–n/a. 10.1002/smll.202003465

Jagiello, K., Sosnowska, A., Stepnik, M., Gromelski, M., & Plonka, K. (2022). *Nano-specific alternative methods in human hazard/safety assessment under different EU regulations, considering the animal testing bans already in place for cosmetics and their ingredients*. **https://echa.europa.eu/documents/2435000/3268573/ECHA-62-**

2022_final_report_published_02aug2023.pdf/4071837e-c4de-b496-b00f-4e5317646713?t=1691138948441

Jain, S., Rachamalla, M., Kulkarni, A., Kaur, J., & Tikoo, K. (2013). Pulmonary fibrotic response to inhalation of ZnO nanoparticles and toluene co-exposure through directed flow nose only exposure chamber. *Inhalation Toxicology, 25*(13), 703–713. 10.3109/08958378.2013.839765

Janković, N. Z., & Plata, D. L. (2019). Engineered nanomaterials in the context of global element cycles. *Environmental Science: Nano, 6*(9), 2697. 10.1039/c9en00322c

Jeong, J., Kim, S., Lee, S., Lee, D., Han, Y., Jeon, S., & Cho, W. (2018). Differential Contribution of Constituent Metal Ions to the Cytotoxic Effects of Fast-Dissolving Metal-Oxide Nanoparticles. *Frontiers in Pharmacology, 9*, 15. 10.3389/fphar.2018.00015

Jeong, M., Jeon, S., Yu, H., Cho, W., Lee, S., Kang, D., Kim, Y., Kim, Y., & Kim, S. (2022). Exposure to Nickel Oxide Nanoparticles Induces Acute and Chronic Inflammatory Responses in Rat Lungs and Perturbs the Lung Microbiome. *International Journal of Environmental Research and Public Health, 19*(1), 522. 10.3390/ijerph19010522

Jiang, J., Oberdörster, G., & Biswas, P. (2009). Characterization of size, surface charge, and agglomeration state of nanoparticle dispersions for toxicological studies. *Journal of Nanoparticle Research, 11*(1), 77–89. 10.1007/s11051-008-9446-4

Jorge Muñoz-Sánchez, & María E. Chánez-Cárdenas. (2019). The use of cobalt chloride as a chemical hypoxia model. *Journal of Applied Toxicology, 39*(4), 556–570. 10.1002/jat.3749

Joseph R Prohaska. (2008). Role of copper transporters in copper homeostasis. *The American Journal of Clinical Nutrition, 88*(3), 826S–829. 10.1093/ajcn/88.3.826s

Kaplan, J., & Maryon, E. (2016). How Mammalian Cells Acquire Copper: An Essential but Potentially Toxic Metal. *Biophysical Journal, 110*(1), 7–13. 10.1016/j.bpj.2015.11.025

Karlsson, H. L., Cronholm, P., Gustafsson, J., & Möller, L. (2008). Copper Oxide Nanoparticles Are Highly Toxic: A Comparison between Metal Oxide Nanoparticles and Carbon Nanotubes. *Chemical Research in Toxicology, 21*(9), 1726–1732. 10.1021/tx800064j

Karlsson, H. L., Gliga, A. R., Calléja, F. M., Gonçalves, C. S., Wallinder, I. O., Vrieling, H., Fadeel, B., & Hendriks, G. (2014). Mechanism-based genotoxicity screening of metal oxide nanoparticles using the ToxTracker panel of reporter cell lines. *Particle and Fibre Toxicology, 11*(1), 41–41. 10.1186/s12989-014-0041-9

Karlsson, Toprak, & Fadeel. (2022). *Toxicity of metal and metal oxide nanoparticles*. Elsevier. 10.1016/b978-0-12-823292-7.00002-4

Kazimirova, A., Baranokova, M., Staruchova, M., Drlickova, M., Volkovova, K., & Dusinska, M. (2019). Titanium dioxide nanoparticles tested for genotoxicity with the comet and micronucleus assays in vitro, ex vivo and in vivo. *Mutation Research, 843*, 57–65. 10.1016/j.mrgentox.2019.05.001

Ke, Q., & Costa, M. (2006). Hypoxia-Inducible Factor-1 (HIF-1). *Molecular Pharmacology, 70*(5), 1469–1480. 10.1124/mol.106.027029

Kendall, M. G. (1945). THE TREATMENT OF TIES IN RANKING PROBLEMS. *Biometrika, 33*(3), 239–251. 10.1093/biomet/33.3.239

Kerr, M. K., & Churchill, G. A. (2001). Experimental design for gene expression microarrays. *Biostatistics (Oxford, England), 2*(2), 183–201. 10.1093/biostatistics/2.2.183

Kessler, R. (2011). Engineered Nanoparticles in Consumer Products: Understanding a New Ingredient. *Environmental Health Perspectives, 119*(3), A120–A125. 10.1289/ehp.119-a120

Kim, Y., Chung, Y., Seo, D., Choi, H., & Lim, C. (2018). Twenty-Eight-Day Repeated Inhalation Toxicity Study of Aluminum Oxide Nanoparticles in Male Sprague-Dawley Rats. *Toxicological Research (Seoul), 34*(4), 343–354. 10.5487/TR.2018.34.3.343

Klemm, D., Schumann, D., Kramer, F., Heßler, N., Koth, D., & Sultanova, B. (2009). Nanocellulose Materials – Different Cellulose, Different Functionality. *Macromolecular Symposia, 280*(1), 60. 10.1002/masy.200950608

Kohl, Y., Rundén-Pran, E., Mariussen, E., Hesler, M., El Yamani, N., Longhin, E. M., & Dusinska, M. (2020). Genotoxicity of Nanomaterials: Advanced In Vitro Models and High Throughput Methods for Human Hazard Assessment—A Review. *Nanomaterials (Basel, Switzerland), 10*(10), 1911. 10.3390/nano10101911

Kokot, Kokot, Sebastijanović, Voss, Podlipec, Zawilska, Berthing, Ballester-lópez, Danielsen, Contini, Ivanov, Krišelj, Čotar, Zhou, Ponti, Zhernovkov, Schneemilch, Doumandji, Pušnik, . . . Štrancar. (2020). *Prediction of Chronic Inflammation for Inhaled Particles: the Impact of Material Cycling and Quarantining in the Lung Epithelium*. Wiley. 10.1002/adma.202003913

Koltermann-Jülly, Keller, Vennemann, Werle, Müller, Ma-Hock, Landsiedel, Wiemann, & Wohlleben. (2018). Abiotic dissolution rates of 24 (nano)forms of 6 substances compared to macrophage-assisted dissolution and in vivo pulmonary clearance: Grouping by biodissolution and transformation. *NanoImpact, 12*, 29. 10.1016/j.impact.2018.08.005

Kononenko, V., Repar, N., Marušič, N., Drašler, B., Romih, T., Hočevar, S., & Drobne, D. (2017). Comparative in vitro genotoxicity study of ZnO nanoparticles, ZnO macroparticles and ZnCl 2 to MDCK kidney cells: Size matters. *Toxicology in Vitro, 40*, 256. 10.1016/j.tiv.2017.01.015

Krämer, A., Green, J., Pollard, J., Jack, & Tugendreich, S. (2014). Causal analysis approaches in Ingenuity Pathway Analysis. *Bioinformatics, 30*(4), 523–530. 10.1093/bioinformatics/btt703

Krewski, D., Yokel, R. A., Nieboer, E., Borchelt, D., Cohen, J., Harry, J., Kacew, S., Lindsay, J., Mahfouz, A. M., & Rondeau, V. (2007). Human Health Risk Assessment for Aluminium, Aluminium Oxide, and Aluminium Hydroxide. *Journal of Toxicology and Environmental Health. Part B, Critical Reviews, 10*(sup1), 1–269. 10.1080/10937400701597766

Kroto, H. W., Heath, J. R., O'Brien, S. C., Curl, R. F., & Smalley, R. E. (1985). C60: Buckminsterfullerene. *Nature (London), 318*(6042), 162–163. 10.1038/318162a0

Kuempel, E. D., Castranova, V., Geraci, C. L., & Schulte, P. A. (2012). Development of risk-based nanomaterial groups for occupational exposure control. *Journal of Nanoparticle Research : An Interdisciplinary Forum for Nanoscale Science and Technology, 14*(9), 1029–15. 10.1007/s11051-012-1029-8

Kuempel, Castranova, Geraci, & Schulte. (2015). Development of risk-based nanomaterial groups for occupational exposure control. *Journal of Nanoparticle Research, 14*(9)10.1007/s11051-012-1029-8

Kuhlbusch, T. A., Asbach, C., Fissan, H., Göhler, D., & Stintz, M. (2011). Nanoparticle exposure at nanotechnology workplaces: A review. *Particle and Fibre Toxicology, 8*(1), 22. 10.1186/1743-8977-8-22

Kunc, F., Bushell, M., Du, X., Zborowski, A., Johnston, L. J., & Kennedy, D. C. (2022). Physical Characterization and Cellular Toxicity Studies of Commercial NiO Nanoparticles. *Nanomaterials (Basel, Switzerland), 12*(11), 1822. 10.3390/nano12111822

Kwon, J., Kim, Y., Choi, S., Yoon, B., Kim, H., Shim, I., & Sul, D. (2022). Pulmonary Toxicity and Proteomic Analysis in Bronchoalveolar Lavage Fluids and Lungs of Rats Exposed to Copper Oxide Nanoparticles. *International Journal of Molecular Sciences, 23*(21), 13265. 10.3390/ijms232113265

Labib, S., Williams, A., Guo, C. H., Leingartner, K., Arlt, V. M., Schmeiser, H. H., Yauk, C. L., White, P. A., & Halappanavar, S. (2016). Comparative transcriptomic analyses to scrutinize the assumption that genotoxic PAHs exert effects via a common mode of action. *Archives of Toxicology, 90*(10), 2461–2480. 10.1007/s00204-015-1595-5

Labib, Williams, Yauk, Nikota, Wallin, Vogel, & Halappanavar. (2015). *Nano-risk Science: application of toxicogenomics in an adverse outcome pathway framework for risk assessment of multi-walled carbon nanotubes*. Springer Science and Business Media LLC. 10.1186/s12989-016-0125-9

Laha, D., Pramanik, A., Maity, J., Mukherjee, A., Pramanik, P., Laskar, A., & Karmakar, P. (2014). Interplay between autophagy and apoptosis mediated by copper oxide nanoparticles in human breast cancer cells MCF7. *Biochimica Et Biophysica Acta (BBA) - General Subjects, 1840*(1), 1–9. 10.1016/j.bbagen.2013.08.011

Lai, X., Wei, Y., Zhao, H., Chen, S., Bu, X., Lu, F., Qu, D., Yao, L., Zheng, J., & Zhang, J. (2015). The effect of Fe2O3 and ZnO nanoparticles on cytotoxicity and glucose metabolism in lung epithelial cells. *Journal of Applied Toxicology, 35*(6), 651–664. 10.1002/jat.3128

Lai, X., Zhao, H., Zhang, Y., Guo, K., Xu, Y., Chen, S., & Zhang, J. (2018). Intranasal Delivery of Copper Oxide Nanoparticles Induces Pulmonary Toxicity and Fibrosis in C57BL/6 mice. *Scientific Reports, 8*(1), 4499–12. 10.1038/s41598-018-22556-7

Langie, S. A. S., Azqueta, A., & Collins, A. R. (2015). The comet assay: past, present, and future. *Frontiers in Genetics, 6*, 266. 10.3389/fgene.2015.00266

Larsen, Jackson, Poulsen, Levin, Jensen, Wallin, Nielsen, & Koponen. (2016). Airway irritation, inflammation, and toxicity in mice following inhalation of metal oxide nanoparticles. *Nanotoxicology, 10*(9), 1254. 10.1080/17435390.2016.1202350

Lebedová, J., Hedberg, Y. S., Odnevall Wallinder, I., & Karlsson, H. L. (2018). Size-dependent genotoxicity of silver, gold and platinum nanoparticles studied using the mini-gel comet assay and micronucleus scoring with flow cytometry. *Mutagenesis, 33*(1), 77–85. 10.1093/mutage/gex027

Leroueil, P. R., Berry, S. A., Duthie, K., Han, G., Rotello, V. M., McNerny, D. Q., Baker, J. R., Orr, B. G., & Banaszak Holl, M. M. (2008). Wide Varieties of Cationic Nanoparticles Induce Defects in Supported Lipid Bilayers. *Nano Letters, 8*(2), 420–424. 10.1021/nl0722929

Li, G., Jiang, J., Liao, Y., Wan, S., Yao, Y., Luo, Y., Chen, X., Qian, H., Dai, X., Yin, W., Min, Z., Yi, G., & Tan, X. (2022). Risk for lung-related diseases associated with welding fumes in an occupational population: Evidence from a Cox model. *Frontiers in Public Health, 10*, 990547. 10.3389/fpubh.2022.990547

Li, H., Yauk, C. L., Chen, R., Hyduke, D. R., Williams, A., Frötschl, R., Ellinger-Ziegelbauer, H., Pettit, S., Aubrecht, J., & Fornace, A. J. (2019). *TGx-DDI, a Transcriptomic Biomarker for Genotoxicity Hazard Assessment of Pharmaceuticals and Environmental Chemicals*. Frontiers Media SA. 10.3389/fdata.2019.00036

Li, Q., Chen, H., Huang, X., & Costa, M. (2006). Effects of 12 metal ions on iron regulatory protein 1 (IRP-1) and hypoxia-inducible factor-1 alpha (HIF-1α) and HIF-regulated genes. *Toxicology and Applied Pharmacology, 213*(3), 245–255. 10.1016/j.taap.2005.11.006

Liu, X., Ruan, W., Wang, W., Zhang, X., Liu, Y., & Liu, J. (2021). The Perspective and Challenge of Nanomaterials in Oil and Gas Wastewater Treatment. *Molecules, 26*(13)10.3390/molecules26133945

Liu, Feng, Wei, Chen, Song, & Shao. (2016). The toxicology of ion-shedding zinc oxide nanoparticles. *Critical Reviews in Toxicology, 46*(4), 348. 10.3109/10408444.2015.1137864

Long, Nascarella, & Valberg. (2013). Carbon black vs. black carbon and other airborne materials containing elemental carbon: Physical and chemical distinctions. *Environmental Pollution, 181*, 271. 10.1016/j.envpol.2013.06.009

Lovell, D. P., Fellows, M., Marchetti, F., Christiansen, J., Elhajouji, A., Hashimoto, K., Kasamoto, S., Li, Y., Masayasu, O., Moore, M. M., Schuler, M., Smith, R., Stankowski, L. F., Tanaka, J., Tanir, J. Y., Thybaud, V., Van Goethem, F., & Whitwell, J. (2018). Analysis of negative historical control group data from the in vitro micronucleus assay using TK6 cells. *Mutation Research. Genetic Toxicology and Environmental Mutagenesis, 825*, 40–50. 10.1016/j.mrgentox.2017.10.006

Luo, Z., Tian, M., Yang, G., Tan, Q., Chen, Y., Li, G., Zhang, Q., Li, Y., Wan, P., & Wu, J. (2022). Hypoxia signaling in human health and diseases: implications and prospects for therapeutics. *Signal Transduction and Targeted Therapy, 7*(1), 218–218. 10.1038/s41392-022-01080-1

Lynch, I., Cedervall, T., Lundqvist, M., Cabaleiro-Lago, C., Linse, S., & Dawson, K. A. (2007). The nanoparticle–protein complex as a biological entity; a complex fluids and surface science challenge for the 21st century. *Advances in Colloid and Interface Science, 134-135*, 167. 10.1016/j.cis.2007.04.021

Ma, Bishoff, Mercer, Barger, Schwegler-Berry, & Castranova. (2019). Role of epithelial-mesenchymal transition (EMT) and fibroblast function in cerium oxide nanoparticles-induced lung fibrosis. *Toxicology and Applied Pharmacology, 323*, 16. 10.1016/j.taap.2017.03.015

Maduraiveeran, G., Sasidharan, M., & Jin, W. (2019). Earth-abundant transition metal and metal oxide nanomaterials: Synthesis and electrochemical applications. *Progress in Materials Science, 106*10.1016/j.pmatsci.2019.100574

Maertens, R. M., Long, A. S., White, P. A., & Benthem, J. v. (2017). Performance of the in vitro transgene mutation assay in MutaMouse FE1 cells: Evaluation of nine misleading ("False") positive chemicals. *Environmental and Molecular Mutagenesis, 58*(8), 582–591. 10.1002/em.22125

MAGAYE, R., ZHAO, J., BOWMAN, L., & DING, M. (2012). Genotoxicity and carcinogenicity of cobalt-, nickel- and copper-based nanoparticles. *Experimental and Therapeutic Medicine, 4*(4), 551–561. 10.3892/etm.2012.656

Magdolenova, Z., Collins, A., Kumar, A., Dhawan, A., Stone, V., & Dusinska, M. (2014). Mechanisms of genotoxicity. A review of in vitro and in vivo studies with engineered nanoparticles. *Nanotoxicology, 8*(3), 233–278. 10.3109/17435390.2013.773464

Magdolenova, Z., Lorenzo, Y., Collins, A., & Dusinska, M. (2012). Can Standard Genotoxicity Tests be Applied to Nanoparticles? *Journal of Toxicology and Environmental Health, Part A, 75*(13-15), 800–806. 10.1080/15287394.2012.690326

Mandriota, S. J., Tenan, M., Nicolle, A., Jankowska, J. D., Ferrari, P., Tille, J., Durin, M., Green, C. M., Tabruyn, S., Moralli, D., & Sappino, A. (2020). Genomic Instability Is an Early Event in Aluminium-Induced Tumorigenesis. *International Journal of Molecular Sciences, 21*(23), 9332. 10.3390/ijms21239332

Marketysers Global Consulting LLP. *Nano Metal Oxide Market Size, Trends & Analysis, by Product, by Application (Energy and Environment, Paints and Coatings, Medical and Personal Care, Electronics and Optics, Others), and by Distribution Channel (Offline Stores, Online Stores), Forecasts to 2027*. Retrieved March 18 2022, from **https://www.reportsanddata.com/report-detail/nano-metal-oxide-market**

Martell, J., & Guidotti, T. L. (2022). Trading One Risk for Another: Consequences of the Unauthenticated Treatment and Prevention of Silicosis in Ontario Miners in the McIntyre Powder Aluminum Inhalation Program. *New Solutions, 31*(4), 422–433. 10.1177/10482911211037007

Martin, A., & Sarkar, A. (2017). Overview on biological implications of metal oxide nanoparticle exposure to human alveolar A549 cell line. *Nanotoxicology, 11*(6), 713–724. 10.1080/17435390.2017.1366574

Maryon, E. B., Molloy, S. A., Ivy, K., Yu, H., & Kaplan, J. H. (2013). Rate and Regulation of Copper Transport by Human Copper Transporter 1 (hCTR1). *The Journal of Biological Chemistry, 288*(25), 18035–18046. 10.1074/jbc.M112.442426

Masoud, G. N., & Li, W. (2015). HIF-1α pathway: role, regulation and intervention for cancer therapy. *Acta Pharmaceutica Sinica. B, 5*(5), 378–389. 10.1016/j.apsb.2015.05.007

Mauvezin, C., Nagy, P., Juhász, G., & Neufeld, T. P. (2015). Autophagosome–lysosome fusion is independent of V-ATPase-mediated acidification. *Nature Communications, 6*(1)10.1038/ncomms8007

Maxwell, P., & Salnikow, K. (2004). HIF-1, An Oxygen and Metal Responsive Transcription Factor. *Cancer Biology & Therapy, 3*(1), 29–35. 10.4161/cbt.3.1.547

May, S., Hirsch, C., Rippl, A., Bürkle, A., & Wick, P. (2022). Assessing Genotoxicity of Ten Different Engineered Nanomaterials by the Novel Semi-Automated FADU Assay and the Alkaline Comet Assay. *Nanomaterials (Basel, Switzerland), 12*(2), 220. 10.3390/nano12020220

Mcclellan, R. O. (1999). KEYNOTE ADDRESS: HUMAN HEALTH RISK ASSESSMENT: A Historical Overview and Alternative Paths Forward. *Inhalation Toxicology, 11*(6-7), 477. 10.1080/089583799196880

Mccormick, Niang, & Dahm. (2023). Occupational Exposures to Engineered Nanomaterials: a Review of Workplace Exposure Assessment Methods. *Current Environmental Health Reports, 8*(3), 223. 10.1007/s40572-021-00316-6

McGarry, T., Biniecka, M., Veale, D. J., & Fearon, U. (2018). Hypoxia, oxidative stress and inflammation. *Free Radical Biology & Medicine, 125*, 15–24. 10.1016/j.freeradbiomed.2018.03.042

Mclean, Mueller, Gosens, Cassee, Rothen-Rutishauser, Boyles, & Tran. (2023). *Establishing relationships between particle-induced in vitro and in vivo inflammation endpoints to better extrapolate between in vitro markers and in vivo fibrosis*. Springer Science and Business Media LLC. 10.1186/s12989-023-00516-y

Miclea, L. C., Mihailescu, M., Tarba, N., Brezoiu, A., Sandu, A. M., Mitran, R., Berger, D., Matei, C., Moisescu, M. G., & Savopol, T. (2022). Evaluation of intracellular distribution of folate functionalized silica nanoparticles using fluorescence and hyperspectral enhanced dark field microscopy. *Nanoscale, 14*(35), 12744. 10.1039/d2nr01821g

Midander, K., Cronholm, P., Karlsson, H. L., Elihn, K., Möller, L., Leygraf, C., & Wallinder, I. O. (2009). Surface Characteristics, Copper Release, and Toxicity of Nano- and Micrometer-Sized Copper and Copper(II) Oxide Particles: A Cross-Disciplinary Study. *Small, 5*(3), 389–399. 10.1002/smll.200801220

Miernicki, M., Hofmann, T., Eisenberger, I., Von Der Kammer, F., & Praetorius, A. (2019). Legal and practical challenges in classifying nanomaterials according to regulatory definitions. *Nature Nanotechnology, 14*(3), 208. 10.1038/s41565-019-0396-z

Mirshafiee, V., Sun, B., Chang, C. H., Liao, Y., Jiang, W., Jiang, J., Liu, X., Wang, X., Xia, T., & Nel, A. E. (2018). Toxicological Profiling of Metal Oxide Nanoparticles in Liver Context Reveals Pyroptosis in Kupffer Cells and Macrophages versus Apoptosis in Hepatocytes. *ACS Nano, 12*(4), 3836–3852. 10.1021/acsnano.8b01086

Miyayama, T., & Matsuoka, M. (2016). Involvement of lysosomal dysfunction in silver nanoparticle-induced cellular damage in A549 human lung alveolar epithelial cells. *Journal of Occupational Medicine and Toxicology, 11*(1)10.1186/s12995-016-0090-0

Mohamed, S. K., Elhgrasi, A. M., & Ali, O. I. (2022). Facile synthesis of mesoporous nano Ni/NiO and its synergistic role as super adsorbent and photocatalyst under sunlight irradiation. *Environmental Science and Pollution Research, 29*(43), 64792. 10.1007/s11356-022-19970-w

Monsé, C., Hagemeyer, O., Raulf, M., Jettkant, B., van Kampen, V., Kendzia, B., Gering, V., Kappert, G., Weiss, T., Ulrich, N., Marek, E., Bünger, J., Brüning, T., & Merget, R. (2018). Concentration-dependent systemic response after inhalation of nano-sized zinc oxide particles in human volunteers. *Particle and Fibre Toxicology, 15*(1), 8. 10.1186/s12989-018-0246-4

Monsé, C., Raulf, M., Jettkant, B., van Kampen, V., Kendzia, B., Schürmeyer, L., Seifert, C. E., Marek, E., Westphal, G., Rosenkranz, N., Merget, R., Brüning, T., & Bünger, J. (2021). Health effects after inhalation of micro- and nano-sized zinc oxide particles in human volunteers. *Archives of Toxicology, 95*(1), 53–65. 10.1007/s00204-020-02923-y

More, Bampidis, Benford, Bragard, Halldorsson, Hernández-jerez, Bennekou, Koutsoumanis, Lambré, Machera, Mennes, Mullins, Nielsen, Schrenk, Turck, Younes, Aerts, Edler, Sand, . . . Schlatter. (2022). Guidance on the use of the benchmark dose approach in risk assessment. *EFSA Journal, 20*(10)10.2903/j.efsa.2022.7584

More, Bampidis, Benford, Bragard, Halldorsson, Hernández-jerez, Hougaard Bennekou, Koutsoumanis, Lambré, Machera, Naegeli, Nielsen, Schlatter, Schrenk, Silano (deceased), Turck, Younes, Castenmiller, Chaudhry, . . . Schoonjans. (2021). Guidance on risk assessment of nanomaterials to be applied in the food and feed chain: human and animal health. *EFSA Journal, 19*(8)10.2903/j.efsa.2021.6768

Moreno-Navarrete, J. M., Ortega, F., Rodríguez, A., Latorre, J., Becerril, S., Sabater-Masdeu, M., Ricart, W., Frühbeck, G., & Fernández-Real, J. M. (2017). HMOX1 as a marker of iron excess-induced adipose tissue dysfunction, affecting glucose uptake and respiratory capacity in human adipocytes. *Diabetologia, 60*(5), 915–926. 10.1007/s00125-017-4228-0

Morrow, G. B., & Mutch, N. J. (2023). Past, Present, and Future Perspectives of Plasminogen Activator Inhibitor 1 (PAI-1). *Seminars in Thrombosis and Hemostasis, 49*(3), 305–313. 10.1055/s-0042-1758791

Moschini, E., Colombo, G., Chirico, G., Capitani, G., Dalle-Donne, I., & Mantecca, P. (2023). Biological mechanism of cell oxidative stress and death during short-term exposure to nano CuO. *Scientific Reports, 13*(1), 2326. 10.1038/s41598-023-28958-6

Moschini, E., Gualtieri, M., Colombo, M., Fascio, U., Camatini, M., & Mantecca, P. (2013). The modality of cell–particle interactions drives the toxicity of nanosized CuO and TiO2 in human alveolar epithelial cells. *Toxicology Letters, 222*(2), 102–116. 10.1016/j.toxlet.2013.07.019

Mothkuri, S., Chakrabarti, S., Gupta, H., Padya, B., Rao, T. N., & Jain, P. K. (2019). Synthesis of MnO2 nano-flakes for high performance supercapacitor application. *Materials Today: Proceedings, 26*, 142. 10.1016/j.matpr.2019.03.236

Mukaka, M. M. (2012). Statistics corner: A guide to appropriate use of correlation coefficient in medical research. *Malawi Medical Journal, 24*(3), 69–71. **https://www.ncbi.nlm.nih.gov/pubmed/23638278**

Murphy, F. A., Johnston, H. J., Dekkers, S., Bleeker, E. A. J., Oomen, A. G., Fernandes, T. F., Rasmussen, K., Jantunen, P., Rauscher, H., Hunt, N., di Cristo, L., Braakhuis, H. M., Haase, A., Hristozov, D., Wohlleben, W., Sabella, S., & Stone, V. (2023). How to formulate hypotheses and IATAs to support grouping and read-across of nanoforms. *ALTEX, 40*(1), 125–140. 10.14573/altex.2203241

Murugadoss, S., Lison, D., Godderis, L., Van Den Brule, S., Mast, J., Brassinne, F., Sebaihi, N., & Hoet, P. H. (2017). Toxicology of silica nanoparticles: an update. *Archives of Toxicology, 91*(9), 2967. 10.1007/s00204-017-1993-y

Naatz, Lin, Li, Jiang, Ji, Chang, Köser, Thöming, Xia, Nel, Mädler, & Pokhrel. (2016). *Safe-by-Design CuO NanoparticlesviaFe-Doping, Cu–O Bond Length Variation, and Biological Assessment in Cells and Zebrafish Embryos*. American Chemical Society (ACS). 10.1021/acsnano.6b06495

Naghdi, M., Metahni, S., Ouarda, Y., Brar, S. K., Das, R. K., & Cledon, M. (2017). Instrumental approach toward understanding nano-pollutants. *Nanotechnology for Environmental Engineering, 2*(1)10.1007/s41204-017-0015-x

Naz, S., Gul, A., & Zia, M. (2020). Toxicity of copper oxide nanoparticles: a review study. *IET Nanobiotechnology, 14*(1), 1–13. 10.1049/iet-nbt.2019.0176

Ndika, J., Ilves, M., Kooter, I. M., Gröllers-Mulderij, M., Duistermaat, E., Tromp, P. C., Kuper, F., Kinaret, P., Greco, D., Karisola, P., & Alenius, H. (2020). Mechanistic Similarities between 3D Human Bronchial Epithelium and Mice Lung, Exposed to Copper Oxide Nanoparticles, Support Non-Animal Methods for Hazard Assessment. *Small (Weinheim an Der Bergstrasse, Germany), 16*(36), e2000527–n/a. 10.1002/smll.202000527

Newman, M. D., Stotland, M., & Ellis, J. I. (2009). The safety of nanosized particles in titanium dioxide– and zinc oxide–based sunscreens. *Journal of the American Academy of Dermatology, 61*(4), 685. 10.1016/j.jaad.2009.02.051

NICNAS. (2014). *Nickel oxide: Human health tier II assessment*. **https://www.industrialchemicals.gov.au/sites/default/files/Nickel%20oxide_Human%20health%20tier%20II%20assessment.pdf**

Nielsen, Baun, Mackevica, Thit, Odnevall Wallinder, Gallego, Westergaard Clausen, Rissler, Skjolding, Castro Nilsson, Cedervall, & Foss Hansen. (2021). Nanomaterials in the European chemicals legislation – methodological challenges for registration and environmental safety assessment. *Environmental Science: Nano, 8*(3), 731. 10.1039/d0en01123a

Nies, A. (2008). *Membrane Transporters*. Springer Berlin Heidelberg. 10.1007/978-3-540-47648-1_3628

Nikota, Banville, Goodwin, Wu, Williams, Yauk, Wallin, Vogel, & Halappanavar. (2017). *Stat-6 signaling pathway and not Interleukin-1 mediates multi-walled carbon nanotube-induced lung fibrosis in mice: insights from an adverse outcome pathway framework*. Springer Science and Business Media LLC. 10.1186/s12989-017-0218-0

NIOSH. (2011). *CURRENT INTELLIGENCE BULLETIN 63 Occupational Exposure to Titanium Dioxide*

NIOSH. (2013). *CURRENT INTELLIGENCE BULLETIN 65 Occupational Exposure to Carbon Nanotubes and Nanofibers*

Niska, K., Zielinska, E., Radomski, M. W., & Inkielewicz-Stepniak, I. (2017). Metal nanoparticles in dermatology and cosmetology: Interactions with human skin cells. *Chemico-Biological Interactions, 295*, 38. 10.1016/j.cbi.2017.06.018

Nuwaysir, E. F., Bittner, M., Trent, J., Barrett, J. C., & Afshari, C. A. (1999). *Microarrays and toxicology: The advent of toxicogenomics*. Wiley. 10.1002/(sici)1098-2744(199903)24:3<153::aid-mc1>3.0.co;2-p

O'Brien, J., Mitchell, C., Auerbach, S., Doonan, L., Ewald, J., Everett, L., Faranda, A., Johnson, K., Reardon, A., Rooney, J., Shao, K., Stainforth, R., Wheeler, M., Dalmas Wilk, D., Williams, A.,

Yauk, C., & Costa, E. (2024). *Bioinformatic workflows for deriving transcriptomic points of departure: current status, data gaps, and research priorities*. Oxford University Press (OUP). 10.1093/toxsci/kfae145

Oberd, G., Rster, J., Ferin, G., Finkelstein, P., Wade, N., & Corson. (1990). INCREASED PULMONARY TOXICITY OF ULTRAFINE PARTICLES? II. LUNG LAVAGE STUDIES.

Oberdörster, G., Maynard, A., Donaldson, K., Castranova, V., Fitzpatrick, J., Ausman, K., Carter, J., Karn, B., Kreyling, W., Lai, D., Olin, S., Monteiro-Riviere, N., Warheit, D., & Yang, H. (2005). Principles for characterizing the potential human health effects from exposure to nanomaterials: elements of a screening strategy. *Particle and Fibre Toxicology, 2*(1), 8. 10.1186/1743-8977-2-8

Oberdorster, G., Oberdorster, E., & Oberdorster, J. (2005). Nanotoxicology: An Emerging Discipline Evolving from Studies of Ultrafine Particles. *Environmental Health Perspectives, 113*(7), 823–839. 10.1289/ehp.7339

Oberdörster, Celein, Ferin, & Weiss. (1995). Association of Particulate Air Pollution and Acute Mortality: Involvement of Ultrafine Particles? *Inhalation Toxicology, 7*(1), 111. 10.3109/08958379509014275

Oberdörster, Oberdörster, & Oberdörster. (2005). Nanotoxicology: An Emerging Discipline Evolving from Studies of Ultrafine Particles. *Environmental Health Perspectives, 113*(7), 823. 10.1289/ehp.7339

Oberdörster, Stone, & Donaldson. (2007). Toxicology of nanoparticles: A historical perspective. *Nanotoxicology, 1*(1), 2. 10.1080/17435390701314761

OECD. (1995). *Test No. 105: Water Solubility*. OECD Publishing. 10.1787/9789264069589-en

OECD. (2009). *No. 15 Preliminary Review of OECD Test Guidelines for their Applicability to Manufactured Nanomaterials*.

OECD. (2014a). *No. 194 GUIDANCE ON GROUPING OF CHEMICALS, SECOND EDITION*

OECD. (2014b). *Test No. 489: In Vivo Mammalian Alkaline Comet Assay*. OECD Publishing. 10.1787/9789264264885-en

OECD. (2015). *CONSIDERATIONS FOR USING DISSOLUTION AS A FUNCTION OF SURFACE CHEMISTRY TO EVALUATE ENVIRONMENTAL BEHAVIOUR OF NANOMATERIALS IN RISK ASSESSMENTS*

OECD. (2016). *OECD TG 476 In Vitro Mammalian Cell Gene Mutation Tests using the Hprt and xprt genes*

OECD. (2018). *Evaluation of In Vitro Methods for Human Hazard Assessment Applied in the OECD Testing Programme for the Safety of Manufactured Nanomaterials*. OECD Publishing. 10.1787/a5da5705-en

OECD. (2019). *GUIDING PRINCIPLES FOR MEASUREMENTS AND REPORTING FOR NANOMATERIALS: PHYSICAL CHEMICAL PARAMETERS*

OECD. (2022a). *No. 103 Important Issues on Risk Assessment of Manufactured Nanomaterials*

OECD. (2022b). *No. 104 Advanced Materials: Working Description*

OECD. (2022c). *Study Report and Preliminary Guidance on the Adaptation of the In Vitro micronucleus assay (OECD TG 487) for Testing of Manufactured Nanomaterials*

OECD. (2023a). *OECD TG 497 Defined Approaches for Skin Sensitisation*. OECD.

OECD. (2023b). Test No. 444A: In Vitro Immunotoxicity. *OECD Guidelines for the Testing of Chemicals, Section 4,* 10.1787/27b10ba3-en

OECD. (2023c). *Test No. 487: In Vitro Mammalian Cell Micronucleus Test*. OECD Publishing. 10.1787/9789264264861-en

OECD. (2024). *OECD GUIDELINE FOR THE TESTING OF CHEMICALS Defined Approaches (DAs) for Serious Eye Damage and Eye Irritation for including a new DA for solids*

Oliver, L. C., Sampara, P., Pearson, D., Martell, J., & Zarnke, A. M. (2022). Sarcoidosis in Northern Ontario hard-rock miners: A case series. *American Journal of Industrial Medicine, 65*(4), 268–280. 10.1002/ajim.23333

Oomen, A. G., Bleeker, E. A. J., Bos, P. M. J., Van Broekhuizen, F., Gottardo, S., Groenewold, M., Hristozov, D., Hund-Rinke, K., Irfan, M., Marcomini, A., Peijnenburg, W. J. G. M., Rasmussen, K., Jiménez, A., Scott-Fordsmand, J. J., Van Tongeren, M., Wiench, K., Wohlleben, W., & Landsiedel, R. (2015). Grouping and Read-Across Approaches for Risk Assessment of Nanomaterials. *International Journal of Environmental Research and Public Health, 12*(10), 13415. 10.3390/ijerph121013415

Ostrowski, A., Nordmeyer, D., Boreham, A., Holzhausen, C., Mundhenk, L., Graf, C., Meinke, M. C., Vogt, A., Hadam, S., Lademann, J., Rühl, E., Alexiev, U., & Gruber, A. D. (2015). Overview about the localization of nanoparticles in tissue and cellular context by different imaging techniques. *Beilstein Journal of Nanotechnology, 6*, 263. 10.3762/bjnano.6.25

Panizzolo, Barbero, Ghelli, Garzaro, Bellisario, Guseva Canu, Fenoglio, Bergamaschi, & Bono. (2024). *Assessing the inhaled dose of nanomaterials by nanoparticle tracking analysis (NTA) of exhaled breath condensate (EBC) and its relationship with lung inflammatory biomarkers*. Elsevier BV. 10.1016/j.chemosphere.2024.142139

Pavan, C., Delle Piane, M., Gullo, M., Filippi, F., Fubini, B., Hoet, P., Horwell, C. J., Huaux, F., Lison, D., Lo Giudice, C., Martra, G., Montfort, E., Schins, R., Sulpizi, M., Wegner, K., Wyart-Remy, M., Ziemann, C., & Turci, F. (2019). The puzzling issue of silica toxicity: are silanols bridging the gaps between surface states and pathogenicity? *Particle and Fibre Toxicology, 16*(1), 32–10. 10.1186/s12989-019-0315-3

Pelclova, D., Barosova, H., Kukutschova, J., Zdimal, V., Navratil, T., Fenclova, Z., Vlckova, S., Schwarz, J., Zikova, N., Kacer, P., Komarc, M., Belacek, J., & Zakharov, S. (2015). Raman microspectroscopy of exhaled breath condensate and urine in workers exposed to fine and nano TiO2 particles: a cross-sectional study. *Journal of Breath Research, 9*(3), 036008. 10.1088/1752-7155/9/3/036008

Pelclova, D., Zdimal, V., Schwarz, J., Dvorackova, S., Komarc, M., Ondracek, J., Kostejn, M., Kacer, P., Vlckova, S., Fenclova, Z., Popov, A., Lischkova, L., Zakharov, S., & Bello, D. (2018). Markers

of Oxidative Stress in the Exhaled Breath Condensate of Workers Handling Nanocomposites. *Nanomaterials, 8*(8), 611. 10.3390/nano8080611

Pelclova, Zdimal, Kacer, Fenclova, Vlckova, Komarc, Navratil, Schwarz, Zikova, Makes, Syslova, Belacek, & Zakharov. (2016). *Leukotrienes in exhaled breath condensate and fractional exhaled nitric oxide in workers exposed to TiO 2 nanoparticles*. IOP Publishing. 10.1088/1752-7155/10/3/036004

Peña, M. D. P. S., Gottipati, A., Tahiliani, S., Neu-Baker, N. M., Frame, M. D., Friedman, A. J., & Brenner, S. A. (2016). Hyperspectral imaging of nanoparticles in biological samples: Simultaneous visualization and elemental identification. *Microscopy Research and Technique, 79*(5), 349. 10.1002/jemt.22637

Petersen, E. J., Reipa, V., Watson, S. S., Stanley, D. L., Rabb, S. A., & Nelson, B. C. (2014). DNA Damaging Potential of Photoactivated P25 Titanium Dioxide Nanoparticles. *Chemical Research in Toxicology, 27*(10), 1877–1884. 10.1021/tx500340v

Piccinno, F., Gottschalk, F., Seeger, S., & Nowack, B. (2012). Industrial production quantities and uses of ten engineered nanomaterials in Europe and the world. *Journal of Nanoparticle Research, 14*(9), 1109–11. 10.1007/s11051-012-1109-9

Pink, Verma, & Schmitz-Spanke. (2020). Benchmark dose analyses of toxic endpoints in lung cells provide sensitivity and toxicity ranking across metal oxide nanoparticles and give insights into the mode of action. *Toxicology Letters, 331*, 218. 10.1016/j.toxlet.2020.06.012

Poland, Duffin, Kinloch, Maynard, Wallace, Seaton, Stone, Brown, Macnee, & Donaldson. (2008). Carbon nanotubes introduced into the abdominal cavity of mice show asbestos-like pathogenicity in a pilot study. *Nature Nanotechnology, 3*(7), 423. 10.1038/nnano.2008.111

Popp, L., Tran, V., Patel, R., & Segatori, L. (2018). Autophagic response to cellular exposure to titanium dioxide nanoparticles. *Acta Biomaterialia, 79*, 354. 10.1016/j.actbio.2018.08.021

Poulsen, S. S., Saber, A. T., Williams, A., Andersen, O., Købler, C., Atluri, R., Pozzebon, M. E., Mucelli, S. P., Simion, M., Rickerby, D., Mortensen, A., Jackson, P., Kyjovska, Z. O., Mølhave, K., Jacobsen, N. R., Jensen, K. A., Yauk, C. L., Wallin, H., Halappanavar, S., & Vogel, U. (2015). MWCNTs of different physicochemical properties cause similar inflammatory responses, but differences in transcriptional and histological markers of fibrosis in mouse lungs. *Toxicology and Applied Pharmacology, 284*(1), 16–32. 10.1016/j.taap.2014.12.011

Q. Vuong, N., Khilji, S., Williams, A., Adam, N., Flores, D., Fulton, K. M., Baay, I., Twine, S. M., Meier, M. J., Kumarathasan, P., Wilkins, R. C., Yauk, C. L., & Chauhan, V. (2025). *Integration of multi-omics and benchmark dose modeling to support adverse outcome pathways*. Informa UK Limited. 10.1080/09553002.2024.2442694

Racette, B. A. (2014). Manganism in the 21st century: The Hanninen lecture. *NeuroToxicology, 45*, 201–207. 10.1016/j.neuro.2013.09.007

Rahman, L., Jacobsen, N. R., Aziz, S. A., Wu, D., Williams, A., Yauk, C. L., White, P., Wallin, H., Vogel, U., & Halappanavar, S. (2017a). Multi-walled carbon nanotube-induced genotoxic, inflammatory and pro-fibrotic responses in mice: Investigating the mechanisms of pulmonary carcinogenesis. *Mutation Research, 823*, 28–44. 10.1016/j.mrgentox.2017.08.005

Rahman, L., Williams, A., Gelda, K., Nikota, J., Wu, D., Vogel, U., & Halappanavar, S. (2020). 21st Century Tools for Nanotoxicology: Transcriptomic Biomarker Panel and Precision-Cut Lung Slice Organ Mimic System for the Assessment of Nanomaterial-Induced Lung Fibrosis. *Small (Weinheim an Der Bergstrasse, Germany), 16*(36), e2000272–n/a. 10.1002/smll.202000272

Rahman, L., Wu, D., Johnston, M., William, A., & Halappanavar, S. (2017b). Toxicogenomics analysis of mouse lung responses following exposure to titanium dioxide nanomaterials reveal their disease potential at high doses. *Mutagenesis, 32*(1), 59–76. 10.1093/mutage/gew048

Rahman, Pittarate, Perumal, Rajula, Thungrabeab, Mekchay, & Krutmuang. (2022). *Larvicidal and Antifeedant Effects of Copper Nano-Pesticides against Spodoptera frugiperda (J.E. Smith) and Its Immunological Response*. MDPI AG. 10.3390/insects13111030

Rasmussen, González, Kearns, Sintes, Rossi, & Sayre. (2015). Review of achievements of the OECD Working Party on Manufactured Nanomaterials' Testing and Assessment Programme. From exploratory testing to test guidelines. *Regulatory Toxicology and Pharmacology, 74*, 147. 10.1016/j.yrtph.2015.11.004

Reed, R. B., Ladner, D. A., Higgins, C. P., Westerhoff, P., & Ranville, J. F. (2012). Solubility of nano-zinc oxide in environmentally and biologically important matrices. *Environmental Toxicology and Chemistry, 31*(1), 93–99. 10.1002/etc.708

Rockey, D. C., Bell, P. D., & Hill, J. A. (2015). Fibrosis — A Common Pathway to Organ Injury and Failure. *New England Journal of Medicine, 372*(12), 1138. 10.1056/nejmra1300575

Rohrs, C. (1957). Metal-Fume Fever from Inhaling Zinc Oxide. *A.M.A. Archives of Industrial Health, 16*(1), 42–47.

Rowan-Carroll, A., Reardon, A., Leingartner, K., Gagné, R., Williams, A., Meier, M. J., Kuo, B., Bourdon-Lacombe, J., Moffat, I., Carrier, R., Nong, A., Lorusso, L., Ferguson, S. S., Atlas, E., & Yauk, C. (2021). High-Throughput Transcriptomic Analysis of Human Primary Hepatocyte Spheroids Exposed to Per- and Polyfluoroalkyl Substances as a Platform for Relative Potency Characterization. *Toxicological Sciences, 181*(2), 199–214. 10.1093/toxsci/kfab039

Ryter, S. W. (2022). Heme Oxygenase-1: An Anti-Inflammatory Effector in Cardiovascular, Lung, and Related Metabolic Disorders. *Antioxidants, 11*(3), 555. 10.3390/antiox11030555

SALDANHA, A. J. (2004). Java Treeview—extensible visualization of microarray data. *Bioinformatics, 20*(17), 3246–3248. 10.1093/bioinformatics/bth349

Sanders, K., Degn, L. L., Mundy, W. R., Zucker, R. M., Dreher, K., Zhao, B., Roberts, J. E., & Boyes, W. K. (2012). In Vitro Phototoxicity and Hazard Identification of Nano-scale Titanium Dioxide. *Toxicology and Applied Pharmacology, 258*(2), 226–236. 10.1016/j.taap.2011.10.023

Santhosh, C., Velmurugan, V., Jacob, G., Jeong, S. K., Grace, A. N., & Bhatnagar, A. (2016). Role of nanomaterials in water treatment applications: A review. *Chemical Engineering Journal, 306*, 1116–1137. 10.1016/j.cej.2016.08.053

Sárközi, L., Horváth, E., Kónya, Z., Kiricsi, I., Szalay, B., Vezér, T., & Papp, A. (2009). Subacute intratracheal exposure of rats to manganese nanoparticles: Behavioral, electrophysiological, and general toxicological effects. *Inhalation Toxicology, 21*(S1), 83–91. 10.1080/08958370902939406

Schinwald, Murphy, Prina-Mello, Poland, Byrne, Movia, Glass, Dickerson, Schultz, Jeffree, Macnee, & Donaldson. (2012). The Threshold Length for Fiber-Induced Acute Pleural Inflammation: Shedding Light on the Early Events in Asbestos-Induced Mesothelioma. *Toxicological Sciences, 128*(2), 461. 10.1093/toxsci/kfs171

Schmid, O., & Stoeger, T. (2016). Surface area is the biologically most effective dose metric for acute nanoparticle toxicity in the lung. *Journal of Aerosol Science, 99*, 133–143. 10.1016/j.jaerosci.2015.12.006

Schubert, J., & Chanana, M. (2018). Coating Matters: Review on Colloidal Stability of Nanoparticles with Biocompatible Coatings in Biological Media, Living Cells and Organisms. *Current Medicinal Chemistry, 25*(35), 4553–4586. 10.2174/0929867325666180601101859

Schulte, P. A., Leso, V., Niang, M., & Iavicoli, I. (2019a). Current state of knowledge on the health effects of engineered nanomaterials in workers. *Scandinavian Journal of Work, Environment & Health, 45*(3), 217–238. 10.5271/sjweh.3800

Schulte, P. A., Leso, V., Niang, M., & Iavicoli, I. (2019b). Current state of knowledge on the health effects of engineered nanomaterials in workers. *Scandinavian Journal of Work, Environment & Health, 45*(3), 217–238. 10.5271/sjweh.3800

Schulz, M., Olubummo, A., & Binder, W. H. (2012). Beyond the lipid-bilayer: interaction of polymers and nanoparticles with membranes. *Soft Matter, 8*(18), 4849–4864. 10.1039/c2sm06999g

Sciau, P. (2012). Nanoparticles in Ancient Materials: The Metallic Lustre Decorations of Medieval Ceramics. InTech. 10.5772/34080

Searle, S. R., Speed, F. M., & Milliken, G. A. (1980). Population Marginal Means in the Linear Model: An Alternative to Least Squares Means. *The American Statistician, 34*(4), 216. 10.2307/2684063

Seaton, A. (1995). *Particulate air pollution and acute health effects Summary*. Lancet (London, England). **https://doi.org/10.1016/s0140-6736(95)90173-6**

Semisch, A., Ohle, J., Witt, B., & Hartwig, A. (2014). Cytotoxicity and genotoxicity of nano - and microparticulate copper oxide: role of solubility and intracellular bioavailability. *Particle and Fibre Toxicology, 11*(1), 10. 10.1186/1743-8977-11-10

Sengul, A. B., & Asmatulu, E. (2020). Toxicity of metal and metal oxide nanoparticles: a review. *Environmental Chemistry Letters, 18*(5), 1659–1683. 10.1007/s10311-020-01033-6

Seo, J., Tryndyak, V., Wu, Q., Dreval, K., Pogribny, I., Bryant, M., Zhou, T., Robison, T. W., Mei, N., & Guo, X. (2019). Quantitative comparison of in vitro genotoxicity between metabolically competent HepaRG cells and HepG2 cells using the high-throughput high-content CometChip assay. *Archives of Toxicology, 93*(5), 1433–1448. 10.1007/s00204-019-02406-9

Shakeel, Jabeen, Shabbir, Asghar, Khan, & Chaudhry. (2015). Toxicity of Nano-Titanium Dioxide (TiO2-NP) Through Various Routes of Exposure: a Review. *Biological Trace Element Research, 172*(1), 1. 10.1007/s12011-015-0550-x

Sharifi, Behzadi, Laurent, Laird Forrest, Stroeve, & Mahmoudi. (2011). Toxicity of nanomaterials. *Chem. Soc. Rev., 41*(6), 2323. 10.1039/c1cs15188f

Shi, X., Wang, X., Huang, R., Tang, C., Hu, C., Ning, P., & Wang, F. (2022). Cytotoxicity and Genotoxicity of Polystyrene Micro- and Nanoplastics with Different Size and Surface Modification in A549 Cells. *International Journal of Nanomedicine, 17*, 4509–4523. 10.2147/IJN.S381776

Shinohara, N., Zhang, G., Oshima, Y., Kobayashi, T., Imatanaka, N., Nakai, M., Sasaki, T., Kawaguchi, K., & Gamo, M. (2017). Kinetics and dissolution of intratracheally administered nickel oxide nanomaterials in rats. *Particle and Fibre Toxicology, 14*(1), 48. 10.1186/s12989-017-0229-x

Sieg, H., Braeuning, C., Kunz, B. M., Daher, H., Kästner, C., Krause, B., Meyer, T., Jalili, P., Hogeveen, K., Böhmert, L., Lichtenstein, D., Burel, A., Chevance, S., Jungnickel, H., Tentschert, J., Laux, P., Braeuning, A., Gauffre, F., Fessard, V., . . . Lampen, A. (2018). Uptake and molecular impact of aluminum-containing nanomaterials on human intestinal caco-2 cells. *Nanotoxicology, 12*(9), 992–1013. 10.1080/17435390.2018.1504999

Sieg, H., Kästner, C., Krause, B., Meyer, T., Burel, A., Böhmert, L., Lichtenstein, D., Jungnickel, H., Tentschert, J., Laux, P., Braeuning, A., Estrela-Lopis, I., Gauffre, F., Fessard, V., Meijer, J., Luch, A., Thünemann, A. F., & Lampen, A. (2017). Impact of an Artificial Digestion Procedure on Aluminum-Containing Nanomaterials. *Langmuir, 33*(40), 10726–10735. 10.1021/acs.langmuir.7b02729

Siegrist, K. J., Reynolds, S. H., Porter, D. W., Mercer, R. R., Bauer, A. K., Lowry, D., Cena, L., Stueckle, T. A., Kashon, M. L., Wiley, J., Salisbury, J. L., Mastovich, J., Bunker, K., Sparrow, M., Lupoi, J. S., Stefaniak, A. B., Keane, M. J., Tsuruoka, S., Terrones, M., . . . Sargent, L. M. (2019). Mitsui-7, heat-treated, and nitrogen-doped multi-walled carbon nanotubes elicit genotoxicity in human lung epithelial cells. *Particle and Fibre Toxicology, 16*(1), 36. 10.1186/s12989-019-0318-0

Siivola, K. M., Suhonen, S., Hartikainen, M., Catalán, J., & Norppa, H. (2020). Genotoxicity and cellular uptake of nanosized and fine copper oxide particles in human bronchial epithelial cells in vitro. *Mutation Research. Genetic Toxicology and Environmental Mutagenesis, 856-857*, 503217. 10.1016/j.mrgentox.2020.503217

Singh, S. (2019). Zinc oxide nanoparticles impacts: cytotoxicity, genotoxicity, developmental toxicity, and neurotoxicity. *Toxicology Mechanisms and Methods, 29*(4), 300–311. 10.1080/15376516.2018.1553221

SINGH, S., TINGMING SHI, SCHINS, R. P. F., DUFFIN, R., ALBRECHT, C., VAN BERLO, D., HOHR, D., FUBINI, B., MARTRA, G., FENOGLIO, I., & BONN, P. J. A. (2007). Endocytosis, oxidative stress and IL-8 expression in human lung epithelial cells upon treatment with fine and ultrafine TiO2: Role of the specific surface area and of surface methylation of the particles. *Toxicology and Applied Pharmacology, 222*(2), 141–151. 10.1016/j.taap.2007.05.001

Sisler, J. D., Li, R., McKinney, W., Mercer, R. R., Ji, Z., Xia, T., Wang, X., Shaffer, J., Orandle, M., Mihalchik, A. L., Battelli, L., Chen, B. T., Wolfarth, M., Andrew, M. E., Schwegler-Berry, D., Porter, D. W., Castranova, V., Nel, A., & Qian, Y. (2016). Differential pulmonary effects of CoO and La2O3 metal oxide nanoparticle responses during aerosolized inhalation in mice. *Particle and Fibre Toxicology, 13*(1), 42. 10.1186/s12989-016-0155-3

Ślosarczyk, A., Klapiszewska, I., Skowrońska, D., Janczarek, M., Jesionowski, T., & Klapiszewski, Ł. (2023). A comprehensive review of building materials modified with metal and metal oxide

nanoparticles against microbial multiplication and growth. *Chemical Engineering Journal, 46*610.1016/j.cej.2023.143276

Smith, A. T., Lachance, A. M., Zeng, S., Liu, B., & Sun, L. (2019). Synthesis, properties, and applications of graphene oxide/reduced graphene oxide and their nanocomposites. *Nano Materials Science, 1*(1), 31. 10.1016/j.nanoms.2019.02.004

Solano, R., Patiño-Ruiz, D., Tejeda-Benitez, L., & Herrera, A. (2021). Metal- and metal/oxide-based engineered nanoparticles and nanostructures: a review on the applications, nanotoxicological effects, and risk control strategies. *Environmental Science and Pollution Research International, 28*(14), 16962–16981. 10.1007/s11356-021-12996-6

Solorio-Rodriguez, Wu, Boyadzhiev, Christ, Williams, & Halappanavar. (2024). *A Systematic Genotoxicity Assessment of a Suite of Metal Oxide Nanoparticles Reveals Their DNA Damaging and Clastogenic Potential*. MDPI AG. 10.3390/nano14090743

SoRelle, E. D., Liba, O., Campbell, J. L., Dalal, R., Zavaleta, C. L., & de la Zerda, A. (2016). A hyperspectral method to assay the microphysiological fates of nanomaterials in histological samples. *eLife, 5*10.7554/eLife.16352

Sotiriou, G. A., Watson, C., Murdaugh, K. M., Darrah, T. H., Pyrgiotakis, G., Elder, A., Brain, J. D., & Demokritou, P. (2014). Engineering safer-by-design silica-coated ZnO nanorods with reduced DNA damage potential. *Environmental Science. Nano, 1*(2), 144–153. 10.1039/c3en00062a

Sousa De Almeida, M., Susnik, E., Drasler, B., Taladriz-Blanco, P., Petri-Fink, A., & Rothen-Rutishauser, B. (2021). Understanding nanoparticle endocytosis to improve targeting strategies in nanomedicine. *Chemical Society Reviews, 50*(9), 5397. 10.1039/d0cs01127d

Stevens, J. P. (2009). *Applied multivariate statistics for the social sciences* (5th ed. ed.). Routledge. 10.4324/9780203843130

Stone, Gottardo, Bleeker, Braakhuis, Dekkers, Fernandes, Haase, Hunt, Hristozov, Jantunen, Jeliazkova, Johnston, Lamon, Murphy, Rasmussen, Rauscher, Jiménez, Svendsen, Spurgeon, . . . Oomen. (2020). A framework for grouping and read-across of nanomaterials- supporting innovation and risk assessment. *Nano Today, 35*10.1016/j.nantod.2020.100941

Strauch, B. M., Hubele, W., & Hartwig, A. (2020). Impact of Endocytosis and Lysosomal Acidification on the Toxicity of Copper Oxide Nano- and Microsized Particles: Uptake and Gene Expression Related to Oxidative Stress and the DNA Damage Response. *Nanomaterials (Basel, Switzerland), 10*(4), 679. 10.3390/nano10040679

Strauch, B. M., Niemand, R. K., Winkelbeiner, N. L., & Hartwig, A. (2017). Comparison between micro- and nanosized copper oxide and water soluble copper chloride: interrelationship between intracellular copper concentrations, oxidative stress and DNA damage response in human lung cells. *Particle and Fibre Toxicology, 14*(1), 28. 10.1186/s12989-017-0209-1

Sun, T., Yan, Y., Zhao, Y., Guo, F., & Jiang, C. (2012). Copper Oxide Nanoparticles Induce Autophagic Cell Death in A549 Cells. *PloS One, 7*(8), e43442. 10.1371/journal.pone.0043442

Sykora, P., Chiari, Y., Heaton, A., Moreno, N., Glaberman, S., Sobol, R. W., & Wilson, D. (2018a). Application of the CometChip platform to assess DNA damage in field-collected blood samples from turtles. *Environmental and Molecular Mutagenesis, 59*(4), 322–333. 10.1002/em.22183

Sykora, P., Witt, K. L., Revanna, P., Smith-Roe, S. L., Dismukes, J., Lloyd, D. G., Engelward, B. P., & Sobol, R. W. (2018b). Next generation high throughput DNA damage detection platform for genotoxic compound screening. *Scientific Reports, 8*(1), 1–20. 10.1038/s41598-018-20995-w

Søs Poulsen, S., Jacobsen, N. R., Labib, S., Wu, D., Husain, M., Williams, A., Bøgelund, J. P., Andersen, O., Købler, C., Mølhave, K., Kyjovska, Z. O., Saber, A. T., Wallin, H., Yauk, C. L., Vogel, U., & Halappanavar, S. (2013). Transcriptomic Analysis Reveals Novel Mechanistic Insight into Murine Biological Responses to Multi-Walled Carbon Nanotubes in Lungs and Cultured Lung Epithelial Cells. *PloS One, 8*(11), e80452. 10.1371/journal.pone.0080452

Tada-Oikawa, S., Ichihara, G., Suzuki, Y., Izuoka, K., Wu, W., Yamada, Y., Mishima, T., & Ichihara, S. (2015). Zn(II) released from zinc oxide nano/micro particles suppresses vasculogenesis in human endothelial colony-forming cells. *Toxicology Reports, 2*(C), 692–701. 10.1016/j.toxrep.2015.04.003

Thoma, T., Ma-Hock, L., Schneider, S., Honarvar, N., Treumann, S., Groeters, S., Strauss, V., Marxfeld, H., Funk-Weyer, D., Seiffert, S., Wohlleben, W., Dammann, M., Wiench, K., Lombaert, N., Spirlet, C., Vasquez, M., Dewhurst, N., & Landsiedel, R. (2024). *Toxicological inhalation studies in rats to substantiate grouping of zinc oxide nanoforms*. Springer Science and Business Media LLC. 10.1186/s12989-024-00572-y

Titma, T., Shimmo, R., Siigur, J., & Kahru, A. (2016). Toxicity of antimony, copper, cobalt, manganese, titanium and zinc oxide nanoparticles for the alveolar and intestinal epithelial barrier cells in vitro. *Cytotechnology (Dordrecht), 68*(6), 2363–2377. 10.1007/s10616-016-0032-9

Todd, N. W., Luzina, I. G., & Atamas, S. P. (2012). Molecular and cellular mechanisms of pulmonary fibrosis. *Fibrogenesis & Tissue Repair, 5*(1), 11. 10.1186/1755-1536-5-11

Tolliver, L. M., Holl, N. J., Hou, F. Y. S., Lee, H., Cambre, M. H., & Huang, Y. (2020). Differential Cytotoxicity Induced by Transition Metal Oxide Nanoparticles is a Function of Cell Killing and Suppression of Cell Proliferation. *International Journal of Molecular Sciences, 21*(5), 1731. 10.3390/ijms21051731

Tossavainen, A. (1976). Metal fumes in foundries. *Scandinavian Journal of Work, Environment &Amp; Health, 2*(1)10.5271/sjweh.2833

U.S. Department of Health and Human Services, Food and Drug Administration, & Office of the Commissioner. (2014). *Guidance for Industry Considering Whether an FDA-Regulated Product Involves the Application of Nanotechnology Contains Nonbinding Recommendations*.

U.S. Department of Labor Occupational Safety and Health Administration. *Zinc Oxide, Dust & Fume.* Retrieved April 2 2024, from **https://www.osha.gov/chemicaldata/215**

US Department of Health and Human Services, Food and Drug Administration Center for Drug Evaluation and Research (CDER), & Center for Biologics Evaluation and Research (CBER). (2022). *Drug Products, Including Biological Products, that Contain Nanomaterials - Guidance for Industry*

Valdiglesias, V., Kiliç, G., Costa, C., Fernández-Bertólez, N., Pásaro, E., Teixeira, J. P., & Laffon, B. (2015). Effects of iron oxide nanoparticles: Cytotoxicity, genotoxicity, developmental toxicity, and neurotoxicity. *Environmental and Molecular Mutagenesis, 56*(2), 125–148. 10.1002/em.21909

Vallotton, P., Angel, B., Mccall, M., Osmond, M., & Kirby, J. (2014). Imaging nanoparticle-algae interactions in three dimensions using Cytoviva microscopy. *Journal of Microscopy, 257*(2), 166. 10.1111/jmi.12199

Van Der Zalm, A. J., Barroso, J., Browne, P., Casey, W., Gordon, J., Henry, T. R., Kleinstreuer, N. C., Lowit, A. B., Perron, M., & Clippinger, A. J. (2022). A framework for establishing scientific confidence in new approach methodologies. *Archives of Toxicology, 96*(11), 2865. 10.1007/s00204-022-03365-4

Van Weeren, L., De Graaff, A. M., Jamieson, J. D., Batenburg, J. J., & Valentijn, J. A. (2004). Rab3D and Actin Reveal Distinct Lamellar Body Subpopulations in Alveolar Epithelial Type II Cells. *American Journal of Respiratory Cell and Molecular Biology, 30*(3), 288. 10.1165/rcmb.2003-0264oc

Vance, M. E., Kuiken, T., Vejerano, E. P., McGinnis, S. P., Hochella, J., Michael F, Rejeski, D., & Hull, M. S. (2015). Nanotechnology in the real world: Redeveloping the nanomaterial consumer products inventory. *Beilstein Journal of Nanotechnology, 6*(1), 1769–1780. 10.3762/bjnano.6.181

Vassal, M., Rebelo, S., & Pereira, M. d. L. (2021). Metal Oxide Nanoparticles: Evidence of Adverse Effects on the Male Reproductive System. *International Journal of Molecular Sciences, 22*(15), 8061. 10.3390/ijms22158061

Vassie, J. A., Whitelock, J. M., & Lord, M. S. (2017). Endocytosis of cerium oxide nanoparticles and modulation of reactive oxygen species in human ovarian and colon cancer cells. *Acta Biomaterialia, 50*, 127–141. 10.1016/j.actbio.2016.12.010

Vecchio, G., Fenech, M., Pompa, P. P., & Voelcker, N. H. (2014). Lab-on-a-Chip-Based High-Throughput Screening of the Genotoxicity of Engineered Nanomaterials. *Small (Weinheim an Der Bergstrasse, Germany), 10*(13), 2721–2734. 10.1002/smll.201303359

Verma, D. K. (2013). Metals in the Lungs of Ontario Hardrock Miners. *Archives of Environmental & Occupational Health, 68*(3), 180–183. 10.1080/19338244.2012.663011

Villeneuve, D. L., Crump, D., Garcia-Reyero, N., Hecker, M., Hutchinson, T. H., Lalone, C. A., Landesmann, B., Lettieri, T., Munn, S., Nepelska, M., Ottinger, M. A., Vergauwen, L., & Whelan, M. (2014). Adverse Outcome Pathway (AOP) Development I: Strategies and Principles. *Toxicological Sciences, 142*(2), 312. 10.1093/toxsci/kfu199

Virlan, M., Miricescu, D., Radulescu, R., Sabliov, C. M., Totan, A., Calenic, B., & Greabu, M. (2016). *Organic Nanomaterials and Their Applications in the Treatment of Oral Diseases*. MDPI AG. 10.3390/molecules21020207

Wall, Seleci, Schworm, Neuberger, Link, Hufnagel, Schumacher, Schulz, Heinrich, Wohlleben, & Hartwig. (2021). Comparison of Metal-Based Nanoparticles and Nanowires: Solubility, Reactivity, Bioavailability and Cellular Toxicity. *Nanomaterials, 12*(1)10.3390/nano12010147

Wang, D., Li, H., Liu, Z., Zhou, J., & Zhang, T. (2017). Acute toxicological effects of zinc oxide nanoparticles in mice after intratracheal instillation. *International Journal of Occupational and Environmental Health, 23*(1), 11–19. 10.1080/10773525.2016.1278510

Wang, M., Li, J., Dong, S., Cai, X., Simaiti, A., Yang, X., Zhu, X., Luo, J., Jiang, L., Du, B., Yu, P., & Yang, W. (2020). *Silica nanoparticles induce lung inflammation in mice via ROS/PARP/TRPM2*

signaling-mediated lysosome impairment and autophagy dysfunction. Springer Science and Business Media LLC. 10.1186/s12989-020-00353-3

Wang, Z., & Tang, M. (2021). Research progress on toxicity, function, and mechanism of metal oxide nanoparticles on vascular endothelial cells. *Journal of Applied Toxicology, 41*(5), 683–700. 10.1002/jat.4121

Wani, M. R., & Shadab, G. (2020). *Titanium dioxide nanoparticle genotoxicity: A review of recent in vivo and in vitro studies*. SAGE Publications. 10.1177/0748233720936835

Waters, K. M., Masiello, L. M., Zangar, R. C., Tarasevich, B. J., Karin, N. J., Quesenberry, R. D., Bandyopadhyay, S., Teeguarden, J. G., Pounds, J. G., & Thrall, B. D. (2009). Macrophage Responses to Silica Nanoparticles are Highly Conserved Across Particle Sizes. *Toxicological Sciences, 107*(2), 553–569. 10.1093/toxsci/kfn250

Watson, C., Ge, J., Cohen, J., Pyrgiotakis, G., Engelward, B. P., & Demokritou, P. (2014). High-Throughput Screening Platform for Engineered Nanoparticle-Mediated Genotoxicity Using CometChip Technology. *ACS Nano, 8*(3), 2118–2133. 10.1021/nn404871p

Wedrychowski, A., Schmidt, W. N., & Hnilica, L. S. (1986). The in vivo cross-linking of proteins and DNA by heavy metals. *The Journal of Biological Chemistry, 261*(7), 3370–3376. 10.1016/S0021-9258(17)35792-7

Weir, A., Westerhoff, P., Fabricius, L., Hristovski, K., & Von Goetz, N. (2012). Titanium Dioxide Nanoparticles in Food and Personal Care Products. *Environmental Science &Amp; Technology, 46*(4), 2242. 10.1021/es204168d

White, P. A., Douglas, G. R., Gingerich, J., Parfett, C., Shwed, P., Seligy, V., Soper, L., Berndt, L., Bayley, J., Wagner, S., Pound, K., & Blakey, D. (2003). Development and characterization of a stable epithelial cell line from Muta™Mouse lung. *Environmental and Molecular Mutagenesis, 42*(3), 166–184. 10.1002/em.10185

White, P. A., Luijten, M., Mishima, M., Cox, J. A., Hanna, J. N., Maertens, R. M., & Zwart, E. P. (2019). In vitro mammalian cell mutation assays based on transgenic reporters: A report of the International Workshop on Genotoxicity Testing (IWGT). *Mutation Research, 847*, 403039. 10.1016/j.mrgentox.2019.04.002

Wight, T. N., Frevert, C. W., Debley, J. S., Reeves, S. R., Parks, W. C., & Ziegler, S. F. (2017). Interplay of extracellular matrix and leukocytes in lung inflammation. *Cellular Immunology, 312*, 1–14. 10.1016/j.cellimm.2016.12.003

Wills, J. W., Johnson, G. E., Doak, S. H., Soeteman-Hernández, L. G., Slob, W., & White, P. A. (2015). Empirical analysis of BMD metrics in genetic toxicology part I:in vitroanalyses to provide robust potency rankings and support MOA determinations. *Mutagenesis, 31*(3), 255. 10.1093/mutage/gev085

Wills, J. W., Johnson, G. E., Doak, S. H., Soeteman-Hernández, L. G., Slob, W., & White, P. A. (2016). Empirical analysis of BMD metrics in genetic toxicology part I: in vitro analyses to provide robust potency rankings and support MOA determinations. *Mutagenesis, 31*(3), 255–263. 10.1093/mutage/gev085

Wils, R. S., Jacobsen, N. R., Di Ianni, E., Roursgaard, M., & Møller, P. (2021). *Reactive oxygen species production, genotoxicity and telomere length in FE1-Muta™Mouse lung epithelial cells exposed to carbon nanotubes*. Informa UK Limited. 10.1080/17435390.2021.1910359

Wongrakpanich, A., Mudunkotuwa, I. A., Geary, S. M., Morris, A. S., Mapuskar, K. A., Spitz, D. R., Grassian, V. H., & Salem, A. K. (2016). Size-dependent cytotoxicity of copper oxide nanoparticles in lung epithelial cells. *Environmental Science. Nano, 3*(2), 365–374. 10.1039/c5en00271k

World Health Organization. (2021). *WHO human health risk assessment toolkit: chemical hazards, second edition* (2nd ed.). World Health Organization.

World Health Organization, & International Programme on Chemical Safety. (2019). *Principles and methods to assess the risk of immunotoxicity associated with exposure to nanomaterials*. World Health Organization.

Wouters, B. G., & Koritzinsky, M. (2008). Hypoxia signalling through mTOR and the unfolded protein response in cancer. *Nature Reviews. Cancer, 8*(11), 851–864. 10.1038/nrc2501

Wu, H., Kerr, M. K., Cui, X., & Churchill, G. A. (2003). MAANOVA: A Software Package for the Analysis of Spotted cDNA Microarray Experiments. *Analysis of Gene Expression Data* (pp. 313–341). Springer. 10.1007/0-387-21679-0_14

Xia, Zhao, Sager, George, Pokhrel, Li, Schoenfeld, Meng, Lin, Wang, Wang, Ji, Zink, Mädler, Castranova, Lin, & Nel. (2011). Decreased Dissolution of ZnO by Iron Doping Yields Nanoparticles with Reduced Toxicity in the Rodent Lung and Zebrafish Embryos. *ACS Nano, 5*(2), 1223. 10.1021/nn1028482

Xu, P., Zeng, G. M., Huang, D. L., Feng, C. L., Hu, S., Zhao, M. H., Lai, C., Wei, Z., Huang, C., Xie, G. X., & Liu, Z. F. (2012). Use of iron oxide nanomaterials in wastewater treatment: A review. *Science of the Total Environment, 424*, 1. 10.1016/j.scitotenv.2012.02.023

Yang, Y., & Westerhoff, P. (2014). Presence in, and Release of, Nanomaterials from Consumer Products. (pp. 1). Springer Netherlands. 10.1007/978-94-017-8739-0_1

Yetisen, A. K., Coskun, A. F., England, G., Cho, S., Butt, H., Hurwitz, J., Kolle, M., Khademhosseini, A., Hart, A. J., Folch, A., & Yun, S. H. (2016). Art on the Nanoscale and Beyond. *Advanced Materials (Weinheim), 28*(9), 1724–1742. 10.1002/adma.201502382

Yoo, N., Jeon, Y., & Choi, S. (2021). Determination of Two Differently Manufactured Silicon Dioxide Nanoparticles by Cloud Point Extraction Approach in Intestinal Cells, Intestinal Barriers and Tissues. *International Journal of Molecular Sciences, 22*(13), 7035. 10.3390/ijms22137035

Yoon, Y., Truong, P. L., Lee, D., & Ko, S. H. (2021). *Metal-Oxide Nanomaterials Synthesis and Applications in Flexible and Wearable Sensors*. American Chemical Society (ACS). 10.1021/acsnanoscienceau.1c00029

Younes, Aquilina, Castle, Engel, Fowler, Frutos Fernandez, Fürst, Gundert-remy, Gürtler, Husøy, Manco, Mennes, Moldeus, Passamonti, Shah, Waalkens-berendsen, Wölfle, Corsini, Cubadda, . . . Wright. (2021). Safety assessment of titanium dioxide (E171) as a food additive. *EFSA Journal, 19*(5)10.2903/j.efsa.2021.6585

Zamora-Perez, P., Pelaz, B., Tsoutsi, D., Soliman, M. G., Parak, W. J., & Rivera-Gil, P. (2021). Hyperspectral-enhanced dark field analysis of individual and collective photo-responsive gold-copper sulfide nanoparticles. *Nanoscale, 13*(31), 13256–13272. 10.1039/d0nr08256b

Zhang, H., Ji, Z., Xia, T., Meng, H., Low-Kam, C., Liu, R., Pokhrel, S., Lin, S., Wang, X., Liao, Y., Wang, M., Li, L., Rallo, R., Damoiseaux, R., Telesca, D., Mädler, L., Cohen, Y., Zink, J. I., & Nel, A. E. (2012). Use of Metal Oxide Nanoparticle Band Gap To Develop a Predictive Paradigm for Oxidative Stress and Acute Pulmonary Inflammation. *ACS Nano, 6*(5), 4349–4368. 10.1021/nn3010087

Zhang, J., Yao, M., Xia, S., Zeng, F., & Liu, Q. (2025). Systematic and comprehensive insights into HIF-1 stabilization under normoxic conditions: implications for cellular adaptation and therapeutic strategies in cancer. *Cellular & Molecular Biology Letters, 30*(1), 2–39. 10.1186/s11658-024-00682-7

Zhang, J., Zou, Z., Wang, B., Xu, G., Wu, Q., Zhang, Y., Yuan, Z., Yang, X., & Yu, C. (2018). Lysosomal deposition of copper oxide nanoparticles triggers HUVEC cells death. *Biomaterials, 161*, 228–239. 10.1016/j.biomaterials.2018.01.048

Zhang, Ji, Xia, Meng, Low-Kam, Liu, Pokhrel, Lin, Wang, Liao, Wang, Li, Rallo, Damoiseaux, Telesca, Mädler, Cohen, Zink, & Nel. (2012). Use of Metal Oxide Nanoparticle Band Gap To Develop a Predictive Paradigm for Oxidative Stress and Acute Pulmonary Inflammation. *ACS Nano, 6*(5), 4349. 10.1021/nn3010087

Zhang, Teng, & Wang. (2020). Multiwalled carbon nanotubes inhibit cell migration and invasion by destroying actin cytoskeleton via mitochondrial dysfunction in ovarian cancer cells.

Zhao, L., Zhu, Y., Chen, Z., Xu, H., Zhou, J., Tang, S., Xu, Z., Kong, F., Li, X., Zhang, Y., Li, X., Zhang, J., & Jia, G. (2018). Cardiopulmonary effects induced by occupational exposure to titanium dioxide nanoparticles. *Nanotoxicology, 12*(2), 169–184. 10.1080/17435390.2018.1425502

Zhao, X., Wei, S., Li, Z., Lin, C., Zhu, Z., Sun, D., Bai, R., Qian, J., Gao, X., Chen, G., & Xu, Z. (2019). Autophagic flux blockage in alveolar epithelial cells is essential in silica nanoparticle-induced pulmonary fibrosis. *Cell Death &Amp; Disease, 10*(2)10.1038/s41419-019-1340-8

Zhong, L., Yu, Y., Lian, H., Hu, X., Fu, H., & Chen, Y. (2017). Solubility of nano-sized metal oxides evaluated by using in vitro simulated lung and gastrointestinal fluids: implication for health risks. *Journal of Nanoparticle Research : An Interdisciplinary Forum for Nanoscale Science and Technology, 19*(11), 1–10. 10.1007/s11051-017-4064-7

Zhou, F., Liao, F., Chen, L., Liu, Y., Wang, W., & Feng, S. (2019). The size-dependent genotoxicity and oxidative stress of silica nanoparticles on endothelial cells. *Environmental Science and Pollution Research International, 26*(2), 1911–1920. 10.1007/s11356-018-3695-2

Zhu, Y., Eaton, J. W., & Li, C. (2012). Titanium Dioxide (TiO2) Nanoparticles Preferentially Induce Cell Death in Transformed Cells in a Bak/Bax-Independent Fashion. *PloS One, 7*(11), e50607. 10.1371/journal.pone.0050607

Zhu, Y., Ji, H., Cheng, H., & Ruoff, R. S. (2017). Mass production and industrial applications of graphene materials. *National Science Review, 5*(1), 90. 10.1093/nsr/nwx055

Zucker, R. M., Ortenzio, J., Degn, L. L., & Boyes, W. K. (2020). Detection of large extracellular silver nanoparticle rings observed during mitosis using darkfield microscopy. *Plos One, 15*(12)10.1371/journal.pone.0240268

Appendices

Appendix I Supplementary Materials (Chapters 2-5)

Supplementary tables and additional files can be accessed through the online version of each study. Captions are included below for reference.

Supplementary Table 2-1. Multi-modal distribution analysis of DLS results from 10 µg/mL CuO NPs suspended in cell culture media + 2% serum and allowed to incubate at room temperature for 0 – 48 h. Values in parentheses indicate standard deviation. Mean DZ-ave: Intensity weighted hydrodynamic diameter. PDI: Poly-dispersity index

Supplementary Table 2-2. Significantly perturbed canonical pathways following 24 h exposure to 5 µg/mL CuO NPs. A pathway was considered significantly perturbed if –log(p-value) ≥ 1.3.

Supplementary Table 2-3. Significantly perturbed canonical pathways following 24 h exposure to 10 µg/mL CuO NPs. A pathway was considered significantly perturbed if –log(p-value) ≥ 1.3**.**

Supplementary Table 2-4. Significantly perturbed canonical pathways following 24 h exposure to 25 µg/mL CuO NPs. A pathway was considered significantly perturbed if –log(p-value) ≥ 1.3.

Supplementary Table 2-5. Significantly perturbed canonical pathways following 48 h exposure to 5 µg/mL CuO NPs. A pathway was considered significantly perturbed if –log(p-value) ≥ 1.3.

Supplementary Table 2-6. Top 100 significantly perturbed canonical pathways following 48 h exposure to 10 µg/mL CuO NPs. A pathway was considered significantly perturbed if –log(p-value) ≥ 1.3.

Supplementary Table 2-7. Significantly perturbed canonical pathways following 48 h exposure to 7 µg/mL $CuCl_2$. A pathway was considered significantly perturbed if –log(p-value) ≥ 1.3.

Supplementary Table 3-1. Percent dissolution of MONPs and MOMPs used in this study after 0 – 48 h of incubation within DMEM + 2% FBS cell culture medium. (-): not assessed.

Supplementary Table 3-2. The top ten most commonly enriched IPA canonical pathways following 2-48 h of exposure to each separate metal oxide form. MONP: metal oxide nanoparticle. MOMP: metal oxide microparticle. MeCl: metal chloride.

Supplementary Table 4-1. Sonication parameters for the metal oxides examined in this study. For all materials, the volume of the stock suspensions was ~8 mL. The sonicator was operated at 80% cycles in all instances (8 seconds on with 2 seconds off). DSE: delivered sonication energy.

Supplementary Table 4-2. Concentration interconversions for pristine MONM, MP, and metal chloride concentrations used for *in vitro* exposure.

Supplementary Table 5-1. Sonication parameters for MONPs and MOMPs stock suspensions in dH_2O.

Supplementary Table 5-2. HD, PDI and ZP in dH_2O determined by DLS and ELS.

Supplementary Table 5-3. % Solubility in DMEM cell culture media, and SSA of all MO particles. NPs: nanoparticles. MP: microparticles. % Solubility data from (Avramescu et al., 2020, 2022).

Supplementary Table 5-4. Endpoint ranking based on µg metal/mL concentration normalized NOEC values. Where NOEC values were not present, LOEC values were used. Red: uncoated NPs. Green: coated NPs. Black: uncoated MPs. Blue: dissolved metal equivalent.

Supplementary Table 5-5. Endpoint ranking based on cm^2 particle / cm^2 well-plate concentration normalized NOEC values. Where NOEC values were not present, LOEC values were used. Red: uncoated NPs. Green: coated NPs. Black: uncoated MPs.

Supplementary File 3-1. Significantly enriched canonical pathways; ZnO NP, MP, $ZnCl_2$

Supplementary File 3-2. Significantly enriched canonical pathways; CuO NP, MP, $CuCl_2$

Supplementary File 3-3. Significantly enriched canonical pathways; NiO NP, MP, $NiCl_2$

Supplementary File 3-4. Significantly enriched canonical pathways; Al_2O_3 NP, MP, $AlCl_3$

Supplementary File 3-5. Significantly enriched canonical pathways; TiO_2 NP, MP

Supplementary File 4-1. R markdowns, model fit graphs, quantile-quantile plots, and residual plots from BMC modelling of CometChip® data. Concentration metric is µg/mL compound.

Supplementary File 4-2. R markdowns, model fit graphs, quantile-quantile plots, and residual plots from BMC modelling of CometChip® data. Concentration metric is µg/mL constituent metal.

Supplementary File 5-1. Spearman's correlation analysis between the physicochemical properties of the MO and genotoxicity.

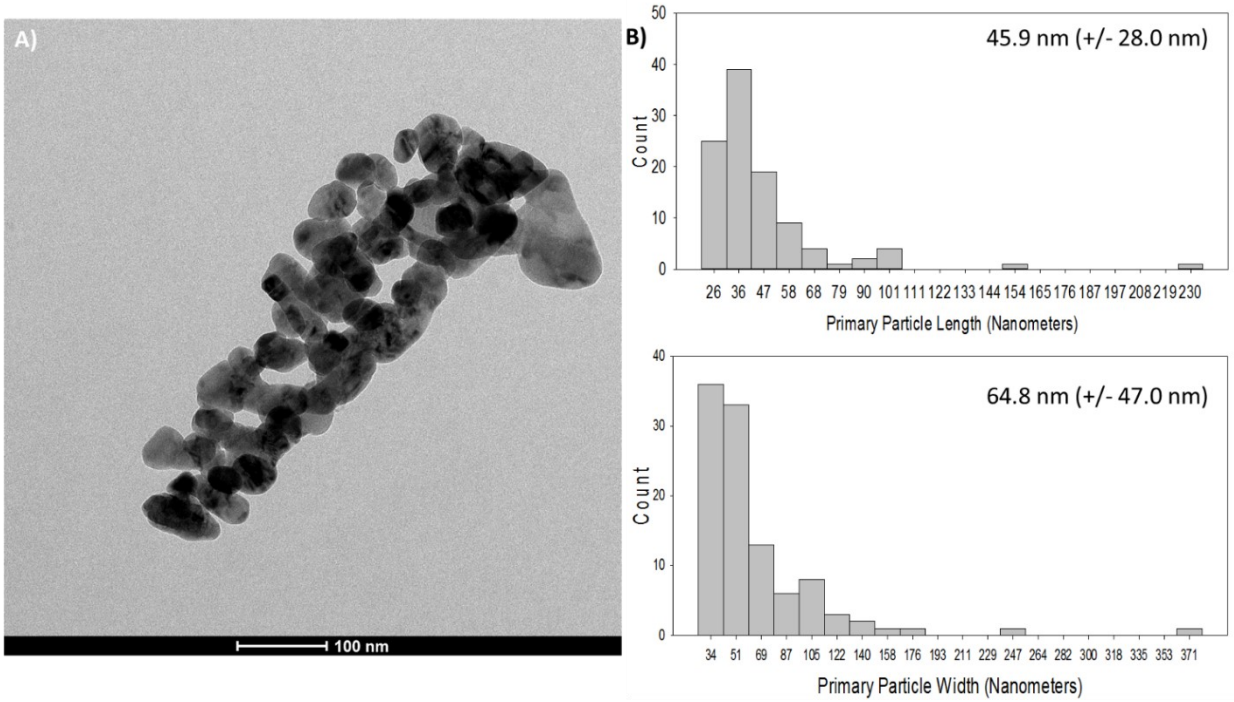

Supplementary Figure 2-1. Transmission electron microscopy and primary particle size distribution of CuO NPs used in this study. A) Representative TEM image showing morphology of NPs. B) Distributions of primary particle length and width determined using ImageJ (n = 105), with mean particle width and length highlighted (values in parentheses indicate standard deviation).

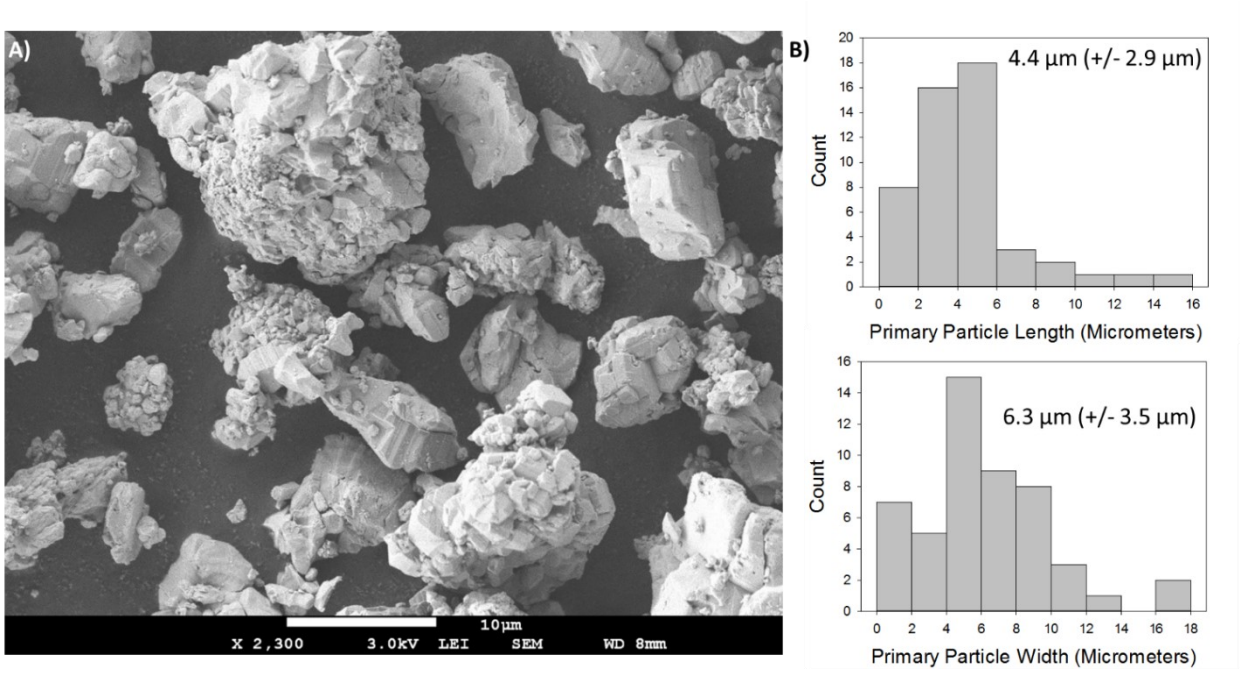

Supplementary Figure 2-2. Scanning electron microscopy and primary particle size distribution of CuO MPs used in this study. A) Representative SEM image showing morphology of MPs. B) Distributions of primary particle length and width determined using ImageJ (n = 50), with mean particle width and length highlighted (values in parentheses indicate standard deviation).

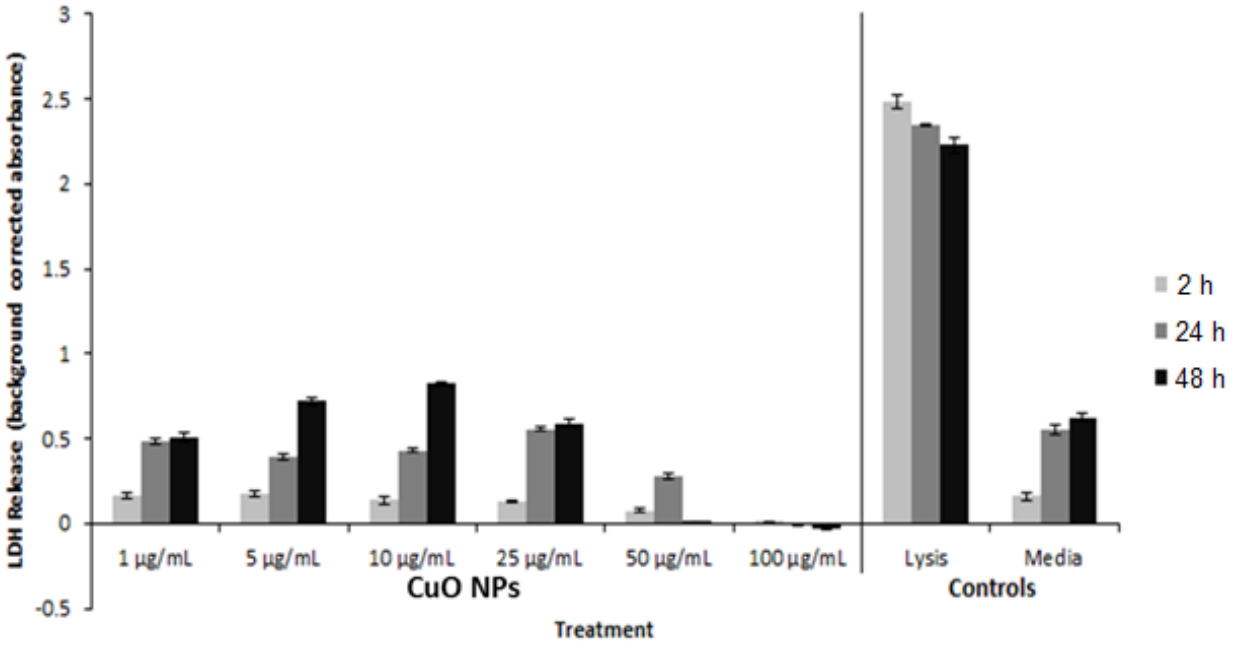

Supplementary Figure 2-3. Cytotoxicity as a function of LDH release for FE1 cells exposed for 2 - 48 h to 1 - 100 µg/mL CuO NPs. Results are inconclusive due to interference from dissolving ions. Error bars represent standard error.

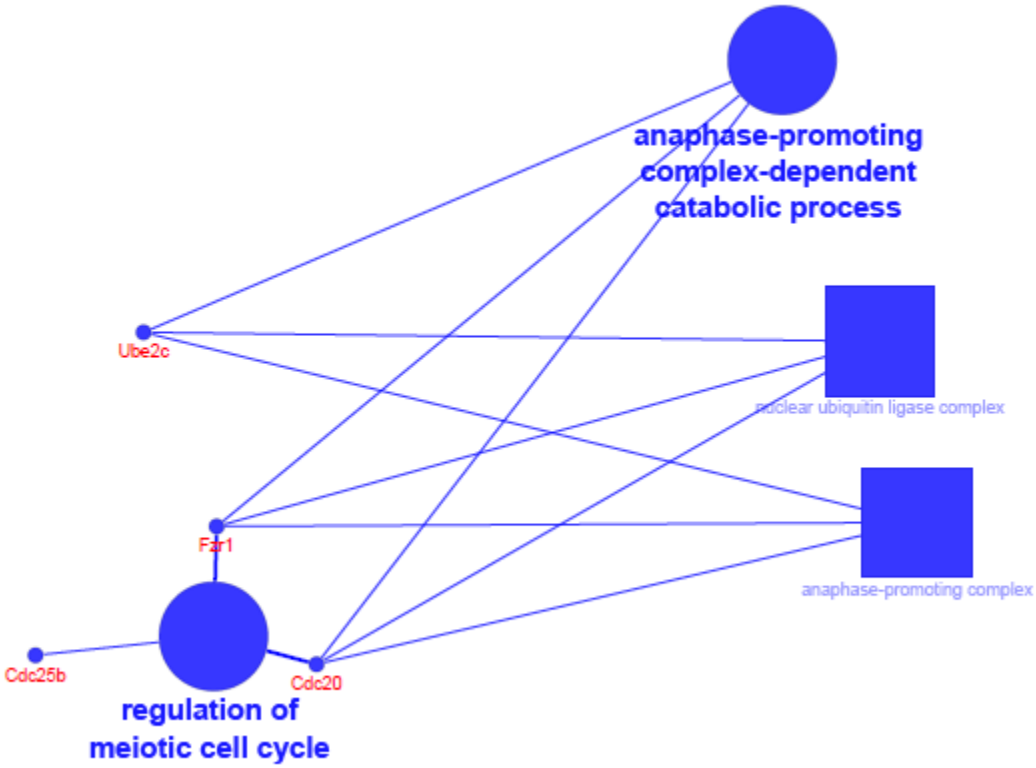

Supplementary Figure 2-4. Cytoscape network visualization of GO enrichment analysis of biological processes (large circle), cellular components (large square) and molecular functions (large triangle, none enriched) of up and down-regulated genes following 2 h exposure to 25 µg/mL CuO MPs. Large blue nodes denote enriched categories from the down-regulated gene list. Small blue nodes with red text denote genes belonging to the enriched categories.

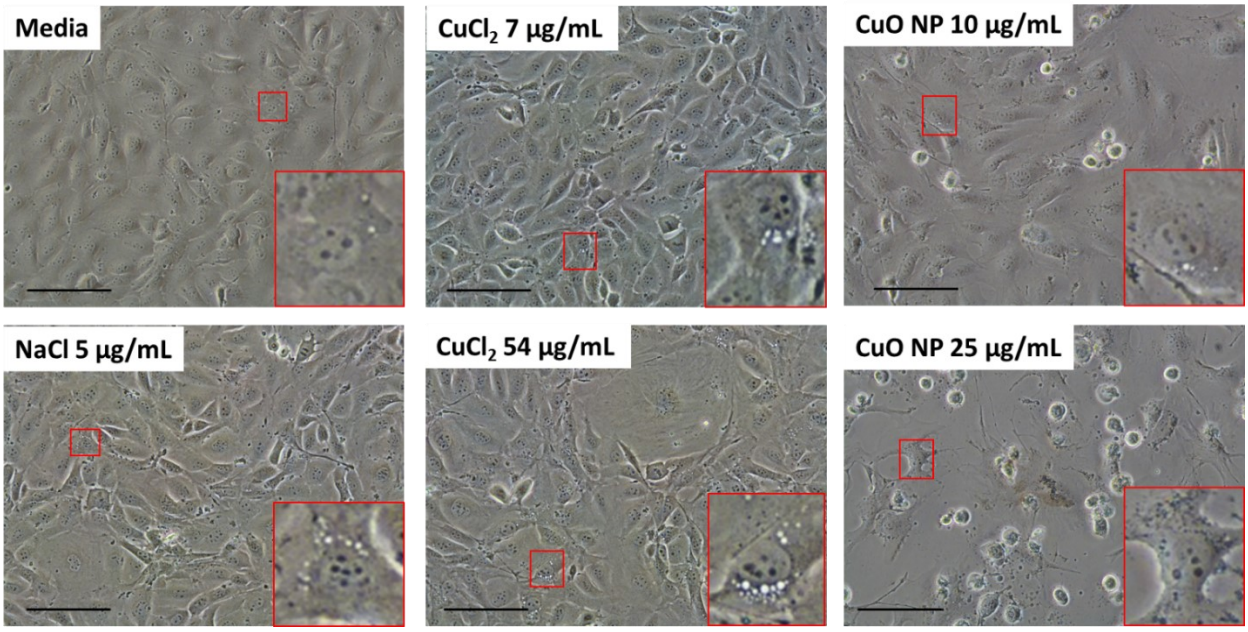

Supplementary Figure 2-5. 20X phase-contrast images of FE1 cells exposed to vehicle media, 5 µg/mL NaCl, 10 & 25 µg/mL CuO NPs, and 7 & 54 µg/mL $CuCl_2$ for 24 h. Scale bar = 125 µm. Insets serve to highlight cytoplasm.

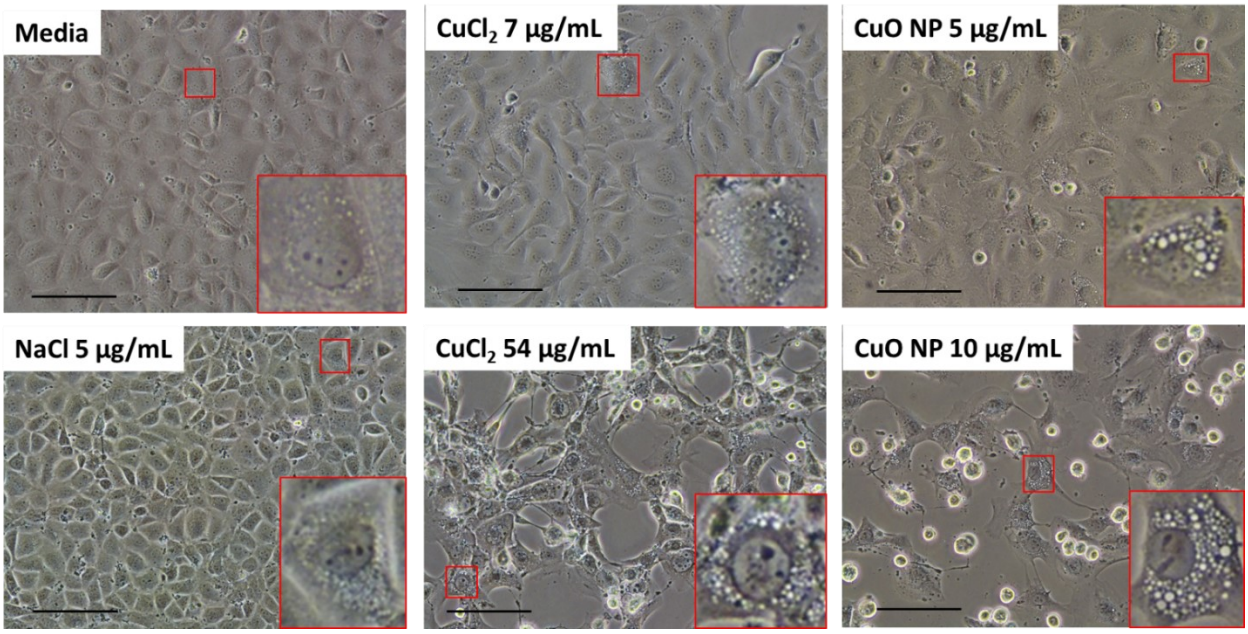

Supplementary Figure 2-6. 20X phase-contrast images of FE1 cells exposed to vehicle media, 5 µg/mL NaCl, 5 & 10 µg/mL CuO NPs, and 7 & 54 µg/mL $CuCl_2$ for 48 h. Scale bar = 125 µm. Insets serve to highlight cytoplasm.

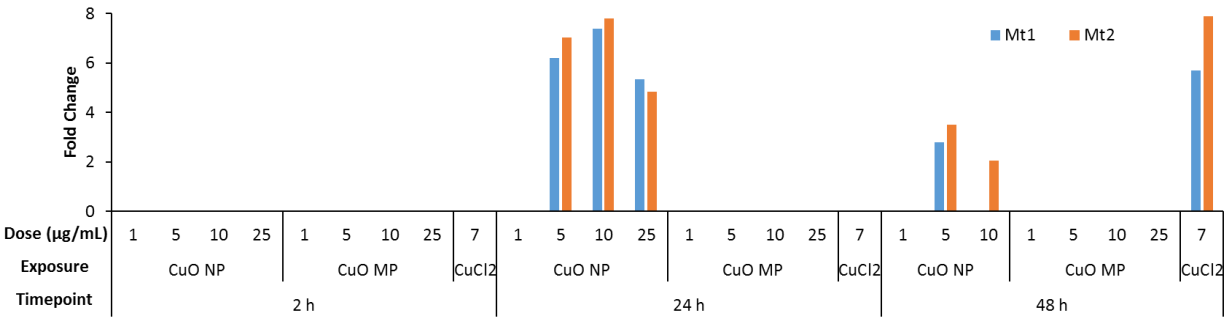

Supplementary Figure 2-7. Differential expression of metallothionein genes *Mt1* and *Mt2* following 2 – 48 h exposure to CuO NPs, CuO MPs, and $CuCl_2$.

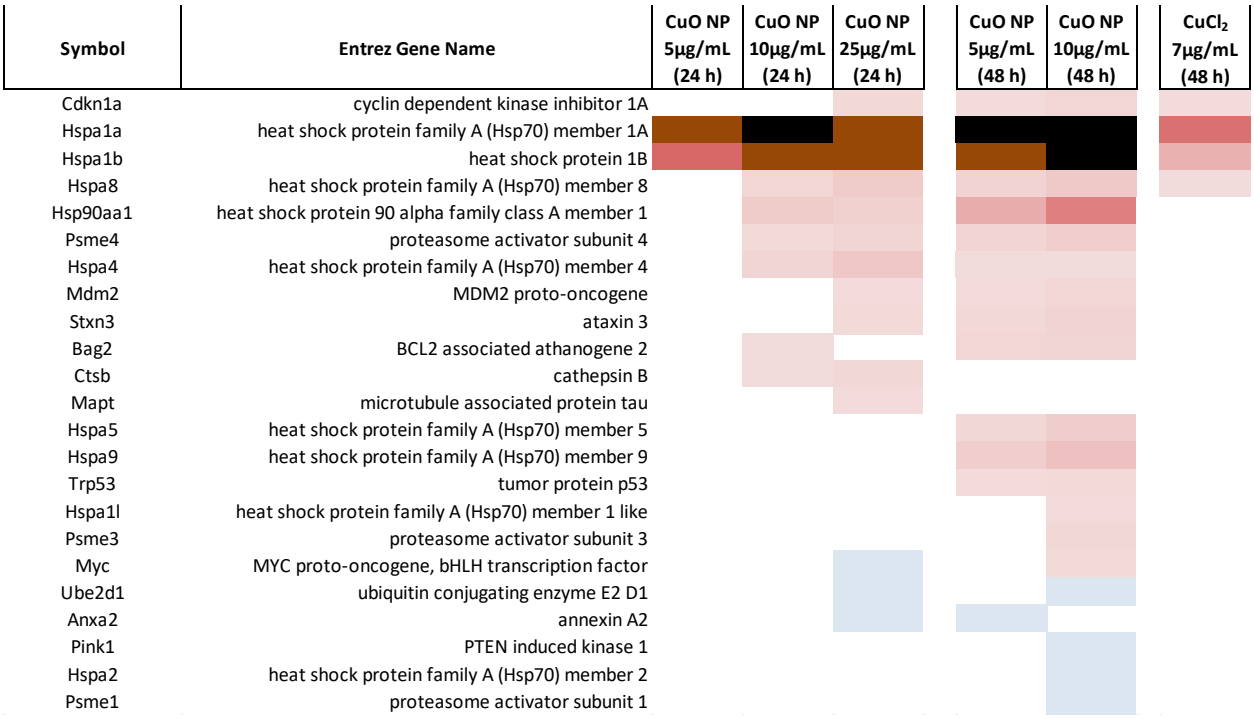

Supplementary Figure 2-8. Differential expression of genes related to the IPA canonical pathway 'Bag2 Signalling Pathway' for samples which induce significant disturbances in the pathway.

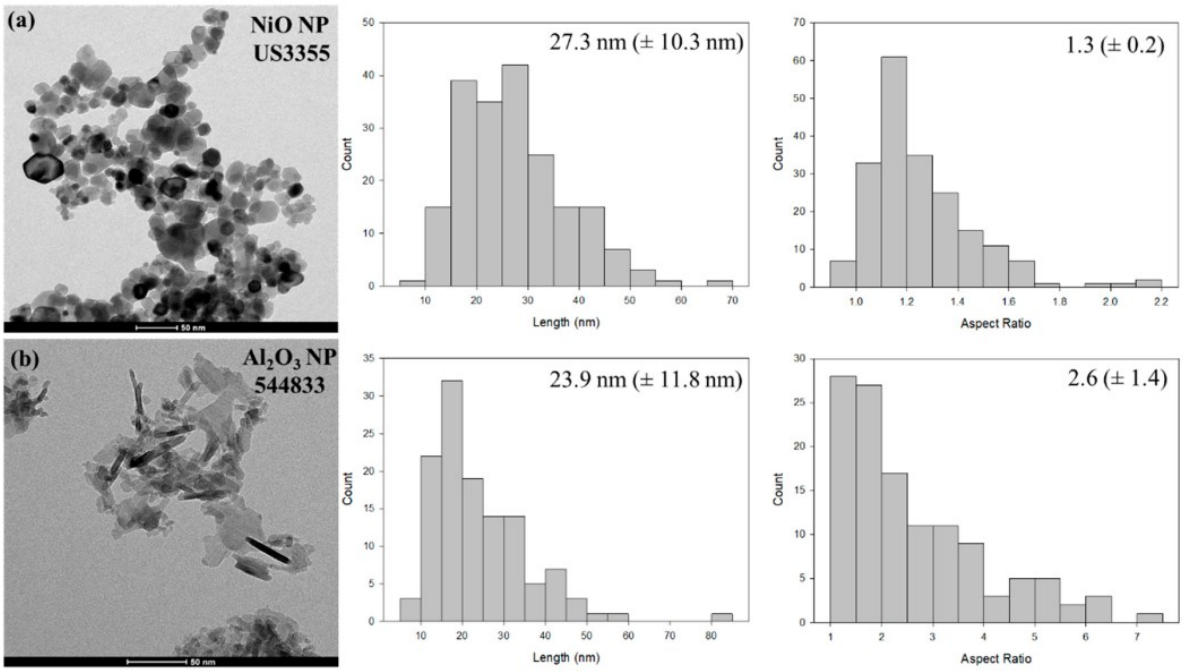

Supplementary Figure 3-1. Representative TEM images of (a) NiO NPs and (b) Al_2O_3 NPs used in this study, along with the average length and aspect ratio based on TEM sizing (± standard deviation). Scale bar: 50 nm.

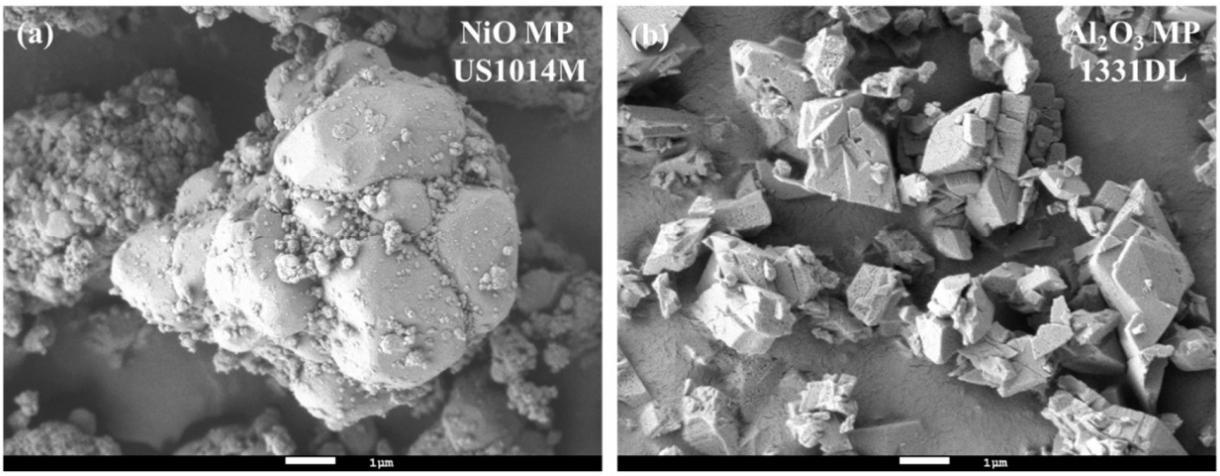

Supplementary Figure 3-2. Representative SEM images of (a) NiO NPs and (b) Al_2O_3 MPs. Scale bar: 1 µm.

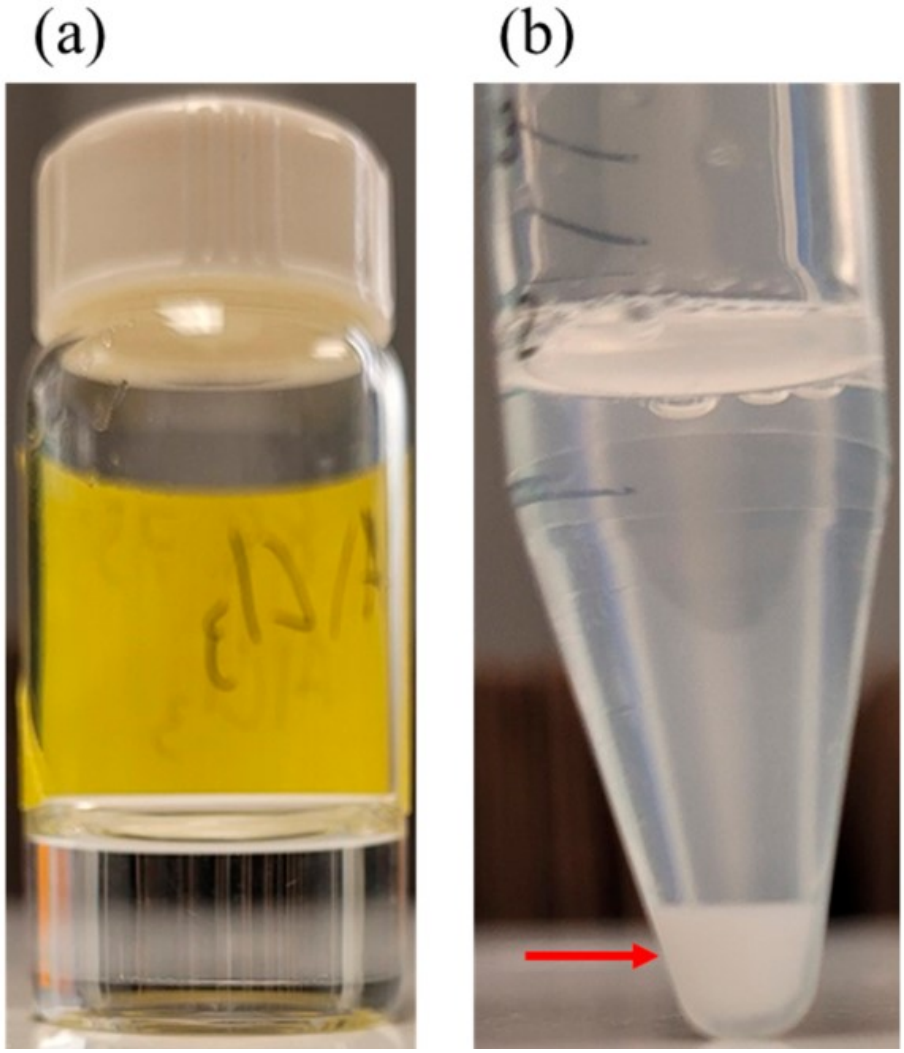

Supplementary Figure 3-3. $AlCl_3$ dissolved in (a) ultrapure water or (b) in cell culture medium with serum. Red arrow: white precipitate formed when $AlCl_3$ dissolved in water was added to medium. Centrifugation was used to collect precipitate at the bottom of the tube.

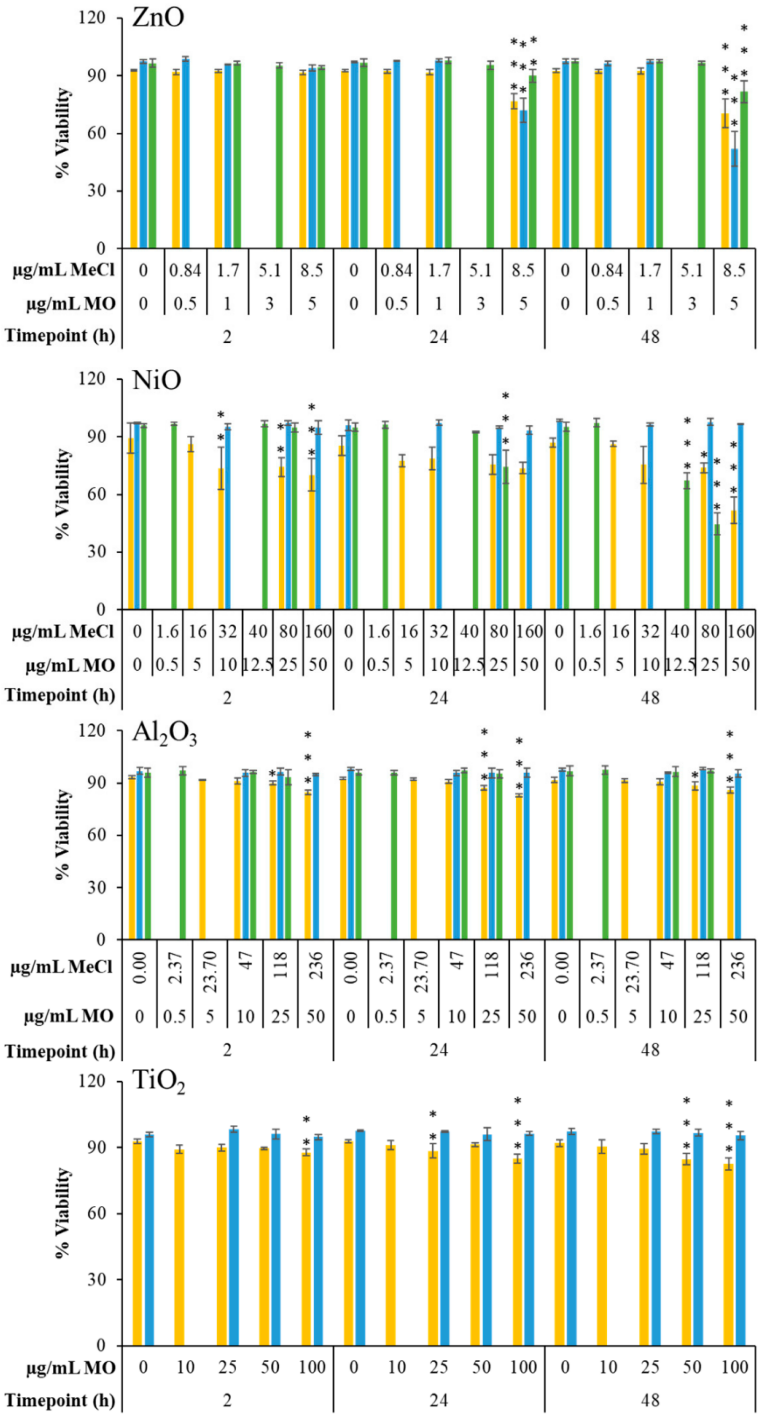

Supplementary Figure 3-4. % Viability of FE1 cells following 2, 24, and 48 h of exposure to MONPs, MOMPs, and metal chlorides compared to time-matched medium controls. Error bars indicate standard deviation (n = 3-4). Graphs were labelled based on the type of metal oxide. Yellow: MONPs. Blue: MOMPs. Green: metal chloride salts. MO: metal oxide. MeCl: metal chloride. Statistical significance against time-matched medium controls were determined through a 2-way ANOVA with a Dunnett's post-hoc. *: $p < 0.05$. **: $p < 0.01$. ***: $p < 0.001$.

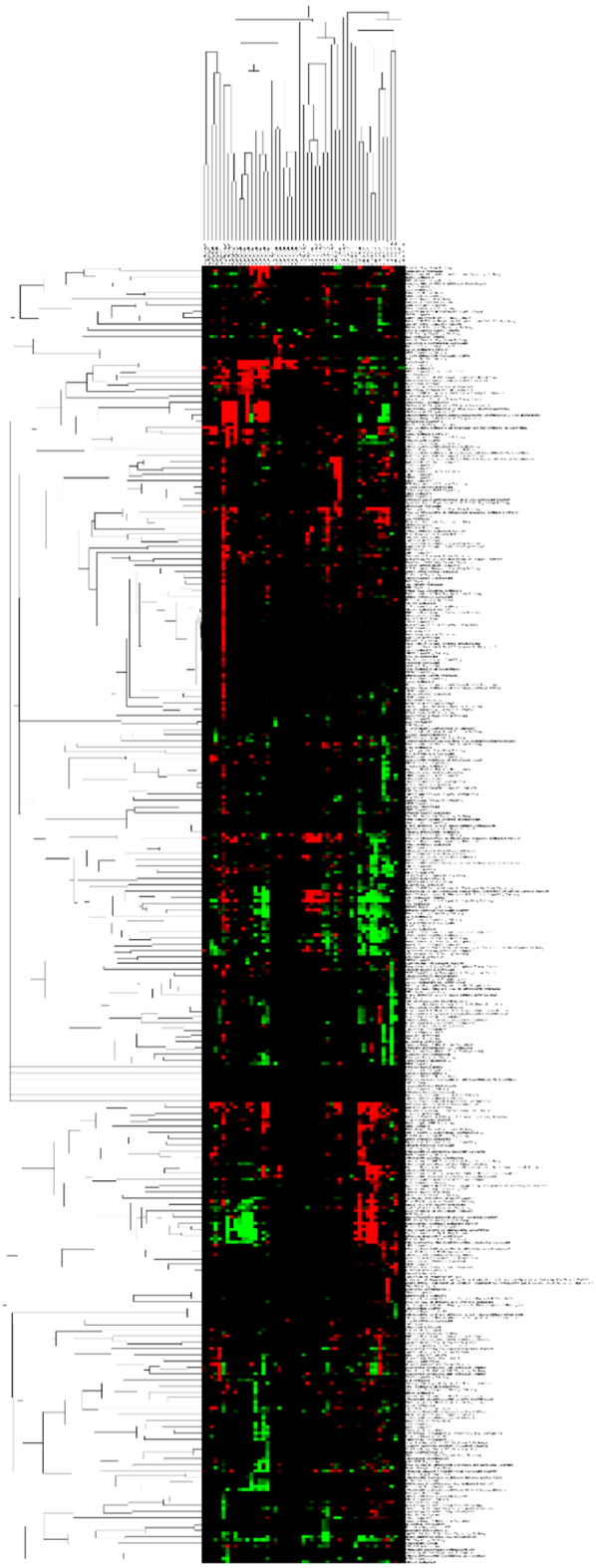

Supplementary Figure 3-5. Hierarchical clustering of exposure groups (x-axis) and significantly enriched IPA canonical pathways (y-axis) using z-score. Green: negative z-score (min: -2), red: positive z-score (max: 2).

Supplementary Figure 3-6. Heatmap depicting differential gene expression in the 'HIF1α Signaling' IPA canonical pathway. Red: positive fold-change (max = 5). Green: negative fold-change (max = -5). A gene was considered differentially expressed if the |FC| > 1.5, with an adjusted $p < 0.05$. The 'HIF1α Signaling' pathway was considered significantly enriched if the -log(pvalue) > 1.3, with at least 3 contained DEGs.

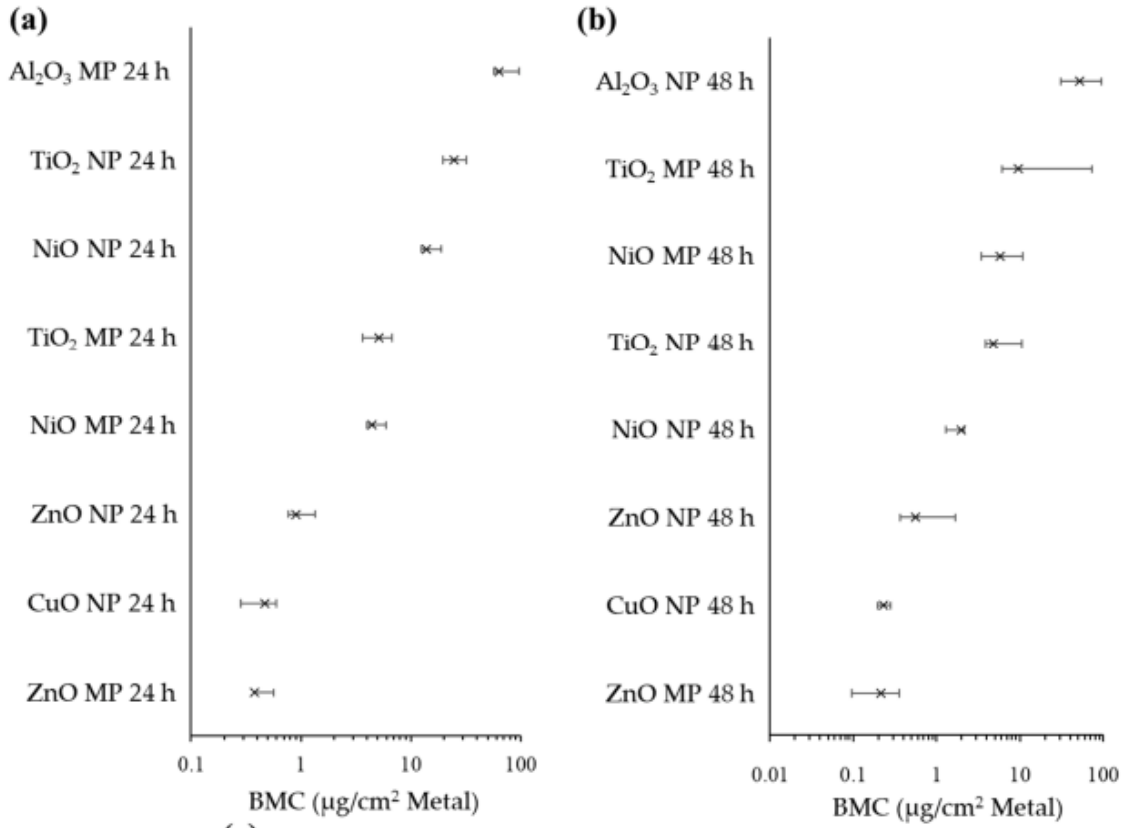

(c)

Metal	24 h Potency Ranking	48 h Potency Ranking
Zn	ZnO MP > ZnO NP	ZnO MP > ZnO NP
Ni	NiO NP ~ NiO MP	NiO NP > NiO MP
Al	(-)	(-)
Ti	TiO_2 MP > TiO_2 NP	TiO_2 NP ~ TiO_2 MP
Cu	(-)	(-)

Supplementary Figure 3-7. BMDS based BMC modelling of decreases in viable cell density following (a) 24 h and (b) 48 h exposure to MONPs and MOMPs, with (c) differences in potency for each metal variety. The concentration is expressed in terms of specific surface area, using the average estimate for MOMPs. Benchmark response: 0.5 (Hybrid extra risk). The 'x' indicates the BMC. Left and right bars indicate BMCL and BMCU values respectively. NP: nanoparticle. MP: microparticle.

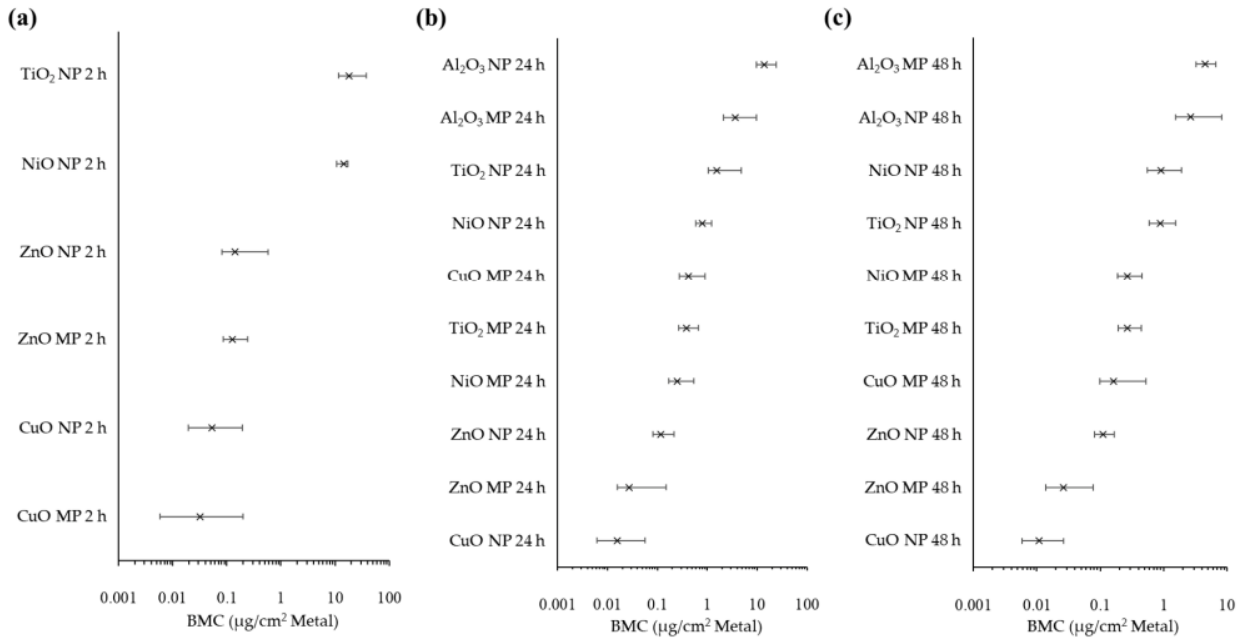

(d)

Metal	2 h Potency Ranking	24 h Potency Ranking	48 h Potency Ranking
Zn	ZnO NP ~ ZnO MP	ZnO NP ~ ZnO MP	ZnO MP > ZnO NP
Ni	(-)	NiO MP > NiO NP	NiO MP > NiO NP
Al	(-)	Al_2O_3 MP ~ Al_2O_3 NP	Al_2O_3 MP ~ Al_2O_3 NP
Ti	(-)	TiO_2 MP > TiO_2 NP	TiO_2 MP > TiO_2 NP
Cu	CuO NP ~ CuO MP	CuO NP > CuO MP	CuO NP > CuO MP

Supplementary Figure 3-8. The 25th ranked gene tPOD determined through BMDExpress2 BMC modelling for (a) 2 h, (b) 24 h, and (c) 48 h MONP and MOMP exposures, with d) differences in potency for each metal variety. The concentration is expressed in terms of specific surface area, using the average estimate for MOMPs. Benchmark response: 1 (Standard deviation). The 'x' indicates the BMC. Left and right bars indicate BMCL and BMCU values respectively. NP: nanoparticle. MP: microparticle.

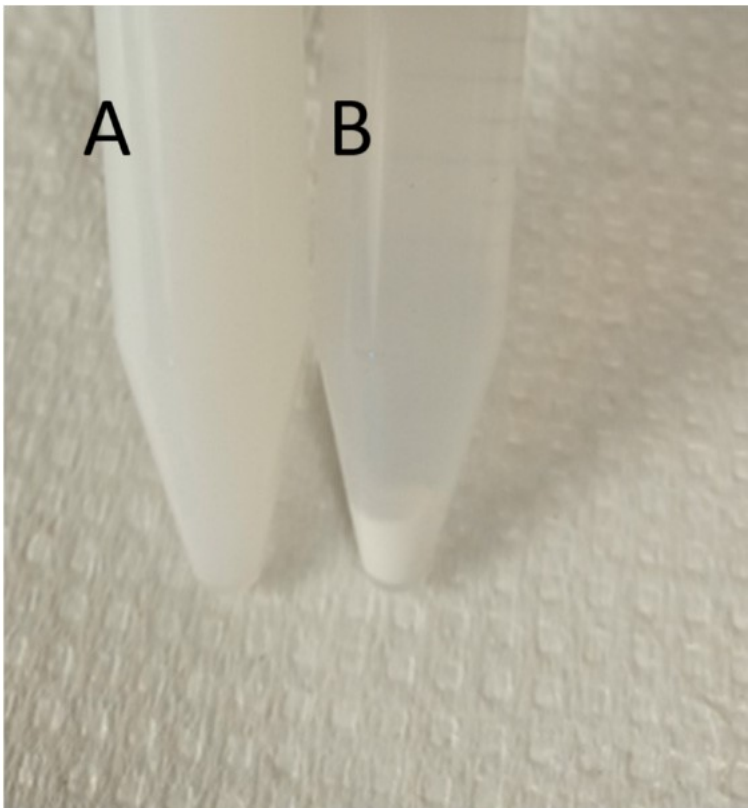

Supplementary Figure 4-1. MK-TiO_2-A050 NPs suspension at 1 mg/mL in DMEM supplemented with 2% FBS A) with or B) without 0.4 mg/mL BSA.

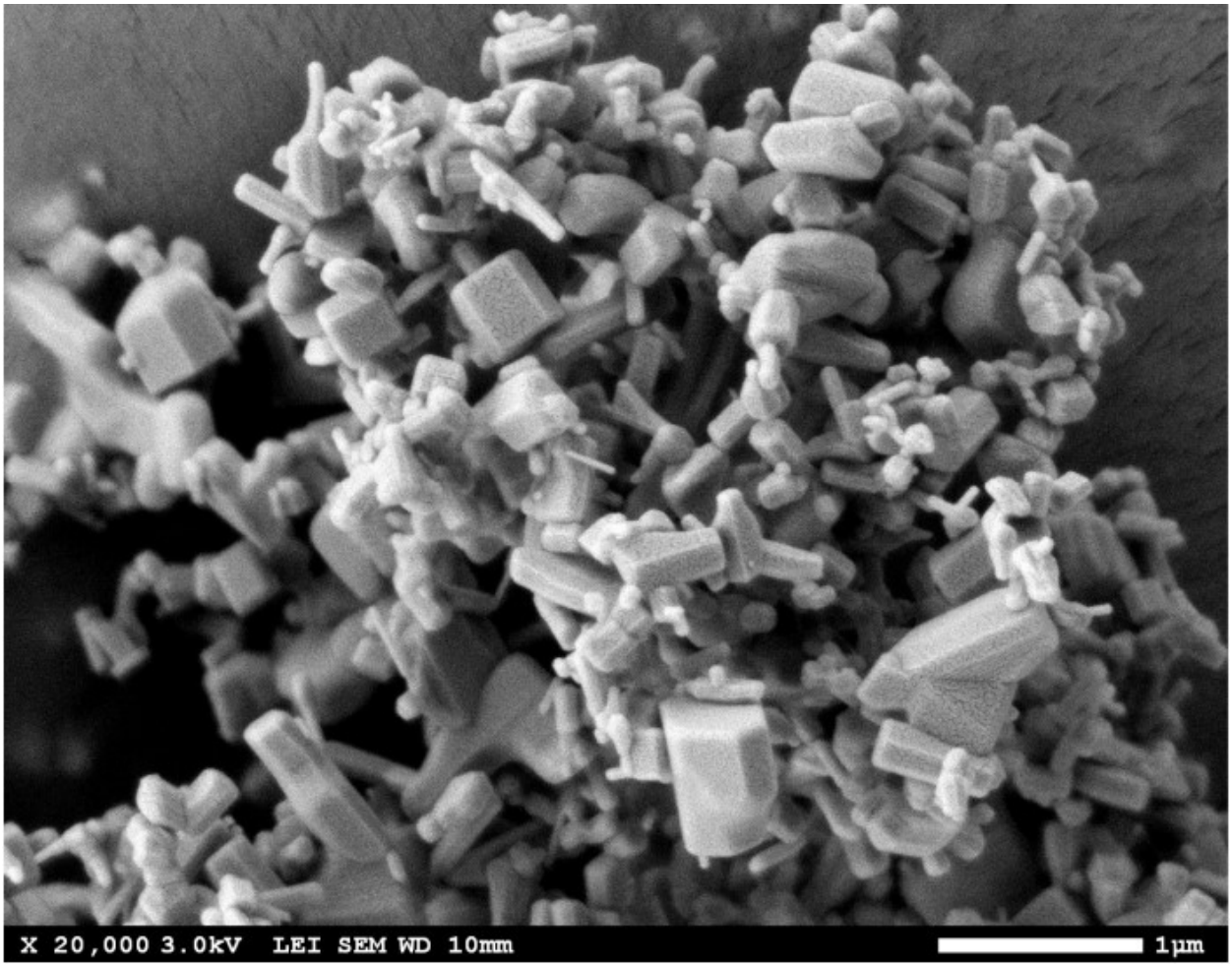

Supplementary Figure 4-2. Representative scanning electron micrograph showing the morphology of the ZnO MPs used in this study.

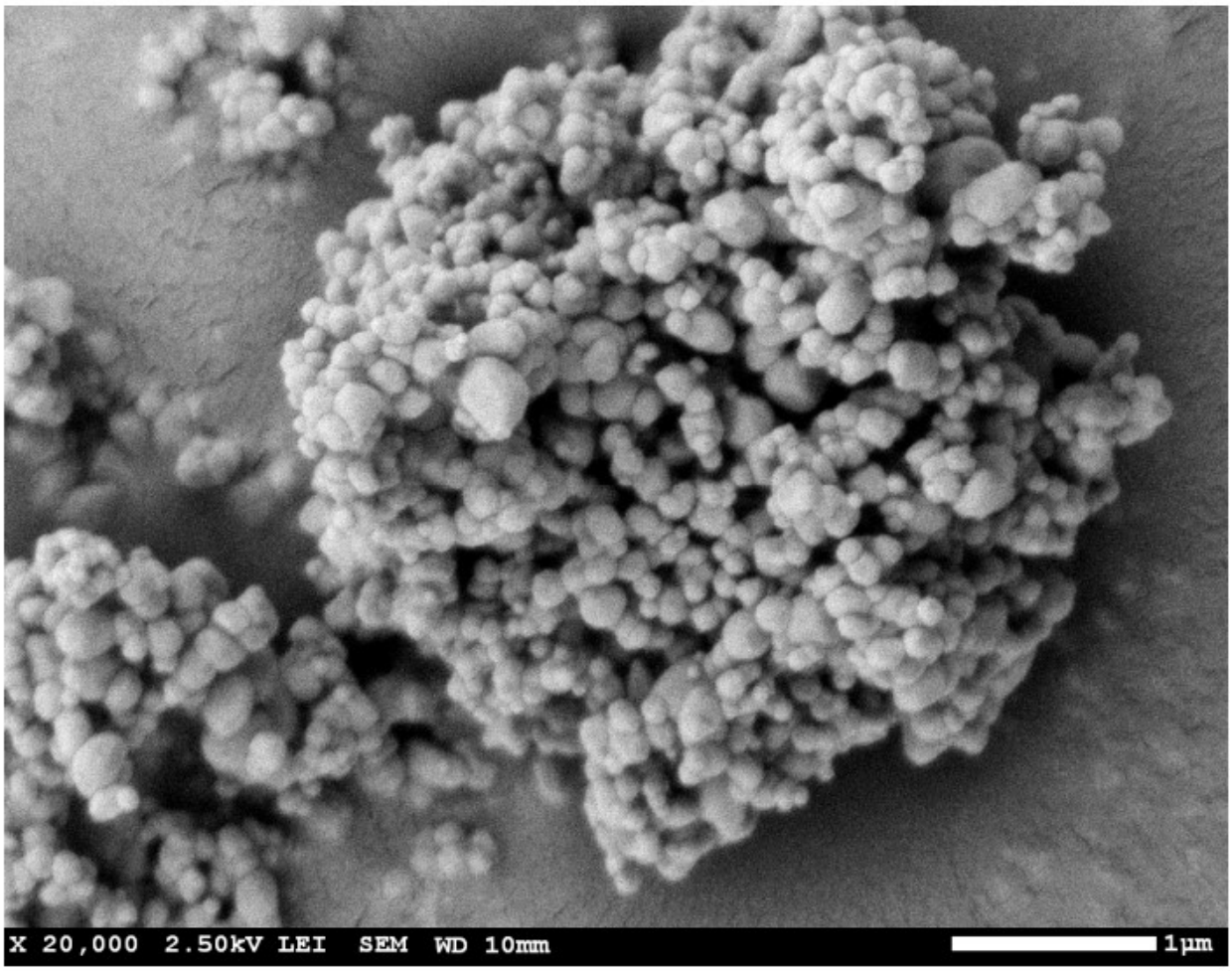

Supplementary Figure 4-3. Representative scanning electron micrograph showing the morphology of the TiO_2 MPs used in this study.

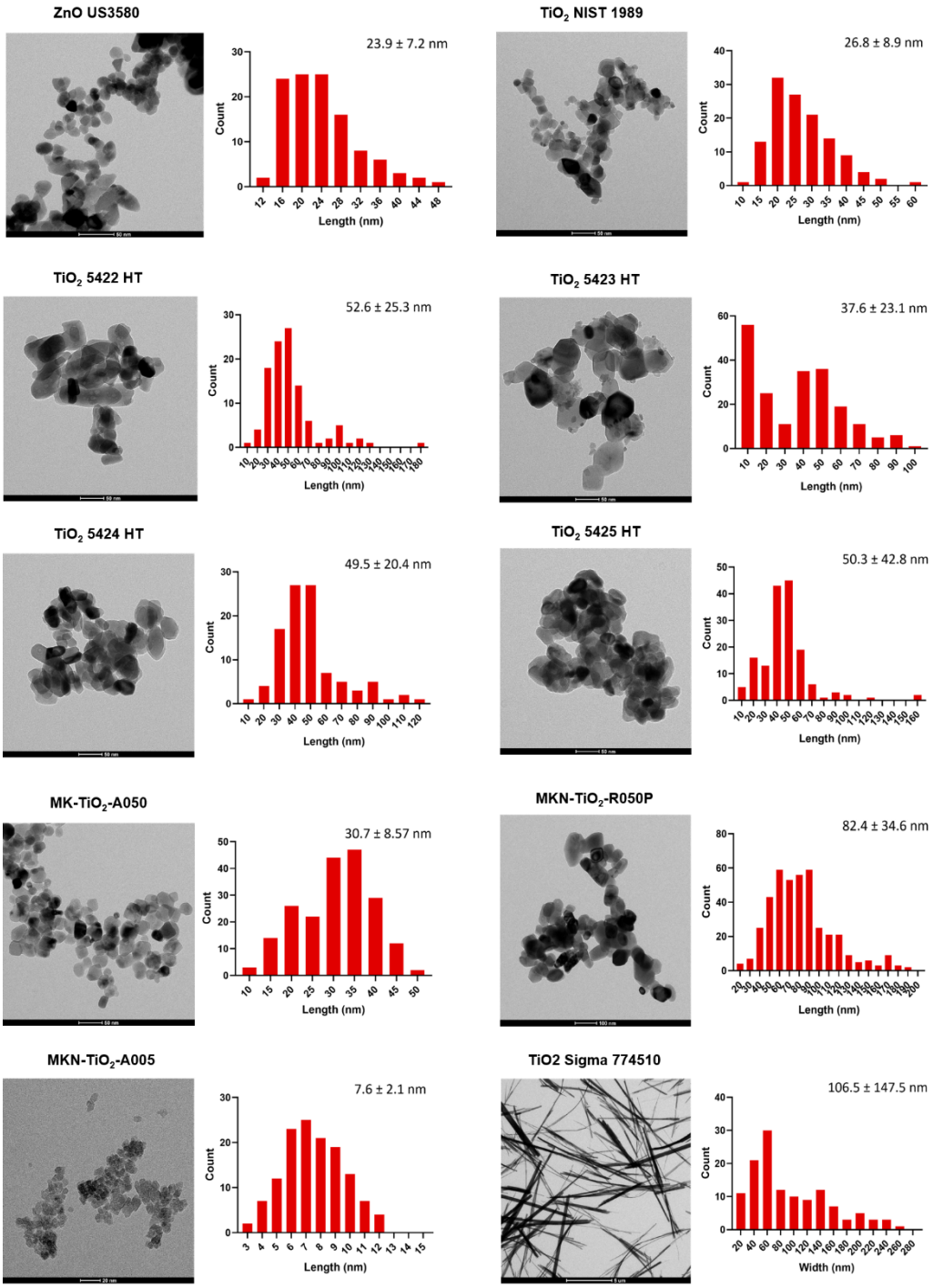

Supplementary Figure 4-4. Transmission electron microscopy and primary particle size distribution of different TiO_2 NPs and one type of TiO_2 NWs used in this study (n = 100-250). Distributions of primary particle length and width were determined using ImageJ. Data represent mean particle length, ± standard deviation. For non-spherical nanoparticles (MKN-TiO_2-R050P), the mean width is also shown. For TiO_2 nanowires (Sigma 774510), the width is shown as the length was not possible to measure due to their tangled nature.

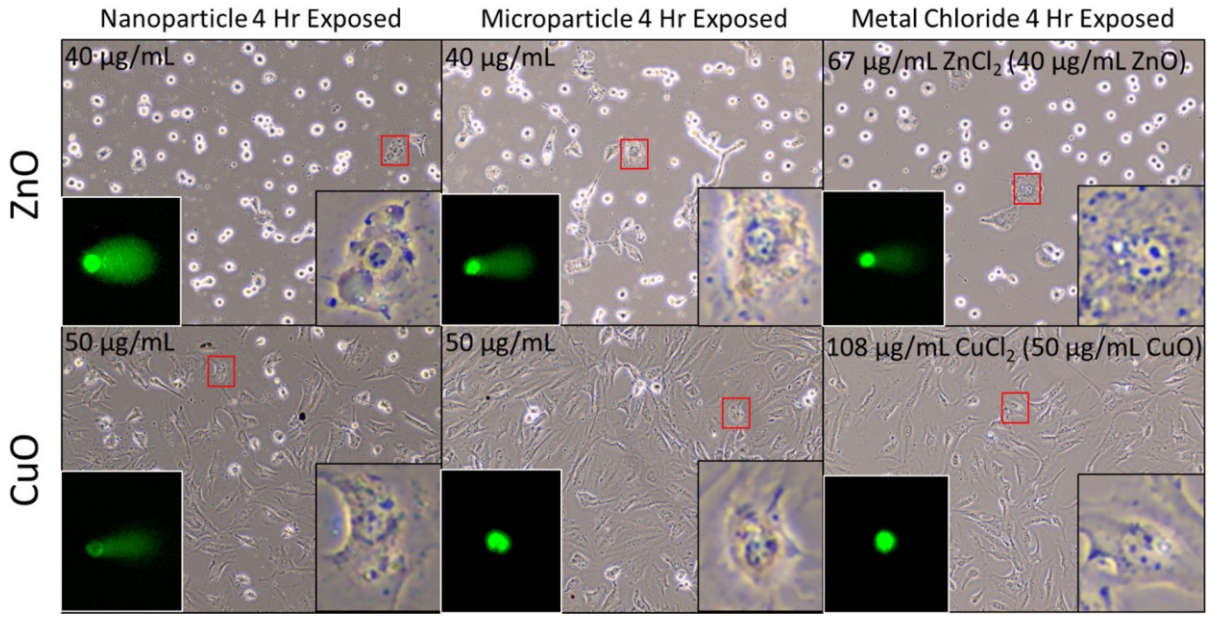

Supplementary Figure 4-5. Phase contrast images (20x) and representative fluorescent comet micrographs of FE1 cells after 4 h exposure to ZnO & CuO NPs, MPs, and metal chloride equivalents. Insets on the bottom right of the micrographs represent an enlargement of the areas highlighted in red. Comet micrographs had brightness and contrast adjusted to aid in visualization.

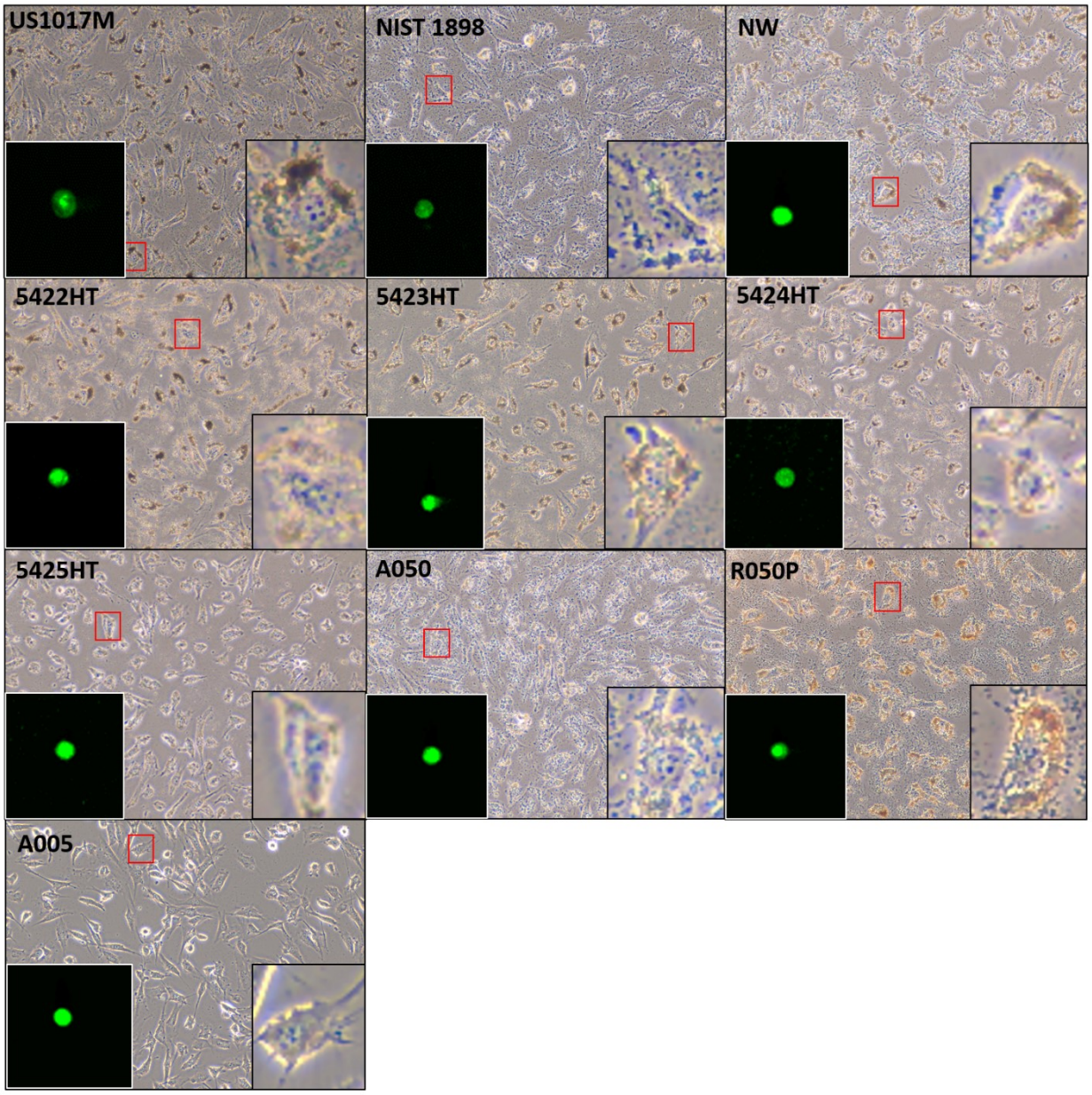

Supplementary Figure 4-6. Phase contrast images (20x) and representative fluorescent comet micrographs of FE1 cells after 4 h exposure to 100 µg/mL TiO_2 nanomaterials and microparticles. NW: nanowires. Insets on the bottom right of the micrographs represent an enlargement of the areas highlighted in red. Comet micrographs had brightness and contrast adjusted to aid in visualization.

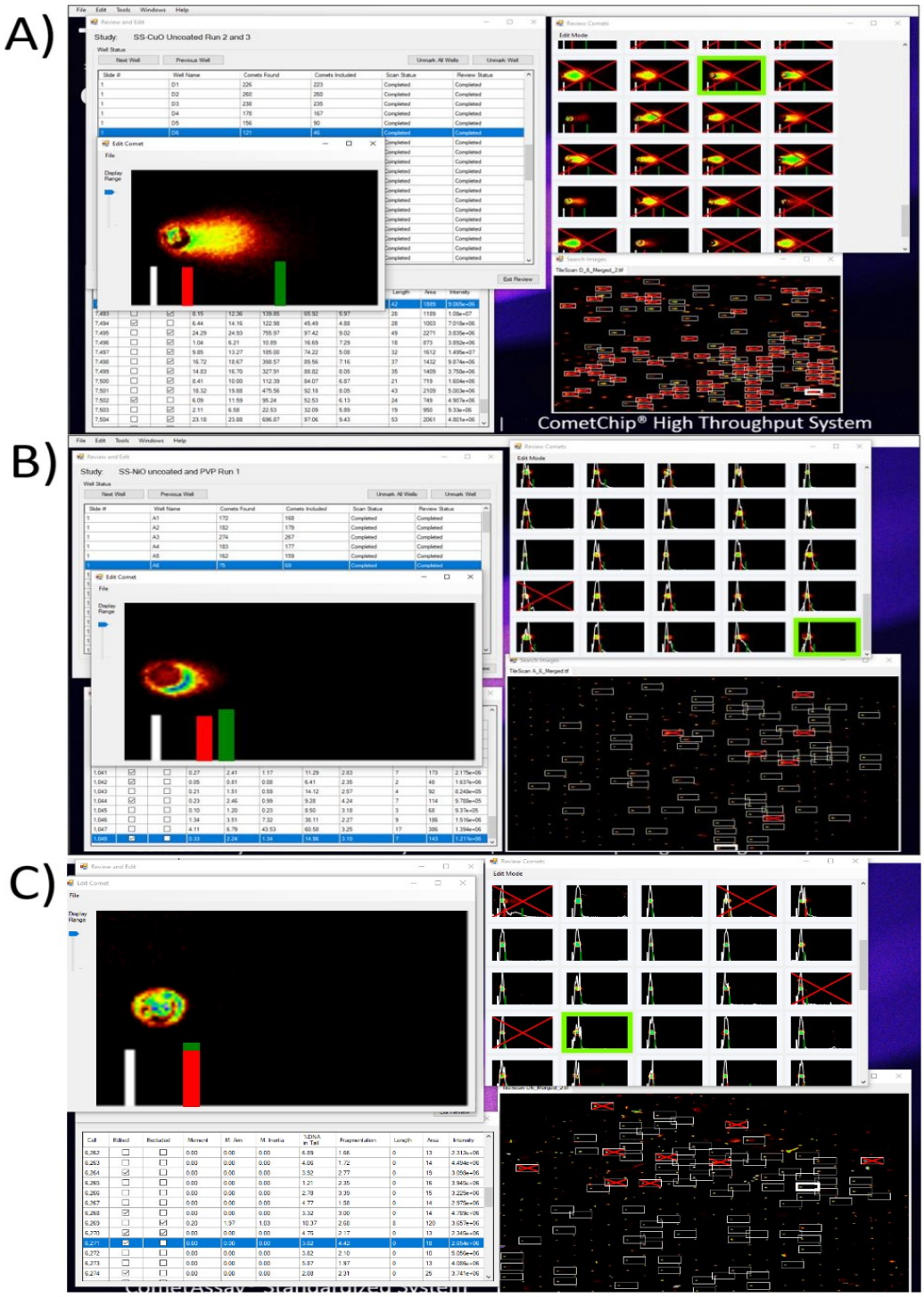

Supplementary Figure 5-1. Representative images of the interference of some MONPs with the SYBR® Gold staining and the analysis of the comet assay at high concentrations. (A) Uncoated CuO NPs (US3070). (B) Uncoated NiO NPs (US3352). (C) Uncoated Fe_2O_3 NPs (US3160). Analysis was conducted using the Trevigen Comet Software.

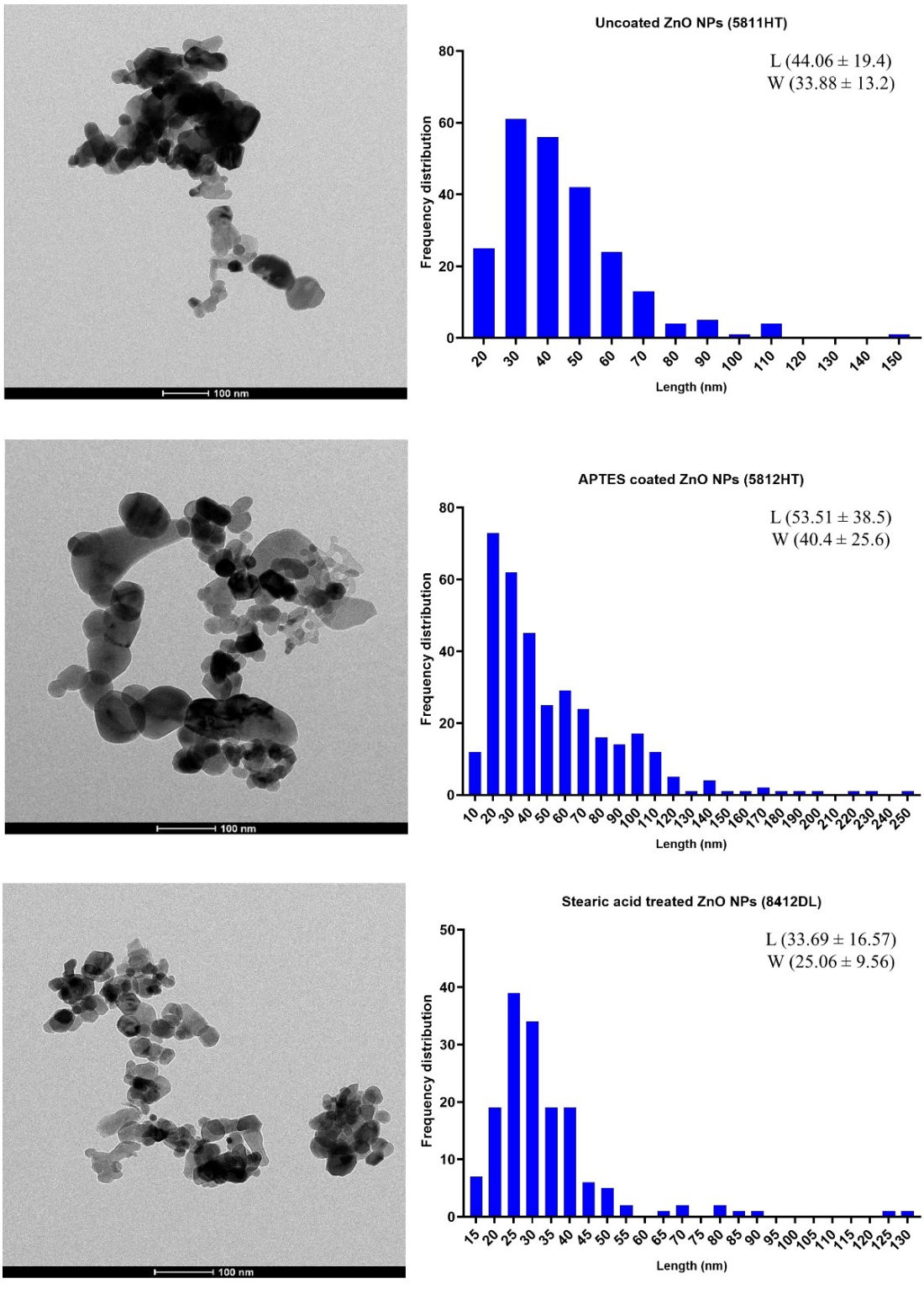

Supplementary Figure 5-2. Representative TEM images and frequency size distribution of ZnO NPs variants. L: Length, W: Width. Scale bar: 100 nm.

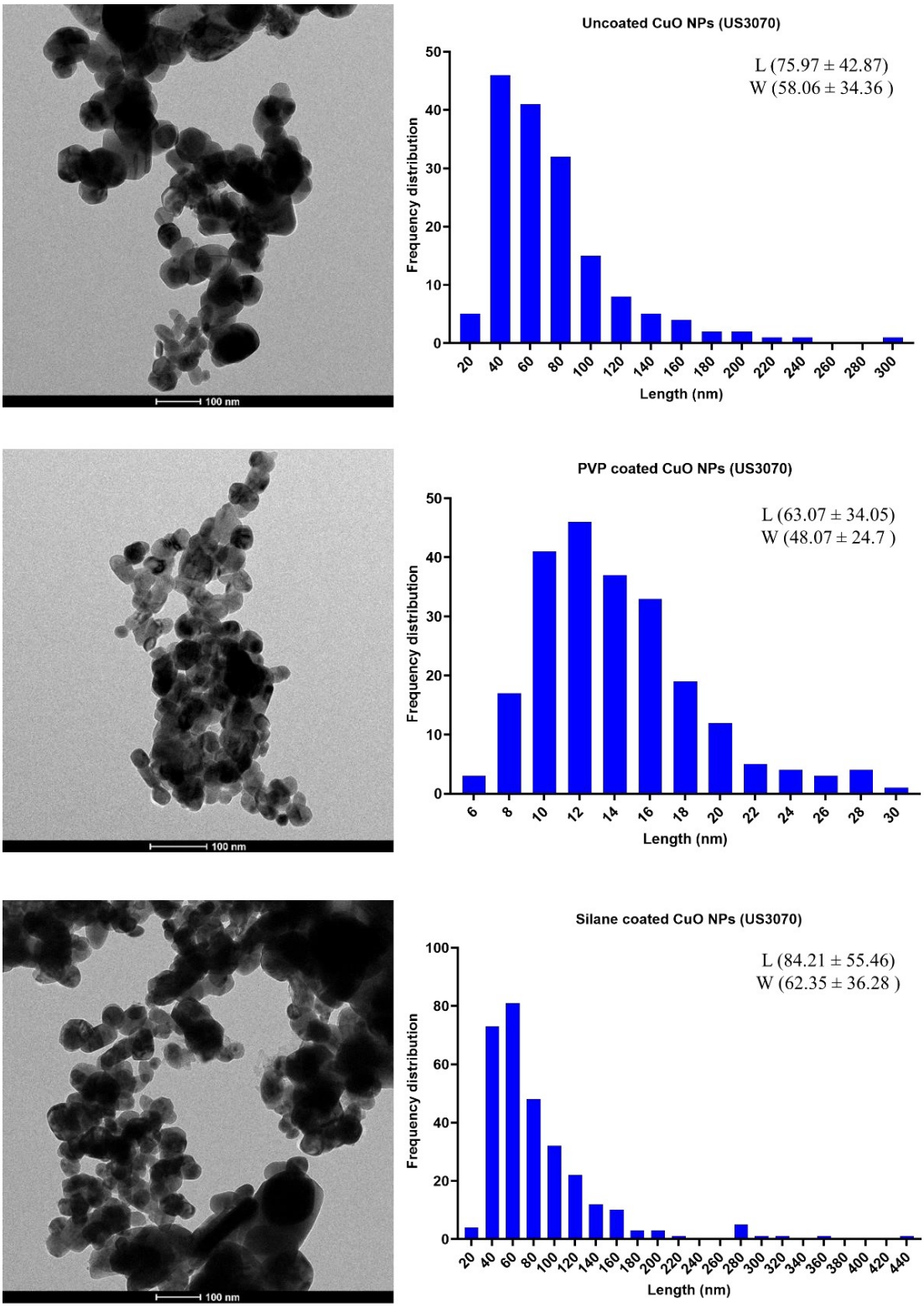

Supplementary Figure 5-3. Representative TEM images and frequency size distribution of CuO NPs variants. L: Length, W: Width. Scale bar: 100 nm.

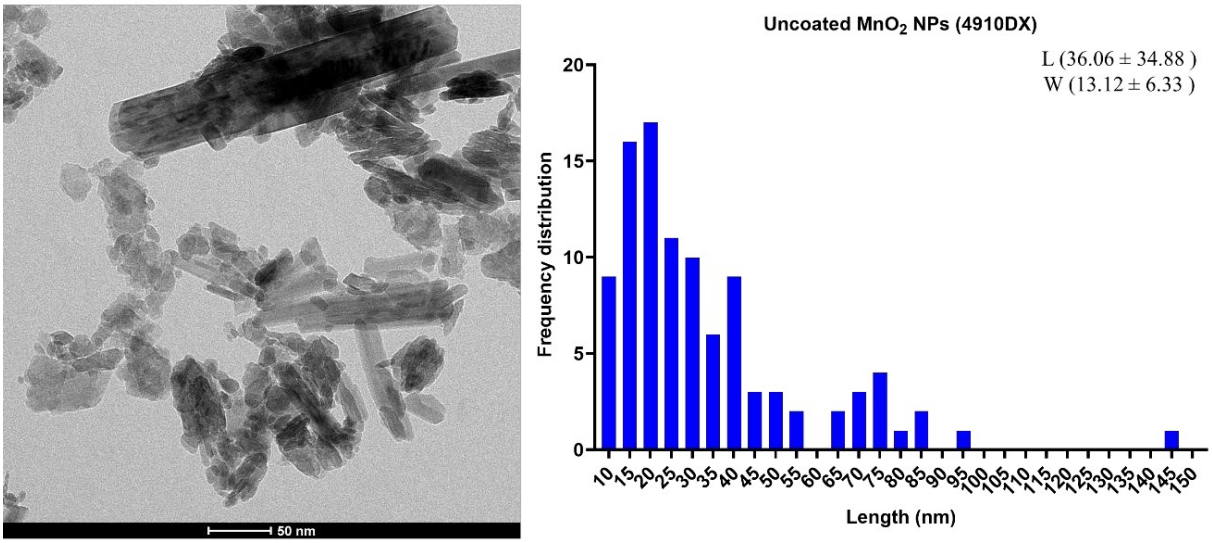

Supplementary Figure 5-4. Representative TEM image and frequency size distribution of MnO_2 NPs. L: Length, W: Width. Scale bar: 50 nm.

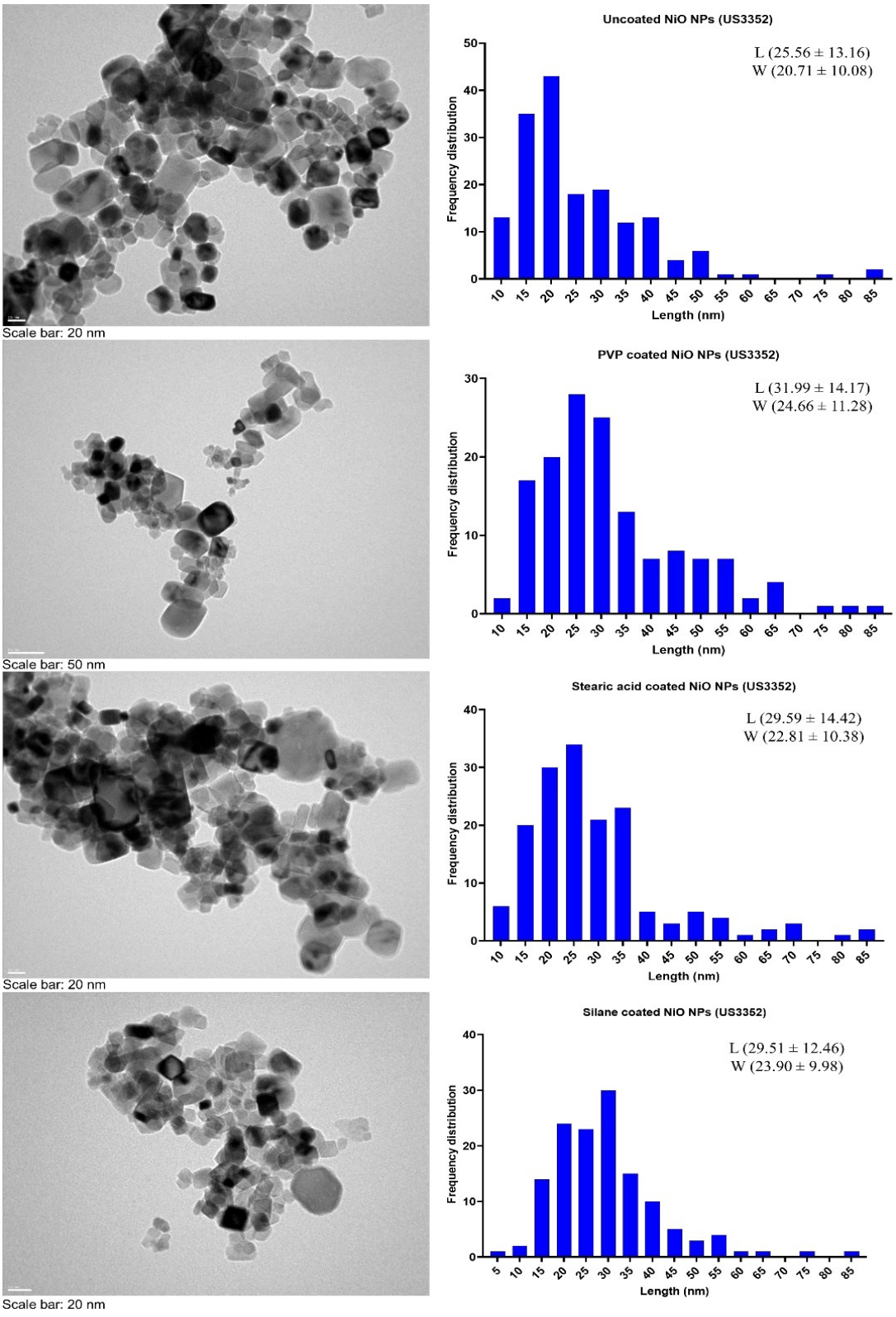

Supplementary Figure 5-5. Representative TEM images and frequency size distribution of NiO NPs variants. L: Length, W: Width.

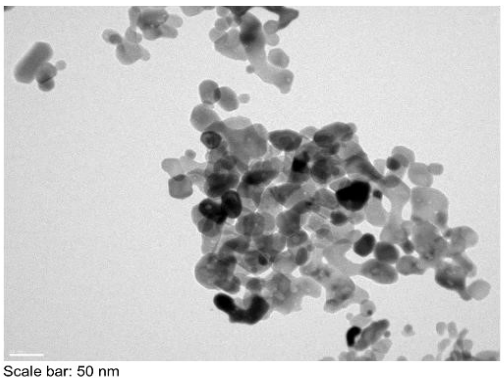

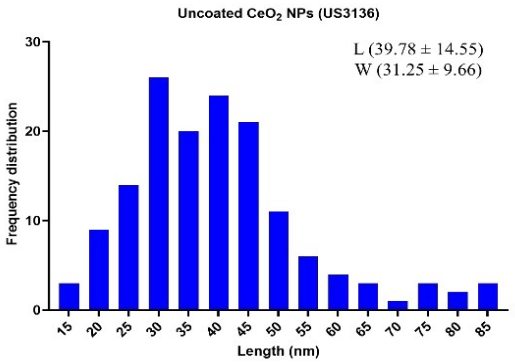

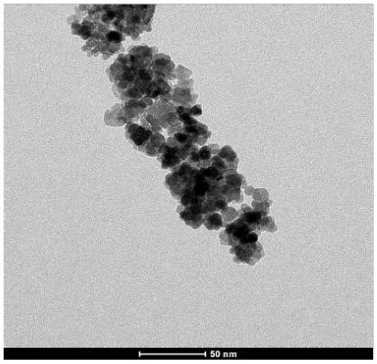

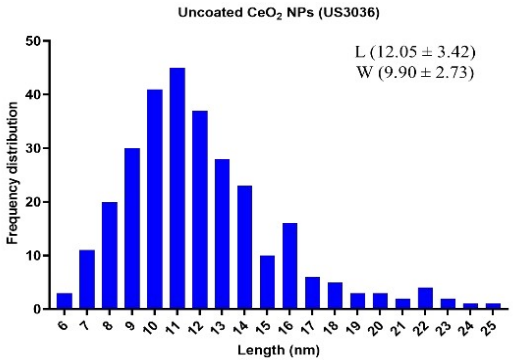

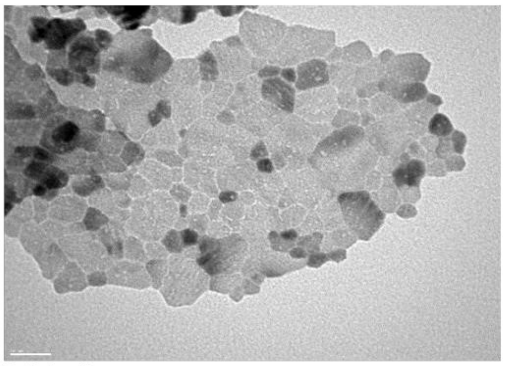

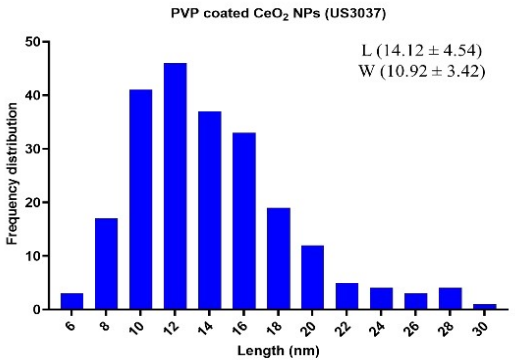

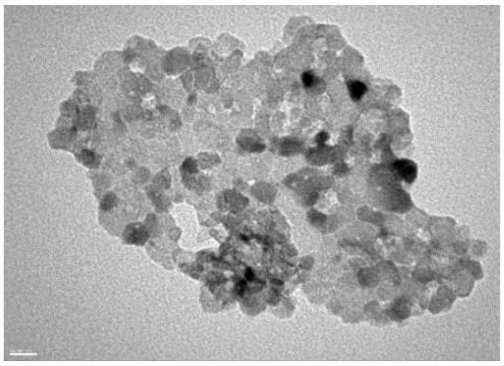

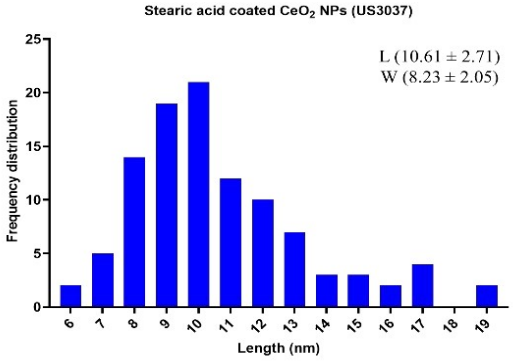

Supplementary Figure 5-6. Representative TEM images and frequency size distribution of CeO_2 NPs variants. L: Length, W: Width.

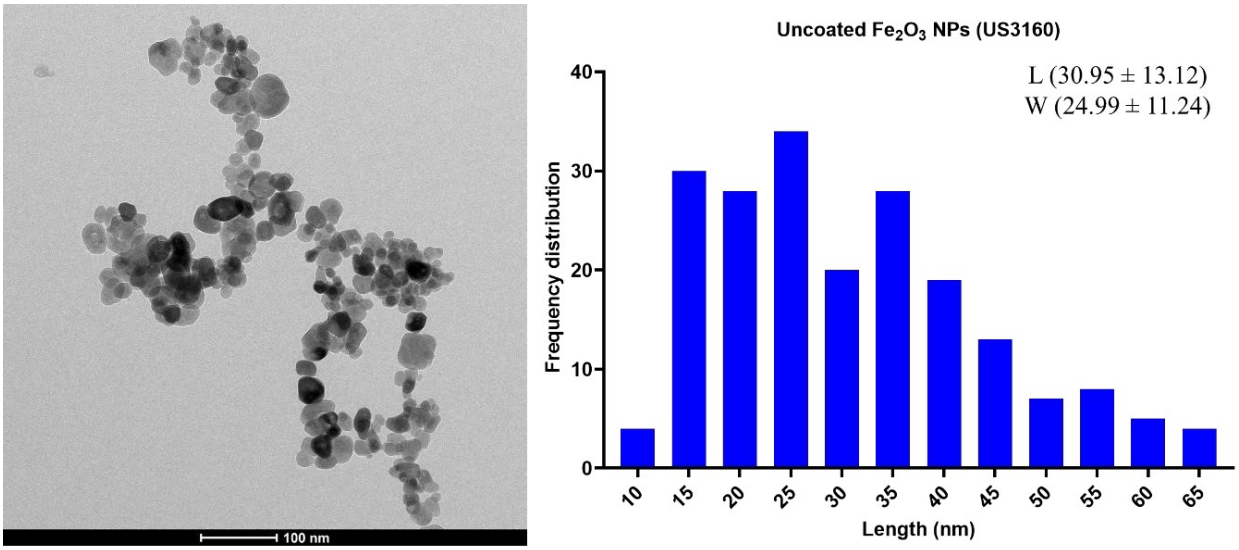

Supplementary Figure 5-7. Representative TEM images and frequency size distribution of Fe_2O_3 NPs. L: Length, W: Width. Scale bar: 100 nm.

MnO_2 4930DX MOMPs

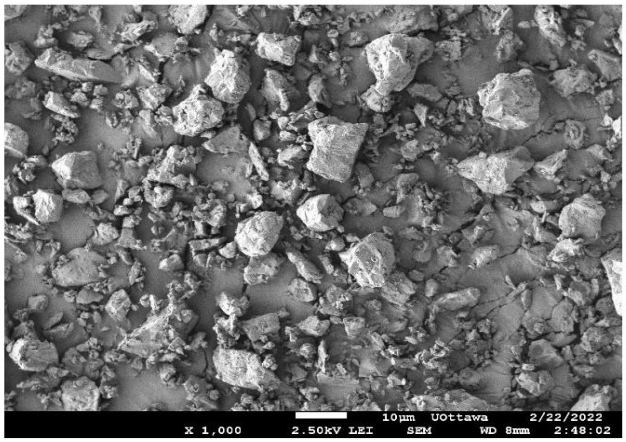

CeO_2 2118CG MOMPs

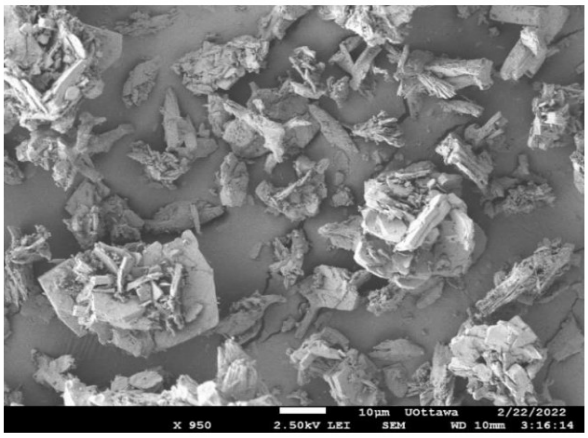

Fe_2O_3 US1139M MOMPs

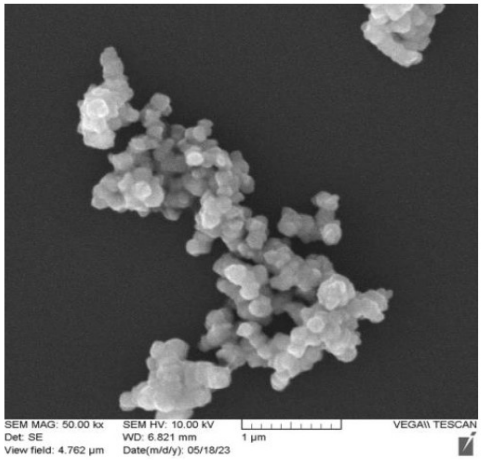

Supplementary Figure 5-8. Representative SEM images of MnO_2 MPs, CeO_2 MPs and Fe_2O_3 MPs.

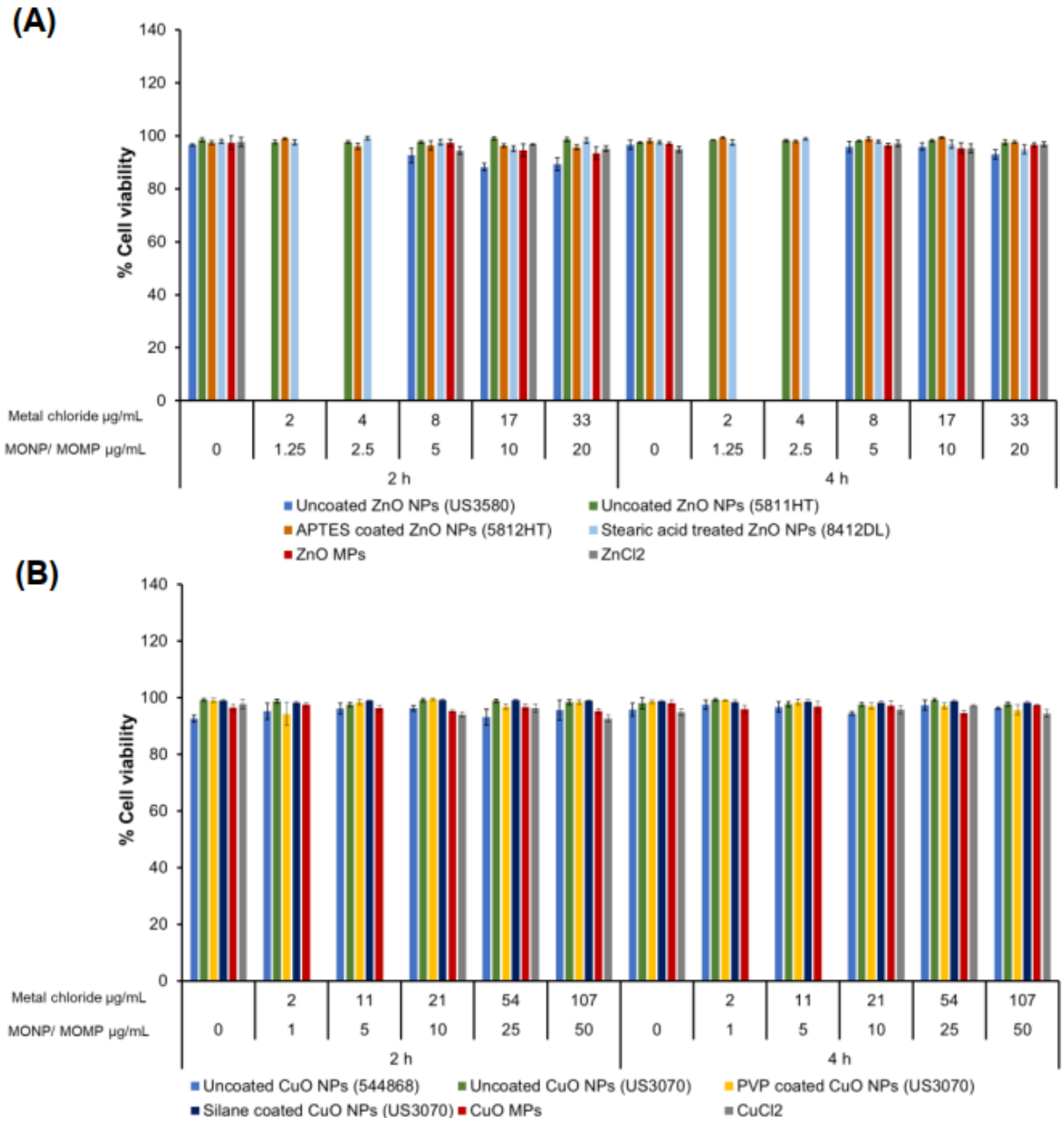

Supplementary Figure 5-9. Percentage of cell viability after exposure to (A) ZnO variants and $ZnCl_2$, (B) CuO variants and $CuCl_2$. Trypan Blue exclusion method was conducted after 2 and 4 h of exposure. Data is presented as mean and standard error (n=3-4 independent experiments). Statistically significant differences between the exposed samples and the matched negative control were determined through Kruskal-Wallis test. Uncoated ZnO NPs (US3580), ZnO MPs, $ZnCl_2$, uncoated CuO NPs (544868), CuO MPs, and $CuCl_2$ were previously published in (Boyadzhiev et al., 2022).

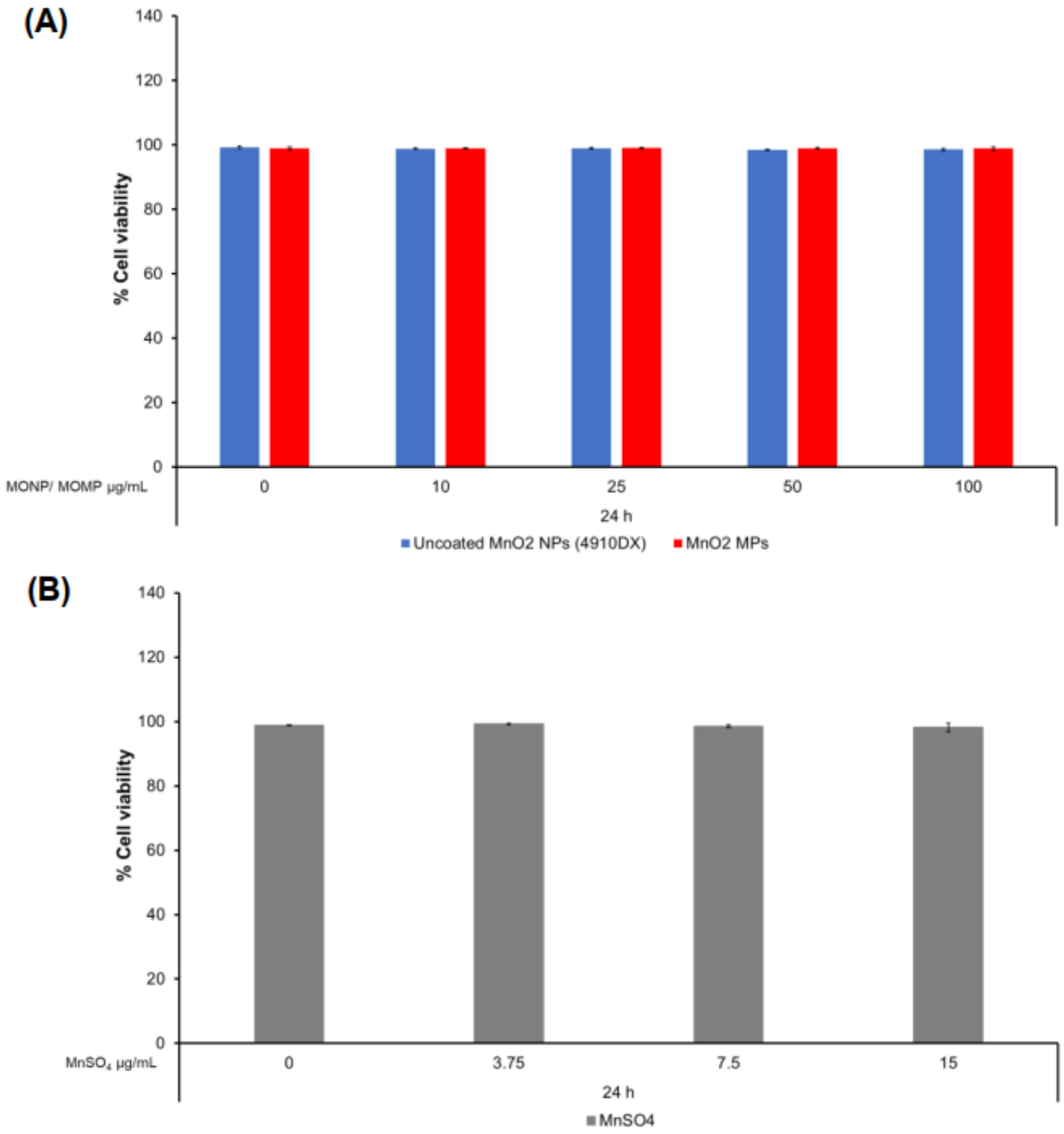

Supplementary Figure 5-10. Percentage of cell viability after exposure to (A) MnO_2 variants and (B) $MnSO_4$ for 24 h. Trypan Blue exclusion method. Data is presented as mean and standard error (n = 3-4 independent experiments). Statistically significant differences between the exposed samples and the matched negative control were determined through Kruskal-Wallis test.

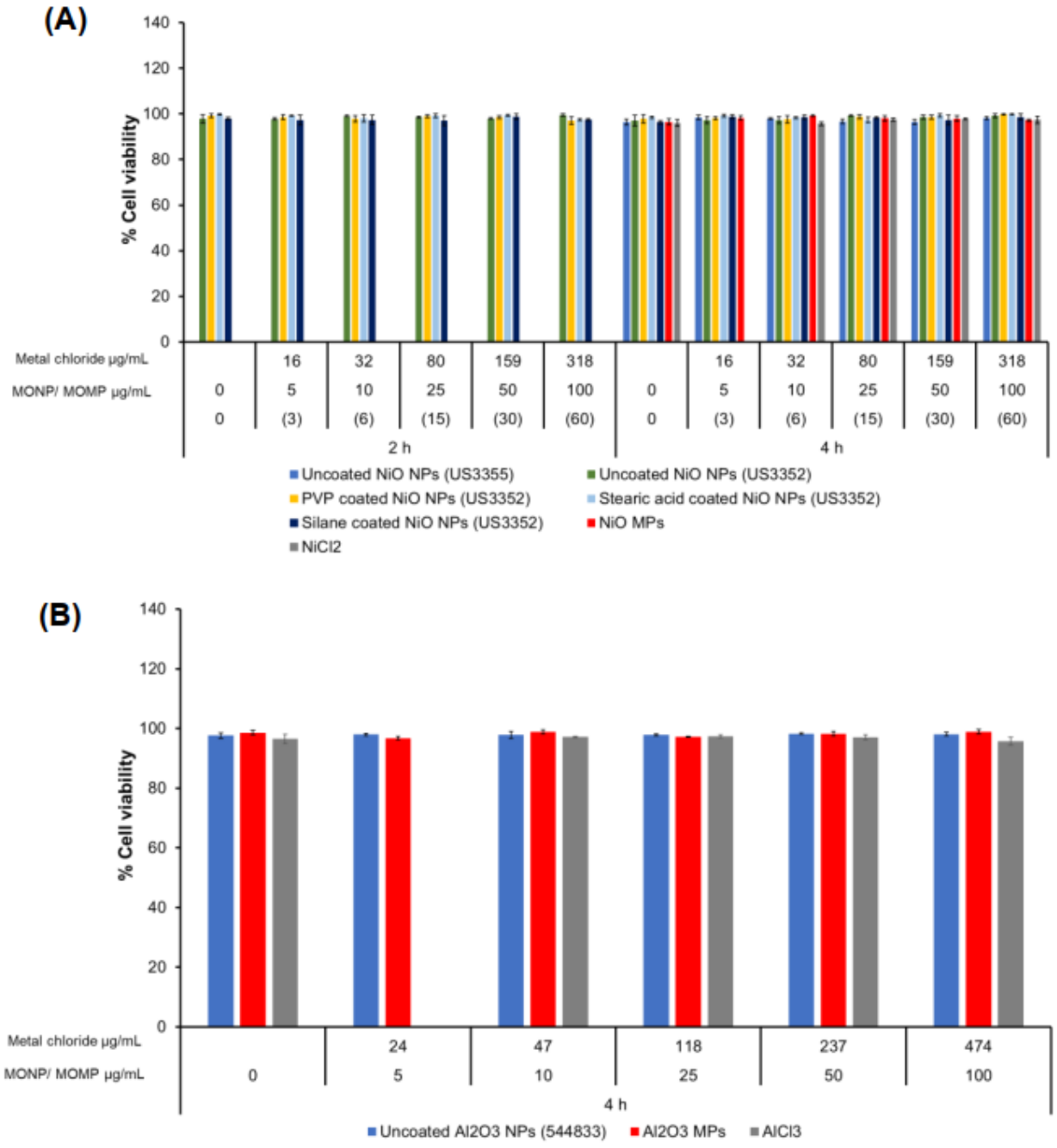

Supplementary Figure 5-11. Percentage of cell viability after exposure to (A) NiO variants and $NiCl_2$ for 2 and 4 h, (B) Al_2O_3 variants and $AlCl_3$ for 4 h. Trypan Blue exclusion method. (A) Data in parenthesis indicates the concentration of stearic acid coated NiO NPs. Data is presented as mean and standard error (n = 3-4 independent experiments). Statistically significant differences between the exposed samples and the matched negative control were determined through Kruskal-Wallis test.

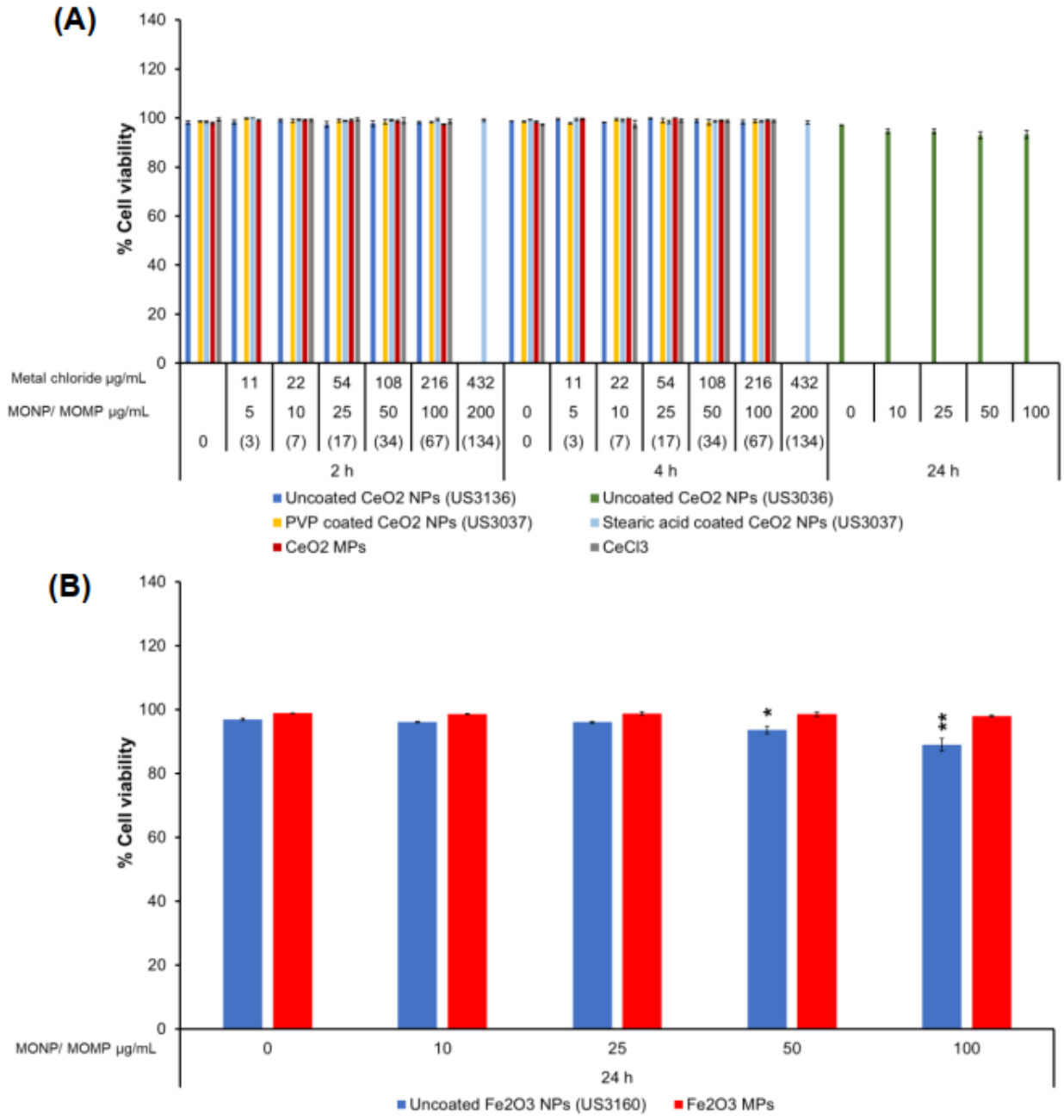

Supplementary Figure 5-12. Percentage of cell viability after exposure to (A) CeO_2 variants and $CeCl_3$, (B) Fe_2O_3 variants. Uncoated CeO_2 NPs (US3036) and Fe_2O_3 variants were only evaluated at 24 h. Uncoated CeO_2 (US3136), coated CeO_2 NPs and $CeCl_3$ were evaluated after 2 and 4 h of exposure. Trypan Blue exclusion method. (A) Data in parenthesis indicates the concentration of stearic acid coated CeO_2 NPs. Data is presented as mean and standard error (n = 3-4 independent experiments). Statistically significant differences between the exposed samples and the matched negative control were determined through Kruskal-Wallis test with a Dunnett's post-hoc. * $p < 0.05$, ** $p < 0.01$.

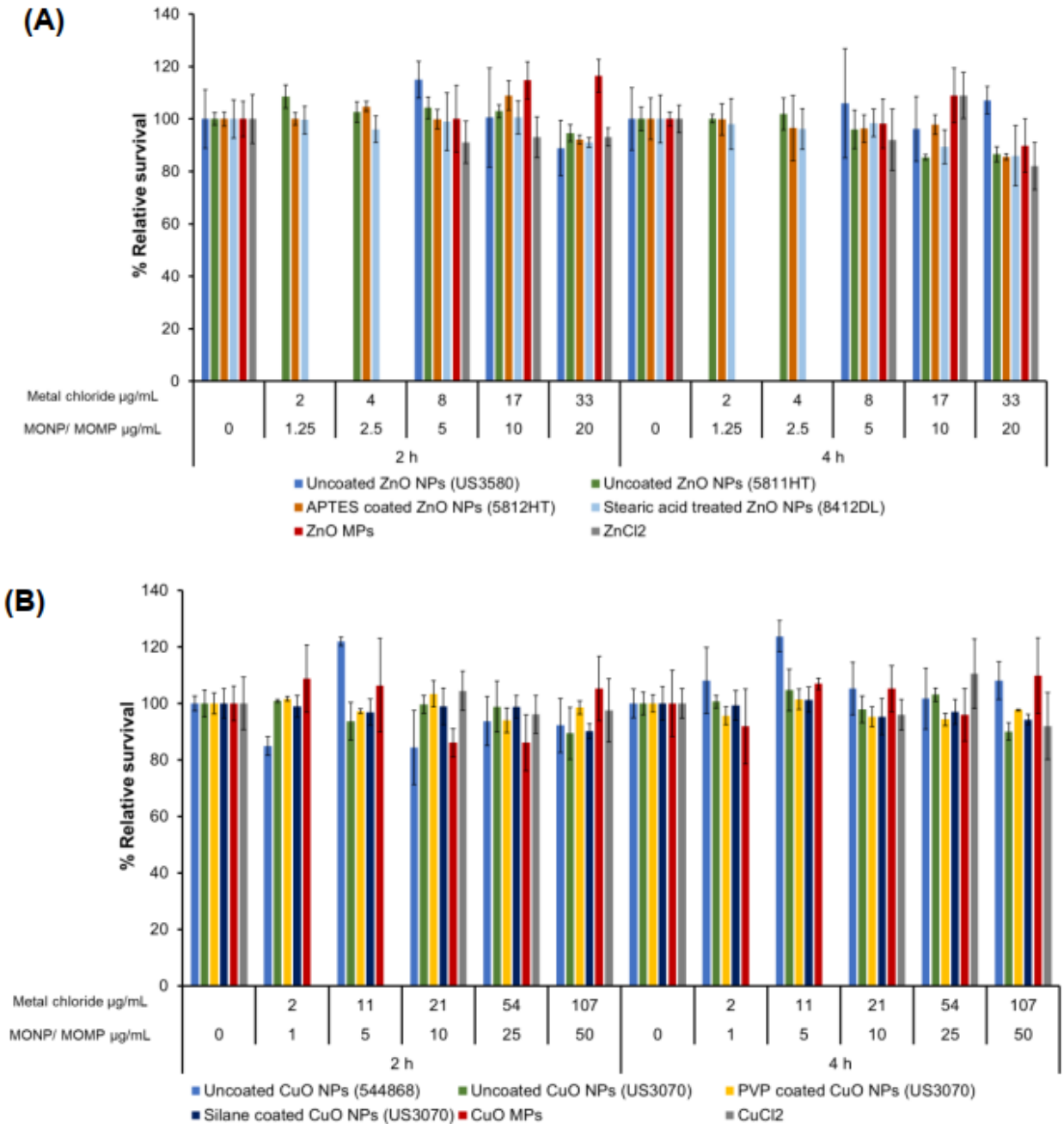

Supplementary Figure 5-13. Percentage of relative survival after exposure to (A) ZnO variants and $ZnCl_2$, (B) CuO variants and $CuCl_2$. Trypan Blue exclusion method was conducted after 2 and 4 h of exposure. Data is presented as mean and standard error (n = 3-4 independent experiments). Statistically significant differences between the exposed samples and the matched negative control were determined through Kruskal-Wallis test.

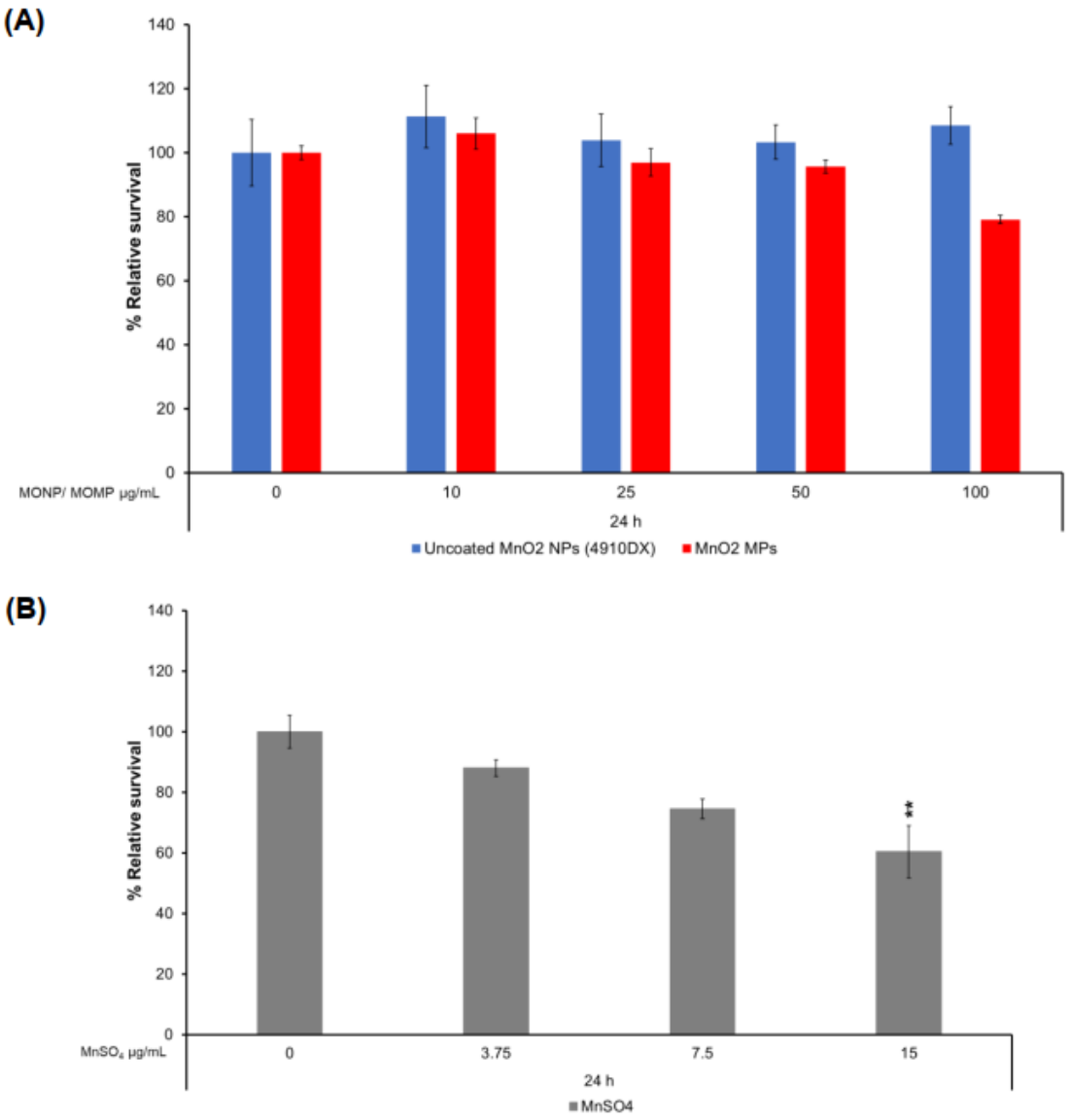

Supplementary Figure 5-14. Percentage of relative survival after exposure to (A) MnO_2 variants and $MnSO_4$ for 24 h. Trypan Blue exclusion method. Data is presented as mean and standard error (n=3-4 independent experiments). Statistically significant differences between the exposed samples and the matched negative control were determined through Kruskal-Wallis test with a Dunnett's post-hoc. ** $p < 0.01$.

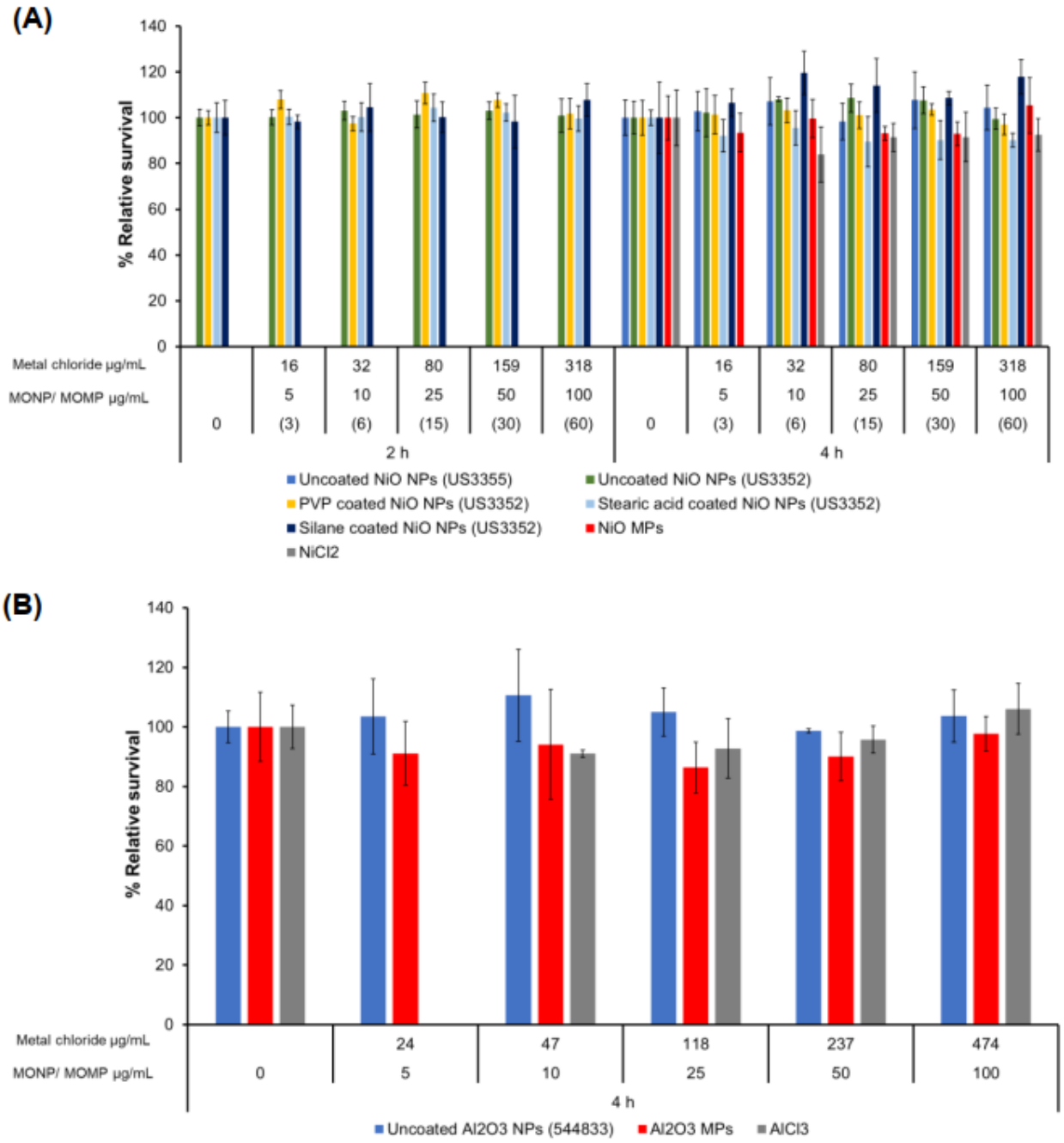

Supplementary Figure 5-15. Percentage of relative survival after exposure to (A) NiO variants and $NiCl_2$ for 2 and 4 h, (B) Al_2O_3 variants and $AlCl_3$ for 4 h. Trypan Blue exclusion method. (A) Data in parenthesis indicates the concentration of stearic acid coated NiO NPs. Data is presented as mean and standard error (n = 3-4 independent experiments). Statistically significant differences between the exposed samples and the matched negative control were determined through Kruskal-Wallis test.

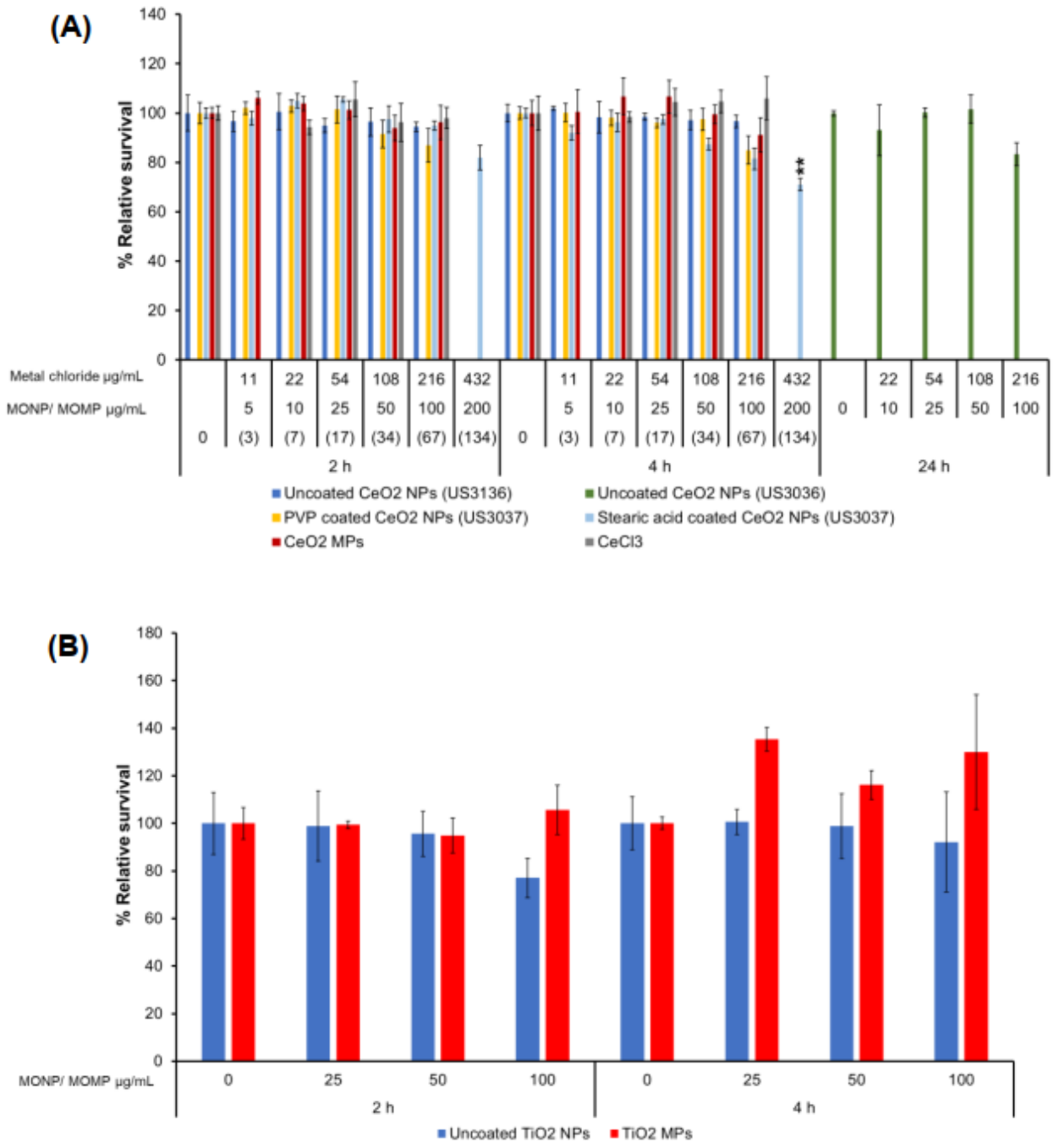

Supplementary Figure 5-16. Percentage of relative survival after exposure to (A) CeO_2 variants and $CeCl_3$ and (B) TiO_2 variants for 2 and 4 h. Uncoated CeO_2 NPs (US3036) were only evaluated after 24 h of exposure. Trypan Blue exclusion method. (A) Data in parenthesis indicates the concentration of stearic acid coated CeO_2 NPs. Data is presented as mean and standard error (n = 3-4 independent experiments). Statistically significant differences between the exposed samples and the matched negative control were determined through Kruskal Wallis test with a Dunnett's post-hoc. ** $p < 0.01$.

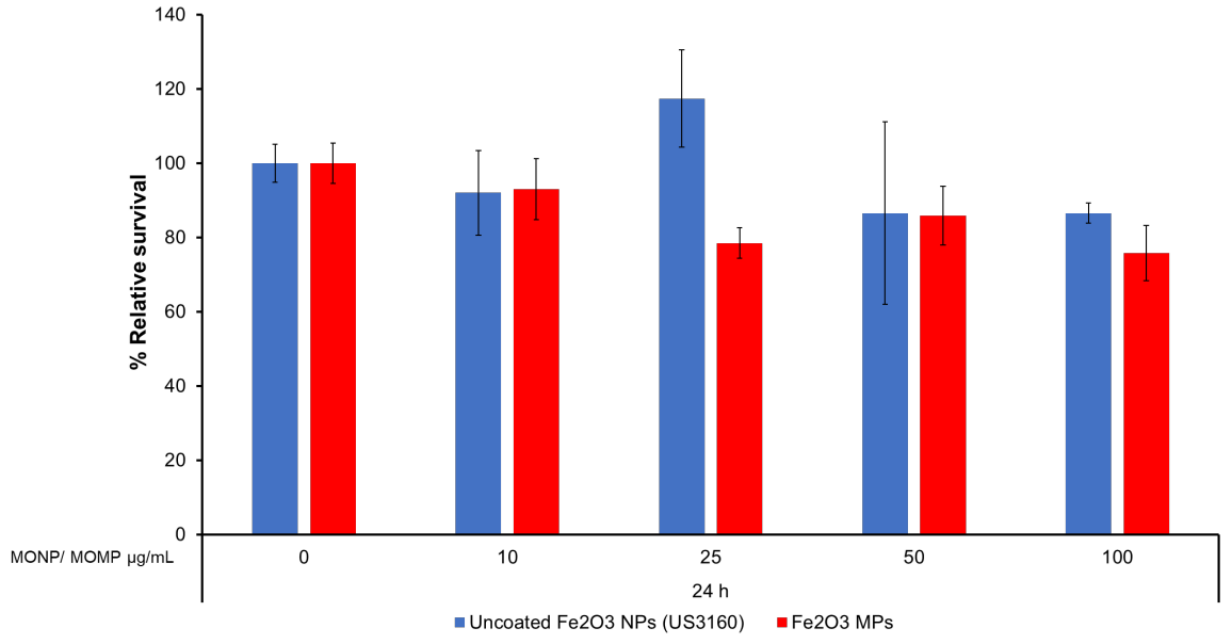

Supplementary Figure 5-17. Percentage of relative survival after exposure to (A) Fe_2O_3 variants for 24 h. Trypan Blue exclusion method. Data is presented as mean and standard error (n=3-4 independent experiments). Statistically significant differences between the exposed samples and the matched negative control were determined through Kruskal-Wallis test.

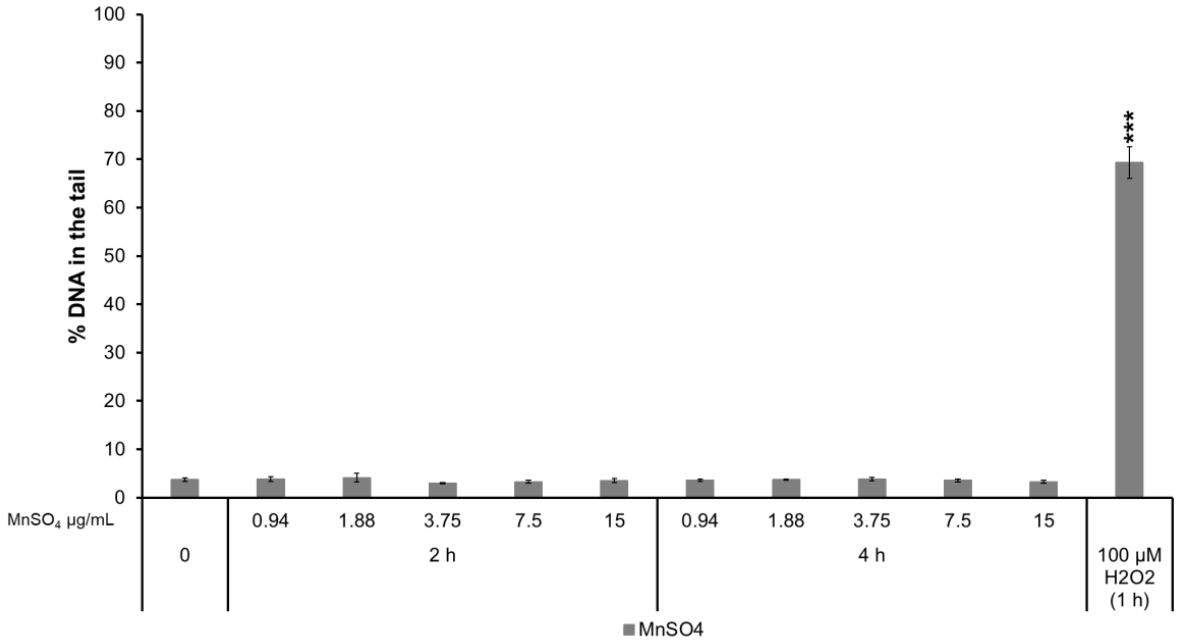

Supplementary Figure 5-18. Percentage of DNA in the tail in FE1 cells after exposure to $MnSO_4$ at 2 and 4 h. Data is presented as mean and standard error (n = 3-4). Statistically significant differences between the exposed samples and the matched negative control were determined through one-way ANOVA with a Dunnett's post-hoc. *** $p < 0.001$.

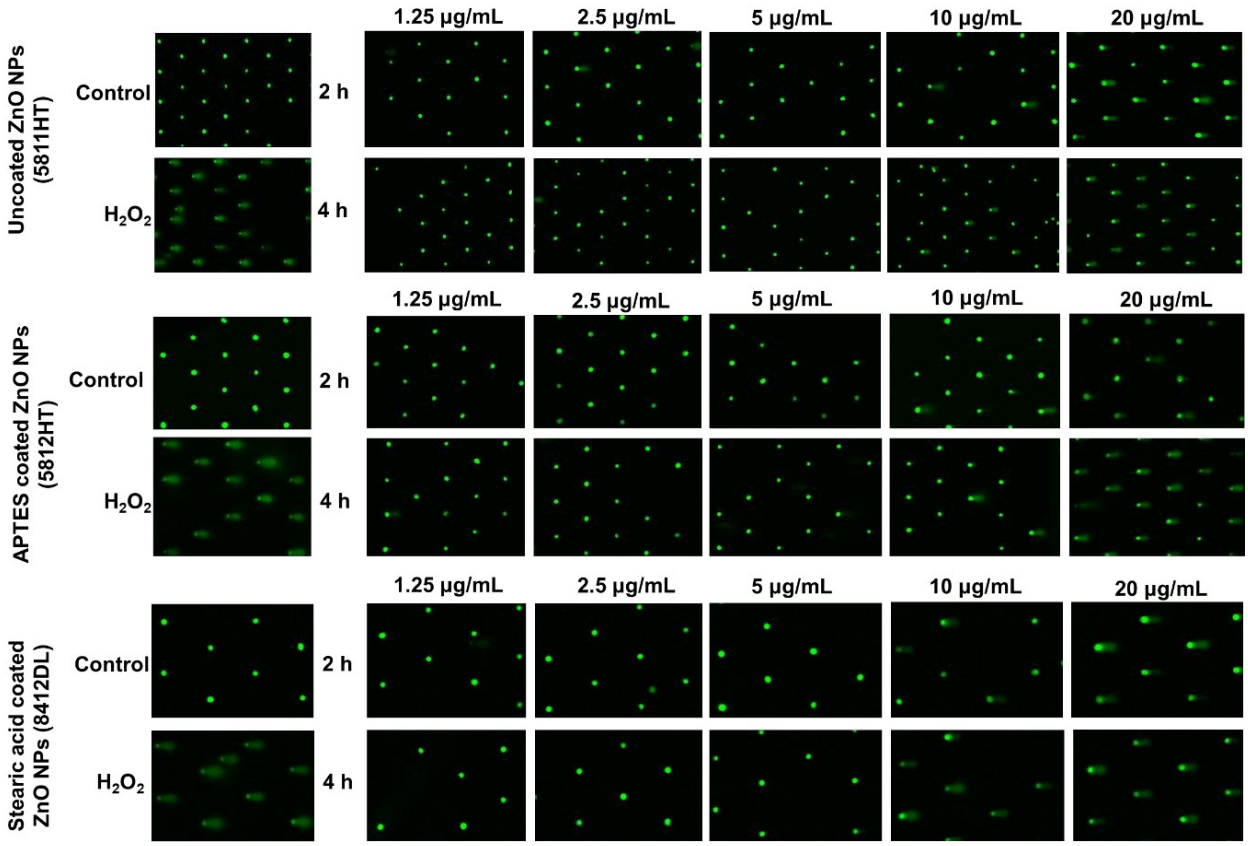

Supplementary Figure 5-19. Representative images of comets after exposure to uncoated ZnO NPs (5811HT), APTES coated ZnO NPs (5812HT), and stearic acid coated ZnO NPs (8412DL). SYBR® Gold staining. Leica DMi8 automated confocal fluorescence microscope 5x.

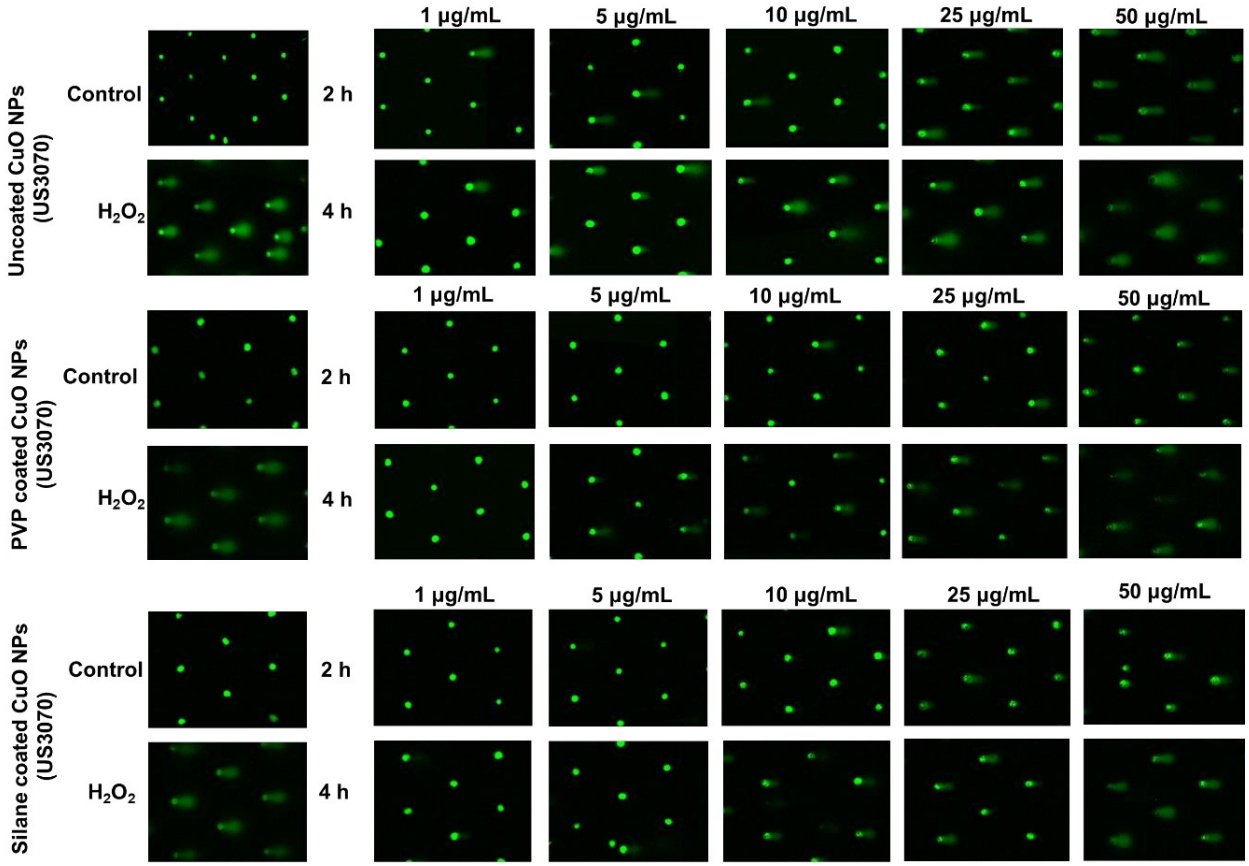

Supplementary Figure 5-20. Representative images of comets after exposure to uncoated CuO NPs (US3070), PVP coated CuO NPs (US3070), and silane coated CuO NPs (US3070). SYBR® Gold staining. Leica DMi8 automated confocal fluorescence microscope 5x.

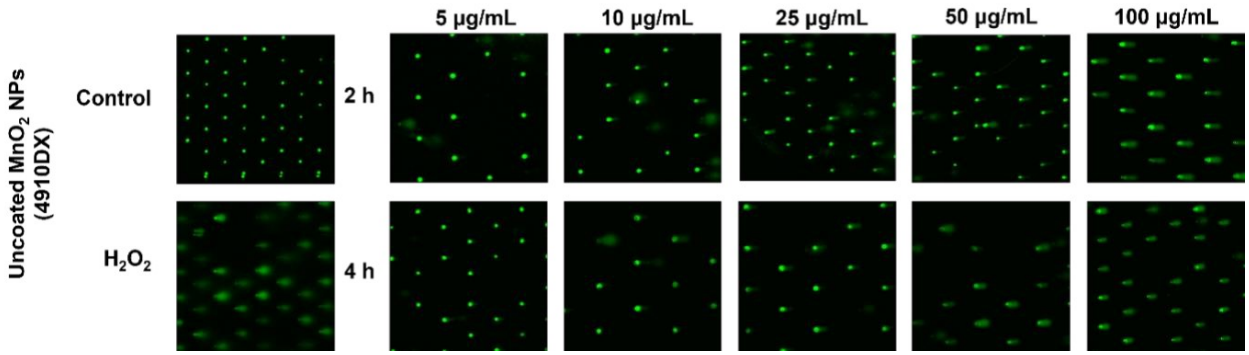

Supplementary Figure 5-21. Representative images of comets after exposure to uncoated MnO_2 NPs (4910DX). SYBR® Gold staining. Leica DMi8 automated confocal fluorescence microscope 5x.

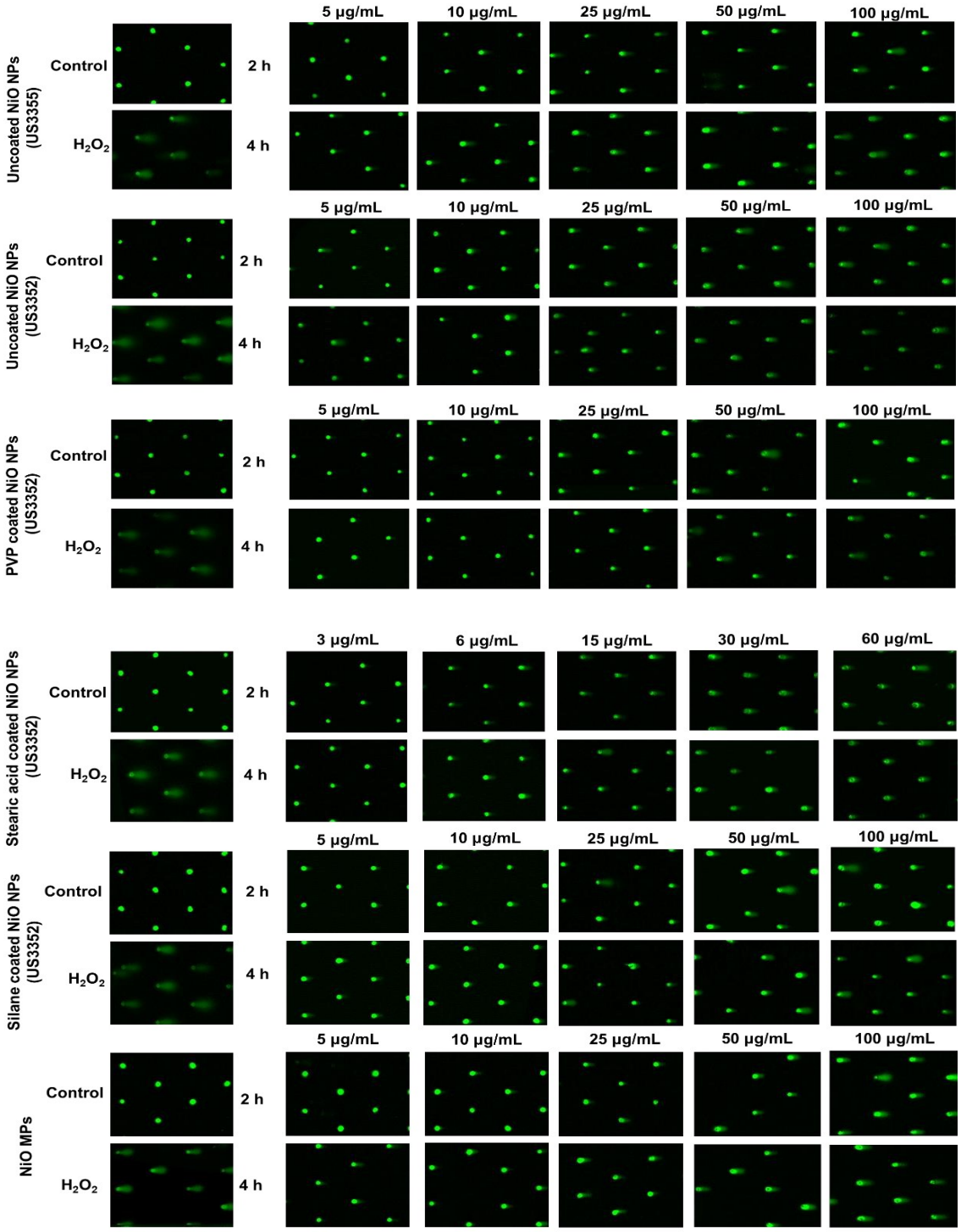

Supplementary Figure 5-22. Representative images of comets after exposure to NiO variants. SYBR® Gold staining. Leica DMi8 automated confocal fluorescence microscope 5x.

Appendix II Chapter 3 Supplementary Document 1

An in depth comparative pathway analysis was carried out as part of Chapter 3, and included as a supplementary document in (Boyadzhiev et al., 2023). The analysis is presented here for completeness.

Enriched Canonical Pathway In-Depth Overview

Overall, the pathway responses seen across exposure conditions were largely compound-specific, with metal chlorides and NPs inducing qualitatively similar responses, albeit with potency and enrichment differences.

ZnO NPs, MPs, $ZnCl_2$

When compared based on the amount of constituent Zn in the exposure media, ZnO MPs present the strongest response at 24 and 48 h, but the weakest response at 2 h (**Supplementary File 3-1**). For both NPs and MPs, the 5 µg/mL concentration was the only one where significantly enriched pathways were seen at any timepoint.

At the early timepoint of 2 h, 5 µg/mL ZnO NPs enriched 98 pathways, many related to cellular stress and death (ex. 'Unfolded protein response', 'NRF2-mediated Oxidative Stress Response', 'Ferroptosis Signaling Pathway', 'HIF1α Signaling'), immune signaling and disease (ex 'IL-10 Signaling', 'IL-6 Signaling', 'Acute Phase Response Signaling'), in addition to multiple metabolic and signaling related responses. For ZnO MPs at 5 µg/mL, the low-fold-change set featured 2 pathways, the 'Aldosterone Signaling in Epithelial Cells', and 'Protein Ubiquitination Pathway', while the high-fold-change set included 9 pathways relating mainly to cellular stress ('HIF1α Signaling', 'NRF2-mediated Oxidative Stress Response', 'Protein Ubiquitination Pathway') and signaling, in addition to the 'Phagosome Formation' pathway. With respect to $ZnCl_2$, 9 and 101 pathways were enriched at 5.1 and 8.5 µg/mL at 2 h. Notably in common between the two concentrations were pathways relating to disease (ex. 'HER-2 Signaling in Breast Cancer', 'Role of PKR in Interferon Induction and Antiviral Response', 'Huntington's Disease Signaling'), in addition to the 'HIF1α Signaling' pathway. Uniquely enriched at the 8.5 µg/mL concentration were 93 pathways, many relating to cellular stress (ex. 'Unfolded protein response', 'NRF2-

mediated Oxidative Stress Response', 'Ferroptosis Signaling Pathway'), immune response, (ex. 'TNFR2 Signaling', 'IL-10 Signaling', 'IL-7 Signaling Pathway'), wound healing and disease (ex. 'Wound Healing Signaling Pathway', 'Pulmonary Fibrosis Idiopathic Signaling Pathway', 'Molecular Mechanisms of Cancer') and general signaling.

By 24 h, response to ZnO NPs increased, with 149 significantly enriched pathways at 5 µg/mL. Many of the same responses from the 2 h timepoint were still present, including cellular stress and cell death related processes (ex. 'Unfolded protein response', 'NRF2-mediated Oxidative Stress Response', 'Ferroptosis Signaling Pathway', 'HIF1α Signaling'), and immune response and disease pathways (ex. 'Acute Phase Response Signaling', 'IL-10 Signaling', 'IL-6 Signaling'). In addition, enrichment of new pathways related to vesicular trafficking was seen ('CLEAR Signaling Pathway', 'Autophagy', 'Caveolar-mediated Endocytosis Signaling', 'Clathrin-mediated Endocytosis Signaling', 'Phagosome Maturation'). The 5 µg/mL ZnO MPs at this timepoint featured 228 unique pathways between both low and high-fold-change sets, with 89 pathways in the low group, 170 pathways in the high group, and 31 pathways shared between the two sets. Response to ZnO MPs at this timepoint was more in line with responses seen for ZnO NPs and $ZnCl_2$ than at 2 h, including pathways relating to cell stress and death (ex. 'NRF2-mediated Oxidative Stress Response', 'Unfolded protein response', 'Ferroptosis Signaling Pathway'), immune response and disease (ex. 'Acute Phase Response Signaling'), vesicular trafficking ('CLEAR Signaling Pathway', 'Caveolar-mediated Endocytosis Signaling', 'Autophagy') and general signaling and metabolic pathways. Finally for $ZnCl_2$ at 24 h, 25 and 177 pathways were enriched at 5.1 and 8.5 µg/mL with high similarity to 5 µg/mL of NPs and MPs. Of those pathways 13 were commonly enriched, mainly relating to immune response (ex. 'Pathogen Induced Cytokine Storm Signaling Pathway', 'Toll-like Receptor Signaling') and metabolism (ex. 'Xenobiotic Metabolism Signaling'). Unique to the high concentration group were an additional 164 pathways related to similar processes seen for NPs and MPs, including cell stress and death (ex. 'Unfolded protein response', 'NRF2-mediated Oxidative Stress Response', 'Ferroptosis Signaling Pathway'), immune response and disease (ex. 'TGF-β Signaling', 'IL-8 Signaling', 'Chemokine Signaling'), vesicular trafficking ('CLEAR

Signaling Pathway', 'Autophagy', 'Caveolar-mediated Endocytosis Signaling', 'Phagosome Maturation', 'Clathrin-mediated Endocytosis Signaling'), as well as signaling and metabolism.

For the latest timepoint of 48 h, a reduced number of pathways was seen with each form of Zn. For 5 μg/mL ZnO NPs, 95 pathways were significantly enriched, with noted induction of DNA repair and damage response pathways (ex. 'Role of BRCA1 in DNA Damage Response', 'Mismatch Repair in Eukaryotes', 'NER (Nucleotide Excision Repair, Enhanced Pathway)', 'ATM Signaling'), cell stress and death responses (ex. 'p53 Signaling', 'Ferroptosis Signaling Pathway', 'HIF1α Signaling', 'Senescence Pathway, 'NRF2-mediated Oxidative Stress Response', 'Unfolded protein response'), immune signaling and disease (ex. 'Pathogen Induced Cytokine Storm Signaling Pathway', 'Interferon Signaling', 'Pancreatic Adenocarcinoma Signaling'), however all pathways relating to vesicular trafficking seen at 24 h were no longer enriched at 48 h. With respect to 5 μg/mL ZnO MPs at 48 h, 199 unique pathways were enriched across both high and low fold-change groups, with 89 pathways in the low-fold-change group, 133 pathways in the high-fold-change group, and 23 pathways shared between the two. Similar responses to 5 μg/mL ZnO NPs were seen, including induction of DNA damage and repair pathways (ex. 'Role of BRCA1 in DNA Damage Response', 'NER (Nucleotide Excision Repair, Enhanced Pathway)', 'Mismatch Repair in Eukaryotes'), cell stress and death signaling (ex. 'p53 Signaling', 'Ferroptosis Signaling Pathway', 'HIF1α Signaling', 'Unfolded protein response', 'NRF2-mediated Oxidative Stress Response'), and immune response and disease (ex. 'Atherosclerosis Signaling', 'Interferon Signaling', 'Pathogen Induced Cytokine Storm Signaling Pathway'). In addition, the 5 μg/mL low-fold-change set notably enriched vesicular trafficking pathways no longer seen in ZnO NPs (ex. 'Caveolar-mediated Endocytosis Signaling', 'Autophagy', 'CLEAR Signaling Pathway). Finally, $ZnCl_2$ at 48 h lead to the enrichment of 36 and 146 pathways at 5.1 and 8.5 μg/mL respectively. Between the two concentrations 28 pathways were shared, which included DNA damage and repair processes (ex. 'DNA damageinduced 14-3-3σ Signaling', 'ATM Signaling', 'Role of BRCA1 in DNA Damage Response'), cell cycle responses (ex. 'Kinetochore Metaphase Signaling

Pathway', 'Mitotic Roles of Polo-Like Kinase', 'Cyclins and Cell Cycle Regulation'), immune signaling and disease, (ex. 'Acute Phase Response Signaling', 'IL-10 Signaling', 'Pulmonary Fibrosis Idiopathic Signaling Pathway'), and cellular stress ('p53 Signaling', 'Senescence Pathway'). Unique to 8.5 µg/mL at 48 h were 118 pathways implicated in DNA repair (ex. 'BER (Base Excision Repair) Pathway', 'NER (Nucleotide Excision Repair, Enhanced Pathway)', 'Mismatch Repair in Eukaryotes), cell stress and death (ex. 'Ferroptosis Signaling Pathway', 'HIF1α Signaling', 'NRF2-mediated Oxidative Stress Response', 'Unfolded protein response'), immune response and disease (ex. 'Interferon Signaling', 'IL-7 Signaling Pathway', 'TGF-β Signaling', 'Molecular Mechanisms of Cancer'), as well as numerous pathways implicated in signaling and metabolic processes.

CuO NPs, MPs, $CuCl_2$

The pathway response to CuO NPs, MPs, and $CuCl_2$ has been described in detail in Boyadzhiev et al., 2021(Boyadzhiev et al., 2021). Analysis of the published data with the most recent version of IPA used in this study resulted in much the same responses with some notable differences (**Supplementary File 3-2**).

At the 2 h timepoint only 25 µg/mL CuO MPs featured significantly two enriched pathways, with 'Mitotic Roles of Polo-like Kinase' and 'Protein Ubiquitination Pathway' being the only perturbed responses. In the previously conducted IPA analysis, CuO MPs were not examined in IPA, but using GO enrichment. Using the GO ontologies, it could be seen that 'regulation of meiotic cell cycle' [GO:0051445] and 'anaphase-promoting complex-dependent catabolic process' [GO:0031145], as well as the cellular components 'nuclear ubiquitin ligase complex' [GO:0000152] and 'anaphase-promoting complex' [GO:0005680] were significantly enriched in the down regulated gene list [34](Boyadzhiev et al., 2021).

At the 24 h timepoint, only CuO NPs presented enriched pathways with 10, 67, and 89 pathways at 5, 10, and 25 µg/mL. At this timepoint, 5, 10, and 25 µg/mL concentrations commonly induced disturbances in 6 pathways relating to vesicular trafficking ('CLEAR Signaling Pathway', 'Phagosome Maturation') and immune function ('IL-10 Signaling', 'Role

of MAPK Signaling in Promoting the Pathogenesis of Influenza'), as well as the iron-mediated cell death pathway 'Ferroptosis Signaling Pathway'. At higher exposure concentrations of 10 and 25 µg/mL 30 pathways were commonly enriched, notably including numerous cell stress pathways (ex. 'HIF1a Signaling', 'NRF2-mediated Oxidative Stress Response', 'Unfolded protein response', 'BAG2 Signaling Pathway'), the vesicular trafficking pathway 'Autophagy', and multiple disease and metabolism related responses. The highest concentration of 25 µg/mL uniquely enriched 53 pathways, including DNA damage and repair responses (ex. 'Role of BRCA1 in DNA Damage Response', 'Mismatch Repair in Eukaryotes'), cell cycle and cancer responses (ex. 'Role of CHK Proteins in Cell Cycle Checkpoint Control', 'Cell Cycle Control of Chromosomal Replication', 'Molecular Mechanisms of Cancer'), and cellular stress and death signaling (ex. 'Immunogenic Cell Death Signaling Pathway', 'p53 Signaling', 'Death Receptor Signaling'). These responses are in line with the previously conducted IPA enrichment with 1, 20, and -1 extra pathways in comparison [34], and the notable enrichment of the 'CLEAR Signaling Pathway' which was not present previously. In addition, the 'BAG2 Signaling Pathway' was not enriched for 5 µg/mL CuO NPs at 24 h due to increases in the total gene count of the pathway (80 genes in IPA content version 81348237 vs 40 genes in IPA content version 48207413).

At the last timepoint of 48 h exposure to 5 and 10 µg/mL CuO NPs resulted in the strongest response with 96 and 170 enriched pathways respectively, whereas for 25 µg/mL no usable RNA was able to be extracted from exposed cells and was therefore not analyzed for transcriptional response (Boyadzhiev et al., 2021). In common to both 5 and 10 µg/mL CuO NP exposures were 74 pathways, including perturbed cell stress signaling responses (ex. 'NRF2- mediated Oxidative Stress Response', 'BAG2 Signaling Pathway', 'Unfolded protein response'), DNA damage and repair pathways (ex. 'GADD45 Signaling', 'ATM Signaling', 'Mismatch Repair in Eukaryotes'), and pathways related to vesicular trafficking and turnover (ex. 'Autophagy', 'CLEAR Signaling Pathway', 'Caveolar-mediated Endocytosis Signaling'), in addition to multiple disease and cancer related pathways and metabolic and signaling responses. Unique to the 10 µg/mL concentration were 96 additional pathways related to cell stress (ex. 'Senescence Pathway', 'Necroptosis Signaling Pathway'), DNA

repair (ex. ‘BER (Base Excision Repair) Pathway’, ‘NER (Nucleotide Excision Repair, Enhanced Pathway)’), immune responses (ex. ‘IL-10 Signaling’, ‘TGF-β Signaling’, ‘Acute Phase Response Signaling’), carcinogenesis (ex. ‘Small Cell Lung Cancer Signaling’, ‘Renal Cell Carcinoma Signaling’), and general signaling and metabolism. Finally, with respect to 7 µg/mL CuCl2, 51 pathways were enriched at 48 h including multiple stress pathways (ex. ‘NRF2-mediated Oxidative Stress Response’, ‘Senescence Pathway’, ‘HIF1α Signaling’), as well as pathways relating to DNA damage response (ex. ‘Cell Cycle: G2/M DNA Damage Checkpoint Regulation’, ‘ATM Signaling’), detoxification (ex. ‘Glutathione-mediated Detoxification’, ‘Superoxide Radicals Degradation’), and cell cycle progression (ex. ‘Cyclins and Cell Cycle Regulation’, ‘Role of CHK Proteins in Cell Cycle Checkpoint Control’). In comparison with the IPA analysis conducted in (Boyadzhiev et al., 2021), 16 and 43 additional pathways are seen for CuO NPs, and 14 additional pathways are seen for $CuCl_2$. Much the same response is seen for 5 and 10 µg/mL CuO NPs, with cell stress, DNA damage, and cell death pathways making up the majority of the highly enriched pathways. Similarly, the most affected processes involved in $CuCl_2$ response at 48 h are akin to the previous IPA enrichment (Boyadzhiev et al., 2021), which include oxidative stress, DNA damage, cell cycle progression, and cellular detoxification.

NiO NPs, MPs, $NiCl_2$

For Ni compounds, NiO NPs and $NiCl_2$ presented much the same response profile, at the same timepoints of assessment, albeit at different concentrations of Ni whereas NiO MPs generally presented a similar but muted response (**Supplementary Data File 3-3**).

At 2 h, no pathway enrichment was seen for any Ni compound.

At 24 h, NiO NPs featured 4, 46, and 80 enriched pathways at 10, 25, and 50 µg/mL. All pathways enriched at 10 µg/mL were commonly enriched at 25 and 50 µg/mL, with ‘Glycolysis’ ‘Gluconeogenesis I’, and ‘Sirtuin Signaling Pathway’ notably enriched. Higher concentrations of 25 and 50 µg/mL commonly enriched 36 pathways, including multiple DNA damage response and repair pathways (ex. ‘NER (Nucleotide Excision Repair, Enhanced Pathway)’, ‘Mismatch Repair in Eukaryotes’, ‘Role of BRCA1 in DNA Damage

Response'), and cell stress pathways ('HIF1α Signaling', 'Senescence Pathway', 'Aryl Hydrocarbon Receptor Signaling'). The highest concentration of 50 µg/mL uniquely enriched 40 additional pathways at this timepoint, including additional cell stress related responses (ex. 'NRF2-mediated Oxidative Stress Response', 'Endoplasmic Reticulum Stress Pathway', 'Unfolded protein response'), and pathways related to vesicular trafficking ('CLEAR Signaling Pathway', 'Phagosome Maturation', 'Autophagy'). For NiO MPs at 24 h, 9 and 50 pathways were significantly enriched at 25 and 50 µg/mL. Common between the two concentrations were 8 pathways, including the 'HIF1a Signaling', 'Sirtuin Signaling Pathway', 'Glycolysis I', and 'Gluconeogenesis I' pathways implicated in hypoxia. The higher concentration of 50 µg/mL further uniquely enriched 42 pathways, 23 of which relate to disease and immune response (ex. 'Interferon Signaling', 'IL-33 Signaling Pathway', 'Neuroinflammation Signaling Pathway'), 7 associated with cell stress / aberrant wound healing (ex. 'Ferroptosis Signaling Pathway', 'NRF2-mediated Oxidative Stress Response', 'Role of Tissue Factor in Cancer'), and the rest comprising metabolic and signaling pathways. With respect to specific pathways related to $NiCl_2$ at 24 h, 58 and 93 pathways were enriched at 40 and 80 µg/mL. Of these pathways, 49 were commonly enriched between the 40 and 80 µg/mL concentrations, including 'HIF1a Signaling', 'Glycolysis I', and 'Gluconeogenesis I' pathways noted for NiO NPs and MPs. The remaining pathways were comprised of DNA damage and repair responses (ex. 'Role of BRCA1 in DNA Damage Response', 'NER (Nucleotide Excision Repair, Enhanced Pathway)', 'GADD45 Signaling'), cell stress and disease (ex. 'p53 Signaling', 'Senescence Pathway', 'Pulmonary Fibrosis Idiopathic Signaling Pathway'), vesicular trafficking processes ('CLEAR Signaling Pathway', 'Autophagy', 'Caveolar-mediated Endocytosis Signaling'), and pathways related to cell cycle control, carcinogenesis, metabolism and signaling. Unique to the 80 µg/mL concentration at 24 h were 44 pathways mainly involved in cell stress, immune signaling, and metabolism, with 'Oxidative Phosphorylation', 'Mitochondrial Dysfunction', and 'NRF2-mediated Oxidative Stress Response' notably enriched.

By 48 h, the concentration-dependent response to NiO NPs increased, with 10, 90, and 147 significantly enriched pathways for 10, 25, 50 µg/mL exposure groups. Common to

all concentrations of NiO NPs at this timepoint were 6 pathways, most of which relate to hypoxia ('Glycolysis I', 'Gluconeogenesis I', 'HIF1α Signaling', 'Sirtuin Signaling Pathway'). At higher concentrations of 25 and 50 μg/mL, 53 pathways were commonly enriched including multiple immune related pathways (ex. 'Acute Phase Response Signaling', 'IL-10 Signaling', 'Pathogen Induced Cytokine Storm Signaling Pathway'), some cell stress pathways ('Senescence Pathway', 'Oxidative Phosphorylation'), and pathways related to DNA damage response ('GADD45 Signaling', 'Cell Cycle: G2/M DNA Damage Checkpoint Regulation'). Unique to 50 μg/mL NiO NPs at 48 h timepoint were 88 additional pathways with notable cell stress responses (ex. 'Mitochondrial Dysfunction', 'NRF2-mediated Oxidative Stress Response', 'Unfolded protein response', 'Ferroptosis Signaling Pathway'), pathways relating to vesicular trafficking ('Autophagy', 'Caveolar-mediated Endocytosis Signaling', 'CLEAR Signaling Pathway'), additional immune related processes (ex. 'Interferon Signaling', 'IL-4 Signaling', 'Chemokine Signaling'), and multiple metabolic and signaling pathways. In terms of NiO MPs at 48 h, 17 and 37 enriched pathways were observed at 25 and 50 μg/mL respectively. Of those pathways, 9 were commonly enriched between both exposure groups, including hypoxia signaling pathways ('Glycolysis I', 'HIF1α Signaling', 'Gluconeogenesis I', 'Sirtuin Signaling Pathway'), and multiple pathways related to immune response and disease (ex. 'Atherosclerosis Signaling', 'Hepatic Fibrosis / Hepatic Stellate Cell Activation'). The high concentration of 50 μg/mL uniquely enriched 28 pathways of which 11 related to immune response and disease (ex. 'Tolllike Receptor Signaling', 'Hepatic Fibrosis Signaling Pathway') and 2 more related to metal homeostasis ('Inhibition of Matrix Metalloproteases', 'Ferroptosis Signaling Pathway'), with the rest being signaling and metabolic in nature. Finally with respect to $NiCl_2$ exposed cells at 48 h, 40 and 80 μg/mL concentrations enriched 81 and 153 pathways respectively, with 57 pathways in common between the two concentrations. These pathways were implicated in hypoxia signaling ('HIF1a Signaling', 'Glycolysis I', 'Gluconeogenesis I', 'Sirtuin Signaling Pathway'), immune and disease (ex. 'Interferon Signaling', 'Pulmonary Fibrosis Idiopathic Signaling Pathway', 'IL-10 Signaling'), and cell stress processes (ex. 'Mitochondrial dysfunction', 'p53 Signaling', 'Ferroptosis Signaling'), in addition to multiple metabolic and

general signaling pathways. At the high $NiCl_2$ concentration of 80 µg/mL, 96 pathways were uniquely enriched including notable cell stress responses ('Unfolded protein response', 'NRF2-mediated Oxidative Stress Response'), vesicular trafficking pathways ('Autophagy', 'CLEAR Signaling Pathway', 'Caveolar-mediated Endocytosis Signaling'), immune processes (ex. 'Acute Phase Response Signaling', 'TGF-β Signaling', 'Pulmonary Healing Signaling Pathway'), and numerous signaling and metabolic pathways.

Al_2O_3 NPs, MPs, $AlCl_3$

With respect to Al exposures, Al_2O_3 NPs presented the weakest response of the MONPs tested (**Supplementary Data File 3-4**). At equivalent concentrations of constituent metal, $AlCl_3$ induced the most pronounced pathway response out of the three materials tested.

At 2 h, no significantly enriched pathways were seen for any Al material.

By the 24 h timepoint, Al_2O_3 NPs featured 3 enriched pathways, which consisted of the 'LPS/IL-1 Mediated Inhibition of RXR Function', 'Regulation Of The Epithelial Mesenchymal Transition By Growth Factors Pathway', and 'NRF2-mediated Oxidative Stress Response'. With respect to Al_2O_3 MPs, they featured their strongest response at 24 h, with 71 enriched pathways at 50 µg/mL. These pathways mainly related to immune responses (ex 'Toll-like Receptor Signaling', 'Th2 Pathway', 'Acute Phase Response Signaling') and metabolism and general signaling, with a few implicated in wound healing and the cytoskeleton ('Wound Healing Signaling Pathway', 'Actin Cytoskeleton Signaling'), and vesicular trafficking ('Phagosome Formation', 'Caveolar-mediated Endocytosis Signaling'). Notably, there was a lack of cell stress signaling, with only the 'NRF2-mediated Oxidative Stress Response' showing significant enrichment. For $AlCl_3$ at 24 h, 1 and 6 pathways were significantly enriched at 47 and 118 µg/mL. The only pathway at 47 µg/mL was 'Glycolysis I', while the higher concentration of 118 µg/mL featured immune signaling (ex. 'Atherosclerosis Signaling', 'IL-17 Signaling'), as well as notable enrichment of the 'HIF1a Signaling' pathway.

At the latest timepoint of 48 h, Al_2O_3 NPs featured a concentration-dependent pathway response with 36 and 46 enriched pathways at 25 and 50 µg/mL respectively. Common to both concentrations at this timepoint were 26 pathways, including the 'HIF1α Signaling' pathway, as well as numerous pathways related to immune response and disease (ex. 'IL-6 Signaling', 'Acute Phase Response Signaling', 'Osteoarthritis Pathway') and aberrant wound healing (ex 'Pulmonary Healing Signaling Pathway', 'Pulmonary Fibrosis Idiopathic Signaling Pathway'). Unique to 50 µg/mL at this timepoint were 20 additional pathways, including the 'GADD45 Signaling' stress pathway and the 'Caveolar-mediated Endocytosis Signaling' internalization pathway, with the remaining pathways implicated in immune responses (ex. 'Toll-like Receptor Signaling', 'Role of IL-17A in Arthritis'), aberrant wound healing (ex. 'Regulation of the Epithelial-Mesenchymal Transition Pathway', 'Wound Healing Signaling Pathway', 'Bladder Cancer Signaling'), and general signaling. With respect to Al_2O_3 MPs at this timepoint, 14 pathways were enriched at 50 µg/mL representing a diverse range of functions including cell stress responses ('p53 Signaling', 'GADD45 Signaling'), immune responses ('LPS/IL-1 Mediated Inhibition of RXR Function'), and numerous cell signaling pathways. Finally with respect to 47 and 118 µg/mL $AlCl_3$, 45 and 60 pathways were significantly enriched. Commonly enriched between the two concentrations were 29 pathways mainly related to aberrant wound healing and disease (ex. 'Pulmonary Fibrosis Idiopathic Signaling Pathway', 'Wound Healing Signaling Pathway', 'Hepatic Fibrosis Signaling Pathway'), as well as the 'Clathrin-mediated Endocytosis Signaling' pathway. Uniquely enriched at 118 µg/mL at 48 h were 31 additional pathways, including immune related responses (ex. 'Acute Phase Response Signaling', 'IL-17A Signaling in Fibroblasts'), pathways implicated in metal ion homeostasis ('Iron homeostasis signaling pathway', 'Ferroptosis Signaling Pathway', 'Inhibition of Matrix Metalloproteases'), and multiple metabolic and signaling responses.

TiO_2 NPs, MPs

Transcriptional response to insoluble TiO_2 was much more pronounced in the case of TiO_2 NPs, as compared to TiO_2 MPs, (**Supplementary Data File 3-5**).

At the earliest timepoint of 2 h, TiO_2 NPs induced mild concentration dependent pathway enrichment with 1, 2, and 5 enriched pathways at 25, 50, and 100 µg/mL concentrations. All concentrations significantly enriched the 'Human Embryonic Stem Cell Pluripotency' pathway, while the 50 and 100 µg/mL concentrations also commonly enriched the 'Mouse Embryonic Stem Cell Pluripotency' pathway. Unique to 100 µg/mL were 2 additional pathways related to diseases, and the calcium signaling pathway 'S100 Family Signaling Pathway'. No significant pathway enrichment was seen for TiO_2 MPs at this timepoint.

By 24 h, concentration dependent enrichment was seen for both NPs and MPs. The response to TiO_2 NPs was more pronounced with 33, 66, and 99 enriched pathways at 25, 50, and 100 µg/mL concentrations. For TiO_2 NPs at this timepoint, 21 pathways were commonly shared between all concentrations including DNA repair pathways ('NER (Nucleotide Excision Repair, Enhanced Pathway)', 'Mismatch Repair in Eukaryotes'), vesicular trafficking responses ('CLEAR Signaling Pathway', 'Phagosome Maturation'), metal ion homeostasis related responses ('Iron homeostasis signaling pathway', 'Ferroptosis Signaling Pathway'), as well as general disease type and metabolic pathways. The two higher TiO_2 NP concentrations (50 & 100 µg/mL) commonly enriched 27 additional pathways, mainly related to DNA repair and damage response (ex. 'Role of BRCA1 in DNA Damage Response', 'GADD45 Signaling', 'BER (Base Excision Repair) Pathway'), and immune signaling (ex. 'IL-10 Signaling', 'IL-17A Signaling in Fibroblasts'), as well as both the 'Autophagy' and 'Senescence Pathway' processes. Unique to the 100 µg/mL exposure group were 50 further pathways implicated in DNA damage responses (ex. 'ATM Signaling', 'Nucleotide Excision Repair Pathway', 'Cell Cycle: G2/M DNA Damage Checkpoint Regulation), cell cycle control, (ex. 'Cyclins and Cell Cycle Regulation', 'Mitotic Roles of Polo-Like Kinase', 'Cell Cycle: G1/S Checkpoint Regulation'), vesicular trafficking ('Caveolar-mediated Endocytosis Signaling', 'Virus Entry via Endocytic Pathways'), as well as the 'p53 Signaling' pathway, and additional metabolic and signaling responses. When examining TiO_2 MPs at 24 h, it can be seen that 6 and 27 pathways were enriched at 50 and 100 µg/mL. All pathways enriched at 50 µg/mL were commonly enriched at 100 µg/mL,

which includes the ‘CLEAR Signaling Pathway’ and 5 pathways related to general immune functions (ex. ‘Granulocyte Adhesion and Diapedesis’). Unique to the 100 µg/mL concentration of TiO2 MPs were 21 pathways related to immune functions (ex ‘Acute Phase Response Signaling’, ‘IL- 17 Signaling), vesicular trafficking (‘Autophagy’, ‘Phagosome Maturation’), cellular stress (ex. ‘NRF2-mediated Oxidative Stress Response’, ‘HIF1α Signaling’), metal ion homeostasis (‘Iron homeostasis signaling pathway’, ‘Inhibition of Matrix Metalloproteases’), and metabolic and signaling responses.

By the final timepoint of 48 h, both TiO_2 NPs and MPs featured concentration dependent pathway enrichment. With respect to TiO_2 NPs at this timepoint, 101, 162, and 262 pathways were significantly enriched at 25, 50, and 100 µg/mL concentrations respectively. Of these pathways, 84 pathways were commonly enriched across all concentrations, including multiple pathways implicated in aberrant wound healing and transformation (ex. ‘Pulmonary Fibrosis Idiopathic Signaling Pathway’, ‘Regulation of the Epithelial-Mesenchymal Transition Pathway’), immune signaling and disease (ex. ‘Acute Phase Response Signaling’, ‘Osteoarthritis Pathway’), vesicular trafficking (‘Caveolar-mediated Endocytosis Signaling’, ‘Clathrin-mediated Endocytosis Signaling’), multiple signaling pathways, and the ‘HIF1a Signaling’ pathway. For the top two TiO_2 NP concentrations of 50 and 100 µg/mL, another 56 pathways were commonly enriched relating to cellular stress (ex. ‘NRF2-mediated Oxidative Stress Response’, ‘BAG2 Signaling Pathway’, ‘GADD45 Signaling’), particle uptake and vesicular trafficking (‘Virus Entry via Endocytic Pathways’, ‘CLEAR Signaling Pathway’), immune type responses (ex. ‘IL- 15 Production’, IL-8 Signaling’, ‘IL-17 Signaling’), in addition to multiple metabolic, signaling and cancer related pathways. Unique to the 100 µg/mL concentration of TiO_2 NPs were 119 pathways, mainly implicated in cellular stress (ex. ‘Apoptosis Signaling’, ‘Unfolded protein response’, ‘Autophagy’), immune responses (ex. ‘IL-1 Signaling’, ‘Chemokine Signaling’, ‘LPS Stimulated MAPK Signaling’), and general signaling and metabolism. Finally, with respect to TiO_2 MPs at this timepoint, 14 and 40 pathways were noted for 50 and 100 µg/mL concentrations respectively. The two concentrations feature 11 common pathways almost all of which relate to immune signaling (ex. ‘Acute Phase Response Signaling’,

'Atherosclerosis Signaling', 'Agranulocyte Adhesion and Diapedesis'). Unique to the 100 µg/mL TiO_2 MP exposure group were 29 enriched pathways, including numerous additional immune signaling and disease pathways (ex. 'Osteoarthritis Pathway', 'Complement System', 'IL-13 Signaling Pathway'), cancer and aberrant wound healing responses (ex. 'Colorectal Cancer Metastasis Signaling', 'Pulmonary Fibrosis Idiopathic Signaling Pathway', 'Molecular Mechanisms of Cancer'), as well as two pathways implicated in metal ion homeostasis ('Iron homeostasis signaling pathway', 'Inhibition of Matrix Metalloproteases').

Appendix III 'HIF1α Signaling' IPA Canonical Pathway

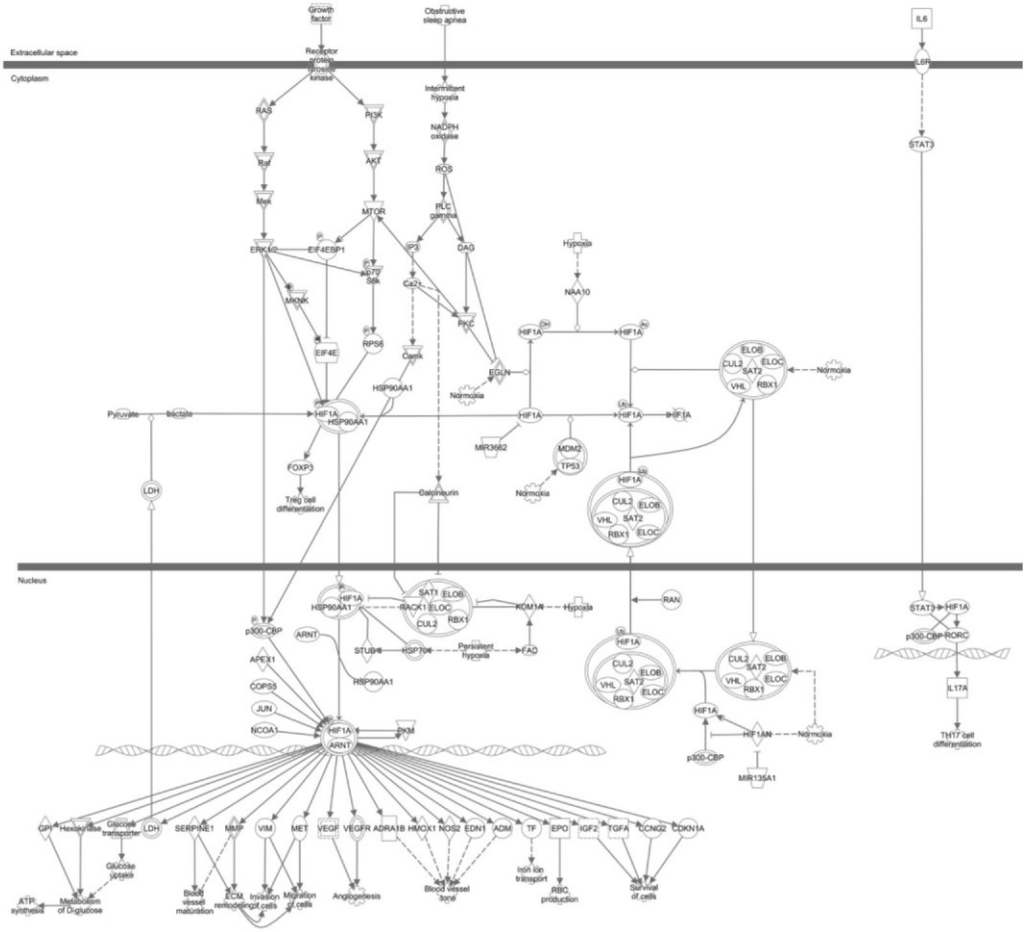

Appendix Figure 3-1. Schematic of the 'HIF1α Signaling' IPA canonical pathway. Corresponds to IPA content version 81348237.

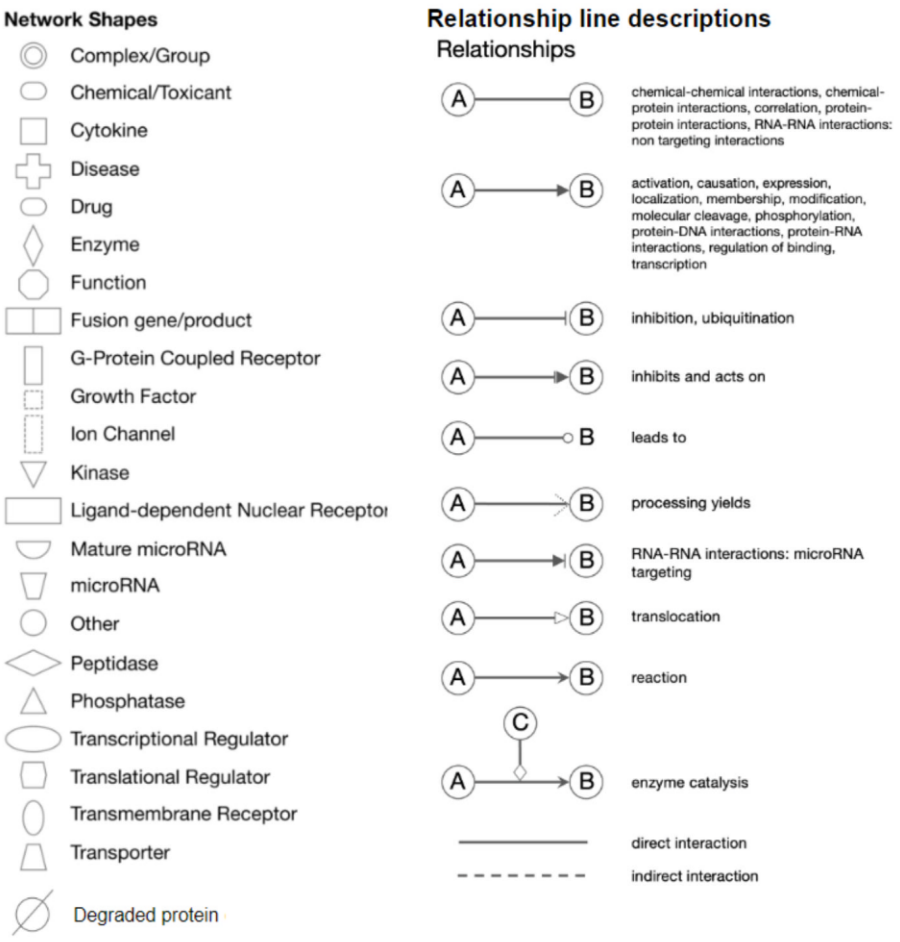

Appendix Figure 3-2. Legend for IPA canonical pathway schematics.

Appendix IV Supplementary Materials (Chapters 4-5)

Supplementary materials for Chapter 6 and Chapter 7 are presented in full, as the data is currently unpublished.

Supplementary Table 7-1. Filtered and Winsorized benchmark concentration (BMC) matrix at a benchmark response (BMR) of 5% extra risk. All concentrations are in μM of the constituent metal. NP: nanoparticle. MP: microparticle. tPOD: transcriptional point of departure. Red: value replaced with upper 95th percentile. Green: value replaced with lower 5th percentile.

Compounds	24 h Viability BMC	48 h Viability BMC	24 h Hif1α (Median)	48 h Hif1α (Median)	MN BMC	2 h Comet BMC	4 h Comet BMC
$ZnCl_2$	32.11	28.42	33.91	36.11	4.74E-05	88.70	29.35
ZnO NP	9.87	8.60	23.05	21.82	3.61E-05	106.76	31.14
ZnO MP	16.45	11.28	20.21	20.87	0.02	135.50	52.38
CuO NP	48.54	24.63	126.39	44.69	0.11	9.79	3.91
CuO MP	515.78	505.38	505.58	397.91	7.48	124.36	217.48
$MnSO_4$	9.37	9.37	16.41	30.92	60.26	135.50	217.48
MnO_2 NP	515.78	58.76	222.58	355.27	3.61E-05	26.13	16.00
MnO_2 MP	463.79	463.79	239.94	222.40	4.63	86.47	48.07
$NiCl_2$	59.07	30.19	58.97	75.44	15.34	135.50	217.48
NiO NP	57.90	13.43	159.77	227.84	0.02	20.82	6.32
NiO MP	117.57	117.57	141.26	163.02	0.02	6.98	4.45
$AlCl_3$	224.54	26.85	505.58	129.94	0.00	135.50	217.48
Al_2O_3 NP	91.35	91.35	505.58	206.91	25.48	7.97	176.38
Al_2O_3 MP	4.47	4.77	505.58	397.91	60.26	135.50	217.48
Fe_2O_3 NP	327.63	327.63	505.58	243.24	60.26	34.45	34.45
Fe_2O_3 MP	5.95	5.95	505.58	382.21	2.27	19.88	19.88
TiO_2 NP	140.36	66.21	502.19	165.55	60.26	10.86	10.86
TiO_2 MP	515.78	505.38	505.58	397.91	60.26	5.04	40.74

Supplementary Table 7-2. Filtered and Winsorized benchmark concentration (BMC) matrix at a benchmark response (BMR) of 10% extra risk. All concentrations are in μM of the constituent metal. NP: nanoparticle. MP: microparticle. tPOD: transcriptional point of departure. Red: value replaced with upper 95th percentile. Green: value replaced with lower 5th percentile.

Compounds	24 h Viability BMC	48 h Viability BMC	24 h Hif1α (Median)	48 h Hif1α (Median)	MN BMC	2 h Comet BMC	4 h Comet BMC
$ZnCl_2$	37.08	32.82	37.35	38.24	2.72E-03	195.38	65.71
ZnO NP	16.12	14.09	27.24	26.72	3.15E-03	140.08	40.86
ZnO MP	34.65	29.76	23.93	25.46	0.18	196.61	65.96
CuO NP	62.71	31.82	158.61	55.14	0.30	19.39	7.00
CuO MP	765.77	752.67	632.38	500.17	10.70	203.92	513.92
$MnSO_4$	18.17	18.17	19.93	38.01	101.98	203.92	711.92
MnO_2 NP	765.77	165.06	312.76	431.26	2.72E-03	23.11	14.47
MnO_2 MP	700.28	700.28	296.70	277.32	8.40	157.93	87.78
$NiCl_2$	84.98	43.46	78.71	104.74	31.27	203.92	711.92
NiO NP	119.61	27.74	214.06	277.40	0.14	25.54	7.66
NiO MP	222.24	222.24	201.89	205.98	0.18	17.71	11.30
$AlCl_3$	427.04	143.27	632.38	171.42	0.03	203.92	711.92
Al_2O_3 NP	275.01	275.01	632.38	283.52	43.39	48.76	711.92
Al_2O_3 MP	15.61	14.09	632.38	500.17	101.98	203.92	711.92
Fe_2O_3 NP	500.47	500.47	632.38	328.69	101.98	146.03	146.03
Fe_2O_3 MP	47.38	47.38	632.38	476.99	7.37	57.62	57.62
TiO_2 NP	238.77	112.64	627.09	259.15	101.98	83.75	83.75
TiO_2 MP	765.77	752.67	632.38	500.17	101.98	16.03	367.49

Supplementary Table 7-3. Filtered and Winsorized benchmark concentration (BMC) matrix at a benchmark response (BMR) of 25% extra risk. All concentrations are in μM of the constituent metal. NP: nanoparticle. MP: microparticle. tPOD: transcriptional point of departure. Red: value replaced with upper 95th percentile. Green: value replaced with lower 5th percentile.

Compounds	24 h Viability BMC	48 h Viability BMC	24 h Hif1α (Median)	48 h Hif1α (Median)	MN BMC	2 h Comet BMC	4 h Comet BMC
$ZnCl_2$	45.36	40.15	43.04	44.58	0.11	286.87	96.48
ZnO NP	32.00	27.86	33.66	34.69	0.16	200.05	58.34
ZnO MP	31.09	25.86	29.38	32.94	3.22	266.16	89.30
CuO NP	94.90	48.16	207.45	69.75	1.26	47.14	14.07
CuO MP	1803.59	1437.79	860.06	671.95	17.29	487.15	1151.17
$MnSO_4$	45.89	45.89	25.47	48.51	201.35	989.27	7701.83
MnO_2 NP	1803.59	698.78	485.09	532.66	0.11	114.92	70.36
MnO_2 MP	1245.73	1245.73	390.78	368.44	29.44	376.37	209.23
$NiCl_2$	153.18	78.30	114.65	148.94	63.19	989.27	7701.83
NiO NP	360.14	83.52	309.97	355.29	1.76	40.10	11.83
NiO MP	541.15	541.15	320.05	278.55	2.41	37.97	21.70
$AlCl_3$	1803.59	497.04	860.06	244.84	0.61	989.27	7701.83
Al_2O_3 NP	1283.44	1283.44	860.06	425.76	89.21	488.23	7701.83
Al_2O_3 MP	1803.59	1437.79	860.06	671.95	201.35	989.27	7701.83
Fe_2O_3 NP	993.80	993.80	854.49	484.77	201.35	916.65	916.65
Fe_2O_3 MP	1361.39	1361.39	860.06	634.81	40.45	289.81	289.81
TiO_2 NP	720.96	340.07	860.06	466.20	201.35	989.27	1124.13
TiO_2 MP	1666.98	1437.79	860.06	671.95	201.35	211.53	6029.18

Supplementary Table 7-4. Filtered and Winsorized benchmark concentration (BMC) matrix at a benchmark response (BMR) of 50% extra risk. All concentrations are in μM of the constituent metal. NP: nanoparticle. MP: microparticle. tPOD: transcriptional point of departure. Red: value replaced with upper 95th percentile. Green: value replaced with lower 5th percentile.

Compounds	24 h Viability BMC	48 h Viability BMC	24 h Hif1α (Median)	48 h Hif1α (Median)	MN BMC	2 h Comet BMC	4 h Comet BMC
$ZnCl_2$	54.13	47.92	48.07	49.28	0.98	385.25	129.57
ZnO NP	58.53	50.96	40.12	42.68	1.36	261.12	76.17
ZnO MP	50.03	42.87	34.91	40.45	24.49	334.23	112.10
CuO NP	147.09	74.66	275.48	88.61	3.95	90.89	27.12
CuO MP	22772.68	16504.43	1113.42	857.74	25.36	932.30	2202.53
$MnSO_4$	103.54	103.54	32.40	58.07	311.43	4614.49	47051.25
MnO_2 NP	22772.68	2483.41	692.34	653.68	0.64	232.35	142.17
MnO_2 MP	2065.87	2065.87	491.25	497.28	70.89	757.22	421.00
$NiCl_2$	285.62	145.99	159.36	177.13	111.24	4614.49	47051.25
NiO NP	1057.40	245.27	419.36	436.57	10.63	73.01	25.38
NiO MP	1182.71	1182.71	461.78	357.47	15.24	69.34	39.88
$AlCl_3$	12173.30	2850.52	1113.42	328.93	6.64	4614.49	47051.25
Al_2O_3 NP	6171.05	6171.05	1113.42	595.43	161.10	2467.63	47051.25
Al_2O_3 MP	22772.68	16504.43	1113.42	857.74	311.43	4614.49	47051.25
Fe_2O_3 NP	2052.73	2052.73	1087.26	668.47	311.43	3336.47	3336.47
Fe_2O_3 MP	22772.68	16504.43	1113.42	803.97	159.18	832.36	832.36
TiO_2 NP	2712.04	5747.13	1113.42	743.88	311.43	4614.49	6987.95
TiO_2 MP	3019.60	3019.60	1113.42	857.74	311.43	1512.93	42970.77

Supplementary Table 7-5. Variance and loading analysis corresponding to PCA analysis of BMR5, 10, 25, and 50% matrices. PC: principle component. Numbers in bold indicate significant loading onto a PC.

		PC1 (BMR5)	PC2 (BMR5)	PC1 (BMR10)	PC2 (BMR10)	PC1 (BMR25)	PC2 (BMR25)	PC1 (BMR50)	PC2 (BMR50)
Variance	Standard Deviation	1.80	1.29	1.87	1.38	2.09	1.38	2.13	1.35
	Proportion of Variance	0.46	0.24	0.50	0.27	0.63	0.27	0.65	0.26
	Cumulative Proportion	0.46	0.70	0.50	0.77	0.63	0.90	0.65	0.91
Loadings	24 h Viability	**0.43**	-0.08	**0.46**	-0.16	**0.45**	-0.23	**0.42**	0.29
	48 h Viability	**0.44**	0.01	**0.46**	-0.03	**0.45**	-0.16	**0.44**	0.19
	24 h 'HIF1α Signaling' tPOD	**0.48**	0.12	**0.48**	-0.01	**0.43**	-0.25	**0.42**	0.30
	48 h 'HIF1α Signaling' tPOD	**0.47**	0.13	**0.48**	-0.01	**0.44**	-0.24	**0.43**	0.27
	Micronucleus	0.26	**0.44**	0.26	**0.46**	0.31	0.38	0.30	**-0.41**
	2 h Comet	-0.33	**0.48**	-0.17	**0.57**	0.20	**0.61**	0.29	**-0.55**
	4 h Comet	-0.06	**0.73**	0.12	**0.66**	0.28	**0.54**	0.31	**-0.51**

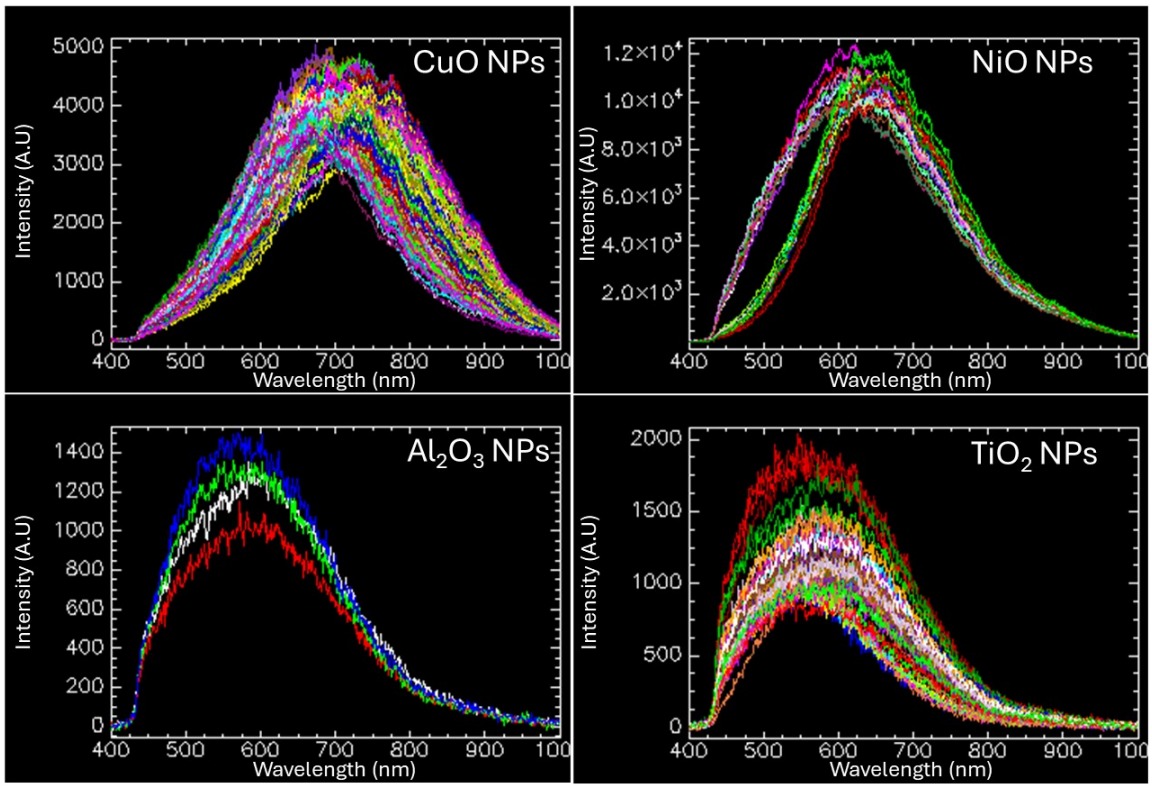

Supplementary Figure 6-1. Filtered hyperspectral libraries of CuO, NiO, Al_2O_3, and TiO_2 NPs used in this study. Each library has 132, 22, 4, and 52 final spectra. Intensity is in arbitrary units.

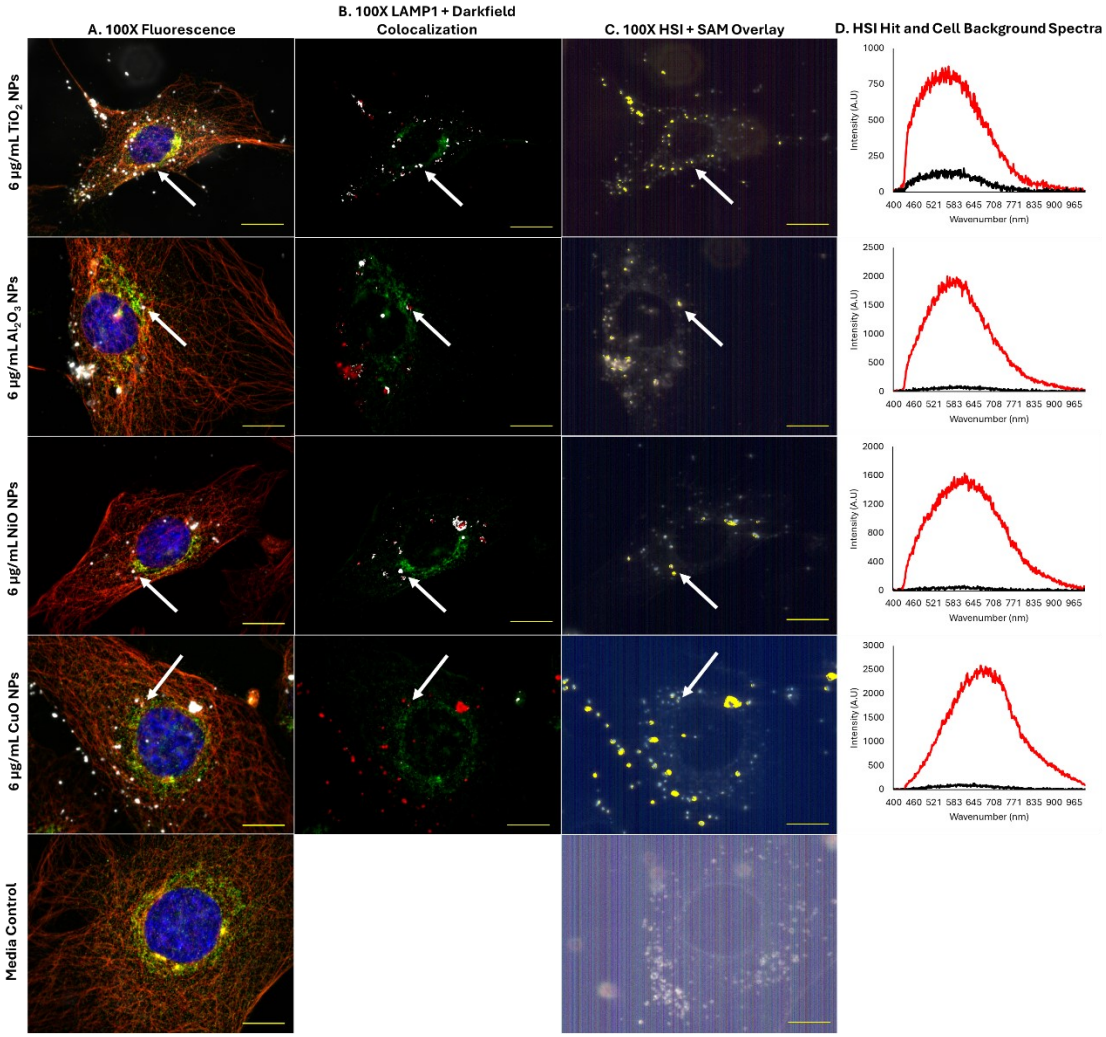

Supplementary Figure 6-2. 100X enhanced darkfield fluorescent imaging of FE1 cells after 24 h of exposure to 6 µg/mL CuO, NiO, Al_2O_3, or TiO_2 NPs. (A: 100X Fluorescence) Red: α-Tubulin; Green: Lysosomes (Lamp1); Blue: Nucleus (Hoechst 33342); White: particles. (B: 100x LAMP + Darkfield Colocalization) Red: intense darkfield scattering objects; Green: Lamp1; White: Areas of overlap between darkfield and LAMP channels. (C: 100x HSI + SAM overlay): Yellow: Areas with spectral match to the MONP of interest. (D: HSI Hit and Cell Background Spectra) Red: representative spectrum identified as a match through SAM mapping. Black: representative spectrum of cellular background. White arrows identify a co-localizing particle. Yellow scale bars = 10 µm in each image.

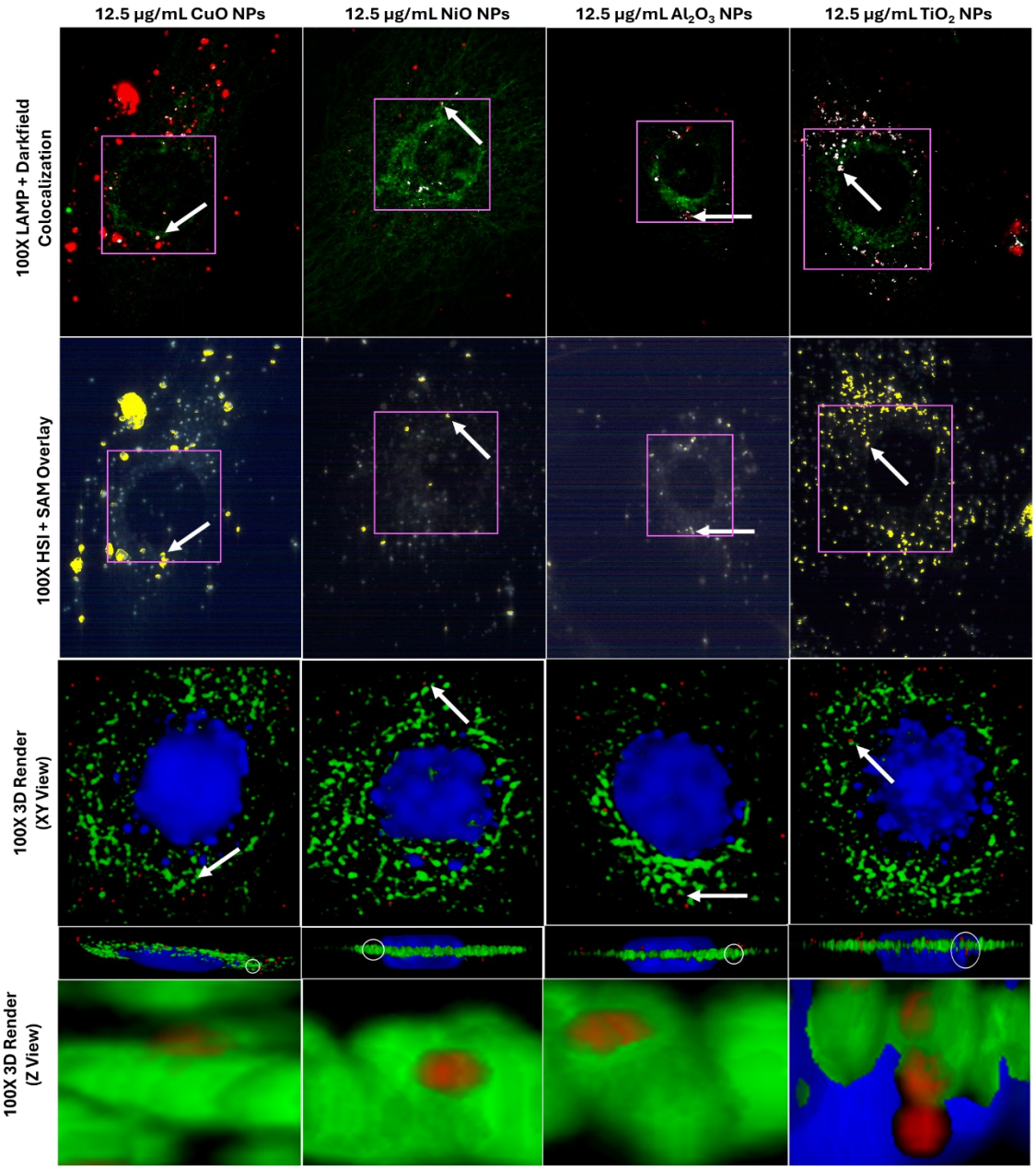

Supplementary Figure 6-3. 100X Co-localization of MONPs with Lamp1 signal. Pink boxes indicate areas which were deconvolved for 3D rendering. White arrow identify particles which show co-localization with Lamp1 signal and positive SAM identification as the material of interest. The white circles in the Z-view 3D images identifies the same particle highlighted in 2D, showing that it is in-plane with the Lamp signal and has overlap with the signal in 3 dimensions. (100x LAMP1 + Darkfield colocalization) Green: Lamp1 signal; Red: particle signal; white: areas of signal overlap determined through auto-thresholding. (100x HSI + SAM Overlay) Yellow: SAM identification of MONP. (100x 3D render (XY View)) Green: Lamp1 signal; Red: particles; Blue: Nucleus. (100x 3D Render (Z View)) Inset is an enlargement of the particle highlighted with a white circle.

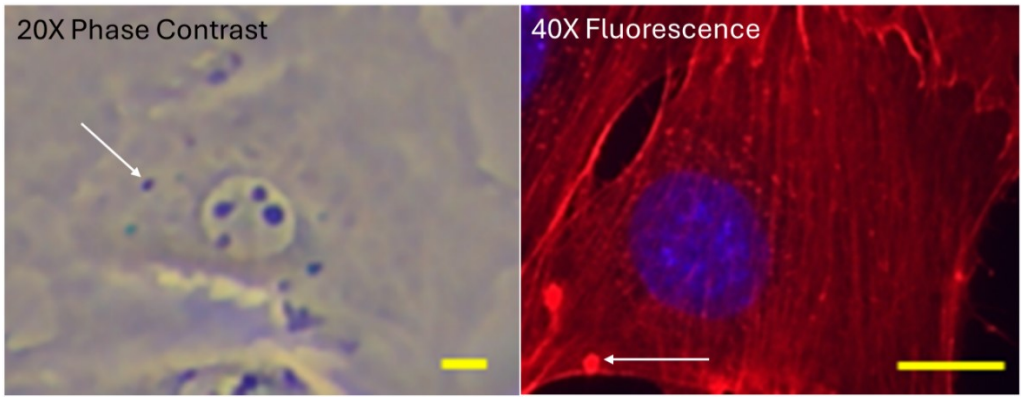

Supplementary Figure 6-4. Comparison between cytoplasmic inclusions visible in phase contrast imaging of FE1 cells, and bright actin aggregates found in media control FE1 cells. White arrows: cytoplasmic inclusions and actin aggregates. Scale bars: 10 µm.

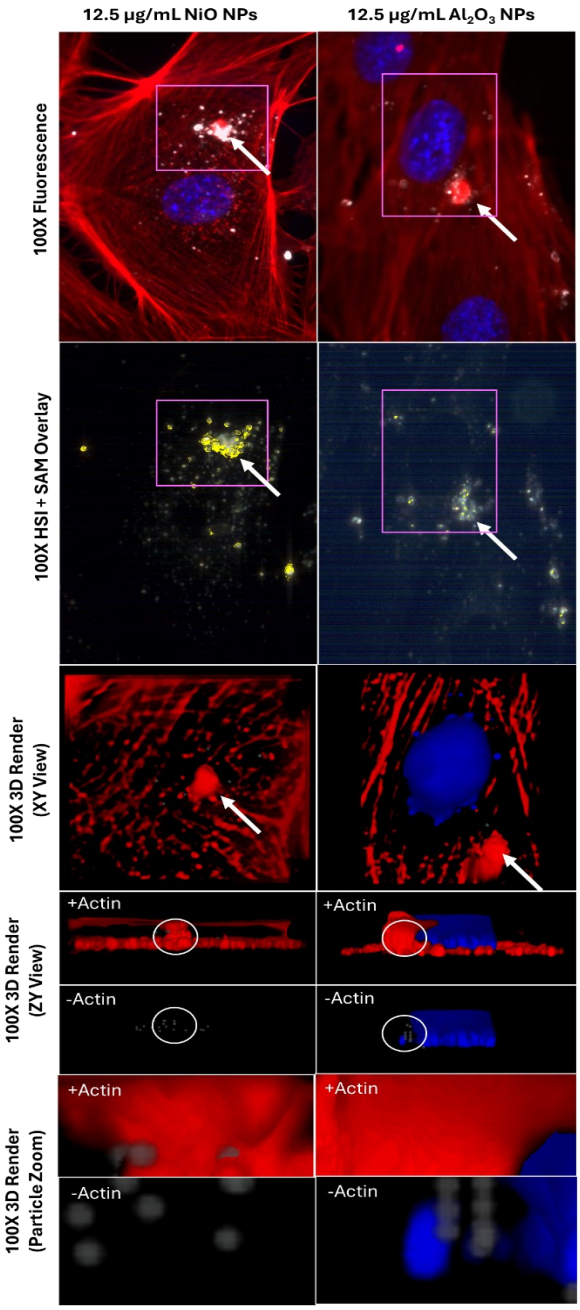

Supplementary Figure 6-5. 100X Co-localization of MONPs with actin aggregates. Pink boxes indicate areas which were deconvolved for 3D rendering. White arrow identifies particles which show co-localization with an actin aggregate and positive SAM identification as the material of interest. The white circles in the Z-view 3D images identifies the same particles highlighted in 2D, showing that they are embedded within the aggregate. (100c Fluorescence) Red: F-actin; blue: nucleus; white: strong scattering darkfield objects. (100x HSI + SAM Overlay) Yellow: SAM identification of MONP. (100x 3D render (XY View)) Red: actin signal; White: particles; Blue: Nucleus. (100x 3D Render (Z View)) Inset is an enlargement of the particles highlighted with a white circle.

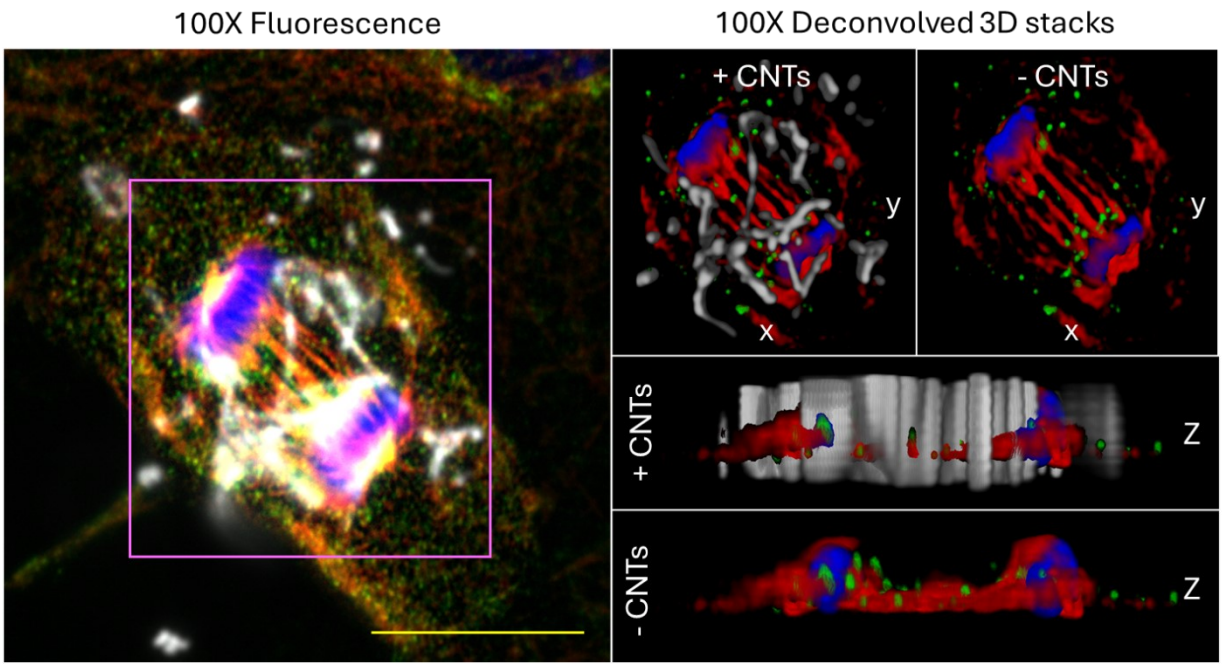

Supplementary Figure 6-6. FE1 cell undergoing mitosis following treatment with 100 µg/mL Mitsui-7 for 24 h. (100x Fluorescence) green: Lamp1. Red: α-tubulin. Blue: nucleus. White: Mitsui-7. Purple box: area deconvolved for 3D visualization. Yellow scale bar: 10 µm.

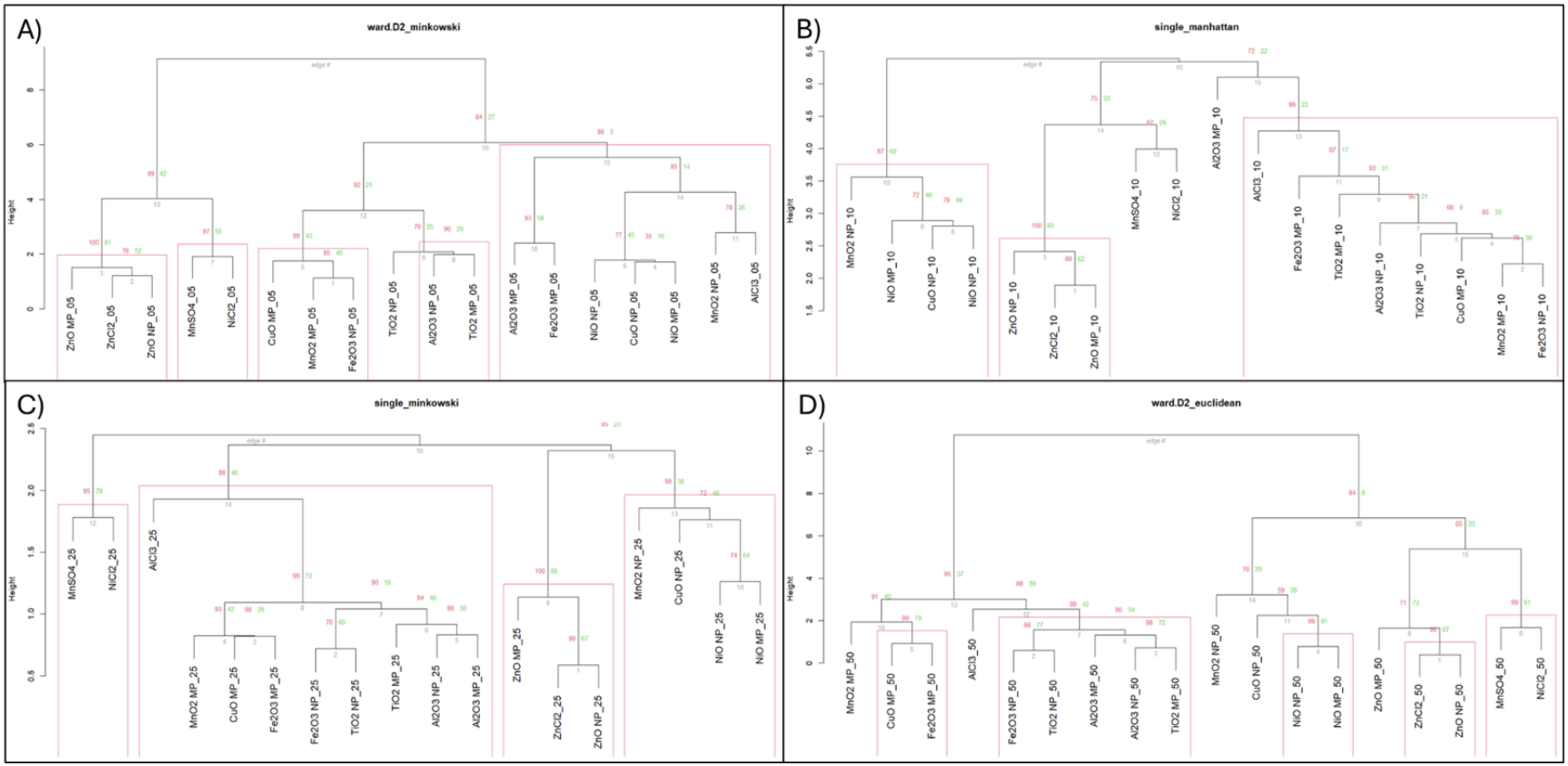

Supplementary Figure 7-1. The best clustering solution based on hierarchical clustering of A) BMR5, B) BMR10, C) BMR25, and D) BMR50 endpoint matrices. Red boxes: Statistically supported groupings based on 1000 bootstraps with an approximately unbiased p>0.95. Grey numbers: edge number. Green: Bootstrap probability. Red: approximately unbiased p value.

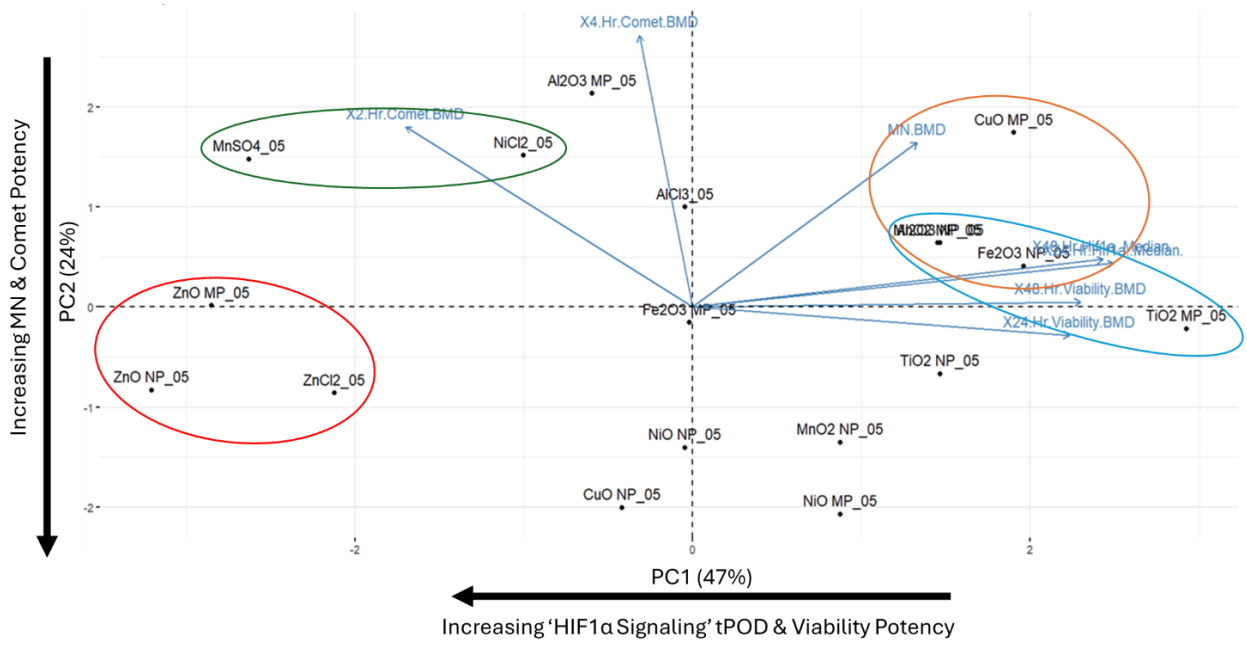

Supplementary Figure 7-2. Biplot showing principle component (PC1) and PC2 from (principle component analysis) (PCA) of filtered, log transformed, and scaled BMR05 BMC matrix. Vectors indicate the direction of loading for each endpoint. 24 h & 48 h viability, and 24 & 48 h 'HIF1α Signaling' tPOD endpoints load significantly and positively onto PC1. 2 & 4 h comet, and micronucleus (MN) endpoints load significantly and positively onto PC2. Numbers in parentheses indicate the amount of variance explained by each PC. Colored circles indicate compounds likely to cluster together based on 12 hierarchical clustering attempts.

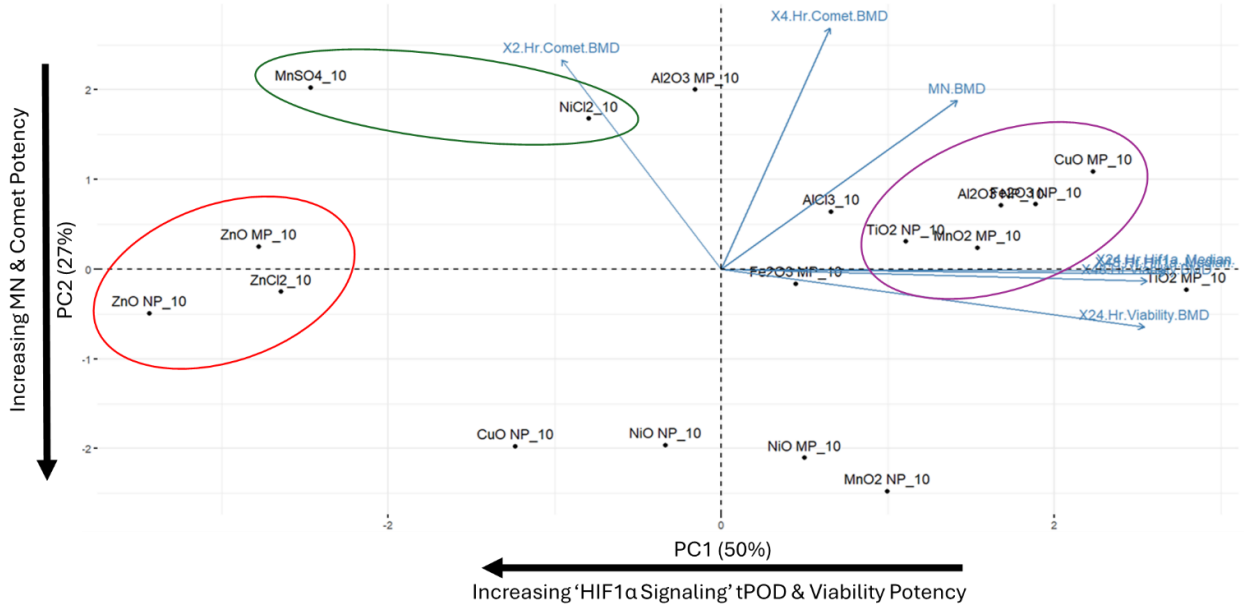

Supplementary Figure 7-3. Biplot showing principle component (PC1) and PC2 from (principle component analysis) (PCA) of filtered, log transformed, and scaled BMR10 BMC matrix. Vectors indicate the direction of loading for each endpoint. 24 h & 48 h viability, and 24 & 48 h 'HIF1α Signaling' endpoints load significantly and positively onto PC1. 2 & 4 h comet, and MN endpoints load significantly and positively onto PC2. Numbers in parentheses indicate the amount of variance explained by each PC. Colored circles indicate compounds likely to cluster together based on 12 hierarchical clustering attempts.

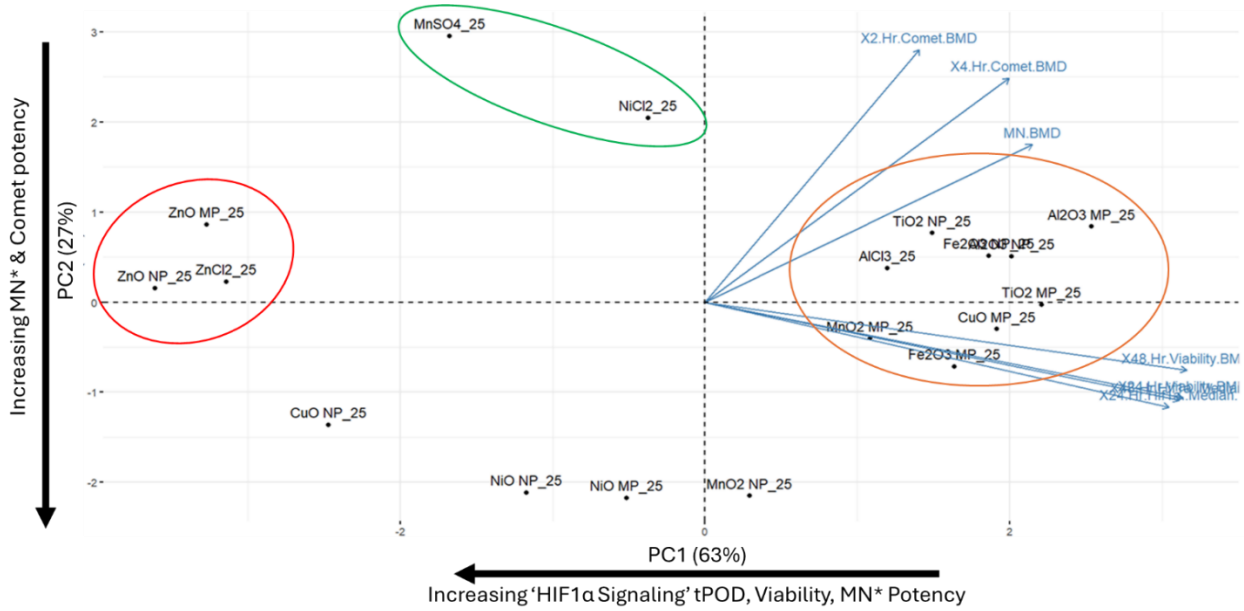

Supplementary Figure 7-4. Biplot showing principle component (PC1) and PC2 from (principle component analysis) (PCA) of filtered, log transformed, and scaled BMR25 BMC matrix. Vectors indicate the direction of loading for each endpoint. 24 h & 48 h viability, and 24 & 48 h 'HIF1α Signaling' endpoints load significantly and positively onto PC1. 2 & 4 h comet endpoints load significantly and positively onto PC2. The micronucleus (MN*) endpoint loads in the same direction as all endpoints and both PCs, but less than the 0.4 cutoff. Numbers in parentheses indicate the amount of variance explained by each PC. Colored circles indicate compounds likely to cluster together based on 12 hierarchical clustering attempts.